Long-term behaviour of twin tunnels in London Clay

by

Richard Laver

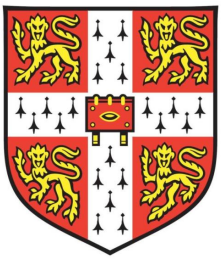

This dissertation is submitted
for the degree of Doctor of Philosophy

September 2010

Department of Engineering

Corpus Christi College, University of Cambridge

“Come to me, all who labour and are heavy laden,

and I will give you rest.

”

Matthew 11:28

I hereby declare that, except where specific reference is made to the works of others, the contents of this dissertation are original and have never been submitted, in part of as a whole, to any other university for any degree, diploma or other qualifications.

This dissertation is the result of my own work and includes nothing which is the outcome of work done in collaboration.

This dissertation contains no more than 65,000 words and 150 figures.

Richard Laver
September 2010

Acknowledgements

I must first thank my supervisor, Prof Kenichi Soga. His insightful vision and experience has fed me with fresh inspirations and priceless advice. Taking a personal interest in his students, he has been unceasingly warm, caring and generous in countless practical ways. My gratitude also goes out to my advisor, Prof Robert Mair, who has always been an inspiring role model in geotechnical engineering.

Big thanks should go to Mr Peter Wright of Tubelines, who has collaborated with us through thick and thin, and kindly donated the unique grout samples. I am also indebted to Dr Jarungit Wongsaroj; with great patience he has answered query after query about ABAQUS. Particular thanks go to Dr Matthew Coop for kindly giving us the London Clay samples from Imperial College, and Dr David Hight for his advice.

There are many others whom I would like to thank for their great help. Dr Kaushal Joshi dedicated incredible amounts of time to help in the laboratory. Mr Chris Knight has always been a fantastically resourceful technician. The CT scans would have been impossible without Mr Alan Heaver. Dr Mark Mann made a remarkable sacrifice to help with SEM. Dr Apollonia Gasparre kindly released her raw thesis data. The department librarians, Dr Martin Liska, Mr Simon Griggs, Dr Satoshi Nishimura, Mr Tim Ablett, Mr Richard Adams and the other Schofield Centre technicians have also assisted much. I am especially touched by the comradeship and faithfulness of friends in the Geotechnical Group, particularly when I have been working from home.

I must say a huge thank you to my dear wife, Shirley, for the uncountable sacrifices she has made for me to finish this thesis. She has also offered endless encouragement, prayers and hugs, and has freed me time to work by caring for our lovely little daughter Hannah, who has spurred me on to finish as soon as possible! Thanks must also go to my mother for dedicating so much to raise me.

The biggest thanks must go to our loving Lord God, who has given me the most wonderful gift of life through Jesus Christ. He has kept my work in perspective, and has helped me to work with integrity. He has renewed my strength every day, and has kept me joyful and hopeful throughout all. May His Name be praised!

Abstract

The assessment of ageing tunnels requires a deeper understanding of the long-term behaviour of twin tunnels, whilst lack of permeability data limits the accuracy of long-term predictions. This thesis therefore investigates long-term twin-tunnel behaviour through finite-element parametric analyses, and provides additional permeability data through laboratory studies.

Permeability tests are performed on fissured London Clay, exploring the effect of isotropic stress cycles on the permeability of fissures. A model explaining the permeability–stress relationship is proposed to explain irrecoverable changes observed in fissure permeability, and is formulated mathematically for numerical implementation.

Laboratory investigations are performed on grout from the London Underground tunnels, investigating permeability, porosity, microstructure and composition. A deterioration process is proposed to explain observations, consisting of acid attack and leaching. The deterioration had appeared to transform the grout from impermeable to permeable relative to the soil. The change in grout permeability with time would strongly influence long-term movements.

The long-term behaviour of single tunnels is investigated in a finite-element parametric study. A new method is formulated to predict long-term horizontal and vertical surface displacements after excavation of a single tunnel, and incorporates an improved measure of relative soil-lining permeability. The study also predicts significant surface movements during the consolidation period, contradicting the lack of further building damage observed in the field.

A further parametric study also investigates the long-term behaviour of twin tunnels. Key interaction mechanisms are identified, leading to the postulation of the long-term interaction behaviour under different tunnelling conditions. Long-term interaction is found to be complex and significant, and should be accounted for in numerical simulations.

List of Figures

List of Tables

Contents

Nomenclature

Roman Symbols

A_{cs}	Cross-sectional area
A_{f}, A_{s}	Coefficients in permeability–stress relationship: for fissure and soil
a_{hd}	Offset of maximum horizontal displacement from tunnel centreline
A_{RS}	Coefficient in relative settlement equation, see equation (8.19)
A_{T}	Cross-sectional area of tunnel
A_{tw}	Multiple of i defining extent of full trough width
B	Pore pressure coefficient for saturation
b	Intermediate principal stress ratio $(\sigma_2 - \sigma_3)/(\sigma_1 - \sigma_3)$
b_{f}, b_{s}	Coefficients in permeability–stress relationship: for fissure and soil
b_{mg}	Parameter for modified Gaussian curve
B_{RS}	Coefficient in relative settlement equation, see equation (8.19)
C	Cover of soil above tunnel crown
C_{b}	Soil parameter controlling initial gradient of isotropic swelling line at load reversal

$C_{\mathrm{b\ max}}$	Maximum value of C_{b}
C_{c}	Compression index
CC	Separation between tunnel centrelines
C_{clay}	Cover of clay above tunnel crown
$\mathbf{C}^{\mathrm{e}}$	Elastic compliance matrix
C_{el}	Characteristic element length
C_{k}	Hydraulic change conductivity index
c_{v}	Coefficient of consolidation
d'	Separation between tunnel centrelines
D	Soil parameter controlling non-linearity during isotropic loading and unloading, or pore diameter
d	Drainage distance, or spacing between atomic planes
$\mathbf{D}^{\mathrm{e}}$, $\mathbf{D}^{\mathrm{e}}_{\mathrm{m}}$	Elastic stiffness matrix in material axis coordinates
$\mathbf{D}^{\mathrm{ep}}$	Elastoplastic stiffness matrix
$\mathbf{D}^{\mathrm{e\ red}}_{\mathrm{m}}$, $\mathbf{D}^{\mathrm{e\ red}}_{\mathrm{f}}$	Softened elastic stiffness matrix: in material axis and in principal stress axis coordinates
$\mathbf{D}^{\mathrm{e}}_{\mathrm{f}}$	Elastic stiffness matrix in coordinate system orthogonal with the fissure plane
d_{fiss}	Width of localised shear region around fissure
DS	Dimensionless surface settlement with respect to extremes of permeability behaviour, see equation (2.2)
D_{T}	Tunnel diameter
E'_{d}	Representative drained soil modulus for consolidating zone

E_{1D}	Modulus for one-dimensional compression
E	Young's modulus—drained in the case of soil
e	Void ratio
E_S, E_T	Young's moduli: for soil and lining
$E_{u\,sec}$, $E_{u\,tan}$	Undrained moduli: secant and tangent
f	Sub-load surface function
$f_{fiss\,min}$	Measure of minimum fissure stiffness
G, G_{hh}, G_{hv}	Shear moduli: isotropic, and in horizontal and vertical planes
G_s	Specific gravity
H	Horizontal displacement
h	Height
$\bar{h}$	Hydraulic head
H_{cmax}	Maximum consolidation horizontal surface displacement in a transverse distribution
I'_0	I' at intersection of yield surface with hydrostatic axis
I'	Hydrostatic stress invariant $3p'$
I	Second moment of area
i	Distance from centreline to inflexion point of transverse surface settlement trough, or hydraulic gradient
I_{eff}	Second moment of area of equivalent uniform concrete lining of same bending stiffness
I_{seg}	Second moment of area of individual segment

$\bar{J}_2$	Deviatoric stress invariant stated relative to rotated yield surface axis
J, J_2	Deviatoric stress invariants: $J_2 = J^2$
J_β	Deviatoric invariant describing rotation of yield surface axis
K, K_0	Earth pressure coefficient, and in-situ value
k, k_S	Representative isotropic soil permeability; $\sqrt{k_\mathrm{v} k_\mathrm{h}}$ if anisotropic
k_h, k_v	Soil permeabilities: horizontally and vertically
K_L	Parameter for width of consolidation settlement trough i/z_0
K_T	Lining seepage coefficient $k_\mathrm{T}/\left(\gamma_\mathrm{w} t_\mathrm{T}\right)$
k_T	Lining permeability
L_c	Tunnel axis depth below water table
L_T	Lag distance between headings of two advancing tunnels
M	Gradient of critical state line in q–p' space, or bending moment in lining about tunnel axis
m	Soil parameter controlling plastic strain within the normal yield surface
M_J	Gradient of critical state line in J–p' space
M_mod	Modification factor devised by Hunt (2005)
M_θ	Stress ratio at failure
N	Lining compression force
NH_cmax	Non-dimensional maximum consolidation horizontal surface displacement
n_j	Number of longitudinal joints around lining ring

$\hat{\mathbf{n}}_{\mathrm{m}}$, $\hat{\mathbf{n}}_{\mathrm{p}}$	Unit normal vector to plane: in material axis and principal stress axis coordinates
NS_{cmax}	Non-dimensional maximum consolidation surface settlement
$\hat{\mathbf{n}}_{\alpha \mathrm{x}}$	Unit normal vector to softening fissure plane
p'_0	Preconsolidation pressure
p', p'_{i}, p'_{rev}	Mean effective stresses: current value, initial value, and at last stress reversal
P	Unsupported excavation length, or penetration pressure
p	Total mean stress
p_{a}	Atmospheric pressure
q	Deviatoric stress $\sigma_1 - \sigma_3$, or volumetric flow rate
q_{i}, q_{o}	Volumetric flow rates: at inlet and at outlet
q_{S}, q_{T}	Volumetric flow rates: through soil and through lining
R	Ratio between sizes of subload and normal yield surfaces
r	Soil parameter controlling non-linearity during isotropic loading and unloading, or radius
R_{eff}	Tunnel radius measured to neutral axis depth of equivalent uniform concrete lining with same bending stiffness
RP	Relative soil-lining permeability
RS_{cmax}	Relative settlement as proportion of steady-state settlement
R_{T}, R_{Ti}	Tunnel radius, and initial value
S	Settlement
$\mathbf{s}$	Deviatoric stress tensor

$\bar{\mathbf{s}}$	Deviatoric stress tensor stated relative to rotated yield surface axis
$S_{\mathrm{c}}^{\mathrm{int}}$, $S_{\mathrm{cmid}}^{\mathrm{int}}$	Additional $S_{\mathrm{cmax(ss)}}$ due to twin-tunnel interaction, and at midline between tunnels, see equation (9.1)
S_{cmax}	Maximum consolidation settlement in a transverse trough
$S_{\mathrm{cmax(ss)}}$	S_{cmax} at steady-state
S_{mod}	Settlement modified by Hunt (2005) to account for tunnel interaction, see equation (3.16)
S_{r}	Saturation ratio
t	Consolidation time
t_{eff}	Thickness of equivalent uniform concrete lining with same bending stiffness
$\mathbf{T}_{\mathrm{fm}}$, $\mathbf{T}_{\mathrm{mf}}$	Transformation tensors for 3-D fissure softening: from fissure plane to material axis coordinates and back
$\mathbf{T}_{\mathrm{pm}}$	Transformation tensor from principal stress axis to material axis coordinates for 2-D fissure softening
t_{T}	Lining thickness
T_{v}	Dimensionless time factor for consolidation
u_0, u_{ff}, u_{ss}	Pore pressures: initial, far-field and steady-state
u_1	Soil parameter controlling plastic strain within the normal yield surface
u	Pore pressure, or displacement
u_{i}, u_{o}	Pore pressures: at inlet and at outlet

u_{norm}	Normalised drop in pore pressure at axis depth midway between tunnels due to seepage, see equation (E.1)
u_{T}	Pore pressure at lining extrados
V_0	Initial specimen volume
$V2_{\mathrm{G}}$	Volume loss for second tunnel excavated in greenfield conditions
$V2_{\mathrm{int}}$	Additional volume loss for second tunnel due to interaction
$V2_{\mathrm{N}}$, $V2_{\mathrm{R}}$	Volume loss for second tunnel excavation: in near and remote limbs of settlement trough
V	Intruded volume
v	Filtration velocity
v_{h}, v_{v}	Vertical direction cosines of normals for planes bounding fissure inclination ranges: for sub-horizontal and sub-vertical ranges
V_{L}	Volume loss as percentage of tunnel cross-sectional area
V_{net}	Net volume of water inflow or outflow
V_{s}	Volume loss per unit length of tunnel
W	Pillar width (minimum separation between lining extradoses)
w	Moisture content
x	Transverse distance from tunnel centreline, or shorthand notation representing either horizontal (h) or vertical (v)
x_{N}	Neutral axis depth
y	Height
z_0	Tunnel axis depth below ground level

z	Depth below ground level or longitudinal distance ahead of tunnel face

Greek Symbols

α	Angle of major principal stress axis to vertical
α_{bs}	Bending stiffness ratio, see equation (D.1)
$\alpha_{\mathrm{d}\sigma}$	Angle of major principal stress increment to vertical, see equation (6.7)
α_{f}	Target value of α
α_{h}, α_{v}	Angles of planes bounding fissure inclination ranges to horizontal: for sub-horizontal and sub-vertical ranges
α_{p}	Angle of plane to horizontal
$\alpha_{\mathrm{ph\ max}}$, $\alpha_{\mathrm{pv\ max}}$	Angles of softening fissure plane to horizontal: for sub-horizontal and sub-vertical ranges
α_{range}	Angle defining bounds of fissure inclination ranges from orthogonal planes
$\boldsymbol{\beta}$	Yield surface rotation tensor
γ	Surface tension
γ_{w}	Bulk unit weight of water
δ_{ij}	Kronecker delta
ε_1, ε_2, ε_3	Major, intermediate and minor principal strains
ε, ε^{p}, ε_{a}	Total strain, plastic strain and axial strain
$\varepsilon^{\mathrm{c}}_{\mathrm{cmax(ss)}}$, $\varepsilon^{\mathrm{f}}_{\mathrm{cmax(ss)}}$	Peak consolidation horizontal strain at steady-state: at centreline and in far-field

$\boldsymbol{\varepsilon}_\mathrm{s}$, $\boldsymbol{\varepsilon}_{\mathrm{s\,rev}}$	Deviatoric strain tensor: current value and at last stress reversal
ε_v, $\varepsilon_{\mathrm{v\,rev}}$	Volumetric strain: current value and at last stress reversal
$\zeta_{\mathrm{fiss\,min}}$	Minimum stiffness reduction factor for a single fissure
ζ_ph, ζ_pv	Stiffness reduction factor for fissure inclination ranges: for sub-horizontal and sub-vertical ranges
$\zeta_{\mathrm{p\,min}}$	Minimum stiffness reduction factor for an element
$\boldsymbol{\eta}$, $\boldsymbol{\eta}_\mathrm{rev}$	Stress ratio tensor $\mathbf{s}/p'$: current value and at last stress reversal
θ	Lode's angle, or diffraction angle
κ	Gradient of swelling line on e–$\ln p'$ plot
λ	Plastic multiplier
μ	Parameter for width of consolidation settlement trough, see equation (3.10)
ν	Poisson's ratio
ξ, ξ_s	Dimensionless distances in stress space: along the hydrostatic axis and in the deviatoric plane
ρ, ρ_b, ρ_d	Density, bulk density and dry density
ρ_c	Gradient of normal compression line in $\log e$–$\log p'$ space
ρ_r	Swelling gradient in $\log e$–$\log p'$ space
σ', σ'_p	Effective stress, and value normal to plane
p'_max	Maximum effective stress experienced normal to fissure plane since misalignment
$\boldsymbol{\sigma}^0$	Tensor defining apex of yield surface

σ_1, σ_2, σ_3	Major, intermediate and minor principal stresses
σ	Total stress
τ, τ_{p}	Shear stress, and value tangential to plane
ϕ'_{crit}, ϕ'_{peak}	Mobilised friction angles: at critical state and the peak value
$\phi'_{\mathrm{bnd\,h}}$, $\phi'_{\mathrm{bnd\,v}}$	Mobilised friction angle on planes defining bounds of the fissure inclination range for 2-D fissure softening
ϕ'_{mob}	Maximum friction angle mobilised on any plane
ϕ'_{p}	Mobilised friction angle on particular plane
$\phi'_{\mathrm{ph\,max}}$, $\phi'_{\mathrm{pv\,max}}$	Maximum friction angle on plane within fissure inclination ranges: for sub-horizontal and sub-vertical ranges
ϕ'_{range}	Range of mobilised friction angle over which stiffness reduces from maximum to minimum during fissure softening
ϕ'_{soft}	Mobilised friction angle at which fissure planes begin softening
χ	Scalar strain amplitude product defining stress reversal
ω_{s}	Soil parameter controlling non-linearity of swelling line

Abbreviations

ASTM	American Society for Testing and Materials
BGL	Below Ground Level
BS	British Standard
CD	Consolidated Drained
CT	Computed Tomography
CU	Consolidated Undrained
DC	Drained Compression

DE	Drained Extension
EB	Eastbound
EPBS	Earth Pressure Balance Shield
FE	Finite Element
GCG	Geotechnical Consulting Group
HCA	Hollow Cylinder Apparatus
IC	Imperial College
ICDD	International Centre for Diffraction Data
JLE	Jubilee Line Extension
LC	London Clay
LG	Lambeth Group
MCC	Modified Cam Clay
MG	Made Ground
MIP	Mercury Intrusion Porosimetry
MRT	Mass Rapid Transit
NATM	New Austrian Tunnelling Method
RAM	Random Access Memory
SEM	Scanning Electron Microscopy
SGI	Spheroidal Graphite Iron
TG	Terrace Gravel
UC	Undrained Compression

UE	Undrained Extension
WB	Westbound
XRD	X-Ray Diffraction

Chapter 1

Introduction

1.1 Background to study

Rapid expansion in cities is increasing the pressure on infrastructure to transport more commuters faster and further than ever before. However, tight demands on space restrict new road construction, resulting in unsustainable congestion. Underground metro systems are proving to be a favoured solution for many cities across the world, providing fast, reliable, mass transport, with minimum surface disruption. Operation of tunnels is therefore indispensable.

Many cities however are now facing the problem of ageing tunnels—the oldest operational tunnel in London dates back to 1863. In many ageing metro systems worldwide, lining distortion and degradation is presenting a safety hazard. Yet preventing failure is difficult; little is known about how tunnels deteriorate, so uncertainty exists concerning how and when to remediate. Those responsible for tunnel upkeep are therefore urgently seeking a solution.

Many researchers have already responded to this need. For instance, there has been a continuous effort at the Cambridge Geotechnical Group to install wireless sensor networks to provide data for real-time condition assessment (Bennett *et al.*, 2010a,b; Stajano *et al.*, 2010). However, questions remain concerning the interpretation of this data: what is causing the degradation, and what can be done to mitigate it? Answering these questions requires an understanding of long-term tunnel behaviour.

Many authors have recognised that significant movements occur after tunnel construction in clays (e.g. Mair, 2008), both in terms of squatting linings and increased settlements; yet, much still remains to be investigated to predict movements accurately.

1.2 Objectives of research

The aim of this thesis is to contribute to the understanding of long-term tunnel behaviour in clay, in the hope of improving the accuracy of long-term prediction. This is done in two areas:

1. **Permeability data** Tunnels act as drains, causing consolidation—this makes long-term behaviour highly dependent upon soil and lining permeability. However, great uncertainty exists concerning field permeabilities, which limits the accuracy of long-term predictions. Laboratory investigations were performed to provide more permeability data for the soil and lining, comprising the following:

   (a) Determination of the permeability–stress relationship for fissured London Clay.

   (b) Determination of the permeability characteristics for London underground tunnel grout.

2. **Long-term behaviour of twin tunnels** A significant contribution was made by Wongsaroj (2005), who characterised the long-term behaviour in the form of normalised charts, derived from a parametric study. Only single-tunnel behaviour was investigated—however, many tunnels are constructed in pairs. No research has yet specifically addressed the influence of twin-tunnel interaction on the long-term behaviour. Numerical studies were conducted to contribute the first insights into long-term twin-tunnel interaction, consisting of the following:

   (a) Development of a soil model for London Clay to match recent laboratory test data obtained by Imperial College (Hight *et al.*, 2007).

(b) Validation of long-term twin-tunnel numerical analysis by simulating the construction of the Jubilee Line Extension beneath St James's Park, London.

(c) Parametric studies investigating factors influencing the long-term behaviour of single and twin tunnels.

1.3 Organisation of thesis

The thesis is organised into ten chapters, this introduction being the first.

Literature review The second and third chapters review the current research relevant to investigating long-term twin-tunnel behaviour. The review is divided into two:

Chapter 2 reviews the long-term behaviour of single tunnels in clay, addressing both causes and effects: the key factors influencing long-term changes are detailed, along with the observed characteristics of these changes.

Chapter 3 reviews the interaction between twin side-by-side tunnels. The effect of interaction is first described, before methods for predicting short-term movements are presented—first for a single tunnel, and then accounting for interaction. The chapter ends by highlighting factors of particular relevance to the long-term numerical modelling of twin tunnels.

Permeability investigations The fourth and fifth chapters present the permeability investigations, and highlight the range of soil and lining permeabilities to assume for the prediction method of Chapter 8:

Chapter 4 describes the laboratory permeability tests on fissured London Clay. A permeability-stress model for fissured clay is proposed, along with a simple mathematical formulation.

Chapter 5 describes a suite of tests to characterise the permeability properties of London underground grout. A deterioration process for the grout is hypothesised to explain observations.

Validation analyses The sixth and seventh chapters describe the validation analyses that lay the foundations for the parametric studies:

Chapter 6 presents the validation of the soil model with laboratory tests on London Clay. The basis of the soil model—formulated by Wongsaroj (2005)—and the recent data from Imperial College (Hight *et al.*, 2007) are first introduced. The performance of modifications to the soil model to fit the data are then evaluated, including the simulation of fissure softening.

Chapter 7 presents the validation of the numerical analysis by simulating tunnel construction at St James's Park. Here, the methodology behind the long-term numerical modelling of twin tunnels is described in detail. The performance of soil models validated in Chapter 6 is compared to select a suitable model for use in the parametric studies. Recommendations to improve the replication of field data are also made.

Parametric studies The eighth and ninth chapters present the parametric studies:

Chapter 8 builds upon the work of Wongsaroj (2005), presenting a further parametric study into long-term single-tunnel behaviour. A new index for relative soil-lining permeability is derived, and an improved method for predicting long-term movements is proposed and validated against two case histories. By studying net surface movements, the effect of long-term changes upon surface structures is also investigated.

Chapter 9 extends the parametric study of Chapter 8 to consider twin side-by-side tunnels. Key long-term interaction mechanisms are identified and related to the twin-tunnel geometry. The influence of long-term interaction on surface structures is also highlighted.

Conclusions

Chapter 10 concludes the thesis, summarising its major contributions. Recommendations having immediate impact upon current practice are also suggested, along with future directions for research.

Chapter 2

Review on the long-term behaviour of tunnels

Further ground movements and increases in lining load have been reported following tunnel construction in clays, continuing upwards of 20 years after construction (Barratt *et al.*, 1994). Field measurements of long-term settlements are relatively scarce because monitoring is often stopped soon after construction (Mair, 2008). Despite this, observations and studies of long-term behaviour have identified the following influential factors (Mair & Taylor, 1997):

- Magnitude and distribution of excess pore pressure generated during construction
- Compressibility and permeability of soil
- Pore pressure conditions, particularly relative soil-lining permeability
- Initial pore pressure distribution

This chapter summarises the current knowledge on the long-term behaviour of tunnels, dividing into two sections: the first reviews factors affecting the long-term behaviour, whilst the second section covers some commonly-observed characteristics of the long-term response.

2.1 Influences on long-term behaviour

2.1.1 Tunnel acting as a drain

The construction of a tunnel introduces a new drainage boundary condition, with zero pore pressure at the lining intrados. Depending upon the lining permeability, this then causes water to flow into the tunnel. Ward & Pender (1981) concluded that tunnels act as drains, after reviewing field observations (De Lory *et al.*, 1979; Eden & Bozozuk, 1969; Palmer & Belshaw, 1980). Both Nyren (1998) and Harris (2002) reported significant ingress of water into the Jubilee Line Extension (JLE) tunnels under St James's Park, confirming that the tunnels were acting as drains.

Indeed, Howland (1980) applied the concept of tunnel drainage to long-term settlement prediction. He assumed 1-D consolidation theory, with effective stress changes determined from a flow net. His predictions agreed well with two case histories, confirming that the tunnels acted as drains in both cases.

2.1.2 Influence of lining permeability

How much a tunnel acts as a drain is determined by the lining permeability. Drainage is greatest when the lining is permeable, which generates a substantial drawdown in pore pressure around the tunnel. However, pore pressure measurement around tunnels suggest that in reality, lining permeability varies across a range of values.

Pore pressure measurements

After monitoring for 11 years, O'Reilly *et al.* (1991) reported a pore pressure drawdown extending only a few metres away from a tunnel. Subsequent finite element (FE) analysis led to the conclusion that the tunnel was acting as a partial drain, achieved by a lining permeability intermediate between fully permeable and fully impermeable.

Low lining permeability is also suggested for the Heathrow Express trial tunnels, around which Bowers *et al.* (1996) noted pore pressures recovering to near-initial values three years after excavation.

More recent measurements around London underground tunnels are presented by Mair (2008), who presented horizontal pore pressure profiles at the axis level of five old tunnels in London Clay, all with bolted cast iron linings and backgrouting; these profiles are shown in Figure 2.1. For four of the tunnels, a marked pore pressure drawdown indicated that these tunnels were acting as drains. However, the fifth tunnel—beneath Kennington Park—showed little pore pressure reduction. Gourvenec *et al.* (2005) attributed this to the founding of the tunnel in the more permeable Unit A2 of London Clay. Here, in-situ measurements suggested a permeability higher than the surrounding layers, consistent with observations of sand partings: this rendered the lining impermeable relative to the soil.

Relative soil-lining permeability

The combined influence of soil and lining permeabilities noted by Gourvenec *et al.* (2005) suggests that relative soil-lining permeability is a key variable influencing long-term behaviour. Wongsaroj (2005) formulated a measure of relative soil-lining permeability (RP) as follows:

$$RP = \frac{k_{\mathrm{T}}}{k_{\mathrm{S}}} \cdot \frac{C_{\mathrm{clay}}}{t_{\mathrm{T}}} \tag{2.1}$$

where:

k_{T}	is the lining permeability
k_{S}	is the soil permeability ($k_{\mathrm{S}} = \sqrt{k_{\mathrm{v}} k_{\mathrm{h}}}$ if anisotropic)
C_{clay}	is the clay cover above the tunnel crown
t_{T}	is the lining thickness

Wongsaroj established bounds for RP corresponding to permeable and impermeable linings by noting the effect on surface settlement. To do this, he defined a dimensionless surface settlement (DS) given by:

$$DS = \frac{NS_{\mathrm{cmax(ss)}} - NS_{\mathrm{cmax(ssi)}}}{NS_{\mathrm{cmax(ssp)}} - NS_{\mathrm{cmax(ssi)}}} \tag{2.2}$$

where:

$NS_{\text{cmax(ss)}}$ is the maximum long-term settlement for a particular case
$NS_{\text{cmax(ssi)}}$ is $NS_{\text{cmax(ss)}}$ for a fully impermeable lining
$NS_{\text{cmax(ssp)}}$ is $NS_{\text{cmax(ss)}}$ for a fully permeable lining

In this way, $DS = 0$ for a fully impermeable lining, whilst $DS = 1$ for a fully permeable one. Wongsaroj conducted many long-term FE analyses trialling different cover-to-diameter ratios, volume losses and lining permeabilities. From these, he plotted DS against RP; Figure 2.2 shows that the results fall within a narrow band. Results from further parametric studies presented by Mair (2008) are superposed, also falling within the same band. The figure shows that an impermeable lining can be represented by $RP < 0.1$, where $DS = 0$, whilst a permeable lining can be represented by $RP > 100$, where $DS = 1$. These ranges provide a useful tool for engineers determining whether a lining-soil system is likely to act impermeably or permeably.

The relative permeability between the tunnel lining and the surrounding ground has large influences on the pore pressure reduction around a tunnel, and hence resulting movements (Harris, 2002). Flow into a permeable lining causes pore pressure drawdown, whereas pore pressures recover to their initial values for an impermeable lining (Mair, 2008). The consequences of these different pore pressure responses are outlined below.

Effect on surface settlement

As mentioned in Section 2.1.2, Wongsaroj used the marked difference in surface settlement to differentiate between a permeable and an impermeable lining, obtaining substantially less settlement with decreasing lining permeability—even heave in the case of fully impermeable linings. This heave is caused by swelling as negative excess pore pressures generated during excavation dissipate. Continuing settlement with a permeable lining is caused by consolidation of the surrounding clay (Shin *et al.*, 2002).

Similar authors conducting FE analyses have noted a similar trend. Investigating factors which influence twin-tunnel construction using plane-strain analyses, Addenbrooke (1996) observed that impermeable tunnels produce surface heave,

whilst permeable tunnels might incur further settlement. For permeable linings, Addenbrooke highlighted the additional complication of initial pore pressure profile: an initially hydrostatic profile resulted in increased settlement, whereas an underdrained profile produced heave.

Harris (2002) also noted similar findings from FE simulations of St James's Park, conducted by the Geotechnical Consulting Group (GCG, 1993). Shin *et al.* (2002) also obtained concurring results when investigating the influence of lining permeability in long-term FE analyses.

Effect on lining behaviour

Lining permeability also influences loads and displacements in the lining itself. Generally, permeable linings are observed to squat, whilst impermeable linings do not (Mair, 2008).

Shin *et al.* (2002) investigated lining loads and ground settlements for three different linings: one impermeable, one permeable and one with intermediate permeability. In addition to causing heave, impermeable linings experienced a gradual increase in lining load. Conversely, permeable linings caused increased surface settlement, but with no significant change in lining load. Only a lining with intermediate permeability reproduced the increases of both lining load and settlement observed in the field.

A similar trend is found by Wongsaroj (2005), with permeable linings squatting more and bearing less lining force in the long-term compared with impermeable linings.

Non-uniformity in lining permeability

Coupled numerical analyses usually assume a uniform permeability around the lining circumference. In reality however, the presence of leaks, joints and cracks will create seepage flow paths, making this assumption an oversimplification (Mair, 2008).

At St James's Park, Nyren (1998) reported persistent dampness inside the tunnel around key segments at knee level. Acting as wedges, these key segments

naturally have gaps around them; although infilled with concrete, these gaps might provide the seepage paths causing the observed dampness.

Simulating the long-term behaviour at St James's Park, Wongsaroj (2005) attempted to replicate the increased permeability at knee level by trialling a non-uniform lining permeability: impermeable above axis level, and permeable below. This distribution matched the field data significantly better, suggesting that modelling seepage points around the lining circumference is important in long-term simulations.

2.1.3 Influence of soil permeability

In addition to the relative soil-lining permeability, the intrinsic nature of soil permeability itself plays an important role in determining long-term behaviour (Wongsaroj, 2005). Authors have focused upon two features of soil permeability in particular: permeability anisotropy, and soil layering.

Permeability anisotropy

Permeability anisotropy was cited by Nyren (1998) as influencing ground movements. Reporting on long-term monitoring data from St James's Park, he attributed the widespread consolidation at tunnel axis level to permeability anisotropy. Harris (2002) also observed that along the Jubilee Line Extension (JLE), the majority of compression during consolidation occurred at tunnel depth. For the relief sewers at Grimsby, consolidation movements were concentrated around tunnel axis level or just below (Glossop & O'Reilly, 1982).

Dimmock (2003) cited permeability anisotropy as also causing the observed pore pressure response at St James's Park, noting markedly different behaviour between pore pressures at crown and axis levels. Pore pressures recovered to almost pre-construction values above the crown, whilst at axis level, pore pressures dropped towards the tunnel, indicating seepage. This behaviour was evident around both westbound and eastbound tunnels.

Attempting to replicate the consolidation period following construction of the westbound tunnel at St James's Park, Wongsaroj (2005) concluded further about

permeability anisotropy. Increasing k_h/k_v from 2 to 5 for Unit A3ii above the tunnel crown improved the replication of pore pressure response there. Investigating further, he conducted parametric studies to systematically investigate the influence of permeability anisotropy on long-term behaviour. By applying higher degrees of anisotropy around a permeable lining, Wongsaroj obtained the consolidating zone at tunnel axis level observed by Nyren (1998). A permeable lining also squatted more with increasing anisotropy. However, permeability anisotropy had much less effect around an impermeable lining due to the reduced flow around the tunnel.

Mair (2008) noted significant deepening and widening of the settlement trough with increasing permeability anisotropy. Presenting results from FE parametric studies, he showed that raising k_h/k_v from 1 to 4 doubled the maximum long-term settlement, whilst also almost doubling the width of the settlement trough.

Soil layering

A large variation in permeability exists in the London Clay between units at different depths, and also at different locations across the London basin, as exemplified in Figure 7.10 (Hight *et al.*, 2007). Harris (2002) therefore noted the necessity to conduct detailed profiling of permeability to obtain realistic predictions. Reporting on ground movements along the JLE tunnels, he highlights greater ground movements occurring when the tunnel passed through Unit A3i than when passing through other units.

In addition, Harris presented results of FE parametric studies conducted by the Geotechnical Consulting Group (GCG), investigating the influence of various factors on long-term tunnel behaviour. The studies pointed to the spatial variation in permeability as playing an important role; the distribution of vertical permeability and the elevation of the tunnel within the strata were highly influential on the rate and magnitude of settlement.

Wongsaroj (2005) specifically addressed the influence of soil layering. He attempted to make the permeability profile more realistic by accounting for differences in both the magnitude and anisotropy of permeability between units of London Clay. Trialling three different profiles, he found significant improvements

in the replication of pore pressures and ground movements in the field. He concluded that correct modelling of both the anisotropy and vertical distribution of permeability was important to realistically simulate long-term behaviour.

2.1.4 Influence of initial pore pressure profile

The initial pore pressure profile also influences long-term behaviour (Mair, 2008). Two extremes for pore pressure regime have generally been considered in the London Clay: hydrostatic and underdrained. An underdrained profile is often observed in London because groundwater has historically been abstracted from the aquifer below the London Clay. Since about 1965 however, there has been a steady rise in water levels owing to the abstraction rate falling below the recharge rate (Simpson *et al.*, 1987). Varying degrees of underdrainage could now exist across London.

Addenbrooke (1996) and Harris (2002) reported on a FE study conducted by GCG investigating factors influencing long-term behaviour (GCG, 1993). In particular, the study compared the long-term behaviour resulting from hydrostatic and underdrained profiles; Figure 2.3 presents the results. Permeable linings were most affected by the pore pressure profile, since a new drainage boundary is introduced. With an underdrained profile, surface settlements reduce in the long-term, but with a hydrostatic profile, further settlement occurs if the lining is permeable; this is due to greater consolidation occurring as the higher pore pressures dissipate.

Mair (2008) compared two case histories in the London Clay where the pore pressure profile was likely to have been influential: St James's Park and Elizabeth House. The JLE tunnels were bored beneath both sites, and movements were monitored for 11 years. St James's Park is a greenfield site, whereas the tunnel at Elizabeth House passes beneath a ten-storey building. Elizabeth House exhibited 80% less long-term settlement than St James's Park by the end of 11 years, as shown in Figure 2.4. Mair suggested two possible reasons for this difference:

Relative soil-lining permeability The ungrouted expanded segments at St James's Park might have resulted in a greater lining permeability than the sprayed concrete lining at Elizabeth House.

Initial pore pressure distribution Elizabeth House was severely underdrained by deep-level pumping, whereas a roughly hydrostatic profile existed at St James's Park, as suggested by Figure 2.5.

Judging from the parametric study conducted by GCG (GCG, 1993) highlighted just before, the pore pressure distribution was likely to have made a significant contribution to the observed difference between the two sites.

2.1.5 Influence of other factors

In addition to investigating relative soil-lining permeability and permeability anisotropy in his long-term FE parametric analyses, Wongsaroj (2005) also studied the effect of stiffness anisotropy, in-situ earth pressure coefficient K_0 and the short-term volume loss. The influence of the other factors is summarised below:

Stiffness anisotropy Compared with isotropic stiffness, adopting anisotropic stiffness increases settlements, and causes squat instead of elongation (lengthening of vertical diameter) of the tunnel. Since squat is almost always observed in London Clay, anisotropy has a key influence upon long-term behaviour.

In-situ earth pressure coefficient Reducing K_0 causes greater settlement, more tunnel squat and reduced lining loads in the long-term; this is due to the soil providing less horizontal restraining force upon the lining.

Short-term volume loss Increasing the short-term volume loss decreases the long-term settlement. A larger volume loss generates greater negative excess pore pressures due to unloading. This leads to more swelling around the tunnel, leading to heave at the ground surface. This was observed at the Heathrow Express Trial Tunnels (Bowers *et al.*, 1996); here, Dimmock (2003) noted that the greatest long-term settlements resulted from the least short-term volume loss. He suggested that the greater negative excess pore pressures resulted in a profile that was closer to the equilibrium profile that resulted from drainage into the tunnel.

2.2 Characteristics of long-term changes

2.2.1 Surface movements

Post-construction movements generally involve the surface settlement trough widening (increasing i: the distance from centreline to point of inflexion) and deepening (increasing $S_{\max}$: the maximum settlement). Also, in general, increases in horizontal displacements and associated differential settlements are small, meaning that further building damage is unlikely to occur (Mair & Taylor, 1997).

The long-term widening of the trough is commonly observed in the field. Reporting on long-term measurements at Grimsby, O'Reilly *et al.* (1991) noted the settlement trough widening by two to three times over the 11-year monitoring period, but with no significant evolution of angular distortions and horizontal strains. Shirlaw (1995) also observed widening of the settlement trough above the Singapore subway tunnels. Above the Heathrow Express trial tunnels, Bowers *et al.* (1996) reported a widening settlement trough, accompanied by only very small development in slopes and horizontal displacement and strain. Nyren (1998) also observed that time-dependent settlements occurred over a wider zone than construction settlements at St James's Park.

Numerical analyses have also simulated the same widening phenomenon; Addenbrooke (1996) found the settlement trough to eventually widen, even if narrowing occurred during the initial stages of consolidation. Analysis results reported by Harris (2002) gave settlements over a much wider zone than volume loss movements: extending to almost 100m away from the tunnels. He states that an increase in slope is also possible during consolidation, so that although further damage might not be initiated, existing damage might be exacerbated. Indeed, he reports further damage having occurred during consolidation in some buildings above the JLE tunnels. Furthermore, the stiffness of ground structures modified the consolidation trough to a lesser extent than the volume loss trough, suggesting that less force is transmitted to buildings. However, he concludes that overall, consolidation movements are less problematic than volume loss movements, with increases in shear strain being relatively small.

The corollary of widening of the trough is that it also becomes less Gaussian in shape. This was noted by Wongsaroj (2005), who instead fitted the more versatile modified Gaussian curve suggested by Vorster *et al.* (2005). From FE parametric studies, Wongsaroj found that trough width increased with a more permeable lining, a deeper tunnel and a greater degree of permeability anisotropy. Mair (2008) also noted the influence of permeability anisotropy on the distribution of settlement; in FE analyses, Mair reported that increasing k_h/k_v from 1 to 4 widened the settlement trough from 60 to 100m.

2.2.2 Subsurface movements

Below the ground surface, consolidation movements also follow a common pattern. A mechanism was suggested by Wongsaroj (2005) from observations made by Nyren (1998) at St James's Park, as illustrated in Figure 2.6. Here, soil in a zone either side of the tunnel consolidates, whilst soil above this zone moves downwards as a rigid body; a small region of swelling also occurs above the crown.

As mentioned in Section 2.1.3, field observations support the concentration of consolidation settlements at tunnel axis level (Glossop & O'Reilly, 1982; Harris, 2002). At the Heathrow Express trial tunnels, Bowers *et al.* (1996) also noted that the fastest rate of consolidation occurred closest to the tunnel. The zone of consolidation settlement can be explained by the permeability anisotropy—if isotropic, radial movement occurs towards the tunnel; anisotropy causes movements over a wider zone (Wongsaroj, 2005).

Unlike the consolidating zone, the existence of the swelling region above the crown (see Figure 2.6) cannot be substantiated due to a lack of long-term subsurface monitoring data available.

2.2.3 Development of settlement with time

Many authors have plotted long-term settlement against log-time, generally obtaining a reverse S-shaped curve. Sometimes, authors have reported initial consolidation settlements developing linearly with respect to log-time. In these cases however, the origin of the time axis appears not to commence from the end of excavation—when consolidation starts—but commences some time later, within

the intermediate portion of the S-shaped curve, giving the false impression of initial linearity. This is further explained below.

Observation of consolidation curves

The first part of an S-shaped curve is apparent when consolidation movements above the sewer tunnels at Grimsby (O'Reilly *et al.*, 1991) are plotted in Figure 2.7a. Here, the time axis commences when short-term movements cease—identified by a sharp change in settlement rate. O'Reilly *et al.* reported a linear plot rather than an S-shaped curve because they plotted consolidation movements from when the compressed air was turned off—100 days after construction; in reality however, some consolidation movements are likely to have already taken place prior to this. Consolidation movements did not curtail until around 7 to 10 years following construction. From long-term FE analyses, O'Reilly *et al.* found that a partially permeable lining matched the observed behaviour best.

The S-shaped curve is also evident for the Heathrow Express trial tunnels, reported by Bowers *et al.* (1996). Once again, the authors interpret a linear development with log-time, since their time axis starts from the commencement of works. If long-term settlements are instead plotted from when the excavation passes beneath the monitoring arrays, the initial portion of an S-shaped curve is produced, as shown in Figure 2.7b. Observations of pore pressure recovering to near-initial values suggest that the tunnels—constructed using the New Austrian Tunnelling Method (NATM)—could be considered impermeable.

The first portion of an S-shaped curve also seems apparent in consolidation settlements at St James's Park, shown in Figure 2.4a (Mair, 2008). This agrees with the S-shaped curves predicted by FE parametric studies at St James's Park (Harris, 2002). However, the slope shows no sign of decaying, even after 11 years, contradicting the FE results that consolidation settlements cease within 5–10 years. The tunnels at St James's Park certainly act as drains, since wet patches were observed inside them across almost the whole section. However, observations of non-zero pore pressures in the field at the crown suggest that the linings might act as partially permeable boundaries.

Idealisation with consolidating soil column

Shirlaw (1995) suggested that the development of settlement could be related to relative soil-lining permeability. He noted that a theoretical S-shaped curve for an impermeable lining fitted settlements above the Singapore subway tunnels, constructed with segmental concrete linings. The theoretical curve used was the C_3 curve—plotted in Figure 2.8—presented by Terzaghi & Peck (1967). This is derived for a consolidating soil column with drainage only from the top boundary, representing the soil above the tunnel crown. Shirlaw contrasted this with earlier tunnels, where settlement developed linearly from the origin on a log-time scale. This trend corresponds to a permeable lining, represented by the C_1 curve given by Terzaghi & Peck, where flow from the base represents the permeable tunnel boundary; this is also plotted in Figure 2.8. Shirlaw surmised that therefore the earlier linings were more permeable, since the later ones adopted hydroswelling gaskets segment joints for more effective waterproofing.

As demonstrated in the preceding section, S-shaped C_3 settlement curves have been more widely reported. This suggests that in practice, linings tend to be partially permeable rather than fully permeable.

These trends might be complicated when twin tunnels are constructed in close proximity; volume loss and consolidation movements from the second excavation would interfere with those from the first (Harris, 2002).

Duration of consolidation

Harris (2002) noted that consolidation settlement is mostly complete within 5–10 years. For the JLE tunnels, consolidation was deemed complete when movements reduced to less than 2mm per year; this criterion was satisfied within 2–5 years from construction, approximately agreeing with the numerical predictions that were made.

In long-term FE studies, Addenbrooke (1996) observed rates of change becoming negligible after 10–15 years for permeable linings, but with pore pressures still not reaching steady-state. With impermeable linings, this period is lengthened to around 20 years, due to the longer drainage distances.

At St James's Park, Mair (2008) reports a long-term settlement of 80mm after 11 years—as shown in Figure 2.4a—with the rate of increase still steady. He concludes that the magnitude and rate of settlement can vary widely between sites in London.

Changes in lining load can continue for even longer than settlements suggest; Barratt *et al.* (1994) still register increases in load after around 20 years.

In summary, the duration for completion of consolidation in London Clay appears to vary between sites, but evidence suggests that it should not exceed a few decades.

2.2.4 Development of lining load with time

Many field observations concur that lining loads increase with time after tunnel construction, with tunnels generally squatting. However, the rate of increase and final magnitudes vary between cases. Ground load acting radially on the lining is often expressed as a proportion of the overburden pressure. The lining thrust at springline is also expressed similarly: as a proportion of the load corresponding to full overburden pressure acting uniformly around the lining (the *full overburden load*).

Observation of lining loads

The development of radial ground load on some linings in London Clay is illustrated in Figure 2.9.

One of the first observations of lining load was reported by Groves (1943), who found that full overburden load in a cast iron lining in London Clay was reached within a fortnight.

Lining loads in a cast-iron tunnel in London Clay were also recorded by Ward & Thomas (1965), over a six-year period. After an initial rapid rise in load within the first year, load accumulated more slowly, reaching 75% of full overburden load after six years. The development of squat followed a similar trend to load. This contrasts markedly with the fast development of lining load reported by Groves.

Collating ground loads for many tunnels, Peck (1969) found that loads increase roughly proportionately with log-time. However, rates varied by four orders of

magnitude or more between cases, as illustrated in Figure 2.9, which includes Peck's plots. Furthermore, Peck (1969) suggested that lining loads in London Clay might rise higher than the full overburden load; his observations show some tunnels approaching or just exceeding full overburden load. This is also seen in the figure.

Barratt *et al.* (1994) monitored lining loads for almost 20 years for a tunnel at Regent's Park, during which time the lining load had increased to 60% and 40% of full overburden load at the springline and crown respectively; the tunnel correspondingly squats with time. Like Peck, they observed an approximately linear increase in lining load when plotted against log-time. Barratt *et al.* also compared lining loads for five further tunnels in London Clay; grouted cast iron linings developed load quicker than expanded concrete linings. They attributed this to the grout providing more intimate contact between lining and soil for load transfer.

Lining loads in the Jubilee Line Extension tunnels beneath St James's Park were reported by Bowers & Redgers (1996); after 100 days, the springline and crown bore 50% and 40% of the overburden load respectively. The ratio between vertical and horizontal ground loading agreed with that noted by Barratt *et al.* (1994).

Ratio of horizontal to vertical ground loading

Mair (1994) provided further insight into the ground loading on linings by stating that the ratio of horizontal to vertical ground loading would not be equal to K_0 immediately after installation or in the long-term. Indeed, Mair & Taylor (1997) noted a lower ratio at Regent's Park: the horizontal loading is about 70% of the vertical, contrasting with K_0 of 1.5–2.0. A lower horizontal than vertical ground loading will generally be the case, even in highly-overconsolidated clays like London Clay, where $K_0 > 1$ (Mair, 1994).

Reporting on lining loads at St James's Park and Elizabeth House, Dimmock (2003) concluded that both horizontal and vertical ground loads on the lining increase during consolidation, but that the vertical load increases by more than the horizontal, leading to the observed squatting. To illustrate transfer of the

overburden load from the soil to the lining, Dimmock portrayed the scenario as three columns: one representing the lining, and the other two the soil on either side. During consolidation, the two soil columns retract support from the lining column, thereby increasing the vertical load borne by the lining.

Influences on lining load

As presented earlier, Shin *et al.* (2002) found that development of lining load is highly dependent upon relative soil-lining permeability. An impermeable lining will accumulate lining load during consolidation; in their FE analyses modelling London Clay, the impermeable lining eventually bore 60% of full overburden load after 14 years. This contrasted with a permeable lining, which accumulated only 45% of full overburden.

Wongsaroj (2005) also observes lower loads in permeable linings, noting further that many interacting factors influence lining load. In his FE parametric studies, Wongsaroj modelled a continuous concrete lining without joints, and trialled various permeabilities ranging from permeable to impermeable. Generally, he found that the springline experienced a large increase in axial force, but a small change in bending moment. However, the crown experienced a small rise—or even reduction—in axial force, but a large reduction in bending moment, which varied considerably, depending upon conditions such as volume loss, RP and permeability anisotropy.

2.3 Summary

2.3.1 The role of permeability

This review has highlighted the significance of both soil and lining permeabilities. This arises from tunnel excavation introducing a new drainage condition to the soil.

The relative soil-lining permeability is a key factor, varying which can lead to a wide range of long-term behaviour, as summarised below:

Permeable lining	Impermeable lining
Surface settlement	Surface heave
Significant squatting	Near-zero squatting
Smaller lining force	Larger lining force

Permeability is also likely to be non-uniform around the lining circumference, so that seepage points might need to be modelled.

The distribution of subsurface movements—particularly the zone of consolidation—is highly dependent upon the stratification of soil permeability. Permeability anisotropy is also highly influential, since it determines flow directions in the soil.

The fundamental role of soil and lining permeabilities presents a challenge: that predictions of long-term behaviour can vary greatly when permeabilities are adjusted within reasonable, credible bounds (Mair, 2008). The validity of numerical analyses is therefore limited by availability of accurate permeability data.

2.3.2 Patterns of long-term behaviour

Common patterns of long-term behaviour have been observed by many authors, for instance:

1. Settlement troughs developing wider and deeper
2. Little further angular distortion and horizontal displacement
3. A zone of consolidation restricted to tunnel axis level
4. Settlement following an S-shaped curve on a log-time plot.
5. Lining load accumulating approximately linearly on a log-time plot.

However, the exact long-term behaviour varies widely between sites, even within the relatively uniform London Clay. Differences between sites cannot usually be attributed to a single factor; this review has shown that a multitude of factors can greatly influence consolidation behaviour. This implies that it may be difficult to obtain accurate long-term predictions from numerical analyses.

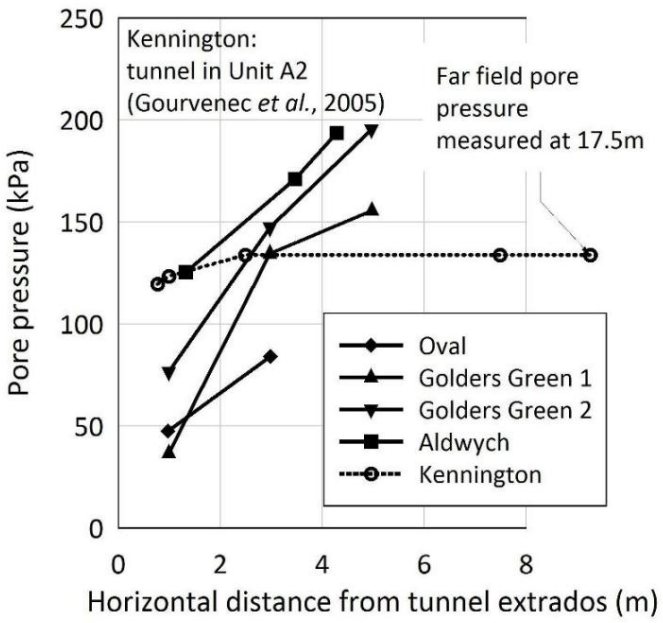

Figure 2.1: Pore pressure variation outside tunnels in London (Mair, 2008)

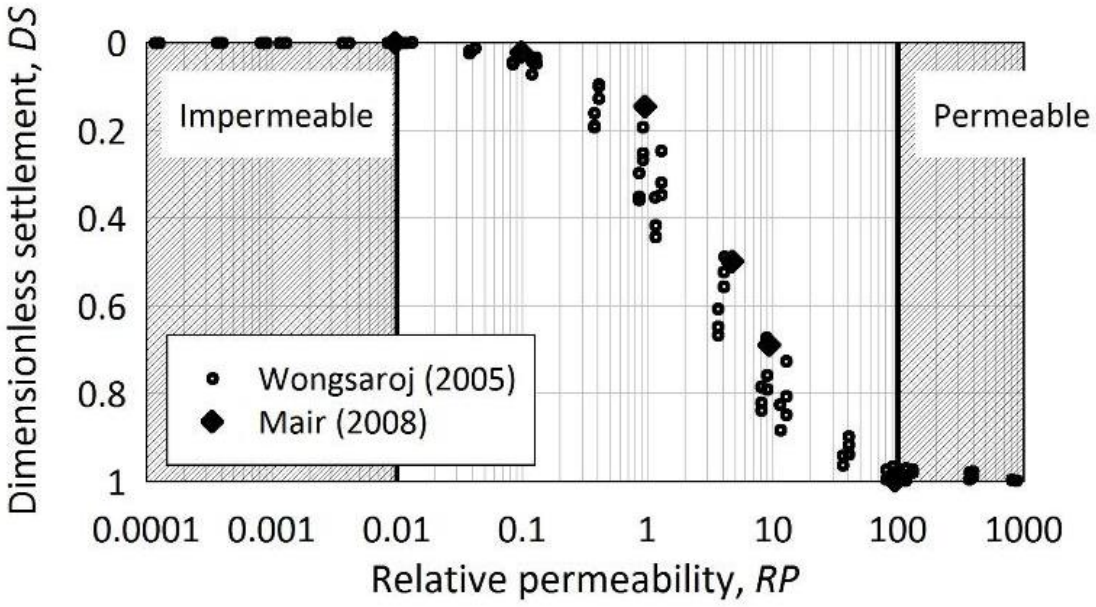

Figure 2.2: Defining lining permeability with relative permeability index (Mair, 2008)

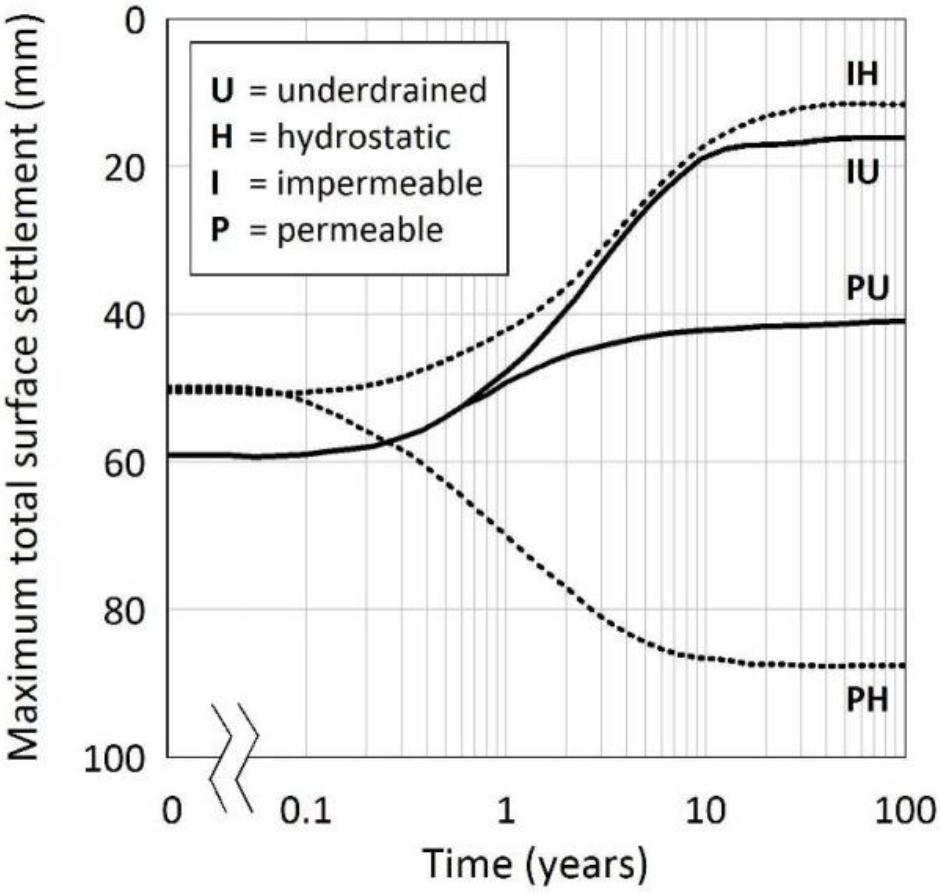

Figure 2.3: Dependence of long-term settlement on initial pore pressure profile (GCG, 1993)

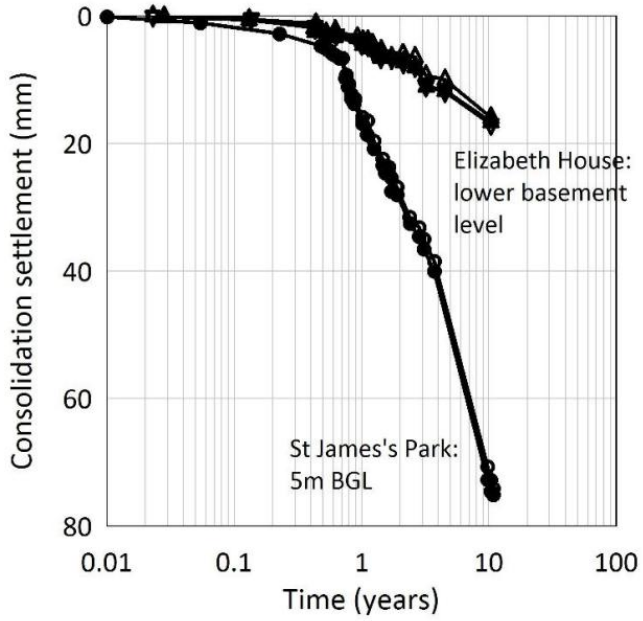

(a) Development of settlement

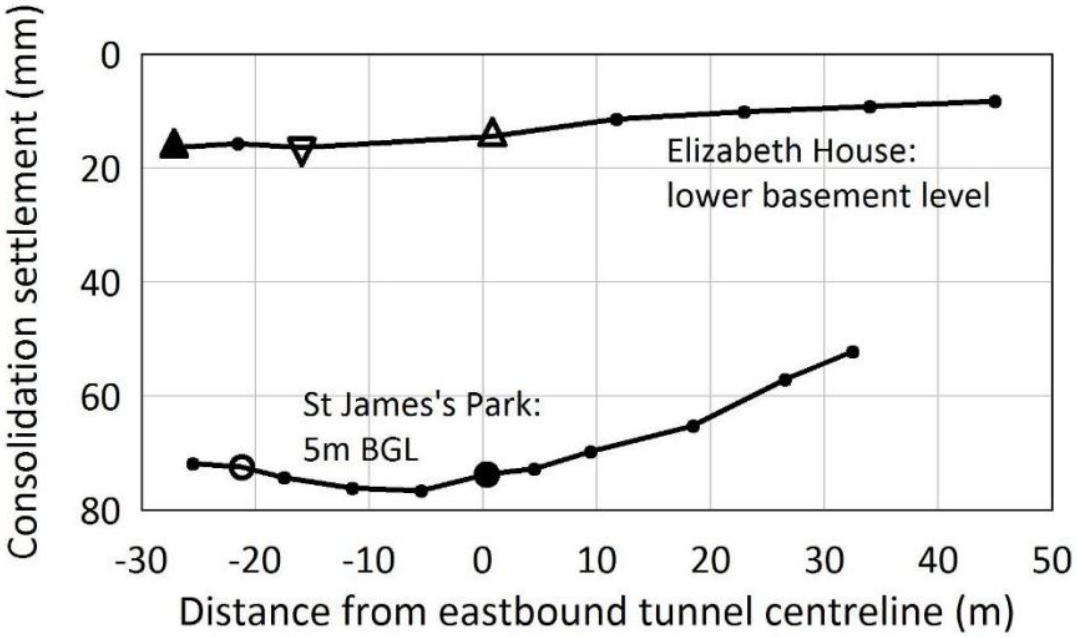

(b) Settlement trough

Figure 2.4: Consolidation settlements at St James's Park and Elizabeth House (Mair, 2008)

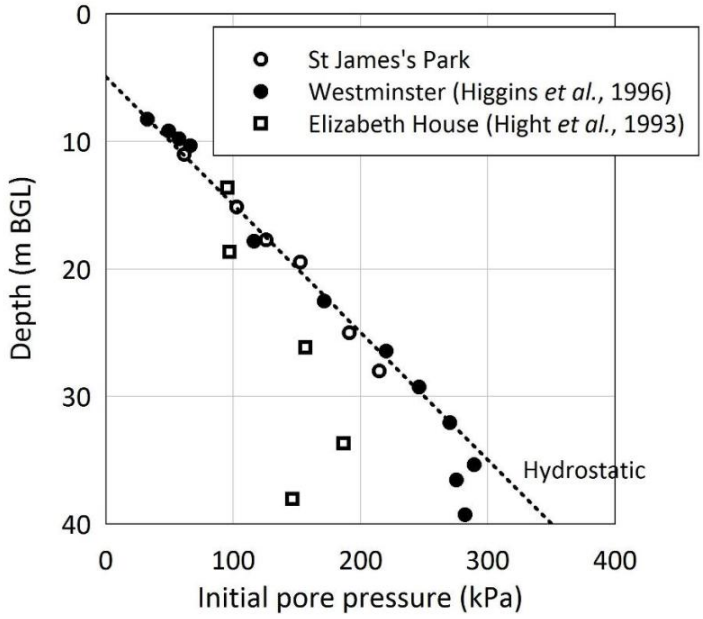

Figure 2.5: Initial pore pressures at St James's Park and Elizabeth House (Mair, 2008)

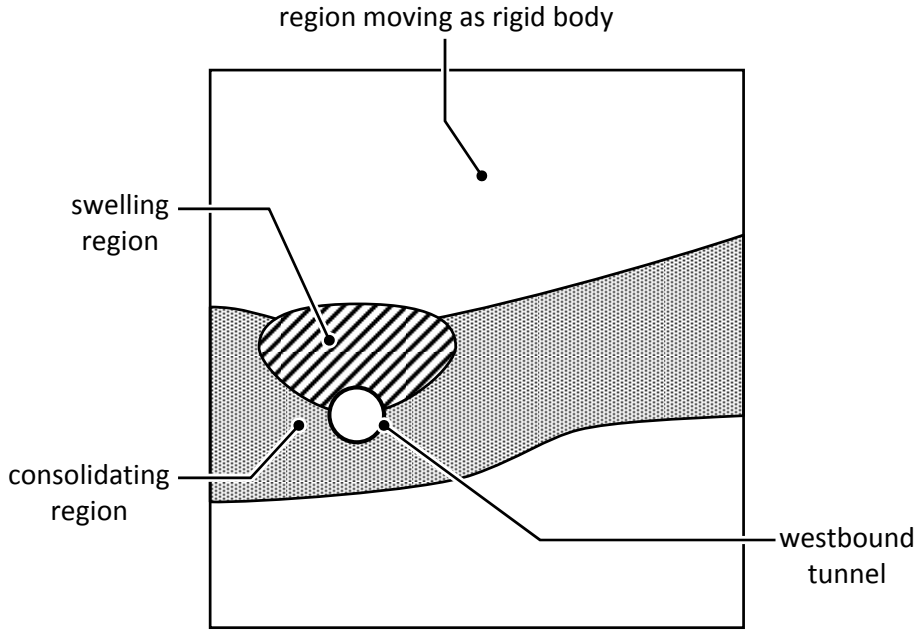

Figure 2.6: Mechanisms of consolidation movement (Wongsaroj, 2005)

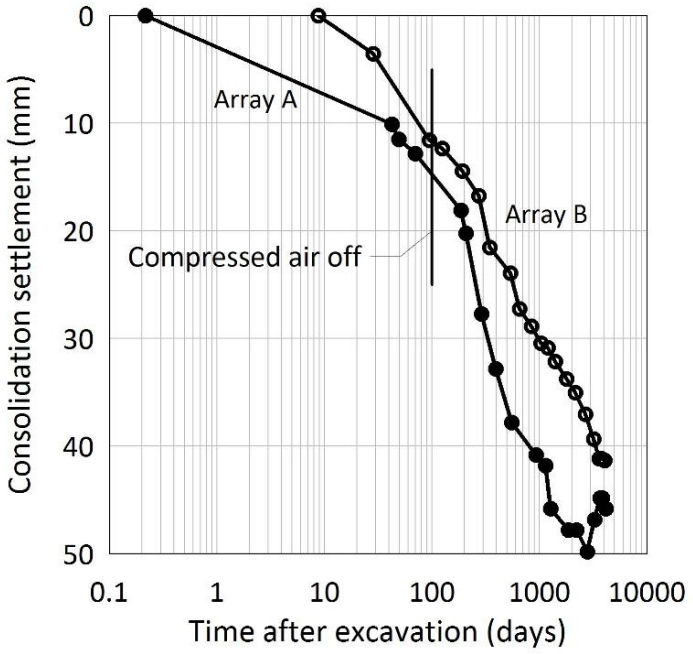

(a) For the Haycroft relief sewer, Grimsby (O'Reilly *et al.*, 1991)

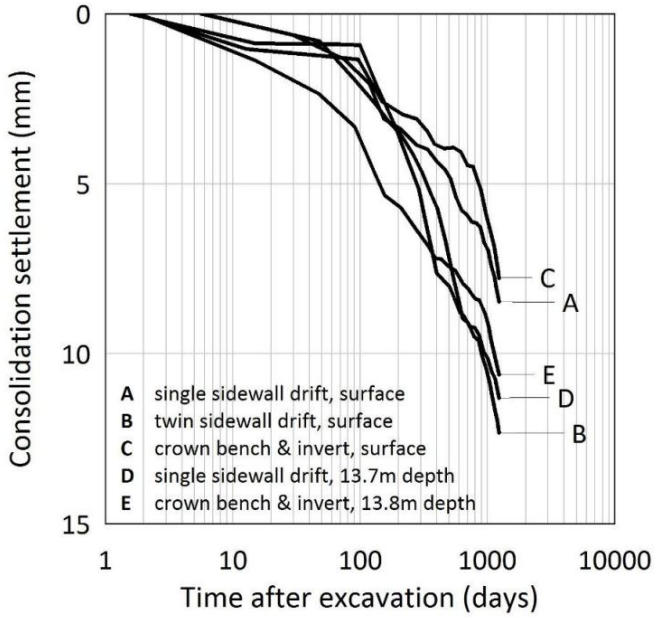

(b) For the Heathrow Express trial tunnels (Bowers *et al.*, 1996)

Figure 2.7: Development of consolidation settlements at Grimsby and Heathrow

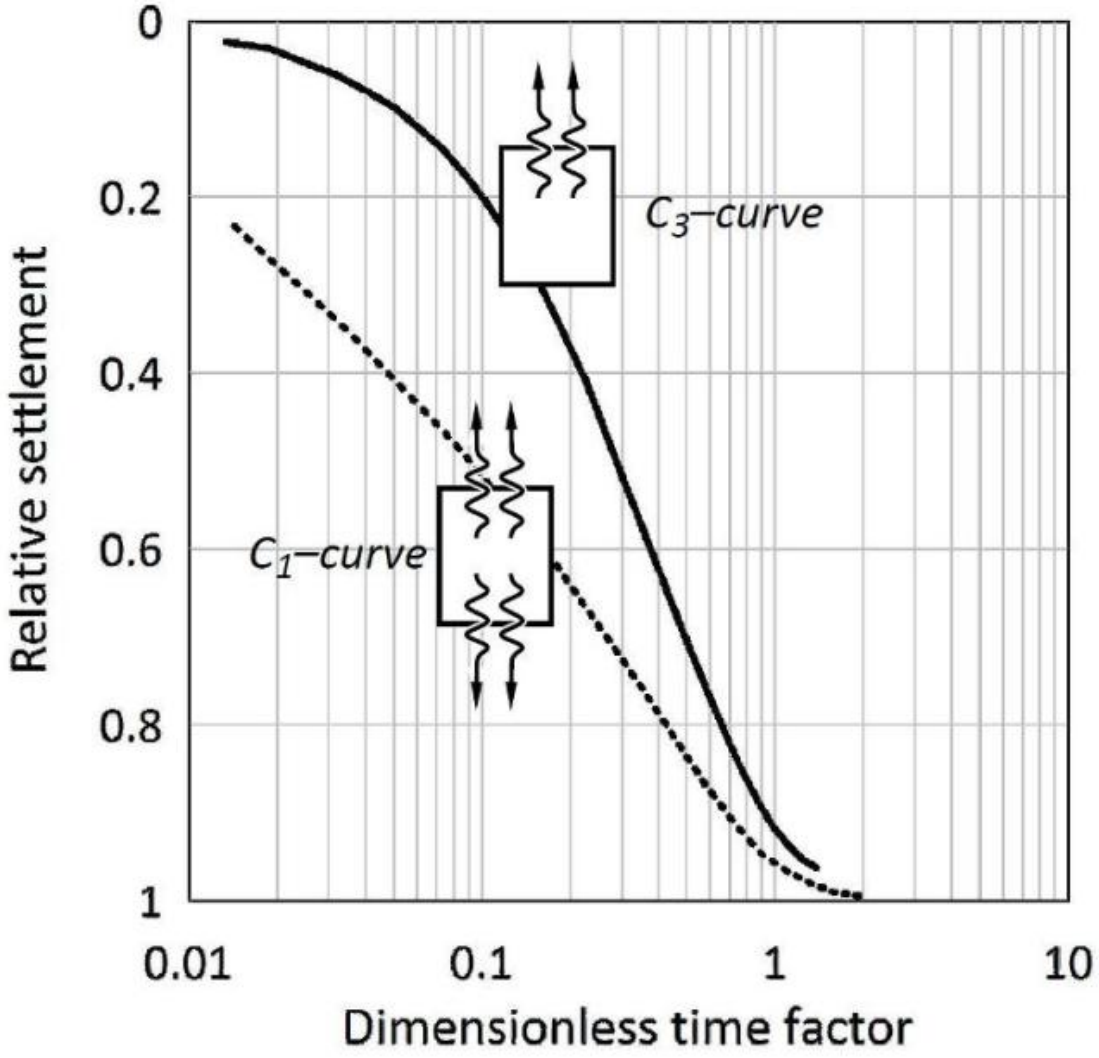

Figure 2.8: Consolidation curves for different drainage conditions (Terzaghi & Peck, 1967)

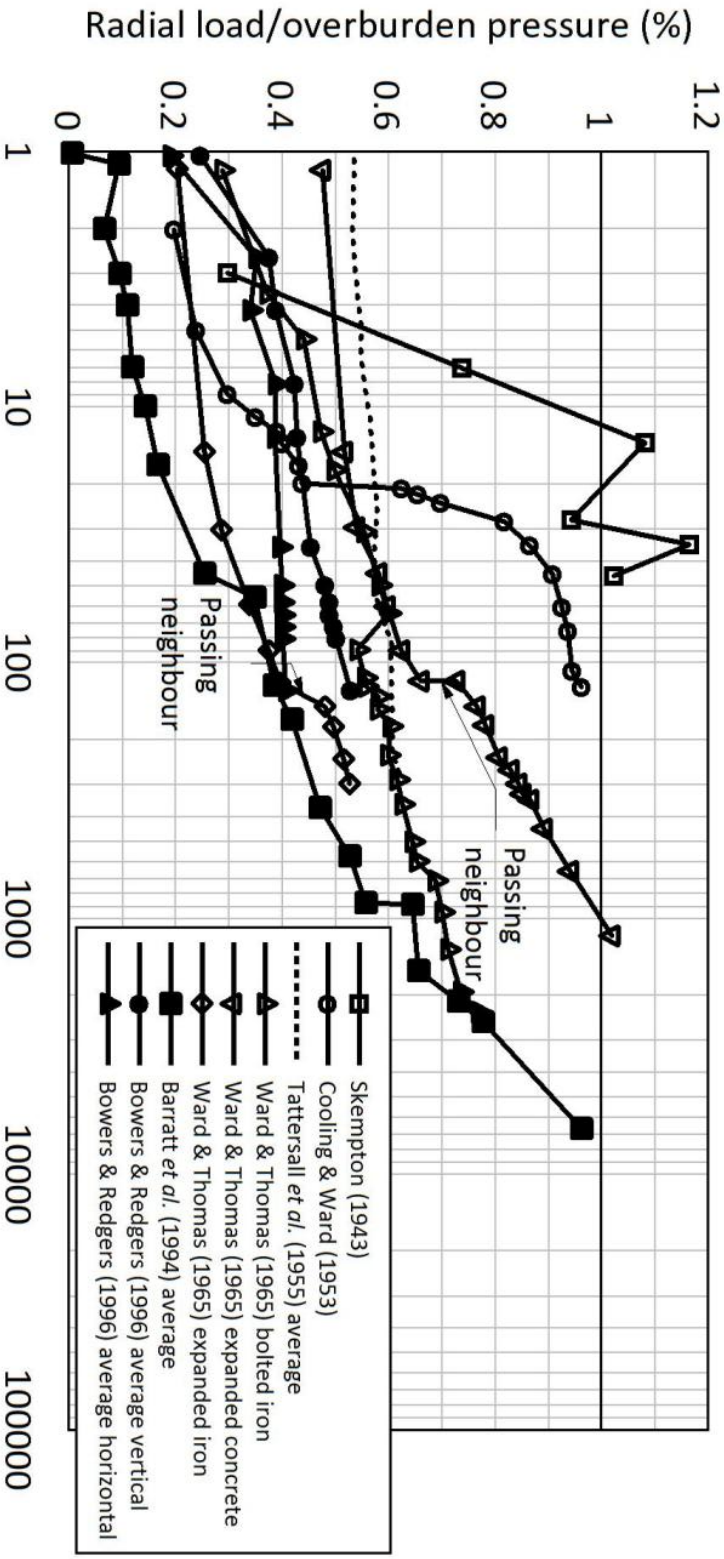

Figure 2.9: Development of ground loading on linings in London Clay

Chapter 3

Review on twin-tunnel interaction

Tunnels are commonly constructed in pairs to enable traffic flow in both directions when tunnels can only admit one-way flow. However, the construction of a tunnel adjacent to another is well-established to affect both the existing tunnel, and the tunnel being excavated. This chapter reviews what has been discovered regarding how twin tunnels interact, specifically focusing upon side-by-side parallel tunnels, since only this arrangement is considered in the parametric study of Chapter 9.

The review splits into three sections: the first summarises the observed characteristic response to twin-tunnelling, both during excavation and the ensuing consolidation period. The second section presents methods to predict the twin-tunnel response; as a foundation for this, the prediction of movements for single tunnels is first described. The final section highlights some aspects of response relevant to the numerical modelling of twin-tunnel interaction, namely the recent stress history, rest period, interaction zone and excess pore pressures.

3.1 Characteristic response

3.1.1 Response during excavation

Increase in volume loss

Many authors have witnessed the second tunnel incurring a larger volume loss than that of a single tunnel excavated in greenfield conditions.

Publishing the first set of field data for twin-tunnel settlements, Terzaghi (1942) reported that settlements incurred during excavation of the second tunnel of the Chicago Subway were two to three times higher than those incurred by the first. Peck (1969) also observed greater settlements due to excavation of the second tunnel, for pairs of tunnels excavated in dense sand. Perez Saiz *et al.* (1981) presented data for the twin tunnels of the Caracas Metro Project, and observed greater maximum settlement and trough volume for the second tunnel. For the sprayed concrete metro tunnels constructed in the stiff clay of Singapore, Shirlaw *et al.* (1988) reported a volume loss four times greater for the second tunnel; the associated settlement trough was also twice as wide as expected. Cooper & Chapman (1998) also noted significantly greater settlement when excavating the Upline tunnel at Heathrow in the region above the previously-excavated Concourse tunnel.

Numerical analyses also reflect a similar trend: Addenbrooke (1996) and Hunt (2005) conducted in-depth numerical investigations into twin-tunnel interaction using plane-strain finite element (FE) models, and both obtained greater volume loss and maximum settlement for the second tunnel, despite the same reduction factor being applied to stresses acting on the tunnel walls when modelling excavation. Hunt attributed this primarily to soil softening due to passage of the first tunnel.

Asymmetry in settlement trough

The greater volume loss for the second tunnel compared with the first would make the trough of net settlements asymmetrical. In addition however, authors have noticed an asymmetry in the trough of incremental settlements caused solely by the excavation of the second tunnel.

Cording & Hansmire (1975) investigated causes of ground movement during tunnel construction, particularly during construction of the twin-tunnel Washington D.C. metro. Noting an asymmetry in the settlement trough from the second tunnel, they introduced the concept of an asymmetrical volume loss $V2_{\text{int}}$ at the surface, additional to the symmetrical greenfield volume loss. This additional volume loss—normalised by the greenfield volume loss for the second

tunnel ($V2_{\text{int}}/V2_{\text{G}}$)—decreased with pillar width, normalised by tunnel diameter (W/D_{T}); pillar width is defined as the horizontal distance between the innermost lining walls. Figure 3.1 illustrates their relationship, along with data from later tunnels added by Cooper & Chapman (2000).

As well as asymmetry in surface settlements, asymmetry was also noted in subsurface displacements. Cording & Hansmire (1975) presented subsurface displacements for the excavation of each tunnel, illustrated in Figure 3.2. The figure shows that—even at depth—displacements are significantly greater on the side closest the first tunnel, although the influence of the first tunnel on the subsurface displacements of the second appears to decrease with depth. Asymmetry in subsurface displacements was also noted by Hanya (1977) for twin shield tunnels in Japan, and by Akins & Abramson (1983) in Atlanta.

Extensive data on ground response was gathered at St James's Park, London, during the construction of the Jubilee Line Extension (JLE) twin tunnels beneath the site. The data was reported by Nyren (1998), who presents an in-depth analysis of the ground response. Nyren noted a greater area for the near limb (closest to the first tunnel) of the settlement trough for the second tunnel compared with the remote limb (furthest from the first tunnel), with the latter embodying just 38% of the total volume loss. Although ground displacements were greater on the side closest the first tunnel, the asymmetry in settlements decreased with depth, as shown in Figure 3.3; the quoted volume losses indicate the asymmetry. This pattern agrees with the subsurface displacements observed by Cording & Hansmire (1975).

Dimmock (2003) also reported on ground movements along the JLE tunnels. At Southwark Park, he noted that the settlement trough due to the second tunnel was skewed towards the first; the near limb embodied a 0.56% volume loss in the near limb, compared to 0.5% for the far limb.

In their numerical analyses, both Addenbrooke (1996) and Hunt (2005) obtained an asymmetrical settlement trough due to the second tunnel, with the position of maximum settlement being offset from its centreline. Analysing more in-depth, Hunt noted that the largest increase in settlement for the second tunnel—compared with a greenfield excavation—occurred around the centreline of the first

tunnel. The relative increase varied between 60% and 150%, increasing if the tunnels were constructed closer together.

Cooper *et al.* (2002) noted that asymmetry in the settlement trough was also manifested in the volume loss at the surface. The authors collated case history data from twin-tunnel excavations, finding greater area in the near limb of the trough than in the remote limb. The same finding was made in the FE analyses conducted by Hunt (2005). Compared to greenfield displacements, the near limb tended to experience larger vertical and horizontal movements, whereas the remote limb experienced smaller movements.

Similar trends have also been observed in laboratory tests. Chapman *et al.* (2007) conducted $1g$ tests investigating the interaction between multiple tunnels constructed side-by-side. The settlement trough due to the second tunnel was skewed towards the first, whilst maximum settlement and volume loss were also larger for the second tunnel. Chapman *et al.* used marker beads to monitor subsurface displacements, finding that the offset for the second trough reduced, and its overlap with the first trough lessened, with increasing depth. All of these findings agree with observed behaviour in the field.

Complexity of horizontal displacements

Horizontal surface strains have the potential to cause severe building damage, yet investigation into the influence of twin-tunnel interaction has been sparse. Hunt (2005) made the first dedicated attempt through running FE analyses of twin-tunnel excavation, finding that interaction affected horizontal displacement in a complex way.

In Hunt's analyses, the transverse profile of horizontal displacement generally widened during construction of the second tunnel. For a single tunnel, symmetry about the centreline ensures that the position of zero horizontal displacement coincides with that of maximum settlement; however, for the second of two tunnels, the two positions no longer coincided. Instead, the position of zero horizontal displacement shifted closer to the first tunnel at shallow depths, but shifted further away at deeper depths; Figure 3.4 captures this behaviour for one of his analyses.

Transfer of lining load

Field measurements of lining load have shown that loads in an existing tunnel increase when a second tunnel is constructed nearby.

Ward & Thomas (1965) reported on lining loads and deformations for an experimental section of the Victoria line in London, noting an increase in lining load as a second tunnel passed; this is highlighted in Figure 2.9.

Reviewing the development of lining load in a number of cases, Peck (1969) postulates that the lining load in an existing tunnel could exceed that corresponding to the full overburden pressure when a second tunnel passes. Tunnels in close proximity to each other, within one tunnel diameter, exhibited a rapid build-up of ground loading—equivalent to the full overburden pressure—within a few weeks to one year.

Numerical analysis has also provided insights into the lining behaviour of twin tunnels. Through FE analyses, Addenbrooke (1996) observed increasing squatting in the first tunnel when the second is excavated, with accompanying increases in bending moment. Bending moments were asymmetric, with the greatest moments being generated closest to the second tunnel. Hoop thrust was also redistributed; the pattern of redistribution suggested that during the second excavation, vertical ground loading increased whilst horizontal loading decreased. The interaction between the tunnels reduced as the tunnel separation increased. Addenbrooke also noted that loads were less in the lining of the first tunnel compared with a greenfield excavation.

Ng *et al.* (2003) modelled the excavation of a new NATM tunnel alongside an existing tunnel in a centrifuge. The existing tunnel was wished-in-place so that the influence of soil softening could not be ascertained. They found that the existing tunnel deformed into an elliptical shape, with the greatest bending moments developing at the springline closest to the new tunnel.

3.1.2 Response during consolidation

Mair (2008) remarked on the importance of understanding how time-dependent settlements caused by construction of an earlier tunnel might affect the ground through which a later tunnel is constructed. Consolidation behaviour for a single

tunnel was reviewed in Chapter 2; however, monitoring of consolidation following twin-tunnel construction has been rare.

Field observations

Consolidation of twin tunnels was recorded during construction of the Singapore Mass Rapid Transit (MRT) system; the tunnels were excavated in soft marine clay using an Earth Pressure Balance Shield (EPBS). Although the influence of interaction was not specifically addressed, Hulme *et al.* (1990) identify different types of consolidation behaviour in Singapore: that due to drainage into the tunnel, which causes the settlement trough to widen, and the more local consolidation due to excess pore pressure dissipation around the tunnel, which generates a Gaussian settlement trough. This implies that the more widespread consolidation caused by tunnel drainage would promote more interaction between the tunnels than that due to excess pore pressure dissipation.

The monitoring of displacements for over two years at St James's Park enabled Nyren (1998) to analyse the long-term behaviour of twin tunnels. The tunnels at St James's Park were diagonally juxtaposed in elevation, so conclusions concerning the interaction must account for the influence of drainage distance—the shallower second tunnel had a shorter drainage distance to the ground surface.

Nyren found a good match when fitting a Gaussian curve to the settlement troughs for each excavation, and also for the consolidation period between them. Greater errors were obtained when fitting to the final consolidation trough after both tunnels have been excavated; consolidation progressed faster on the side nearest the first tunnel, resulting in a wider settlement trough that was offset towards the first. Nyren noted an additive effect here, with continuing consolidation from the first tunnel superposing that of the second. He also suggested that excess pore pressures generated around the first tunnel during the second excavation might have caused further local movements around the first as they dissipated.

Harris (2002) also remarked on the interaction of consolidation troughs at St James's Park. He observed that long-term movements reduced where the tunnels diverged, suggesting that consolidation movements from closely-spaced adjacent tunnels at different elevations were, to a degree, additive. Harris also noted larger

consolidation movements occurring during the twin-tunnel construction of station tunnels (40–60mm) than during that of running tunnels (5–10mm). He attributed this to the close proximity of the station tunnels, and also because the tunnels were larger, and at different elevations.

Finite element studies

Like the field observations, few FE studies have focused on interaction between tunnels during the consolidation period.

Addenbrooke (1996) modelled a consolidation period after excavating twin tunnels in coupled plane-strain FE analyses. He noted continuing ground settlement, with the tunnels moving closer together and experiencing further squatting; however, he did not conclude further about influencing factors.

Harris (2002) reported findings from parametric FE analyses conducted by the Geotechnical Consulting Group (GCG, 1993), which modelled the construction of multiple tunnels and the resulting consolidation. They found that clay cover and tunnel spacing were important parameters which governed movements. They also noted that consolidation movements from a first tunnel can continue whilst a second tunnel is constructed, resulting in the rate of consolidation movement increasing following completion of the second tunnel.

3.2 Prediction methods

This section outlines methods proposed to predict the response—particularly movements—to twin tunnelling. The framework behind twin-tunnel prediction methods is first outlined by describing those for a single tunnel alone.

3.2.1 Prediction for a single tunnel

Gaussian approximation

The Gaussian curve is widely used to describe the transverse settlement trough shape:

$$S(x) = S_{\max} \exp\left(\frac{-x^2}{2i^2}\right) \tag{3.1}$$

where

S = settlement
$S_{\max}$ = maximum settlement on tunnel centreline
x = horizontal distance from tunnel centreline
i = horizontal distance of inflexion point from tunnel centreline

The Gaussian curve was first trialled by Martos (1958) to fit settlements above mine openings; Peck (1969), and subsequently many other authors, have since obtained good fits to field data using the same curve. The settlement trough shape can therefore be predicted by evaluating suitable values of $S_{\max}$ and i.

The volume V_s (per unit tunnel length) of the trough is derived by integrating Equation 3.1:

$$V_s = \sqrt{2\pi}\, i S_{\max} \tag{3.2}$$

For an undrained excavation, as is commonly assumed in clay, the soil will incur no volume change. V_s is then equal to the area swept by the converging tunnel circumference during excavation. This is often expressed as a fraction V_L of the tunnel area, where V_L is termed the *volume loss*, so that:

$$V_s = V_L \cdot \frac{\pi {D_T}^2}{4} \tag{3.3}$$

Maximum settlement $S_{\max}$ can therefore be derived from an estimate of V_L.

Evaluating trough width parameter

A relationship to estimate the parameter i was first proposed by Peck (1969), accounting for tunnel diameter, depth and ground conditions; since then, many other authors have performed similar investigations (Clough & Schmidt, 1981; Cording & Hansmire, 1975; Fujita, 1981; O'Reilly & New, 1982; Rankin, 1988). Reviewing them all, Mair & Taylor (1997) recommended the simple relationship suggested by O'Reilly & New (1982), relating i to tunnel depth z_0:

$$i = K_L z_0 \tag{3.4}$$

Mair & Taylor (1997) confirmed the applicability of this relationship by extensively validating against case history data, finding $K_L = 0.5$ to give a good fit for most clays; this was confirmed by Fujita (1981) for case histories in Japan.

Predicting subsurface settlements

Prediction of subsurface settlements was addressed by Mair *et al.* (1993). Like the surface settlement trough, they assumed that subsurface troughs also adopt a Gaussian curve, but with $(z_0 - z)$ instead of z_0 substituted for the depth to the tunnel, where z is the trough depth. The parameter i therefore becomes:

$$i = K_{\mathrm{L}}(z_0 - z) \tag{3.5}$$

Field measurements revealed that K_{L} increased towards the tunnel, as shown in Figure 3.5, so that subsurface troughs become proportionately wider closer to the tunnel. Figure 3.5 illustrates that Mair *et al.* (1993) found a good fit with the equation:

$$K_{\mathrm{L}} = \frac{0.175 + 0.325(1 - z/z_0)}{1 - z/z_0} \tag{3.6}$$

Knowing that the volume of subsurface settlement troughs at different depths is the same, that is V_{s}, they found the maximum settlement $S_{\max}$ of a trough at depth z from Equations 3.2–3.6:

$$\frac{S_{\max}}{R_{\mathrm{T}}} = \frac{1.25V_{\mathrm{L}}}{0.175 + 0.325(1 - z/z_0)} \cdot \frac{R_{\mathrm{T}}}{z_0} \tag{3.7}$$

where R_{T} is the tunnel radius.

Alternative trough shapes

The Gaussian curve is not the only mathematical representation that has been proposed for the settlement trough shape. Celestino *et al.* (2000) found that a yield density curve provided more flexibility to fit the settlement trough, described by:

$$S(x) = \frac{S_{\max}}{1 + \left(\dfrac{|x|}{a}\right)^b} \tag{3.8}$$

For stiff clays, b varies in the range 2.0–2.8, whilst a is found from the equation:

$$\frac{a}{D_{\mathrm{T}}} = 0.39\left(\frac{z}{D_{\mathrm{T}}}\right) + 0.31 \tag{3.9}$$

Rather than proposing a new curve to improve the fit, Vorster *et al.* (2005) incorporated an additional parameter into the Gaussian trough formulation:

$$S(x) = \frac{b_{\text{mg}}}{(b_{\text{mg}} - 1) + \exp\left[\mu \left(\frac{x}{i}\right)^2\right]} \cdot S_{\max} \tag{3.10}$$

where:

$$b_{\text{mg}} = e^{\mu}\frac{2\mu - 1}{2\mu + 1} + 1 \tag{3.11}$$

Here, parameter b_{mg} controls the decay of the trough away from the centreline, whilst parameter μ ensures that i remains the distance to the inflexion points from the centreline. In his investigation of long-term tunnel behaviour, Wongsaroj (2005) adopted this modified Gaussian curve to fit the wider long-term settlement troughs obtained during his FE consolidation analyses.

Both the yield density and modified Gaussian curves employ three parameters, compared to the two for the unmodified Gaussian curve; this improves the chances of finding a better fit for both.

Predicting horizontal displacements

Methods for the prediction of horizontal displacements assume a common focus for soil displacement vectors, termed a *vector focus*. The horizontal displacements can then be directly determined from the settlement trough. O'Reilly & New (1982) suggested a focus at the tunnel centre, so that horizontal displacement H at a depth z is given by:

$$H(x) = S(x)\frac{x}{z_0 - z} \tag{3.12}$$

where $S(x)$ is the settlement at a transverse distance x from the tunnel centreline.

Taylor (1995) noted that Mair *et al.* (1993) identified a deeper vector focus at a depth $(1 + 0.175/0.325)z_0$ below axis level, from Equation 3.6; this led to the horizontal displacements:

$$H(x) = S(x) \cdot \frac{x}{\left(1 + \dfrac{0.175}{0.325}\right) z_0} \tag{3.13}$$

Grant & Taylor (2000) suggested three vector focus points, each corresponding to a different horizon, to account for the non-linear variation of trough width with

depth noted by the authors. However, they concluded that assuming a single focus at the depth suggested by Mair *et al.* (1993) yielded adequate predictions of horizontal displacement.

3.2.2 Prediction for twin tunnels

Principle of superposition

To obtain the total settlement profile for twin tunnels, New & O'Reilly (1991) simply added the Gaussian troughs due to the first and second tunnels, assuming them to be identical:

$$S(x) = S_{\max}\left[\exp\frac{-x^2}{2i^2} + \exp\frac{-(x-d')^2}{2i^2}\right] \tag{3.14}$$

where d' is the separation between tunnel centrelines. They do the same superposition to predict horizontal displacements as well.

Accounting for interaction

Superposition of the greenfield troughs alone—such as proposed by New & O'Reilly (1991)—might be sufficient for settlement predictions above tunnels excavated simultaneously, if stress-strain non-linearity is disregarded. However, delay between the excavations causes settlements due to the second tunnel to be affected by excavation of the first; examples of such interaction were reviewed in Section 3.1. Attempts have therefore been made to account for this interaction.

Introducing offset for second trough

New & Bowers (1994) attempted to fit a transverse Gaussian trough to settlements above the Heathrow Express trial tunnels, which trialled the New Austrian Tunnelling Method (NATM) with three different excavation sequences. An offset trough resulted from advancing one sidewall drift ahead of the other, requiring them to modify the Gaussian curve with an offset parameter β_{x}:

$$S(x) = S_{\max}\exp\left(\frac{-(x-\beta_{\mathrm{x}})^2}{2i^2}\right) \tag{3.15}$$

Altering shape of second trough

Hunt (2005) made a concerted attempt to examine the effect of interaction on movements induced by the second tunnel, by conducting plane-strain FE analyses of multiple tunnels at different spacings and depths. From his observations, he introduced a modification factor to adjust the greenfield trough shape, as shown in Figure 3.6.

The modification factor skews the settlement trough due to the second tunnel by increasing settlements in a region around the first, which represents the zone of interaction between the tunnels. The shape of the distribution for the modification factor was derived from the FE analysis results, which showed that the maximum relative increase in settlement due to interaction occurs above the centreline of the first tunnel, and is independent of tunnel spacing. Subsurface settlements at a depth z can also be predicted by using $i = K_{\mathrm{L}}(z - z_0)$ instead of $i = K_{\mathrm{L}}z$; the modified trough shape for the second tunnel is then given by:

$$S_{\mathrm{mod}}(x) = \left(1 + \left(M_{\mathrm{mod}}\left(1 - \frac{|d' + x|}{A_{\mathrm{tw}}K_{\mathrm{L}}(z - z_0)}\right)\right)\right) S_{\mathrm{max}} \exp\left(-\frac{x^2}{2{K_{\mathrm{L}}}^2(z - z_0)^2}\right) \tag{3.16}$$

where M_{mod} is the modification factor, taken as 0.6; A_{tw} is the multiple of i defining the full trough width, typically 2.5 or 3; and d' is the centreline separation. Equation 3.16 also allows a different value of K_{L} to be used for each limb of the settlement trough to account for asymmetry in trough width.

The modified trough was also applied to predict horizontal displacements by assuming a vector focus for displacements due to the second tunnel, which Hunt translated to account for the interaction. However, this translation away from the tunnel centreline is not consistent with constant volume deformation associated with undrained behaviour (Grant & Taylor, 2000). To the author's knowledge, Hunt is the only researcher who investigated in-depth the effect of interaction on horizontal displacements, despite them having a major influence on building damage.

Using three case studies, Hunt demonstrated an improved fit to field data compared with the unmodified superposition method suggested by New & O'Reilly (1991). Chapman *et al.* (2007) also applied Hunt's modification factor to match

trough shapes for side-by-side multiple tunnels modelled in the laboratory at $1g$. They confirmed that the modification factor greatly improved the fit to observed surface settlements when K_{L} is factored by 1.5 for the near limb, and 0.6 for the remote limb. However, the input parameters required for the derivation—namely, the widths of remote and near limbs of the second settlement trough, and the position of vector focus for the second tunnel—are difficult to evaluate for predictive purposes in the field.

Empirical prediction

An empirical approach is adopted by Cooper *et al.* (2002) to account for the asymmetry of the second settlement trough. The authors collated case history data from twin-tunnel excavations, finding the ratio of the areas of the remote and near limbs of the settlement trough due to the second tunnel ($V2_R/V2_N$). As plotted in Figure 3.7, the authors correlated this ratio with the centreline separation CC, normalised in two different ways: firstly, with tunnel diameter ($CC/2R$), and secondly, with depth from the trough to the tunnel axis (CC/Z).

The authors proved that trough predictions made using these correlations approximated well to field data from the Piccadilly Line tunnels, demonstrating the potential of empirical prediction. However, the large scatter of data points in Figure 3.7 suggests that more case histories are required for validation. In addition, an alternative dimensionless parameter incorporating both diameter and depth might give a stronger correlation; this is explored later in Section 3.3.3.

Lining behaviour

By conducting FE analyses of twin tunnels with pillar widths of $0.5D_{\mathrm{T}}$ and $0.25D_{\mathrm{T}}$, Soliman *et al.* (1993) presented charts to estimate lining loads and deflections during twin-tunnel excavation. They used the single-tunnel case as a reference solution so that twin-tunnel behaviour could be readily determined from any tunnel analysis. The authors recognised the cost of conducting 3-D analysis over 2-D, and therefore presented lining behaviour predictions for both 2-D and 3-D analyses. In this way, the accuracy of the more easily-obtainable solutions from 2-D analyses could be improved.

They found that 2-D analyses gave adequate accuracy for tunnels excavated in soft soil with a stiff lining. Since many of the London underground tunnels have flexible linings—and because the London Clay is stiff—this finding confirms that 3-D analysis is necessary to give accurate predictions in London.

3.3 Aspects relevant to numerical modelling

3.3.1 Consideration of recent stress history

Through plane-strain FE studies, Addenbrooke (1996) investigated the influence of modelling recent stress history on twin-tunnel interaction. He achieved this by reintroducing zero-strain stiffness in selected regions between the excavation of the first and second tunnels, trialling two strategies of stiffness renewal: firstly, over the entire mesh; and secondly, only in regions of load reversal.

Although Addenbrooke (1996) did not comprehensively conclude about the two methods, Addenbrooke *et al.* (1997) later made more definitive conclusions by implementing the methods in numerical analyses of the JLE construction beneath St James's Park. Both methods produced deeper and narrower settlement troughs, more like that in the field. Despite this, reintroducing high stiffness globally over the entire mesh was more unrealistic than selective reintroduction in regions of load reversal. The resulting second settlement trough also lacked the asymmetry observed in the field, since stiffnesses were restored to their uniform greenfield condition.

These observations illustrate that—with realistic implementation—modelling recent stress history has the potential to improve twin-tunnel numerical predictions.

3.3.2 Significance of rest interval

The significance of rest interval—between the construction of the tunnels—on twin-tunnel interaction is addressed in two FE studies: Addenbrooke (1996) and Ng *et al.* (2004). The authors defined the rest interval in two different ways:

1. Addenbrooke (1996) used plane-strain models, and defined the rest interval as a period of time: the *rest period*.

2. Excavating in a 3-D model however, Ng *et al.* (2004) defined a *lag distance* between the faces of the two advancing tunnels.

Both studies are described below. By considering the outcomes of both together, the influence of the rest interval is found to vary between four distinct zones.

Significance of rest period: Addenbrooke (1996)

Addenbrooke (1996) investigated factors influencing twin-tunnel interaction in London Clay using coupled plane-strain FE analyses, and trialled three rest periods: 22 days, 207 days ($\approx$ 7 months) and 6590 days ($\approx$ 18 years). Extending the rest period from 22 days to 7 months had no influence on changes due to the second excavation; however, beyond this time, a longer rest period made the settlement profile wider and flatter.

This effect can be attributed to accumulated consolidation from the first tunnel: before 7 months, consolidation had begun, but accumulated changes were insufficient to produce an effect; beyond this period, the accumulation of consolidation changes was large enough to affect the second excavation. In accordance with this, Addenbrooke anticipated that if the rest period were to be extended even further—until consolidation nears completion before the second excavation—then varying the rest period would again be unlikely to have an influence.

The rest period also had a slight influence on the lining behaviour, as shown in Figure 3.8a; a longer period caused loads in both tunnel linings to interact less.

Significance of lag distance: Ng *et al.* (2004)

Ng *et al.* (2004) investigated interactions between twin parallel tunnels with a pillar width of $1.0D_{\mathrm{T}}$, modelling the NATM in stiff London Clay using coupled FE analyses. Unlike Addenbrooke (1996), they used 3-D models, and so incorporated a rest interval by introducing a lag distance L_{T} between the advancing tunnel faces. As L_{T} increased, more load was borne by the leading tunnel and less by the lagging one. The final total settlement trough was also offset from the line

bisecting the tunnels: being zero when L_T is zero, increasing to a constant value of $32\%D_T$ when $L_T \geq 2.5D_T$, as pictured in Figure 3.8b. A longer lag also led to less horizontal movement around the tunnel, whereas the change in vertical diameter was unaffected. Greater negative excess pore pressures were also generated around the lagging tunnel.

Load transfer and longitudinal interaction

Ng *et al.* introduced the concept of load transfer between the tunnels to explain their observations: simultaneous advance occurred when $L_T = 0$, with the overburden load being shared equally between the tunnels; as L_T approached $2.5D_T$, the excavation tended towards a staggered advance, with the leading tunnel bearing a greater share of the load. The advancement of one tunnel ahead of the other subjected the virgin soil to a stress history, thus modifying stresses and stiffnesses in the soil before the next tunnel arrived. Interaction between the tunnels in the longitudinal direction therefore caused the load transfer behaviour. Such a gradual transition between simultaneous and staggered excavation can only be achieved in a 3-D model—by varying the lag distance; 2-D modelling can only model either one or the other.

The load transfer behaviour is more obvious in Figure 3.8b, which plots the maximum incremental bending moment, ΔM_{max}, against L_T. Ng *et al.* defined ΔM_{max} as the difference between the maximum bending moment in each lining and that for excavation of a single tunnel alone. The slight asymmetry in ΔM_{max} when $L_T = 0$ is due to asymmetrical construction of drifts. The figure shows that increasing load was being borne by the first tunnel, and less by the second, even beyond $L_T = 3.5D_T$; this value is greater than $L_T = 2.5D_T$ at which longitudinal interaction ceased to affect the settlement trough. Excess pore pressures around the second tunnel also appeared to be affected beyond $L_T = 3.5D_T$, with magnitudes continuing to increase above those around the first tunnel.

In quoting the lag distances above, it must be considered that each NATM tunnel was excavated in two drifts, staggered by $2.3D_T$. However, Ng *et al.* measure L_T between headings of the first drifts for each tunnel. Therefore, were each

tunnel to be constructed in one drift, the value of $L_T = 3.5D_T$ mentioned above should be corrected to $L_T = 1.2D_T$.

Defining lag distance for staggered advance

Both excess pore pressures and lining loads still appear to interact longitudinally beyond a lag distance of $L_T = 1.2D_T$. This raises the question of the lag distance beyond which tunnel advance can be considered to be completely staggered. Further clarification is provided by observing excess pore pressure generation, which almost ceases 8 days after the face of the last drift passes. By considering the excavation rate, the eight days corresponds to an advance of $2.3D_T$, suggesting an upper bound of $L_T = 2.3D_T$ to define the limit of longitudinal interaction.

Zones defining influence of rest period

Considering the findings of Addenbrooke (1996) and Ng *et al.* (2004) together suggest that the influence of rest interval differs distinctly between four zones:

Zone 1 A very short rest interval—where $0 \leq L_T \leq 2.3D_T$—influences load transfer between the tunnels: simultaneous advancement occurs at $L_T = 0$ and staggered advancement at $L_T \geq 2.3D_T$. Load transfer at intermediate lag distances is governed by longitudinal interaction between the tunnel headings, which depends upon soil stiffness and tunnel diameter as well.

Zone 2 With $L_T \geq 2.3D_T$, advance of the tunnels can be considered as staggered, so that the stress history after the first excavation influences the second. Consolidation has already begun, but accumulated changes are insufficient to make a difference to the second excavation. Addenbrooke suggests that accumulated changes only have an influence after 7 months; this period is more intuitively defined with dimensionless time according to Wongsaroj (2005):

$$T_v = \frac{E'_d k_S}{\gamma_w} \cdot \frac{t}{{C_{clay}}^2} \tag{3.17}$$

where C_{clay} is the clay cover, E'_d the drained stiffness at a depth $C_{clay}/2$ above the tunnel and k_S is the equivalent isotropic permeability, defined as $\sqrt{k_v k_h}$. For Addenbrooke's analyses, seven months corresponds to $T_v = 0.05$.

Zone 3 For $T_v > 0.05$, accumulated consolidation changes begin to influence the second excavation, so rest interval becomes influential again.

Zone 4 After a sufficiently long time, a steady-state condition will have been reached—signifying the end of consolidation. Beyond this, any further delay in excavating the second tunnel will have little effect on the response; however, twin-tunnel construction with such a long delay is highly improbable, unless new tunnels are constructed alongside existing ones.

3.3.3 Interaction zone

Many authors have related the geometry of twin side-by-side tunnels and their interaction. This section reviews their work, concluding that both depth and separation of the tunnels determines interaction behaviour. A value for the separation-to-depth ratio is then proposed, beyond which interaction becomes negligible.

Review of influences on interaction zone

Through a series of 2-D linear elastic analyses, Ghaboussi & Ranken (1977) investigated the effect of pillar width, tunnel depth and construction sequence on twin side-by-side tunnels. The authors found that settlement trough interaction between shallow tunnels (depth-to-diameter ratio $z_0/D_T = 1.5$) became negligible for pillar widths greater than two diameters. For deeper tunnels, at $z_0/D_T = 5.5$, a greater pillar width was required to prevent the wider troughs from overlapping. Tunnel depth appeared to have less influence on interaction between the linings: this is expected, since lining interactions depend less upon the zone of interaction above the tunnels, which itself depends upon tunnel depth. In most cases, interaction became negligible at pillar widths greater than two diameters.

Addenbrooke (1996) ran a series of plane-strain FE analyses of twin-tunnel excavation and consolidation with different configurations. He also compared the effect of different soil model features: elastic anisotropy, non-linear small-strain stiffness and recent stress history. Interaction between side-by-side tunnels became negligible if the pillar width W was greater than $7D_T$ (seven diameters); however, his criterion for negligible interaction might have been too lenient. Figure 3.9

plots the variation of additional volume loss $V2_{\text{int}}$ due to interaction for the second tunnel—normalised by the greenfield volume loss $V2_{\text{G}}$—against normalised pillar width. At $W/D_{\text{T}} = 7$, $V2_{\text{int}}/V2_{\text{G}}$ is still about 8%. The figure shows that a more stringent criterion might be when $V2_{\text{int}}/V2_{\text{G}} = 3\%$; in this case, interaction can be considered negligible when $W/D_{\text{T}} > 14$.

Addenbrooke trialled tunnels at different separations, but at the same depth ($z_0/D_{\text{T}} = 8.2$). Ghaboussi & Ranken (1977) found that interaction depended upon tunnel depth as well as separation, suggesting that Addenbrooke's criterion for interaction involving only pillar width is too simplistic.

Hunt (2005) also conducted plane-strain FE investigations into twin-tunnel interaction. He found that the eccentricity of the total settlement trough about the line bisecting the tunnels fell to zero when the separation-to-depth ratio d'/z_0 exceeded 1.9. The relationship between lining interaction and separation agreed well with Ghaboussi & Ranken (1977); in Hunt's analyses, any large lining displacements in the first tunnel due to interaction abruptly decrease when pillar widths exceeded two diameters.

Relating tunnel geometry to interaction

The literature reviewed above illustrated that interaction between tunnels should depend upon both depth and separation. The interaction zone where settlement troughs overlap is illustrated by Hunt (2005) in Figure 3.6; the width of the zone at the ground surface increases with tunnel depth, suggesting that the parameter d'/z_0 might be related to the interaction between surface settlement troughs. At the ground surface, the tunnels would interact if $d' < A_{\text{tw}} z_0$, where A_{tw} is the trough half-width—expressed as a multiple of i—at which overlap with a neighbouring trough would cause interaction. Values of A_{tw} defining the limit of interaction between tunnels have been collated from the literature reviewed above:

Source	A_{tw}	
Addenbrooke (1996)	1.7	(adopting $W/D_{\text{T}} = 14$)
Ghaboussi & Ranken (1977)	2.0	
Cooper *et al.* (2002)	1.5–2.1	(shown in Figure 3.7)
Hunt (2005)	1.9	

Values of A_{tw} vary between 1.5 and 2.1; negligible interaction between side-by-side tunnels might therefore be assumed when $d'/z_0 > 2.0$. Conversely, interaction might be significant when $d'/z_0 < 1.5$. Even so, Cooper *et al.* (2002) state that the remote limb of the second settlement trough might not be significantly affected until $d'/z_0 < 0.8$ for tunnels in clay. Interaction during consolidation should persist to larger values of d'/z_0 since movements are more widespread than during excavation.

3.3.4 Excess pore pressure development

Little investigation has been conducted concerning the effect of interaction on excess pore pressures generated during excavation, despite their dissipation determining post-construction movements. As far as the author is aware, Ng *et al.* (2004) presented the only dedicated attempt to describe the influence of interaction on excess pore pressures.

Ng *et al.* (2004) reported excess pore pressures around pairs of NATM tunnels with a pillar width of $1.0D_{\mathrm{T}}$, each excavated in two staggered drifts using 3-D coupled FE analyses. Negative excess pore pressures were generated during excavation due to the decrease in total stress around the tunnel; the authors stated that those due to shear straining were relatively insignificant, since mobilised shear strains were small. More negative excess pore pressures were generated around the second tunnel, particularly on the side nearest the first, so indicating a greater stress reduction around the second tunnel compared with the first. Also, the magnitude of negative excess pore pressure around the first tunnel increased on the side nearest the second after it passed. This suggested that stress relief associated with excavation of the second tunnel was also influencing the first.

The observations of Ng *et al.* demonstrate that stress changes due to the excavation of a second tunnel clearly influence excess pore pressures around both tunnels. This implies that twin-tunnel interaction certainly affects the consolidation period, not only through the interaction between drainage boundaries of the two tunnels, but also through the interaction of excess pore pressures.

3.4 Summary

3.4.1 Need to investigate long-term interaction

The interaction behaviour between twin side-by-side tunnels has certain characteristic features, namely:

- The settlement trough for the second tunnel is skewed towards the first.
- The volume of the near limb of the second settlement trough tends to be greater than that of the remote limb.
- The position of maximum settlement in the second settlement trough is also shifted towards the first tunnel.
- The influence of the first tunnel on the second decreases as tunnel separation increases.
- The influence of the first tunnel on the second decreases with depth.
- Lining loads of the first tunnel increase during excavation of the second.
- Consolidation due to drainage into the first tunnel adds to that due to drainage into the second.

Although many observations during the twin-tunnel excavation have been made, relatively little monitoring has continued into the ensuing consolidation period. This is also reflected in numerical studies, where long-term coupled analyses of twin tunnels have been scarce. This lack of knowledge presents an opportunity to discover more about the long-term interaction behaviour between twin tunnels.

3.4.2 Need for improved prediction

Settlement predictions for a single tunnel are commonly based upon a Gaussian trough; horizontal displacements derive from these by assuming a vector focus for displacements.

However, predictions for twin tunnels require more than just the simple superposition of the individual greenfield settlement troughs for each tunnel; interaction

effects must also be considered. Furthermore, interaction between the horizontal displacements is difficult to characterise.

The application of a modification factor by Hunt (2005) most comprehensively accounted for the interaction by increasing settlements due to the second excavation, in a region around the centreline of the first tunnel. Although successful in improving the fit to field data, the input variables are hard to determine for prediction purposes. Empirical methods (Cooper *et al.*, 2002) provide an alternative, but lack specificity to ground conditions at a particular site.

Much scope therefore exists for the improvement of displacement predictions for twin-tunnel excavation, and especially for the resulting consolidation period, where no methods exist at all to account for interaction. The prediction of horizontal displacements has also been widely neglected, despite their potential to damage surface structures. A need therefore exists for improving twin-tunnel displacement predictions.

3.4.3 Aspects to consider for numerical modelling

This review has highlighted a number of aspects pertinent to numerical modelling of twin-tunnel interaction:

Modelling of recent stress history Modelling the recent stress history—namely the stiffness renewal upon load reversal—is important to the realistic simulation of twin-tunnel interaction.

Influence of rest period Compared with constructing a single tunnel, twin-tunnelling also introduces the additional variable of rest period. The influence of rest period depends upon the interval between construction of the two tunnels, giving rise to four distinct zones of behaviour. These zones are determined by the longitudinal interaction during excavation, and the progress of consolidation thereafter.

Prediction of interaction Interaction across a transverse plane between side-by-side tunnels can be predicted from the separation-to-depth ratio, d'/z_0. Interaction can be considered negligible for $d'/z_0 > 2.0$, whereas for $d'/z_0 < 1.5$, interaction should be considered as significant.

Influence of excess pore pressures Excess pore pressure generation is also affected by interaction; this implies that the ensuing consolidation phase would also be influenced as the pore pressures dissipate.

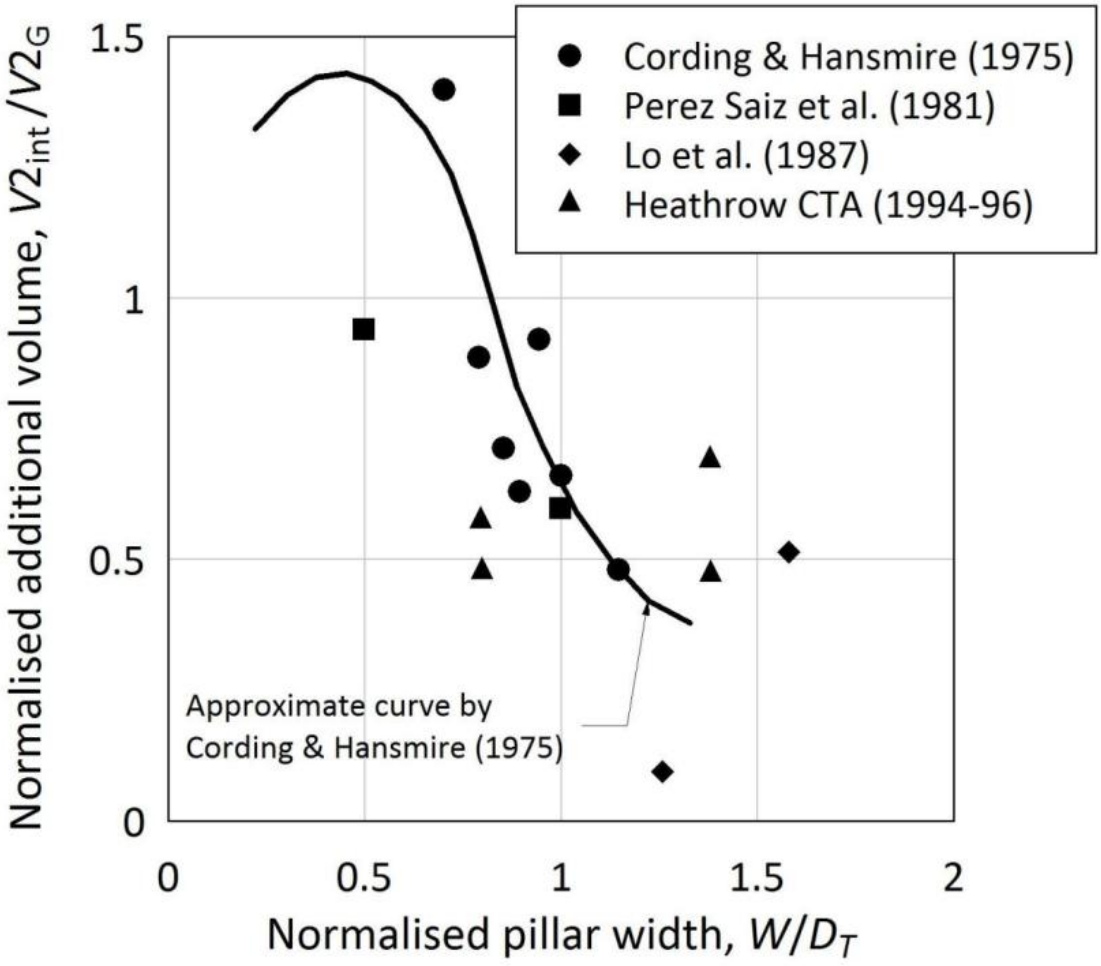

Figure 3.1: Variation of additional volume loss due to interaction with pillar width observed in the field (Cooper & Chapman, 2000)

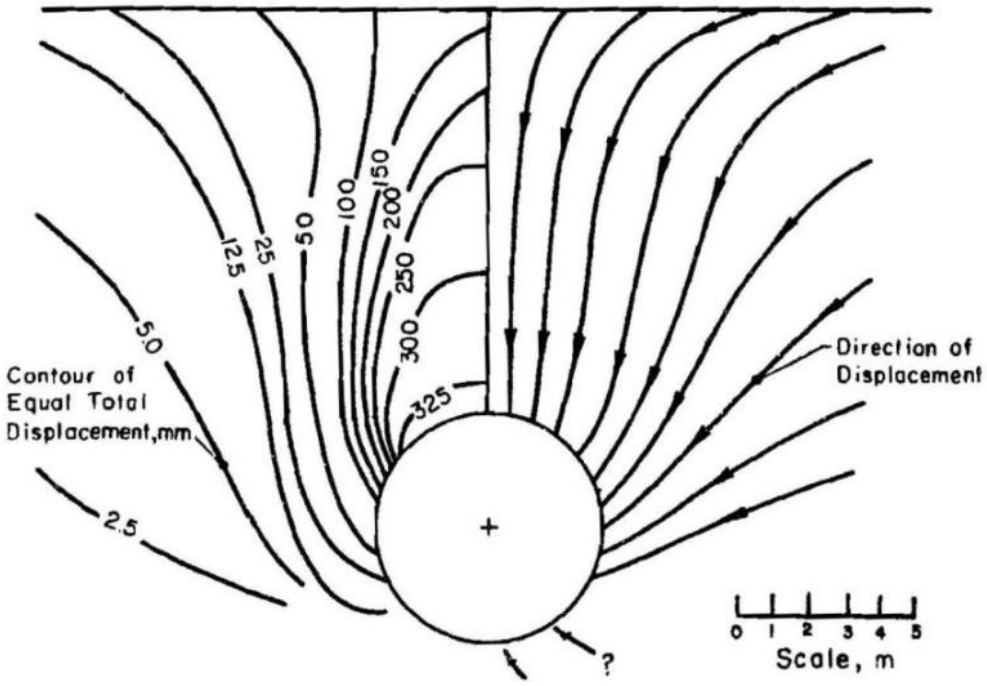

(a) After excavation of first tunnel

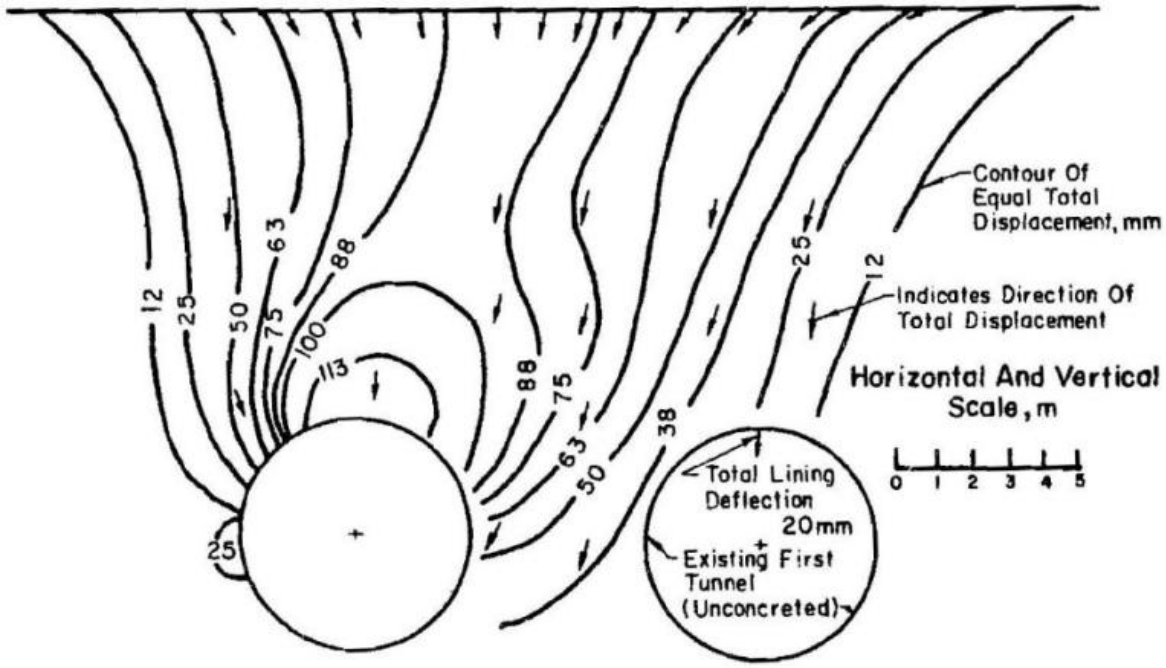

(b) After excavation of second tunnel

Figure 3.2: Accumulated subsurface displacements around the Washington D.C. metro tunnels (Cording & Hansmire, 1975)

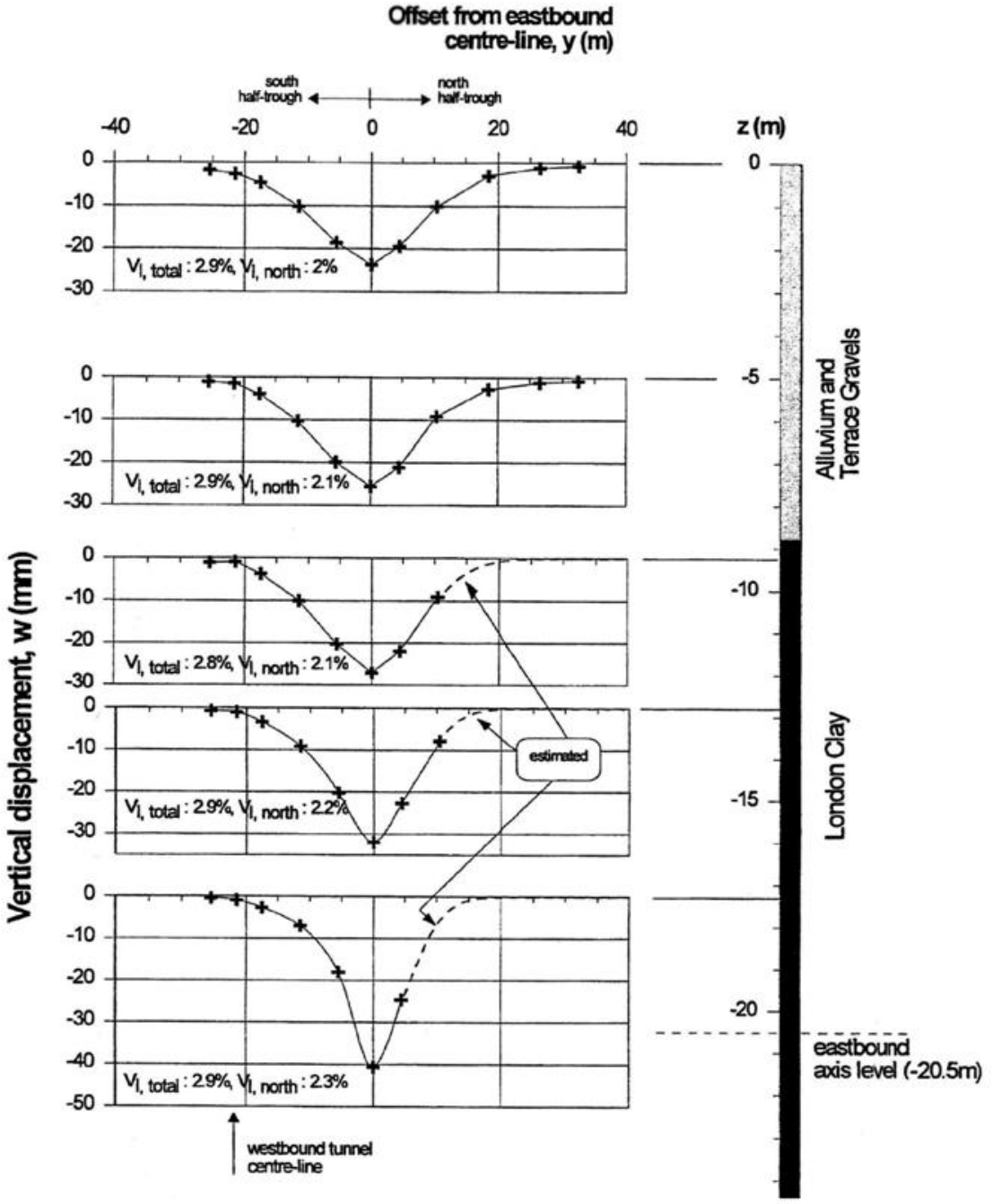

NOTES:

a. Remote north half-trough assumed to represent greenfield settlements such that $V_{l,\,north}$ gives the greenfield volume loss.

b. Westbound tunnel driven first before eastbound.

Figure 3.3: Subsurface settlement troughs above the second tunnel at St James's Park (Nyren, 1998)

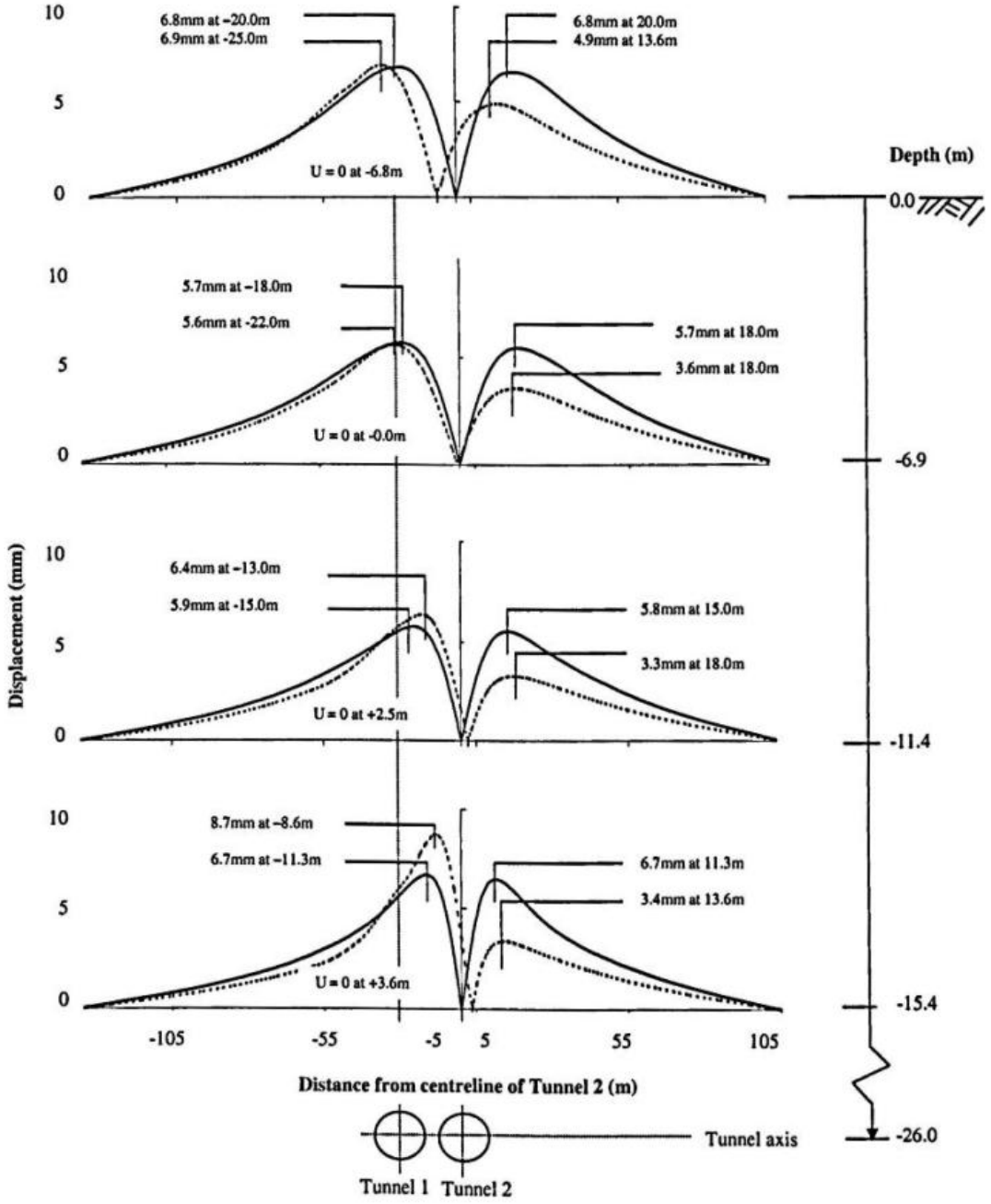

Surface and sub-surface horizontal displacements above Tunnel 2 when considering twin 9.0m diameter tunnels at 26.0m depth with a 20.0m centre-to-centre spacing (V_1 and V_2 = 1.3%)

Figure 3.4: Subsurface horizontal displacements from numerical simulations by Hunt (2005)

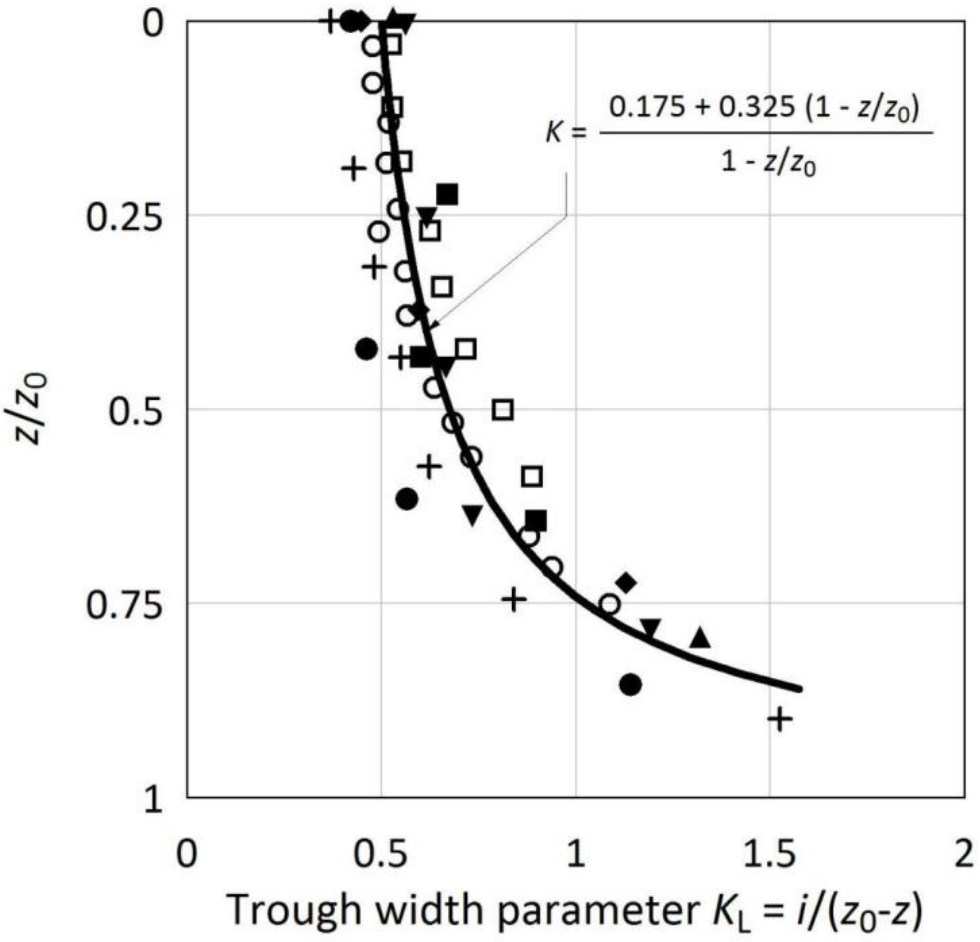

Figure 3.5: Variation of trough width parameter with depth for subsurface settlement profiles in clays (Mair & Taylor, 1997)

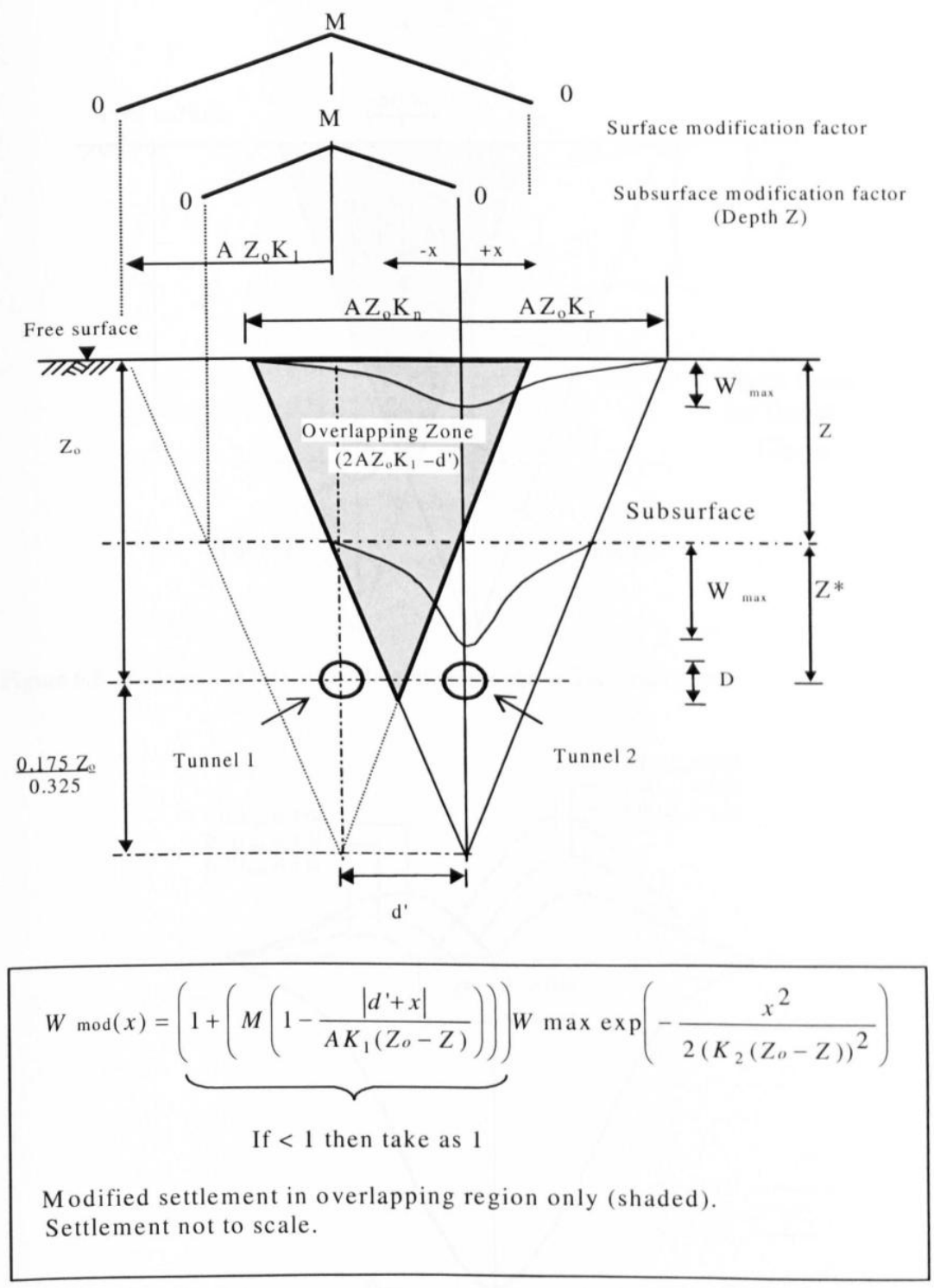

Figure 3.6: The modification factor prediction method for twin tunnels (Hunt, 2005)

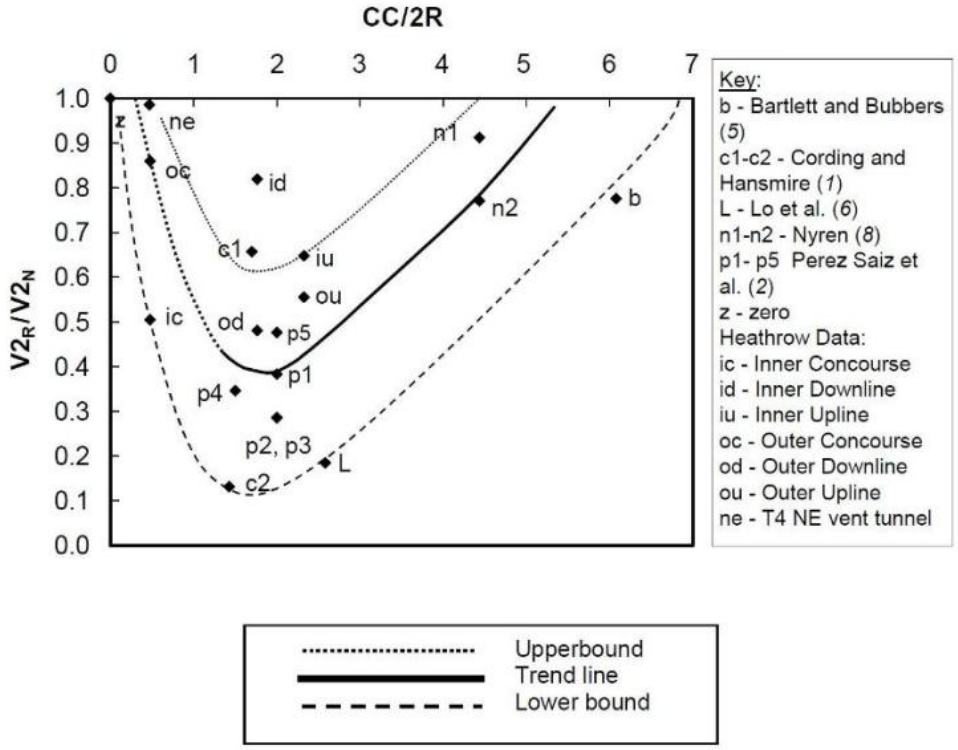

(a) By centreline separation normalised by diameter

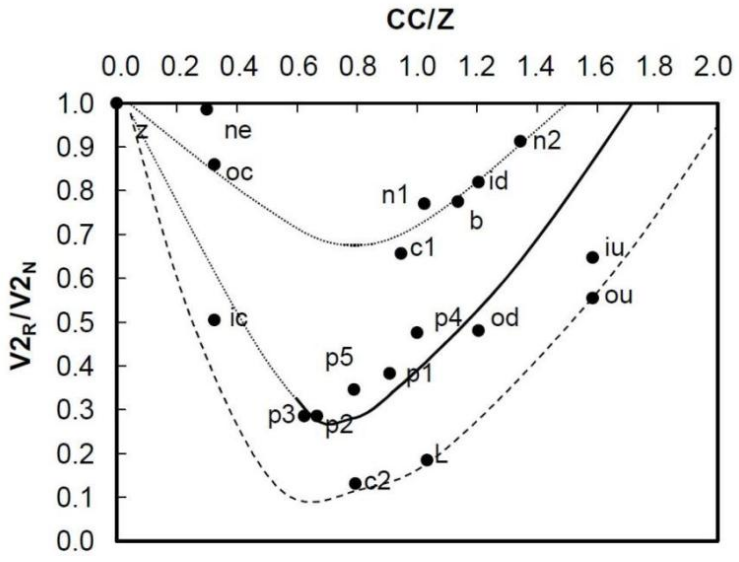

(b) By centreline separation normalised by depth

Figure 3.7: Charts for empirical prediction of volume loss asymmetry (Cooper *et al.*, 2002)

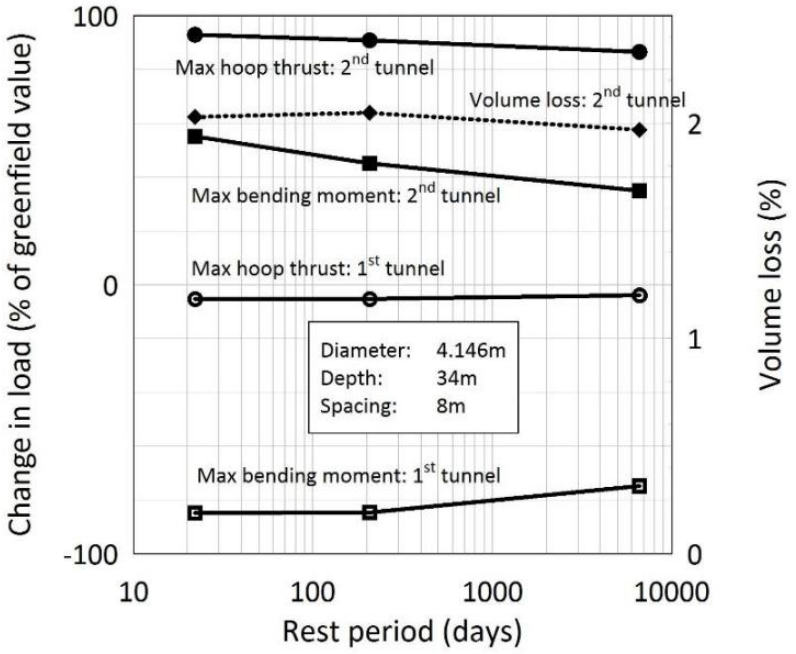

(a) Influence of rest period on lining loads and volume loss (Addenbrooke, 1996)

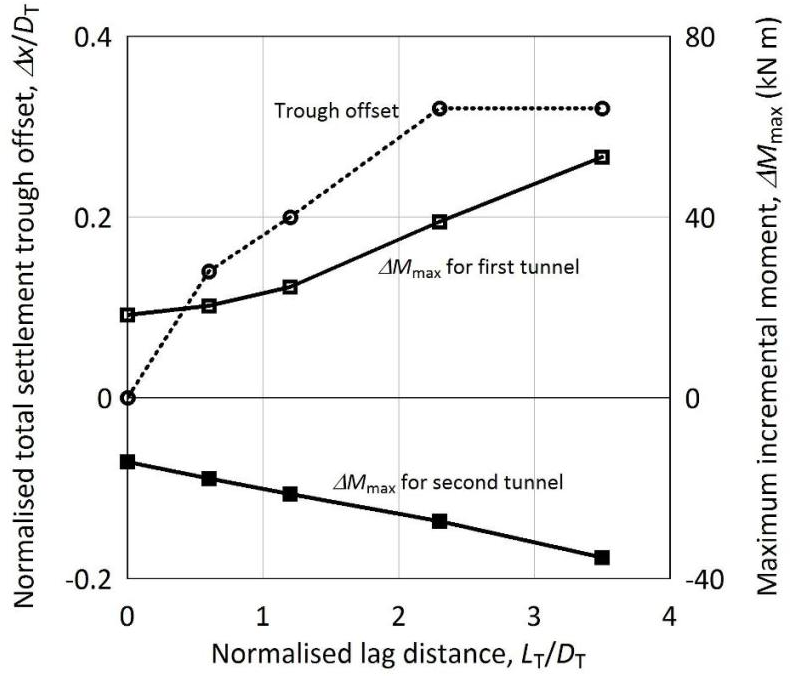

(b) Influence of lag distance on lining moment and settlement trough offset (Ng *et al.*, 2004)

Figure 3.8: Influence of rest interval on twin-tunnel interaction

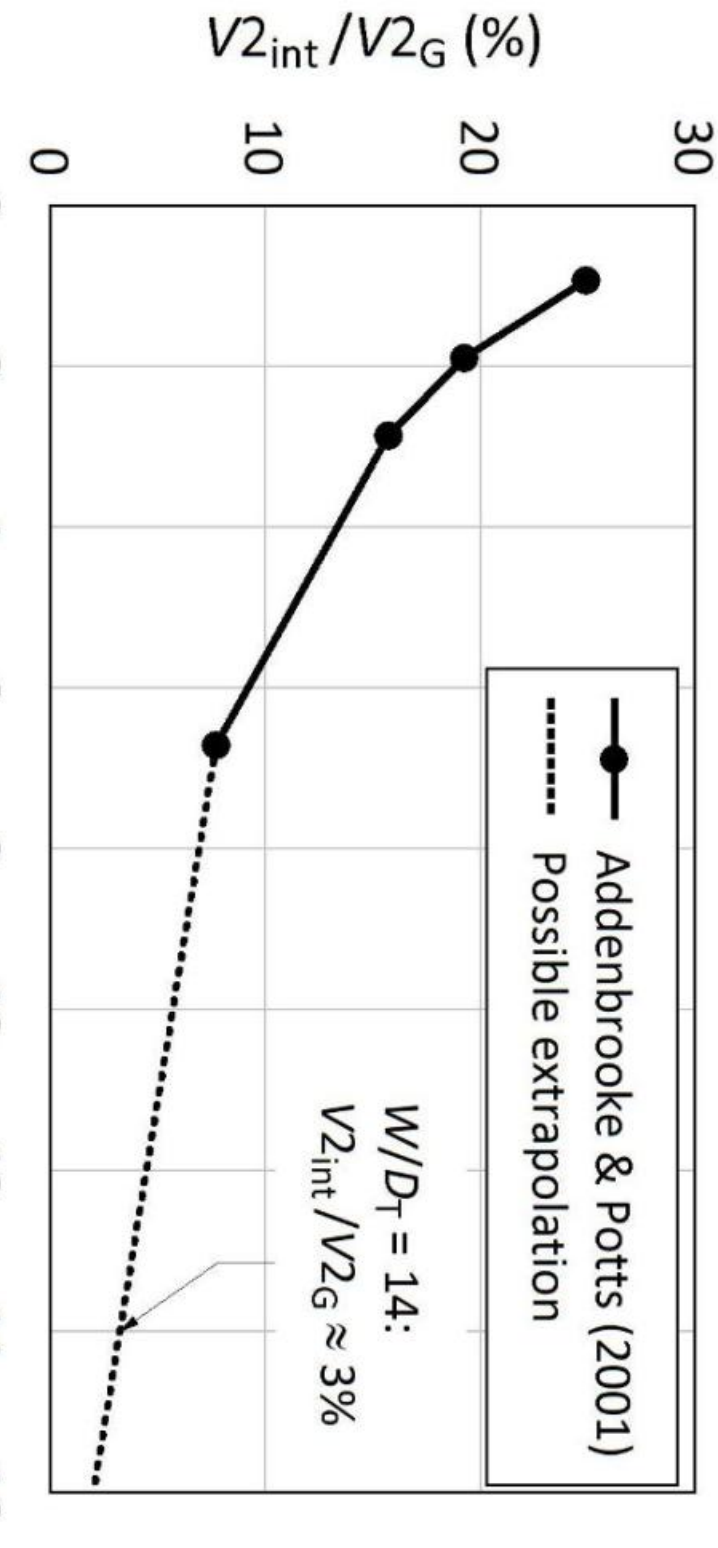

Figure 3.9: Variation of additional volume loss due to interaction with pillar width in numerical analyses by Addenbrooke (1996)

Chapter 4

Permeability tests on fissured London Clay

4.1 Introduction

Despite playing an essential role in determining post-construction movements (Mair & Taylor, 1997; Wongsaroj, 2005), in-situ permeability remains difficult to evaluate, presenting a challenge to the prediction of post-construction behaviour. Fissure disturbance caused by stress changes during tunnelling can change the mass permeability by several orders of magnitude, thus affecting the fluid flow regime that is so influential to post-construction behaviour, and also influencing the choice of soil permeability in the prediction method of Chapter 8. This chapter describes a permeability investigation on fissured London Clay to examine how the permeability of fissures evolves under tunnelling stress changes.

4.2 Overview

4.2.1 Specimen origin

Six specimens were tested, as detailed in Table 4.1. The specimens tested were cut from high-quality rotary cores and block samples kindly donated by Prof Matthew Coop from Imperial College, London; these were extracted at the site of Heathrow Terminal 5 (Hight *et al.*, 2007).

The block samples were recovered near the ground surface in Unit C, and were densely fissured; the Unit C of London Clay corresponds to the lithological divisions identified by King (1981). In contrast, no fissures were present in the rotary core samples extracted from the deeper Unit B2a—the presence of fissures was detected by X-ray scanning. This variation of fissure intensity with depth matched observations made by Skempton *et al.* (1969).

The unfissured specimens provided a baseline to compare with the fissured specimens, to identify the permeability change due to the fissures alone. The first letter of the specimen name given in Table 4.1 identifies the origin as either Unit C (C) or Unit B2a (B). Thus, four fissured specimens (CFV, CFH, CHV & CHH) and two control specimens without fissures (BHV & BHH) were tested.

To capture information about the permeability anisotropy of London Clay, two orientations of specimen were cut from the same sample: horizontal (H) and vertical (V). In this way, the third letter of the specimen name in Table 4.1 indicates its orientation.

4.2.2 Method of permeability measurement

Darcy's Law states that $v = ki$, where v is the filtration velocity through a specimen, i is the hydraulic gradient across it, and k, its coefficient of permeability. Darcy's Law is assumed to be valid for these experiments so that two types of test can be conducted on a specimen:

Constant-flow test maintains a constant flow rate v whilst measuring the hydraulic gradient i developed.

Constant-head test maintains a constant hydraulic gradient i whilst measuring the flow rate v induced.

The second letter of the specimen name in Table 4.1 identifies the test type as either constant-head (H) or constant-flow (F).

A constant-flow test was selected for the first two specimens (CFH & CFV) out of the six. This type of test is shorter because flow rate need not be recorded, which would require a minimum volume to pass for acceptable accuracy. However,

excessive hydraulic gradients were encountered in these tests because the minimum flow rate possible with the available syringe pump was too great. Therefore, constant-head tests were applied for the last four specimens (CHH, CHV, BHH & BHV), where the hydraulic gradient could be controlled.

4.2.3 Test series

In reality, tunnel construction generates complex stress changes. However, to simplify testing, only isotropic effective stress changes were applied to the specimens.

To capture any hysteresis, cycles of isotropic effective stresses were applied. Each cycle consisted of progressive increases and decreases in effective stress, interrupted at particular effective stresses to measure the permeability. Each series therefore required several permeability measurements, each following a consolidation or swelling stage.

Ideally, horizontal and vertical permeabilities would be measured on the same specimen. Indeed, Chan & Kenney (1973) pioneered a cubic specimen—rotatable by 90°—for this purpose. However, confining stresses are hard to change in this set-up, so in the present experiments, different specimens were tested to determine horizontal and vertical permeabilities.

Using triaxial cells, two flexible-wall permeameters were set-up, allowing horizontally- and vertically-cut specimens from the same sample to be tested concurrently. Since a total of six specimens were tested, this led to the following three test series:

1. **Constant-flow tests on two fissured specimens (CFV & CFH)** These tests generated excessive hydraulic gradients.

2. **Constant-head tests on two fissured specimens (CHV & CHH)** Performed with constant-head tests to reduce the hydraulic gradient.

3. **Constant-head tests on two unfissured specimens (BHV & BHH)** Ran as control tests, so that effects of the fissures and the soil matrix could be distinguished.

The specimens were trimmed to the largest possible size to contain the most representative variety of fissures in the field. To this end, specimens were trimmed

to 50mm in both diameter and length—this being the largest size that horizontally-aligned specimens could be cut from the rotary cores.

4.2.4 X-ray scanning

The location of fissures and inclusions inside all six specimens were mapped in 3-D using X-rays in a Computed Tomography (CT) scanner. The X-Tek HMX160 scanner employed was designed for inspecting mechanical devices to a resolution of 1 micron. Selected scan images are presented in Figure 4.1. For calibration purposes, some specimens were scanned with a metallic marker mounted.

4.3 Experimental procedures

4.3.1 Specimen preparation

Clay samples begin to dry upon exposure to air, causing cracking. Special care was therefore taken to minimise moisture loss during specimen preparation.

Specimens were trimmed from rotary core and block samples kindly donated by Imperial College. Investigators there had already preserved the samples with great care (Gasparre, 2005; Nishimura, 2006). Both block samples and rotary cores were wrapped in cellophane film and coated with wax to prevent moisture loss. In addition, the block samples were sealed in plywood boxes, and polyurethane foam was injected into the resulting cavity between the sample and plywood to provide shock protection.

Figure 4.2 illustrates the specimen preparation process. The block sample from Unit C—used to prepare the four specimens CFH, CFV, CHH & CHV—was first cut into octant blocks using an electric bandsaw (Figure 4.2a) and immediately coated with wax and film to minimise drying (Figure 4.2b). Specimens were then cut from the rotary cores and octant blocks. A soil lathe was first used to trim to the correct diameter (Figure 4.2c) before immediate coating (Figure 4.2d). The ends were then trimmed in a V-block (Figure 4.2e) before applying a final protective coating.

Preparation of these specimens required special care, since the clay from Unit C was intensely fissured, and hard inclusions were frequently encountered, as illustrated in Figure 4.3. More delicate cuts were necessary to avoid crumbling along existing fissure planes.

The moisture content of specimen trimmings was determined according to BS 1377-2:1990: trimmings were weighed before and after drying in an oven for a period exceeding 24 hours. From the moisture content values, the initial void ratios and degree of saturation could be estimated. Moisture contents, along with dry and bulk densities, initial void ratios and saturation ratios are given in Table 4.1. A specific gravity of 2.75 was assumed (Bishop *et al.*, 1965; Gasparre, 2005).

4.3.2 Equipment set-up

Two sets of apparatus were assembled so that two tests could be conducted concurrently, as illustrated in Figure 4.4. Figure 4.5 shows a schematic diagram of one set.

Permeability cell

The permeability cell is pictured at the centre of Figure 4.5. The cell used was a triaxial cell for 100mm-diameter specimens, fitted with a pedestal adaptor to mount the 50mm clay specimens. Figure 4.6 illustrates how the specimen was set-up in the permeability cell. During testing, water was injected upwards to assist removal of undissolved air.

Cell, back and injection systems

Figure 4.5 illustrates the cell, back and injection systems. In a constant-head test, the water in each system was pressurised by an air-water interface, with a regulator governing the air pressure transferred to the water. For a constant-flow test however, Figure 4.5 the air-water interface on the injection system was replaced with a syringe pump. A branch in the delivery line from the syringe allowed refilling of the syringe without disconnection, which could have resulted in undesirable entry of air.

Pressure transducers

Three pressure transducers monitored the pressure within each of the cell, back and injection systems. The transducers were mounted in de-airing blocks at the same elevation. Each transducer had a working range of 0 to 1000kPa (10 bar).

Volume change transducers

Flow rate through the specimen was measured using a pair of volume change transducers—measuring inflow and outflow.

Data-logging

DASYLab software was used to process transducer data. Data was sampled at 20Hz, then averaged over a time period depending upon the stage of testing.

Calibration of transducers

Accurate calculation of permeability required meticulous calibration of both pressure and volume change transducers. Relative pressure measurement is important for permeability testing, so the calibration procedures reduced errors between pressure transducers to under 0.1kPa when subjected to the same pressure. For the volume change transducers, errors of under 1% of the measured flow rate were obtained.

Leakage check

Before each set of tests, a leakage check was conducted, consisting of maintaining a pressure of 200kPa for a minimum of 24 hours, whilst monitoring flow rates in the two volume change transducers. The worst-case rate of leakage of 0.07mL day^{-1} could then be deduced. Comparing with the maximum permissible rate suggested in BS 1377-6:1990 of 0.2mL day^{-1}, the set-up was deemed sufficiently watertight.

Specimen set-up

Specimen set-up followed guidelines recommended in BS 1377-6:1990; the guidelines minimise trapped air, which compromises accurate measurement. Figure 4.6 illustrates the specimen during and after set-up.

Before set-up, the height, diameter and mass of each specimen was measured. De-aired water was used to flush out any undissolved air in the equipment, and porous stones were pre-boiled in de-ionised water for 30 minutes before being soaked in de-aired water, along with the filter paper.

The order of assembly for the specimen and associated components can be visualised in Figure 4.6. Great care was taken to minimise trapped air: the lower porous stone was slid onto a layer of water on the base pedestal, both porous stones were maintained fully saturated throughout set-up, and the top cap was moistened before fitting. Furthermore, air bubbles trapped between the membrane and specimen were expelled by stroking the membrane.

Vertical alignment of the specimen was also ensured before commencing saturation. De-aired water was used in all procedures.

4.3.3 Saturation

The saturation method outlined in BS 1377-6:1990 was adopted, consisting of incremental applications of cell and pore pressure; pore pressure was applied through both back and injection systems.

During all saturation stages, the cell pressure was maintained at 10kPa above the pore pressure to apply a positive effective stress. The first stage began with a cell pressure of 50kPa. At each successive stage, the pressures were increased by 50kPa, up to a maximum cell pressure of 400kPa. After this point, further stages alternated between cell pressures of 400kPa and 350kPa so that the greater pore pressures also applied could more quickly dissolve air.

Following each saturation stage, the pore pressure coefficient B was obtained to test the degree of saturation. This was obtained by applying an increment of cell pressure $\Delta\sigma$ and monitoring the subsequent rise in pore pressure Δu with the back and injection valves shut. Then, $B = \Delta\sigma/\Delta u$; $\Delta\sigma = 50$kPa was adopted.

Figure 4.8 plots the progress of saturation for all six specimens. Full saturation is indicated when $B = 1.0$, however, adequate saturation is generally accepted when $B \geq 0.95$ (ASTM D5084-90; BS 1377-6:1990). Such a high value of B might not be attainable for stiff fissured clays, in which case BS 1377-6:1990 considers saturation as acceptable if three successive stages exceed a threshold of $B = 0.90$, superposed on Figure 4.8. However, the figure shows that only half of the specimens (CFV, CFH & CHH) met this criterion.

The probable cause of the low B values is the volume change transducers, rather than insufficient saturation; Nishimura (2006) and Gasparre (2005) use similar specimens but no volume change transducers, and attain minimum B-values of 0.92 and 0.95 respectively. Measurement of B assumes that only compression of undissolved air causes volume change in the pore water, causing the soil matrix to bear some of the cell pressure increment as effective stress, rather than increasing the pore pressure. However, the inlet and outlet chambers of the volume change transducers incorporate rubber belloframs; these rolling diaphragms enable the chambers to expand and contract. Slight deformation of the rubber bellofram during a pressure increment would cause the volume change necessary for the low B-value readings. Therefore, the low B values are likely to be misleading.

Considering this, the long saturation periods and eventual stabilisation of B-values indicated in Figure 4.8 suggest that adequate saturation had in fact been attained. Indeed, for incompressible materials, ASTM D5084-90 considers saturation complete if the B-value remains unchanged in successive saturation stages.

4.3.4 Consolidation and swelling

After saturation, the effective stress was set to different levels, at which permeability was measured.

Effective stress levels

For each specimen, Figure 4.9 shows successive effective stresses applied during each series. The *target* effective stress refers to the desired difference between cell and back pressures during permeability measurement. However, the *mean* effective stress always fell short of the target value because the injection pressure needed

to be elevated to promote flow. The mean effective stress is also indicated in Figure 4.9, along with individual injection and back pressures in Figures 4.9a & b. The premature termination of series BHV compared with BHH in Figure 4.9d was due to leakage between cell and back systems.

Control of hydraulic gradient

A large difference between back and injection pressures is evident for the constant-flow tests in Figures 4.9a & b. This indicates that the minimum flow rate of 1μL min^{-1} deliverable by the syringe pumps was too high, allowing excessive hydraulic gradients (≈ 300) to develop.

In the constant-head tests, hydraulic gradient was maintained at 29, with the injection pressure set 15kPa above the back pressure. This complied with the maximum gradient of 30 recommended in ASTM D5084-90; furthermore, mean effective stresses were only 7.5kPa below the target values, as shown in Figures 4.9c & d.

Limitations in the compressed air supply restricted the maximum attainable cell pressure, leading to effective stresses lower than the highest target value of 350kPa being applied in test 5 of series CFH, tests 4, 10 & 16 of series CHV & CHH, and tests 4 & 10 of series BHV & BHH.

Pressure control strategy

Between levels, the effective stress was changed by incrementing cell pressure by 100kPa each time, whilst maintaining back and injection pressures within the range 150–165kPa.

One-way and two-way drainage

For most of the constant-head tests, two-way drainage was adopted to attain more complete pore pressure dissipation. Dissipation was declared complete when the net flow rate reduced below 6μL hr^{-1}. This limit was decided by adding 5% of the initial flow rate (around 3μL hr^{-1}) to the leakage rate of 0.07mL day^{-1} (3μL hr^{-1}) determined prior to set-up.

One-way drainage was only adopted for the constant-flow tests, and for the first four tests of series CFV & CFH. The BS 1377-6:1990 recommendation of 95% excess pore pressure dissipation was adopted as a completion criterion.

Figure 4.10 shows that the net flow rate after two-way drainage was significantly more satisfactory than for one-way drainage. In the figure, all dimensionless time factors T_{v} exceed unity, suggesting that at least 94% of full dissipation had occurred, if parabolic isochrone theory is assumed. T_{v} was estimated from:

$$T_{\mathrm{v}} = \frac{3V_0\Delta p'}{V_{\mathrm{net}}} \cdot \frac{kt}{\gamma_{\mathrm{w}} d^2} \tag{4.1}$$

where:

d	maximum drainage distance: specimen height if one-way or half-height if two-way
γ_{w}	unit weight of water
$\Delta p'$	change in effective stress applied
t	drainage time
V_0	initial specimen volume
V_{net}	net volume of water outflow or inflow

4.3.5 Permeability measurement

Following each change in effective stress, permeability was measured either by applying a constant flow rate or a constant head difference across the specimen, depending upon the test series. Permeability measurements will be referenced by the series name followed by the test number; for instance, CHV04 refers to the fourth test in series CHV.

Constant-flow rate series

The constant-flow rate test was initially adopted to give short test periods, since it does not depend upon accuracy of flow rate measurement—derived from volume passed in a given time.

Flow was applied with a syringe pump. The syringe diameter and pumping rate were selected to deliver the slowest achievable flow rate of 1μL min^{-1} to minimise

the hydraulic gradient. The first few tests however used a faster flow rate: 6, 2 and 2μL min^{-1} for CFH01, CFH02 and CFV01 respectively, before the need for a slower flow rate was recognised.

After initiation of flow, a head difference gradually developed across the specimen. The rising injection pressure was monitored to determine an equilibrium value for permeability calculation. Permeation typically lasted 1–4 days.

Constant-head series

Despite adopting the slowest attainable flow rate, hydraulic gradients were still excessive in the constant-flow tests ($i \simeq 300$). Subsequent tests were therefore performed by applying a constant-head instead, providing control of the hydraulic gradient. Pressures were controlled using air-water interfaces, maintaining a head difference of 15kPa across the specimen, with a minimum pore pressure of 150kPa. Permeation lasted 3–6 days.

Inflow and outflow check

In both constant-flow and constant-head series, flow rates were determined by plotting volume change with time through the back and injection volume change transducers. The inflow rate usually exceeded the outflow, so an average was typically taken to calculate permeability.

Figure 4.11 plots inflow rate against outflow rate for the constant-flow and constant-head tests, superposing the range within which the difference between rates could be attributed to leakage.

For the constant-head tests, almost all data points fall within this range, suggesting that leakage between the volume change transducers caused the flow rates to differ. This implies that the apparatus was approaching the lowest permeability capable of measurement.

For the constant-flow tests, Figure 4.11 shows that data points fall outside the leakage-attributable range, suggesting that the inflow-outflow difference is due to a further cause. In these tests, inflow rates agreed with those applied, but outflow rates were always significantly slower. Excessive hydraulic gradients might have

caused significant swelling at the injection end, encouraging accumulation of water in the specimen, and hence a lower outflow than inflow.

Calculation of permeability

Calculation of permeability assumed that Darcy's Law was valid, leading to the following expression being adopted:

$$k = \frac{q_\mathrm{i} + q_\mathrm{o}}{2A_\mathrm{cs}} \cdot \frac{1}{\frac{u_\mathrm{i} - u_\mathrm{o}}{\gamma_\mathrm{w} h} + 1} \tag{4.2}$$

where:

A_cs	mean cross-sectional area of specimen
γ_w	unit weight of water
h	mean height of specimen
u_i	pore pressure at inlet
u_o	pore pressure at outlet
q_i	volumetric flow rate at inlet
q_o	volumetric flow rate at outlet

4.4 Results

4.4.1 Validity of results

To make reliable conclusions from the results, the validity of the data is first assessed in light of the following observations:

Excessive hydraulic gradient The relatively high flow rate applied in the constant-flow rate tests led to excessive hydraulic gradients (≈ 300) developing, which may have encouraged:

- Washing of fines through the specimen, leading to clogging of flow paths.
- Large variation in effective stress across the specimen, leading to lack of confidence in associating the measured permeability to a unique effective stress.

- Significant swelling of the specimen, leading to the outflow being significantly lower than the inflow.
- Negative effective stress around the injection end of the specimen; the lack of confinement would allow bypass flow between the specimen and membrane, as well as enabling flow to disturb the soil fabric.

Hydraulic gradients in the constant-head tests were fixed much lower ($i = 29$). These tests were therefore considered more reliable than the constant-flow tests.

Influential leakage rate In the constant-head tests, leakage was the likely cause for difference between inflow and outflow rates. In series CHV, CHH & BHH, the flow through the specimen was fast enough to make the influence of leakage rate acceptable. However, the low permeability of specimen BHV resulted in the flow rate through the specimen being comparable to the leakage rate. Results for specimen BHV were therefore considered unreliable, as confirmed by the large scatter in permeability data (Figure 4.12e) compared with specimen BHH (Figure 4.12f).

In summary, series CHV, CHH & BHH gave results sufficiently reliable to draw conclusions from. Experimental difficulties encountered during series CFV, CFH & BHV rendered them suitable only for confirming trends.

4.4.2 Observations

Figure 4.12 plots the variation in permeability with effective stress for each series; comparison is facilitated by the identical axis scales. Data for specimen BHH has been superimposed on the plots for specimens CHV and CHH for immediate comparison between fissured and unfissured specimens. Below are observations from the figure, presented for later discussion:

1. **Initial permeabilities** Figures 4.12c & d illustrate that before consolidation, the fissured specimens begin with a permeability an order of magnitude higher than the unfissured specimen. Figures 4.12a, b & e confirm higher values for fissured specimens CFV & CFH, and a lower value for the unfissured

specimen BHV. Theory presented later proposes that fissure permeability increases after excavation, when fissure surfaces can open and misalign.

2. **Permeability change due to initial consolidation** Initial consolidation in Figures 4.12c, d & f gradually reduces the initial permeability. During this reduction, the effective stress and permeability are related approximately linearly in $\log k$–$\log p'$ space, suggesting a relationship of the form $k = Ap'^{-b}$. The reduction is around 17 times steeper for the fissured specimens (Figures 4.12c & d) than for the unfissured specimen (Figure 4.12f). As explained later, this might be due to fissure surfaces closing under increasing effective stress. Ratnam (2002) made similar observations when applying constant-flow tests to Gault Clay: the initial permeability at 30kPa effective stress was an order of magnitude higher for intentionally-fractured specimens than for intact specimens; increasing effective stress to 111kPa then reduced permeability to the intact value.

3. **Magnitude of permeability changes** Figures 4.12c & d illustrate that for the fissured specimens CHV & CHH, further changes in permeability are around 20 times smaller than the reduction observed during initial consolidation; Figures 4.12a & b confirm this for specimens CFV & CFH as well. In all fissured specimens therefore, the initial high permeability of the fissured specimens is not restored. Theory presented later suggests this is due to plastic fracture of asperities between fissure surfaces.

4. **Direction of permeability changes** In all series presented in Figure 4.12, increasing effective stress causes permeability to decrease. However, permeability change when effective stress decreases can follow one of two trends. The first trend is steadily increasing permeability with progressive swelling, as Figure 4.12f shows for specimen BHH. The second trend is exhibited in specimens CHV & CHH (Figures 4.12c & d), where the swelling stages immediately following consolidation (CHV05, CHV11, CHV17, CHH05 & CHH06) exhibit a continuing decrease in permeability before increasing. This may be due to local swelling or continuing asperity fracture on fissure surfaces, as

proposed later. The unexpectedly low permeability in test CHV12 suggests an anomalous reading.

5. **Hysteresis in permeability** Corresponding points on successive cycles of effective stress show a gradual reduction in permeability. For instance, tests BHH01 & BHH07 in Figure 4.12f exhibit a decreasing permeability, as do tests CHV07, CHV13 & CHV19 in Figure 4.12c and tests CHH07, CHH13 & CHH19 in Figure 4.12d. For the fissured specimens, the change in permeability during each cycle is around an order of magnitude less than the steep drop during initial consolidation.

6. **Specimen orientation** For the deeper specimens from Unit B2a, the permeabilities recorded for the vertically-cut specimen (BHV) are 1.55 times less on average than those for the horizontally-cut specimen (BHH). The actual permeability of specimen BHV is likely to be even less because leakage in the apparatus limited the measurement of lower permeabilities. A reverse trend applies to the shallower specimens from Unit C: the average permeability for CHV being 1.35 times greater than that for CHH. A possible reason for this is presented later.

4.5 Analysis & discussion

4.5.1 Permeability–stress theory

Relative influences of soil matrix and fissures

As shown in Figures 4.12c & d, the steep decrease in permeability during initial consolidation in specimens CHV & CHH is followed by less severe changes in successive stress cycles. The distinct change in behaviour suggests that either the soil matrix or fissures dominate permeability changes, depending upon conditions. The following three points present evidence to support this:

1. **Laboratory investigation** Using an oedometric permeameter, Dewhurst *et al.* (1998) recorded the permeability changes in two intact specimens of London Clay during K_0-consolidation to 33MPa effective stress, and then during swelling as

the stress was relieved. The two specimens differed in their depths of extraction—17m and 60m, resulting in different clay fractions of 47% and 67% respectively. Permeability was measured both directly, using a constant-head test following each stage of drainage, and indirectly, deriving from compressibility measurements during drainage itself. Figure 4.14 superposes the permeability results on data from series CHV & CHH. Only indirect permeability measurements are plotted, since the authors take direct measurements only after the estimated preconsolidation effective stress of 1.5MPa has been exceeded.

The figure shows that rates of permeability change are similar to specimens CHV & CHH after their initial consolidation. No fissures were recorded by the authors, and fissures are relatively sparse at the depths of recovery, so the data can be taken to represent the permeability change due to the soil matrix alone. This suggests that changes after initial consolidation are dominated by the soil matrix, contrasting with the steeper changes during initial consolidation when fissure permeability dominates.

2. Mathematical prediction From laboratory studies, Tavenas *et al.* (1983) discovered that the hydraulic conductivity change index, $C_\mathrm{k} = \Delta e / \Delta \log k$, is approximately half the initial void ratio e_0 (*log* represents the logarithm to the base 10). Also, since soil is stressed below yield in these current experiments, the elastic compressibility relation for isotropic compression can be assumed: $\Delta e = -\kappa \Delta \ln p'$. Combination of these two relationships yields k as a function of p':

$$k = A_\mathrm{s} p'^{-b_\mathrm{s}} \qquad \text{where} \qquad b_\mathrm{s} = \frac{\kappa}{0.5 \log \mathrm{e}\, e_0} \tag{4.3}$$

Such interaction between effective stress, void ratio and permeability is also highlighted by Vaughan (1994).

On a $\log k$–$\log p'$ plot, Equation 4.3 plots as a straight line with a gradient of $-b_\mathrm{s}$. The value of b_s given by Equation 4.3—which applies to the soil matrix—can be compared with the permeability changes observed in CHV, CHH & BHH to investigate the influence of the soil matrix. To derive b_s, values of κ and e_0 must first be determined: isotropic compression tests on London Clay conducted by Gasparre (2005) gave $\kappa = 0.064$ for units A to C, and $e_0 = 0.74$, averaged from the void ratios presented in Table 4.1; these values predict that $b_\mathrm{s} = 0.40$.

In Figures 4.15b & c, values of $b_s = 0.30$, 0.23 and 0.33 respectively were fitted to stages following initial consolidation of specimens CHV, CHH & BHH. The similarity of these values to the prediction suggests that the soil matrix dominates permeability changes here. During initial consolidation for specimens CHV & CHH however, the relatively high values of $b_s = 1.3$ and 1.8 fitted in Figure 4.15a imply that fissures contribute to steepen the initial permeability decrease.

3. Fissured and unfissured specimens Comparison of the fissured specimens CHV & CHH with the unfissured specimen BHH in Figures 4.12c & d reveals that the high initial permeability and its subsequent rapid reduction is characteristic only of the fissured specimens. Following initial consolidation, permeability changes are approximately the same magnitude for fissured and unfissured specimens, implying that fissures play a major role during first consolidation, but thereafter, the soil matrix dominates more.

In conclusion, both soil matrix and fissures determine how permeability changes with effective stress. Relative to the fissures, the influence of the soil matrix is weak during initial consolidation. Subsequent stress cycling below the initial consolidation stress reduces the influence of fissure permeability, allowing the soil matrix to dominate changes. This hypothesis is illustrated in Figure 4.13, and each component of the figure is discussed below.

Fissure misalignment with stress relief

The high initial permeability suggests that to begin with, the fissures are significantly more conductive than the soil matrix. However, this is unlikely to be the case in-situ, due to interlocking: Skempton *et al.* (1969) encounter 95% of fissure surfaces in London Clay exhibiting a matt texture, created by mounds and depressions. Very few fissure surfaces were found to be polished, prompting the authors to suggest that no appreciable relative movements had occurred along fissures, implying that surfaces interlock.

Instead, stress relief after extraction would allow surfaces to separate and misalign, leaving gaps for flow between non-interlocking surfaces (Box A of Figure 4.13). Visible separation of the fissure surfaces before testing is evident in

the X-ray scans of Figures 4.1a–d; as a low density medium, air between fissure surfaces appears darker.

This has implications on excavations in fissured clay: stress relief on an excavated face might increase permeability in the direction parallel to it.

Fissure flow restriction with increasing confining stress

Asperity crushing Figures 4.12c & d show that during initial consolidation, flow between fissure surfaces becomes restricted. This can be explained by crushing of the asperities holding fissure surfaces apart (Box B of Figure 4.13). This crushing is aided by the low contact area between surfaces, which subjects the asperities to intense stresses.

Plasticity of fissure closure The figures also show that the high initial fissure permeability is not recovered during subsequent swelling. Convergence of the fissure surfaces therefore exhibits little elasticity, probably due to plastic crushing of fissure asperities caused by high contact stresses. Therefore Box D of Figure 4.13 only portrays recovery of the soil matrix as contributing to the permeability increase.

Multiple mechanisms after initial consolidation

Permeability changes are more complex during swelling than during consolidation, suggesting the existence of various opposing mechanisms. Three such mechanisms are postulated below:

Mechanism 1. Recoverable changes in soil matrix The soil matrix deforms almost recoverably at stresses below yield so that recoverable permeability changes are also expected. Strong permeability recovery is demonstrated for tests CHV06–19 and BHH04–11, in Figures 4.12c & f. This recoverability can be attributed to the soil matrix, since fissure closure is irrecoverable (Boxes C and D of Figure 4.13).

Mechanism 2. Shear deformation across fissures Effective stress varies within the specimen throughout testing, both spatially, and with time. This non-uniformity would induce small shearing stresses across fissures in the specimen. Furthermore, the specimens possess inherent stiffness anisotropy endowed by in-situ K_0-consolidation; therefore, the applied isotropic compression would induce shearing as well as volumetric strain. Such shearing is likely to erode weak asperities on fissure surfaces (Box C of Figure 4.13), and under the applied effective stress, resulting fissure closure would constrict flow. This possibly explains the permeability reduction witnessed in tests CHH05, CHH11 & CHH17 conducted after swelling (see Figure 4.12d), which opposes the trend of increasing permeability prevailing in almost all other swelling stages.

Mechanism 3. Expansion of fissure surfaces During the swelling stage, the expansion of regions adjacent to fissures may force opposing fissure surfaces to encroach into the gap between them (Box C of Figure 4.13). The resulting constriction of flow could also cause the permeability reductions in tests CHH05, CHH11 & CHH17.

Mechanism 2 might have more influence during tunnel construction, where significantly greater shear stresses would be induced. These would erode larger asperities, allowing a continuing reduction in permeability, even under diminishing mean effective stress.

The concepts of asperity interlock and erosion theorised here might also apply to other fissure properties; for instance, the friction angle at which shear stiffness between fissure surfaces might reduce. This would begin low at low confining pressures due to lack of interlock between fissure surfaces, but might increase as contact area and interlocking develop with rising effective stress; it might reduce again if shearing fractures asperities.

Hysteresis effects

Hysteresis in permeability is evident in series CHV, CHH & BHH in Figures 4.12c, d & f, due to irrecoverable changes. In the soil matrix, irrecoverability is introduced

by particles or agglomerates of clay progressively weakening at each stress cycle, with some even fracturing. Plastic changes might develop even quicker on fissure surfaces, where more intense contact stresses exacerbate asperity fracture.

Construction processes—such as pile driving—subject the soil to multiple stress cycles, and so hysteresis could be significant in reducing the permeability. Although in many construction processes the stresses do not cycle, cyclic stresses might be significant during operation. For example, cyclic stresses arising from traffic through tunnels could result in diminishing permeability in the surrounding soil.

Specimen orientation

The inherent anisotropy of London Clay causes a greater horizontal than vertical permeability. The two unfissured specimens BHH & BHV exhibit this trend. However, fissured specimens CHH & CHV demonstrate the reverse pattern; here, the difference in fissure permeabilities eclipses the permeability anisotropy of the soil matrix. In his tests on fractured specimens, Ratnam (2002) also finds that permeability depends upon fracture geometry, and influences both horizontal and vertical permeabilities. The presence of open fissures is therefore likely to make the permeability anisotropy ratio dependent upon fissure geometry, rather than the soil matrix.

4.5.2 Fissure permeability model

The prevalence of Mechanism 1 over Mechanisms 2 & 3 in section 4.5.1 implies that a simple permeability model could neglect Mechanisms 2 & 3. Figure 4.16 presents such a model, comprising two distinct types of behaviour: solid lines labelled "A" model irrecoverable behaviour when permeability is fissure-dominated, whereas dashed lines labelled "B" replicate recoverable permeability changes governed by the soil matrix.

Evolution of fissure-dominated permeability

It was hypothesised that stress relief would misalign fissures surfaces and augment permeability. Therefore, a near-zero threshold for mean effective stress is intro-

duced; below it, the permeability is elevated to a high value, represented by the top of line A in Figure 4.16.

Thereafter, the permeability reduces every time the mean effective stress experienced since fissure misalignment attains a new maximum, denoted by $p'_{\max}$ in Figure 4.16. This reduction is represented by progression down line A, where the downward-pointing arrows indicate irrecoverable decreases.

From Figure 4.15a, linearity of the gradient during initial consolidation for specimens CHV & CHH in $\log k$–$\log p'$ space suggests the relationship:

$$k = A_{\mathrm{f}} \left(\frac{p'_{\max}}{p_{\mathrm{a}}} \right)^{-b_{\mathrm{f}}} \tag{4.4}$$

Values of A_{f} and b_{f} are suggested in Figure 4.15a, where relationships are fitted to data for series CHV & CHH. Although depending upon the degree of disturbance causing fissure opening and misalignment, the figure suggests a representative value of A_{f} to be around 2×10^{-10}m s^{-1}; the figure also suggests $b_{\mathrm{f}} = 1.5$ as representative.

Evolution of soil-dominated permeability

The elastic changes of Mechanism 1 above occur when the mean effective stress, p', falls below the maximum experienced since initial misalignment, $p'_{\max}$. The permeability state then leaves line A and follows one of the dashed lines B in Figure 4.16, which intersects line A at $p' = p'_{\max}$. Line B follows the relationship:

$$k = A_{\mathrm{f}} \left(\frac{p'_{\max}}{p_{\mathrm{a}}} \right)^{-b_{\mathrm{f}}} \left(\frac{p'}{p'_{\max}} \right)^{-b_{\mathrm{s}}} \tag{4.5}$$

where adopting the mean effective stress (p') for the independent variable ensures recoverable behaviour, symbolised by the two-way arrows in Figure 4.16. Values of b_{s} are suggested in Figures 4.15b & c, where permeability changes following initial consolidation are linear in $\log k$–$\log p'$ space; a value of $b_{\mathrm{s}} = 0.3$ is most representative.

Limitations of model

The simplified model presented here was derived from permeability changes observed during isotropic stress changes. In reality however, tunnelling stress changes will also have a deviatoric component, which would complicate permeability changes. Implementation of the model in numerical analyses at this stage might therefore not give realistic results; further laboratory investigation into the effect of deviatoric stress changes on fissure permeability may be necessary.

4.6 Summary

Long-term movements are highly sensitive to permeability, so experiments were conducted to investigate how stress changes affect the permeability of fissured London Clay. Cycles of isotropic stress were applied to fissured and unfissured specimens to compare their permeability responses. Also, X-ray scans enabled the fissure networks to be visualised.

A high initial fissure permeability resulted from opening and misalignment of fissure surfaces after excavation. The fissure permeability then reduced irrecoverably as applied stress progressively caused asperities to crush and fracture. In contrast, the permeability of the soil matrix appeared to vary almost elastically.

This theory led to the proposal of a permeability model for fissured soil, combining irrecoverable changes in fissure permeability with recoverable changes in the soil matrix. Relationships between permeability and isotropic stress were derived from the experimental data. However, further development is recommended to account for deviatoric stress changes before they can realistically represent fissured soil in numerical analyses.

The permeability of fissured soil can change by more than two orders of magnitude due to stress changes; this makes it difficult to estimate a realistic soil permeability for the prediction method presented in Chapter 8.

SPECIMEN NAME	ORIENTATION	TEST TYPE	UNIT	MOISTURE CONTENT	BULK DENSITY	DRY DENSITY	SPECIFIC GRAVITY	INITIAL VOID RATIO	INITIAL SATURATION RATIO*
				w	ρ_b	ρ_d	G_s	e_0	S_r
				%	Mg m^{-3}	Mg m^{-3}			
CFV	Vertical	Constant flow	C	25.20	1.990	1.590	2.75	0.73	0.95
CFH	Horizontal	Constant flow	C	25.28	1.971	1.573	2.75	0.75	0.93
CHV	Vertical	Constant head	C	23.31	1.939	1.572	2.75	0.75	0.86
CHH	Horizontal	Constant head	C	25.22	1.956	1.562	2.75	0.76	0.91
BHV	Vertical	Constant head	B2a	26.01	2.037	1.616	2.75	0.70	1.02
BHH	Horizontal	Constant head	B2a	26.28	2.042	1.617	2.75	0.70	1.03

* The presence of voids caused an overestimation of water mass, and hence of saturation ratio

Table 4.1: Test details and index properties for specimens

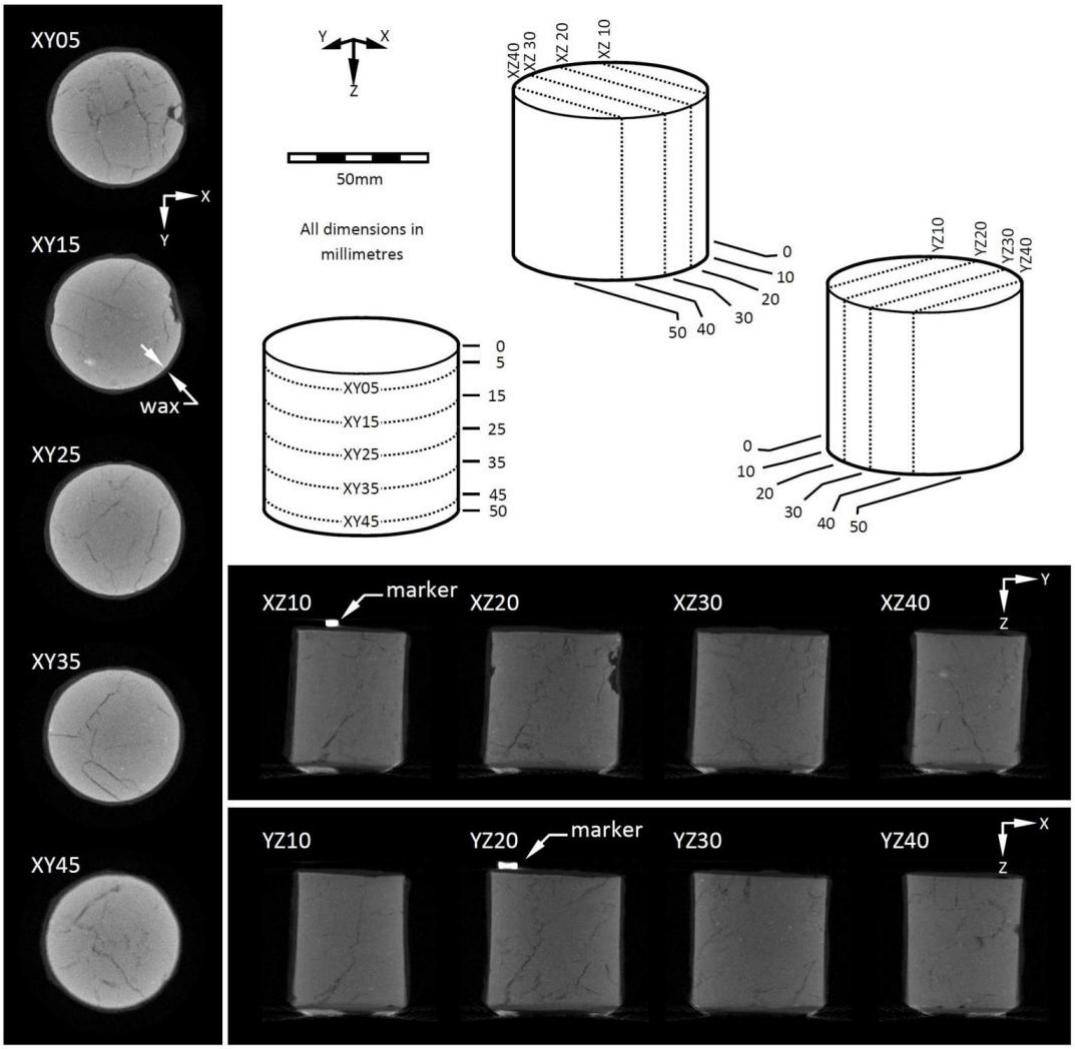

(a) Specimen CFV

Figure 4.1: CT scan cross-sections of specimens

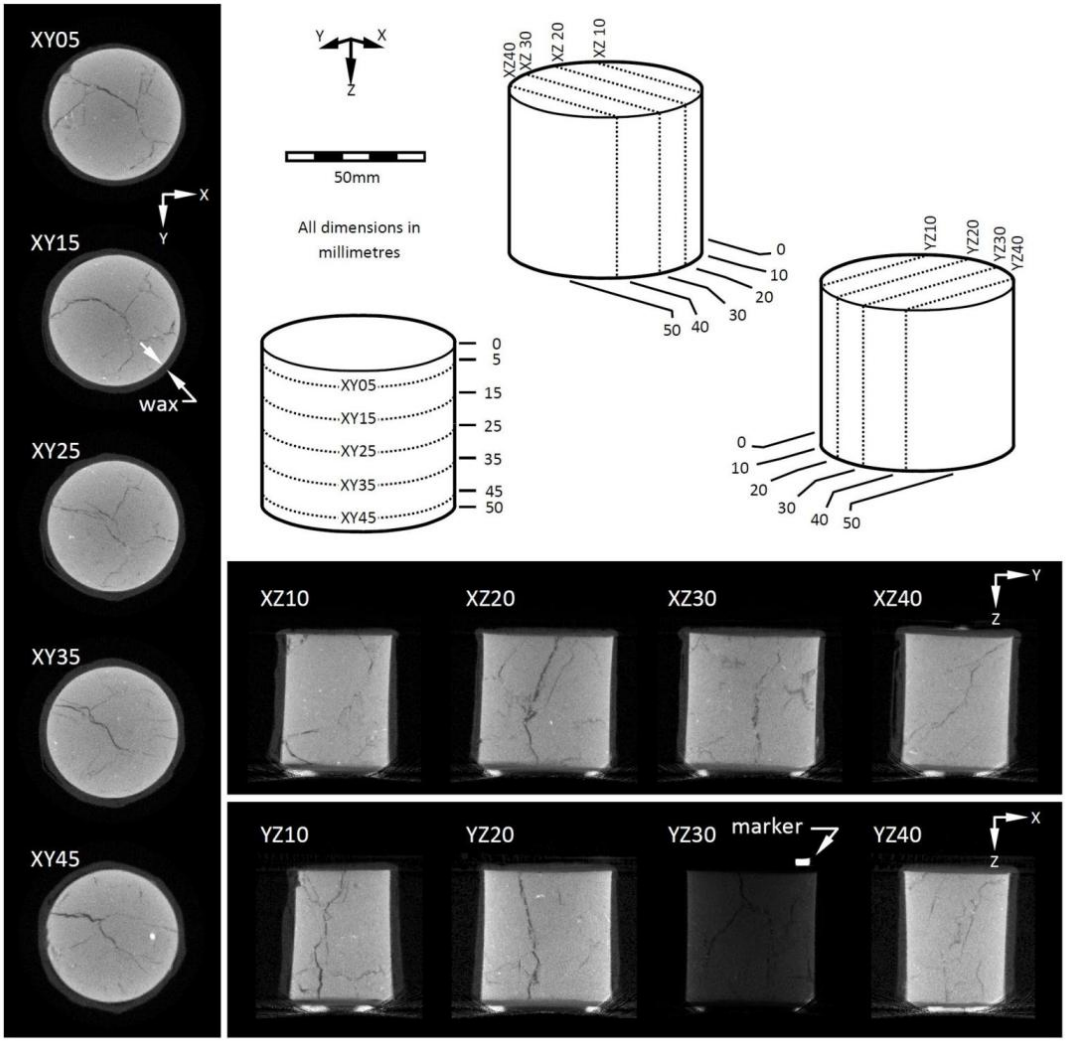

(b) Specimen CFH

Figure 4.1: *cont...* CT scan cross-sections of specimens

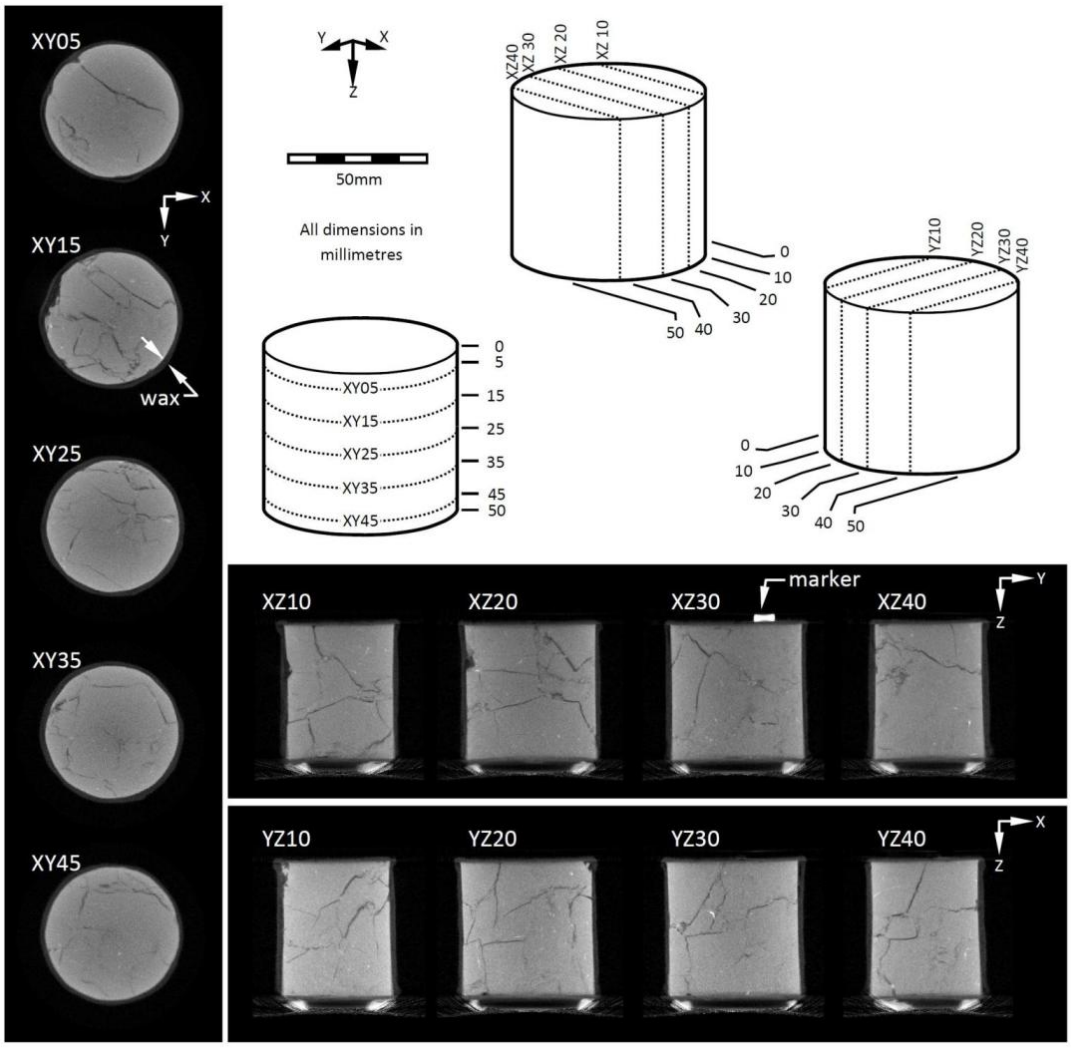

(c) Specimen CHV

Figure 4.1: *cont...* CT scan cross-sections of specimens

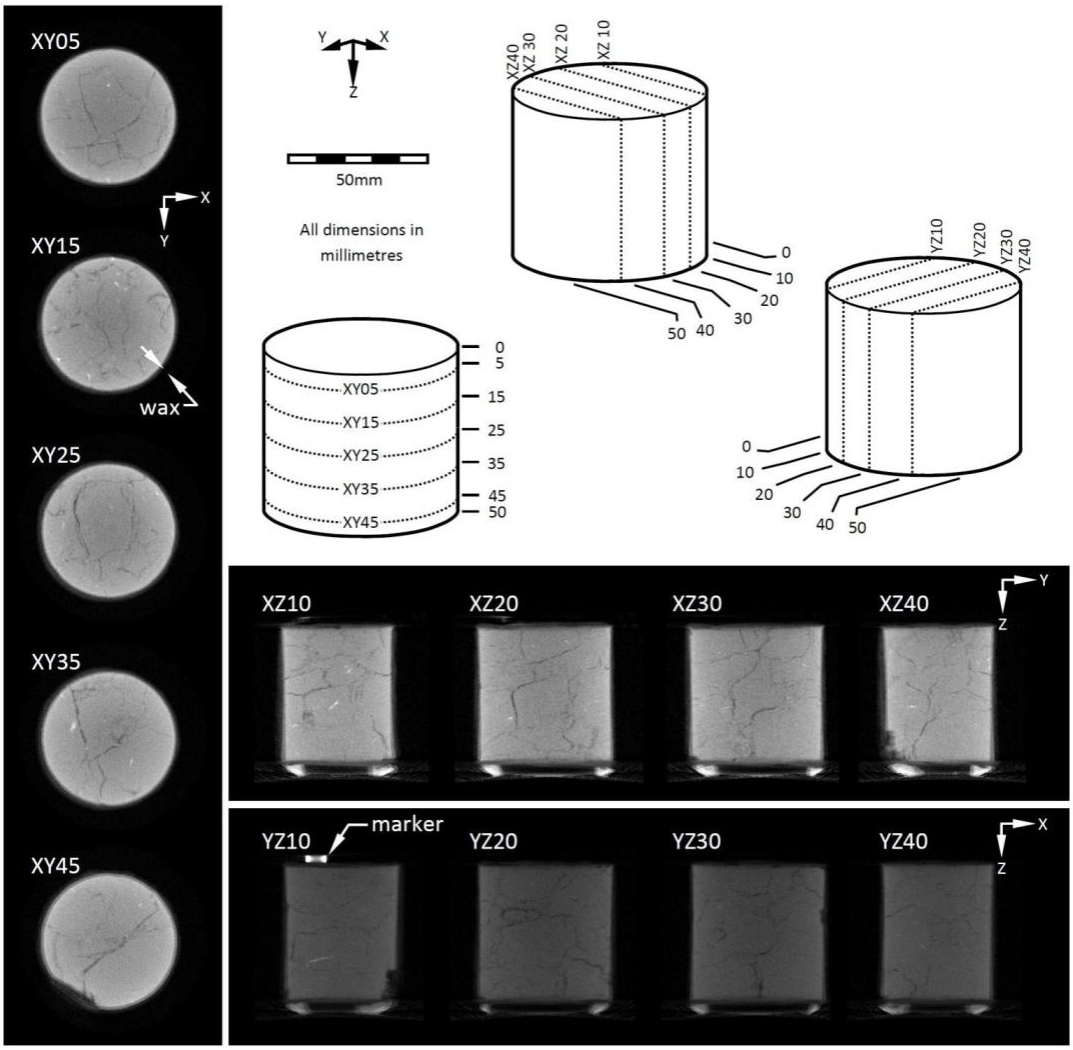

(d) Specimen CHH

Figure 4.1: *cont...* CT scan cross-sections of specimens

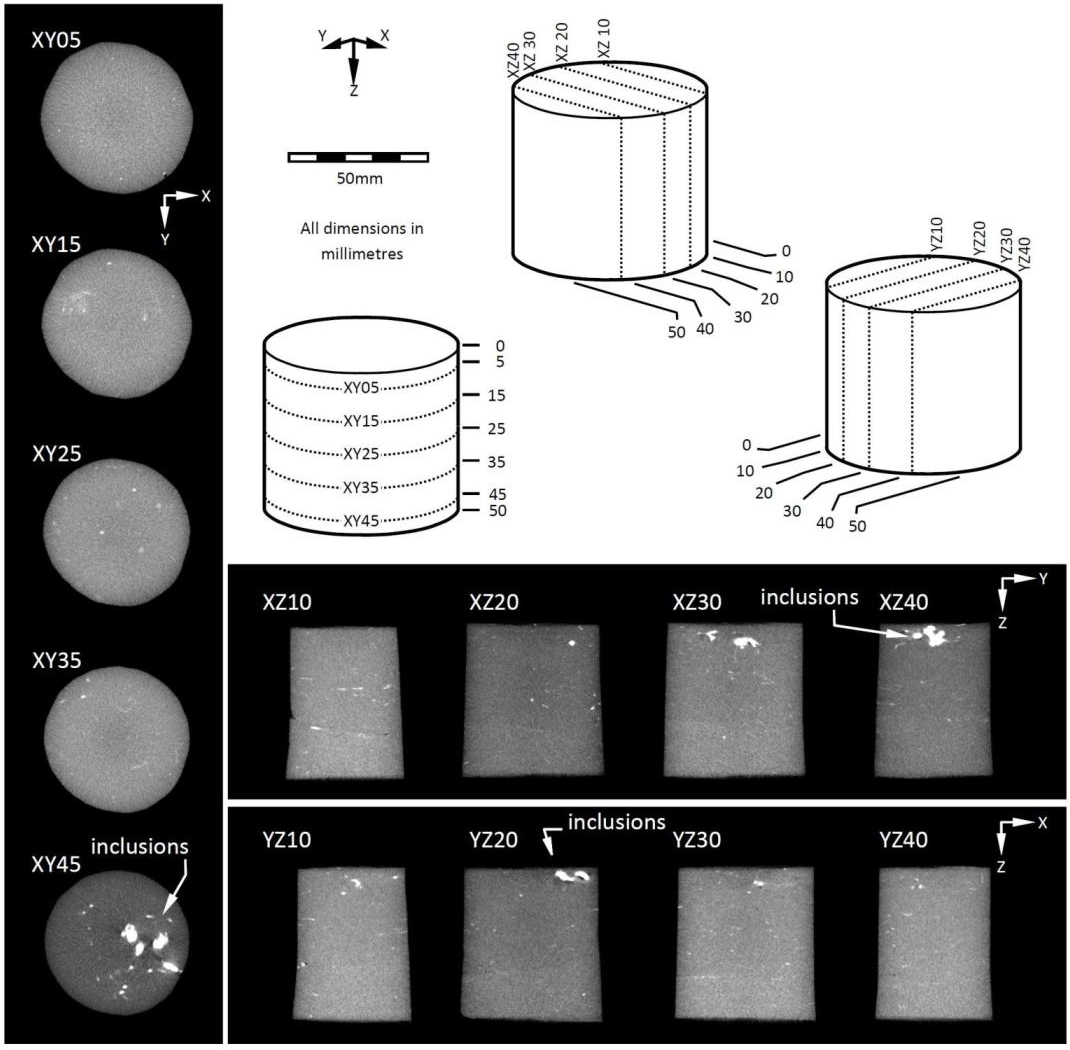

(e) Specimen BHV

Figure 4.1: *cont...* CT scan cross-sections of specimens

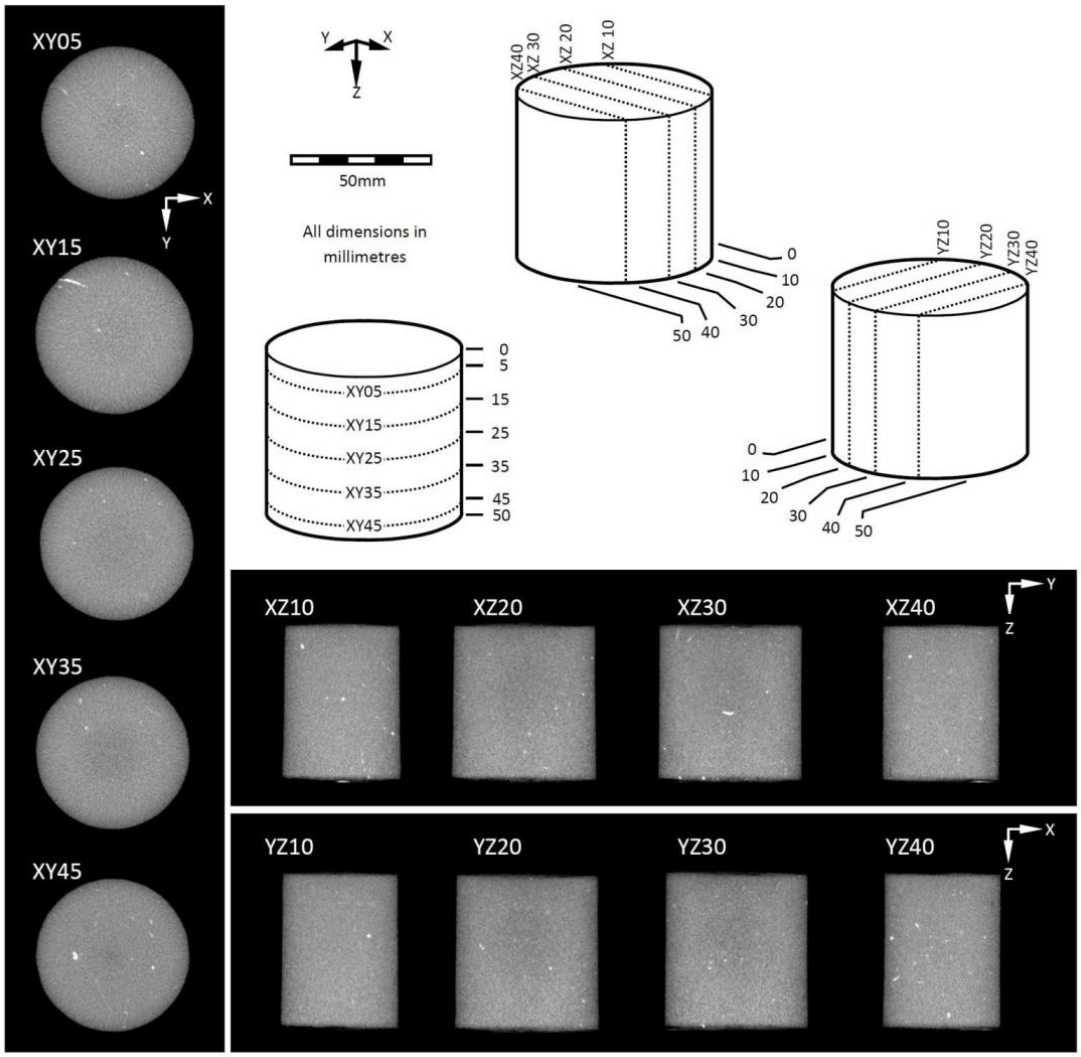

(f) Specimen BHH

Figure 4.1: *cont...* CT scan cross-sections of specimens

(a) Octant from block sample with protective layers

(b) Octant from block sample after removal of protective layers

Figure 4.2: Photographs of specimen preparation

(d) Applying wax and cellophane film

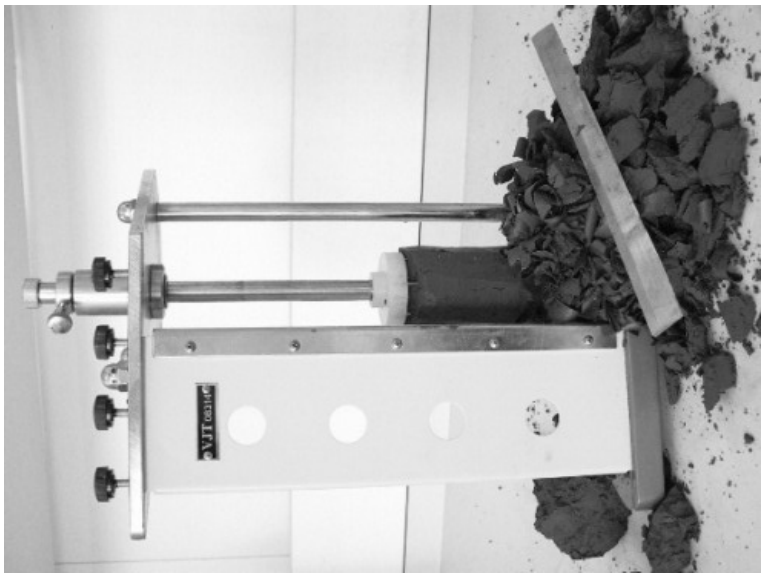

(c) Trimming diameter in lathe

Figure 4.2: *cont...* Photographs of specimen preparation

(e) Trimming ends in V-block

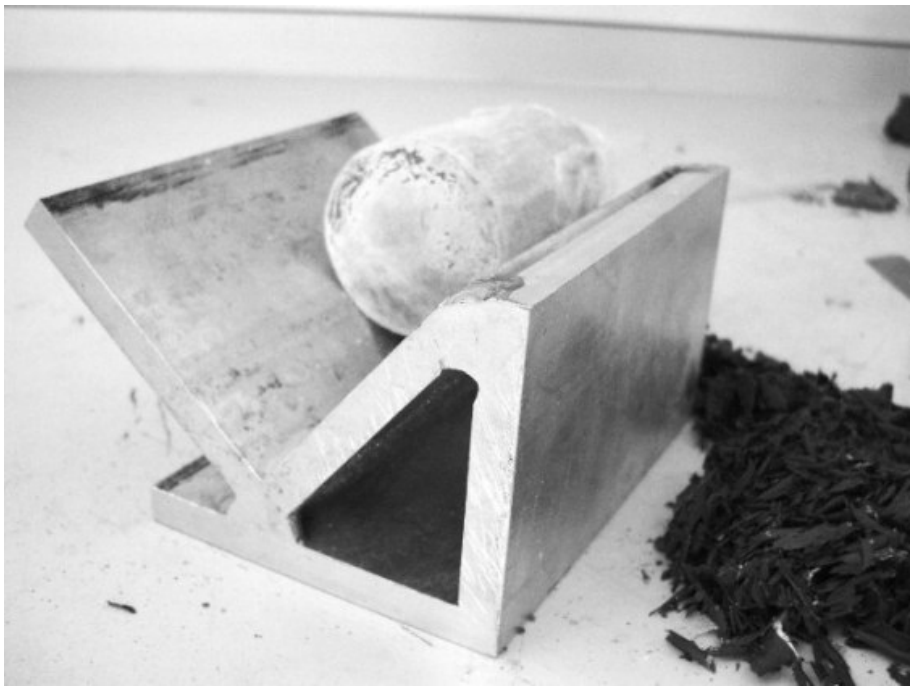

(f) Minimising moisture loss by wrapping

Figure 4.2: *cont...* Photographs of specimen preparation

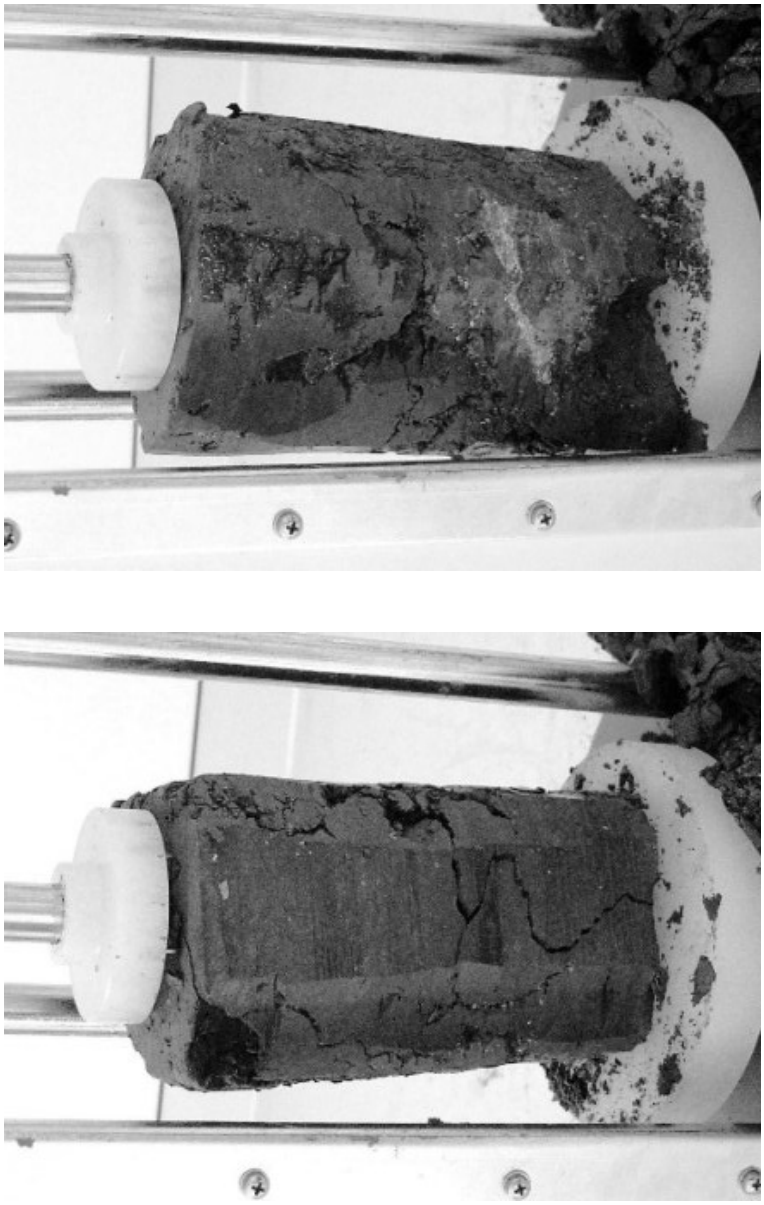

(a) Dense fissuring

(b) Hard inclusions

Figure 4.3: Photographs of inhomogeneities in Unit C specimens

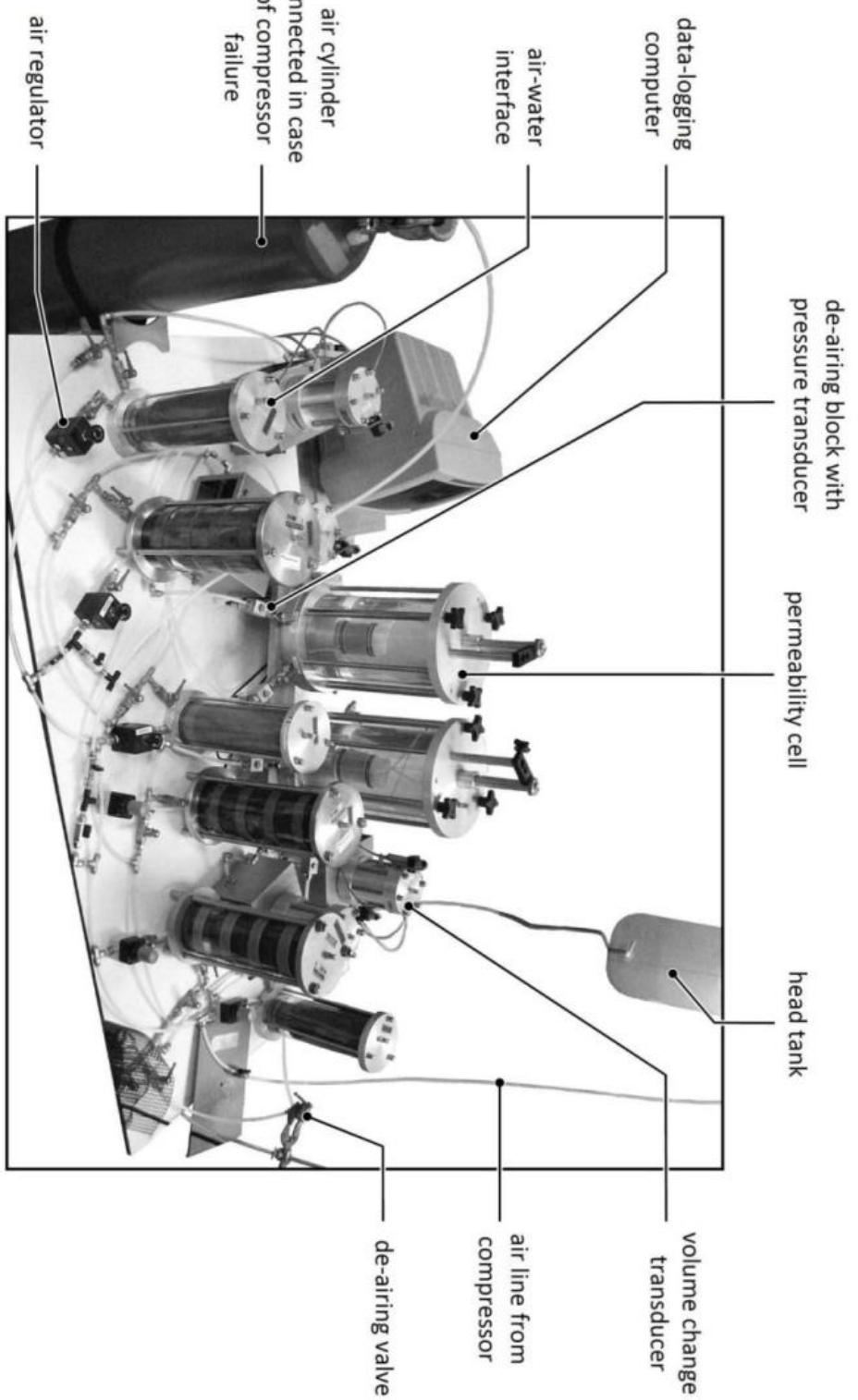

Figure 4.4: Photograph of permeability test apparatus

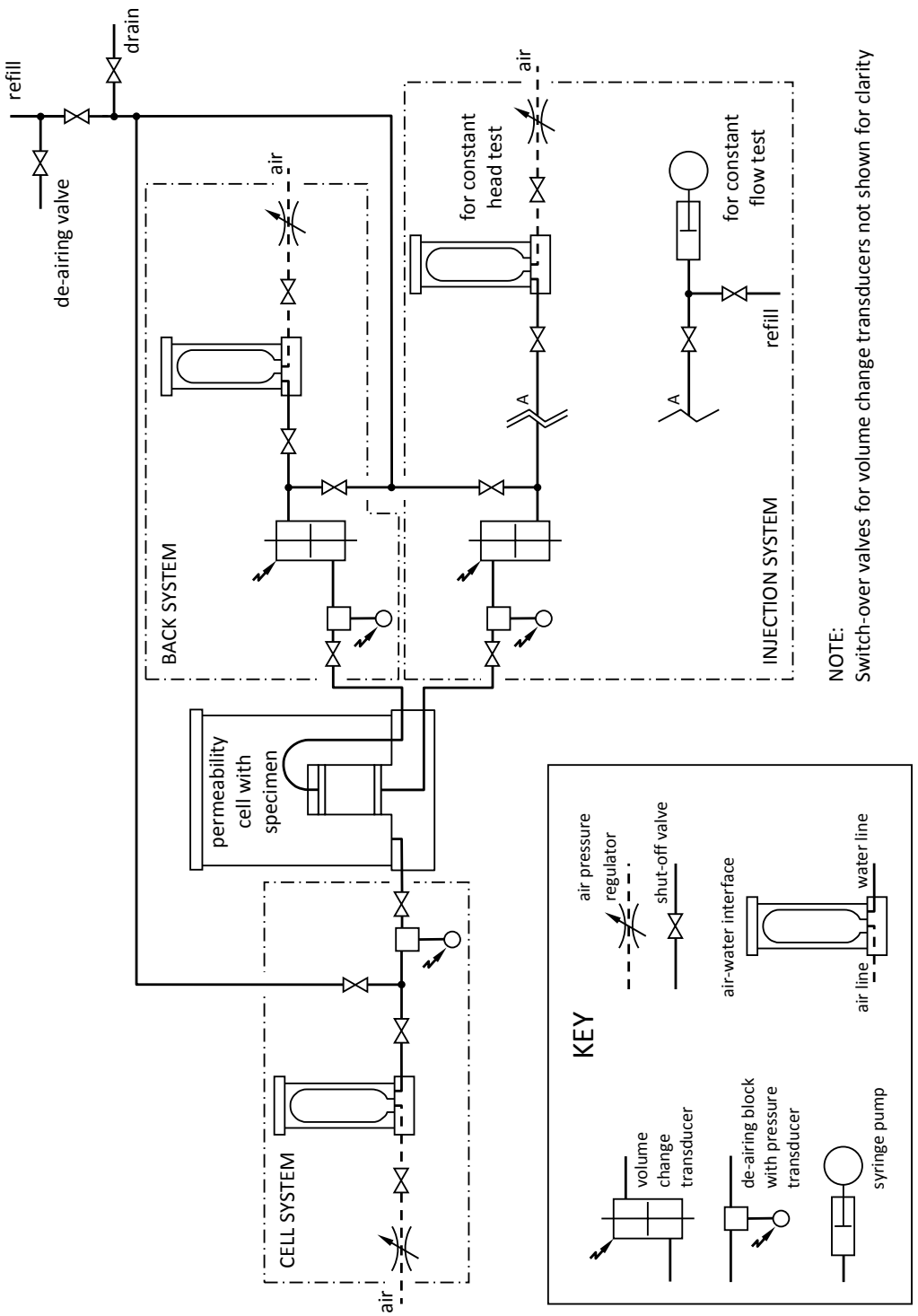

Figure 4.5: Schematic diagram of permeability test apparatus

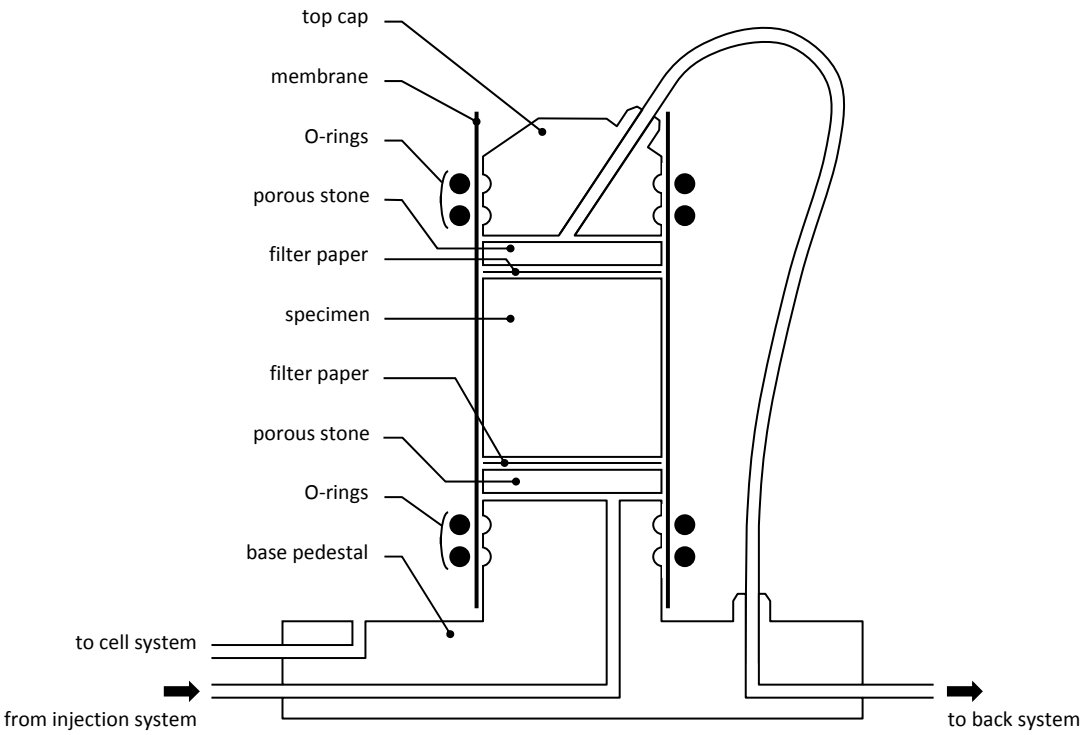

Figure 4.6: Schematic diagram of specimen set-up

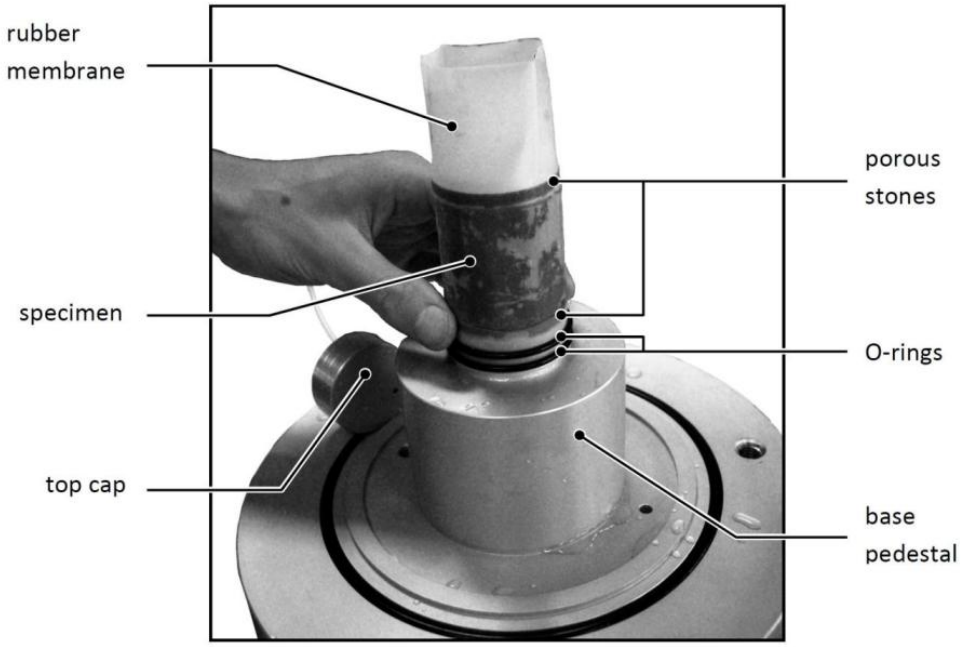

(a) Before removing air and placing top cap

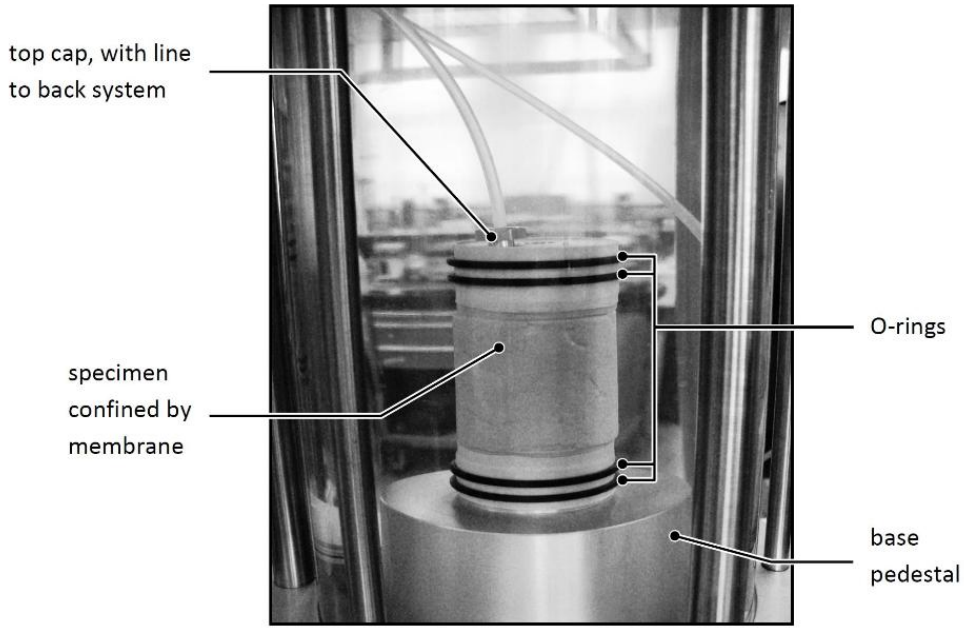

(b) After set-up is complete

Figure 4.7: Photographs of specimen set-up

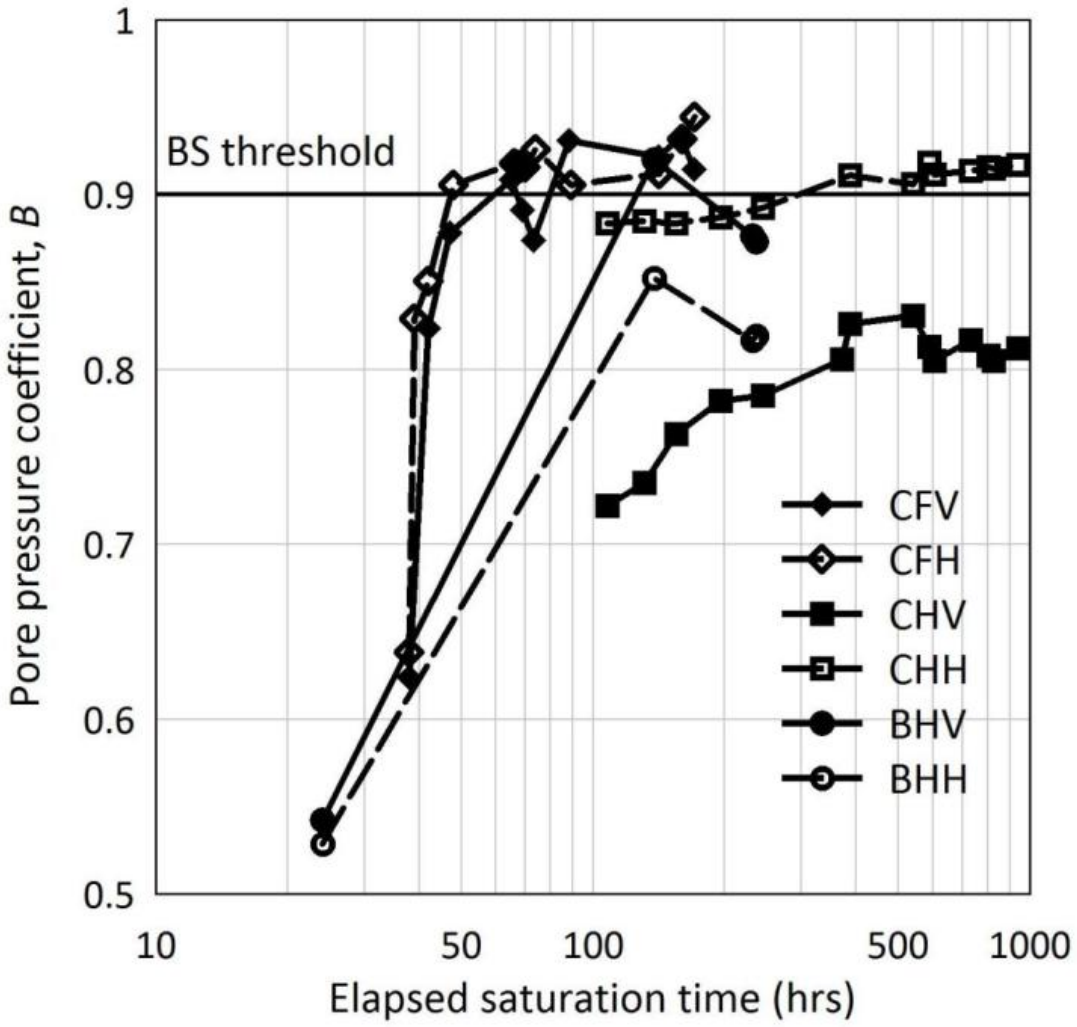

Figure 4.8: Variation of pore pressure coefficient during saturation

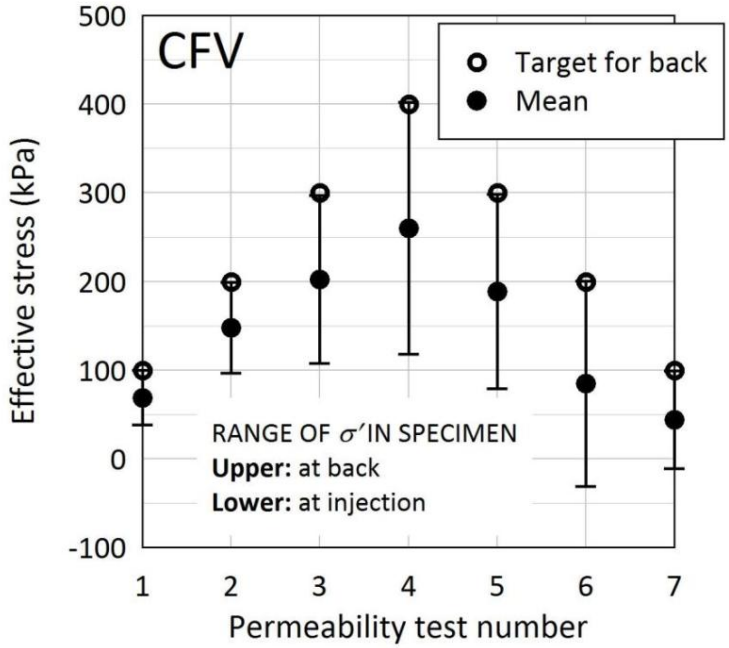

(a) Specimen CFV

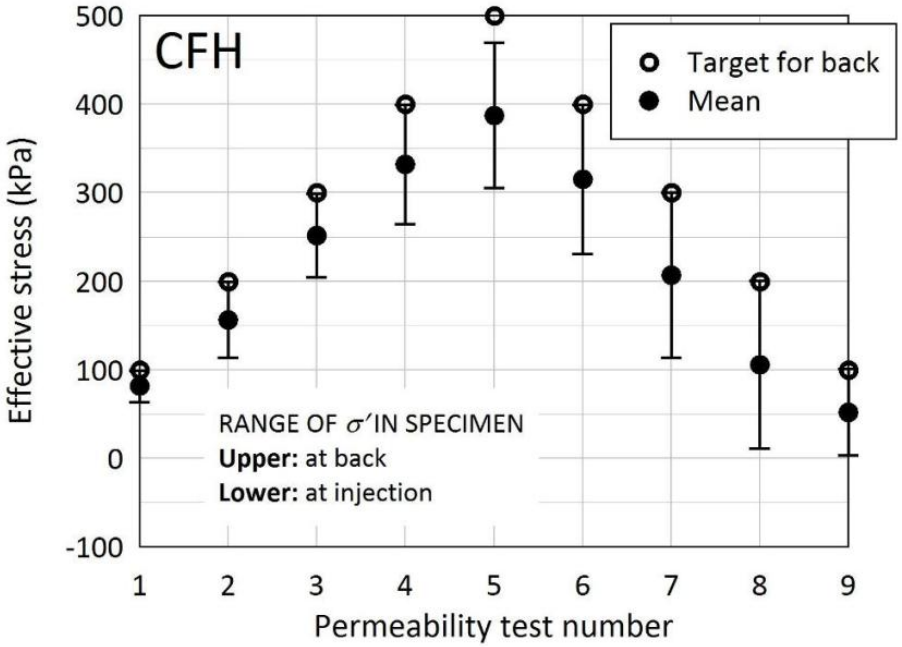

(b) Specimen CFH

Figure 4.9: Effective stresses applied during permeability tests

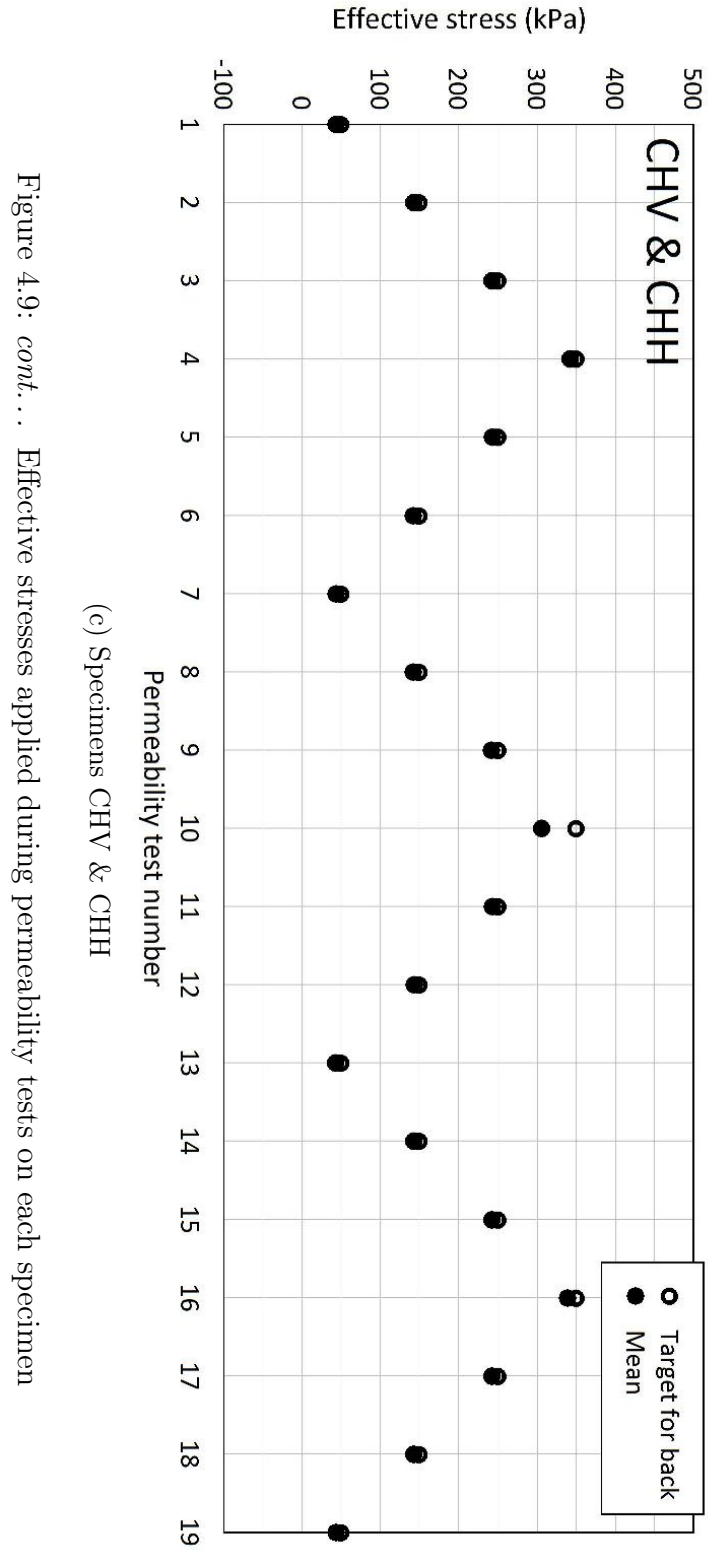

(c) Specimens CHV & CHH

Figure 4.9: *cont...* Effective stresses applied during permeability tests on each specimen

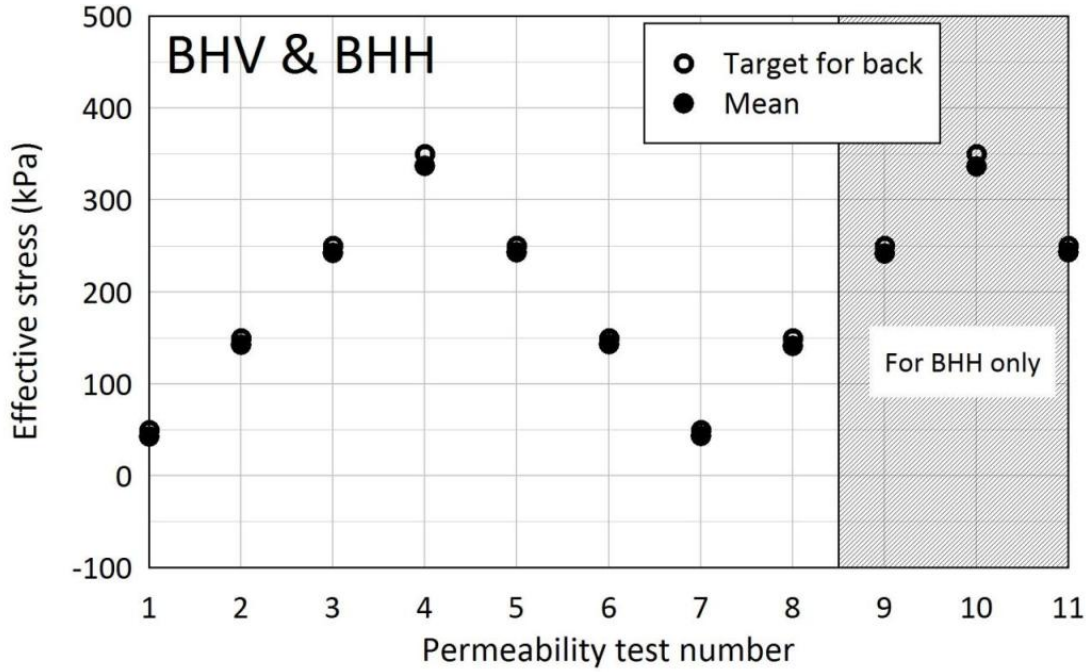

(d) Specimens BHV & BHH

Figure 4.9: *cont...* Effective stresses applied during permeability tests on each specimen

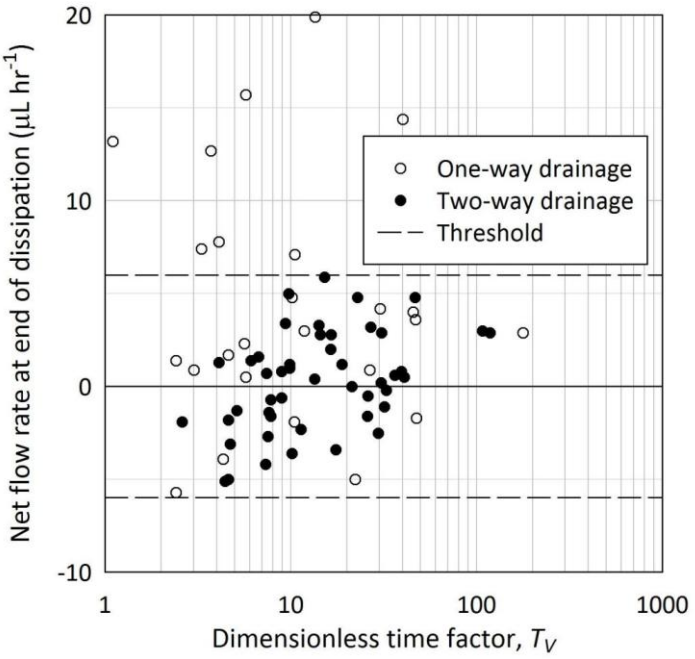

Figure 4.10: Net flow rates after completion of consolidation and swelling

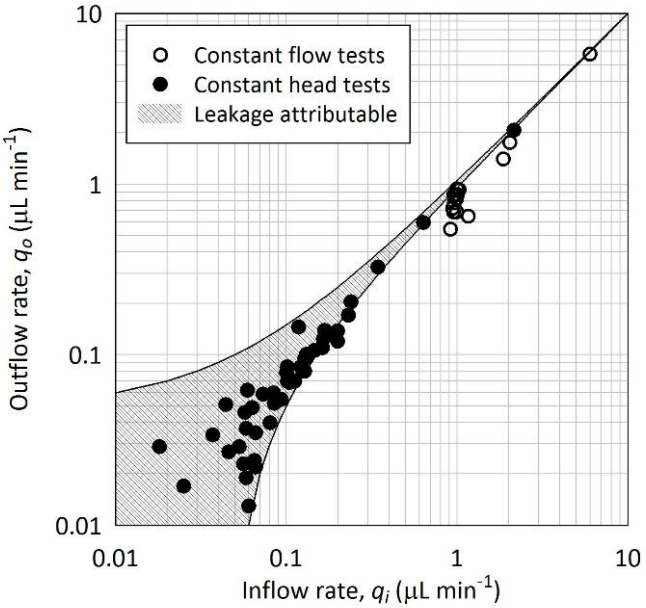

Figure 4.11: Inflows and outflows during permeability measurements

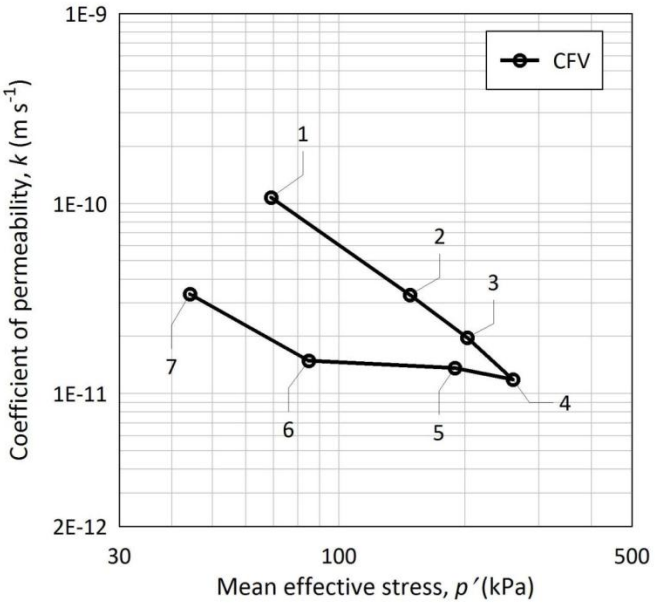

(a) Specimen CFV

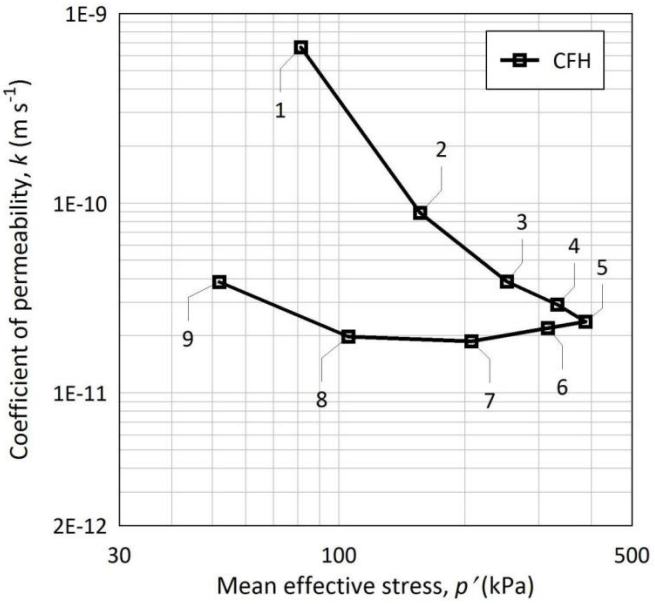

(b) Specimen CFH

Figure 4.12: Variation of permeability with effective stress

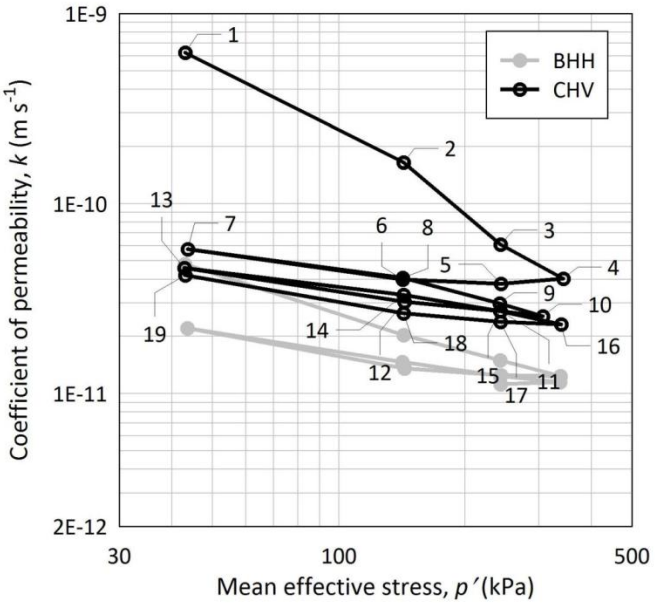

(c) Specimen CHV

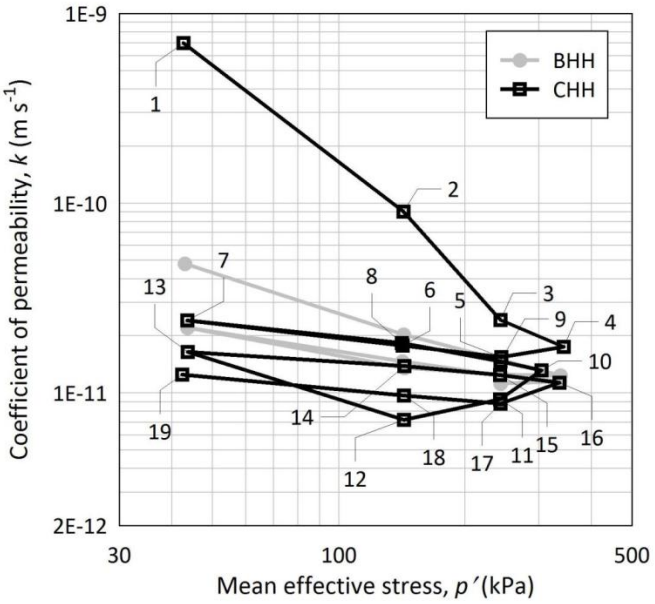

(d) Specimen CHH

Figure 4.12: *cont...* Variation of permeability with effective stress

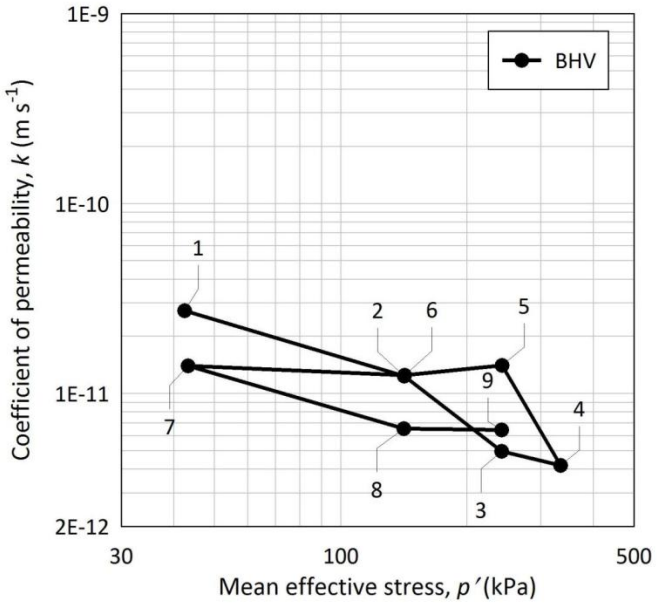

(e) Specimen BHV

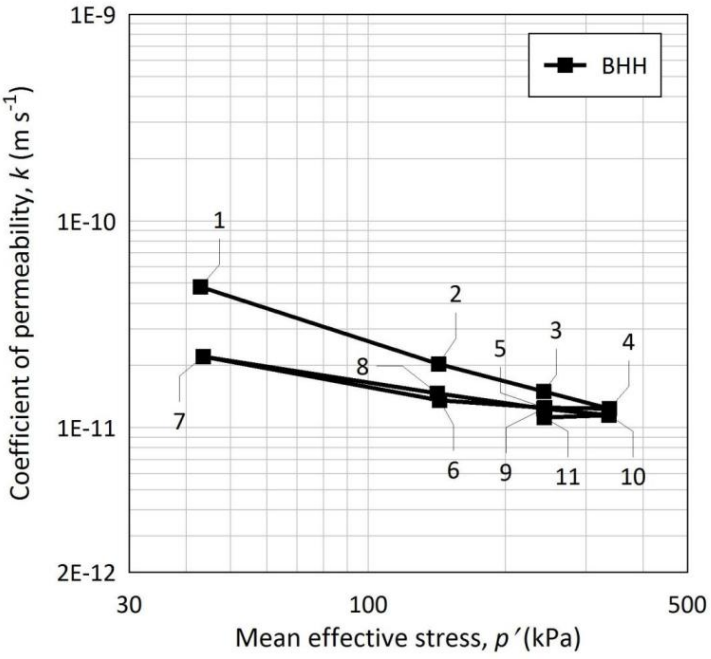

(f) Specimen BHH

Figure 4.12: *cont...* Variation of permeability with effective stress

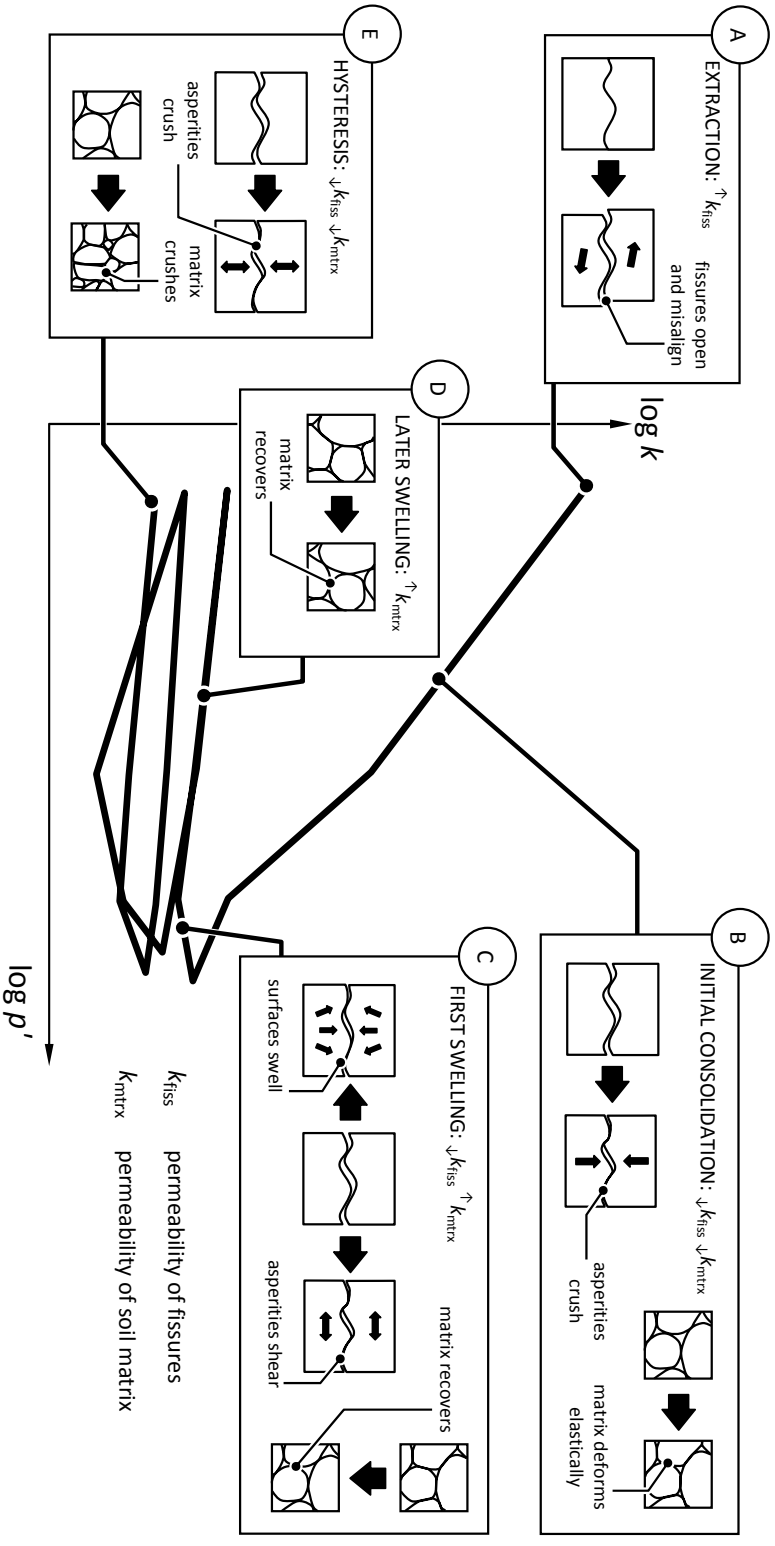

Figure 4.13: Permeability–stress theory for fissured clay

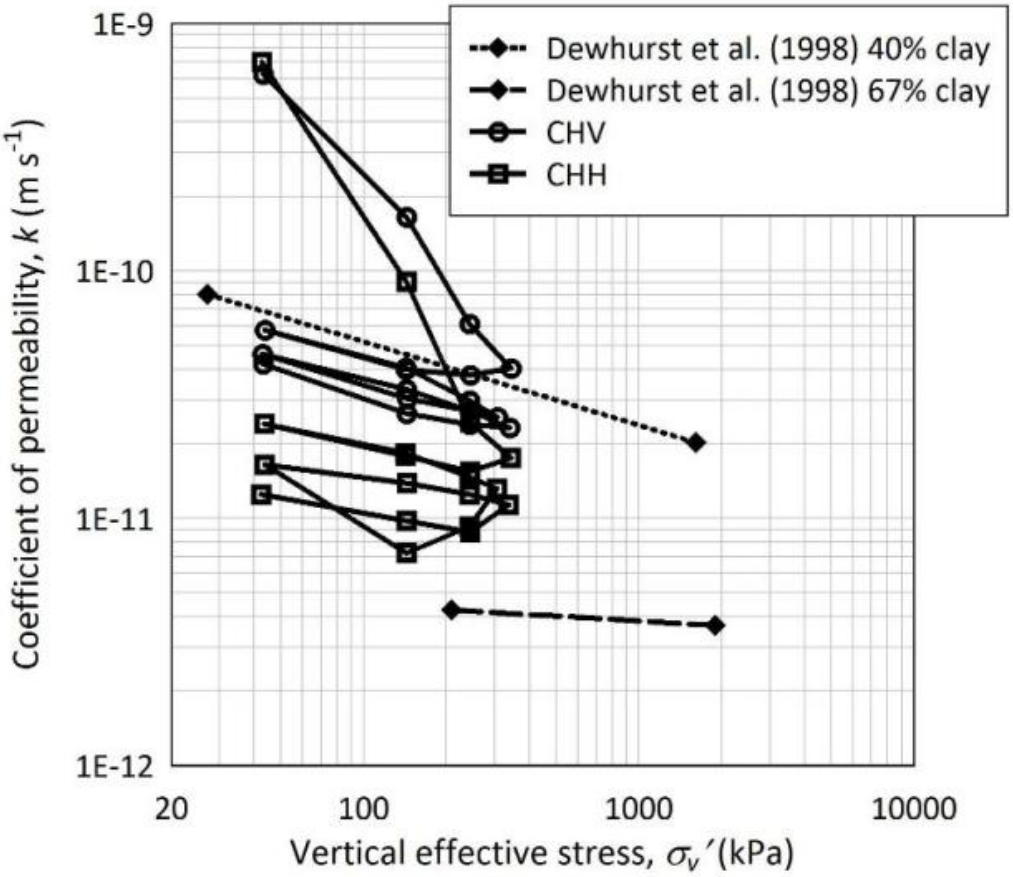

Figure 4.14: Comparison of observed permeabilities with Dewhurst *et al.* (1998)

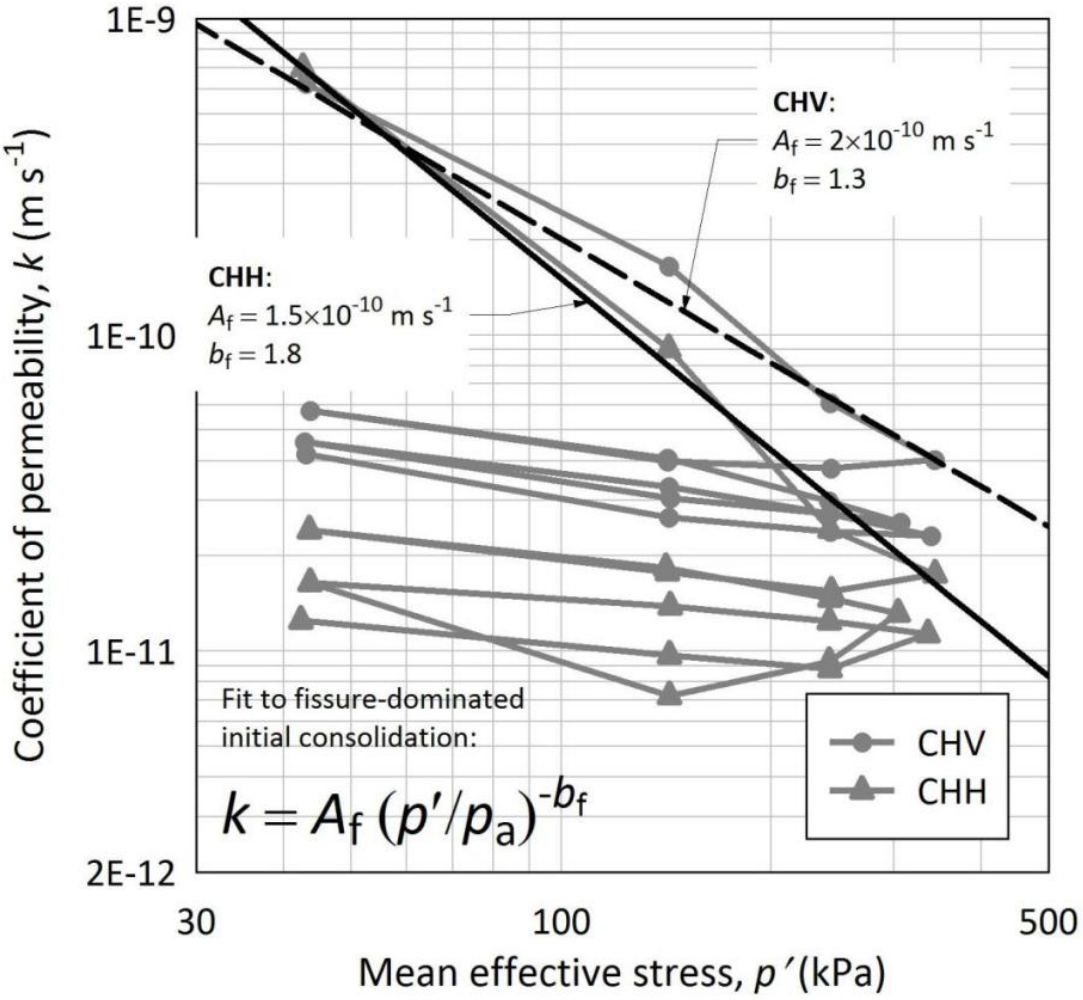

(a) During initial consolidation for specimens CHV & CHH

Figure 4.15: Permeability–stress relationships from experimental data

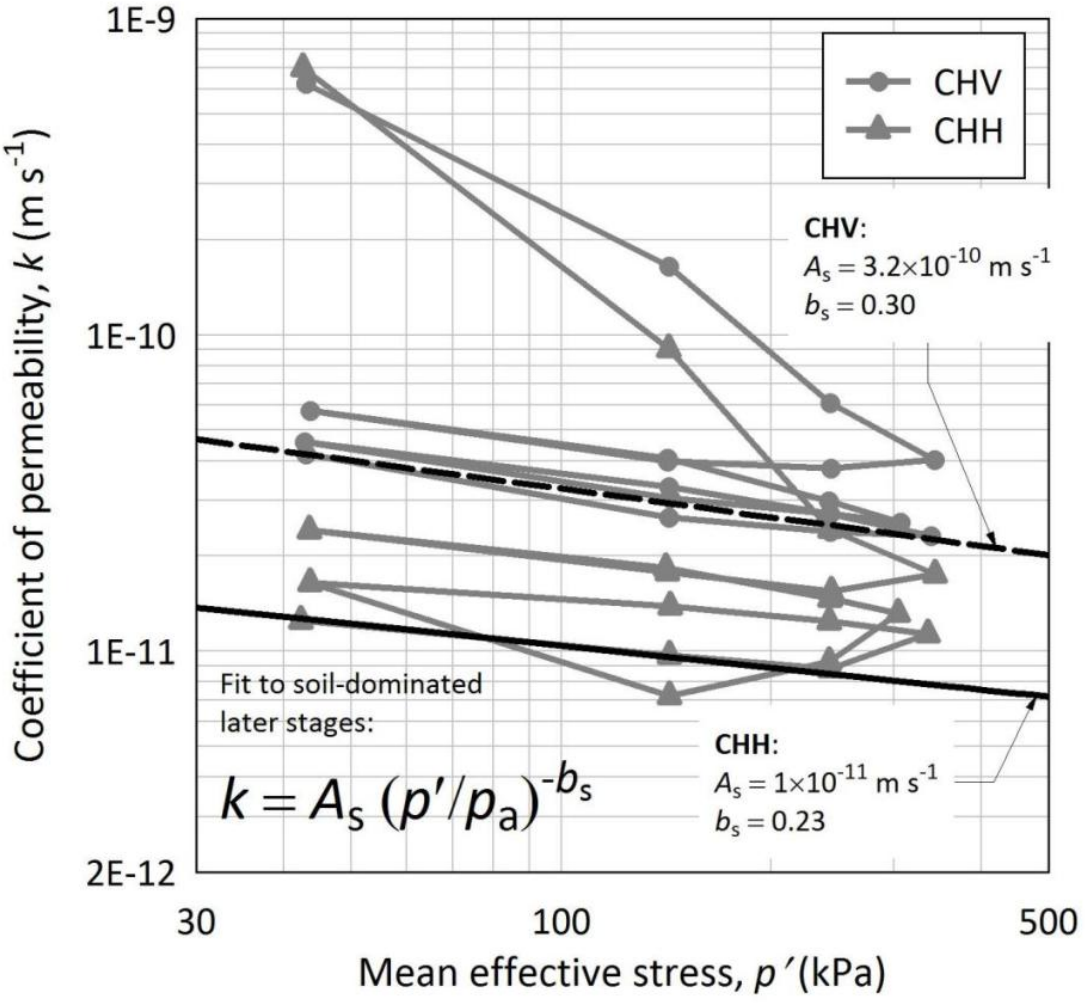

(b) After initial consolidation for specimens CHV & CHH

Figure 4.15: *cont...* Permeability–stress relationships from experimental data

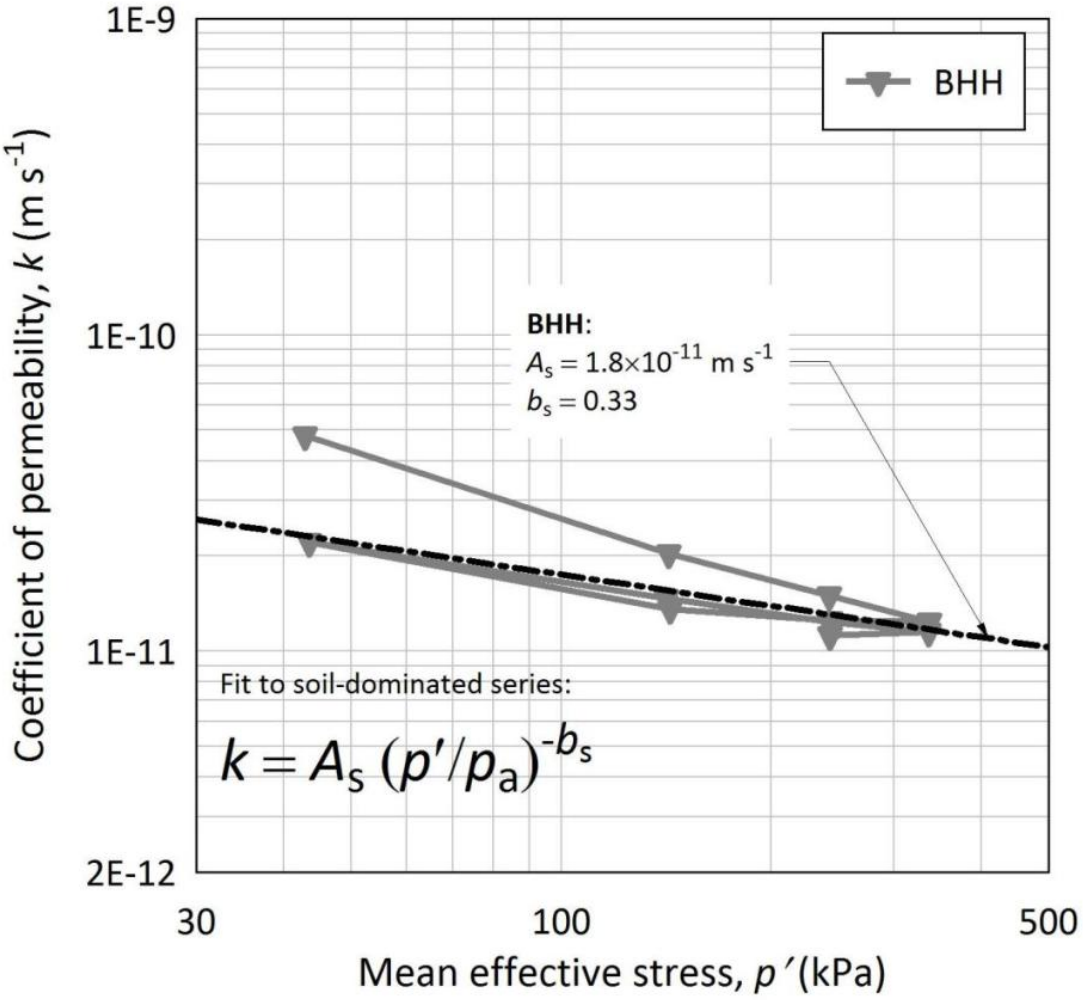

(c) After initial consolidation for specimen BHH

Figure 4.15: *cont...* Permeability–stress relationships from experimental data

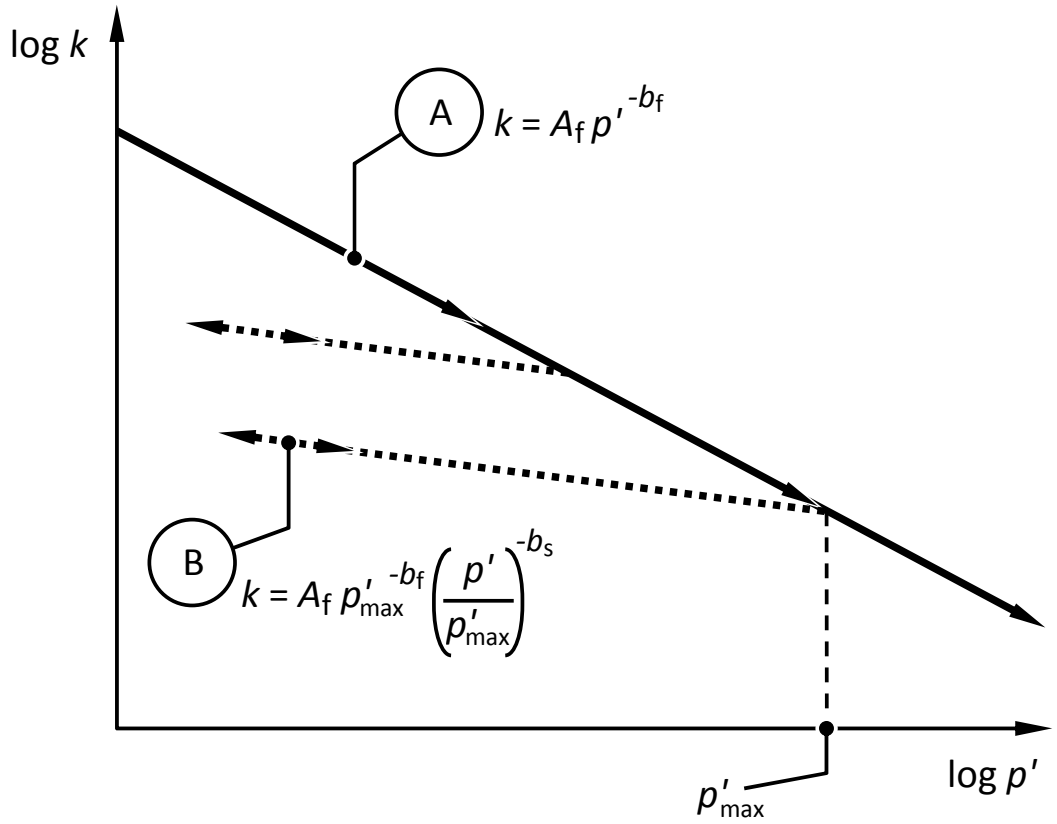

Figure 4.16: Permeability–stress mathematical model for fissured clay

Chapter 5

Characterisation of tunnel grout

5.1 Introduction

Most tunnel linings act as drains (Harris, 2002; Ward & Pender, 1981), and so lining permeability greatly influences post-construction movements. Furthermore, the permeability of the lining is likely to vary around its circumference, depending upon the location of joints and gaps. This can drastically alter regions of consolidation and swelling in the soil (Wongsaroj, 2005). However, little is known concerning the distribution of permeability around the circumference.

A key contributor to this uncertainty is the permeability of grout injected between the tunnel lining and the soil. The grout can have one of two effects, depending upon its permeability relative to the soil: a more permeable grout facilitates water ingress by acting as a circumferential or longitudinal flow path toward joints and gaps, whereas a less permeable grout impedes water flow by acting as a drainage barrier. To identify which behaviour is occurring, grout samples extracted from London Underground tunnels were characterised with the following four tests:

- Constant-flow rate permeability tests investigated permeability.
- Mercury intrusion porosimetry (MIP) investigated porosity.
- Scanning electron microscopy (SEM) investigated microstructure.
- X-ray diffraction (XRD) investigated mineral composition.

Better knowledge of the grout permeability would help in estimating the lining conductivity to apply in the prediction method of Chapter 8.

5.2 Sample details

The grout samples were kindly provided by Peter Wright from Tube Lines: the consortium responsible for maintaining the London Underground deep-tube tunnels. As shown in Figure 5.1, the grout was cut as discs during horizontal corings drilled from within the tunnel; they usually fractured during coring. The rarity of extracting such samples presented a unique opportunity to perform tests on the grout.

Table 5.1 presents the origins of each grout sample, illustrating extraction from a range of deep-tube tunnels, with most specimens dating from the early 20^{th} century. The origin of sample NK is unknown since it was not labelled before storage. The table also presents the colour and hardness of freshly-cut faces for each sample. Sample BB is distinctly different, being harder, and with a darker and greyer appearance.

5.3 Permeability tests

5.3.1 Test procedures

A constant flow-rate test was used to measure permeability. The set-up is identical to that described in Section 4.3.2 for the London Clay tests, with the apparatus set-up as shown in Figure 4.5.

Before mounting inside the cell, the grout specimens were first soaked in de-aired water for at least 30 minutes to minimise undissolved air. The grout specimens were then set-up like the London Clay specimens, described in Section 4.3.2.

The specimens were left to saturate in the permeability cell overnight before conducting the constant-flow test. An effective stress of 200kPa was applied to prevent flow between the specimen and the membrane. Table 5.2 presents details of each permeability test.

The inlet and outlet flow rates were monitored to check for leakage through the membrane. Table 5.2 notes that leakage occurred in three tests: S02, S06 & S18, indicated by the mean flow rate through the specimen being significantly greater than that applied by the syringe pump; results from these three tests were therefore disregarded.

The permeabilities of the three sample BB specimens (S20–S22) were so low that flow was forced between the membrane and specimen; this is indicated by the excessive hydraulic gradient recorded in Table 5.2 for these tests. The measured permeabilities therefore provide an upper bound for the specimen permeability.

Since the grout permeability was initially unknown, the minimum attainable flow rate of 1μL min^{-1} was applied to the first specimen (S01) to ensure against an excessive hydraulic gradient. As tests progressed, the applied flow rate was gradually stepped up to 4μL min^{-1}, to reduce the time required for the injection pressure to reach equilibrium. The flow rate could safely be increased since the hydraulic gradients developed were not excessive, reaching a maximum of 45. The minimum flow rate of 1μL min^{-1} was once again applied in specimens S21 & S22, which exhibited extremely low permeabilities, to minimise the hydraulic gradient induced.

5.3.2 Specimen preparation

Cylindrical specimens were cut from the grout discs. Specimen height was limited by the disc thickness, which varied between 10 and 24mm; the specimens were cut to the smallest possible diameter—38mm—so that specimen thickness could be maximised. The cylinders were orientated to measure permeability for radial flow into the tunnel.

A water-cutter was first used to cut oversized cylinders from the discs. The specimens were then turned to the required diameter of 38mm in a metal-working lathe, in which the end faces were also squared. During preparation, some of the specimens fractured on a plane running through the disc; this plane of weakness could be due to delays between stages of grout injection. Figure 5.2 illustrates some prepared specimens; some planes of weakness are discernable on the circumference of some specimens as distinctive layering.

Details of each specimen are tabulated in Table 5.2. The number of specimens cut from each sample depended upon the sample size and the degree of fracturing, which caused some specimens to disintegrate during manufacture. The density of each specimen was determined from measurements of dimensions and mass.

5.3.3 Results & analysis

Figure 5.3 plots the coefficient of permeability for each specimen against its density. The clustering of data points for specimens from the same sample confirms the reliability of both density and permeability measurements. Permeability also correlates well with density: permeability reduction accompanies an increase in density.

The permeabilities of the sample BB specimens—which are upper bounds—were at least two orders of magnitude less than that of the other samples. The specimens were also about 50% more dense.

Superposed on Figure 5.3 is the range of permeabilities for London Clay measured in Chapter 4. The range is divided into fissured and unfissured clay, taken from test series CHH and BHH respectively; series CHH records the highest reliable permeability measurement for fissured clay, whilst series BHH is the most reliable series for unfissured clay.

Also superposed on Figure 5.3 is the range of in-situ horizontal permeabilities for London Clay, taken from Hight *et al.* (2007) (see Figure 7.10). To represent clays at tunnelling depths, the range ignores the near-surface measurements at Guildford by Hutchinson (1984).

Except for sample BB, all of the grout samples exhibited greater permeabilities than the unfissured London Clay tested in Chapter 4, and exhibited permeabilities comparable to both the fissured London Clay and the in-situ permeabilities collated by Hight *et al.* (2007).

In general, the grout from these samples can be considered more permeable than the London Clay; it must be considered that for tunnel construction, the fissure permeability is likely to be relative low, due to soil stresses closing the fissures. Hence, out of the London Clay tested in Chapter 4, the unfissured range should be taken as more representative of the London Clay during the consolidation

period. Also, the in-situ permeabilities from Hight *et al.* (2007) were measured horizontally, so the equivalent isotropic permeability for London Clay would be lower due to anisotropy.

Being more permeable than the London Clay, the grout would therefore act as a flow path into the lining, facilitating flow into joints and gaps around the circumference.

Providing upper bounds for permeability, the data points for sample BB suggest a permeability lower than unfissured London Clay. This grout therefore acts as a flow barrier, obstructing flow into the lining.

5.4 Mercury intrusion porosimetry

5.4.1 Test procedures

Mercury intrusion porosimetry (MIP) characterises the pore space of a porous specimen by forcing mercury into the empty pores under pressure. With a high surface tension, the mercury requires a force to penetrate the pores. Assuming the pore opening to have a circular cross-section, the pressure P required to penetrate a pore opening of diameter D is given by the Washburn equation:

$$P = \frac{-4\gamma \cos\theta}{D} \tag{5.1}$$

where γ is the surface tension of mercury, and θ its contact angle; the negative sign of the equation arises because $\theta > 90°$. Recording the intruded volume of mercury as the pressure is increased therefore provides information about the pore size distribution. (Webb & Orr, 1977)

The Micromeritics AutoPore IV 9500 series porosimeter was used. The specimen was placed inside the sample cup of the porosimeter, which was first evacuated so that compression of air in the pores did not resist the intrusion of mercury. The sample cup was then filled with mercury, whose pressure was steadily increased in increments from 0.1psi (690Pa) to 30,000psi (210MPa) of absolute pressure, to infiltrate the pores of the specimen. At each increment during this intrusion cycle, the pressure was maintained for 40s to allow the flow of mercury to curtail.

The intrusion cycle was followed by an extrusion cycle, where the pressure was ramped down in a similar fashion, allowing the mercury to re-emerge. The porosimeter automatically recorded the intruded and extruded volumes at each pressure increment. By assuming a cylindrical pore shape, the porosimeter was able to generate plots relating pore size diameter, area and volume. Porosity was also calculated.

5.4.2 Specimen preparation

The cuboid specimens, pictured in Figure 5.4, were cut from each sample using a tile saw. The faces were finished with emery paper so that typical dimensions were less than 1cm, to fit inside the sample cup of the porosimeter. Six specimens were prepared and tested, one from each of the samples listed in Table 5.1.

5.4.3 Results & analysis

Specimen porosities are presented in Figure 5.5, showing that the porosity of sample BB was 4–5 times lower than the other samples, which have porosities of around 40–50%. This agrees with observations noted earlier of a higher density and lower permeability for sample BB.

Figure 5.6 presents plots of log differential intrusion $dV/d(\log D)$ versus pore diameter D for each sample. Such a plot indicates the pore size distribution: ranges of pore size containing the same volume in the specimen will plot as peaks with equal areas. The distribution of area on the graph therefore indicates how pore volume is distributed in terms of pore size. Log differential intrusion is given per unit mass of specimen, and therefore has units of mL g^{-1}.

Consistent with its lower porosity, sample BB demonstrated less intruded volume than the other samples, indicated by the smaller total area of the peaks. The sample exhibited two distinct pore sizes: one at 50nm, and the other almost 2000 times larger, at 90μm. The smaller pore size might correspond to the grain size, whilst the larger pore size might relate to gaps between agglomerates of grains; the smaller pore space is observable in the SEM images of Figure 5.7. Pore size in the other samples fell in the range 80–120nm; the existence of just one peak for these samples indicates a more homogeneous structure than sample BB.

5.5 Scanning electron microscopy

5.5.1 Test procedures

A JEOL 5800 LV SEM machine was employed to produce magnified images of the grout surface by scanning electron microscopy (SEM). Specimens from five of the samples listed in Table 5.1 were scanned: BB, CH135, CH142, OS & TT; all material from sample NK—the smallest sample—had been consumed to make samples for the preceding tests.

The specimens were scanned in different forms: the specimen from sample CH135 was formed as a smooth thin tablet, with sub-centimetre dimensions to fit on the specimen stub of the SEM machine, whilst the other four specimens—BB, CH142, OS & TT—were scanned as powder specimens. A magnification factor of $\times 5000$ was adopted.

Two methods of scanning were trialled:

1. **Back-scattered electrons** The tablet-shaped specimen from sample CH135 was scanned using back-scattered electrons: fast-moving electrons from the scanning beam that reflect back from the surface. This was performed under low-vacuum conditions; the long period of pumping required to attain a high vacuum proved to be impractical.

2. **Secondary electrons** The powdered specimens—BB, CH142, OS & TT—were scanned using secondary electrons: slow-moving electrons emitted from the scanned material as electrons from the beam repel them away. Images produced from secondary electrons have greater depth of field than those produced from back-scattered electrons, and depict the 3-D surface topology more clearly. High-vacuum conditions were adopted, since air molecules spread and attenuate the slow-moving secondary electrons.

5.5.2 Specimen preparation

Two methods of specimen preparation were trialled to ensure that the preparation method would not influence the images:

1. The tablet-shaped specimen from sample CH135 was manufactured using a tile saw and emery paper. The specimen was attached to an SEM stub using conductive carbon tape, enabling conduction of electrons away from the scanned surface. The stub, together with the specimen, was then sputter-coated with platinum; the conducting platinum surface prevented accumulation of charge from the electron beam, and improved image resolution by enhancing electron emission.

2. The other four specimens—AH, CH142, OS & TT—were ground to a fine powder using an agate pestle and mortar. Four pieces of conductive carbon tape were fixed to a stub, and the four powders from each sample were sprinkled on each piece. Excess powder was tapped off, taking care not to contaminate the other specimens. The entire stub—with the powders on top—was then sputter-coated with gold.

During specimen preparation, great care was taken to prevent cross-contamination between samples: tools were regularly cleaned with solvent, and specimens immediately sealed in clean containers after preparation.

5.5.3 Results & analysis

Figure 5.7 present the SEM images for all specimens.

Sample BB (Figure 5.7a) mainly consisted of plate-like crystals, which were absent in the other samples. These are likely to be portlandite (calcium hydroxide) crystals, which was confirmed in X-ray diffraction tests described later in Section 5.6. The highly fractal agglomerates observable in the other samples featured needle-like crystals, and could be hydrated calcium silicates. (Lea, 1970)

Pore size distributions from the MIP tests (Figure 5.6) indicate a pore diameter of around 0.1μm in all specimens; this pore size could be observed in all SEM images. The pore size distributions indicate no larger pore spaces for specimens CH135, CH142, OS & TT, yet larger spaces are evident in the SEM images for powder specimens CH142, OS & TT (Figures 5.7c–e). Since the tablet-like specimen CH135 exhibit no such larger spaces in Figure 5.7b, this suggested that these larger spaces were formed between particles broken during the grinding required

for powder preparation. These larger spaces are also absent in sample BB (Figure 5.7a); the harder calcium hydroxide in this sample may have resisted breakage better, resulting in larger particles.

The calcium hydroxide crystals in sample BB form relatively large and dense structures which extend beyond the field of view in Figure 5.7a, indicating that the structures must be larger than 40μm. Indeed, Figure 5.6 indicates a larger pore space for sample BB—of the order of 0.1mm—which might indicate the extent of these structures.

The dense plate-like structure of sample BB contrasts with the porous fractal crystal clusters in the other samples, illustrated in Figures 5.7b–e. This difference in structure explains the differences in permeability, porosity and density noted earlier.

5.6 X-ray diffraction

5.6.1 Test procedures

X-ray diffraction (XRD) was used to identify compounds present in the samples using a Bruker D8 X-ray diffractometer. During XRD, X-rays are emitted from a copper target when it is bombarded by electrons. The copper target emits a characteristic spectrum of X-ray wavelengths, which is filtered to monochromatic radiation with a wavelength of 1.5418Å. For these XRD scans, the tungsten filament used to produce the electrons was supplied with a current of 40mA and a voltage of 40kV.

An XRD pattern is constructed by inclining the tube emitting the X-rays at different angles of incidence to the sample. At each angle of incidence, the intensity of diffracted radiation is measured with a detector. The detector is also inclined at the same angle, since the angles of incidence and emergence are equal. Constructive interference between the diffracted rays produces peaks in intensity at certain angles. Each lattice structure has a unique pattern of peaks, enabling compounds in the sample to be identified.

If the angle of incidence is θ, angles are usually expressed in terms of 2θ, since this is the total change in angle between incident and emergent rays. In these

scans, samples were scanned at angles of incidence $5° \leq 2\theta \leq 50°$, at increments of 0.049°. At each increment, the angle was maintained for 0.88s so that the detector could determine the intensity of the diffracted ray. This increment size and dwell time were sufficient to identify compounds present in each sample. Determination of weight fractions would have taken significantly longer—requiring smaller increments and longer dwell times—but this information was not required.

5.6.2 Specimen preparation

Specimens were prepared from five of the samples listed in Table 5.1: BB, CH135, CH142, OS & TT. There was insufficient material from sample NK to make a specimen, due to the small sample size.

The specimens were prepared as fine powders, to ensure homogeneity and to prevent crystalline grains from aligning in a preferred orientation. Specimens were ground with an agate pestle and mortar, and tools were meticulously cleaned between preparation of each sample, to eliminate cross-contamination. Each specimen was packed inside a sample holder, and the top surface made flush with the rim using a glass slide.

5.6.3 Results & analysis

The XRD patterns from each sample are compared in Figure 5.8. Phases were identified by comparing patterns of peaks—peak positions and relative intensities—with known characteristic XRD patterns for pure phases. These characteristic XRD patterns are stored in a database compiled by the International Centre for Diffraction Data (ICDD), who assigned each phase a characteristic ICDD number. The diffraction patterns were retrieved using the software PcPdfWin.

Three phases could confidently be identified:

- Portlandite, or calcium hydroxide, $Ca(OH)_2$
- Calcite, or calcium carbonate, $CaCO_3$
- Calcium sulphate hydrate, $CaSO_4.2H_2O$

Figure 5.8 shows the presence of portlandite only in sample BB, confirmed by the plate-like crystals observed in SEM (Figure 5.7a). Conversely, calcite and calcium sulphate hydrate is only evident in samples CH135, CH142, OS & TT.

It should be noted that the main hydration product of portland cement, tobermorite (consisting of calcium silicate hydrates), is highly amorphous and difficult to detect with XRD, which characterises crystalline phases.

5.7 Discussion

5.7.1 Review of observations

Before discussing the causes for the difference between sample BB and the other samples, CH135, CH142, OS & TT, the differences are first reviewed below:

Colour Sample BB was darker and greyer.

Hardness Sample BB was significantly harder.

Permeability The permeability of sample BB was around two orders of magnitude less.

Porosity Sample BB exhibited a porosity around 4–5 times less. Its pore size distribution suggested the presence of agglomerates, which were absent in the other samples.

Microstructure Sample BB exhibited a dense structure of plate-like portlandite crystals, whilst the other samples exhibited a more porous and open structure.

Composition Portlandite was present only in Sample BB, whilst calcite and calcium sulphate hydrate were present only in the other samples.

The discussion below presents how sample BB might represent an intact grout, whilst the grout in the other samples appears to have degraded.

5.7.2 Formation of portlandite

The XRD and SEM scans confirmed the presence of portlandite, $Ca(OH)_2$, in sample BB; this could have arisen from two sources:

1. **Hydration of lime** Lime (CaO) hydrates via the following process:

$$CaO + H_2O \rightarrow Ca(OH)_2 \tag{5.2}$$

2. **Hydration of Portland cement** In Portland cement, portlandite is produced by the complex hydration of calcium silicates. For instance, hydration of tricalcium silicate ($3CaO.SiO_2$) follows the simplified process (Lea, 1970):

$$2(3CaO.SiO_2) + 6H_2O \rightarrow 3Ca.2SiO_2.3H_2O + 3Ca(OH)_2 \tag{5.3}$$

The portlandite in sample BB is therefore expected as a hydration product in lime and cement grouts.

5.7.3 Formation of calcite

Calcite ($CaCO_3$) was identified in samples CH135, CH142, OS & TT by XRD. Calcite results from the carbonation of existing portlandite with carbonic acid (H_2CO_3). The carbonic acid forms when carbon dioxide dissolves in water. The carbonation reaction is:

$$H_2CO_3 + Ca(OH)_2 \rightarrow CaCO_3 + 2H_2O \tag{5.4}$$

Carbonation is highly feasible, since groundwater containing carbonic acid can permeate through the grout into the tunnel—carbonic acid would have been introduced as the rain water dissolves carbon dioxide in the air before seeping into the ground.

Carbonation can be beneficial: a mass increase accompanies carbonation due to absorption of carbon dioxide, which reduces porosity and permeability. The fine network of calcite crystals also provides more resistance to water flow, which also contributes to permeability reduction (Arandigoyen *et al.*, 2006). Furthermore, carbonation imparts greater strength to lime mortars (Lea, 1970).

Carbonation in samples CH135, CH142, OS & TT—but not in sample BB—explains the absence of portlandite and the presence of calcite in the former. However, these samples are also less dense, weaker and more porous than sample BB, contradicting the beneficial effects of carbonation mentioned above. The greater porosity observed in these samples must therefore be due to a further process, proposed below.

5.7.4 Weathering of calcite

The greater porosity observed in samples CH135, CH142, OS & TT can be explained by weathering of the calcite generated by carbonation. Acid present in the groundwater can transform the calcite into the more soluble calcium bicarbonate $Ca(HCO_3)_2$. The bicarbonate can then leach away with the groundwater, increasing the porosity of the grout. A continuing supply of carbonic acid could achieve this:

$$H_2CO_3 + CaCO_3 \rightleftharpoons Ca(HCO_3)_2 \tag{5.5}$$

It is likely that the bicarbonate leaches through the lining into the tunnel, as deposits are frequently observed inside the tunnel at seepage points, as shown in Figure 5.9. Here, contact with the air allows calcium carbonate to reform, following the reverse reaction of Equation 5.5. As a weak acid, dissolved sulphur dioxide can also cause leaching of calcite—the sulphur dioxide from air pollutants can dissolve in rain water, before seeping into the ground (Domone & Jefferis, 1994).

5.7.5 Sulphate attack

The presence of calcium sulphate hydrate ($CaSO_4.2H_2O$) indicates that sulphate attack has occurred in samples CH135, CH142, OS & TT. Calcium sulphate hydrate is produced when sulphuric acid $Na_2SO_4.10H_2O$ (aqueous sodium sulphate) attacks portlandite in the grout:

$$Ca(OH)_2 + Na_2SO_4.10H_2O \rightarrow CaSO_4.2H_2O + 2NaOH + 8H_2O \tag{5.6}$$

This could also explain the lack of portlandite in samples CH135, CH142, OS & TT, compared with sample BB. This reaction can consume all available portlandite,

given a constant supply of sodium sulphate in the groundwater and a continuous removal of sodium hydroxide (Lea, 1970). Collepardi (2003) suggests that the main hydration product, calcium silicate hydrate, may also be decalcified in this reaction.

Collepardi records that other kinds of sulphate attack can produce ettringite, thaumasite or brucite. However, these compounds are absent in the XRD patterns, indicating that these types of sulphate attack did not occur.

5.7.6 Origin of grouts

Table 5.1 shows that sample BB—exhibiting little degradation—originated from the Jubilee Line, which was constructed in the 1970s. The other samples—with degraded grout—were extracted from much older tunnels, constructed in the early 1900s. The older grout had clearly degraded, whilst the newer grout remained intact, suggesting the following explanations:

1. The grout degraded with time.

2. Grout technology had improved with time, such that the grout used for the Jubilee Line was more resistant to attack.

5.7.7 Summary of proposed degradation mechanisms

Samples CH135, CH142, OS & TT appear to be more degraded than sample BB. The presence of calcite and calcium sulphate hydrate in these samples indicates that carbonation and sulphur attack from acidic groundwater had taken place. The high porosity suggests that groundwater had also leached away much of the degradation products. The absence of portlandite in these samples suggests its total consumption in the processes of carbonation and sulphur attack. However, the presence of portlandite and the absence of degradation products only in sample BB confirms that this grout is more intact.

5.7.8 Implications on long-term behaviour

Intact grout—like that of sample BB—has a permeability lower than that of London Clay; such grout behaves as a barrier, impeding flow into the tunnel. In contrast, degradation of the grout can cause its permeability to rise higher than that of London Clay. The degraded grout then behaves as a flow path, facilitating flow into joints and gaps around the circumference of the lining.

The change in grout permeability with time has implications on movements and stresses in both the ground and lining. A lining might be considered as fully impermeable relative to the surrounding soil with freshly-set grout. This is likely to promote swelling around the tunnel as negative excess pore pressures after construction dissipate (Wongsaroj, 2005). However, as the grout degrades, its porosity will increase, until eventually the grout could behave as if fully permeable relative to the soil. If joints between the lining segments are permeable, the tunnel will then act as a drain, causing widespread consolidation at tunnel axis depth.

The range of possible grout permeabilities also influences the choice of lining conductivity in the prediction method of Chapter 8. Not only can the conductivity vary from site to site, but it can also evolve with time. A conservative approach might be to assume a fully permeable lining, since this tends to produce the most severe displacements.

5.8 Summary

Six samples of grout were extracted from different sites around the London underground tunnels. The permeability, porosity, microstructure and composition of the grout were investigated using permeability testing, mercury intrusion porosimetry, scanning electron microscopy and X-ray diffraction.

Five of the samples were found to have degraded by carbonation and sulphate attack. Subsequent leaching of the degradation products led to increased porosity and permeability; as a result, the grout could be considered fully permeable relative to the surrounding clay. The remaining sample had not degraded, retaining its low porosity such that it was fully impermeable relative to the clay.

These observations suggest that immediately following construction, the freshly-set grout would behave as an impermeable barrier. The increase in grout permeability with progressive degradation could then transform the grout to act as a flow path instead. This change in flow regime would have a drastic impact on long-term movements; for the prediction method of Chapter 8, it may be conservative to assume a fully permeable lining when assessing displacement response, and a fully impermeable lining to obtain worst-case lining loads.

Only the permeability characteristics of intact grout have been investigated here. Cracking of the grout after injection might also contribute to an increase in permeability with time.

SAMPLE NAME	BETWEEN STATIONS	RING NO.	LINE OF ORIGIN	DIRECTION OF LINE	CONSTRUCTION PERIOD †	COLOUR	MOHS HARDNESS ‡
BB	Bond Street - Baker Street	61	Jubilee	N/K	1971 - 1979	Dark grey	5
CH135	Covent Garden - Holborn	135	Piccadilly	Eastbound	1902 - 1906	Pale grey	3
CH142	Covent Garden - Holborn	142	Piccadilly	Eastbound	1902 - 1906	Medium brown	3
NK	N/K	N/K	N/K	N/K	N/K	Pale grey	3
OS	Oval - Stockwell	1504	Northern	Northbound	1923 - 1924	Pale brown	3
TT	Tooting Bec - Tooting Broadway	1909	Northern	Northbound	1924 - 1926	Pale grey	3

N/K = not known

† Source: Tube Lines (2005). *Historical study report* . Tube Lines report, TLL-L001-N416-DTAAWP2-TUN-RPT-00013

‡ Estimated from an approximate comparison with materials of similar Mohs hardness

Table 5.1: Origins and characteristics of grout samples

SPECIMEN	SAMPLE	DENSITY	HEIGHT	FLOW RATE		HYDRAULIC GRADIENT	COEFFICIENT OF PERMEABILITY	NOTES
				FROM SYRINGE PUMP	MEAN			
		ρ	h	q_{pump}	q_{mean}	i	k	
		Mg m^{-3}	mm	µL min^{-1}	µL min^{-1}		m s^{-1}	
S01	CH142	1.21	11.4	1	0.88	8.4	3.57E-10	
S02	CH142	1.26	10.5	1	5.78	8.6	3.21E-10	Membrane leakage
S03	CH142	1.27	13.5	2	1.89	26.3	2.90E-10	
S04	CH142	1.31	13.1	2	1.91	18.7	3.91E-10	
S05	CH142	1.34	13.7	2	1.89	14.1	5.32E-10	
S06	CH142	1.27	12.2	2	2.10	17.2	3.92E-10	Membrane leakage
S07	CH142	1.24	17.1	2	1.90	22.6	4.27E-10	
S08	CH142	1.32	18.4	2	1.93	17.4	5.88E-10	
S09	OS	1.16	18.7	2	1.94	2.5	3.13E-09	
S10	OS	1.17	21.7	2	2.14	4.5	2.32E-09	
S11	OS	1.15	23.6	2	1.92	4.9	2.38E-09	
S12	OS	1.14	22.6	2	1.94	7.2	1.64E-09	
S13	CH135	1.47	11.7	4	3.92	32.0	4.24E-10	
S14	CH135	1.48	12.3	4	3.45	26.8	5.28E-10	
S15	CH135	1.42	13.2	4	3.94	13.3	1.09E-09	
S16	CH135	1.43	12.6	4	3.97	25.7	5.60E-10	
S17	TT	1.43	13.0	4	3.91	45.3	3.29E-10	
S18	TT	1.41	13.4	4	4.72	70.5	2.22E-10	Membrane leakage
S19	NK	1.23	17.9	4	3.91	38.9	5.32E-10	
S20	BB	2.06	9.7	4	4.17	385.1	2.97E-11	⎫ Flow between membrane and
S21	BB	2.04	15.3	1	0.44	359.6	1.25E-11	⎬ specimen: permeability is an
S22	BB	1.94	16.0	1	0.28	978.4	4.83E-12	⎭ upper bound

Table 5.2: Details of permeability tests

Figure 5.1: Photographs of grout discs

Figure 5.2: Photographs of permeability test specimens

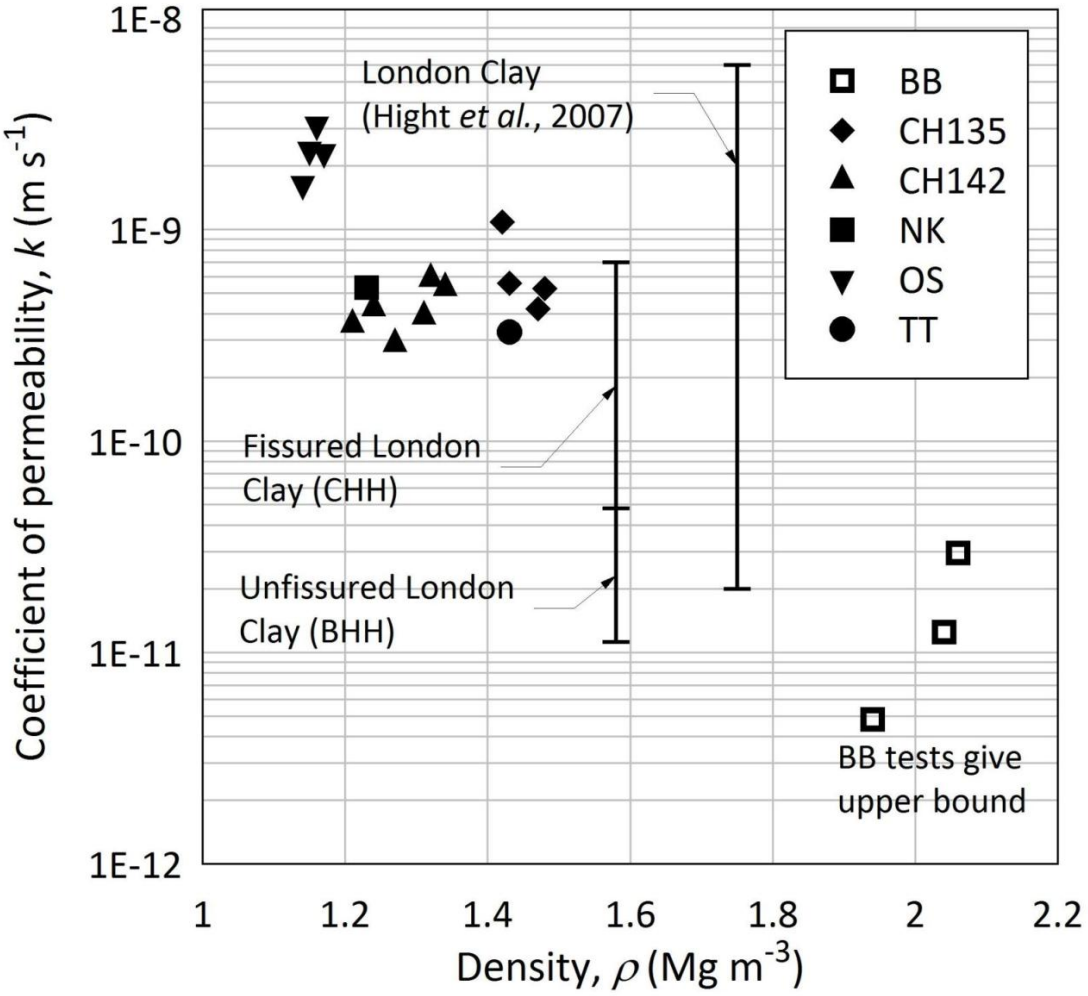

Figure 5.3: Permeabilities and densities of grout

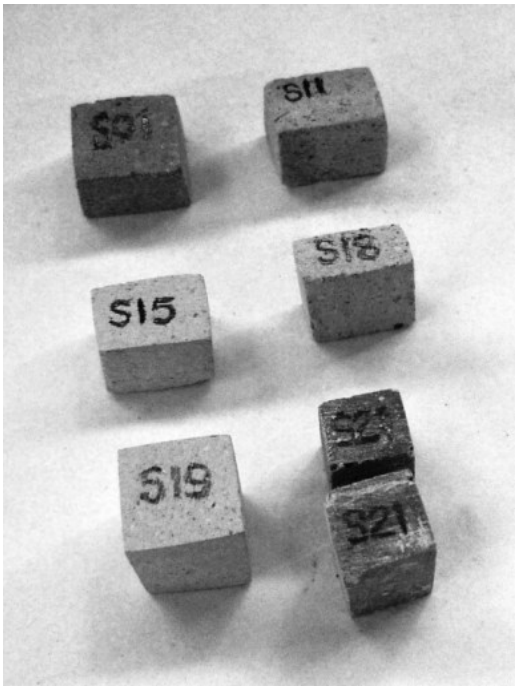

Figure 5.4: Photographs of mercury intrusion porosimetry specimens

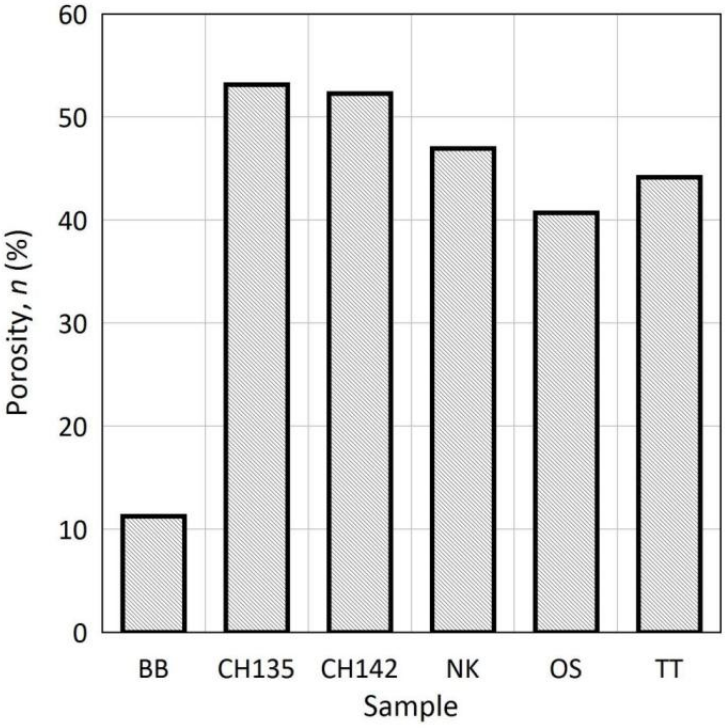

Figure 5.5: Porosities of grout

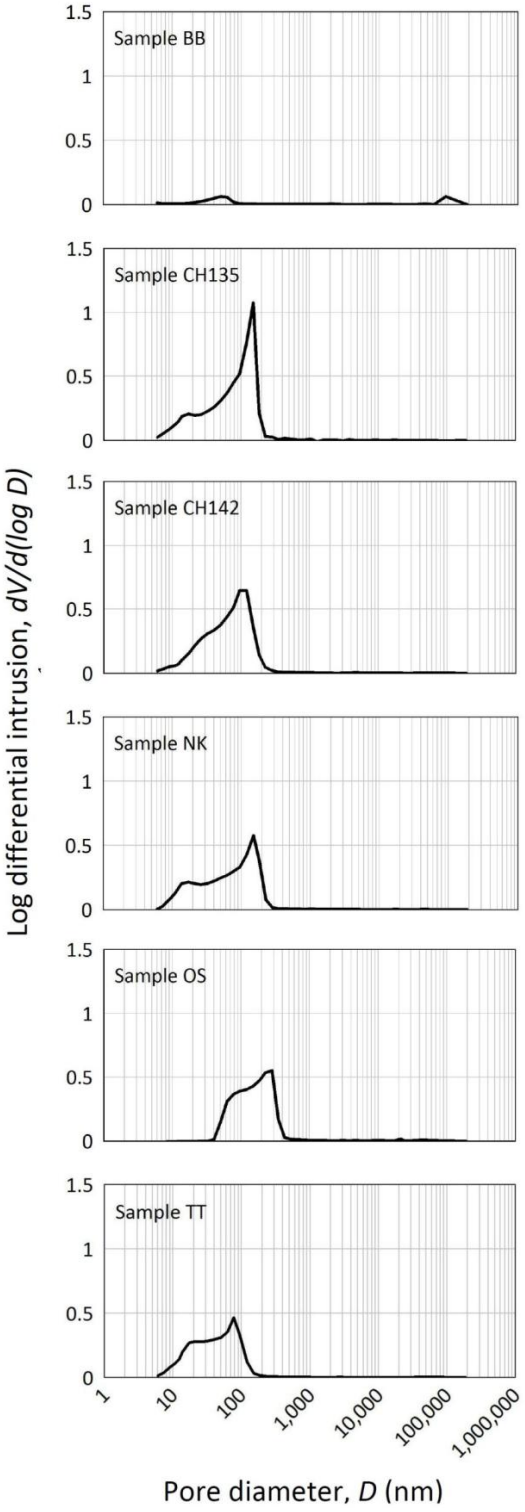

Figure 5.6: Pore size distributions of grout

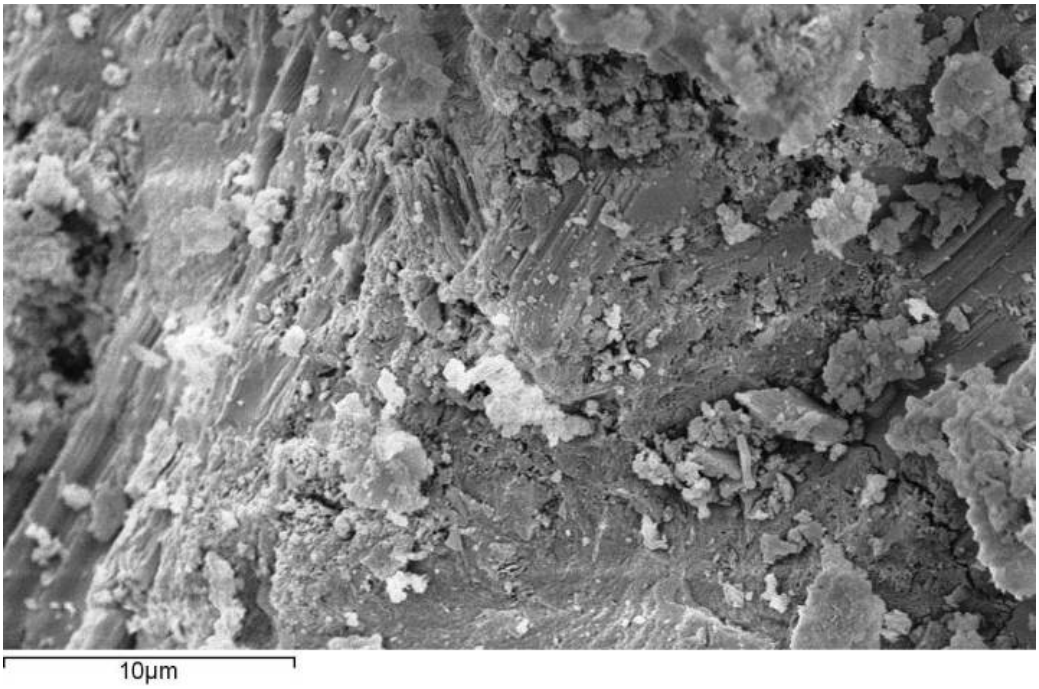

(a) Sample BB

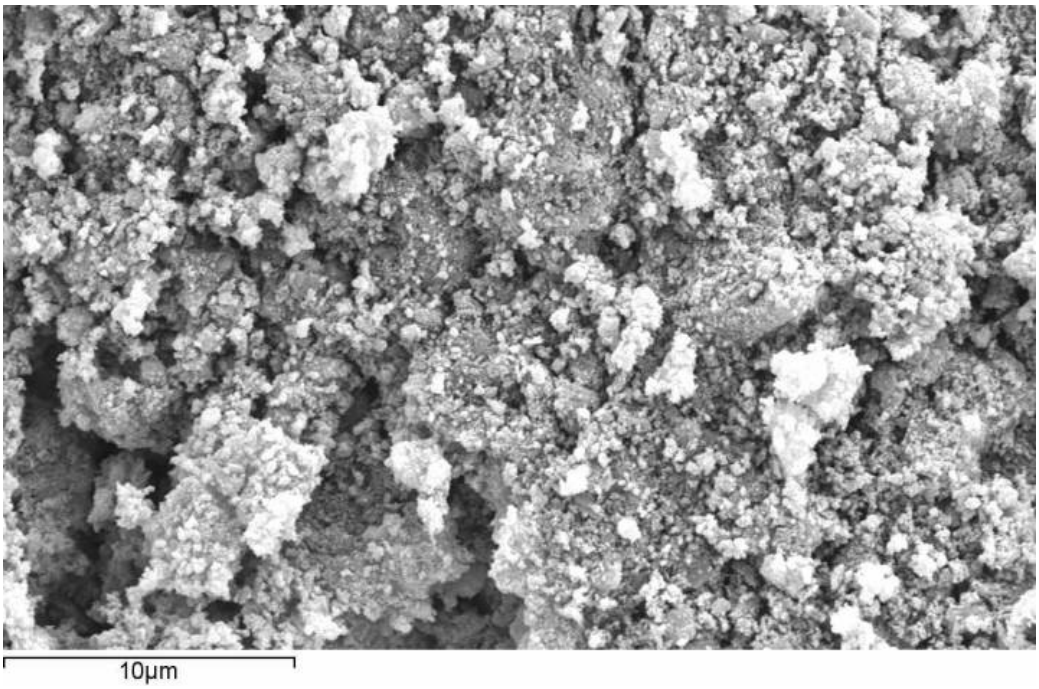

(b) Sample CH135

Figure 5.7: Scanning electron microscopy images of grout

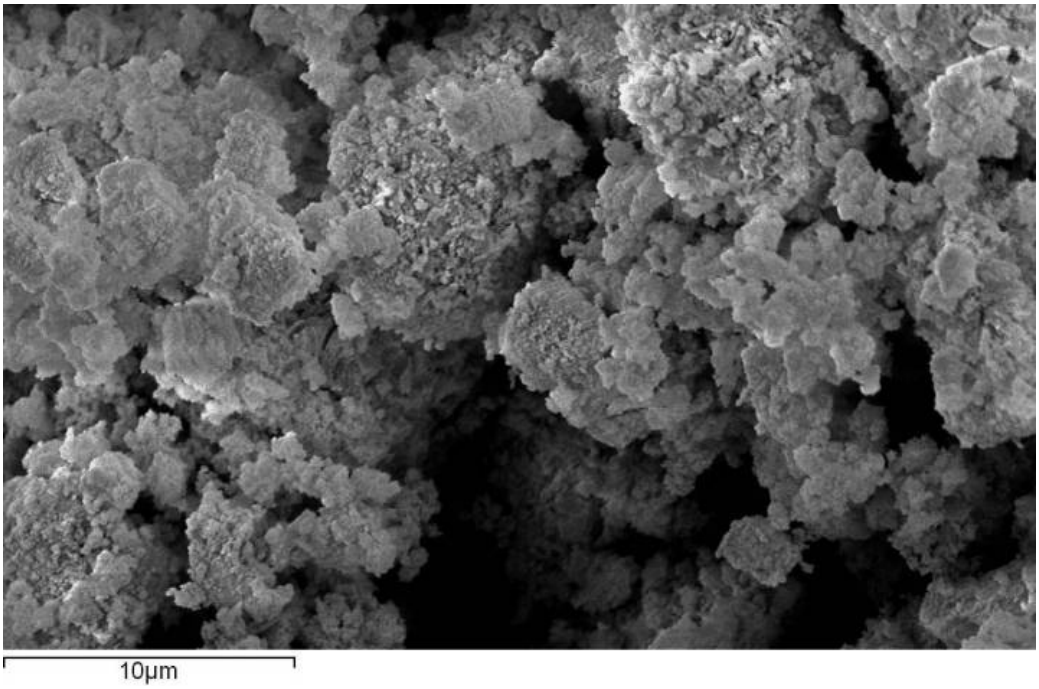

(c) Sample CH142

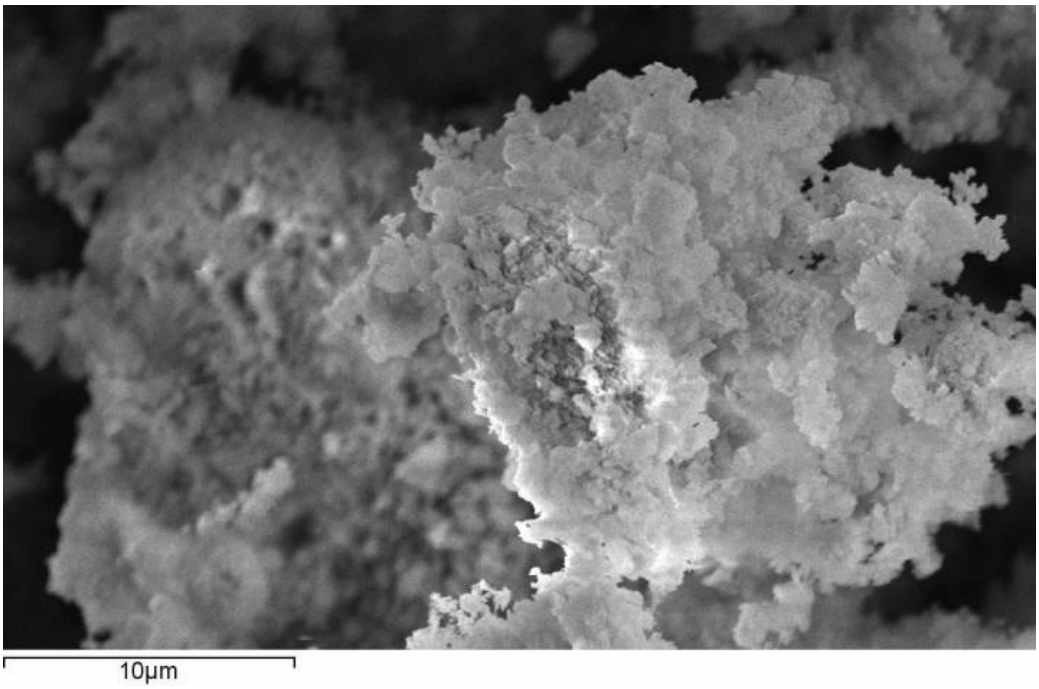

(d) Sample OS

Figure 5.7: *cont...* Scanning electron microscopy images of grout

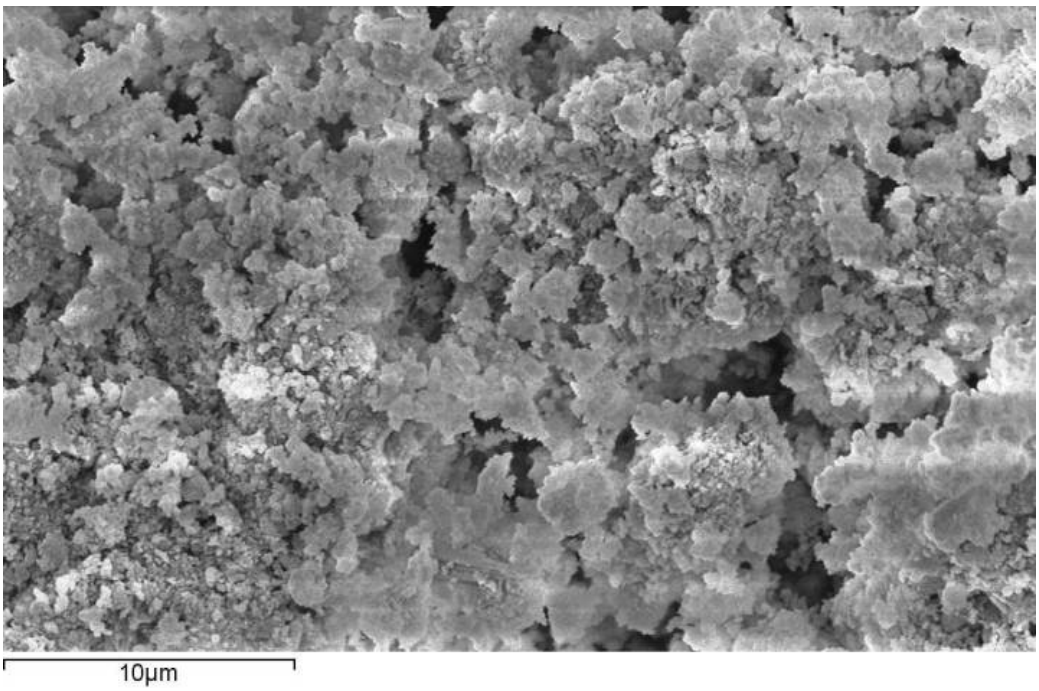

(e) Sample TT

Figure 5.7: *cont...* Scanning electron microscopy images of grout

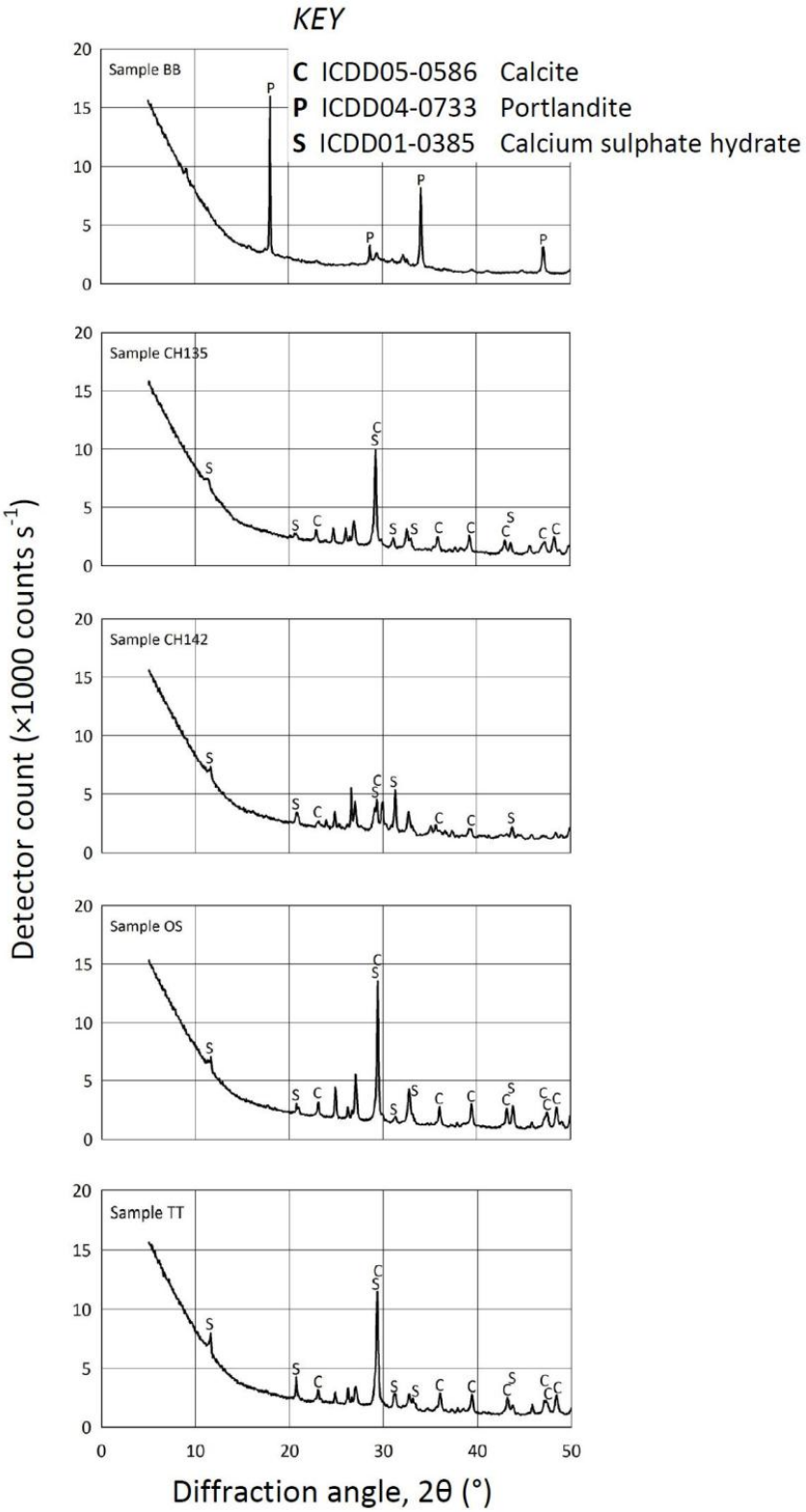

Figure 5.8: X-ray diffraction patterns of grout

Figure 5.9: Lining deposits in a London underground tunnel

Chapter 6

Soil constitutive model

6.1 Introduction

This chapter describes the development of a realistic soil model for London Clay. The model builds upon that devised by Wongsaroj (2005), so his original formulation and parameters are first outlined. Developments to the model are then presented in the light of new findings from recent high-quality laboratory test data. Finally, the performance of the modified models is evaluated through numerical simulations of a range of laboratory tests. Comparison with test data exposes the capabilities and limitations of each model.

6.2 Requirements

A soil model for use in long-term tunnelling simulations should ideally exhibit the following features:

Good fitting up to 1% shear strain Nyren (1998) notes a maximum of around 1.0% shear strain during tunnel construction at St James's Park. The soil model should therefore replicate actual behaviour well up to this strain level.

Good prediction of pore pressures Since dissipation of excess pore pressures during construction determines changes during consolidation (Wongsaroj, 2005), pore pressures should be predicted accurately.

Good drained and undrained predictions In clays, rapid construction is practically undrained, whilst long-term consolidation is drained. The soil model must therefore model both behaviours well.

Good prediction of variety of stress paths Soil surrounding a tunnel undergoes a variety of complex stress paths during its construction (Wongsaroj, 2005). The soil model should therefore match a wide range of stress paths.

6.3 Formulation

Wongsaroj (2005) developed a soil model for London Clay to investigate the long-term behaviour of tunnels in clay. He noticed that previous researchers had improved trough shape or excess pore pressure predictions through including non-linear small-strain stiffness, elasto-plastic behaviour, elastic anisotropy and recent stress history effects. Building upon a critical-state foundation, Wongsaroj selected implementations of these aspects from other authors' work to assemble an accurate soil model. These components and their relation to the input parameters of his model are described below. Full details of Wongsaroj's model can be found in Appendix A.

Stress space Wongsaroj defined his model in general stress space, describing stress state with six components of Cauchy stress.

Yield surface The Modified Cam Clay (MCC) yield surface developed by Wheeler (1997) was adopted. The modified yield surface allowed strength anisotropy to be modelled by enabling the elliptical Cam Clay surface to rotate; however, Wongsaroj did not invoke rotation. Where the surface crosses the hydrostatic axis defines its initial size; the mean effective stress here is termed the preconsolidation pressure p'_0.

Failure criterion in π-plane The Matsuoka & Nakai failure criterion was chosen since it fitted failure in triaxial tests on Toyoura sand closer than the Mohr-Coulomb criterion (Matsuoka & Nakai, 1985). The input parameter M determines the size of the failure envelope, and is the gradient of the critical state line in q–p' space.

Elasto-plasticity Wongsaroj combined elastic and plastic behaviour within the yield surface by implementing the sub-load surface of Hashiguchi & Chen (1998). The sub-load surface is geometrically similar to the yield surface, but scaled down by a factor R so that it passes through the current stress point. Its growth is related to its relative size, such that dR is a function of R:

$$dR = u_1(\frac{1}{R^m} - 1) \parallel d\varepsilon^{\mathrm{p}} \parallel \tag{6.1}$$

where $d\varepsilon^{\mathrm{p}}$ is the plastic strain increment. The two parameters u_1 and m therefore determine the degree of plasticity within the yield surface. The evolution of plastic strain within the yield surface can be accelerated by increasing u_1 or decreasing m.

Non-linear small-strain stiffness The degradation of stiffness was that used in the MIT-S1 model of Pestana (1994). Formulated in $\log e$–$\log p'$ space, the swelling gradient ρ_{r} degrades according to:

$$\rho_{\mathrm{r}} = \frac{1 + \omega_{\mathrm{s}}\xi_{\mathrm{s}}}{C_{\mathrm{b}}} \left(\frac{p'}{p_{\mathrm{a}}}\right)^{\frac{1}{2}} + D(1 - \xi^r) \tag{6.2}$$

The constant p_{a} is the atmospheric pressure. The variables ξ and ξ_{s} are dimensionless distances in stress space since the last stress reversal, defined by:

$$\xi = \begin{cases} p'/p'_{\mathrm{rev}} & \text{for} \quad p' < p'_{\mathrm{rev}} \\ p'_{\mathrm{rev}}/p' & \text{for} \quad p' \geq p'_{\mathrm{rev}} \end{cases}, \xi \leq 1 \tag{6.3}$$

$$\xi_{\mathrm{s}} = \{(\boldsymbol{\eta} - \boldsymbol{\eta}_{\mathrm{rev}}) : (\boldsymbol{\eta} - \boldsymbol{\eta}_{\mathrm{rev}})\}^{\frac{1}{2}}, \boldsymbol{\eta} = \mathbf{s}/p' \tag{6.4}$$

so that ξ represents the distance along the hydrostatic stress axis, and ξ_{s} the distance in the deviatoric stress plane. Therefore, the first term on the right-hand side of Equation 6.2 controls the stiffness degradation due to deviatoric stresses; parameters C_{b} and ω_{s} describe this. The second term controls degradation due to hydrostatic stresses, determined by the parameters D and r. The modelling of stiffness degradation due to both hydrostatic and deviatoric stresses is similar to the behaviour observed in clay. The gradient ρ_{r} enables the bulk and shear stiffnesses to be calculated; use of ρ_{r}

to define the degradation of both stiffnesses maintains the elastic Poisson's ratios constant.

Stress path reversal criterion The dimensionless stress distances in Equation 6.2 are reset and the initial stiffness restored when the stress path reverses; in Section 3.3.1, this was identified as essential to realistic twin-tunnel modelling. A stress path reversal is defined according to Pestana (1994), chosen for consistency with the stiffness degradation rule. It is defined by the scalar product of the current strain increment vector with the vector of accumulated strains since the last reversal (see Appendix A). Thus, whether this product is positive or negative defines when the strain direction changes.

Hardening rule To be consistent with the definition of stiffness in $\log e$–$\log p'$ space, the yield surface grows according to the plastic volumetric strain increment $d\varepsilon_{\mathrm{v}}^{\mathrm{p}}$:

$$dp'_0 = \frac{1+e}{e(\rho_{\mathrm{c}} - \rho_{\mathrm{r}})} p'_0 \, d\varepsilon_{\mathrm{v}}^{\mathrm{p}} \tag{6.5}$$

This introduces another model parameter ρ_{c} as the gradient of the normal compression line. The initial void ratio e_0 must also be defined.

Elastic anisotropy Adopting a cross-anisotropic elastic stiffness matrix requires the definition of five elastic parameters. Three Poisson's ratios are defined: ν_{vh}, ν_{hv} and ν_{hh}. The variable ρ_{r} then defines the bulk modulus as a further parameter; along with ν_{hh}, this also determines the shear modulus in the plane of deposition, G_{hh}. The last parameter, $G_{\mathrm{hh}}/G_{\mathrm{vh}}$, defines the degree of anisotropy in shear stiffness, yielding G_{hv} from G_{hh}.

Knowledge of the meaning of these soil model parameters helps in adjusting them to better match true London Clay behaviour.

6.4 Parameter selection

To represent London Clay accurately in his tunnel analyses, Wongsaroj (2005) established realistic ranges for each of his soil model parameters. These ranges were based upon findings from past laboratory test data and literature. Guided

by these ranges, he then selected parameters which fitted laboratory test data the closest. The ranges for D and r were established using data from reconstituted specimens. To simulate intact clay therefore, Wongsaroj chose values outside of these bounds.

The soil model was calibrated with drained and undrained triaxial compression data (Yimsiri, 2001), and also with results from a wide range of oedometer tests. Specimens for the triaxial tests were cut both horizontally and vertically, enabling Wongsaroj to evaluate his anisotropic parameters. Some of the oedometer tests involved swelling so that unloading behaviour could also be calibrated. The resulting parameters selected by Wongsaroj to fit Yimsiri's data are given in Table 6.1.

Wongsaroj needed to validate the performance of his tunnel simulation with field data. St James's Park was monitored extensively as the Jubilee Line Extension was constructed beneath the site, and data from this (Nyren, 1998) was used. Wongsaroj adjusted parameters M, e_0 and ρ_c to match soil properties specific to the site; in addition, ω_s was increased to enhance dilation and softening at peak strength. These parameters are also listed in Table 6.1. The same set of parameters was applied to the entire thickness of London Clay, with only preconsolidation pressure p'_0 varying with depth. This variation was derived by averaging estimates given in the literature.

6.5 New data

Since Wongsaroj calibrated his soil model, new data from laboratory tests on London Clay has been published (Hight *et al.*, 2007). Fresh insights from this data suggest that the original soil model can be developed to improve its realism.

Researchers at Imperial College extracted high-quality samples at the site of Heathrow Terminal 5, consisting of rotary cores and block samples for minimal disturbance. Specimens were then subjected to an extensive series of hollow cylinder tests, advanced triaxial stress path tests and dynamic tests. Amongst the many discoveries about the behaviour of London Clay (Gasparre *et al.*, 2007a,b; Hight *et al.*, 2007; Nishimura *et al.*, 2007), the following new information suggests improvements to Wongsaroj's original soil model.

Strength anisotropy data Nishimura (2006) investigated the anisotropy of shear strength in London Clay by performing hollow cylinder tests on the Heathrow Terminal 5 specimens; to address the lack of data on strength anisotropy. The hollow cylinder apparatus (HCA) enables full control over parameters defining the anisotropy of applied stress: the angle α between the major principal stress direction and the vertical, and the intermediate principal stress ratio $b = (\sigma_2 - \sigma_3)/(\sigma_1 - \sigma_3)$, where σ_1, σ_2 and σ_3 symbolise the major, intermediate and minor principal stresses respectively. This new dataset offered to calibrate anisotropic behaviour of the soil model more comprehensively than was previously possible.

Softening during triaxial extension The advanced triaxial tests performed by Imperial College included extension as well as compression tests (Gasparre, 2005; Nishimura, 2006). By comparing the failure envelopes of Figure 6.1, Hight *et al.* (2007) noticed that the strength in extension is closer to the fissure strength than that in compression, concluding that orientation of loading influences failure along fissures. Also, both Gasparre (2005) and Nishimura (2006) observe the early formation of sub-horizontal shear planes in extension tests, due to fissures orientated in these directions. The laboratory data in Figures 6.19, 6.20 and 6.22 illustrate that this reduced the peak strength and dilatancy. Therefore, a modification is required in Wongsaroj's soil model to simulate this.

Variation with depth Although stiffness is expected to increase with mean effective stress, Gasparre (2005) concluded that the structure of each lithological unit also influences behaviour. The rotary core samples from Heathrow Terminal 5 spanned across the sub-units C, B2c, B2b, B2a, A3ii and A3i, enabling calibration of Wongsaroj's parameters to individual units.

6.6 Laboratory test simulations

In the light of the findings from Imperial College, modifications were made to Wongsaroj's model. The performance of these was evaluated by numerically modelling laboratory tests and comparing the results with data from Imperial College.

The finite element program ABAQUS was used for single-element modelling of triaxial, oedometer and hollow cylinder tests. These tests are detailed below.

6.6.1 Triaxial tests

Both compression and extension tests were modelled since tunnel construction induces both types of shearing. Also, the need to model both short- and long-term soil response meant that both undrained and drained tests were simulated. Gasparre (2005) performed these different types of triaxial test upon specimens from a range of depths, with a variety of approach paths, so many of her tests were modelled.

Gasparre applied approach paths to replicate the geological history. Only tests preceded by such an approach path were considered for validation because the following shearing phase would better represent in-situ shearing. This led to the selection of thirteen triaxial tests to model: one drained and four undrained extension tests, and two drained and six undrained compression tests.

The sudden reduction in stiffness during extension tests demanded further characterisation. Therefore eight undrained triaxial extension tests were simulated from Nishimura (2006) to supplement Gasparre's test data. Like Gasparre's tests, Nishimura's specimens were extracted from a range of depths. Altogether, Gasparre's and Nishimura's triaxial specimens cover five sub-units: C, B2c, B2b, B2a and A3ii.

Approach stress paths for the validated tests were regenerated faithfully to ensure the correct stress history. Details are tabulated in Table 6.2, corresponding to the labelling in Figure 6.2a. All approach paths are drained, typically beginning with an increase in p alone (isotropic compression) followed by an increase in q alone. To generate the recent stress history, Gasparre also performs one or two unload-reload loops after these paths. Gasparre kindly provided her raw test data so that test conditions could be simulated exactly.

6.6.2 Oedometer tests

Oedometer tests can reveal the capability of the soil model to simulate drained consolidation and swelling, important for the modelling of long-term changes. Gas-

parre (2005) performed eleven oedometer tests spanning from Unit C down to Unit A3i, with initial swelling stages in four of the tests. Table 6.3 details the stresses used to model the state paths pictured in Figure 6.2b.

The value of $K = \sigma'_{\mathrm{v}}/\sigma'_{\mathrm{h}}$ to apply at the beginning of the oedometer test simulations is hard to judge because the initial effective stresses are unknown. Figure 6.3 follows the specimen through the set-up stages to establish the bounds $0.6 \leq K \leq 1.0$, assuming that in-situ K_0 is 1.5.

The sensitivity of oedometer test simulations to initial K is presented in Figures 6.4 and 6.5 for tests without and with initial swelling respectively. Two of the soil models evaluated in this chapter are considered: models ORIG and MODU, which are explained later. The extremes for initial K of 0.6 and 1.0 are considered, alongside behaviour with the mean value of 0.8 for comparison. The figures show that varying initial K makes only a slight difference to one-dimensional compression behaviour, suggesting that the performance of soil models at larger strains with the same initial K value can be compared adequately. For these analyses therefore, the mean value of $K = 0.8$ was applied initially, before the specimens were consolidated in 1-D to simulate the oedometer tests.

6.6.3 Hollow cylinder tests

The anisotropic behaviour of the soil model can be assessed through hollow cylinder tests. Nishimura performed two series of stress path tests in the hollow cylinder apparatus (HCA): one upon isotropically-consolidated specimens, and the other upon anisotropically-consolidated ones. For the latter series, the shearing stage is more likely to be representative of field behaviour since the initial stresses are closer to the in-situ condition. Therefore the anisotropically-consolidated series was modelled, comprising ten tests. All specimens were taken from block samples at the same depth, in Unit B2. Test details are given in Table 6.4.

A stress path can be uniquely defined by p, q, b and α. The measures b and α are explained in Section 6.5. Each test followed a shearing stress path with different values of b and α, as plotted in 3-D stress space in Figure 6.6. Along the shearing path, b and p are kept constant, whilst α changes to attain the final target value, α_{f}. Although α changes during shearing, the direction of the stress

vector in the τ–$\frac{1}{2}(\sigma_{zz} - \sigma_{\theta\theta})$ plane, defined by $\alpha_{d\sigma}$, is kept constant. Values of $\alpha_{d\sigma}$ defined for each test are presented in Table 6.4. Figure 6.6 illustrates the difference between α and $\alpha_{d\sigma}$, which is also apparent from their equations:

$$\alpha_{d\sigma} = \frac{1}{2}\arctan\left(\frac{2\delta\tau_{\theta z}}{\delta\sigma_{zz} - \delta\sigma_{\theta\theta}}\right) \tag{6.6}$$

$$\alpha = \frac{1}{2}\arctan\left(\frac{2\tau_{\theta z}}{\sigma_{zz} - \sigma_{\theta\theta}}\right) \tag{6.7}$$

Test AC0000 is the exception to b being kept constant; in this test, changes in principal stress ratios cause b to abruptly change during shearing. To finish at the desired $b = 0.0$ therefore, Nishimura starts shearing at $b = 1.0$, as shown in Figure 6.6.

Considering test AC6705 as an example can clarify the difference between defining α_f and $\alpha_{d\sigma}$. The "67" in the name indicates that $\alpha_f = 67°$, whilst "05" indicates that $b = 0.5$. This means that α decreases from 90° at the start of shearing until reaching its target value $\alpha_f = 67°$. During this change, the angle of the stress increment vector in the τ–$\frac{1}{2}(\sigma_{zz} - \sigma_{\theta\theta})$ plane ($\alpha_{d\sigma}$) stays constant at 55°.

Before the shearing stress paths, each specimen underwent three set-up phases. The first phase changed p alone to the desired value for shearing, whilst keeping q, b and α constant. The second and third phases then changed only q and only b respectively to set-up the correct initial stresses before shearing. The first two p- and q-change phases were drained, whilst the third b-change phase was undrained. Shearing in all tests started from the same p and q, but b could take a value of 0.0, 0.5, 0.7 or 1.0.

The boundary conditions for implementing a hollow cylinder test in a single-element simulation are summarised in Figure 6.7. Constraint equations were enforced to ensure correct kinematic behaviour.

6.7 Developments

The numerical simulations helped to evaluate the success of developments in improving Wongsaroj's original soil model; these developments are described below.

6.7.1 Yield surface size

Hight *et al.* (2007) noted a higher fissure intensity prevailing at shallower depths at Heathrow Terminal 5, agreeing with observations by Skempton *et al.* (1969). This imparted a lower stiffness and strength to samples from the uppermost unit, Unit C. This softer behaviour can be replicated by defining a smaller initial yield surface for this unit.

For his laboratory test simulations, Wongsaroj assumed a preconsolidation pressure p'_0 of 3000kPa. This value was adopted for Units A & B since it produced the best fit, but for Unit C, a value of 1000kPa was chosen. Although such a sudden variation in preconsolidation pressure does not represent the actual variation, it was found to replicate the softer behaviour imparted by the higher fissure intensity well.

6.7.2 Yield surface rotation

Wongsaroj (2005) used a yield surface that was symmetrical about the hydrostatic stress axis, such that strength anisotropy was not modelled. The original model was therefore modified to impart initial rotation to the yield surface.

The rotation is defined by a tensor β_{ij}. Figure 6.8 illustrates the meaning of this tensor, both in general stress space and in q–p' space. Figure 6.8a shows that β_{ij} defines the deviatoric offset of the yield surface axis from the hydrostatic axis. The rotation tensor was therefore defined to lie in the deviatoric stress plane, with no hydrostatic component.

The six components of the rotation tensor in Cauchy stress space, (β_{11}, β_{22}, β_{33}, β_{12}, β_{13} and β_{23}) can be reduced to three components β_{hh}, β_{vv} and β_{vh} because of cross-anisotropy. These were chosen to replicate the observed anisotropy of London Clay, which imparts greater strength in triaxial compression than in extension for vertically-cut specimens (Hight *et al.*, 2003). The best fit was found by applying $\beta_{\mathrm{hh}} = -0.05$, $\beta_{vv} = 0.1$ and $\beta_{\mathrm{vh}} = 0$. The fact that $2\beta_{\mathrm{hh}} + \beta_{vv} = 0$ ensured that the rotation tensor lies in the deviatoric stress plane.

6.7.3 Modified parameters

In addition to yield surface size and rotation, the other parameters of Wongsaroj's model were also changed to those listed in Table 6.1, in the column "MODU". These new values were determined by trial-and-error to best-fit behaviour across the whole spectrum of laboratory tests described above.

The following strategy was adopted to determine the new parameter values:

1. The yield surface rotation influences the relative stiffness and strength between stress paths with different $\alpha_{d\sigma}$. Trialling different values of $\alpha_{d\sigma}$, the yield surface rotation tensor β_{ij} was therefore calibrated with the hollow cylinder tests conducted by Nishimura (2006).

2. Influencing the direction of stress paths in the undrained tests, the Poisson's ratios ν_{vh} and ν_{hv} were then adjusted to match the undrained triaxial compression data from Gasparre (2005). The ratio ν_{hh} was found to have little influence.

3. The yield surface size, p'_0, was next reduced to match the reduced strength of the Unit C specimens.

4. The initial stiffnesses for the oedometer, drained triaxial and undrained triaxial tests from Gasparre (2005) were then matched by increasing the parameter C_b in Equation 6.2.

5. Following this, the degradation in stiffness for the same tests was corrected by changing the parameter ω_s in Equation 6.2.

6. Lastly, reducing m—which accelerates the onset of plasticity—also helped to match stiffness degradation and the curvature of stress paths in q–p' space.

The remaining parameters of Wongsaroj's model were not adjusted, since the effects of adjusting them could be replicated by instead adjusting the selected parameters above.

The elastic parameters—in particular, Poisson's ratios—might be quite unrealistic for the small-strain behaviour of London Clay. Bender element tests and static probes (Gasparre, 2005) indicated that ν_{hh} and ν_{vh} were around zero, whilst ν_{hv}

increases with depth from about 0.5 to 1.0. However, these Poisson's ratios apply only to small-strain behaviour; applying them in elastic simulations of laboratory tests produced a poor fit at larger strains. This implies that the Poisson's ratios evolve with strain; replicating this variation was considered too complicated, so instead Poisson's ratios were maintained constant and chosen to best-fit the data.

6.7.4 Fissure models

Wongsaroj's original soil model yielded a poor fit to the triaxial extension data from Imperial College. Figures 6.19, 6.20 and 6.22 illustrate that upon reaching a certain strain, the stiffness suddenly reduced in nearly all laboratory tests. This abrupt softening was attributed to fissures, based upon evidence given by the authors of the tests.

Gasparre (2005) observed that all of her extension specimens failed on pre-existing fissures, whilst Nishimura (2006) attributed early shear plane formation in tests TE1, TE2 and TE8 (Figure 6.22) to natural discontinuities. Both authors were able to derive a fissure strength envelope from these tests.

The inclination of shear planes provides further support for the influence of fissures. In the extension tests of both authors, the shear planes were inclined significantly closer to the horizontal than the planes of maximum stress ratio, upon which a homogeneous specimen would fail. This indicates a lower shear resistance in the sub-horizontal directions, at which fissures in London Clay are orientated.

Hight *et al.* (2003) and Hight *et al.* (2007) also attribute strength loss in extension to fissures.

The soil model was therefore modified according to two theories, both based upon fissure softening: fissure models ModF and ModG, which are described below.

6.8 Fissure models

In this section, explanation of the fissure models is divided into two parts. The first part describes the implementation; supporting evidence for this is then presented

in the second part. Details of the mathematical formulation can be found in Appendix B.

6.8.1 Implementation

Overview Both fissure models attempt to model the softening associated with fissures. Both models assume that fissures only exist on planes at orientations commonly found in London Clay, i.e. sub-horizontal and sub-vertical. Softening on these fissures is initiated according to a criterion of friction angle on these planes. After initiation, the degree of softening depends upon the element size, to model the local behaviour of softening correctly. The two fissure models differ in the way that softening is executed: in model MODF, softening is isotropic, whereas in model MODG only the shear stiffnesses on the softening fissure planes are softened.

With this overall picture in mind, each component of the fissure model will now be presented more comprehensively, with reference to Figure 6.9.

Ranges for fissure plane inclination The fissures in London Clay predominate within two ranges of inclination (Skempton *et al.*, 1969). One range is within a small angle from the horizontal (sub-horizontal), whilst the other range is within a small angle from the vertical (sub-vertical). In the fissure models, fissures are assumed to be perfectly flat planes, existing only at inclinations within these two ranges (Box A of Figure 6.9).

Frictional criterion for fissure softening Both fissure models implement softening when a fissure plane meets certain conditions. Firstly, the inclination of the plane must be within the sub-horizontal or sub-vertical ranges (Box B of Figure 6.9). Secondly, the friction angle mobilised on the plane must exceed a threshold value, termed the softening friction angle ϕ'_{soft} (Box G of Figure 6.9).

Identification of softening fissure planes Within each of the sub-horizontal and sub-vertical ranges, softening is implemented when the friction angle mobilised on any plane within that range (ϕ'_{p}) exceeds the softening friction angle ϕ'_{soft}. The

angle α_{range} defines the boundaries for the sub-horizontal and sub-vertical ranges (Box A of Figure 6.9). This angle is measured from the horizontal and vertical planes respectively, and is a material parameter.

Within each of the two ranges, the fissure plane with the greatest mobilised friction angle is sought (Box B of Figure 6.9). This angle is termed $\phi'_{\text{ph max}}$ and $\phi'_{\text{pv max}}$ for the sub-horizontal and sub-vertical ranges respectively. Since they mobilize the greatest angle of friction, these two fissure planes represent the inclinations at which the fissures are most likely to soften. If the mobilised friction angle on one of these planes exceeds the softening friction angle ($\phi'_{\text{ph max}} > \phi'_{\text{soft}}$ or $\phi'_{\text{pv max}} > \phi'_{\text{soft}}$), softening is implemented on that plane. Therefore, only one sub-horizontal and one sub-vertical fissure plane is allowed to soften at any one time.

Because the stress state changes during the analysis, the orientations of these planes, together with the friction angles that they mobilize, can evolve as the analysis progresses.

Derivation of stiffness reduction factors Softening is implemented by defining factors to reduce stiffness, termed *stiffness reduction factors*. Two stiffness reduction factors are determined: ζ_{ph} for the sub-horizontal range, and ζ_{pv} for the sub-vertical range.

The stiffness reduction factor for each range is related to the greatest mobilised friction angle found on any plane within that range, either $\phi'_{\text{ph max}}$ if sub-horizontal or $\phi'_{\text{pv max}}$ if sub-vertical; the preceding section described how these values are found. The relationship between $\phi'_{\text{ph max}}$ or $\phi'_{\text{pv max}}$ and the corresponding stiffness reduction factor, ζ_{ph} or ζ_{pv}, is a ramped step function consisting of three ranges (Box G of Figure 6.9):

1. If the mobilised friction angle is less than the corresponding softening friction angle, that is ($\phi'_{\text{ph max}} < \phi'_{\text{soft}}$) or ($\phi'_{\text{pv max}} < \phi'_{\text{soft}}$), no softening occurs and the corresponding reduction factor, ζ_{ph} or ζ_{pv}, is unity.

2. If the mobilised friction angle exceeds the corresponding softening friction angle, that is ($\phi'_{\text{ph max}} \geq \phi'_{\text{soft}}$) or ($\phi'_{\text{pv max}} \geq \phi'_{\text{soft}}$), the corresponding reduction factor reduces from unity to a minimum value $\zeta_{\text{p min}}$ linearly over the

friction angle range ϕ'_{range}. This range is a material parameter (Box F of Figure 6.9), and helps to avoid convergence problems resulting from an abrupt change in stiffness during the analysis.

3. Full softening is implemented if the mobilised friction angle exceeds the sum of the softening friction angle plus this range, that is ($\phi'_{\text{ph max}} > (\phi'_{\text{soft}} + \phi'_{\text{range}})$) or ($\phi'_{\text{pv max}} > (\phi'_{\text{soft}} + \phi'_{\text{range}})$). Here, the stiffness reduction factor attains its minimum value ($\zeta_{\text{pv}} = \zeta_{\text{p min}}$ or $\zeta_{\text{ph}} = \zeta_{\text{p min}}$).

Accounting for element size Fissure softening is a local phenomenon, but finite element modelling implements softening across a whole element. The minimum value of stiffness reduction factor ($\zeta_{\text{p min}}$), characterising fully softened behaviour, must therefore by scaled so that localised stiffness reduction can be represented within an element (Box C of Figure 6.9). The scaling rule assumes a shearing element with characteristic length C_{el} (Box E of Figure 6.9) containing a localised shearing region of width d_{fiss} representing the fissure, as pictured in Figure 6.10. The minimum stiffness reduction factor for the element $\zeta_{\text{p min}}$ is thus:

$$\zeta_{\text{p min}} = \frac{1}{1 + \dfrac{f_{\text{fiss min}}}{C_{\text{el}}}} \tag{6.8}$$

where $f_{\text{fiss min}} = d_{\text{fiss}}/\zeta_{\text{fiss min}}$ is a material property defined for the fissure (Box D of Figure 6.9). In this way therefore, the minimum reduction factor for the element ($\zeta_{\text{p min}}$) is scaled from the analogous quantity for the fissure ($\zeta_{\text{fiss min}}$).

Implementation of softening All of the preceding steps to define stiffness reduction factors are common to both fissure models: ModF and ModG. However, the models differ in the way that these factors are applied, as outlined below:

Model MODF Model ModF factors all components of the stiffness matrix uniformly by the same stiffness reduction factor, so that softening is isotropic, as illustrated in Figure 6.11. The reduction of all stiffness components in ModF models how a softening fissure might lead to secondary isotropic softening of neighbouring regions. This is achieved by modifying the parameter C_{b} in

Equation 6.2, from which all stiffness components are derived (Box H of Figure 6.9). Since there is one factor for each range—ζ_{ph} and ζ_{pv}—model MODF reduces the stiffness matrix twice: once for each factor. Softening is therefore applied equally in all directions, regardless of fissure plane orientation.

Model MODG Softening is directional in model MODG, modelling the fissure plane as a weaker slip surface, whilst all other stiffnesses are maintained (Box J of Figure 6.9). This type of softening, affecting only the shear stiffness along the fissure plane, is pictured in Figure 6.11. To achieve this, the stiffness matrix is first transformed to a coordinate system aligned with the fissure plane. The components relating shear stress to shear strain on the fissure plane are then reduced by the stiffness reduction factor, before the stiffness matrix is transformed back to the original coordinate system. Since there is one factor for each range—ζ_{ph} and ζ_{pv}—this operation of transformation and stiffness reduction is performed twice: once for the sub-horizontal fissure range, and once for the sub-vertical range.

6.8.2 Supporting evidence

Evidence supporting the formulation of the fissure models is presented below.

1. Ranges for fissure orientation Skempton *et al.* (1969) observed that in London Clay, fissures tend to concentrate at inclinations below 20° to the bedding plane, and between 70° and 90° to it. These two bounds indicate the sub-horizontal and sub-vertical ranges for fissure orientation respectively.

No bias is applied to fissure inclination when locating the softening fissure plane within these ranges. The occurrence of fissure inclinations within these ranges is therefore modelled as a rectangular distribution by the fissure models; however, a normal distribution is more realistic, as portrayed in Figure 6.12. Therefore, assuming ±20° for the range of the rectangular distribution would overestimate the occurrence of fissures with orientations towards the extremities of the range, relative to those towards the middle. To model the distribution more realistically, bounds were fixed at $\alpha_{range} = \pm 16°$, as shown in Figure 6.12. Using this range, the standard deviations of the rectangular and normal distributions are the same,

assuming that 85% of fissures in the normal distribution dip at inclinations within $\pm 20°$.

2. Friction angle for softening Gasparre (2005) and Nishimura (2006) both attribute the pre-mature softening in their extension tests to sub-horizontal fissures. So for each of these tests, at the initiation of softening, the shear stress on a sub-horizontal plane was plotted against the effective stress normal to it. This is illustrated in Figure 6.13, where a plane at an inclination of 16° to the horizontal is assumed. At the onset of softening, friction angles on this plane fall between 8.5° and 14°, with a best fit of 12.5°—this narrow range supports the onset of softening at a unique friction angle.

The onset of softening at about 12.5° was modelled by choosing $\phi'_{\text{soft}} = 11.5°$ and $\phi'_{\text{range}} = 1.5°$, so that the material gradually softens over a range of friction angle. A plane inclined at 16° was chosen for Figure 6.13 because it represents an upper bound to possible inclinations. The upper bound was used because the most inclined fissure plane mobilises the greatest friction angle in extension tests, and will therefore soften first.

Many authors cite a fissure strength envelope with a friction angle greater than that derived here—for instance, Nishimura (2006) finds $\phi'_{\text{mob}} = 17°$. However, these envelopes refer to the friction angle mobilised on the plane of maximum stress ratio, which tends to be more inclined in triaxial tests than the sub-horizontal and sub-vertical ranges considered here.

3. Determination of softening factors Values of $f_{\text{fiss min}}$ in Table 6.1 were selected to best-fit behaviour after softening. For model ModF, a lower value (less severe softening) best-fitted the hollow cylinder tests compared with the triaxial tests; the hollow cylinder geometry might have attenuated the effects of fissures, as explained in Section 6.9.4. For model ModG however, a similar reduction of $\zeta_{\text{p min}}$ in the hollow cylinder tests produced no improvement.

6.9 Model performance

The suitability of four models to represent London Clay behaviour in long-term tunnelling simulations was evaluated by simulating the laboratory tests detailed earlier. All four models were based upon the formulation by Wongsaroj (2005), with various developments also described earlier. The four models are summarised below, with their parameters listed in Table 6.1:

1. **Model ORIG** The original model by Wongsaroj, with his original parameters.

2. **Model MODU** The original model by Wongsaroj, with parameters modified to best-fit the laboratory data. The yield surface was rotated, with its size depending upon the lithological unit.

3. **Model MODF** Based upon model MODU, with isotropic softening of fissures.

4. **Model MODG** Based upon model MODU, with directional softening along the fissure plane alone.

The parameters for model ORIG were selected here to represent London Clay from many different sites, rather than to match specimens tested by Yimsiri (2001) alone. Many of Wongsaroj's parameters were derived from the literature on London Clay, and so could be taken as representative of London Clay in general. The exception is the stiffness degradation parameter ω_s, which Wongsaroj calibrated to best-fit stiffness degradation curves for Yimsiri's specimens only. However, when selecting ω_s to use in his St James's Park simulations, Wongsaroj considered degradation curves collated by Hight *et al.* (2003) from a range of investigations. This latter value was therefore chosen to represent general London Clay behaviour in model ORIG.

The performance of these models will now be compared.

6.9.1 Oedometer tests

Simulations Figure 6.14 compares the simulation of eleven oedometer tests to assess performance in drained consolidation and swelling, which is important for

long-term modelling. The test name provides the specimen depth in metres. Gasparre (2005) performed tests on specimens spanning from Unit C down to A3i, providing data from a range of depths. Together, Table 6.3 and Figure 6.2b detail the precise stress state paths modelled.

Performance Figure 6.15 compares the compressibility after yielding for each model, and illustrates that model ModU is far more capable than model Orig at replicating drained behaviour. On average, model ModU predicts compressibility correctly, whilst model Orig overpredicts by about 2.5 times. In four of the eleven tests, Gasparre swells the specimen before the first consolidation; all models cannot accurately model the ensuing consolidation, they overestimate compressibility. However, Figure 6.15 shows that model ModU overpredicts by only 1.5 times, compared to 2.5 times for model Orig. The stiffer behaviour of model ModU compared with model Orig is due mainly to a greater value (300 instead of 200) for parameter C_b, which defines the stiffness behaviour from Equation 6.2. Adopting a lower value (10 instead of 20) for parameter ω_s—which determines the rate of stiffness degradation—also contributes to the greater stiffness of model ModU at later strains. In practice, the choice of stiffness parameter is likely to be site-specific, as exemplified in Section 7.6.1, which questions the stiffness parameter C_b applied in the numerical simulation of tunnel excavation at St James's Park.

Fissure softening Fissure softening is only initiated in test O25 (Figure 6.14e), which causes an unrealistically abrupt change in compressibility. A likely explanation for the lack of fissure softening in reality considers the nature of boundary conditions: fissures might soften in triaxial tests because the confining membrane allows relative movement between fissure surfaces; in contrast, the rigid walls in oedometer tests might prevent this, and hence inhibit softening in real oedometer tests. However, such rigidity in boundary displacement would be rare in tunnelling simulations, so that the fissure models would still apply.

Convergence Figure 6.14 also shows that most simulations stop converging and terminate after about 2MPa due to large volumetric strains developing, which

causes the yield surface to collapse. Stresses in tunnel analyses are unlikely to reach this level, so this should not present a problem.

6.9.2 Drained triaxial tests

Simulations In addition to oedometer tests, the drained performance was also evaluated with three drained triaxial tests: two in compression and one in extension. Details are given in Table 6.2 and Figure 6.2a. The first number in the test name indicates the specimen depth in metres.

Performance of ModU Comparison of Figures 6.16a and 6.17a with Figures 6.16b and 6.17b confirm that model ModU is superior to model Orig in replicating drained behaviour. The figures show that model ModU produces around twice the drained stiffness of model Orig, and is also able to predict peaks in stress and volumetric strain.

As with the oedometer tests, the greater drained stiffness exhibited by model ModU can be attributed to increasing C_b and reducing ω_s. The earlier softening—which enables model ModU to predict a peak in stress and volumetric strain—is due to the reduced Poisson's ratio ν_hv.

Performance of ModF As demonstrated in Figures 6.16c and 6.17c, model ModF can replicate the softening behaviour in extension, but prevents strength and volumetric strain from attaining a peak.

Performance of ModG Figures 6.16d and 6.17d show that model ModG makes no improvement to model ModU. The triaxial loading condition mobilises only a low shear stress on the sub-horizontal and sub-vertical fissure planes; since model ModG reduces only the shear stiffness parallel to these planes, the softening has little influence.

6.9.3 Undrained triaxial tests

Simulations Validation was performed against a total of eighteen undrained triaxial tests. They consisted of six compression and four extension tests from Gas-

parre (2005), and eight additional extension tests from Nishimura (2006). These additional tests were included to confirm that the fissure models could replicate the observed fissure softening behaviour. All triaxial tests are detailed in Table 6.2 and Figure 6.2a. For Gasparre's tests, the test name indicates the specimen depth and labels compression and extension paths as UC and UE respectively. Nishimura's triaxial extension tests are labelled TE1, TE2 *etc.*.

For Gasparre's tests, Figures 6.18, 6.19 and 6.20 compare the performance of each soil model with the laboratory data, presenting stress paths, stress-strain behaviour and pore pressure evolution respectively. Figures 6.21 and 6.22 present the performance for Nishimura's tests, showing stress paths and stress-strain paths. Stiffness degradation curves are also compared in Figure 6.23. For Nishimura's tests, pore pressure development could not be compared because such plots were unavailable.

Curves for Gasparre's tests were plotted from raw data, which required smoothing to remove noise at very small strains. Nishimura's data was digitized from plots, so stiffnesses at small strains are less accurate.

Performance of ModU Figure 6.24 facilitates immediate comparison between the stress-strain performance of models Orig and ModU. The plot presents two performance measures: the fit to small-strain stiffness, and the fit to medium-strain stiffness. The stiffness at 0.01% axial strain was taken as the small-strain stiffness, being the lowest strain where noise allowed a confident value of stiffness to be determined. Medium-strain stiffness was taken at 0.5% axial strain. The error ratio for both initial stiffness and stiffness degradation is the ratio between the value for the model simulation and that for the laboratory data, so that an error of unity represents perfect agreement. Figure 6.25 presents analogous measures for the rate of excess pore pressure generation. Nishimura's tests are not plotted because at small strains, the digitized data was not reliable.

Figures 6.24 and 6.25 illustrate that model ModU gives a slightly improved overall fit compared with model Orig, with errors centred closer around unity. The comparative fit of each individual test depends upon the approach path, but overall, Figure 6.24 shows that model ModU produces almost twice the small-

strain stiffness as model ORIG, with medium-strain stiffness much the same. A similar trend with pore pressure development is demonstrated in Figure 6.25.

The stiffer response of MODU is due to a higher value of C_{b}, which determines initial stiffness behaviour. The faster stiffness degradation is attributable to the different Poisson's ratios, and also to earlier plasticity imparted by the lower value of m; the parameter m in Equation 6.1.

Figure 6.25 highlight the two extension tests 7gUE and 23gUE as exceptions to this trend, with model MODU instead predicting softer behaviour. Originating from the shallowest unit, model MODU endowed specimen 7gUE with a smaller yield surface than model ORIG gave, reducing the stiffness and dilatancy. For specimen 23gUE, the additional unload-reload loop included in its approach path might have induced yield surface contraction.

Comparison of Figures 6.18a and b also illustrates that model MODU is able to generate more realistic stress paths than model ORIG. Stress paths of model MODU are characterised by rightward curvature, in contrast to the constant gradients of model ORIG. The curvature with model MODU corresponds to late development of dilation. This is the reduced parameter m, which encourages the earlier onset of plasticity.

Performance of MODF A key purpose of the validation was to replicate the abrupt softening evident in most of the extension tests in Figures 6.19 and 6.22. Figures 6.19c, 6.20c and 6.22c demonstrate that model MODF could approximate the sudden reductions in stiffness and dilatancy.

The strain at softening and the post-softening behaviour varies widely according to the natural variability in occurrence, orientation and complexity of the fissures. The perceived points of softening in the laboratory extension tests indicated on the stiffness degradation curves of Figure 6.23 can be compared with the points of softening modelled by model MODF, marked by the departure of MODF from model MODU. The modelled softening follows a similar drop in stiffness, but can only approximate the strain at softening due to this natural variability.

Performance of MODG Unlike model MODF, model MODG exhibited notable undesirable features. The model was unable to replicate the desired fissure

softening in the extension tests of Figures 6.19d and 6.22b. This is because only the shear component on the softened fissure plane is reduced. Since the extension tests mobilised only very low shear stresses on sub-horizontal planes, the effect on strength was negligible.

Whereas stress paths from model ModF were more realistic—with rightward curvature—model ModG imparts a leftward curvature around the yield point as seen in Figure 6.18d. This unrealistic increase in dilatancy is not observed in the laboratory.

The unusual dilatancy observed in model ModG is due to changes in Poisson's ratios when fissures soften. In model ModF, all components of the stiffness matrix degrade uniformly, so that elastic Poisson's ratios remain unaltered. However, model ModG effects only softening along a plane; the directionality of this softening can drastically distort the elastic Poisson's ratios, and hence the evolution of undrained stress paths as well.

6.9.4 Hollow cylinder tests

Simulations Ten undrained hollow cylinder tests performed by Nishimura (2006) were simulated to encompass a variety of stress paths, since during tunnel construction, the soil undergoes complex stress changes. The tests were described in Section 6.6.3, with details given in Table 6.4. The test names indicate the stress path followed: the third and fourth digits give $\alpha_{d\sigma}$ in degrees, whilst the last two digits indicate the value of b.

Figures 6.26 and 6.27 compare the stress paths and stress-strain behaviour for each model simulation with the laboratory data. The initial mean effective stress was offset from the laboratory value in many of the simulations, most notably for AC4507. This was due to the approximation in modelling the preceding undrained b-change step; Nishimura observed high creep strains following this step, and stress relaxation could have changed effective stresses. This suggests that a creep model is needed to replicate the correct stress and strain history during set-up.

Figure 6.28 presents stiffness degradation curves for each test, whilst the error plots of Figure 6.29 summarise the match of stiffness at small and medium strains. The small-strain stiffness was taken at the lowest possible deviatoric strain

of 0.01%, where the stiffness derived from the digitized data seemed sufficiently reliable. A stiffness at a deviatoric strain of 0.5% was chosen to represent the medium-strain behaviour.

The potential for deviatoric stress to both rise and fall in the same hollow cylinder test means that stiffness can alternate between positive and negative during a test. The ratio error—defined in Section 6.9.3—would be misleading in such tests. Instead, the error plotted in Figure 6.28 was defined as the absolute difference between laboratory and model stiffnesses, normalised by the laboratory value. In this way, errors of zero indicate perfect agreement.

Performance of ModU In Figure 6.29, error increases with distance from the origin, suggesting that overall, model ModU simulated stiffness no better than model Orig. Model ModU generally modelled much higher stiffnesses at lower angles of $\alpha_{d\sigma}$. This was due to the rotated yield surface, which makes compression behaviour (where $\alpha_{d\sigma} = 0°$) stiffer than extension behaviour (where $\alpha_{d\sigma} = 90°$). Model ModU therefore models some tests better, and some tests worse: higher stiffnesses at low angles of $\alpha_{d\sigma}$ are more realistic, whilst stiffness in torsional modes with $\alpha_{d\sigma} = 45°$ is severely overestimated.

This reveals a need to model less stiff behaviour for mid-range values of $\alpha_{d\sigma} \simeq 45°$. Consideration of a cuboid specimen provides a physical interpretation for this. When aligned with the material axes, the specimen is softer under simple shear ($\alpha_{d\sigma} = 45°$), where shear stresses parallel to the faces cause shearing, than under direct shear ($\alpha_{d\sigma} = 0°$ or $90°$), where normal stresses on the faces cause the shearing. This could arise due to the horizontal orientation of particles within the clay, which could allow them to slide more easily under simple shearing.

Model ModU imparts a slightly more realistic curvature to stress paths, as illustrated by comparing Figures 6.26a and b. As with the undrained triaxial tests, this is likely to be due to the different Poisson's ratios applied.

Performance of ModF Compared with the triaxial cell, the influence of fissuring is less obvious in the HCA, so that Nishimura could not explain the abrupt softening in tests such as AC4505. He suggested that the geometry of torsional shearing effectively transforms a sub-horizontal planar fissure into a discontinuity

whose height varies sinusoidally around the circumference. The sinusoidal geometry would mobilize the softening friction angle only at isolated locations rather than across an entire plane at once; this might suppress fissure softening. Nishimura noted that discontinuities might be less active in tests where $b = 0.5$ since the asymmetry of loading reduces the number of possible orientations for the failure planes compared with the infinite number of planes possible with the axisymmetric loading of tests where $b = 0.0$ or 1.0.

Although it is inconclusive whether or not fissures cause premature softening in the HCA, the clustering of errors around zero in Figure 6.29c indicates that model ModF fits the stress-strain behaviour significantly better than model Orig. The stiffness degradation curves in Figures 6.28b–f highlight that this is particularly true for tests where $\alpha_{d\sigma} \leq 45°$. For most tests, fissure softening begins in the undrained b-change step. This might explain the absence of sudden softening during the shearing stage of many of the laboratory tests. Figures 6.26a and 6.26c show that the stress paths of model ModF are also more realistic in general than model Orig.

The improved fit of model ModF is due to softer behaviour for $\alpha_{d\sigma} \simeq 45°$ stress paths compared with other stress paths. Stress paths with $\alpha_{d\sigma} \simeq 45°$ correspond to simple shearing on a cuboid specimen aligned with the material axes, and mobilise greatest shear stresses on horizontal and vertical planes. This causes earlier softening along the sub-horizontal and sub-vertical fissures modelled by model ModF. For other stress paths, the planes of maximum shear stress are more inclined, and fissure softening is less likely.

Performance of ModG Despite improving the realism of stress-strain paths shown in Figure 6.27d, Figure 6.26d shows that model ModG introduces undesirable leftward curvature to stress paths, most notably in torsional modes where $\alpha_{d\sigma} = 45°$. Like model ModF, ModG can soften stress paths with $\alpha_{d\sigma} \simeq 45°$ preferentially to other stress paths. However, the non-isotropic adjustment of stiffness components in model ModG leads to the Poisson's ratios evolving in an unrealistic manner, causing adverse curvature in the stress paths.

6.10 Model suitability

The suitability of models ModU, ModF and ModG for use in long-term simulations is summarised below. The performance of each model is compared to that of Orig.

Model ModU The most significant improvement is the improved drained behaviour, which should yield more realistic results during consolidation following tunnel construction. This was achieved by adjusting parameters C_b and ω_s, which determine the elastic stiffness matrix. Also, the model's stiffer response in stress and pore pressure generally fits undrained compression behaviour better. Although C_b and ω_s also influenced this, the adjusted Poisson's ratios and the lower value of m, which imparted earlier plasticity, helped accelerate the stiffness degradation for a more realistic match.

Model ModF Being based upon model ModU, model ModF inherits the improved drained behaviour. It is capable of replicating the observed fissure softening in extension tests, and can also fit the wide variety of hollow cylinder stress paths significantly better. The improved fit to hollow cylinder tests is due to preferential softening when $\alpha_{\mathrm{d}\sigma} \simeq 45°$, which encourages fissure planes to soften. These benefits make model ModF the most favoured to model tunnel excavation and consolidation.

Model ModG Model ModG exhibits features undesirable for tunnel simulation, despite inheriting improved drained behaviour from model ModU. Fissure softening is accompanied by adverse pore pressure changes due to the directional nature of softening, which cause drastic changes in Poisson's ratios. The reduction of only the shear stiffness component along the fissure also means that significant shear stress on the fissure plane must be mobilised before softening becomes noticeable. The softening in model ModG is therefore unrealistic and unsuitable.

6.11 Summary

Long-term tunnelling simulations need a constitutive model which can accurately represent strains and pore pressures under a wide range of stress paths and drainage conditions. For his long-term tunnel analyses, Wongsaroj (2005) formulated a model for London Clay behaviour. However, new information for London Clay (Hight *et al.*, 2007) was since published concerning its strength anisotropy, fissure softening and variation with depth.

In this chapter, three new models based upon Wongsaroj's original model were developed and validated against the new data. One model demonstrated that modifying the yield surface size and rotation, and using alternative parameters, imparted superior behaviour in drained tests. The other two models built upon this modified model by adding fissure softening. The fissure softening model used a frictional criterion to soften either isotropically in the first model, or solely along the fissure plane in the second.

The model that softened directionally gave poor results, but the model that softened isotropically demonstrated an improvement by modelling fissure softening, in addition to improved drained behaviour inherited from the modified model. This makes it the prime candidate for use in tunnelling simulations.

DESCRIPTION	PARAMETER	UNITS	MODEL					
			Wongsaroj (2005) to match Yimsiri (2001)	Wongsaroj (2005) to match St James's Park	ORIG	MODU	MODF	MODG
Elastic parameters								
Poisson's ratio of horizontal strain under vertical straining	ν_{vh}	-	0.07	0.07	0.07	0.015	0.015	0.015
Poisson's ratio of vertical strain under horizontal straining	ν_{hv}	-	0.16	0.16	0.16	0.04	0.04	0.04
Poisson's ratio of horizontal strain under horizontal straining	ν_{hh}	-	0.12	0.12	0.12	0.12	0.12	0.12
Shear stiffness anisotropy ratio	G_{hh}/G_{vh}	-	1.5	1.5	1.5	1.5	1.5	1.5
Initial gradient of isotropic swelling line at load reversal	C_b	-	200	200	200	300	300	300
Non-linearity of swelling line	ω_s	-	3	20	20	10	10	10
Gradient of normal consolidation line in log e - log p' space	ρ_c	-	0.225	0.3	0.225	0.225	0.225	0.225
Factor for non-linearity during isotropic loading and unloading	D	-	0.05	0.05	0.05	0.05	0.05	0.05
Factor for non-linearity during isotropic loading and unloading	r	-	2	2	2	2	2	2
Plastic parameters								
Factor for evolution of plastic strain	u_1	-	300	300	300	300	300	300
Factor for evolution of plastic strain	m	-	0.2	0.2	0.2	0.05	0.05	0.05
Yield surface parameters								
Gradient of critical state line in q-p' space	M	-	0.89	0.814	0.89	0.89	0.89	0.89
Yield surface rotation towards σ_{vv}-direction	β_{vv}	-	0	0	0	0.1	0.1	0.1
Yield surface rotation towards σ_{hh}-direction	β_{hh}	-	0	0	0	-0.05	-0.05	-0.05
Yield surface rotation towards τ_{vh}-direction	β_{vh}	-	0	0	0	0	0	0
Initial preconsolidation pressure for Unit C	$p'_{0\,(C)}$	kPa	3000	-	3000	1000	1000	1000
Initial preconsolidation pressure for Unit B	$p'_{0\,(B)}$	kPa	3000	vary	3000	3000	3000	3000
Initial preconsolidation pressure for Unit A	$p'_{0\,(A)}$	kPa	3000	vary	3000	3000	3000	3000
Fissure model parameters								
Maximum inclination of fissure plane to either vertical or horizontal directions	α_{range}	°	-	-	-	-	16	16
Fissure friction angle at onset of softening	ϕ_{soft}	°	-	-	-	-	11.5	11.5
Range of fissure friction angle over which stiffness reduction factor ramps to minimum value	ϕ_{range}	°	-	-	-	-	1.5	1.5
Measure of minimum fissure stiffness, default	$f_{fiss\ min}$	-	-	-	-	-	3.6	0.66
Measure of minimum fissure stiffness, in hollow cylinder tests for better match	$f_{fiss\ min\ (HCA)}$	-	-	-	-	-	0.66	0.66

Table 6.1: Comparison of original and adjusted soil model parameters

TEST NAME	INITIAL VOID RATIO	DEPTH	UNIT	TEST TYPE	AUTHOR	SET-UP STAGE A P'-CONSOLIDATION		B Q-REDUCTION		C UNLOAD		D RELOAD		E P'-INCREASE		F UNLOAD		G RELOAD	
	e_0	z m				p' kPa	q kPa	p' kPa	q kPa	p' kPa	q kPa	p' kPa	q kPa	p' kPa	q kPa	p' kPa	q kPa	p' kPa	q kPa
7gUE	0.758	7.0	C	UE	G	260	0	260	-85										
11gDE	0.684	11.0	B2c	DE	G	260	0	260	-85										
13gUE	0.666	13.0	B2b	UE	G	250	0	250	-120										
23gUE	0.739	23.0	B2a	UE	G	420	0	420	-195	365	-209	411	-167						
31.4gUE	0.798	31.4	B2a	UE	G	510	0	510	-125										
7gUC	0.758	7.0	C	UC	G	260	0	260	-85										
11gUC	0.674	11.0	B2c	UC	G	260	0	260	-85										
12.5gUC	0.674	12.5	B2c	UC	G	260	0	260	-85										
24g37DC	0.721	24.0	B2a	DC	G	420	0	420	-195	365	-209	420	-155	475	-155	455	-178	510	-125
25gUC	0.681	25.0	B2a	UC	G	420	0	420	-195	365	-209	420	-155						
36.5gDC	0.580	36.5	A3ii	DC	G	420	0	420	-195	365	-209	507	-125						
36lgUC	0.641	36.0	A3ii	UC	G	820	0			365	-209	518	-126						
38.7lgUC	0.715	38.7	A3ii	UC	G	820	0			365	-209	502	-121						
TE1	0.729	20.9	B2b	UE	N	371	0	371	-138										
TE2	0.680	16.1	B2c	UE	N	323	0	323	-165										
TE3	0.683	27.9	B2a	UE	N	430	0	430	-160										
TE4	0.710	8.2	C	UE	N	242	0	242	-123										
TE6	0.656	13.6	B2c	UE	N	294	0	294	-149										
TE7	0.707	10.6	B2c	UE	N	277	0	277	-141										
TE8	0.691	29.1	B2a	UE	N	438	0	438	-151										
TE9	0.651	28.2	B2a	UE	N	429	0												

Key

UE	Undrained extension
DE	Drained extension
UC	Undrained compression
DC	Drained compression
G	Gasparre (2005)
N	Nishimura (2006)

Table 6.2: Implementation details for triaxial test simulations(see Figure 6.2a)

TEST NAME	INITIAL VOID RATIO	DEPTH	UNIT	VERTICAL EFFECTIVE STRESS					
				O	S	A	B	C	D
	e_0	z		$\sigma'_{v\,(O)}$	$\sigma'_{v\,(S)}$	$\sigma'_{v\,(A)}$	$\sigma'_{v\,(B)}$	$\sigma'_{v\,(C)}$	$\sigma'_{v\,(D)}$
		m		kPa	kPa	kPa	kPa	kPa	kPa
O7	0.658	7	C	100		3500	100	15000	
O10	0.747	10	B2	160		2500	160	10000	150
O12S	0.784	12	B2	75	25	4000	75	11000	25
O17	0.726	17	B2	217		5200	1300	10400	25
O25	0.717	25	B2	260		7000	260	17000	50
O25s	0.714	25	B2	150	25	1500	150	8500	25
O28	0.718	28	B2	220		3500	220	14000	220
O28s	0.731	28	B2	220	10	11500	10		
O35	0.684	35	A3ii	425		3000	425	8000	25
O35s	0.571	35	A3ii	425	25	2000	50	10000	25
O51	0.568	51	A3i	550		4400	550	14000	550

Table 6.3: Implementation details for oedometer test simulations (see Figure 6.2b)

TEST	INITIAL VOID RATIO	DEPTH	UNIT	MEAN EFFECTIVE PRESSURE	DEVIATORIC STRESS	INTERMEDIATE PRINCIPAL STRESS RATIO	INCLINATION OF MAJOR PRINCIPAL STRESS TO VERTICAL	
							INCREMENT	FINAL VALUE
	e_0	z		p'	q	b	$\alpha_{d\sigma}$	α_f
		m		kPa	kPa		°	°
AC0005	0.631	16.3	B2	323	165	0.5	0	0
AC2305	0.671	16.3	B2	323	165	0.5	15	23
AC4505	0.649	16.3	B2	323	165	0.5	30	45
AC6705	0.679	16.3	B2	323	165	0.5	55	67
AC9005	0.620	16.3	B2	323	165	0.5	90	90
AC0000	0.720	16.3	B2	323	165	0.0	0	0
AC4507	0.698	16.3	B2	323	165	0.7	30	45
AC4510	0.684	16.3	B2	323	165	1.0	30	45
AC6710	0.702	16.3	B2	323	165	1.0	55	67
AC9010	0.641	16.3	B2	323	165	1.0	90	90

Stress path:

1. Isotropic consolidation
2. Drained q-reduction with constant p'
3. Undrained b-change with constant p' and q
4. Shearing at constant p', b and $\alpha_{d\sigma}$

Table 6.4: Implementation details for hollow cylinder test simulations (see Figure 6.6)

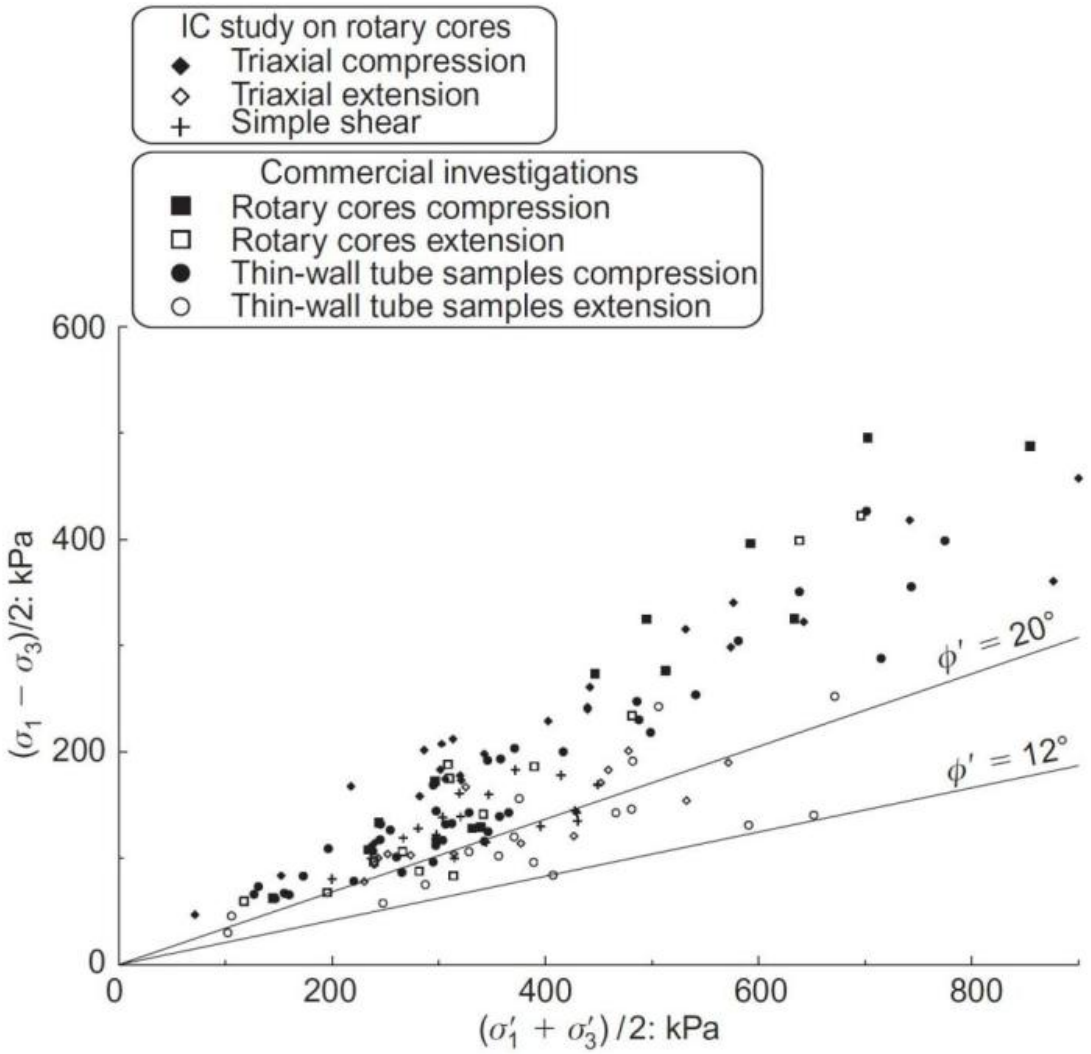

Figure 6.1: Effective stresses at failure points for undrained stress paths (Hight *et al.*, 2007)

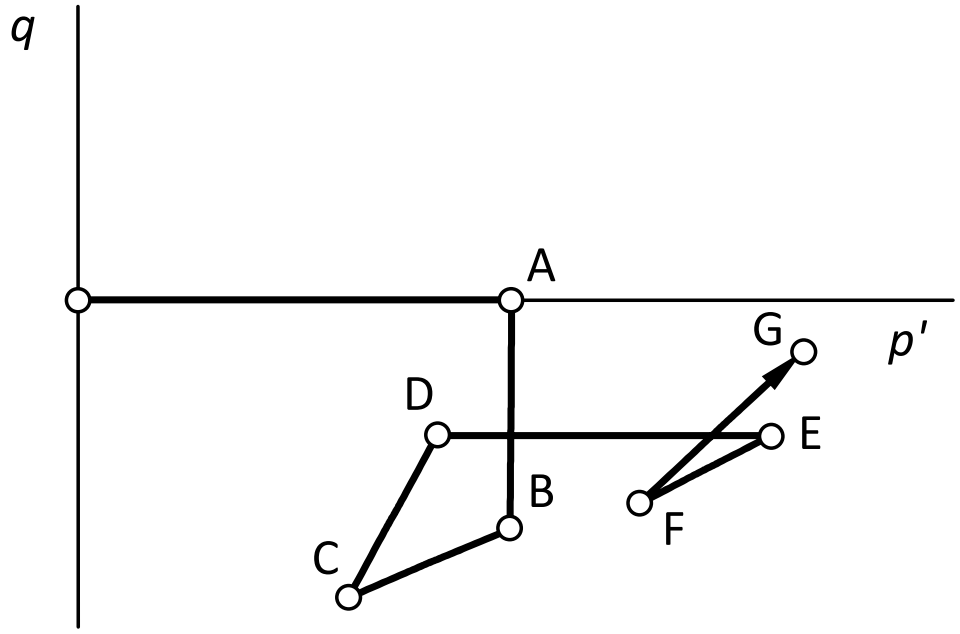

(a) Triaxial approach path

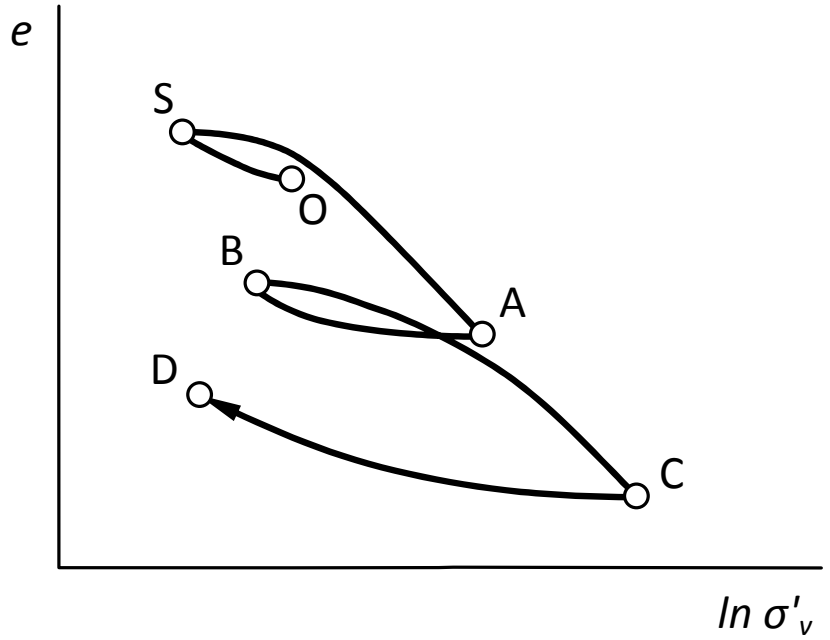

(b) Oedometer approach path

Figure 6.2: Approach paths for triaxial and oedometer test simulations (see Tables 6.2 & 6.3)

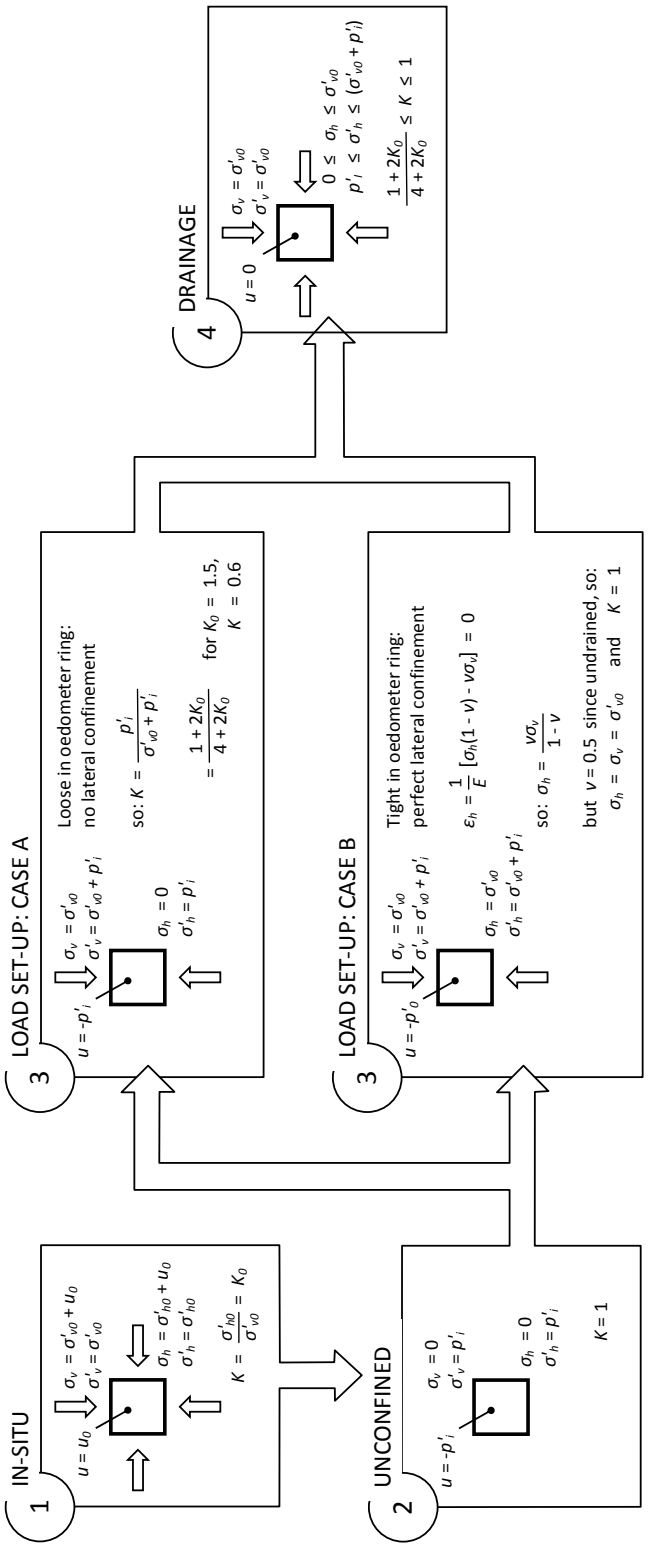

Figure 6.3: Evolution in K during oedometer test set-up

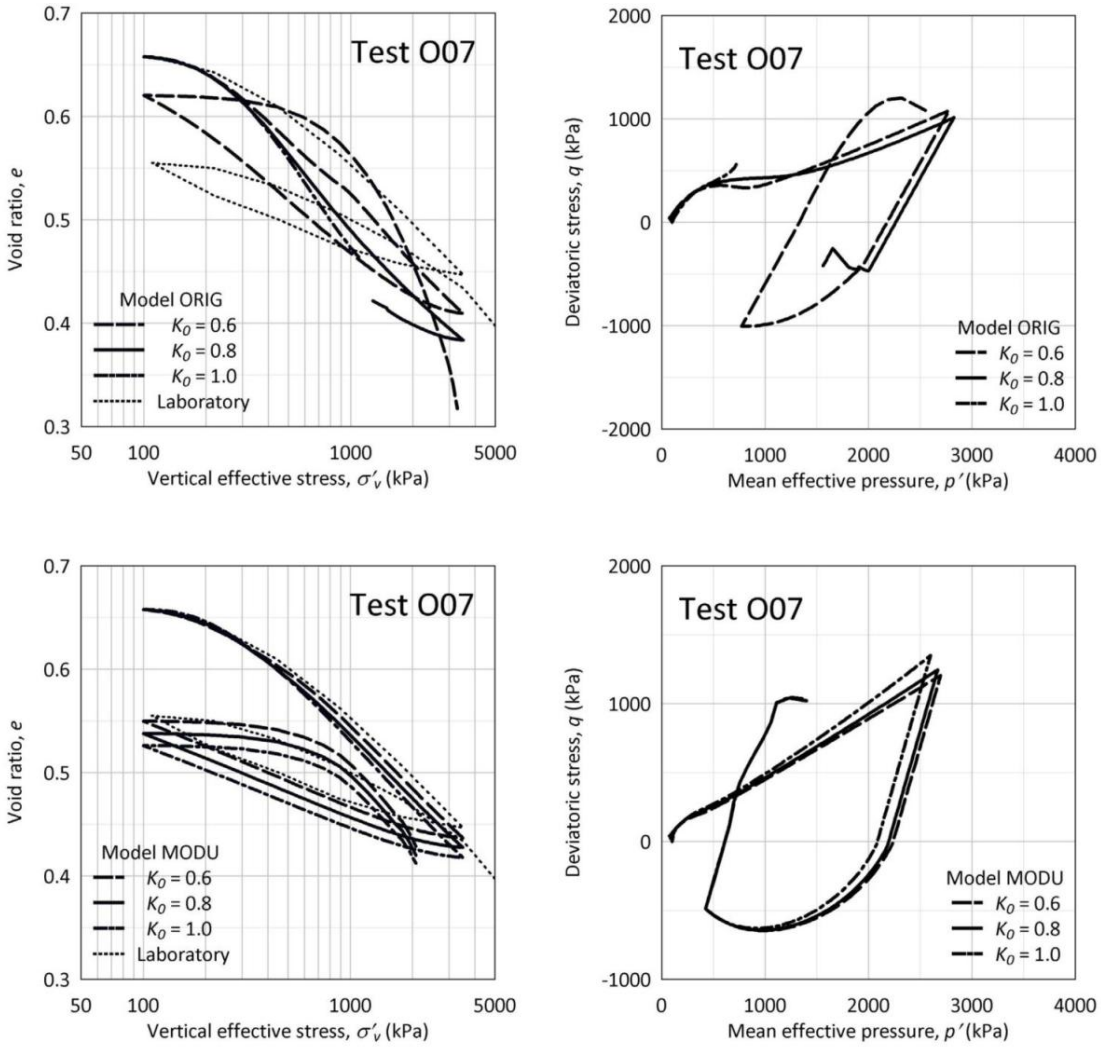

Figure 6.4: Effect of initial K_0 on oedometer simulation: without initial swelling

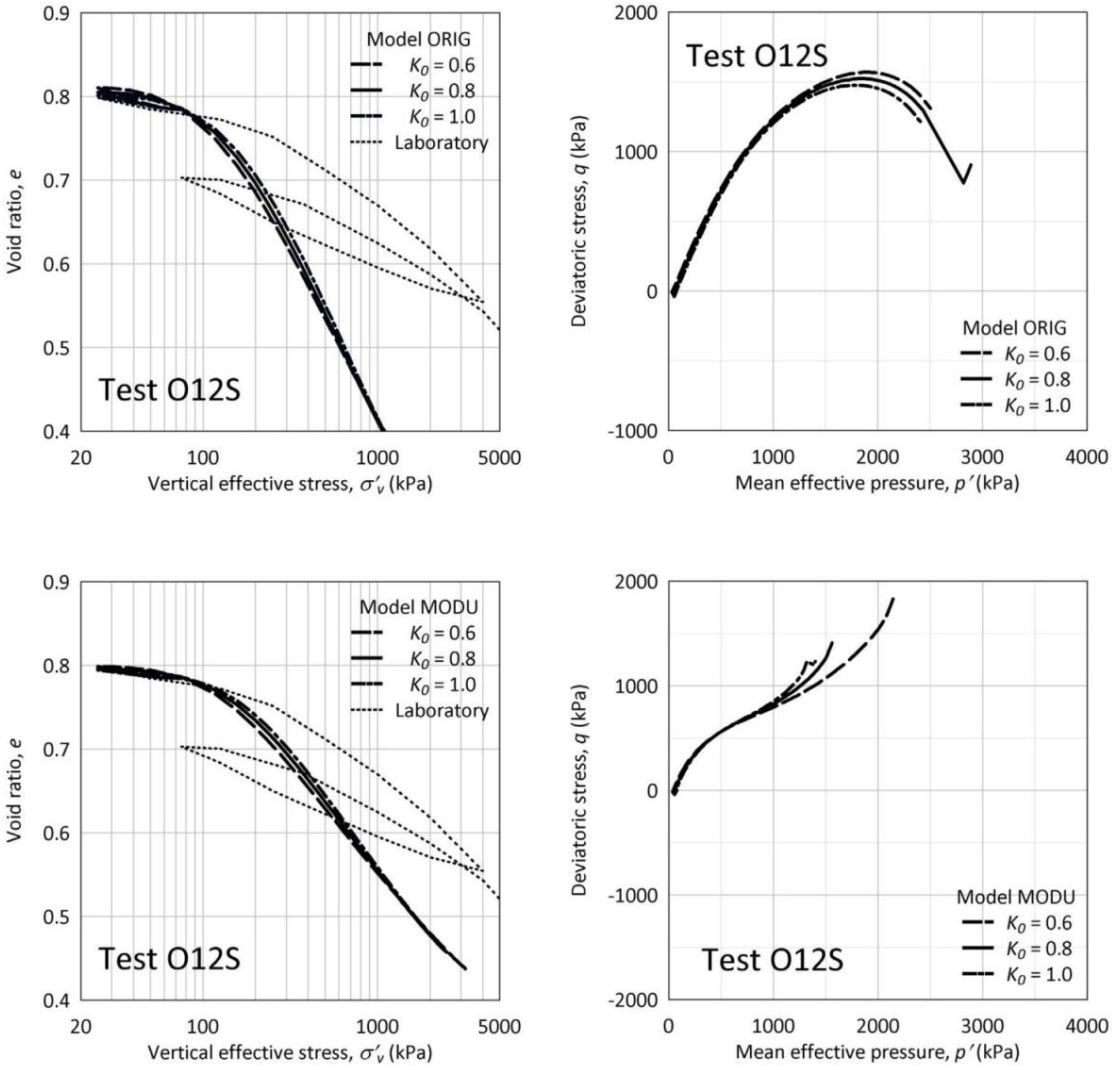

Figure 6.5: Effect of initial K_0 on oedometer simulation: with initial swelling

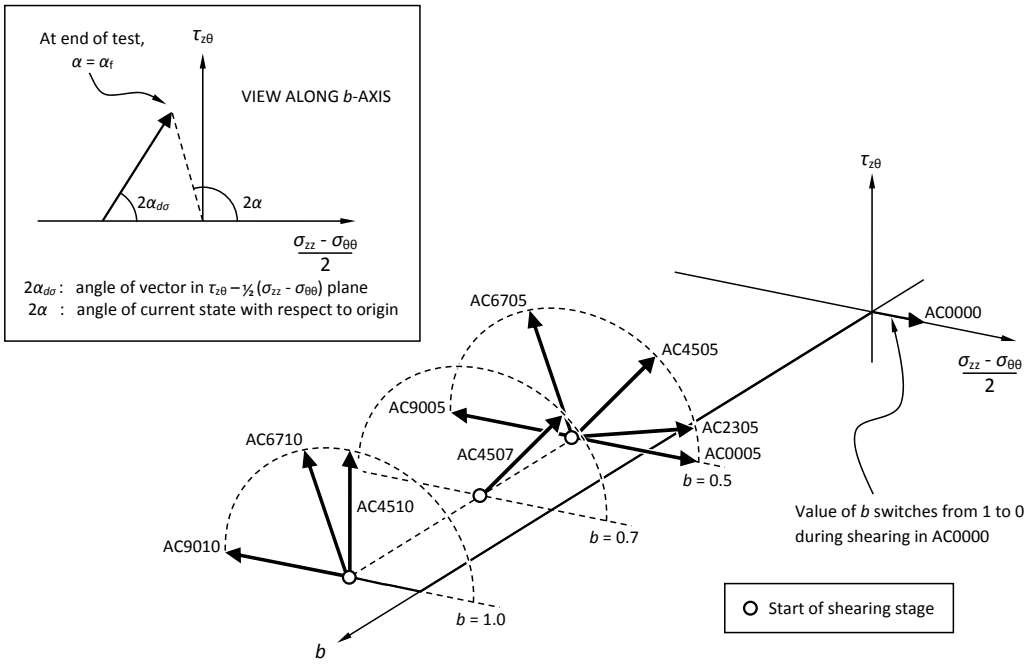

Figure 6.6: Undrained shear stress paths for hollow cylinder tests, adapted from Nishimura (2006) (see Table 6.4)

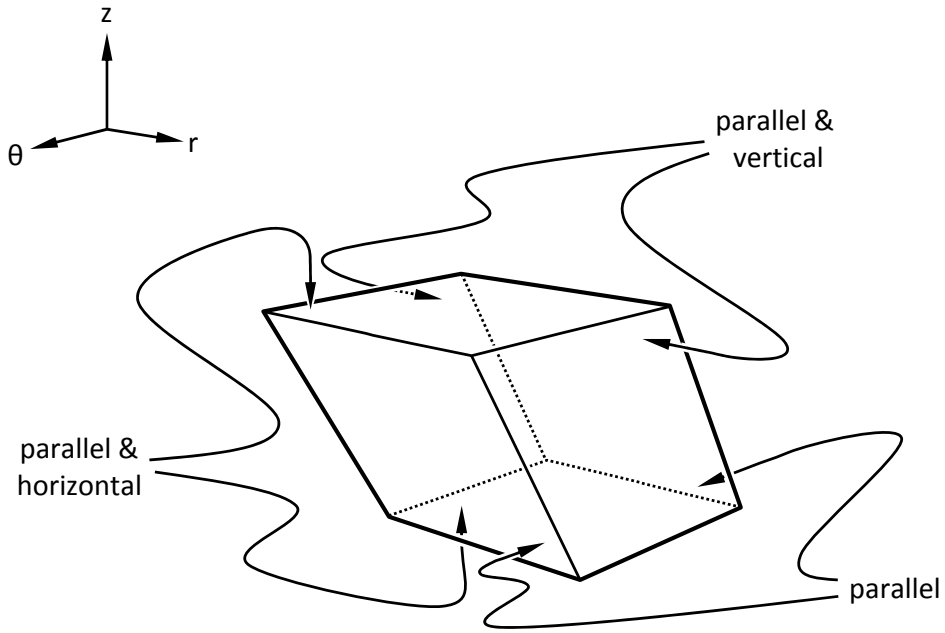

Figure 6.7: Boundary conditions for hollow cylinder tests in single-element simulation

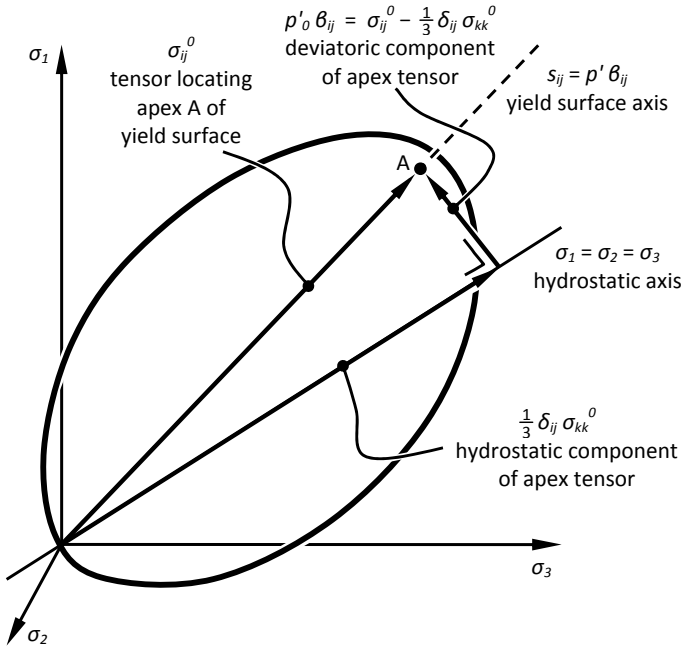

(a) In general stress space

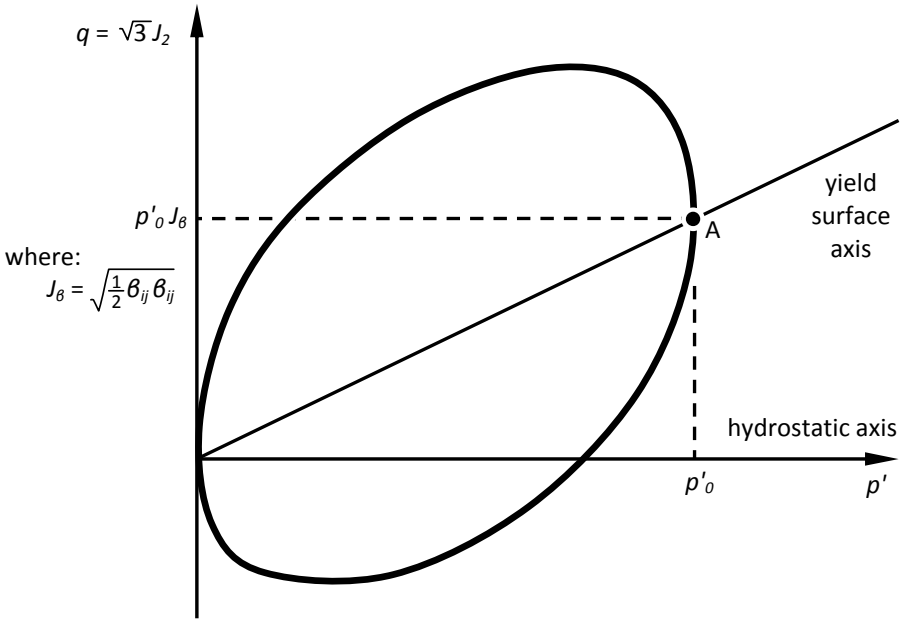

(b) In q–p' space

Figure 6.8: Interpretation of rotation tensor β_{ij} in stress space

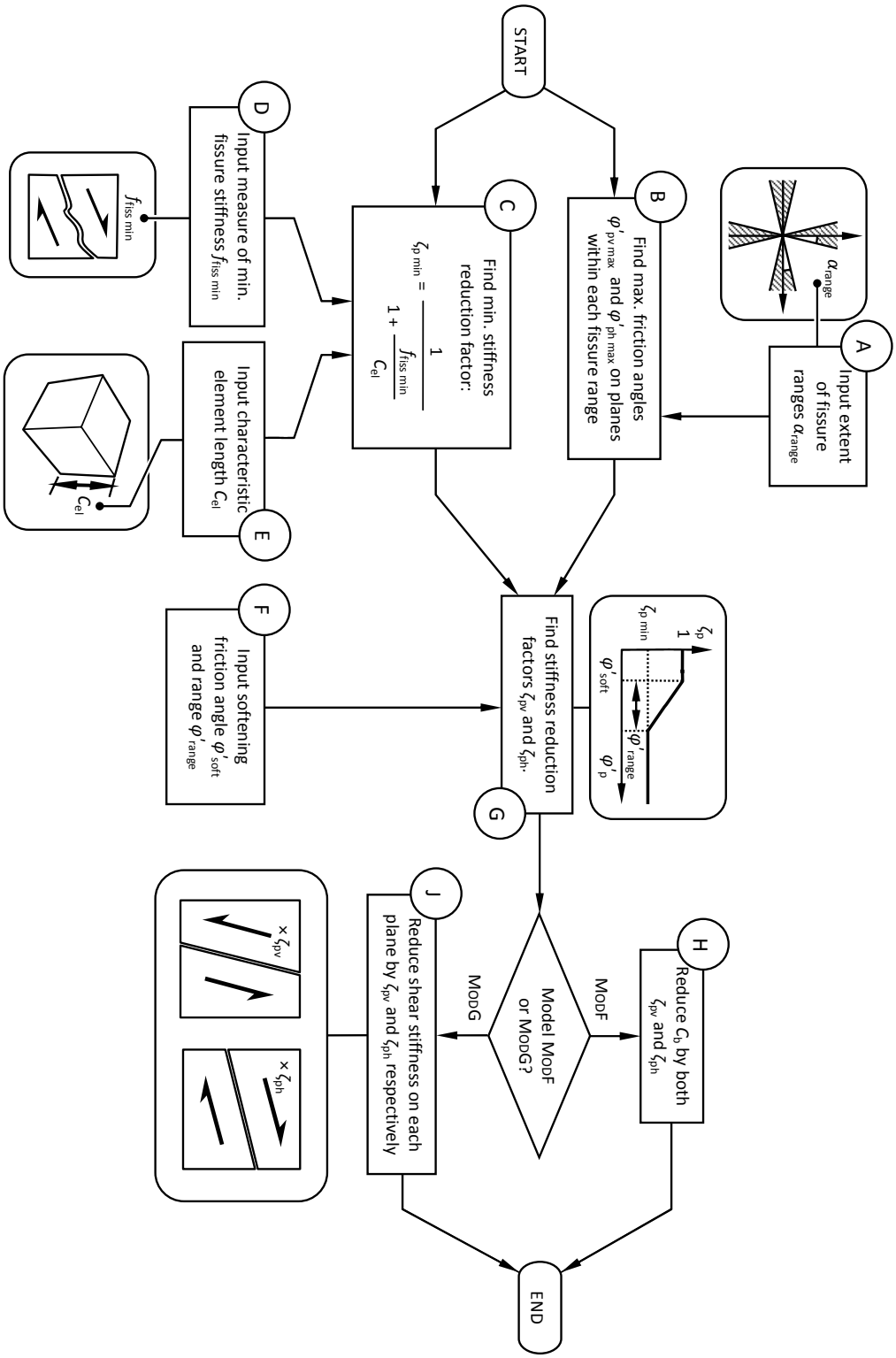

Figure 6.9: Flowchart for implementation of fissure softening

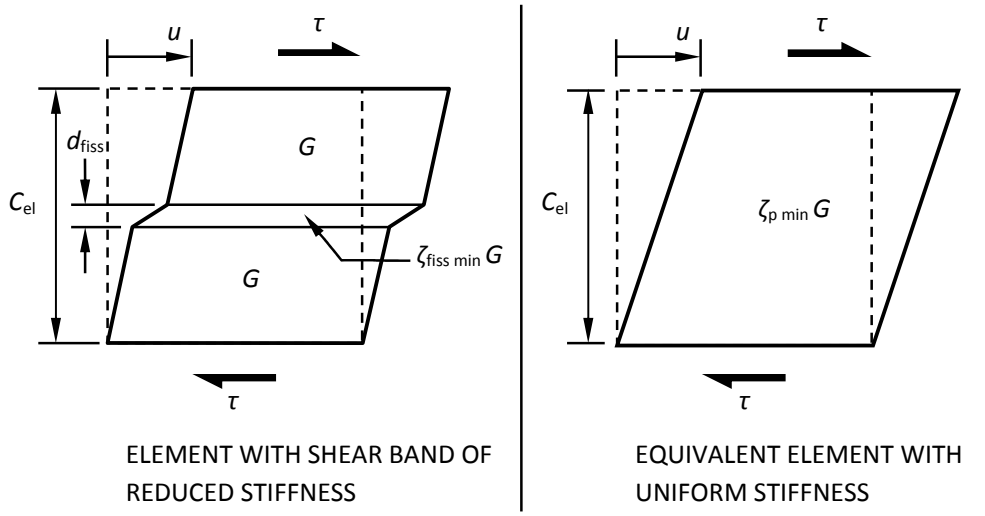

$$u = \frac{\tau}{\zeta_{p\,min}\,G}\,C_{el} \approx \frac{\tau}{\zeta_{fiss\,min}\,G}\,d_{fiss} + \frac{\tau}{G}\,C_{el} \qquad \text{for } d_{fiss} \ll C_{el}$$

$$\text{so} \qquad \zeta_{p\,min} = \frac{1}{\frac{d_{fiss}}{\zeta_{fiss\,min}\,C_{el}} + 1}$$

Figure 6.10: Scaling rule for softening factor according to element length

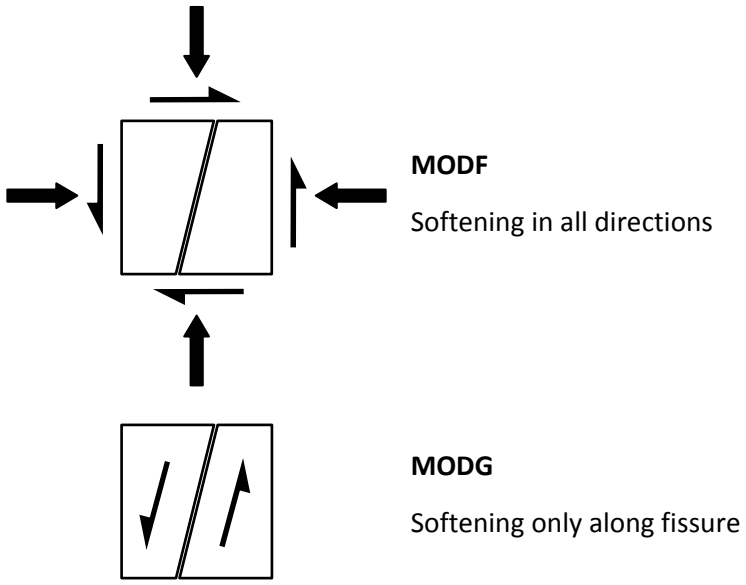

Figure 6.11: Illustration of fissure softening in models ModF and ModG

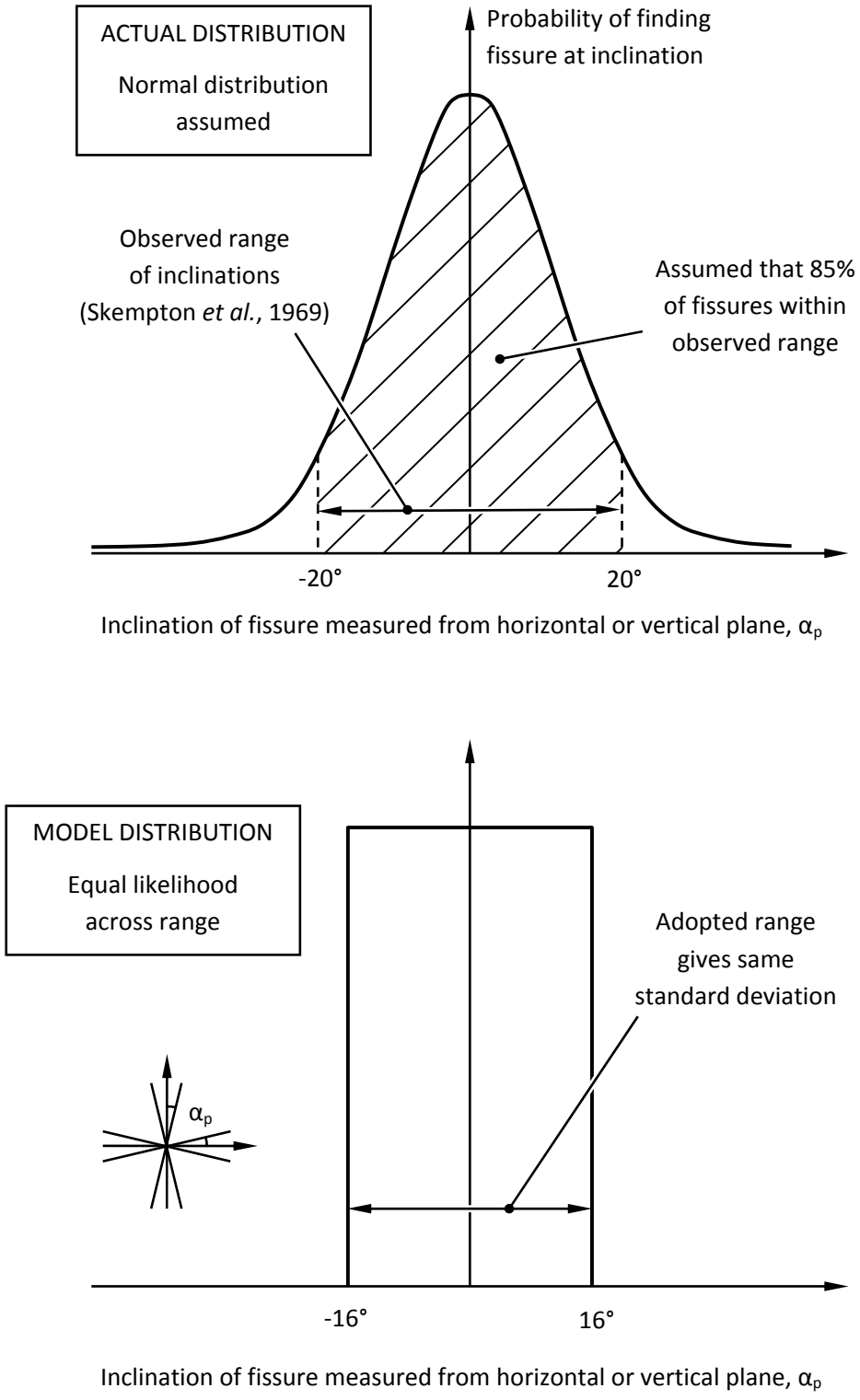

Figure 6.12: Correction to fissure inclination range to account for distribution of inclinations

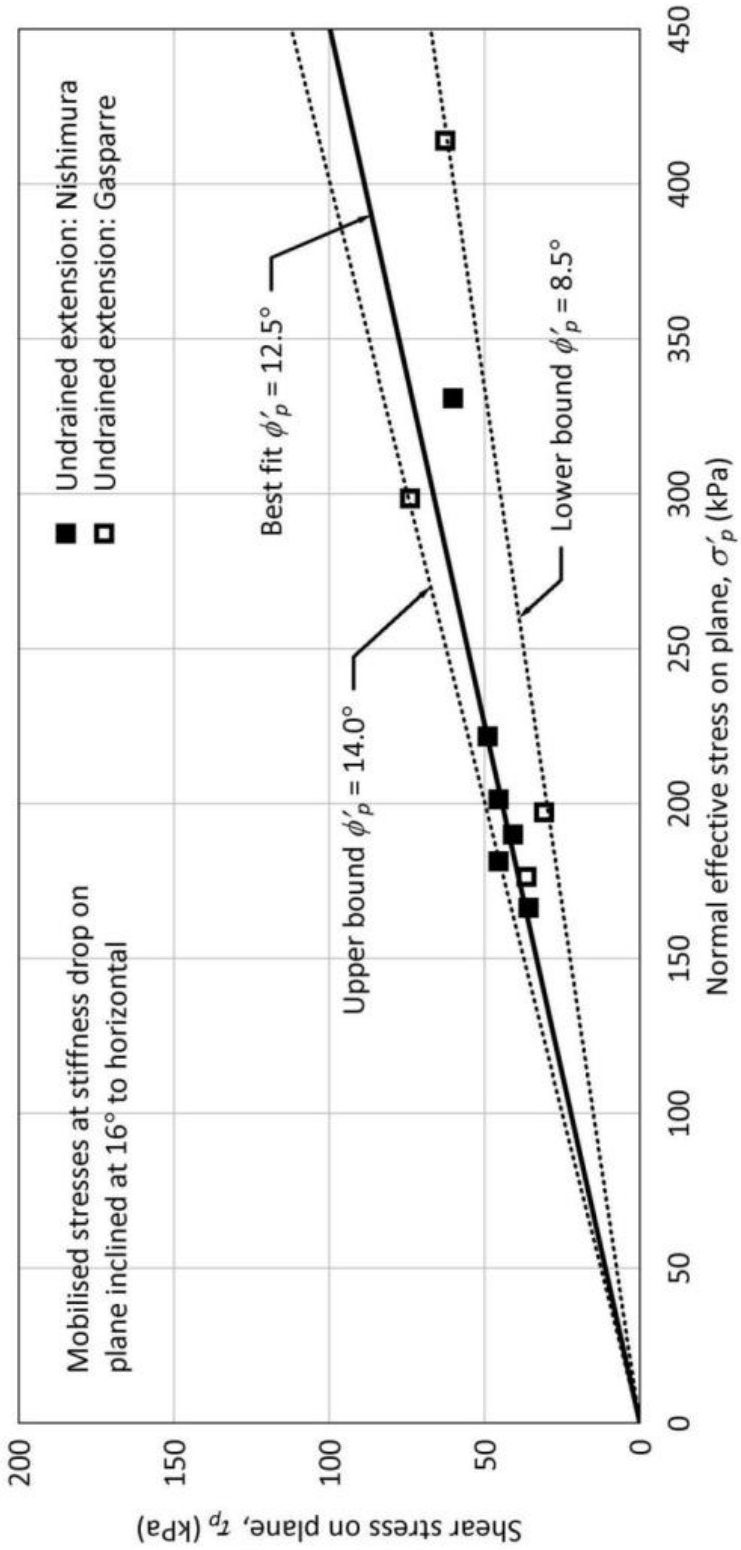

Figure 6.13: Effective stress envelope for fissure slippage in triaxial extension tests

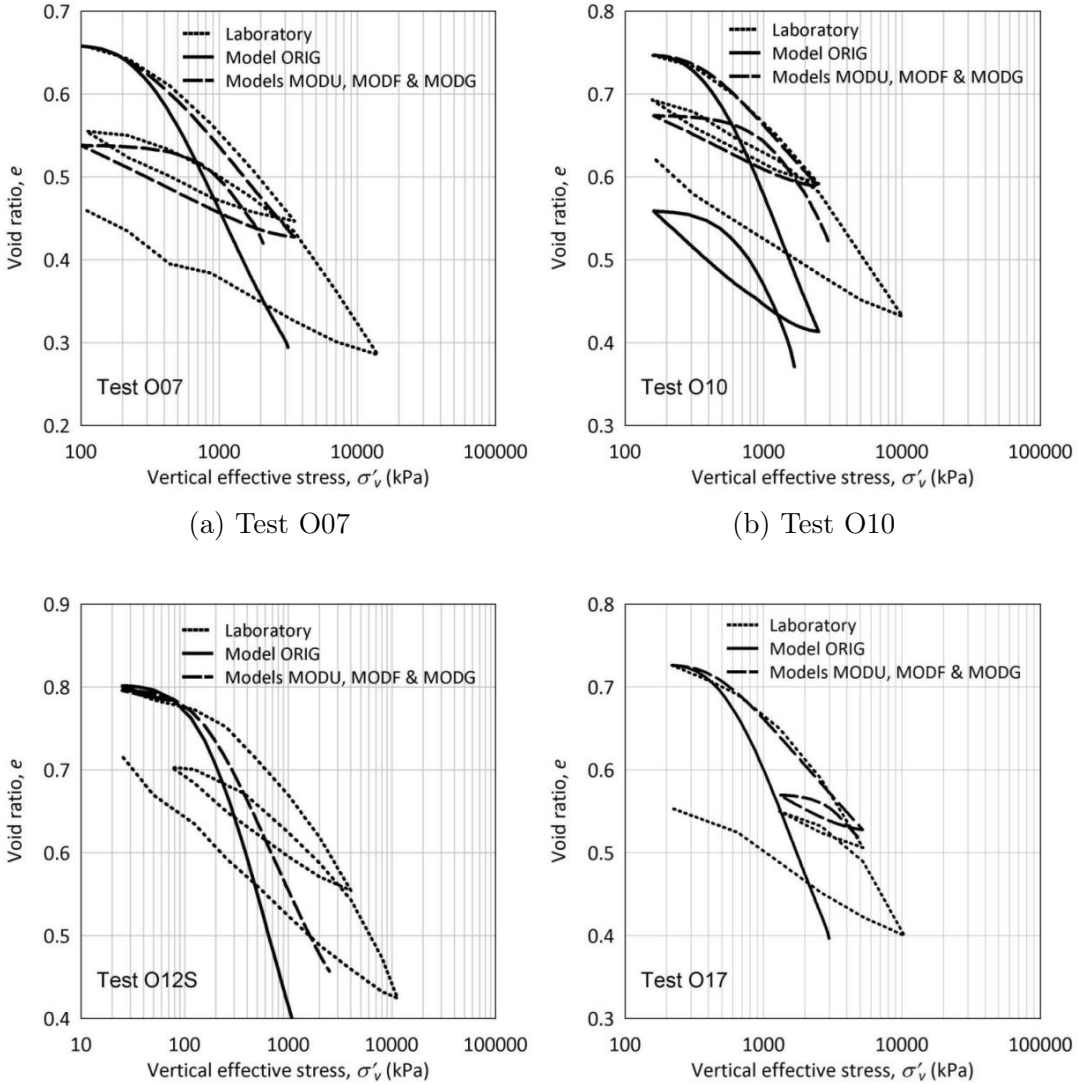

(a) Test O07

(b) Test O10

(c) Test O12S

(d) Test O17

Figure 6.14: Simulation of consolidation curves for oedometer tests of Gasparre (2005)

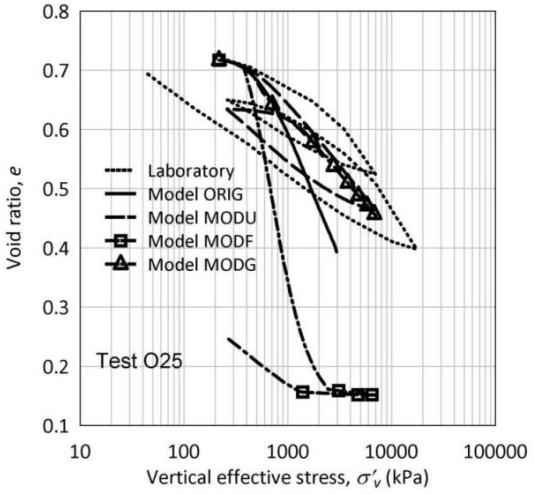

(e) Test O25

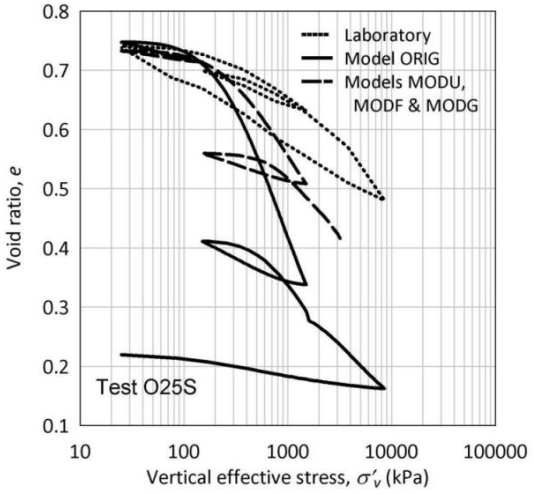

(f) Test O25S

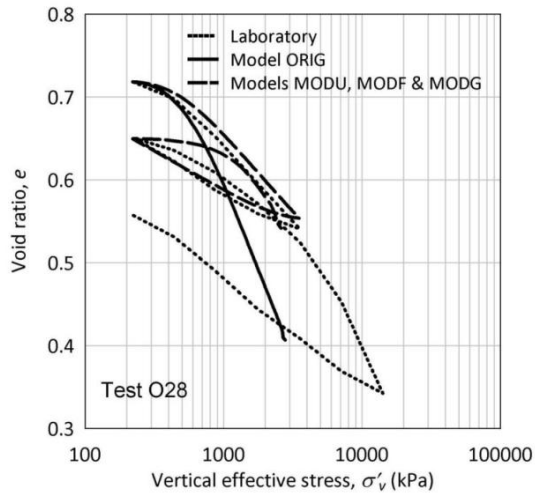

(g) Test O28

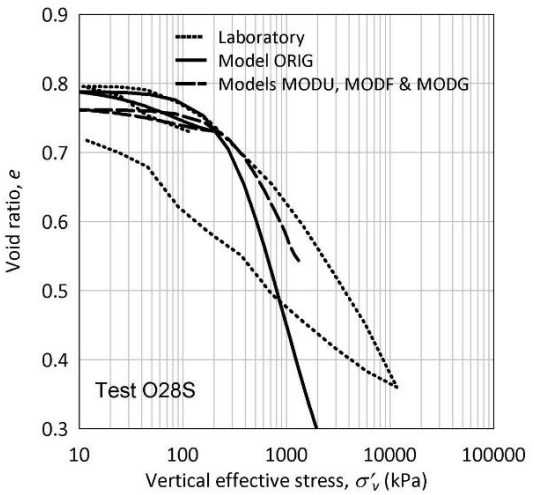

(h) Test O28S

Figure 6.14: *cont...* Simulation of consolidation curves for oedometer tests of Gasparre (2005)

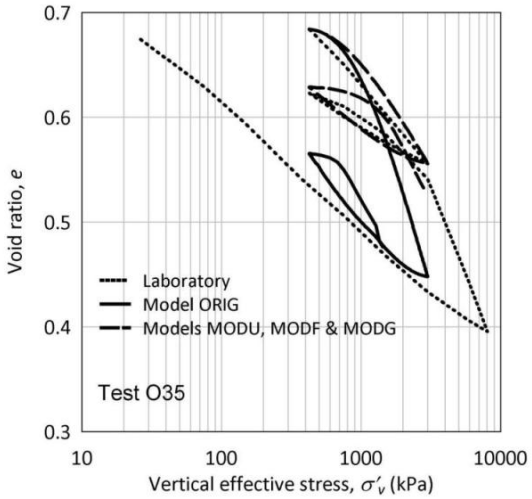

(i) Test O35

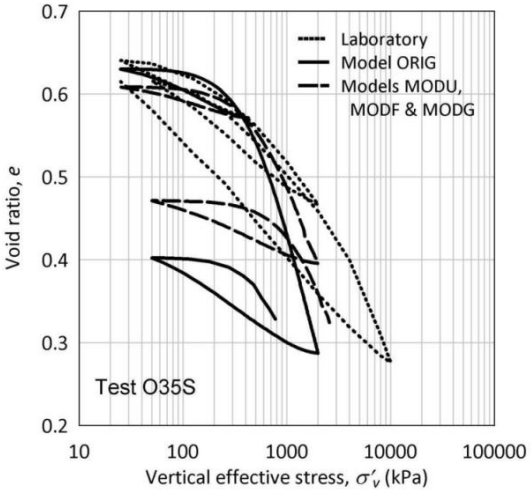

(j) Test O35S

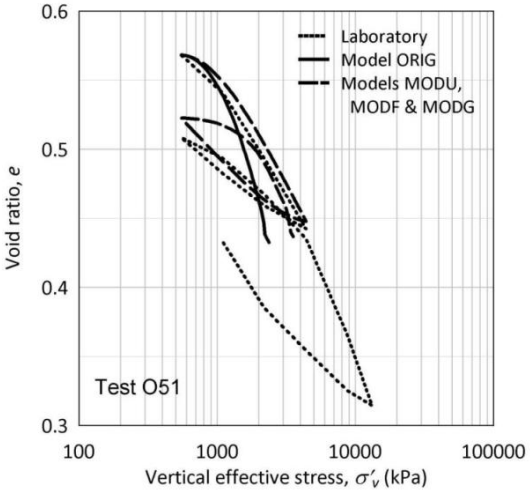

(k) Test O51

Figure 6.14: *cont...* Simulation of consolidation curves for oedometer tests of Gasparre (2005)

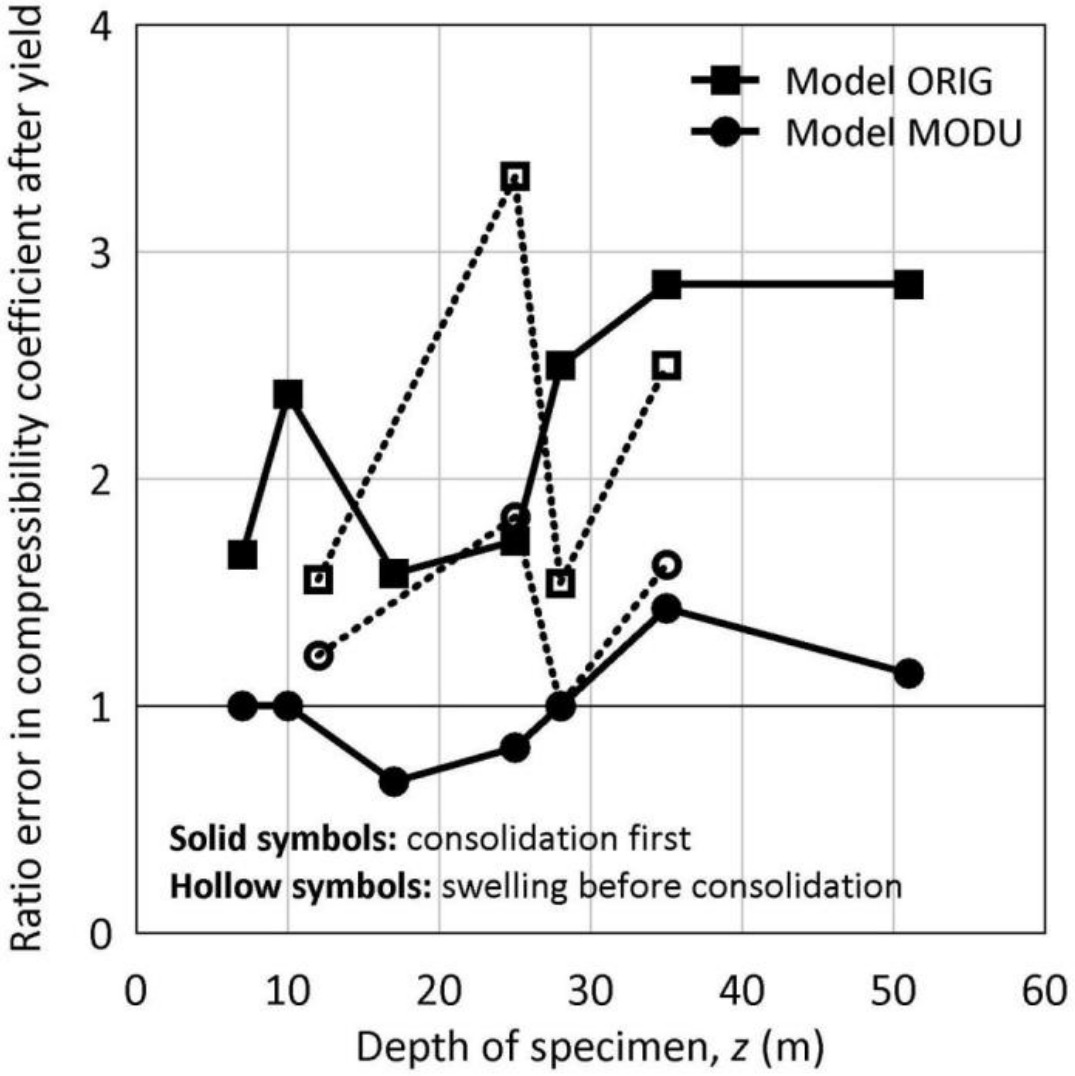

Figure 6.15: Comparison of simulated compressibilities in oedometer tests of Gasparre (2005)

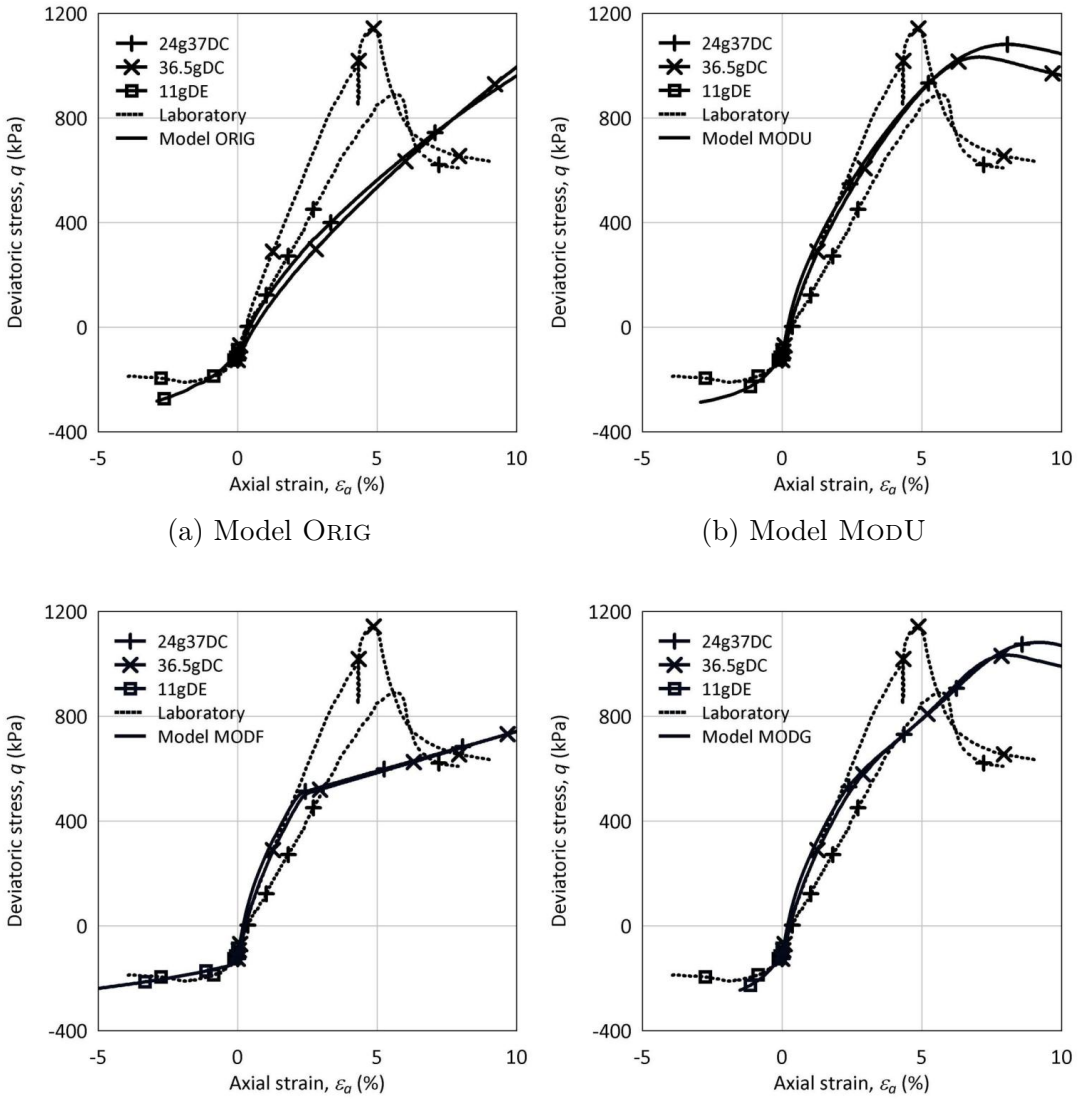

(a) Model Orig

(b) Model ModU

(c) Model ModF

(d) Model ModG

Figure 6.16: Simulation of stress-strain behaviour for drained triaxial tests of Gasparre (2005)

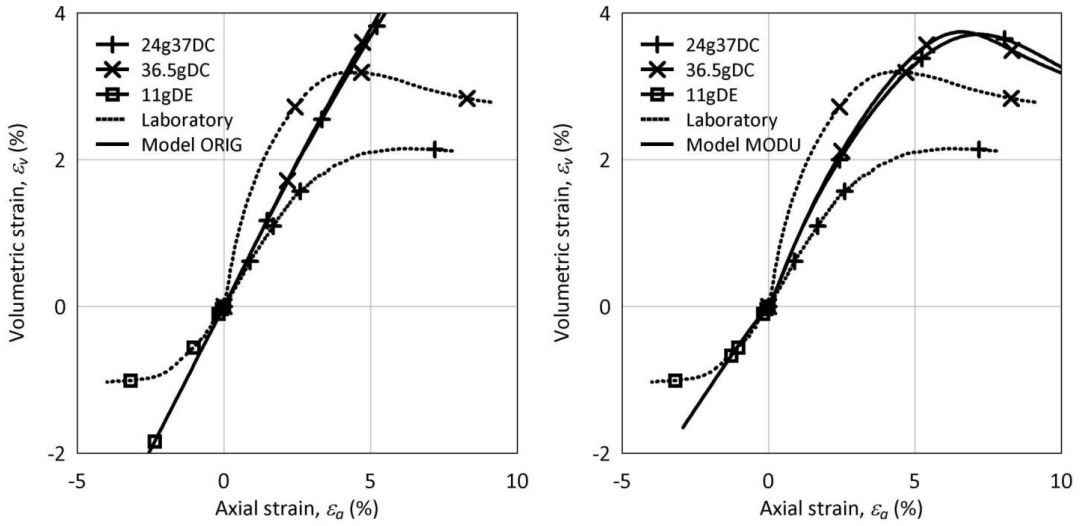

(a) Model Orig

(b) Model ModU

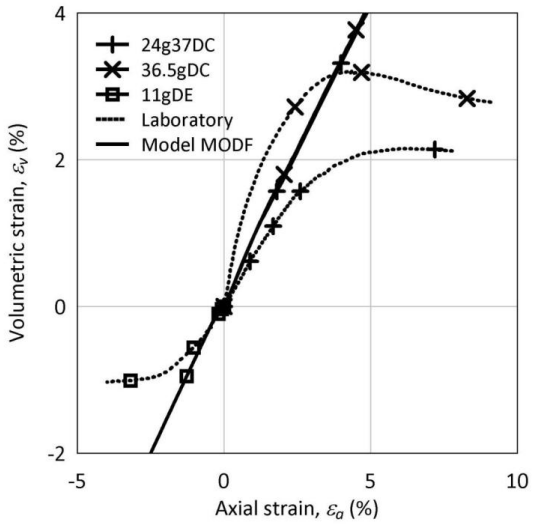

(c) Model ModF

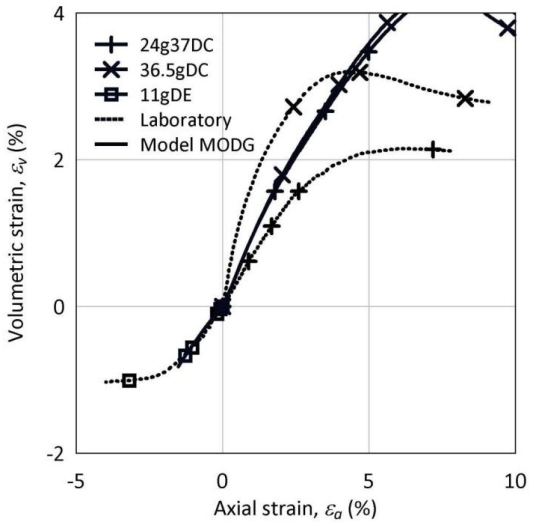

(d) Model ModG

Figure 6.17: Simulation of volumetric strains for drained triaxial tests of Gasparre (2005)

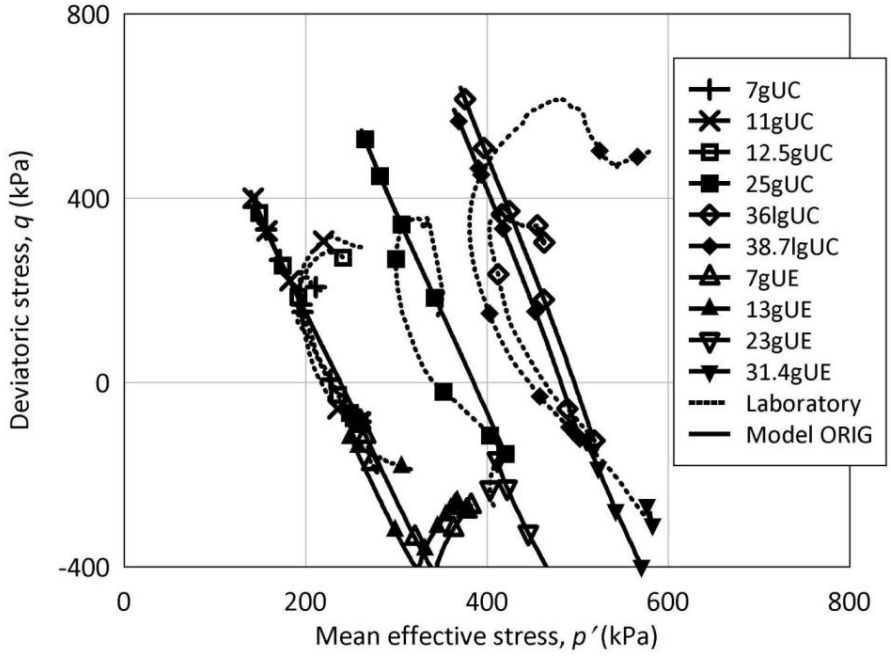

(a) Model ORIG

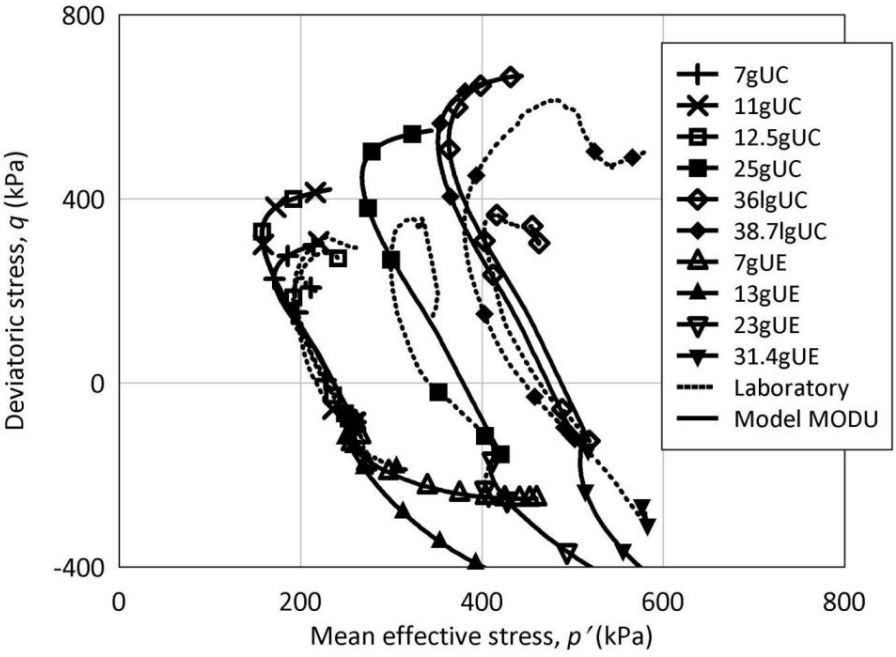

(b) Model MODU

Figure 6.18: Simulation of stress paths for undrained triaxial tests of Gasparre (2005)

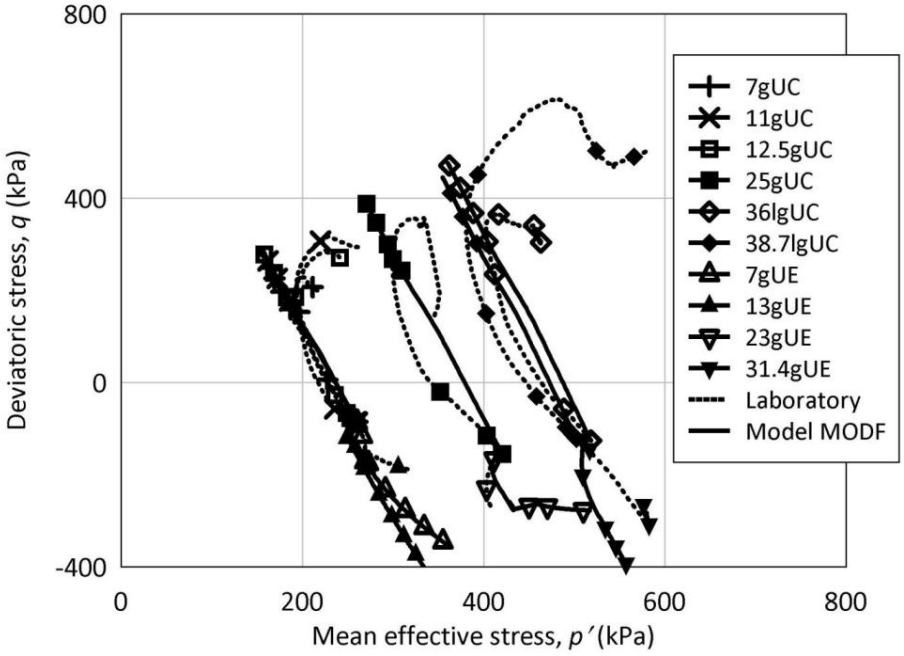

(c) Model MODF

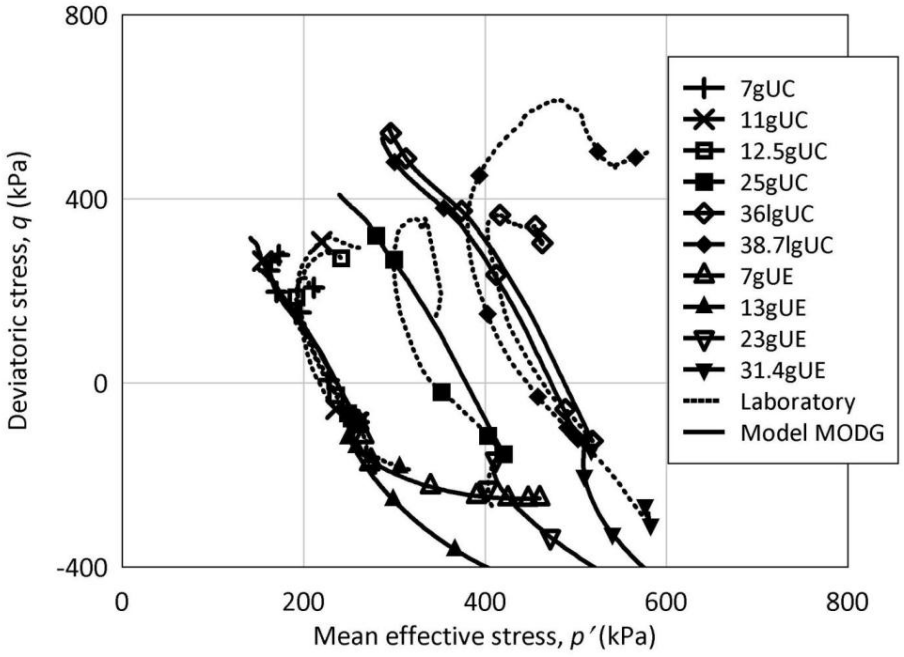

(d) Model MODG

Figure 6.18: *cont...* Simulation of stress paths for undrained triaxial tests of Gasparre (2005)

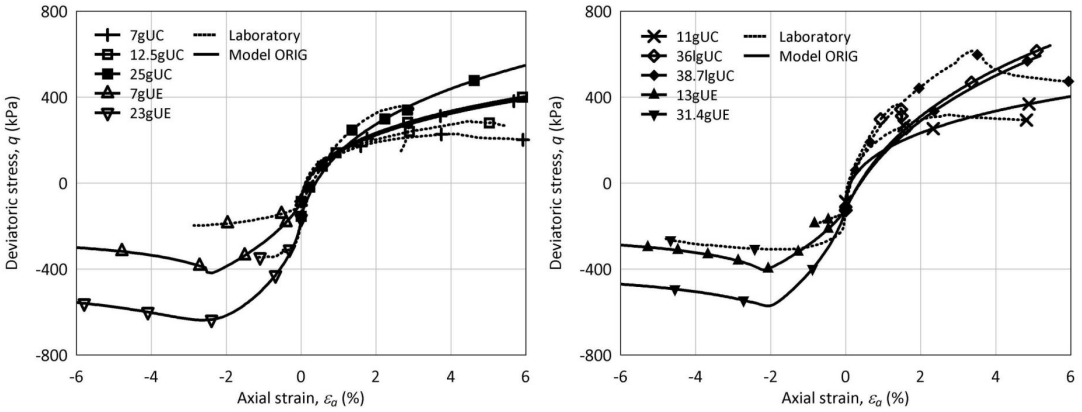

(a) Model Orig

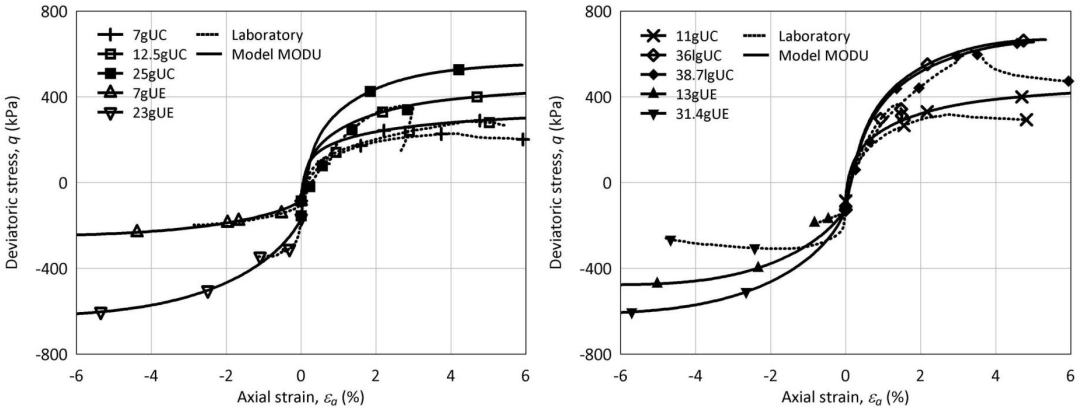

(b) Model ModU

Figure 6.19: Simulation of stress-strain behaviour for undrained triaxial tests of Gasparre (2005)

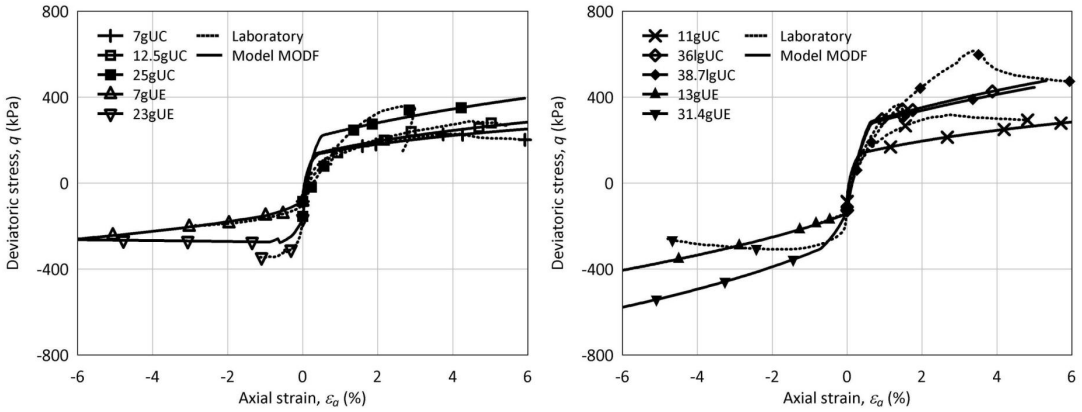

(c) Model ModF

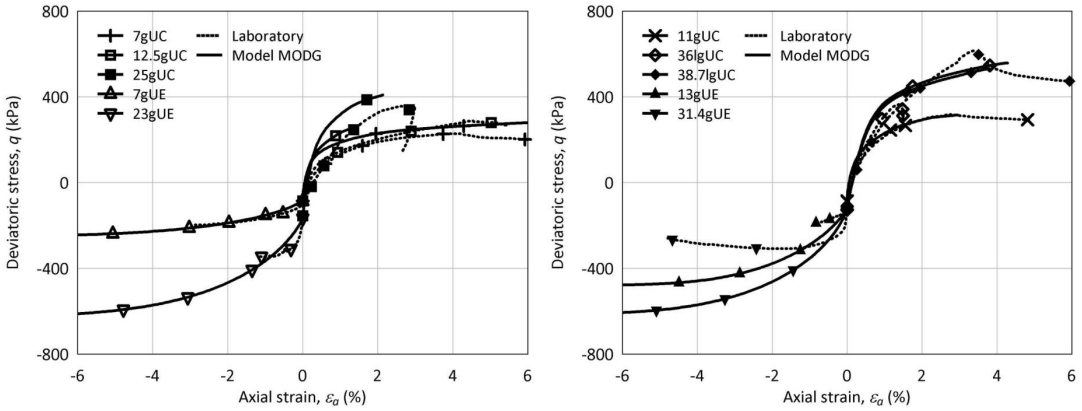

(d) Model ModG

Figure 6.19: *cont...* Simulation of stress-strain behaviour for undrained triaxial tests of Gasparre (2005)

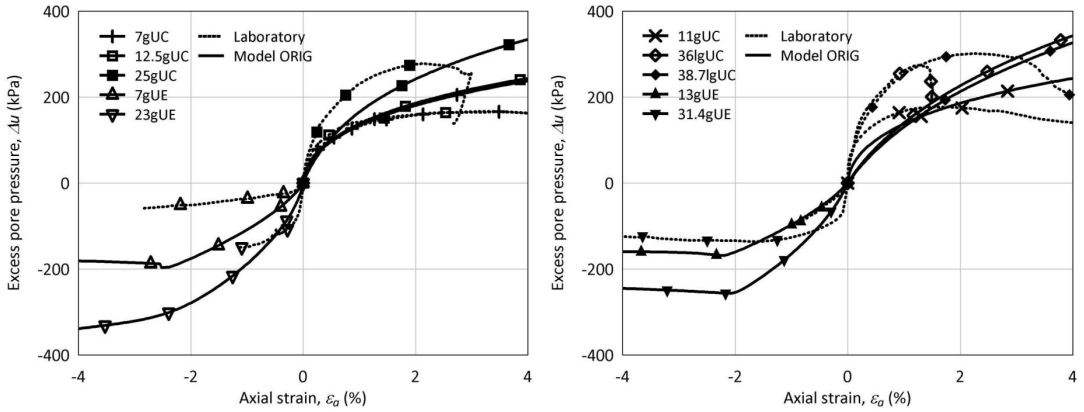

(a) Model Orig

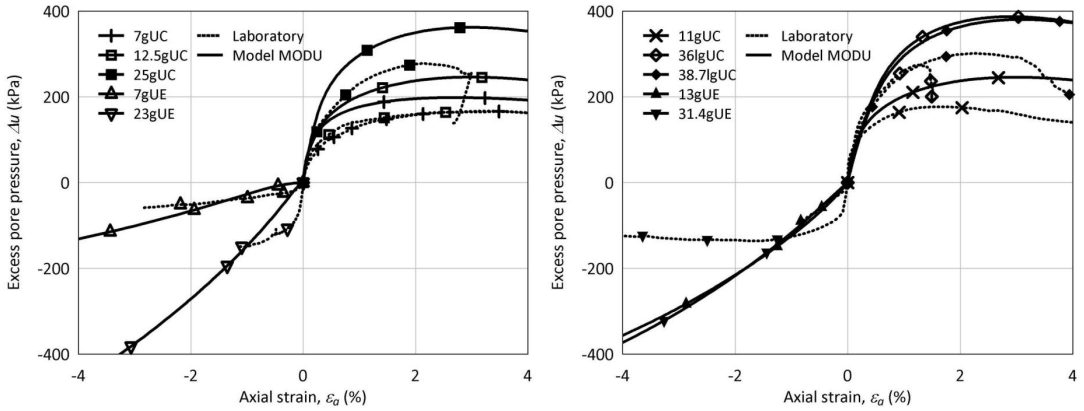

(b) Model ModU

Figure 6.20: Simulation of pore pressure for undrained triaxial tests of Gasparre (2005)

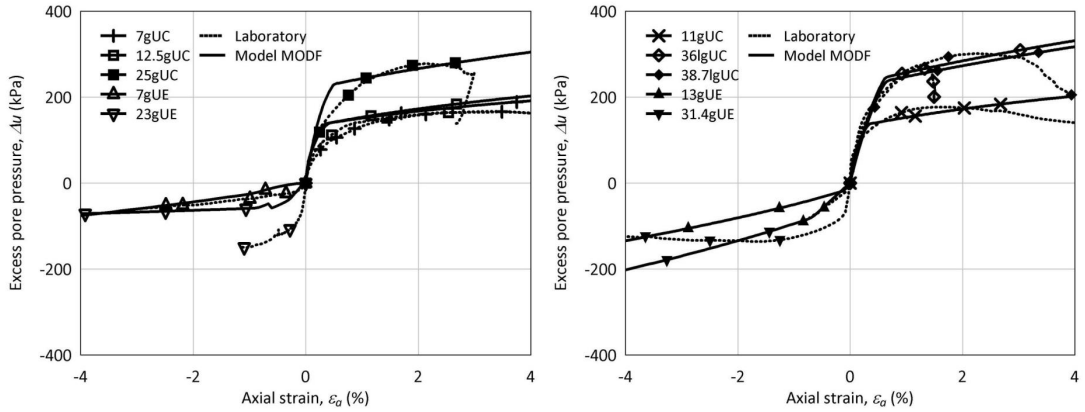

(c) Model ModF

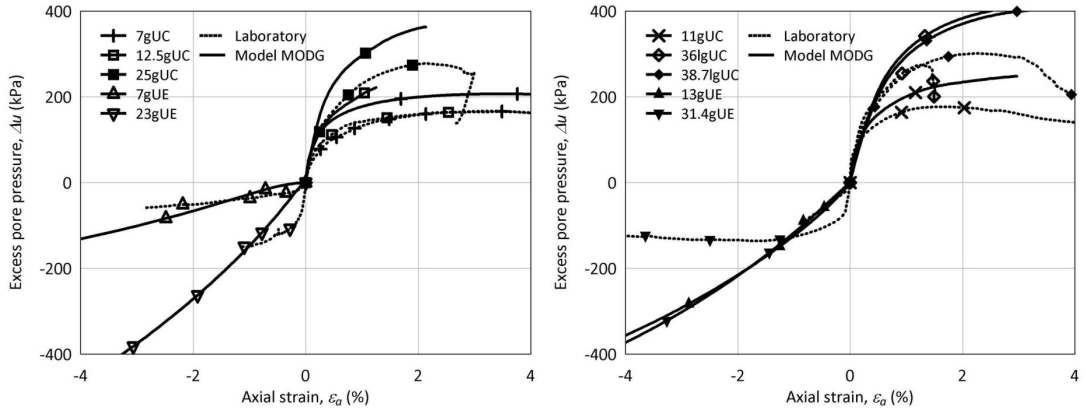

(d) Model ModG

Figure 6.20: *cont...* Simulation of pore pressure for undrained triaxial tests of Gasparre (2005)

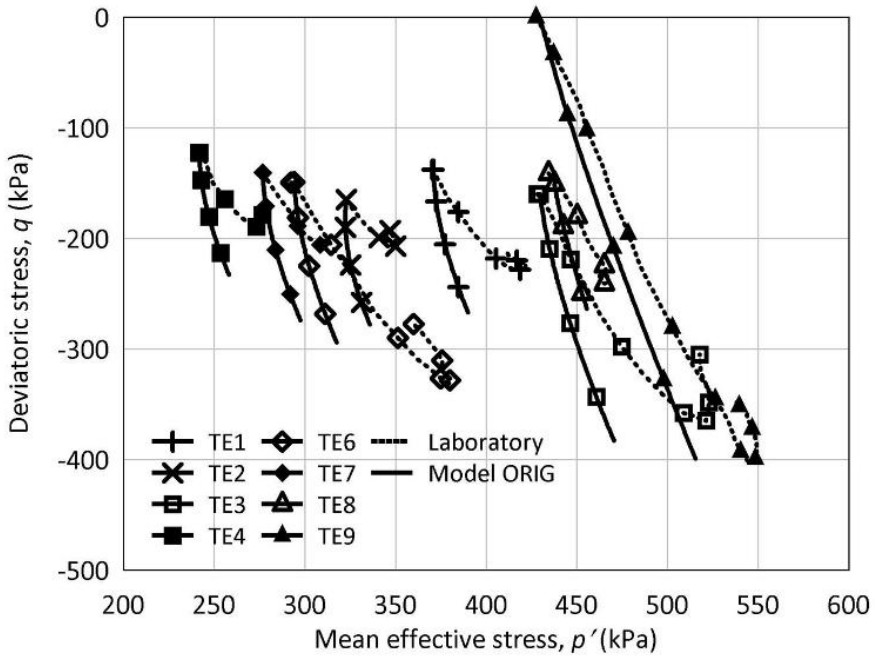

(a) Model Orig

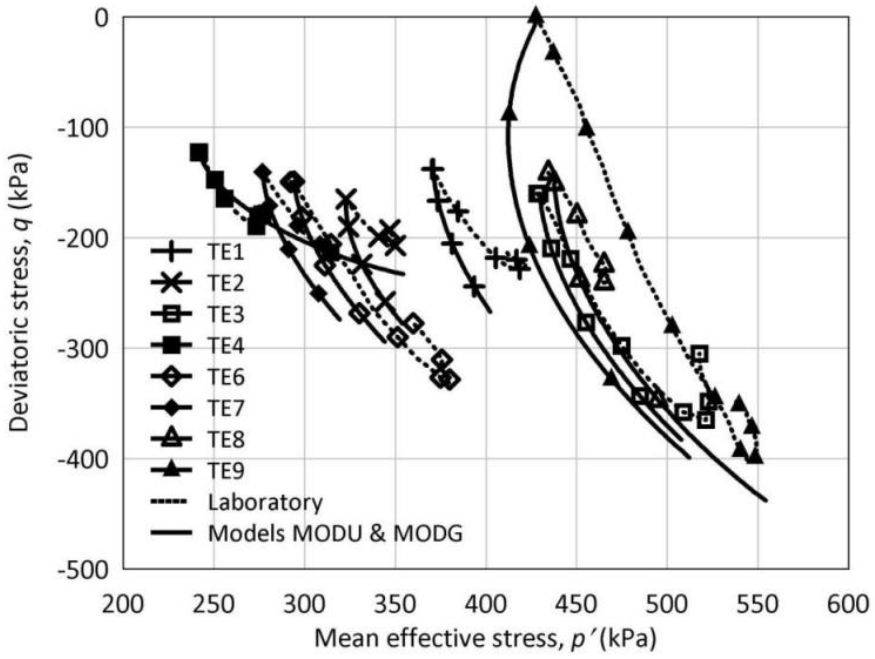

(b) Models ModU & ModG

Figure 6.21: Simulation of stress paths for undrained triaxial tests of Nishimura (2006)

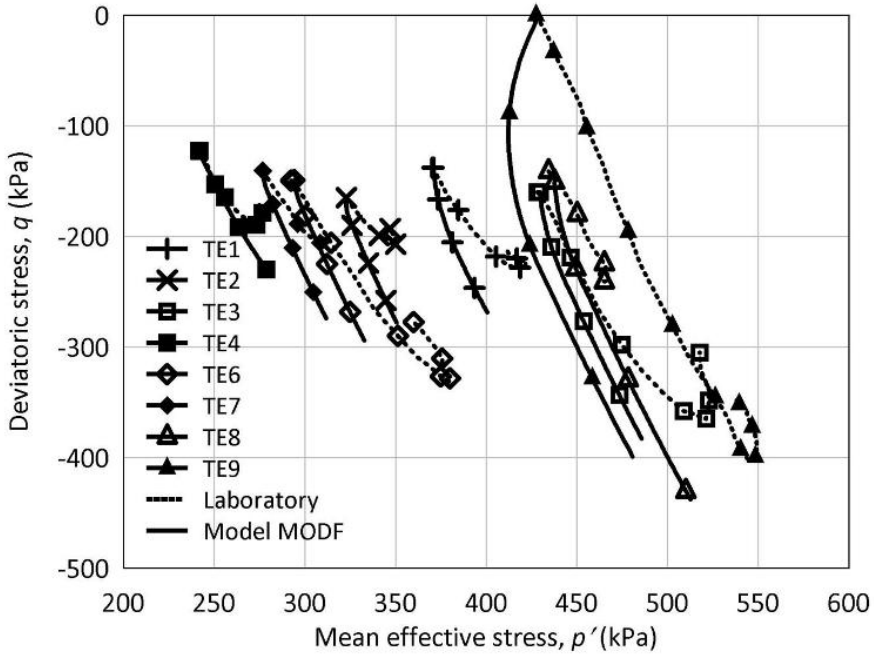

(c) Model MODF

Figure 6.21: *cont...* Simulation of stress paths for undrained triaxial tests of Nishimura (2006)

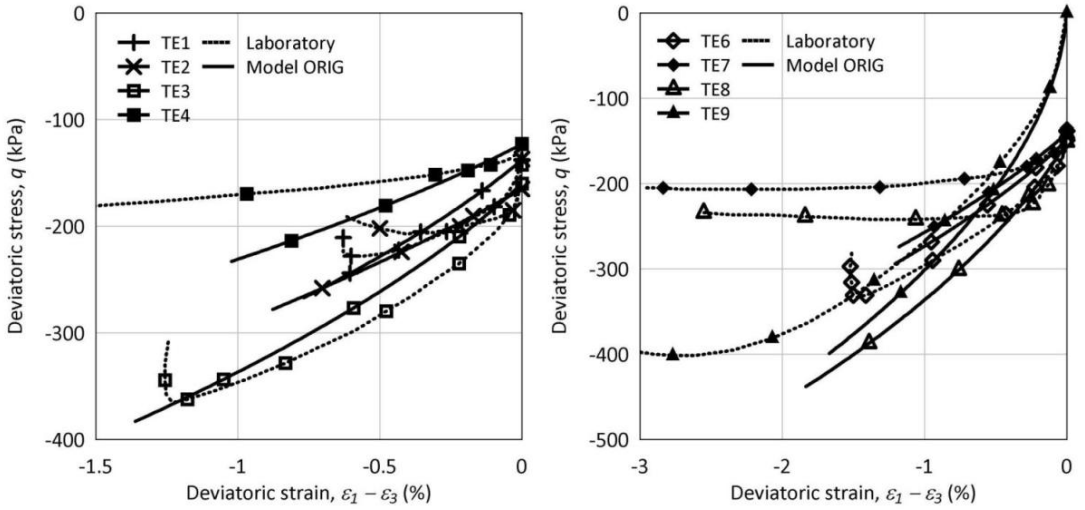

(a) Model Orig

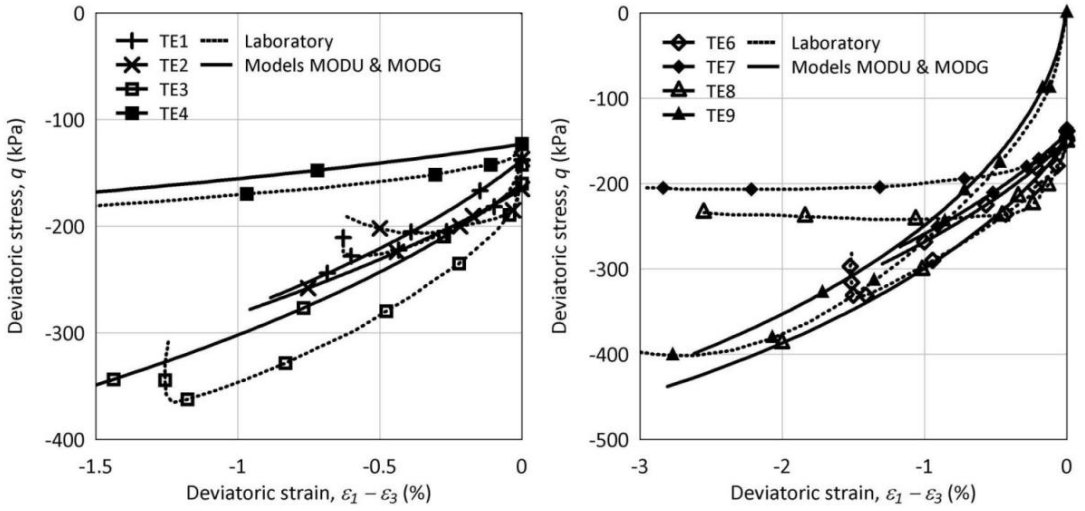

(b) Models ModU & ModG

Figure 6.22: Simulation of stress-strain behaviour for undrained triaxial tests of Nishimura (2006)

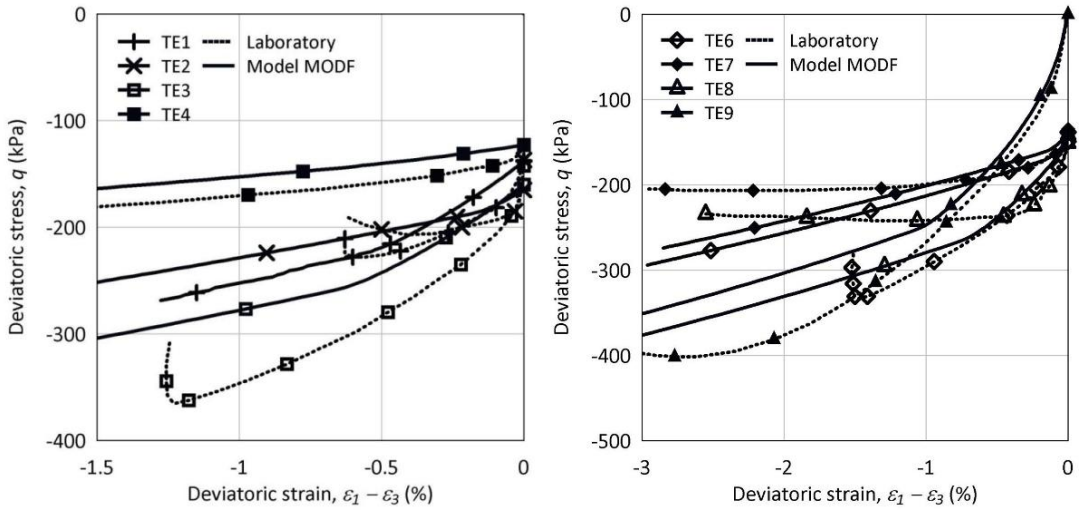

(c) Model MODF

Figure 6.22: *cont...* Simulation of stress-strain behaviour for undrained triaxial tests of Nishimura (2006)

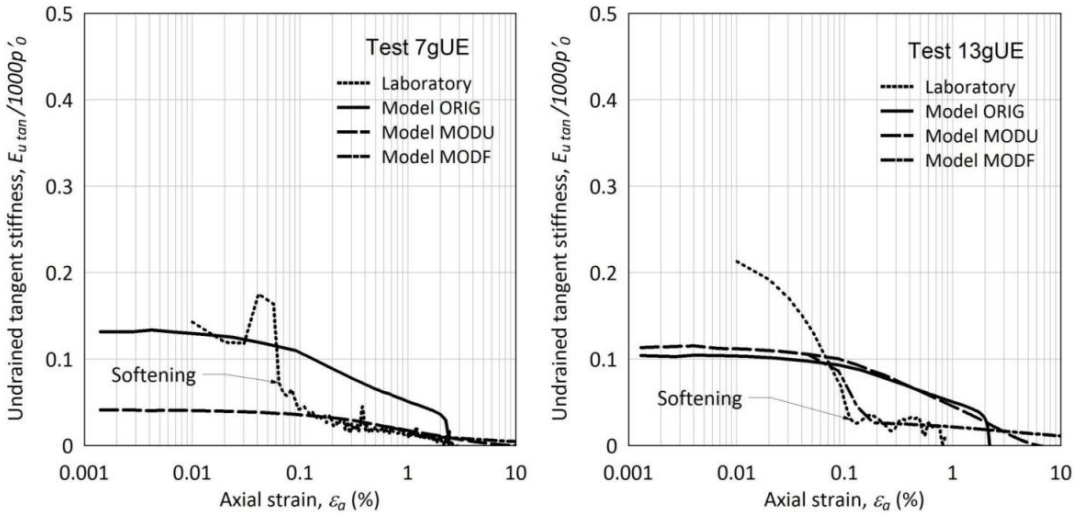

(a) Test 7gUE

(b) Test 13gUE

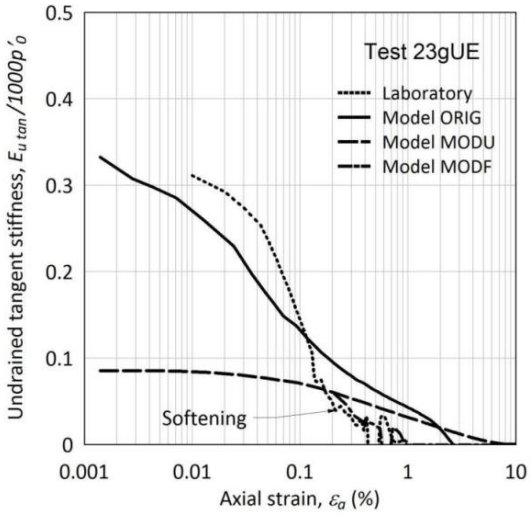

(c) Test 23gUE

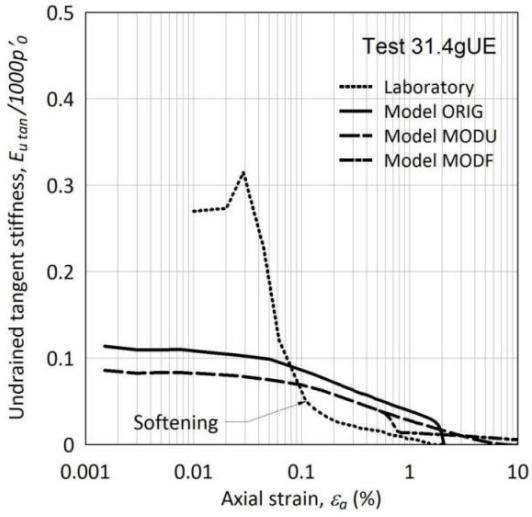

(d) Test 31.4gUE

Figure 6.23: Simulation of stiffness degradation for undrained triaxial tests of Gasparre (2005)

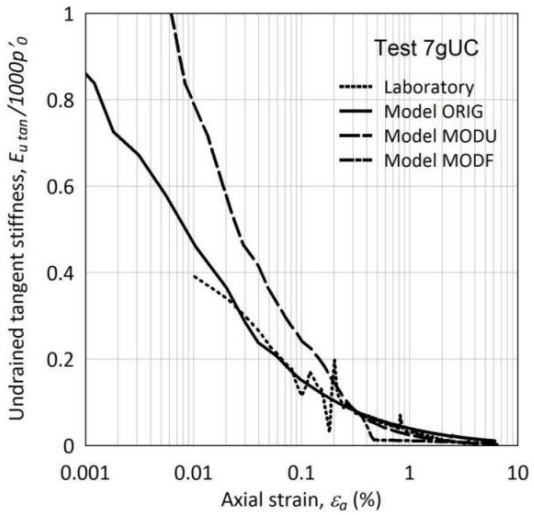

(e) Test 7gUC

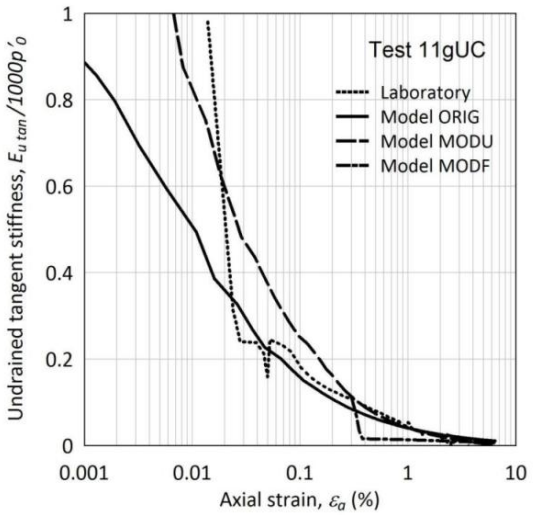

(f) Test 11gUC

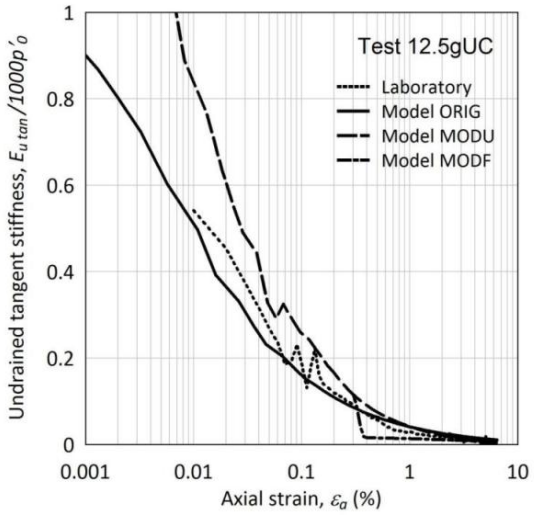

(g) Test 12.5gUC

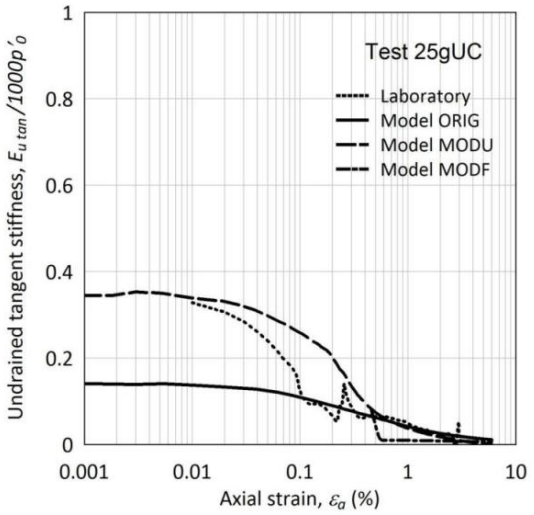

(h) Test 25gUC

Figure 6.23: *cont...* Simulation of stiffness degradation for undrained triaxial tests of Gasparre (2005)

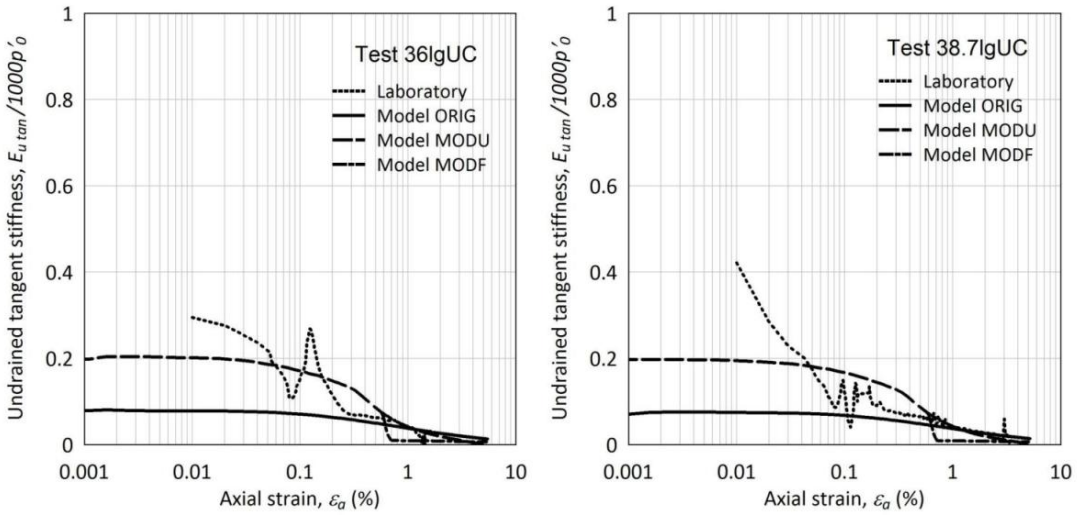

(i) Test 36lgUC (j) Test 38.7lgUC

Figure 6.23: *cont...* Simulation of stiffness degradation for undrained triaxial tests of Gasparre (2005)

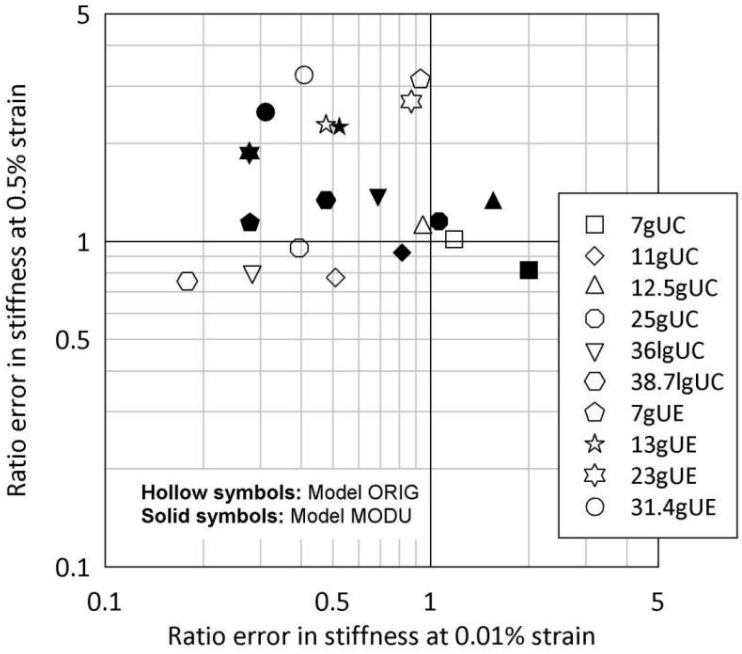

Figure 6.24: Comparison of errors in simulated small- and medium-strain stiffnesses for undrained triaxial tests of Gasparre (2005)

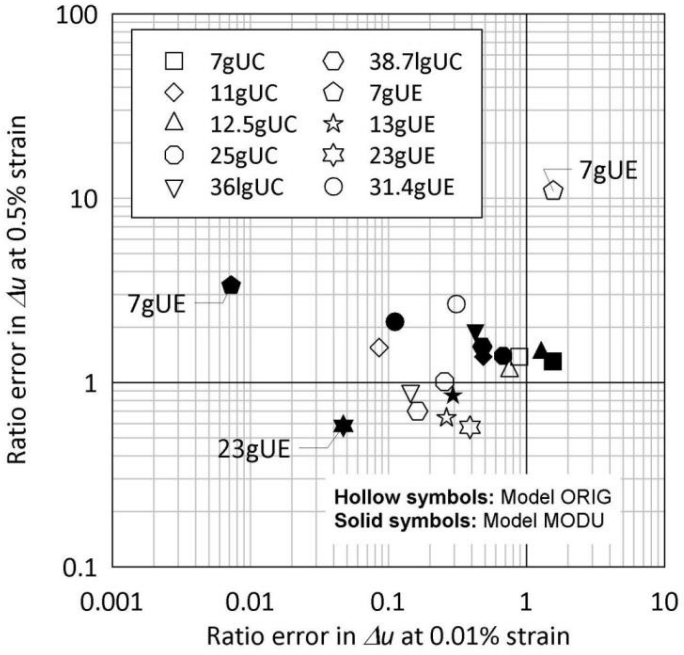

Figure 6.25: Comparison of errors in simulated small- and medium-strain pore pressures for undrained triaxial tests of Gasparre (2005)

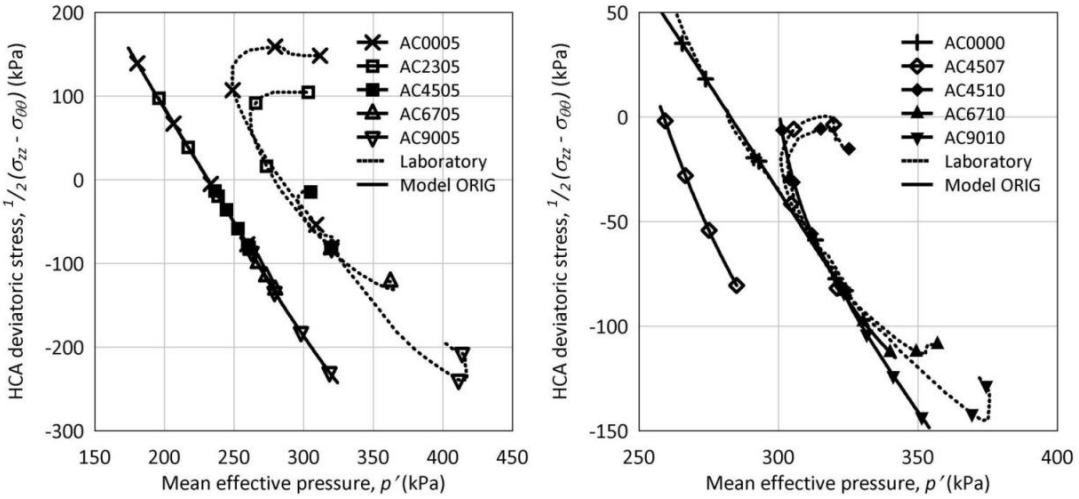

(a) Model Orig

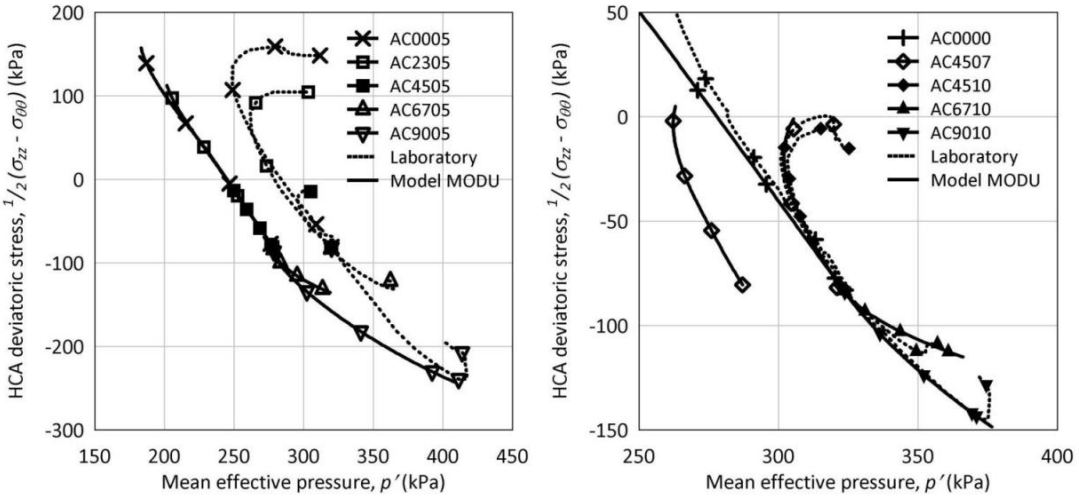

(b) Model ModU

Figure 6.26: Simulated stress paths for hollow cylinder tests of Nishimura (2006)

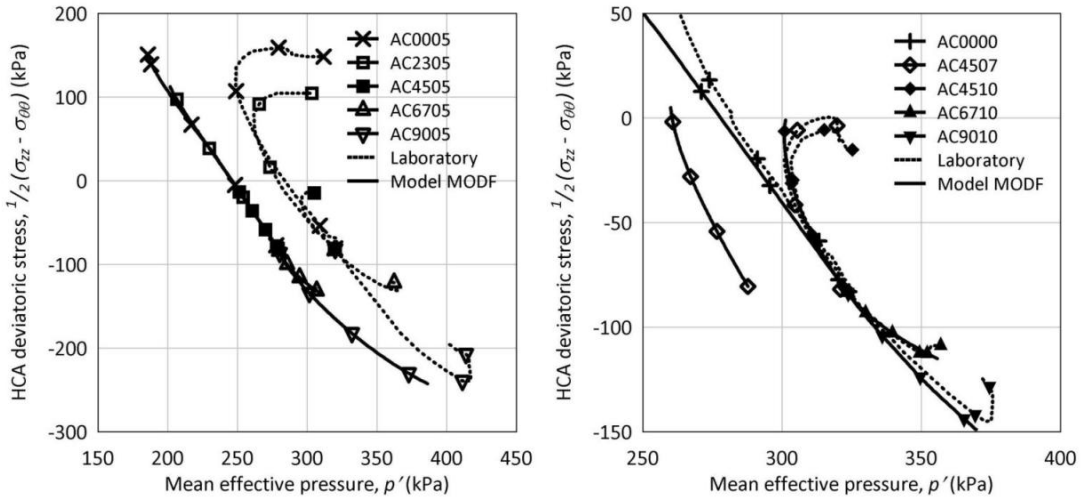

(c) Model ModF

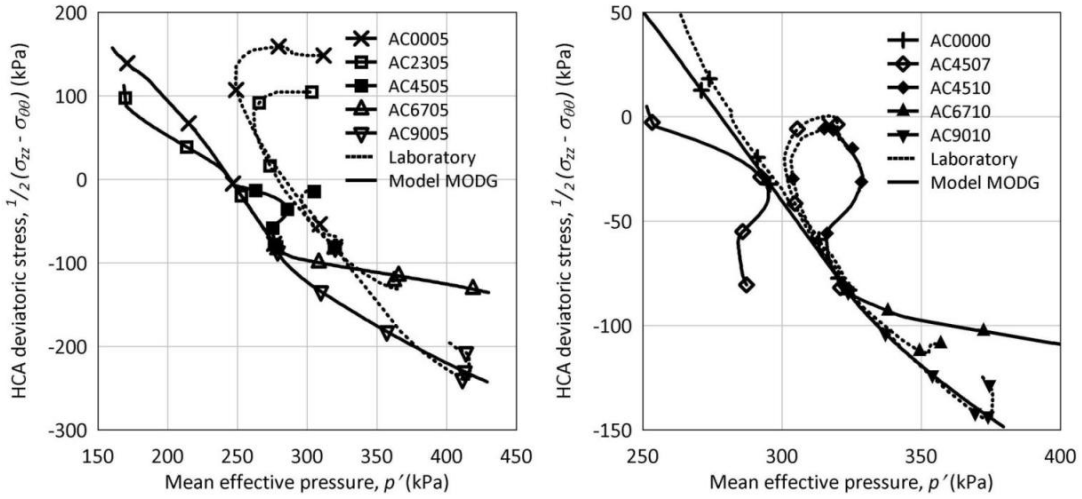

(d) Model ModG

Figure 6.26: *cont...* Simulated stress paths for hollow cylinder tests of Nishimura (2006)

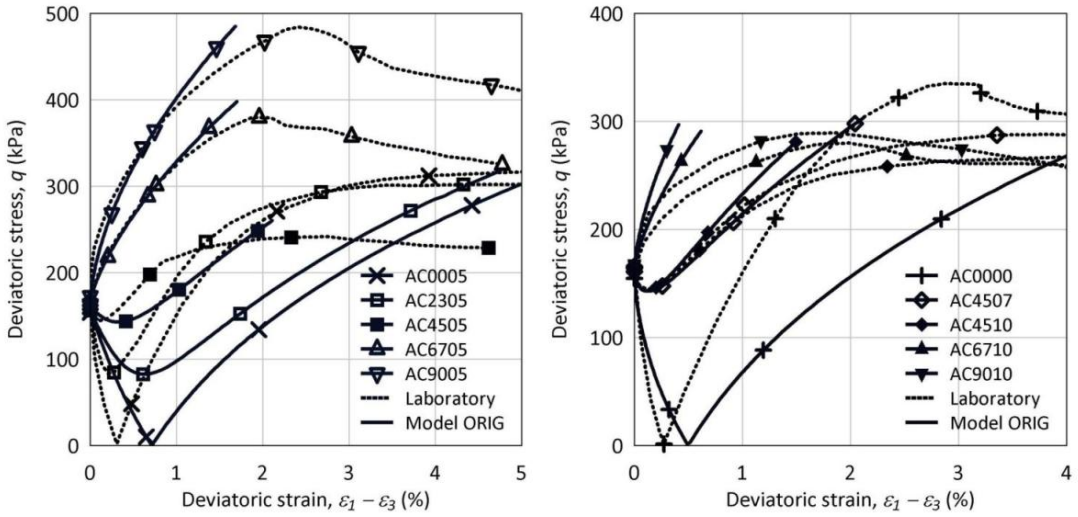

(a) Model Orig

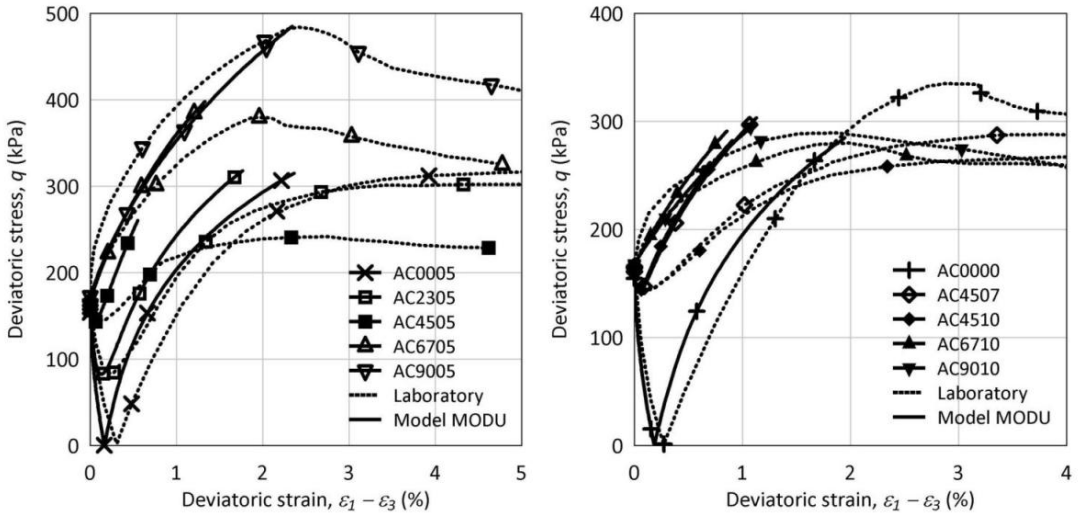

(b) Model ModU

Figure 6.27: Simulated stress-strain behaviour for hollow cylinder tests of Nishimura (2006)

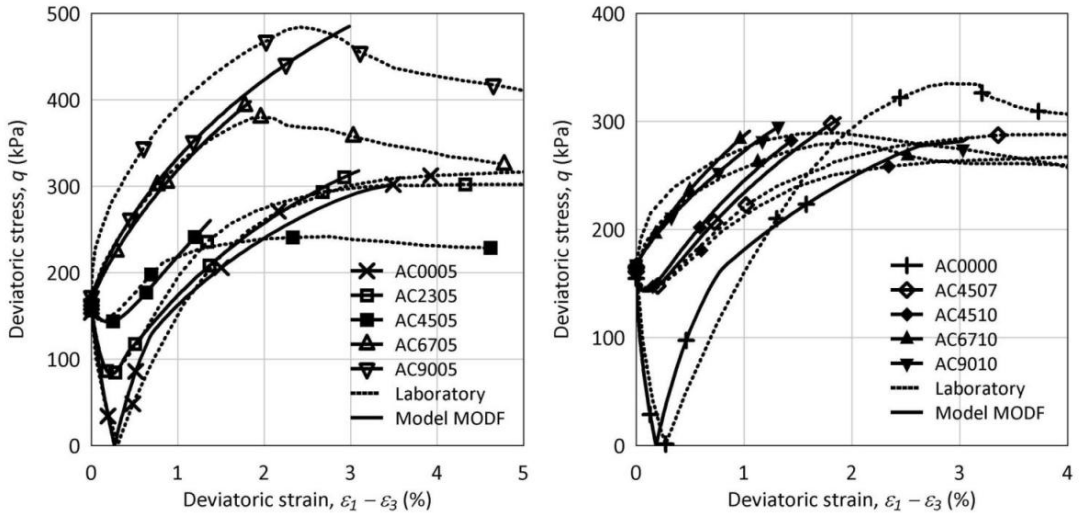

(c) Model ModF

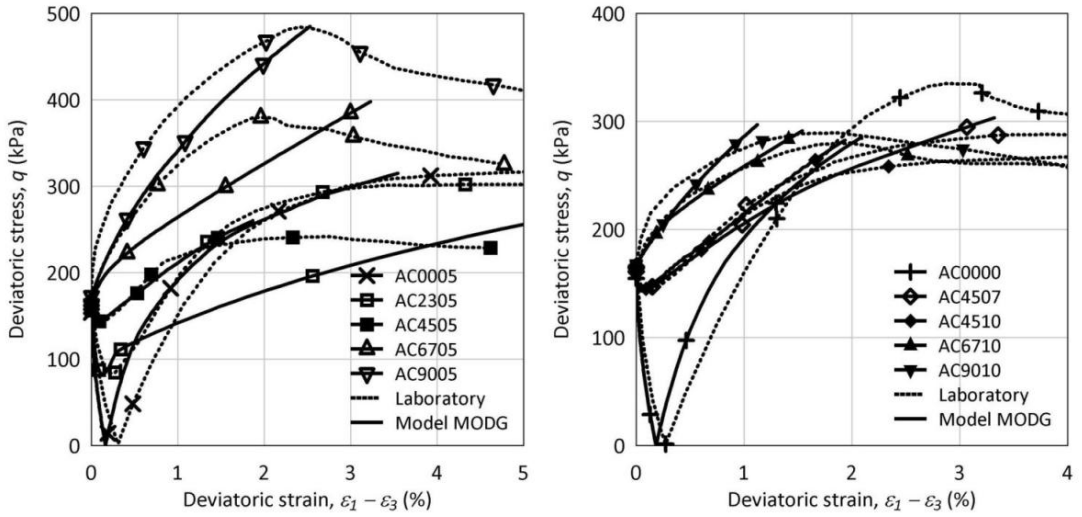

(d) Model ModG

Figure 6.27: *cont...* Simulated stress-strain behaviour for hollow cylinder tests of Nishimura (2006)

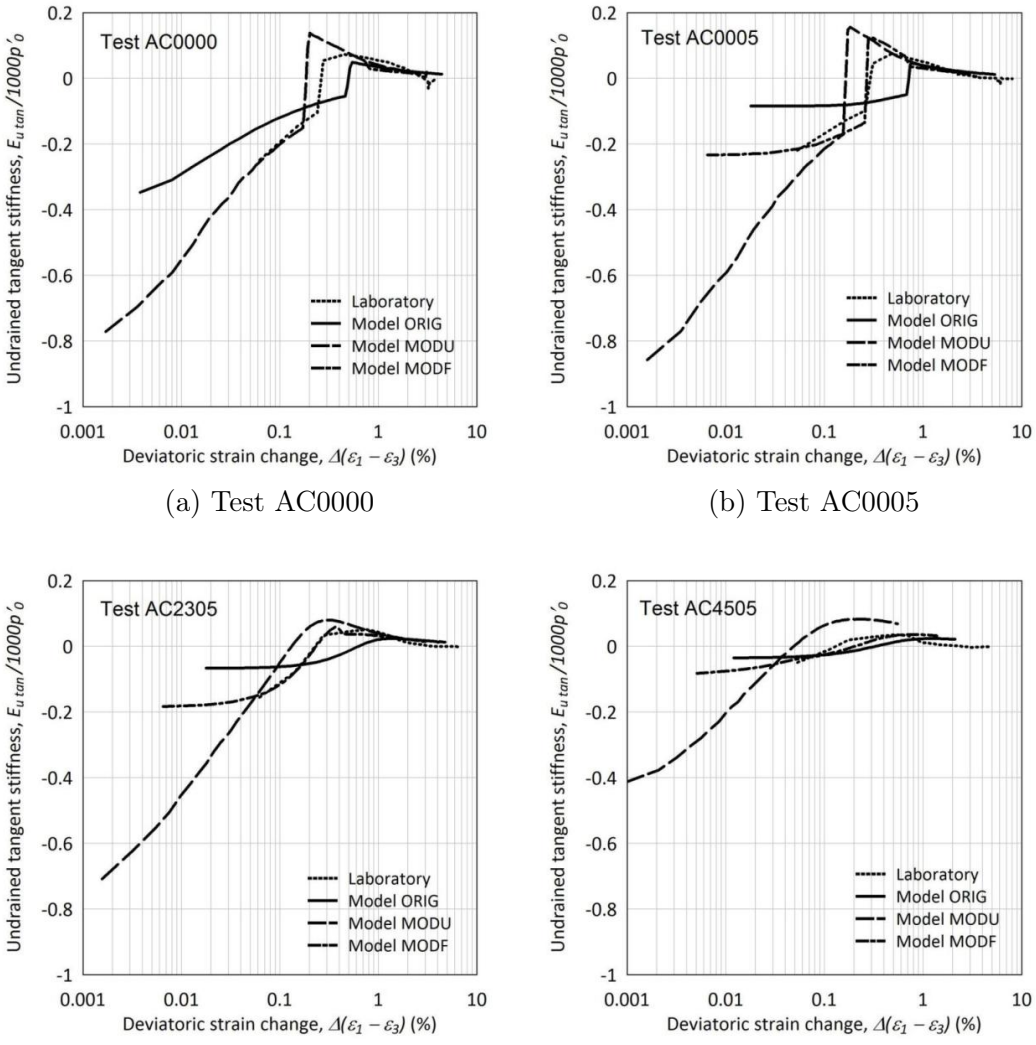

(a) Test AC0000

(b) Test AC0005

(c) Test AC2305

(d) Test AC4505

Figure 6.28: Simulated stiffness degradation for hollow cylinder tests of Nishimura (2006)

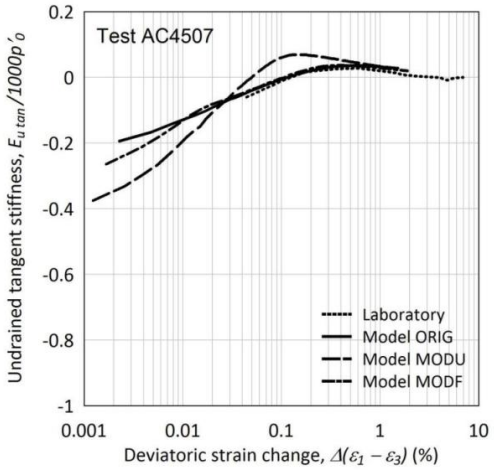

(e) Test AC4507

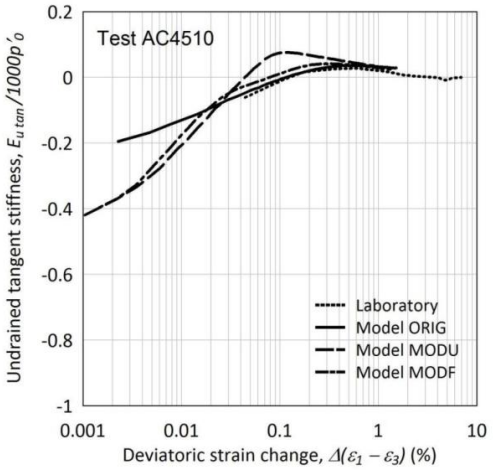

(f) Test AC4510

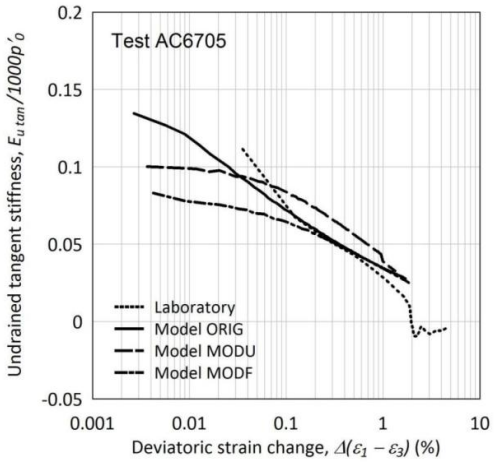

(g) Test AC6705

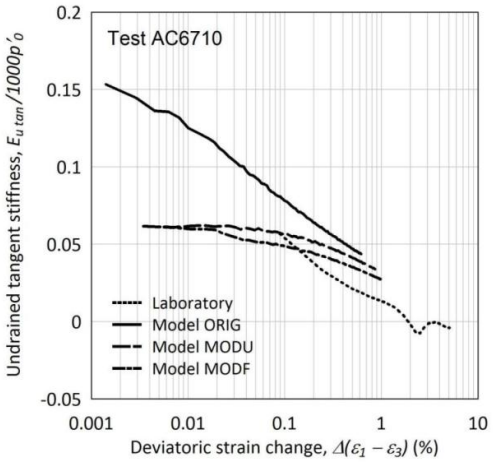

(h) Test AC6710

Figure 6.28: *cont...* Simulated stiffness degradation for hollow cylinder tests of Nishimura (2006)

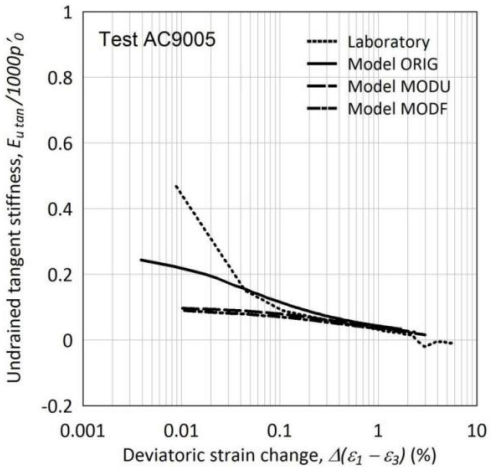

(i) Test AC9005

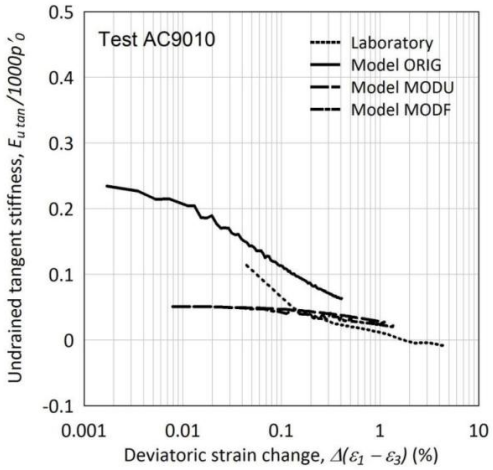

(j) Test AC9010

Figure 6.28: *cont...* Simulated stiffness degradation for hollow cylinder tests of Nishimura (2006)

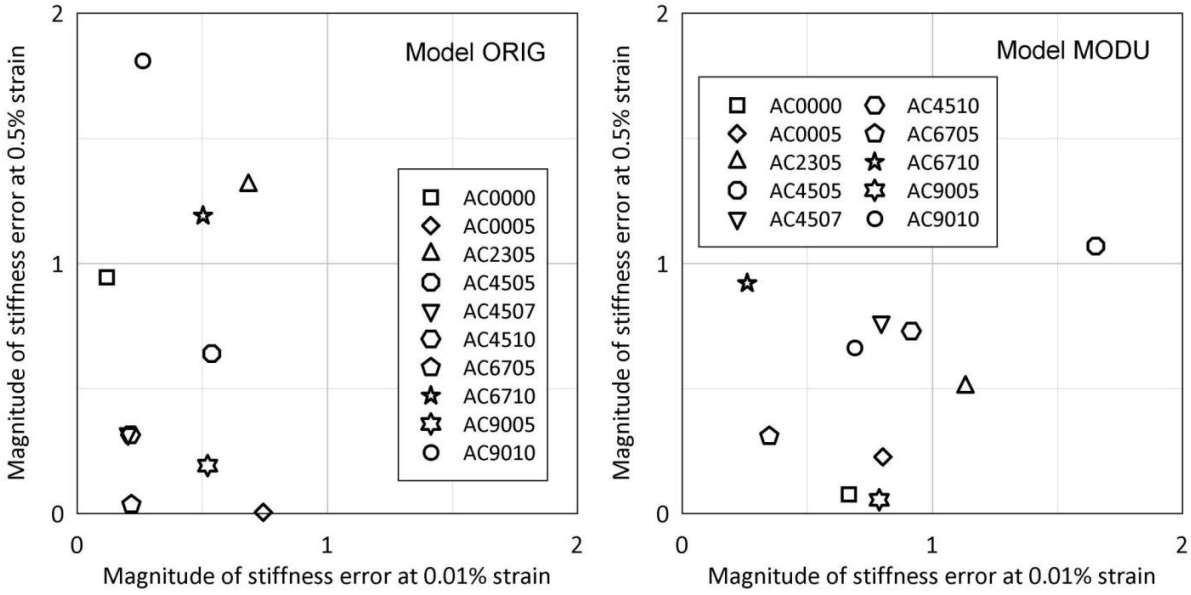

(a) Model Orig

(b) Model ModU

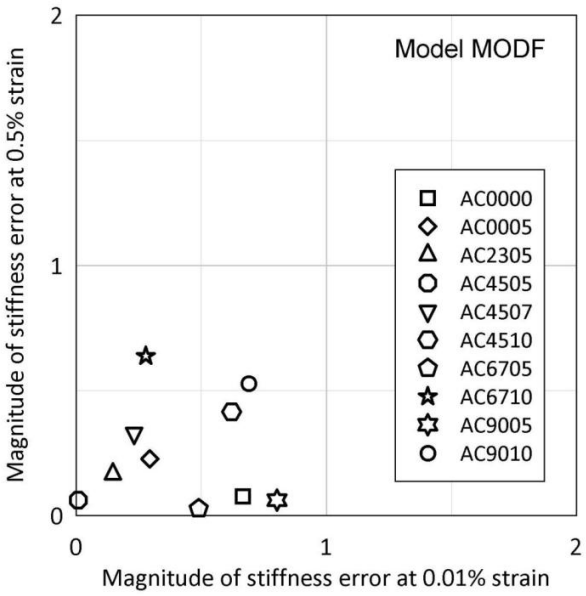

(c) Model ModF

Figure 6.29: Errors in simulated small- and medium-strain stiffnesses for hollow cylinder tests of Nishimura (2006)

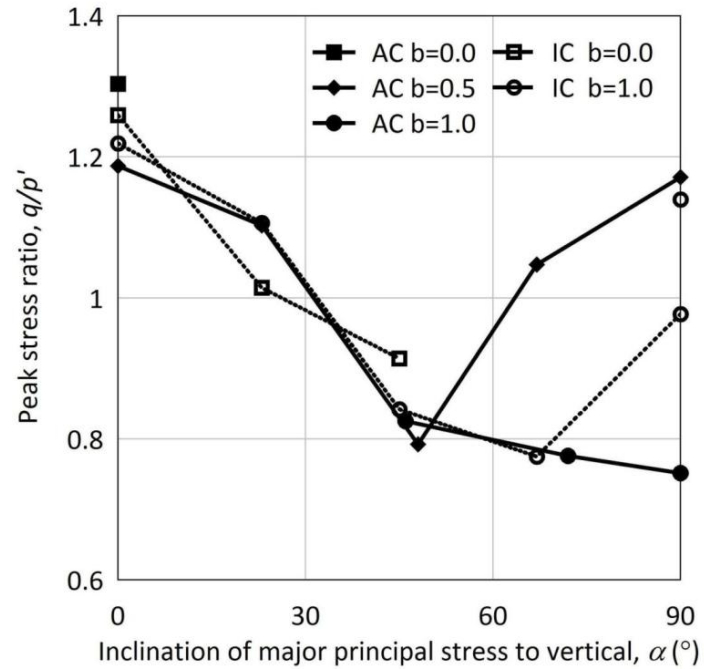

(a) For drained strength

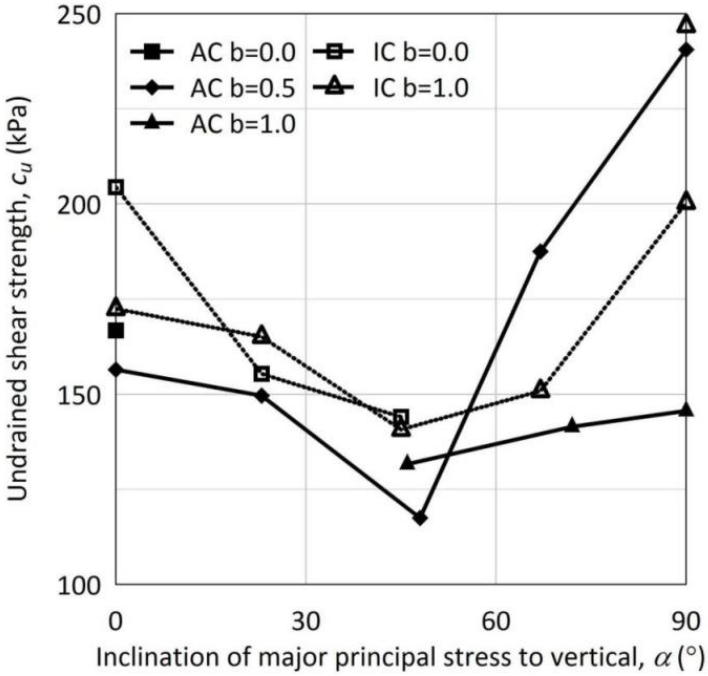

(b) For undrained strength

Figure 6.30: Peak shear strength anisotropy in hollow cylinder tests (Nishimura *et al.*, 2007)

Chapter 7

St James's Park validation

7.1 Introduction

To be feasible, a numerical analysis can require many simplifications, which can limit the realism of the analysis. Validation analyses can reveal the validity of these simplifications by attempting to simulate a field scenario.

This chapter presents validation analyses simulating twin-tunnel construction of the Jubilee Line Extension beneath St James's Park, London. The analyses assessed the suitability of simulations in conducting the parametric studies in Chapters 8 & 9. The analyses compared the abilities of soil models presented in Chapter 6 to replicate field data gathered during the excavation and consolidation periods. The analyses highlighted the most suitable soil model to use in the parametric studies.

7.2 Field data from St James's Park

Although much field data collected during tunnel construction has been published, monitoring tends to cease thereafter, resulting in very few sources of data covering long-term changes.

This chapter uses the data reported by Nyren (1998) for the twin-tunnel construction of the Jubilee Line Extension (JLE) beneath St James's Park (1995–96), for the following reasons:

- The twin open-face shield tunnels were constructed in heavily fissured London Clay: the same material simulated by the soil models proposed in this thesis.
- The instrumentation was comprehensive, providing high-quality sub-surface settlements, horizontal soil stresses, pore pressures, along with lining diameters and loads, for up to two years or more.
- Being a greenfield site, St James's Park was relatively simple to simulate.
- Wongsaroj (2005) also validated his numerical simulation against the St James's Park data, providing a foundation for numerical modelling.

Details of the site and construction will now be presented.

7.2.1 Construction

The twin 4.85m-diameter running tunnels were excavated using backhoes in open-face shields, leading to volume losses of 3.3% and 2.9% respectively for westbound and eastbound tunnels; these exceeded the expected losses of 1–2% in London Clay (Mair, 1996). Figure 7.1 shows the orientation of the tunnels, and Figure 7.2 the instrumentation layout; the instrumentation was installed along a plane perpendicular to the tunnels. At 31m depth, the advancement of the deeper westbound tunnel past the instrument plane was followed 256 days later by the 21m-deep eastbound tunnel. Being diagonally juxtaposed in elevation, the tunnels are separated by 21.5m in plan. Unlike its perpendicular crossing with the eastbound tunnel, the instrument plane intersects the westbound tunnel at an angle of around 80°.

The lining was erected from unbolted concrete segments, which were expanded against the soil by inserting wedge-shaped key segments at knee level, as shown in Figure 7.3.

7.2.2 Instrumentation

The instrumentation included 24 surface monitoring points (SMPs), providing 3-D surface displacements which agreed with total station surveys to within ±1mm.

Subsurface horizontal and vertical displacements were monitored by nine electrolevel inclinometer holes (designated Ai to Hi, and Ji) and eleven extensometer arrays (Ax to Hx). Five piezometers installed above the tunnels and four spade cells at eastbound tunnel axis level gave pore pressures and horizontal stresses.

Such breadth and accuracy of instrumentation provided a comprehensive comparison with numerical analysis output.

7.2.3 Geology

Figure 7.4 presents the soil profile found at borehole 109, located less than 50m from the instrumented section. The other profiles presented are from boreholes sunk around the St James's Park site. Topsoil and sandy man-made fill (Made Ground) is underlain by sandy Alluvium and coarse to fine flint gravel (Terrace Gravel) to around 6–8m BGL. Beneath this, London Clay extends to over 40m depth, successively giving way to the Lambeth Group, Thanet Sands and Chalk bedrock.

7.2.4 Hydrogeology

Two aquifers persist across London: a deep aquifer in the Thanet Sands and Chalk below the London Clay and Lambeth Group, and a perched aquifer in the Terrace Gravels, recharged by precipitation and from the river Thames. The pore pressure profile shown in Figure 7.5 nearby the site indicates a water table rising to about 5m BGL. However, the sub-hydrostatic pore pressures towards the base of the London Clay indicates slight underdrainage from the deeper aquifer below. Water strikes in several boreholes suggest the presence of water in claystone and sand partings.

7.3 Single-tunnel modelling by Wongsaroj (2005)

Wongsaroj (2005) investigated the long-term behaviour of single tunnels in London Clay, using the field data from St James's Park to validate his simulations before applying similar models in parametric studies. He conducted his analyses using the finite element package Abaqus.

Modelling the westbound and eastbound tunnels individually, he did not account for interaction between tunnels, which would influence behaviour significantly. This thesis builds upon Wongsaroj's work by modelling this interaction, and uses his numerical implementation as a foundation for constructing the twin-tunnel models. It is therefore helpful to describe his single-tunnel models here, along with discussion regarding which features to replicate, and which to develop.

7.3.1 Model geometry

Wongsaroj attempted to accurately replicate in-situ soil behaviour from information provided by Nyren (1998), and also by Standing & Burland (1999), who conducted a later ground investigation at St James's Park. By extrapolating borehole logs, he derived the following representative soil profile for his models:

Made Ground & Alluvium (MG)	0–5m
Terrace Gravel (TG)	5–8m
London Clay (LC)	8–43m
Lambeth Group (LG)	43–50m

Modelled together as a uniform stratum, Made Ground & Alluvium are collectively termed "Made Ground".

To accurately represent tunnel construction, Wongsaroj used a 3-D mesh for modelling excavation. He extracted data at a plane through which he excavated the tunnel, representing the instrument plane at St James's Park. The meshes he adopted for the westbound and eastbound tunnels are illustrated in Figure 7.6, showing how he harnessed the symmetry about the tunnel centreline to halve the mesh size.

So that the proximity of the model boundaries did not introduce significant errors, Wongsaroj trialled different model dimensions. For the 3-D mesh, a model length of 140m, with a lateral vertical boundary located at a distance $4z_0$ from the tunnel centreline, gave acceptable errors, where z_0 is the tunnel depth.

An element length of 2m was adopted in the longitudinal direction for the purposes of modelling the excavation.

7.3.2 Element types

To reduce computational time, Wongsaroj mainly used 8-node linear-strain elements, but employed 20-node reduced-integration quadratic-strain elements in a zone surrounding the tunnel to provide a smoother pore pressure response. The nodes of these quadratic elements were located at the midpoints of each edge and at the vertices. The tunnel lining was modelled with 8-node quadratic-strain continuum shell elements, which allowed better resolution of strains. The lining and soil elements shared the same nodes at the tunnel boundary, thus simulating no-slip contact.

7.3.3 Boundary conditions

All analyses restricted out-of-plane displacements on the vertical boundaries, whilst displacements at the model base were fixed. In addition, rotation of the lining about the longitudinal direction was restricted on the plane of symmetry. Pore pressures were maintained at the ground surface and base of the model to locate the water table at 5m below the ground surface, defining +50kPa at the base to impart slight underdrainage to the hydrostatic profile. After completion of construction, Wongsaroj applied a drainage-only seepage condition around the tunnel boundary, which allowed pore fluid to flow into the tunnel only, rather than out of it; this was necessary to simulate the ensuing consolidation.

7.3.4 Constitutive law

Wongsaroj developed his own soil model for London Clay, which he applied to all strata—Made Ground, Terrace Gravel and the Lambeth Group—but with different parameters for each; these are summarised in Table 7.1, along with other non-constitutive parameters. Appendix C explains how Wongsaroj selected these parameters. For London Clay, Wongsaroj validated his soil model against undrained and drained triaxial compression tests on horizontally- and vertically-cut specimens conducted by Yimsiri (2001), and with oedometer test data from a range of sources.

His validation results give good fits, and his extensive use of literature, laboratory and field test data adds confidence to his calibration. However, evaluation with the wider range of tests in Chapter 6 identified the inability to model fissure softening in triaxial extension tests, the potential for improving drained behaviour, and scope for improving the simulation of hollow cylinder stress paths.

Appendix C describes that for the other strata, where possible, Wongsaroj derived parameters from values estimated in the literature. He also matched stiffness degradation curves to lie within ranges established by other authors.

Wongsaroj assumed the variation of preconsolidation pressure p'_0 with depth shown in Figure 7.8. He based this upon the average of estimates by Skempton & Henkel (1957), Skempton (1961) and Bishop *et al.* (1965) for London Clay, and Bolton *et al.* (1998) for the Made Ground and Terrace Gravel. The simulation results for laboratory tests in Chapter 6 affirmed his choice of values: with the exception of Unit C, the value of $p'_0 = 3000$kPa adopted for all specimens fitted acceptably. This value compares well with the range of 3000–3350kPa applied to the London Clay in Wongsaroj's analyses, shown in Figure 7.8.

A linear elastic model was applied to the tunnel lining to model concrete, with an isotropic Young's modulus of 28GPa and Poisson's ratio of 0.15, as used by Addenbrooke (1996). Concrete density was taken as 2400kg m^{-3} and the actual lining thickness of 0.2m in the field was modelled.

7.3.5 Excavation modelling

Wongsaroj attempted to accurately reproduce the excavation by applying observations noted by Nyren (1998) during construction. Based upon these, he assumed a 6m unsupported length for the tunnel heading. The element length along the tunnel would need to be 1m to accurately model the actual progression of the shield in 1m increments. To reduce computational time however, Wongsaroj modelled the excavation using a 2m element length, according to the process illustrated in Figure 7.7. Lining elements were installed simply by activating them, so that lining expansion was not replicated. Compared to other uncertainties, the longer unsupported section seemed to have only a small influence, but the lack of jacking

stress in the lining following its erection might influence strains accompanying the transfer of stress from the soil.

Wongsaroj also trialled modelling a horizontal restraint on the soil below the tunnel axis, imposed by the presence of the shield. However, poorer results using this variant led to the original model being favoured for excavation modelling.

7.3.6 Remeshing technique

Wongsaroj models tunnel excavation in a 3-D mesh. However, a steady-state is reached after the tunnel has advanced far beyond the instrument plane, after which the ensuing consolidation is plane-strain. Desiring to reduce computational time therefore, Wongsaroj modelled the consolidation period with a 2-D mesh, as illustrated in stages 1–3 of Figure 7.11 (this figure illustrates all mappings required for twin-tunnel modelling; only stages 1–3 were performed by Wongsaroj).

The transformation from 3-D to 2-D analysis required defining a new 2-D mesh with the same geometry as the instrument plane of the 3-D mesh. This facilitated mapping of data, since nodes of each mesh were in direct correspondence. Wongsaroj refers to this technique as *remeshing*. Complete definition of the initial condition for the 2-D mesh required mapping of soil and lining stresses, pore pressures, void ratio and the soil model variables (so-called *state dependent variables*) necessary to define the stress and strain history of the soil.

7.3.7 Permeabilities

Permeability plays a vital role in determining consolidation movements since they control excess pore pressure dissipation and drainage resulting from the new seepage condition introduced at the lining. However, the range of permeabilities for both the lining and surrounding soil can be large and difficult to measure. This posed a challenge to Wongsaroj when deciding realistic permeabilities to model for the consolidation phase after westbound tunnel construction. Wongsaroj initially assumed homogeneous permeabilities for both soil and tunnel lining, but these failed to replicate field observations. In the field, consolidation is restricted to a zone located at tunnel axis level, whilst soil swells above the tunnel crown, accompanied by a corresponding pore pressure rise. Wongsaroj therefore trialled

different permeability definitions for the soil and lining to best match the field data.

Regarding the soil, he applied different permeabilities across the units of London Clay. From borehole data collected at St James's Park by Standing & Burland (1999), Wongsaroj located the units in London Clay as follows:

Unit B2	8–20.5m
Unit A3ii	20.5–28m
Unit A3i	28–35m
Unit A2	35–43m

He then proposed three different permeability profiles for these units, shown in Figure 7.9, and compared their performance in analyses. These profiles were determined by researching ranges of permeability measured for each unit from literature. From Standing & Burland (2005), Wongsaroj noted that:

$$k_{\text{A3ii(top)}} > k_{\text{A3i}} \approx k_{\text{A3ii(base)}} > k_{\text{B}} \tag{7.1}$$

he also considered permeability ranges from Hight *et al.* (2003) (this data is shown in Figure 7.10, along with more recent measurements and Wongsaroj's profile 2), and Burland & Hancock (1977) to derive realistic profiles.

Regarding the tunnel lining, Wongsaroj applied a non-homogeneous lining permeability. Figure 7.3 illustrates that key segments were inserted at knee level, leaving gaps which were later infilled with concrete. Nyren's observations of wet patches below the tunnel springline therefore led Wongsaroj to suggest an ingress of water through the infill concrete, which might possess a higher permeability than the surrounding precast segments.

His postulation was supported by his need to use a lining with a homogeneous permeability two orders of magnitude higher than concrete to match the pore pressure recovery above the tunnel crown. To model the augmented permeability around the key segments therefore, Wongsaroj made the lower half of the lining fully permeable relative to the soil, and the upper half fully impermeable.

After conducting trials comparing homogeneous and non-homogeneous lining permeabilities, in combination with different permeability profiles, Profile 2 of Figure 7.9 with a non-homogeneous lining was found to match field data the best.

7.3.8 Results for short-term analyses

Through comparing different analyses, Wongsaroj confirmed the importance of modelling certain features. Inclusion of stiffness anisotropy led to an improved trough shape and pore pressure response. Also, 3-D modelling of excavation made a difference to tunnel lining loads and the mean effective stress in sheared soil, as well as improving surface settlements.

The pore pressure response of Wongsaroj's simulations agreed well with the field, along with profiles of vertical and horizontal subsurface movements. However, his simulations still produced transverse settlement troughs that were too wide.

Despite this, Wongsaroj was able to narrow the transverse trough significantly by adopting a lower shear stiffness G_{vh}. These results seem to suggest that soil above the tunnel should be encouraged to move more like a column: in a vertical rather than a horizontal direction, and that this could be achieved by softening the shear modulus. This is especially important when investigating the interaction between settlement troughs of successive tunnels.

Wongsaroj also noted complex deformations occurring around the tunnel shoulder, confirming the necessity to validate the soil model across the wider range of hollow cylinder stress paths considered in Chapter 6.

7.3.9 Results for long-term analyses

A homogeneous concrete model for lining permeability certainly seems too impermeable to be realistic. Instead, Wongsaroj defined the lining to be impermeable relative to the soil above tunnel axis level, and relatively permeable below. Although this distribution is still unrealistic, it has the benefit of reproducing effects similar to the actual key segment gaps. His long-term analyses suggested that non-uniformity in both soil and lining permeability greatly influence drainage, and hence further ground movements.

Wongsaroj deduced the mechanism illustrated in Figure 2.6 for long-term ground movements at St James's Park, consisting of:

- Swelling immediately above the tunnel crown caused by the relatively impermeable lining here, which allows pore pressure to recover

- Widespread consolidation on either side of the tunnel, governed by inflow near the key segments at knee level
- Downward rigid body movement above the consolidating zone

The depth of the consolidating zone depended upon the soil permeability profile, with the rate of consolidation depending upon the permeability of the stratum at axis level.

There are many uncertainties in the actual variation of soil and lining permeability, including the varying geology across the site, the quality of the key segment infill concrete, and joint tolerances. Added to this, the permeability of the surrounding soil is likely to evolve with tunnelling-induced strain, as discussed in Chapter 4. The high sensitivity of consolidation analyses to permeability would therefore make accurate replication of field data difficult.

Wongsaroj's eventual choice of soil and lining permeabilities produced a good fit with field data, and so seemed suitable to apply for the long-term analysis of the westbound tunnel. However, this particular combination might be just one of many possibilities that could match behaviour well. Different ground conditions around the eastbound tunnel might favour the adoption of different permeabilities to realistically model the eastbound tunnel consolidation.

7.4 Twin-tunnel modelling

Modelling the westbound and eastbound tunnels separately, Wongsaroj (2005) did not account for twin-tunnel interaction. However, Chapter 3 highlighted that this could be significant; the first tunnel softens the ground through which the second tunnel is advanced, whilst disturbance due to the second tunnel induces additional movements in the first.

Nyren (1998) noted the influence of the first tunnel on the highly asymmetrical and deeper settlement trough of the second. Twin-tunnel interaction is therefore influential at St James's Park, making it a suitable case to validate the twin-tunnel analyses of this thesis.

The success of many features used in Wongsaroj's single-tunnel analyses made his model a suitable foundation for formulating the twin-tunnel model. However,

certain aspects of his analyses were also developed. The features of the twin-tunnel model will now be described, and compared with his single-tunnel model.

7.4.1 Mesh design

Figure 7.12 presents the twin-tunnel mesh geometry, comparing it with Wongsaroj's mesh for westbound tunnel construction; this section explains differences and similarities between the meshes.

Broadening of the mesh width

Figure 7.12 shows that the 3-D twin-tunnel mesh is significantly wider than Wongsaroj's single-tunnel mesh. This was necessary for the following reasons:

1. No plane of symmetry Analysis of a single tunnel can be simplified by harnessing the plane of symmetry along the tunnel centreline; by halving the model size, computational time is significantly reduced. For a twin-tunnel analysis however, the excavation of the second tunnel through soil disturbed by the first removes this plane of symmetry, so reducing the mesh size is not possible.

2. Width influenced by consolidation For the excavation period, Wongsaroj noted that locating the lateral vertical boundaries at a distance $4z_0$ from the tunnel centreline made boundary effects negligible. However, permeability anisotropy encourages more horizontal flow during the ensuing consolidation period, causing the zone of influence to widen. Investigating this, Wongsaroj concluded that the lateral vertical boundary must be located at distances of $5z_0$, $7z_0$ and $10z_0$ away from the tunnel centreline, when $k_\mathrm{h}/k_\mathrm{v}$ is 2, 4 and 10 respectively.

In light of these findings, Wongsaroj made his 2-D mesh wider than his 3-D mesh. Since the far-field regions of the 2-D mesh extended beyond the lateral boundaries of the 3-D mesh, these regions were assigned a greenfield condition during remeshing before commencing the consolidation analysis.

Unlike Wongsaroj's analysis however, the twin-tunnel analyses must adopt a wider 3-D model as well. This is because changes in the far-field regions during the consolidation analysis would influence excavation of the second tunnel, and so

the greenfield condition applied by Wongsaroj can no longer be defined in these regions. This concerns the remeshing step illustrated in step 4 of Figure 7.11, and is explained further in Section 7.4.3. The width of the 3-D and 2-D meshes must therefore be identical for the initial conditions of each mesh to be defined correctly.

For the twin-tunnel analyses, $k_h/k_v \leq 5$ applies, implying that lateral boundaries should be located at a distance of around $8z_0$ from the tunnel centrelines. Instead, a value of $10z_0$ was adopted—as shown in Figure 7.12—to further ensure that the initial conditions for the second excavation were defined correctly.

Simplifications to the mesh

The twin-tunnel mesh needed to be significantly wider than Wongsaroj's single-tunnel mesh. To keep the computational time feasible therefore, the mesh for the twin tunnels was simplified in comparison to Wongsaroj's mesh. Two simplifications were introduced, pictured in Figure 7.12:

1. The mesh density was reduced.

2. The region of quadratic soil elements was limited to a zone of elements immediately surrounding each tunnel.

Total excavated length

Unlike Wongsaroj, the tunnels were progressed through the entire mesh length. This was done in anticipation of modelling excavation and consolidation with the same 3-D mesh. In the end however, a 2-D mesh was used for the consolidation stages.

Similarities with Wongsaroj

The following features of Wongsaroj's mesh were incorporated because of their success in his simulations:

1. **Construction modelling** The same construction procedure was adopted, including incremental excavation length, unsupported length, and order of element removal and activation. Like Wongsaroj, lining expansion was not

modelled. This could influence load transfer from the soil to the lining, so a trial was conducted to activate the lining with a compression pre-stress. However, the time available did not allow for the numerical implementation of lining expansion with sufficient consistency.

2. **Mesh length and depth** The mesh was constructed to the same 140m length and 50m depth, since Wongsaroj had already affirmed these as giving adequately small boundary errors. For the same reason, the instrument plane was located at the same longitudinal distance as he used.

3. **Soil profile** The same soil profile was applied because Wongsaroj's soil profile gave a good approximation of strata at St James's Park; this is pictured in Figure 7.12.

7.4.2 Constitutive law

London Clay formulations

In Chapter 6, four soil models were proposed to replicate the behaviour of London Clay in the laboratory, and model ModF was identified as fitting the behaviour best. To ensure adequate realism in the twin-tunnel parametric analyses, this model is first validated in a twin-tunnel analysis. The simulation results are compared with behaviour in the field, and with those from the other soil models.

Four different constitutive formulations for London Clay were applied in four separate simulations to compare their performance; these are described below. The analysis names correspond to the soil models introduced in Chapter 6, except for ModX, which is a modified version of ModF:

1. **Analysis Orig** The original model by Wongsaroj (2005), using his original parameters.

2. **Analysis ModU** The original model by Wongsaroj (2005), with parameters modified to best fit the laboratory data. The yield surface is rotated, and its size depends upon the lithological unit.

3. **Analysis ModF** Based upon model ModU, with isotropic softening of fissures. The friction angle at which fissures begin to soften is $\phi_{\text{soft}} = 11.5°$.

4. Analysis ModX Model ModF, but with $\phi_{soft} = 10°$.

Soil model ModG was not trialled because it is unsuitable for modelling London Clay, as concluded in Chapter 6.

Parameter selection

The parameters applied to each model for the St James's Park simulations are displayed in Table 7.1. These parameters are similar to those applied in the laboratory test simulations of Chapter 6 (listed in Table 6.1), which were selected to represent the general behaviour of London Clay. However, Wongsaroj (2005) modified some of the parameters he used for his laboratory tests before applying them to his St James's Park analyses, to match ground investigation data. Likewise, parameters are also modified here before applying them in the twin-tunnel analyses:

- M, the gradient of the critical state line in q–p' space, was chosen to be 0.814 by Wongsaroj. This was based upon the suggestion by Nyren (1998) that the peak angle of shearing resistance for the site was 21°, assumed by Wongsaroj to equal the critical state angle. Since this value is specific to St James's Park, $M = 0.814$ was adopted in the twin-tunnel analyses.

- ρ_c, the gradient of the normal consolidation line in $\log e$–$\log p'$ space, was chosen to be 0.3 by Wongsaroj. Using an empirical relation between virgin compression index C_c and initial void ratio e_0, Wongsaroj discovered that this value of ρ_c matched values of C_c and e_0 derived from oedometer specimens taken at St James's Park (Standing & Burland, 1999). Since this value is specific to the site, $\rho_c = 0.3$ was adopted in the twin-tunnel analyses.

Here, applying identical parameters to all units (except Unit C) replicated behaviour well. The parameters chosen by Wongsaroj were applied to the Made Ground, Terrace Gravel and Lambeth Group, since his selection procedure derived the best estimate from available data, as described in Appendix C.

Lining models

An unjointed lining model was adopted, identical to Wongsaroj's. The material was therefore isotropic, homogeneous and linear-elastic, with a Young's modulus of 28GPa, Poisson's ratio of 0.15, density of 2400kg m^{-3} and uniform thickness of 0.2m.

A jointed lining was also trialled, because the additional flexibility in bending due to longitudinal joints might affect soil and lining deformations. The limitation on thesis size means that a full description of this trial cannot be presented here. However, the trial showed that the assumption of an unjointed lining is acceptable only if the soil response outside a distance of two tunnel diameters from the tunnel axis is of interest. More investigation is necessary to ascertain the effect of assuming an unjointed lining.

7.4.3 Remeshing technique

Wongsaroj (2005) pioneered a remeshing technique to transfer data from the instrument plane of the 3-D mesh to a 2-D mesh representing the plane, as described in Section 7.3.6. The 3-D mesh was necessary to accurately represent the 3-D effects of tunnel excavation, but a 2-D mesh was sufficient to model the ensuing consolidation, which was effectively plane-strain. Computation using the 2-D mesh resulted in significant time savings.

Extending the technique

To facilitate modelling of the twin tunnels, Wongsaroj's remeshing technique was extended to remesh data from a 2-D to a 3-D mesh, as shown in step 4 of Figure 7.11; this enabled the second tunnel to be excavated using a 3-D mesh. The complete process for modelling twin-tunnel construction is presented in Figure 7.11, dividing into the four stages outlined below:

1. **ExcWB** Excavation of westbound tunnel in a 3-D mesh (step 1 of Figure 7.11), followed by remeshing to a 2-D mesh (step 2).

2. **CslWB** Consolidation after westbound tunnel excavation in a 2-D mesh (step 3), followed by remeshing to a 3-D mesh (step 4).

3. **ExcEB** Excavation of eastbound tunnel in a 3-D mesh (step 5), followed by remeshing to a 2-D mesh (step 6).

4. **CslEB** Consolidation after eastbound tunnel excavation in a 2-D mesh (step 7).

The transformation from 3-D to 2-D, and vice versa, required defining a new 2-D mesh with the same mesh geometry as the instrument plane of the 3-D mesh. This facilitated mapping of data, since nodes and integration points were in direct correspondence. Complete definition of the initial condition for the 2-D mesh required mapping of the variables listed in Table 7.2: soil and lining stresses, pore pressures, void ratio and the soil model variables necessary to define the stress and strain history of the soil.

In the 3-D mesh, the instrument plane intersects nodes rather than integration points. Therefore, as a nodal variable, pore pressures at nodes in one mesh could be directly copied to corresponding nodes in the other. However, the remaining variables were integration and section point variables. Before the 3-D to 2-D remeshing therefore, the variables to be mapped required interpolation from the integration and section points lying immediately on either side of the instrument plane.

Rather than being defined at integration points, the void ratio definition for the numerical solver required one void ratio per element; this was obtained by averaging values across the integration points of an element. Displacements were transferred by defining nodes of the new mesh to have the same deformed coordinates as those of the old mesh.

Improvement to interpolation

A key development to Wongsaroj's remeshing technique addresses the interpolation of integration point variables during 3-D to 2-D remeshing. Since no integration points lie on the instrument plane, integration point variables must be interpolated to obtain values to represent the condition on the instrument plane. Two possibilities for the interpolation method are compared in Figure 7.13.

Wongsaroj interpolated integration point variables for the 2-D mesh from nodal output, as illustrated in the figure. This nodal output was in turn obtained by interpolation from the integration point output from the 3-D mesh. Thus, Wongsaroj's remeshing involved two successive stages of interpolation, which introduced errors, as illustrated in Figure 7.14. These errors applied only to soil stresses and soil model variables; lining stresses were remeshed using output from section points themselves, requiring no interpolation within the instrument plane. For each continuum element, the section points defined the stress and strain state at different depths throughout the lining thickness. Five section points were located at each integration point.

To eliminate this interpolation error, the twin-tunnel analyses in this thesis use integration point output from either side of the instrument plane, as shown in Figure 7.13. To obtain values at correct points on the plane therefore, output is interpolated perpendicular to the plane, rather than within it. An approximate plane-strain condition exists across the instrument plane by the end of excavation, so there is very little variation in variables in this direction. Errors associated with interpolation across the plane are therefore small compared with the errors associated with Wongsaroj's remeshing.

7.4.4 Permeability profiles

Excavation stages: ExcWB & ExcEB The excavation period is short relative to the time required for clay to drain, so the clay was considered to behave as undrained. For simplicity therefore, soil permeability was assumed to be uniform and isotropic during stages ExcWB and ExcEB; a low value of $k = 2 \times 10^{-11}$m s^{-1} was defined.

First consolidation stage: CslWB For the first consolidation stage following westbound tunnel excavation, CslWB, the same permeability profile adopted by Wongsaroj (2005) was applied, detailed in Profile 2 of Figure 7.9. No other permeability profiles were trialled, since Wongsaroj had already trialled three different profiles, and researched the profile at the site, as explained in Section 7.3.7.

For the lining, permeability was specified using a seepage coefficient K_{T}, defined as:

$$K_{\mathrm{T}} = \frac{k_{\mathrm{T}}}{\gamma_{\mathrm{w}} t_{\mathrm{T}}} \tag{7.2}$$

where k_{T} is the lining permeability, t_{T} the lining thickness, and γ_{w} the unit weight of water. K_{T} relates the pore pressure outside the lining (u_{T}) to the filtration velocity through the lining (v) with the equation $v = K_{\mathrm{T}} u_{\mathrm{T}}$. The one-way drainage condition is applied so that water can only flow into—not out of—the tunnel. For the westbound tunnel, Wongsaroj's lining seepage coefficients were also adopted: relatively impermeable above axis level, with $K_{\mathrm{T}} = 10^{-12}\mathrm{kN^{-1}m^3s^{-1}}$; and relatively permeable below, with $K_{\mathrm{T}} = 10^{-5}\mathrm{kN^{-1}m^3s^{-1}}$. This is illustrated in Figure 7.15.

Final consolidation stage: CslEB For stage CslEB, Wongsaroj's permeability definition was trialled first; however, his permeability definition was optimised only for stage CslWB. Hence, to find a better fit to field data for stage CslEB, several other definitions for soil and lining permeability were also trialled. The best combination that was compatible with the soil permeabilities adopted for stage CslWB was to reduce the conductivity of the eastbound lining, without modifying the soil permeabilities. This was achieved by shortening the permeable circumference at the tunnel invert, represented in Figure 7.15. Thus, $K_{\mathrm{T}} = 10^{-5}\mathrm{kN^{-1}m^3s^{-1}}$ was applied across a region $\pm 45°$ from the invert, outside of which $K_{\mathrm{T}} = 10^{-12}\mathrm{kN^{-1}m^3s^{-1}}$.

7.5 Presentation of results

Output from the simulations is presented in Figures 7.18–7.33, grouped according to the modelling stage: Figures 7.18–7.20 present output for the first excavation stage, ExcWB, and output for the intermediate consolidation stage, CslWB, is presented in Figures 7.22–7.24. Figures 7.25–7.27 present output for the second excavation stage, ExcEB, and output for the final consolidation stage, CslEB, is presented in Figures 7.26–7.31.

The figures for each excavation stage present volume losses, centreline vertical displacement profiles, horizontal displacement profiles to one side of the tunnel, surface settlement troughs, lining displacements, lining forces, lining moments and the centreline pore pressure profiles. For each consolidation stage, the figures show vertical displacement profiles, settlement troughs just below the Made Ground, the development of settlement with time, lining displacements, lining forces, lining moments, centreline pore pressure profiles and the variation of pore pressure above the crown. The lining forces and moments are calculated by ABAQUS, and outputted directly at each integration point of the lining. It should be noted that the assumption of an unjointed lining means that lining response is not representative of that in the field. The lining response is presented to compare the behaviour imparted by the different soil models.

Finally, Figures 7.32 & 7.33 illustrate the regions softened by fissures in analyses MODF and MODX respectively.

Coordinate system Data is plotted according to the Cartesian coordinate system shown in Figure 7.16, with the origin at the ground surface. The x-, y- and z-directions represent the transverse distance from the midline between the two tunnels, height above ground level and longitudinal distance ahead of the tunnel face of interest respectively.

Normalisation of data To compare displacement distributions, displacement data is normalised using two different methods:

1. **By maximum displacement** Here, displacements of a distribution are given relative to the maximum of the distribution. This enables the shape of distributions to be readily compared, for instance, narrowness of settlement trough.

2. **By volume loss** Displacements are scaled by a factor $V_{\mathrm{L\,ref}}/V_{\mathrm{L}}$, where V_{L} is the volume loss in the analysis, and $V_{\mathrm{L\,ref}}$ the volume loss for a reference case, in this instance, the excavation in the field. Figure 7.17 explains that V_{L} is proportional to displacement, if movements are small and material behaviour is linear. If this is the case, normalising with respect to volume loss

accounts for the different magnitudes of movement induced, enabling direct comparison of displacement directions; this was also noted by Nyren (1998). Volume losses for both excavations are presented in Figures 7.18 & 7.25, calculated directly from tunnel displacements incurred during excavation.

Incremental displacement and load Displacement and lining load plots show incremental displacements and loads incurred during each stage. This isolates the effect of a stage, and helps in identifying mechanisms associated with the stage.

Sign convention The following sign conventions are adopted:

- Lining forces are positive in tension
- Lining moments are positive if moments increase curvature of the lining about the tunnel axis
- Soil stresses are positive in compression

Settlement output for consolidation For the consolidation stages, seasonal fluctuations in the Made Ground made comparison of surface settlements unreliable. Therefore, settlements below the Made Ground, at around 5m depth, are compared to validate the consolidation stages. The development of settlement with time is presented at depths of 5.6m and 5.1m in stages CslWB and CslEB respectively, corresponding to the depths at which displacements were recorded by Nyren (1998).

7.6 Performance of soil models

To compare the different soil models, four analyses were conducted, as outlined in Section 7.4.2. The performance of the soil models in replicating the field data is evaluated in three sections:

1. **Limitations of all models** This section presents deficiencies in simulating the field data that are common to all of the models.

2. **Comparison of ModU with Orig** The two models which neglect fissure softening are first compared to observe how the modified parameters and rotated yield surface of model ModU compare with Wongsaroj's original model, model Orig.

3. **Comparison of ModF & ModX with ModU** Models ModF & ModX are the same as model ModU, but with additional fissure softening. By comparing these models with model ModU, the influence of fissure softening can be identified.

7.6.1 Limitations of all models

All soil models can simulate the field data with some degree of success; this section highlights limitations which none of the soil models could overcome. The notable limitations are described briefly below:

1. The volume losses for the westbound and eastbound tunnels (Figures 7.18 & 7.25) are generally lower in the field, indicating that the unsupported length assumed in the excavation analyses was too long. The excavation length was therefore reduced in the parametric study described in Chapters 8 and 9. Such over-prediction of volume loss might influence patterns of ground response due to the non-linearity in stress-strain behaviour.

2. The soil column above each tunnel experienced less strain in the field (Figures 7.19a & 7.26a), and is therefore more akin to rigid body movement. Figure 7.35 portrays simplified stress paths during excavation, suggesting that simple-shear modes—where shearing forces act in horizontal and vertical directions—are active along the sides of the soil column. Softer shearing in these modes would assist the downward movement of the column as a rigid body; this implies that in the field, soil is softer in simple shear.

3. For the westbound tunnel, maximum horizontal displacement in the field occurs at the tunnel shoulder, rather than at axis level, as predicted by the simulations (Figure 7.19b). This is probably due to soil variability, since maximum displacement during the eastbound tunnel excavation occurs at axis level in the field.

4. Settlement troughs are narrower in the field (Figures 7.19c & 7.26d). However, the normalised trough width is unusually narrow at St James's Park, with $K_L \approx 0.35$ for both tunnels (Nyren, 1998); usually for clays, $K_L = 0.5$ is expected (Mair *et al.*, 1993); troughs with $K_L = 0.5$ are included in the figures for comparison. The stress paths postulated in Figure 7.35 suggest that the settlement zone above the tunnel could be made narrower if the soil was made softer in simple shear. This supports the earlier conclusion that in the field, the soil is softer in simple shear.

5. During westbound tunnel consolidation, the swelling zone above the crown is both thicker and narrower in the field (Figures 7.22a & b). This leads to the reduction of settlement towards the centreline, illustrated in the transverse settlement troughs of Figure 7.22c; this unique trough shape is not replicated in simulations. Replication of the swelling region might be improved by reducing the vertical permeability of the soil above the crown.

6. Settlement in the field continues at a steady rate—even 10 years after construction, yet all simulations predict that settlement rate becomes negligible after around 20 years (Figure 7.29e). Simulations conducted by GCG (1993) predict roughly the same period.

   This could be due to the overestimation of coefficient of consolidation (c_v) in the field; also plotted on Figure 7.29e is an analysis adopting model MODF, with both stiffness and permeability back-analysed to fit the field data; the stiffness parameter C_b for London Clay was reduced from 300 to 100, whilst both horizontal and vertical permeabilities of Unit A3ii—encompassing the permeable portion of the eastbound lining—were halved. The plot demonstrates that the field data can be fitted by reducing c_v of the soil. However, whether the back-analysed permeability and stiffness is realistic of soil behaviour in the field remains to be ascertained, since these properties are likely to be site-specific. It should also be noted that the back-analysed plot does not represent a realistic simulation: parameters were only modified in the final consolidation stage; the plot is therefore only demonstrative.

7. The steady-state pore pressure in the field above the eastbound crown is difficult to replicate (Figure 7.31a). Piezometer FP3 is likely to be unreliable; Dimmock (2003) suggested that the surrounding sand pocket was clipped by the tunnel shield during excavation. Considering this, pore pressures appear to almost fully recover to the greenfield condition, indicating relatively little seepage occurring. Reducing the vertical permeability above the crown in simulations would reproduce this better; permeability anisotropy in the field might thus be higher than previously thought.

In summary, these limitations suggest the following:

- Soil in the field is softer in simple shear ($\alpha_{\mathrm{d}\sigma} \simeq 45°$) than in direct shear ($\alpha_{\mathrm{d}\sigma} \simeq 0°$ or $90°$).
- Consolidation behaviour near the tunnel crown is particularly difficult to model, and suggests a higher permeability anisotropy in the field than previously thought.
- Soil compressibility is likely to be site-specific. The determination of soil stiffness and permeability would therefore limit the accuracy of analyses simulating consolidation in the field.

7.6.2 Comparison of ModU with Orig

Soil model behaviour Model ModU generally exhibits stiffer drained and undrained behaviour than Orig, except in extension, where behaviour is softer. The greater overall stiffness is mainly due to the greater elastic stiffness parameter C_{b} (see Chapter 6), whilst the rotated yield surface makes extension behaviour softer relative to that in compression. These aspects of soil model behaviour will now be discussed in light of the simulation results.

Greater overall undrained stiffness during excavation Soil model ModU is stiffer than model Orig in most shearing modes, including simple shear ($\alpha_{\mathrm{d}\sigma} \simeq 45°$), as demonstrated in the hollow cylinder simulations of Chapter 6. The stiffer behaviour in simple shear explains the following observations:

1. **Trough width** Analysis MODU gives a wider settlement trough than analysis ORIG (Figure 7.19c). The stiffer behaviour of model MODU in simple shear would distribute the downward movement over a wider zone, according to the shearing modes identified in Figure 7.35.

2. **Volume loss** Analysis MODU predicts the least volume losses in both excavations (Figures 7.18 & 7.25). Figure 7.34 shows how the stiffer simple-shear behaviour of model MODU reduces the volume loss.

3. **Lining force** Figure 7.34 also illustrates how the stiffer soil of model MODU redistributes more overburden force onto the lining; this is confirmed in Figures 7.20a & 7.27b. Peck (1969) noted that the short-term ground loading experienced by the lining is inversely proportional to the volume loss incurred before its installation; this was confirmed by Negro *et al.* (1996) when monitoring lining loads in Sao Paulo.

Softer extension behaviour during excavation Figure 7.35 proposes simplified stress paths that might occur during excavation. Extension behaviour is less stiff in model MODU than model ORIG, giving softer behaviour at the crown. Conversely, compression behaviour is more stiff, giving stiffer behaviour at the springline.

For the westbound excavation, the vertical displacement profile (Figure 7.19a) illustrates the softer zone above the crown. Likewise, the horizontal displacement profile (Figure 7.19b) confirms the stiffer compression behaviour at the springline. A similar pattern is found for the eastbound tunnel in Figures 7.26a, c & f.

This imbalance in stiffness behaviour around the lining explains the following observations:

1. **Tunnel squat** Analysis MODU predicts more squatting of the tunnel than analysis ORIG (Figure 7.19d), due to the softer extension behaviour at the crown augmenting the vertical displacement. It should be noted that much of this squatting occurs before the lining is placed.

2. **Lining moment** For the westbound excavation, lining moments (Figure 7.20b) follow a different trend to lining forces (Figure 7.20a): analysis MODU gives

greater lining force than analysis ORIG, but less lining moment. This indicates a more even distribution of soil forces around the lining for analysis MODU, which could have resulted from the different stiffness behaviour around the lining.

Greater overall drained stiffness during consolidation The drained behaviour of model MODU is stiffer than that for model ORIG, except for extension paths. Since an extension path only occurs above the tunnel crown, consolidation behaviour for analysis MODU is generally stiffer. This explains the following observations:

1. **Consolidation strain** Consolidation strains both above and below the westbound tunnel for analysis MODU are less than in analysis ORIG (Figure 7.22b), due to the stiffer drained behaviour.

2. **Lining moment** Moments developed during consolidation are less for analysis MODU than for analysis ORIG (Figures 7.23b & 7.30d). As consolidation progresses, vertical load on the lining increases, deflecting the springline outwards against the soil. In analysis MODU, the stiffer soil at the springline is able to resist this deflection, resulting in a more even distribution of soil forces around the lining, and less lining moment.

3. **Lining force** During the final consolidation, both linings develop greater lining forces for analysis MODU than for analysis ORIG (Figure 7.23a, 7.30a & 7.30b). Imposing the same consolidation strain would relieve more force from the soil to the lining in analysis MODU, due to the higher drained stiffness; this load transfer mechanism was proposed by Dimmock (2003).

4. **Pore pressure dissipation** Following excavation, excess pore pressures initially dissipate faster for analysis MODU (Figures 7.24b & 7.31b); the higher drained stiffness increases the coefficient of consolidation according to the equation: $c_{\mathrm{v}} = kE_{\mathrm{1D}}/\gamma_{\mathrm{w}}$.

7.6.3 Comparison of ModF & ModX with ModU

Regions of fissure softening Figures 7.32a–d plot the stiffness parameter C_b using model ModF following each stage; a low value of C_b indicates fissure softening. These figures highlight the following observations for analysis ModF:

1. **Effect on settlement trough** Fissure softening above the crown (Figure 7.32a) causes a narrower settlement trough for the westbound excavation (Figure 7.19c); however, the trough is still much wider than in the field. The reduced clay cover above the eastbound crown offers less opportunity for the fissure-softened region shown in Figure 7.32c to influence trough width for the eastbound excavation, so that the trough is not appreciably narrower (Figure 7.26d).

2. **Asymmetry in softening** More fissure softening occurs on the remote side above the eastbound tunnel (away from the westbound tunnel) than on the near side during the eastbound excavation (Figure 7.32c). Figure 7.36 demonstrates how the passage of the westbound tunnel mobilises greater shear stresses on the remote side, initiating more widespread fissure softening here.

3. **Analogy with annealing** Fissure softening is triggered by mobilisation of high friction angles on sub-horizontal and sub-vertical planes; therefore, regions with fissure softening can highlight regions with high friction angle. Mobilised friction angle reduces during consolidation (cf. Figures 7.32a & b and 7.32c & d) due to the increase in mean effective stress, mimicking an annealing process.

ModX v. ModF Model ModX initiates fissure softening at a lower friction angle than model ModF in an attempt to improve the fit to field data. However, the earlier onset of fissure softening in model ModX made little difference: for instance, the settlement trough in (Figure 7.19c)became only slightly narrower. In other figures, such as Figure 7.20b, the improvement is barely discernable, such that plots for models ModF & ModX practically overlap. This is due to the

fissured-softened regions for both models being almost identical (cf. Figures 7.32a & 7.33).

Softer undrained simple shearing Fissure softening in model ModF softens undrained behaviour in simple shear ($\alpha_{d\sigma} \simeq 45°$). Section 7.6.1 suggested that such softening might improve the fit to field data—this is confirmed by closer replication of ground movements in analysis ModF than in other analyses. In summary, fissure softening causes the following observations:

1. **Volume loss** Analysis ModF incurs significantly greater volume losses than analysis ModU (Figures 7.18 & 7.25). Figure 7.34 illustrates how the softer shearing behaviour of model ModF increases volume loss.

2. **Lining force** The corollary of greater volume loss is that the lining bears less force. This is confirmed by lower lining forces for model ModF after installation (Figures 7.20a & 7.27b).

3. **Trough width** The settlement trough for westbound excavation is significantly narrower in analysis ModF than in analysis ModU (Figure 7.19c), due to softer behaviour in the simple shear regions indicated in Figure 7.35; the narrower trough improves the fit to field data. Despite this, patterns of lining deformation are practically identical between the two analyses (Figure 7.19d); Figure 7.35 indicates that simple-shear modes have less influence close to the tunnel since they are combined with extension and compression modes, so softening in these modes has less effect on the lining. The narrower settlement trough is less obvious for the eastbound excavation (Figure 7.26d) because the shallower depth of the eastbound tunnel allows less opportunity for fissure softening to influence trough width.

4. **Vertical displacement profile** The soil column above the crown in analysis ModF moves downward with less vertical strain than in analysis ModU (Figures 7.19a & 7.26a). The softer simple-shear behaviour of model ModF allows soil on the sides of the column to shear more, allowing it to move more like a rigid body. Analysis ModF is most alike the field behaviour in this regard.

5. **Lining moments after installation** Immediately after installation, lining moments are greater for analysis ModF than for analysis ModU (Figures 7.20b & 7.27d). Fissure softening around the tunnel increases the imbalance of soil forces around the lining, leading to larger moments: the softened soil would carry less load, increasing the vertical force bearing on the crown, whilst simultaneously weakening horizontal restraining forces at the springline.

6. **Westbound lining loads during stage ExcEB** The westbound lining also bears more additional load during the eastbound tunnel excavation in analysis ModF compared with analysis ModU (Figures 7.27a & c), with lining force exhibiting almost double the increase in analysis ModF. Figure 7.32c illustrates a region of fissure softening around the westbound tunnel, which would encourage the westbound lining to bear more load.

Softer drained behaviour The drained triaxial test simulations presented in Chapter 6 demonstrated that fissure softening causes softening of drained as well as undrained behaviour. Figures 7.32b & d indicate regions of fissure softening after the consolidation stages. This softening explains the following observations:

1. **Vertical displacement profile** Greater vertical strains are incurred around the tunnel for analysis ModF compared with analysis ModU (Figures 7.22b, 7.29b & 7.29c); this correspond to regions of fissure softening around each tunnel, highlighted in Figures 7.32b & d.

2. **Lining moment** Lining moments developed during consolidation, are significantly greater in analysis ModF than in analysis ModU (Figures 7.23b, 7.30c & 7.30d). Squatting during consolidation causes the lining to push against soil at the springline. Fissure softening in analysis ModF reduces the horizontal resistance of the soil, so that a greater lining moment is required to support the vertical force bearing upon the crown.

3. **Pore pressure dissipation** Excess pore pressures in analysis ModF dissipate slower initially than in analysis ModU (Figures 7.24b & 7.31b). This is due to the softer drained stiffness reducing the coefficient of consolidation, according to the equation: $c_{\mathrm{v}} = kE_{\mathrm{1D}}/\gamma_{\mathrm{w}}$.

4. **Trough offset** During the final consolidation stage, analysis ModF exhibits a settlement trough with a greater offset towards the westbound tunnel than in analysis ModU (Figure 7.29d). This is because the fissure-softened region encompasses the westbound as well as the eastbound tunnel in Figure 7.32d, causing more consolidation here.

Excess pore pressure inaccuracies Excess pore pressures after eastbound excavation show marked differences between the analysis predictions and the field behaviour, as shown by the centreline profile of Figure 7.28. These inaccuracies could be due to pore pressure nodes being too sparse around the tunnels. For this reason, the regions of quadratic elements around each tunnel were extended in the parametric study described in Chapters 8 and 9. Excess pore pressure generation might also be complicated by interaction, since excess pore pressures after the westbound excavation are well-predicted in Figure 7.21. However, the inaccuracies in modelling excess pore pressure generation had little influence on the following consolidation stage (e.g. vertical displacement profiles in Figures 7.29a & b). This is due to movements arising from two mechanisms:

1. **Excess pore pressure dissipation** Dissipation of excess pore pressures generated during excavation affects movements only in the immediate vicinity of the tunnel, and occurs only at the very start of consolidation.

2. **Drainage into tunnel** Drainage into the tunnel induces consolidation over a wide zone, and determines the steady-state condition.

The long-term behaviour therefore demonstrated little sensitivity to generation of excess pore pressure because its dissipation was transient and localised.

7.7 Implications

7.7.1 Softer simple-shear behaviour

Simulation of the narrow settlement trough observed in the field has long since presented a challenge. Past authors have found that adopting a soft shear modulus G_{vh} produced a narrower trough (Addenbrooke *et al.*, 1997; Franzius, 2003; Lee

& Rowe, 1989; Simpson *et al.*, 1996); however, it needed to be unrealistically low to match trough widths in the field. Lee & Rowe (1989) found that adopting $G_{\mathrm{vh}}/E_{\mathrm{v}}$ in the range 0.2–0.25 gave a reasonable fit to centrifuge test data; however laboratory tests on London Clay give $G_{\mathrm{vh}}/E_{\mathrm{v}}$ varying from 0.23 to 0.44, with an average of 0.38.

This chapter agrees with this finding: more accurate simulation of excavation required softer behaviour in simple-shear modes ($\alpha_{\mathrm{d}\sigma} \simeq 45°$) compared with other shearing modes; Simpson *et al.* (1996) recognised that this corresponded to adopting a soft G_{vh}.

Elastic values of G_{vh} from bender element tests on London Clay could not justify the reduction in G_{vh} required to fit the field data (Simpson *et al.*, 1996). However, at larger strains, a low value can be justified: preferential softening in simple shear was observed by Nishimura (2006) in hollow cylinder tests on London Clay, presented in Chapter 6.

This implies that G_{vh} degrades faster with strain than E_{v} and E_{h}. This deterioration in shear modulus at large strains indicates that adjusting the plastic flow rule might be effective at preferentially softening simple-shear behaviour. One way to achieve this is to apply the tangential stress rate effect (Hashiguchi & Tsutsumi, 2001). This would make plastic strain evolution dependent upon the stress increment component tangential to the yield surface, as well as upon the normal component. This formulation is particularly attractive considering that without fissure softening—at very low volume losses or in the absence of fissures—a narrow trough still results.

In this chapter, soil models ModF & ModX implemented simple-shear softening through a fissure model, and therefore replicated narrower settlement troughs compared with model ModU, which lacked the fissure model. Softening of bulk modulus in models ModF and ModX might be unrealistic since the fissures are maintained in a state of compression. These models might be improved by softening only the shear stiffness components by the same reduction factor.

7.7.2 Soil model selection for parametric analyses

In all models, there is significant scope to improve the prediction of excess pore pressure generation. However, the excess pore pressures had little influence on the steady-state condition after consolidation, implying that the parametric studies should not be compromised by the inaccuracies.

Overall, soil model ModU replicated the St James's Park simulation poorer than model Orig, despite fitting laboratory test data better in Chapter 6. This is because relative stiffnesses between the modes illustrated in Figure 7.35—simple shear, extension and compression—was imbalanced.

Model ModF attempted to rectify this by softening behaviour in simple shear ($\alpha_{d\sigma} \simeq 45°$). Model ModF therefore demonstrated significant improvement over ModU, and still fitted better than Orig, although by less of a margin.

To trial earlier onset of fissure softening, the threshold friction angle at which fissures softened was reduced in model ModX compared with ModF, but made only a slight improvement. Because of this, and since the softening friction angle applied in ModF fitted the laboratory test data well in Chapter 6, model ModF seems the most suitable soil model for London Clay out of all models trialled. Giving the best overall fit in both laboratory tests and field simulations, model ModF is the prime candidate to use in parametric studies.

7.7.3 Knowledge of in-situ parameters

The simulations have highlighted the sensitivity of long-term behaviour to in-situ permeability and stiffness. These parameters are likely to be site-specific, and so long-term predictions will be limited by accurate knowledge of these.

7.8 Summary

The twin-tunnel construction of the Jubilee Line Extension beneath St James's Park was simulated in a series of finite-element coupled-consolidation analyses. The analyses were based upon similar validation analyses conducted by Wongsaroj (2005), for a single tunnel alone.

Comparing the performance of four different soil models, the analyses proved that model MODF (presented in Chapter 6) was the most suitable to use in the parametric analyses described in Chapters 8 & 9. This is due to fissure softening in the model, which preferentially softened the simple-shear behaviour, resulting in a narrower settlement trough.

To replicate field data more realistically, the soil model should simulate softer behaviour in simple shear compared with other shearing modes. This can be achieved by adjusting the plastic flow rule (Hashiguchi & Tsutsumi, 2001), or by implementing fissure softening such as that proposed here. A possible improvement to this implementation might be to soften only shear stiffness components whilst maintaining the bulk modulus. Also, a more in-depth knowledge of the in-situ permeability and stiffness would greatly improve the simulation of consolidation to match field data.

DESCRIPTION	PARAMETER	UNITS	MODEL						
			MADE GROUND	TERRACE GRAVEL	LAMBETH GROUP	LONDON CLAY ORIG	LONDON CLAY MODU	LONDON CLAY MODF	LONDON CLAY MODX
Elastic parameters									
Poisson's ratio of horizontal strain under vertical straining	ν_{vh}	-	0.2	0.2	0.2	0.07	0.015	0.015	0.015
Poisson's ratio of vertical strain under horizontal straining	ν_{hv}	-	0.2	0.2	0.2	0.16	0.04	0.04	0.04
Poisson's ratio of horizontal strain under horizontal straining	ν_{hh}	-	0.2	0.2	0.2	0.12	0.12	0.12	0.12
Shear stiffness anisotropy ratio	G_{hh}/G_{vh}	-	1	1	1	1.5	1.5	1.5	1.5
Initial gradient of isotropic swelling line at load reversal	C_b	-	100	400	900	200	300	300	300
Non-linearity of swelling line	ω_s	-	15	15	50	20	10	10	10
Gradient of normal consolidation line in log e - log p' space	ρ_c	-	0.2476	0.556	0.37	0.3	0.3	0.3	0.3
Factor for non-linearity during isotropic loading and unloading	D	-	0	0	0.05	0.05	0.05	0.05	0.05
Factor for non-linearity during isotropic loading and unloading	r	-	0	0	2	2	2	2	2
Plastic parameters									
Factor for evolution of plastic strain	u_1	-	100	100	100	300	300	300	300
Factor for evolution of plastic strain	m	-	0.1	0.1	0.1	0.2	0.05	0.05	0.05
Yield surface parameters									
Gradient of critical state line in q-p' space	M	-	0.984	1.418	1.07	0.814	0.814	0.814	0.814
Yield surface rotation towards σ_{vv}-direction	β_{vv}	-	0	0	0	0	0.1	0.1	0.1
Yield surface rotation towards σ_{hh}-direction	β_{hh}	-	0	0	0	0	-0.05	-0.05	-0.05
Yield surface rotation towards τ_{vh}-direction	β_{vh}	-	0	0	0	0	0	0	0
Initial preconsolidation pressure	$p'_{0(C)}$	kPa	*varies*	*varies*	*varies*	*varies*	*varies*	*varies*	*varies*
Fissure model parameters									
Maximum inclination of fissure plane to either vertical or horizontal directions	α_{range}	°	-	-	-	-	-	16	16
Fissure friction angle at onset of softening	ϕ_{soft}	°	-	-	-	-	-	11.5	10
Range of fissure friction angle over which stiffness reduction factor ramps to minimum value	ϕ_{range}	°	-	-	-	-	-	1.5	1.5
Measure of minimum fissure stiffness	$f_{fiss\ min}$	-	-	-	-	-	-	3.6	3.6
Non-constitutive properties									
Initial voids ratio	e_0	-	0.65	0.5	0.65	0.7	0.7	0.7	0.7
Earth pressure coefficient at rest	K_0	-	0.6	0.4	1.2	1.2	1.2	1.2	1.2
Bulk unit weight	γ_b	kN m^{-3}	20	20	20	20	20	20	20
Coefficient of vertical permeability	k_v	m s^{-1}	1×10^{-7}	5×10^{-4}	5×10^{-12}	*variable*	*variable*	*variable*	*variable*

Table 7.1: Soil parameters applied to strata

VARIABLE TO REMESH				SYMBOL	METHOD OF DEFINITION
For numerical solver					
Displacement				$\Delta x, \Delta y, \Delta z$	defines new nodal coordinates
Pore pressure				u	mapped to nodes
Void ratio				e	mapped to elements
Stresses in soil				$\sigma_{xx}, \sigma_{yy}, \sigma_{zz}, \sigma_{xy}$	mapped to integration points
Lining:	EITHER	stresses,	if unjointed lining	$\sigma_{cc}, \sigma_{zz}, \sigma_{cr}$	mapped to section points
	OR	forces and moments,	if jointed lining	N_{cc}, N_{zz}, M_{zz}	mapped to integration points
For constitutive model code					
Yield surface variables					
Intersection of yield surface with hydrostatic axis				p'_0	
Current strain variables					
Current volumetric strain				ε_v	
Current deviatoric strain				$\varepsilon_{s\,11}, \varepsilon_{s\,22}, \varepsilon_{s\,33}, \varepsilon_{s\,12}, \varepsilon_{s\,13}, \varepsilon_{s\,23}$	
Void ratio				e	
Stress reversal variables					
Volumetric strain at last stress reversal				$\varepsilon_{v\,rev}$	
Deviatoric strain at last stress reversal				$\varepsilon_{s\,rev\,11}, \varepsilon_{s\,rev\,22}, \varepsilon_{s\,rev\,33}, \varepsilon_{s\,rev\,12}, \varepsilon_{s\,rev\,13}, \varepsilon_{s\,rev\,23}$	
Mean effective stress at last stress reversal				p'_{rev}	
Ratio of deviatoric to mean effective stress at last stress reversal				$\eta_{rev\,11}, \eta_{rev\,22}, \eta_{rev\,33}, \eta_{rev\,12}, \eta_{rev\,13}, \eta_{rev\,23}$	
Fissure softening variables					
Friction angle mobilised on softening sub-vertical fissure plane				$\phi'_{pv\,max}$	mapped to integration points
Friction angle mobilised on softening sub-horizontal fissure plane				$\phi'_{ph\,max}$	
Vertical direction cosine of normal to softening sub-vertical fissure plane				v_{qv}	
Vertical direction cosine of normal to softening sub-horizontal fissure plane				v_{qh}	

Key to coordinate directions:

x	Transverse: perpendicular to excavation direction
y	Vertical
z	Longitudinal: parallel to excavation direction
c	Circumferential
r	Radial

Table 7.2: Variables mapped between meshes during remeshing

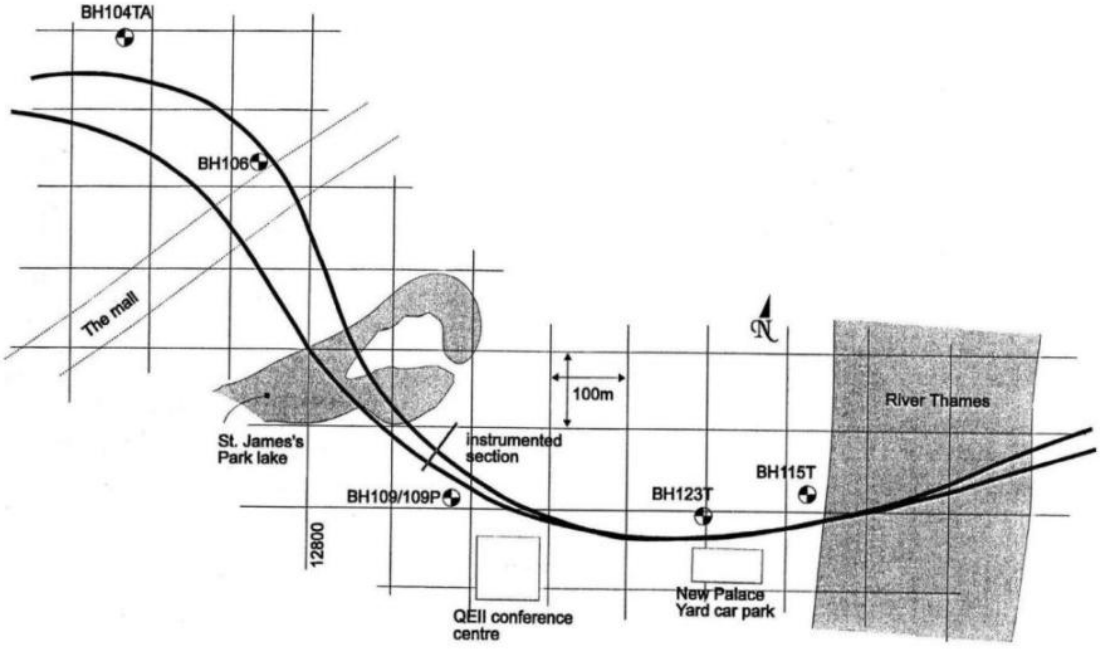

Figure 7.1: Site plan of St James's Park (Nyren, 1998)

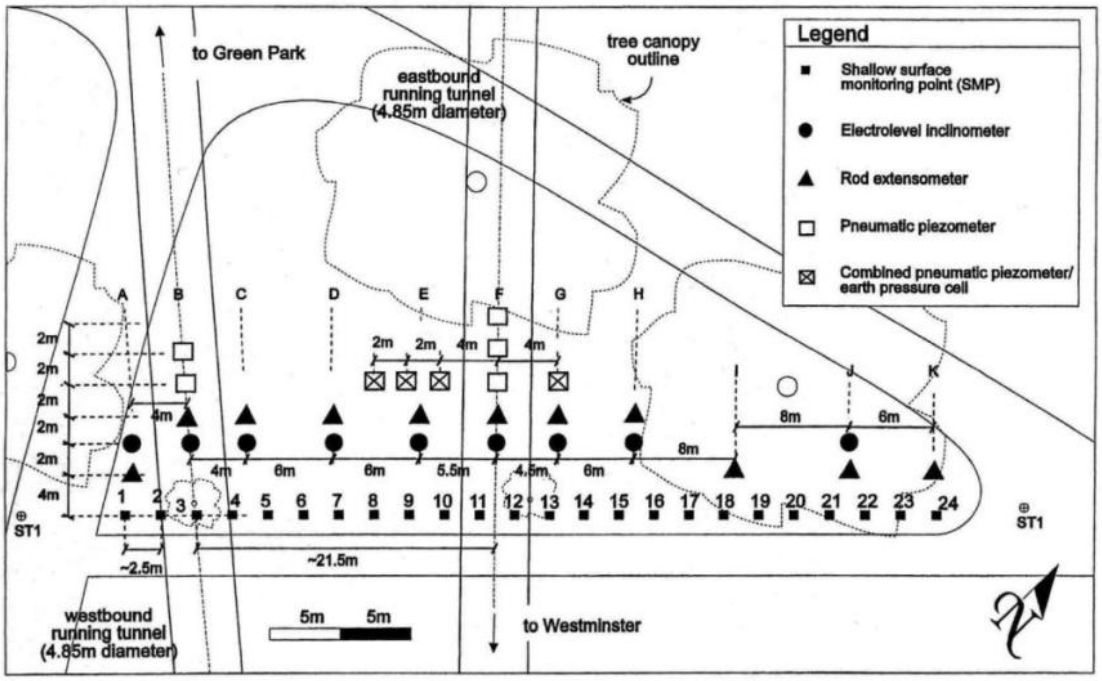

(a) Plan

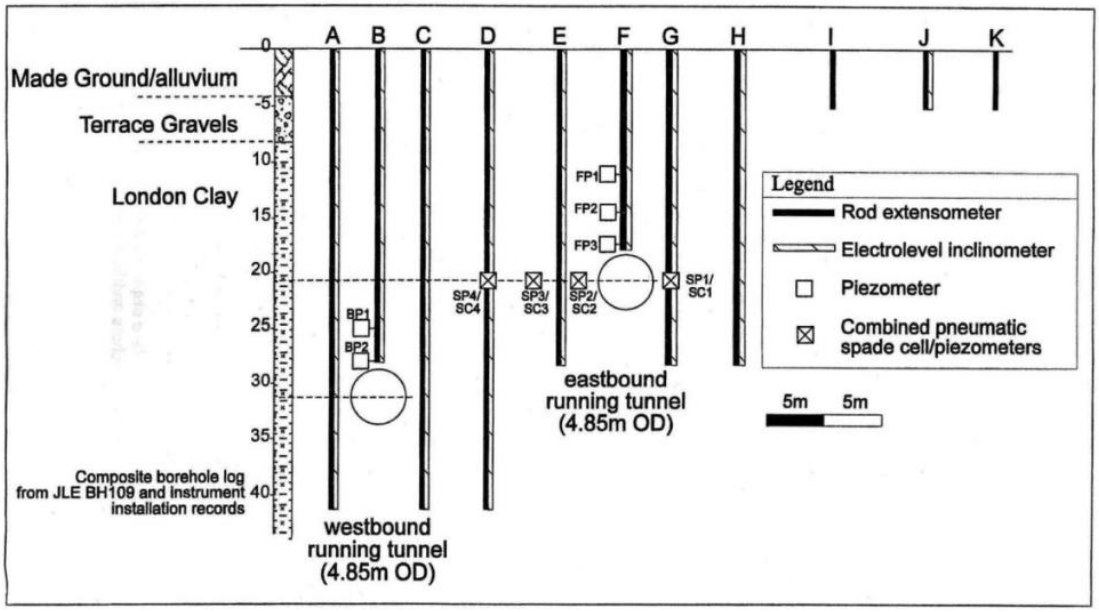

(b) Elevation

Figure 7.2: Instrumentation layout at St James's Park (Nyren, 1998)

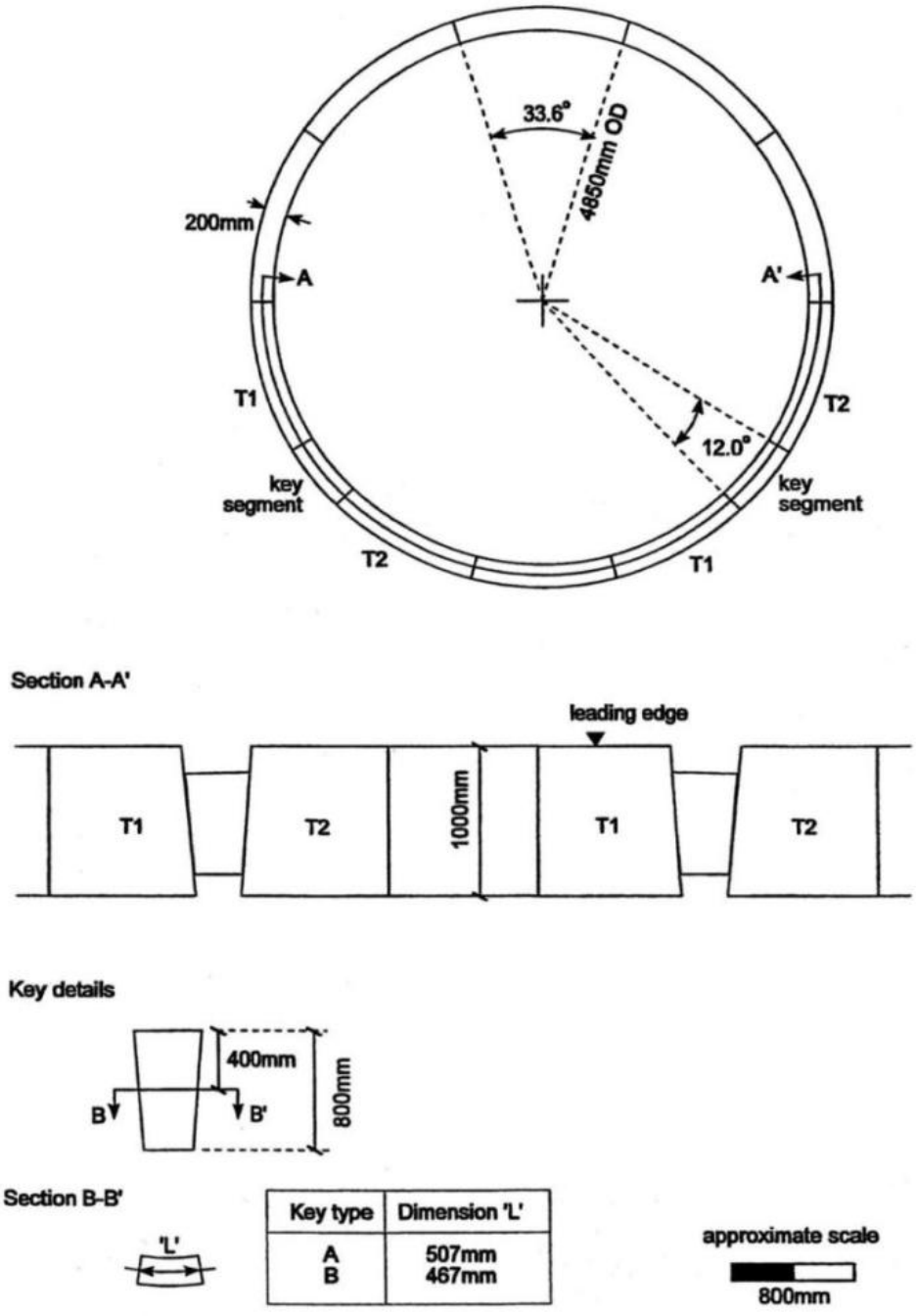

Figure 7.3: Arrangement of lining segments at St James's Park (Nyren, 1998)

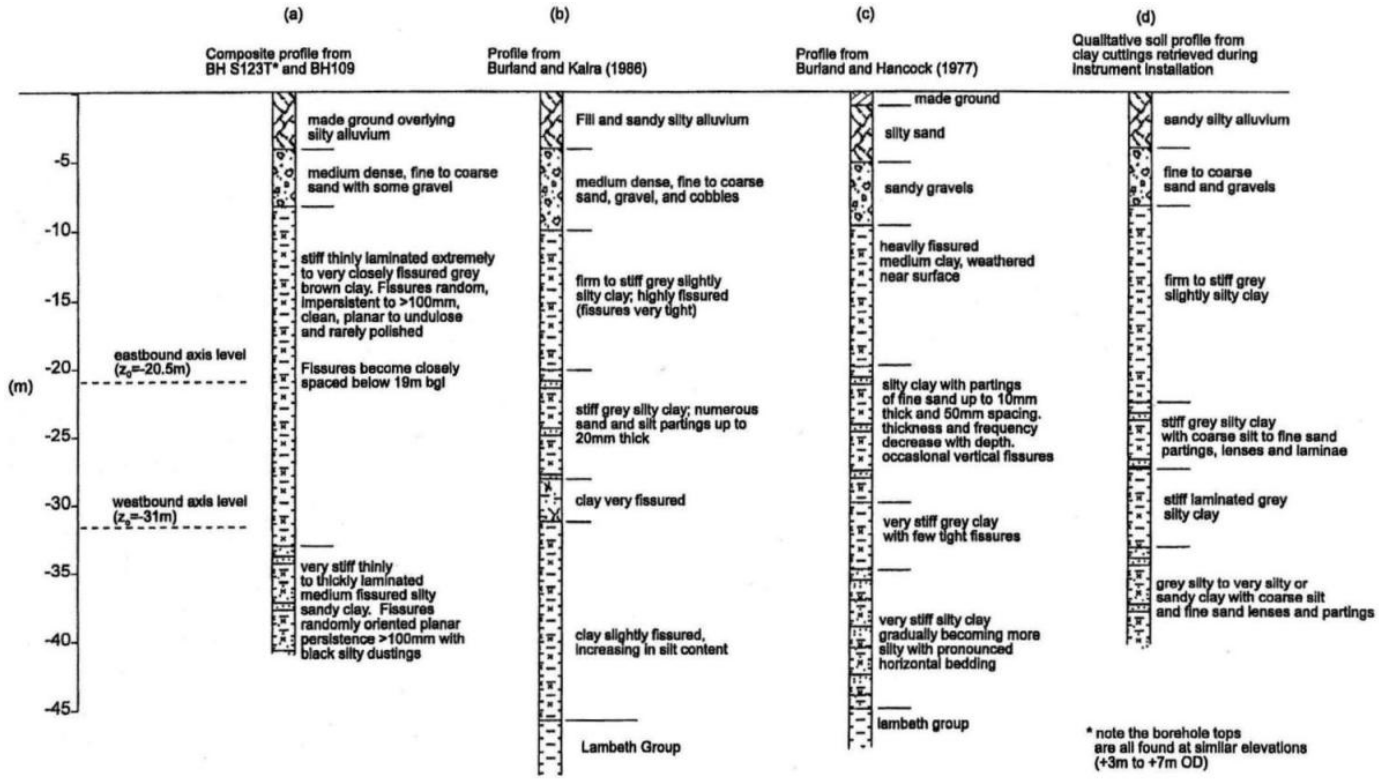

Figure 7.4: Borehole profiles from around St James's Park (Nyren, 1998)

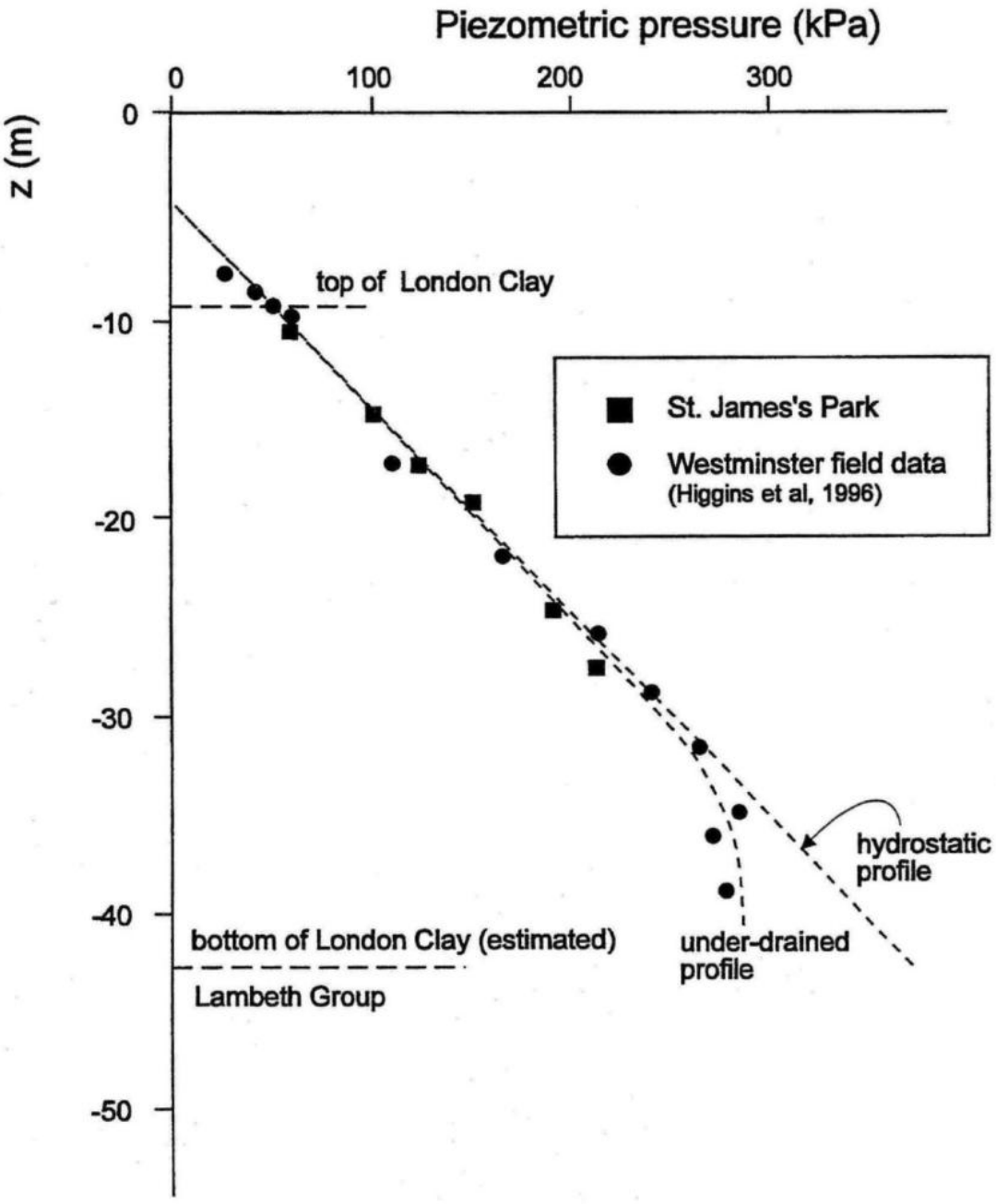

Figure 7.5: Pore pressure profile at St James's Park (Nyren, 1998)

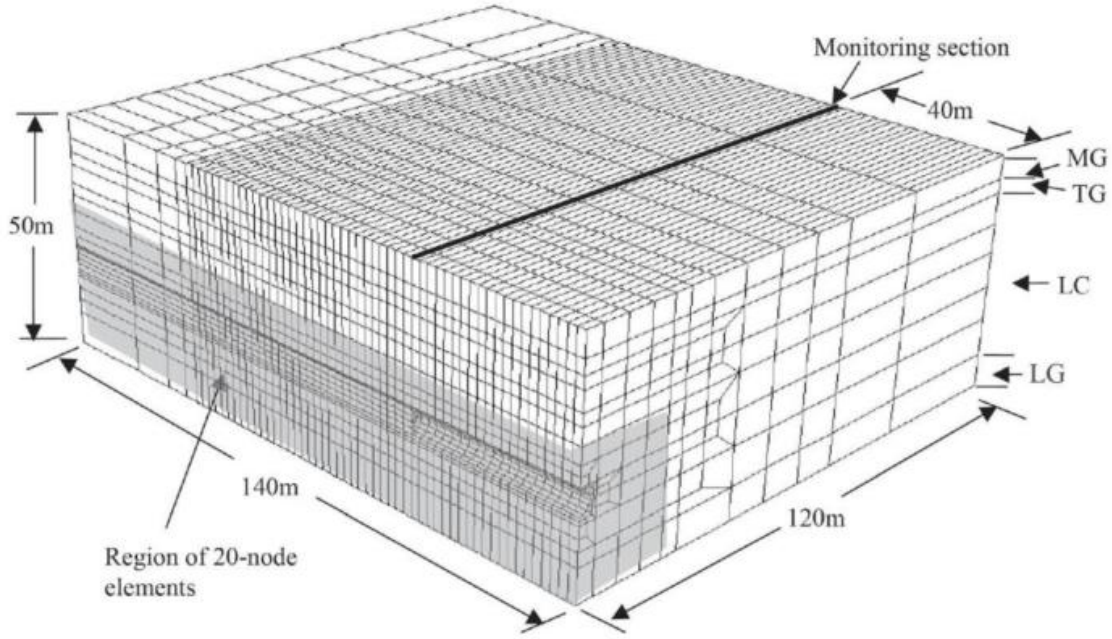

(a) For westbound excavation

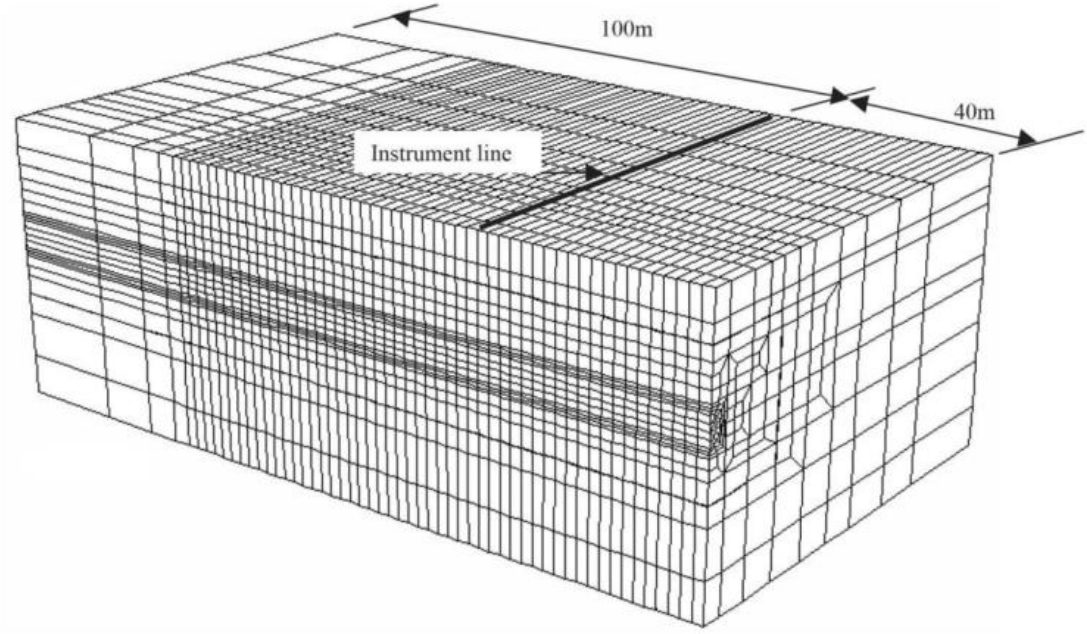

(b) For eastbound excavation

Figure 7.6: 3-D meshes adopted by Wongsaroj (2005)

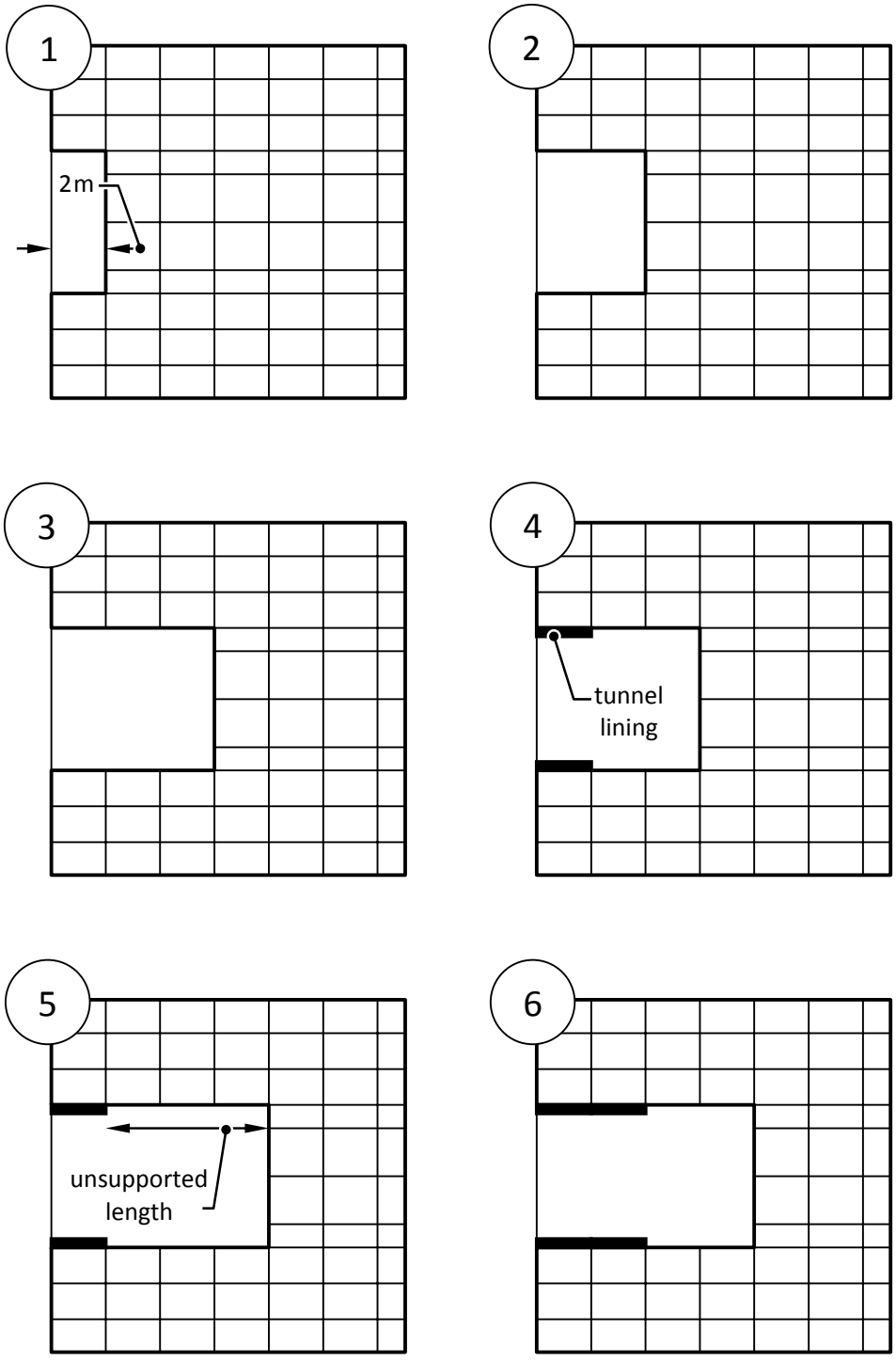

Figure 7.7: Procedure for modelling excavation

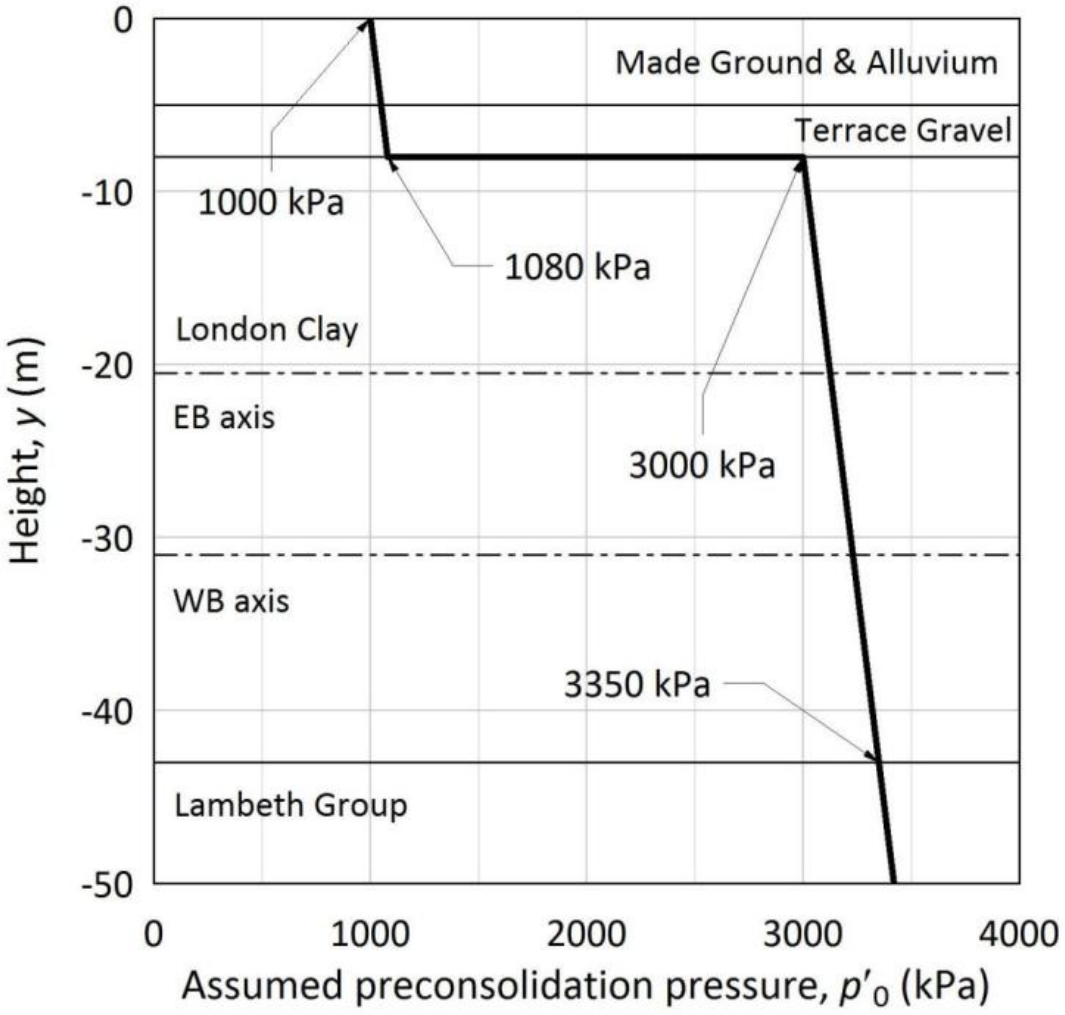

Figure 7.8: Profile of preconsolidation pressure with depth

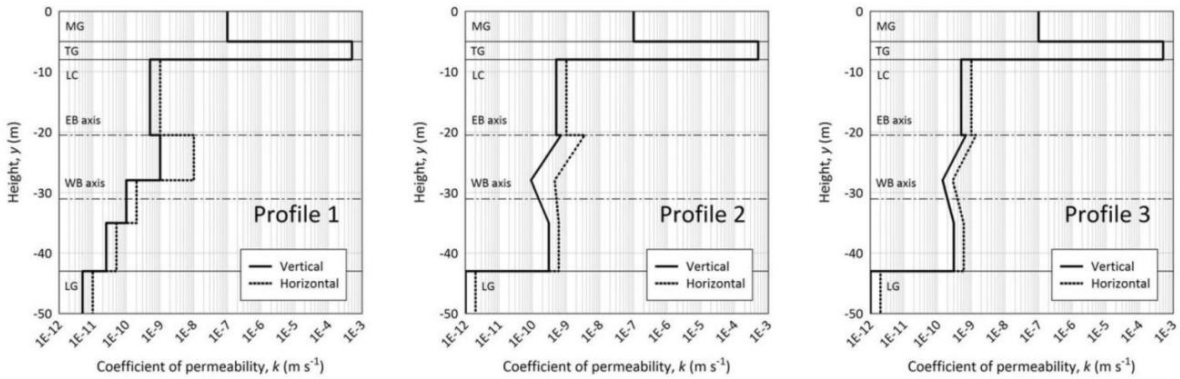

Stratum		Depth	Permeability profile 1		Permeability profile 2		Permeability profile 3	
			k_v	k_h	k_v	k_h	k_v	k_h
		m	m s^{-1}	m s^{-1}	m s^{-1}	m s^{-1}	m s^{-1}	m s^{-1}
Made ground & alluvium		0 – 5	5×10^{-7}	5×10^{-7}	5×10^{-7}	5×10^{-7}	5×10^{-7}	5×10^{-7}
Terrace gravel		5 – 8	1×10^{-4}	1×10^{-4}	1×10^{-4}	1×10^{-4}	1×10^{-4}	1×10^{-4}
London Clay	Unit B	8 – 20.5	5×10^{-10}	1×10^{-9}	5×10^{-10}	1×10^{-9}	5×10^{-10}	1×10^{-9}
	Unit A3ii	20.5 – 28	1×10^{-9}	1×10^{-8}	7×10^{-10} to 9×10^{-11}	3.5×10^{-9} to 4.5×10^{-10}	7×10^{-10} to 1.41×10^{-10}	1.4×10^{-9} to 2.83×10^{-10}
	Unit A3i	28 – 35	1×10^{-10}	2×10^{-10}	9×10^{-11} to 3×10^{-10}	4.5×10^{-10} to 6×10^{-10}	1.41×10^{-10} to $\times10^{-10}$	2.83×10^{-10} to 6×10^{-10}
	Unit A2	35 – 43	2.5×10^{-11}	5×10^{-11}	3×10^{-10}	6×10^{-10}	3×10^{-10}	6×10^{-10}
Lambeth group		43 – 50	5×10^{-12}	1×10^{-11}	1×10^{-12}	2×10^{-12}	1×10^{-12}	2×10^{-12}

Figure 7.9: Permeability profiles trialled by Wongsaroj (2005)

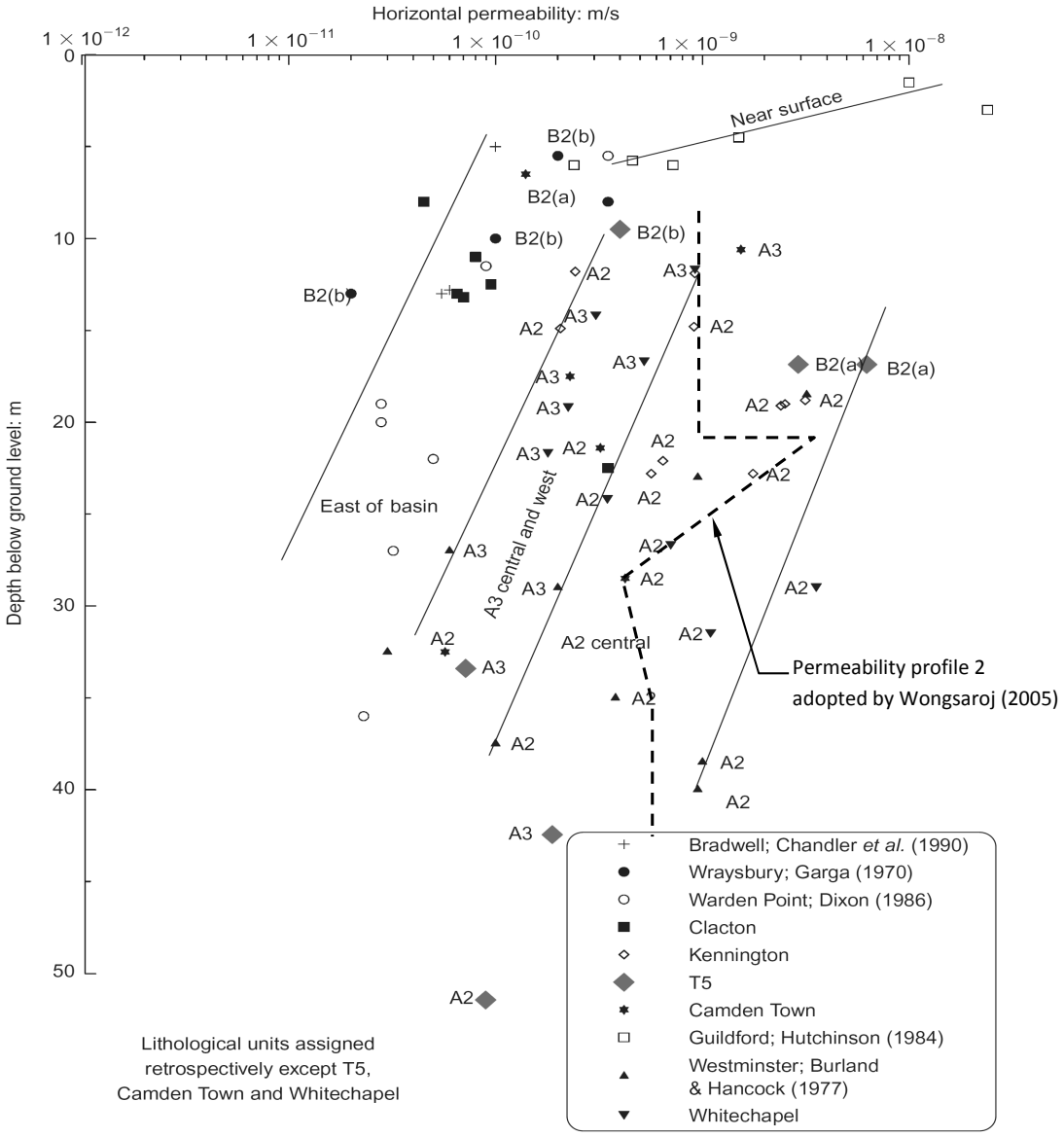

Figure 7.10: In-situ permeability data for London Clay (Hight *et al.*, 2007)

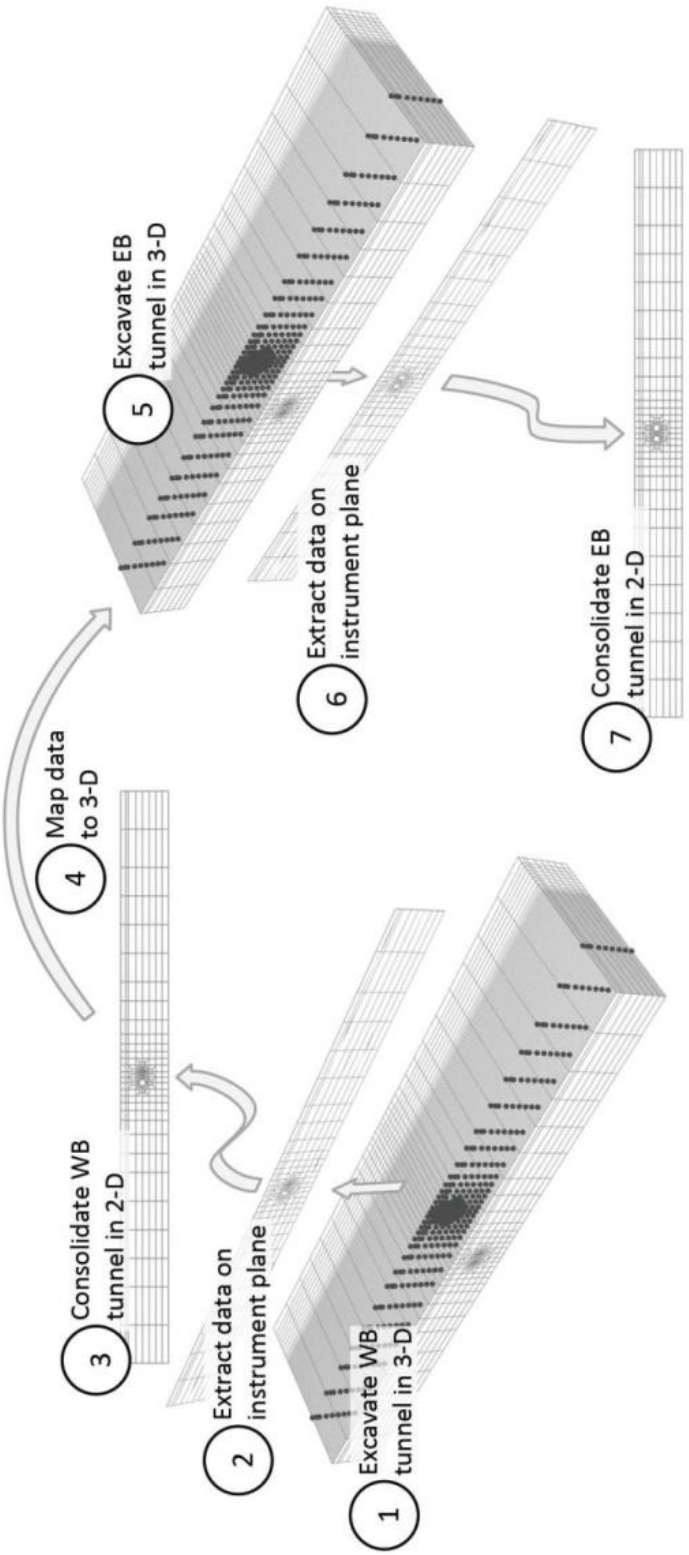

Figure 7.11: Steps in remeshing between 3-D and 2-D meshes

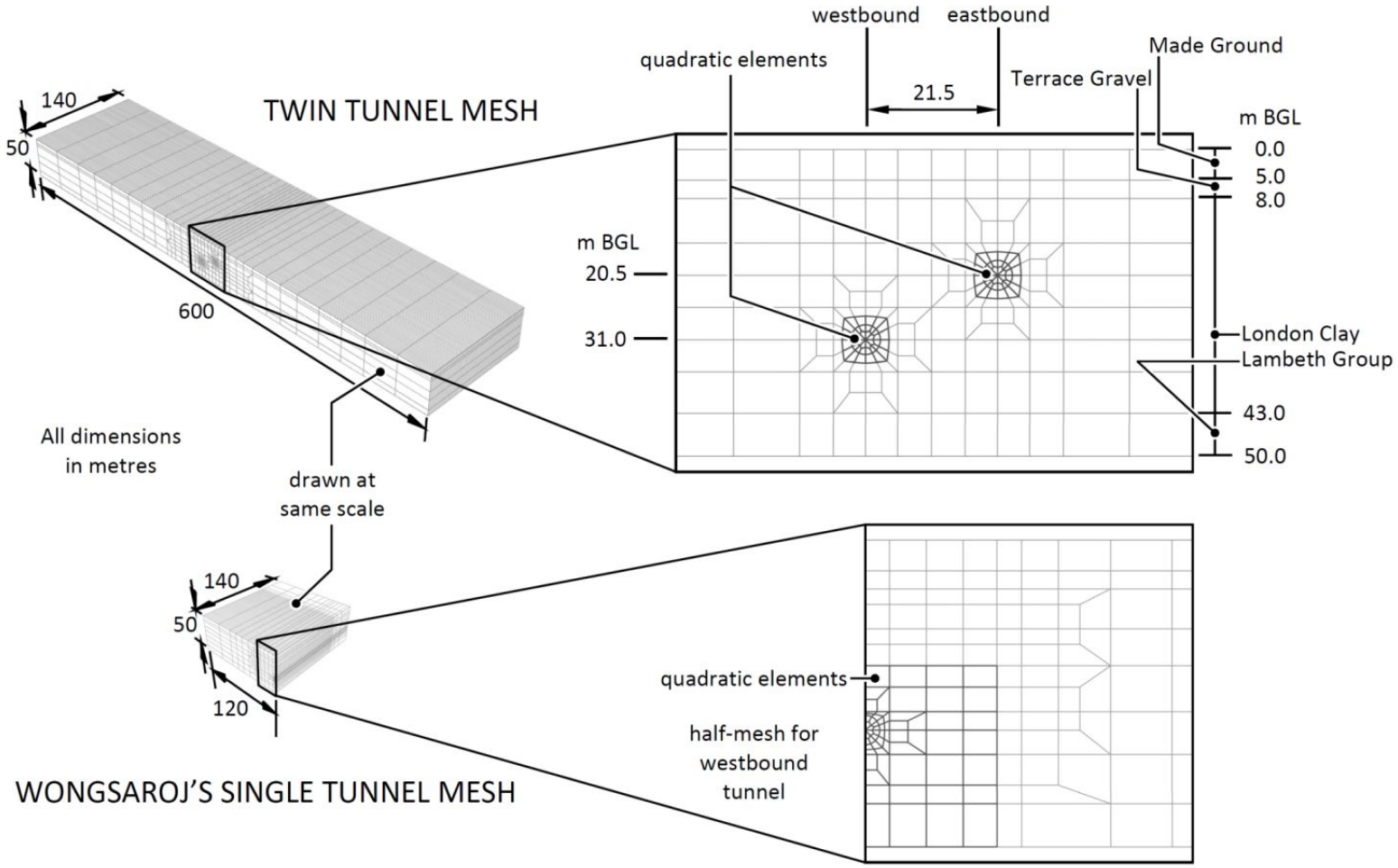

Figure 7.12: Comparison of twin-tunnel mesh with single-tunnel mesh adopted by Wongsaroj (2005)

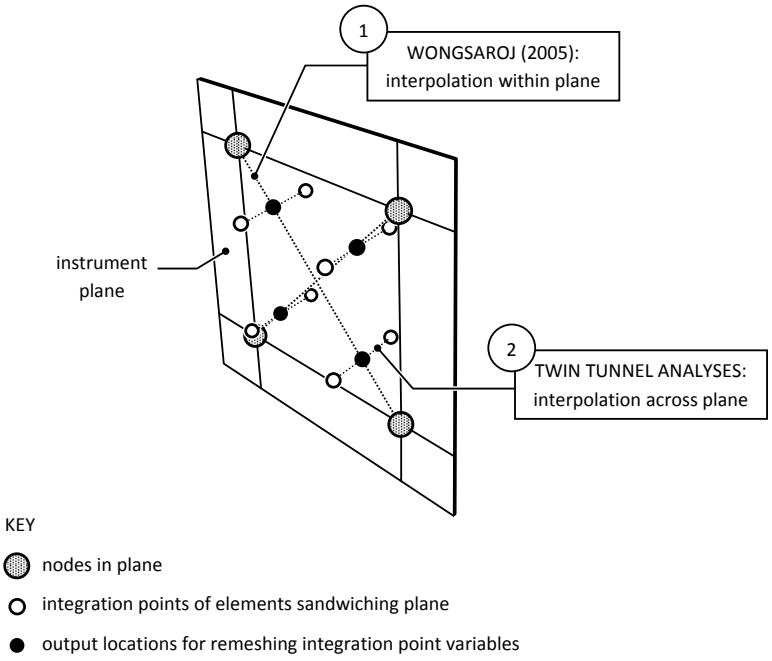

Figure 7.13: Two methods for interpolating integration point variables on the instrument plane

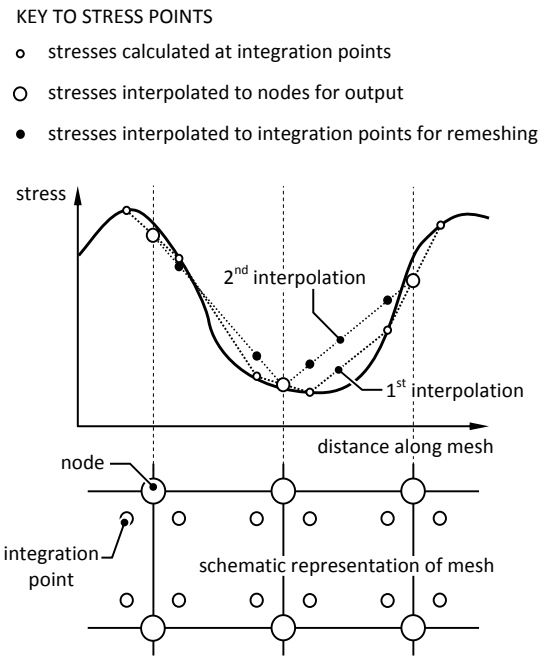

Figure 7.14: Interpolation error in remeshing of Wongsaroj (2005)

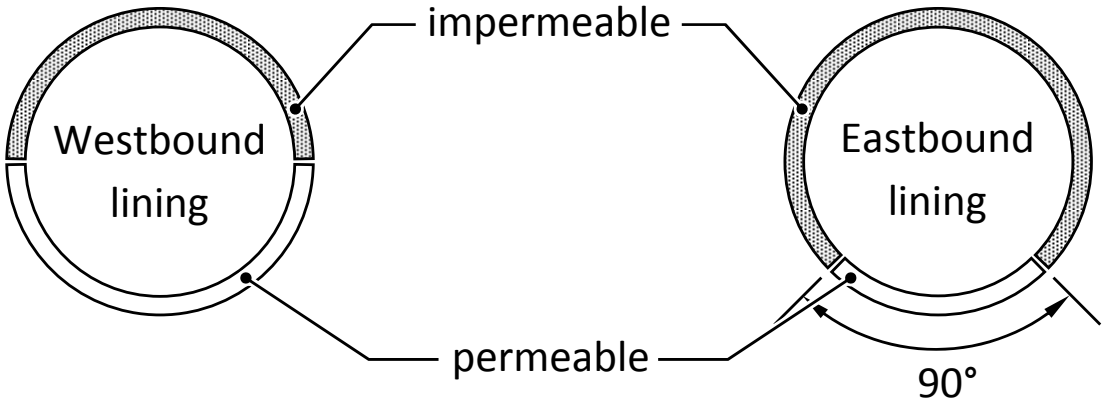

Figure 7.15: Simulated lining permeability distributions

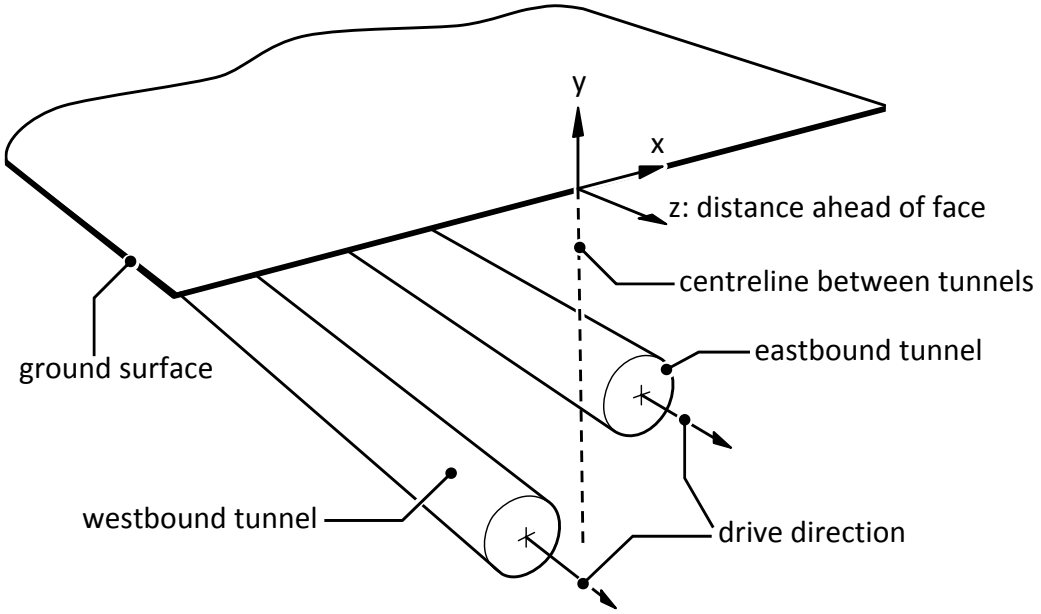

Figure 7.16: Coordinate system for presenting simulation output

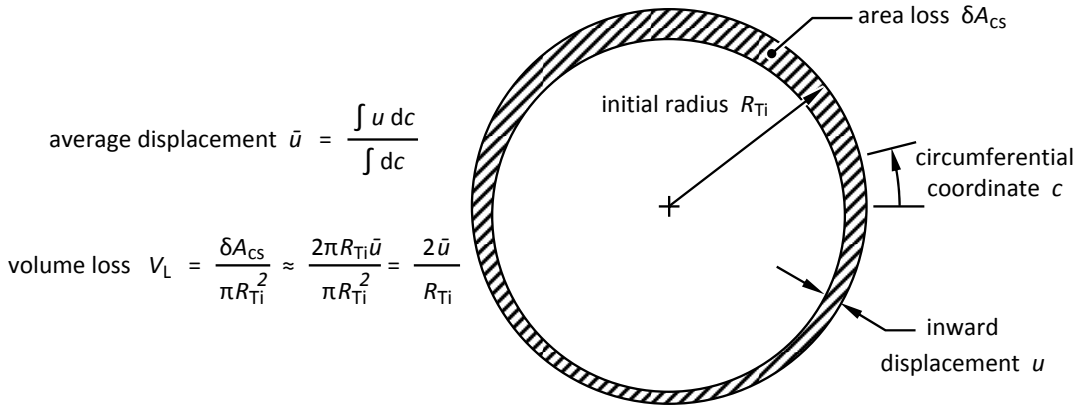

Figure 7.17: Methodology behind normalisation by volume loss

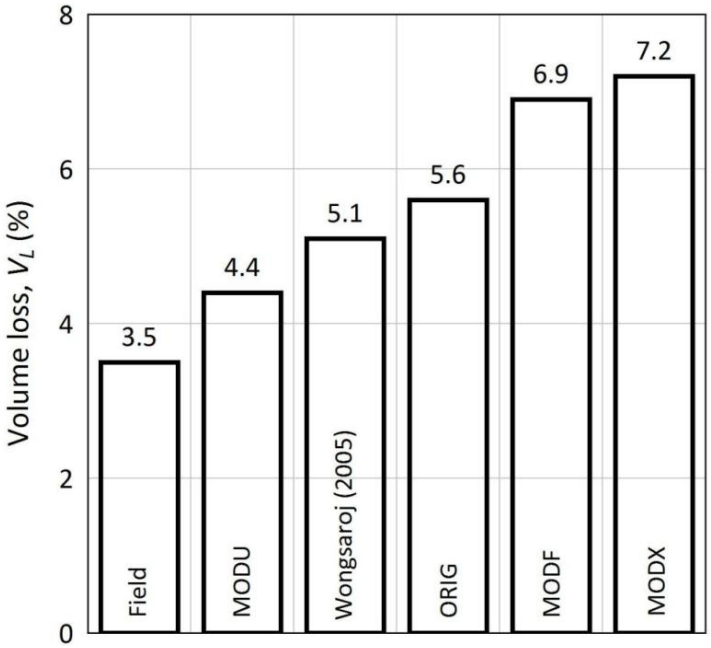

Figure 7.18: Volume losses for westbound tunnel during stage ExcWB

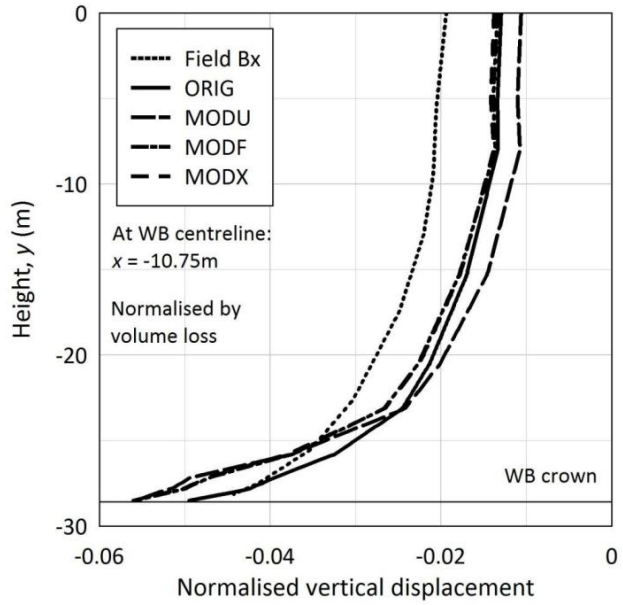

(a) Vertical displacement profiles above westbound tunnel

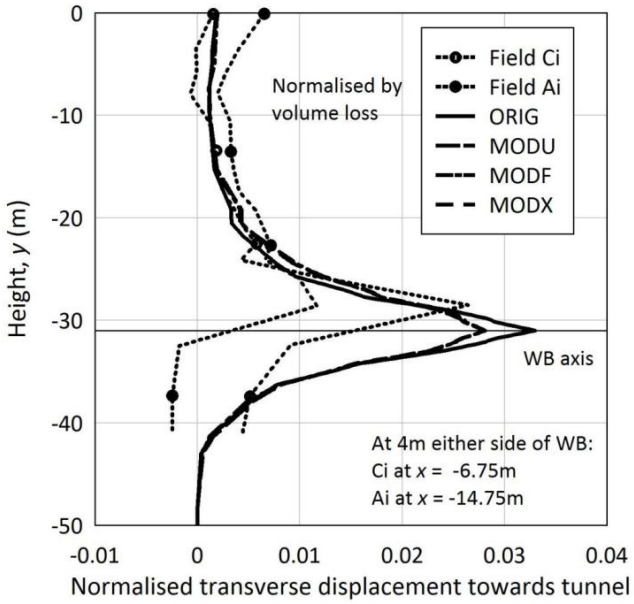

(b) Horizontal displacement profiles adjacent to westbound tunnel

Figure 7.19: Plots of displacement normalised by volume loss for stage ExcWB

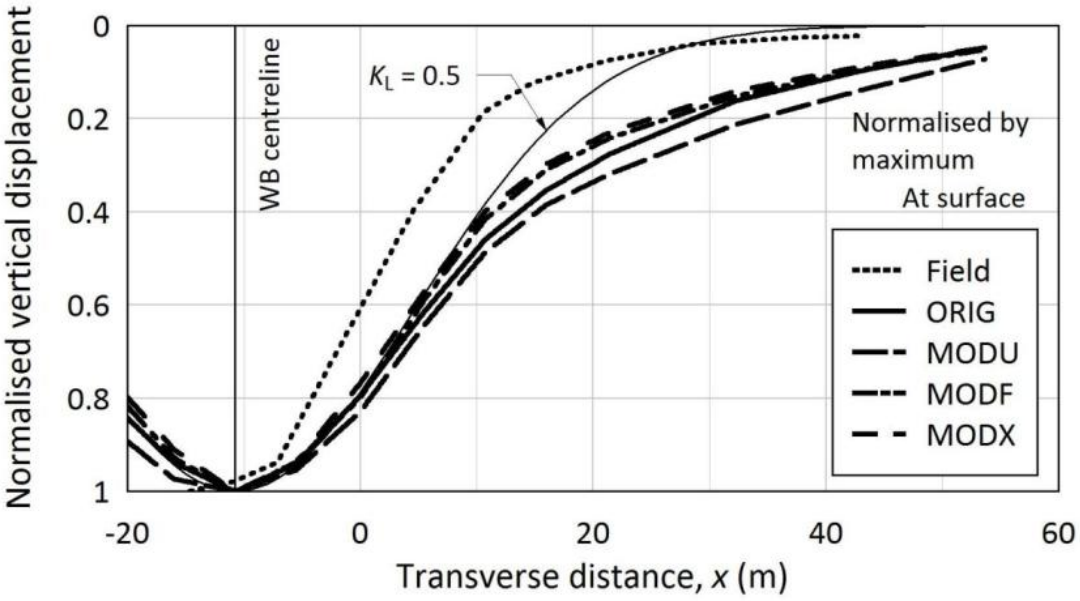

(c) Transverse surface settlement troughs

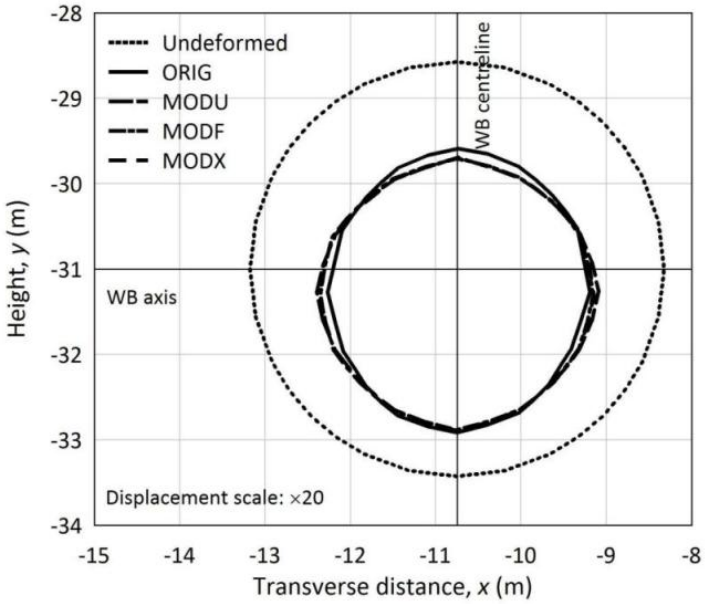

(d) Tunnel displacements for westbound tunnel

Figure 7.19: *cont...* Plots of displacement normalised by volume loss for stage ExcWB

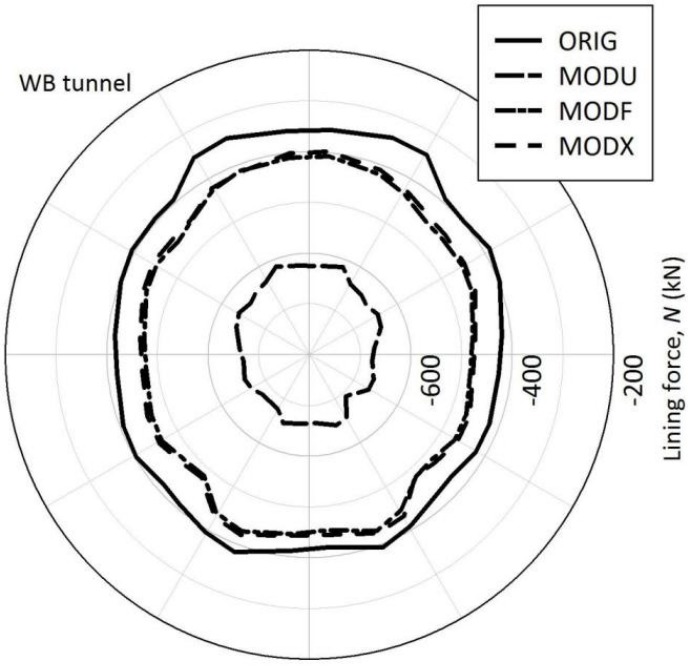

(a) Forces around westbound tunnel lining

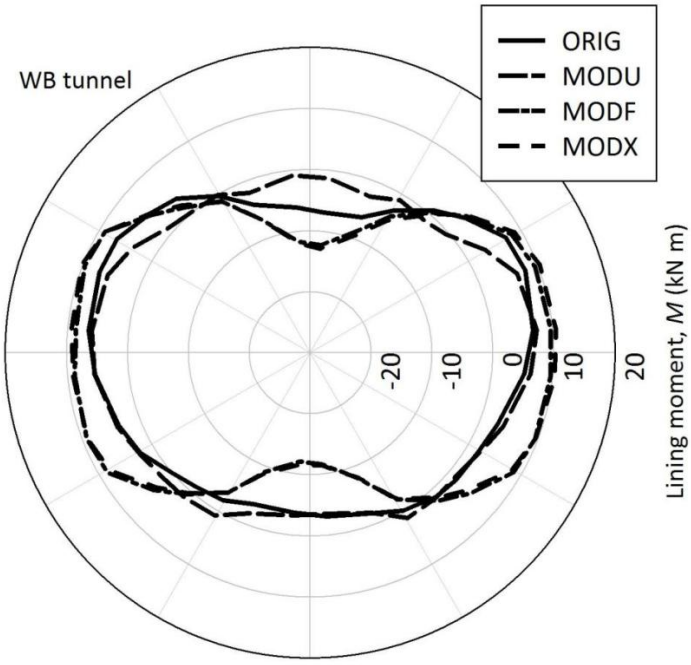

(b) Moments around westbound tunnel lining

Figure 7.20: Distributions around lining of load contributed by stage ExcWB

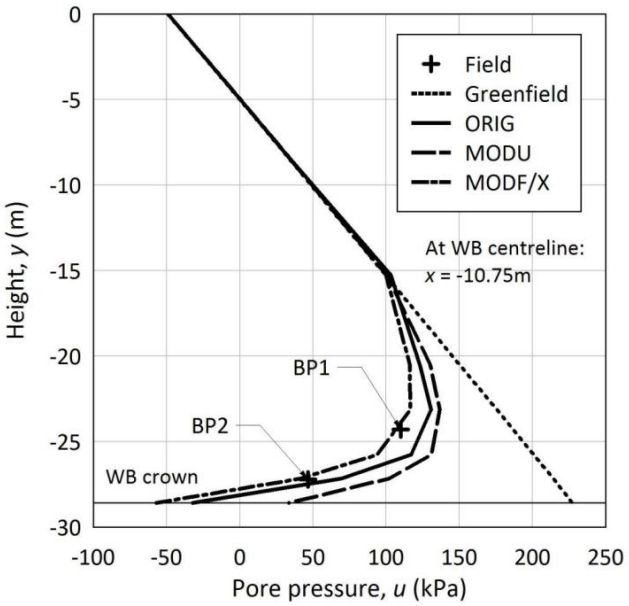

Figure 7.21: Pore pressure profiles along westbound tunnel centreline for stage ExcWB

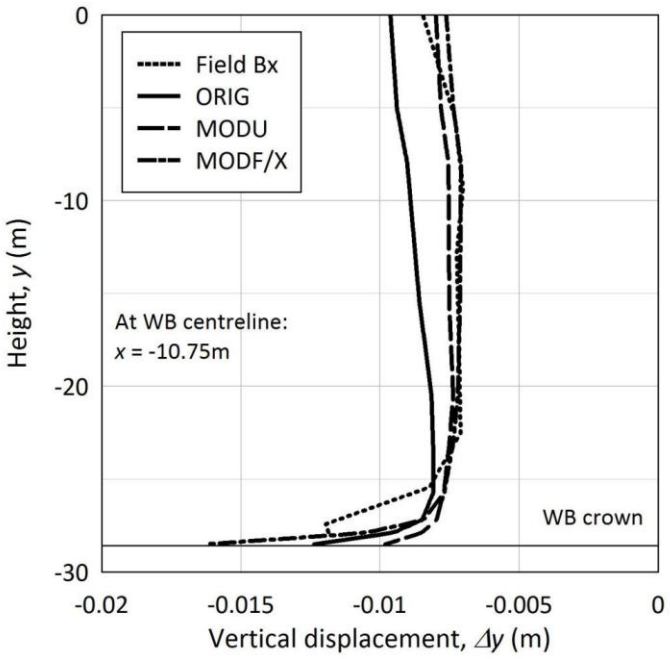

(a) Vertical displacement profiles above westbound tunnel

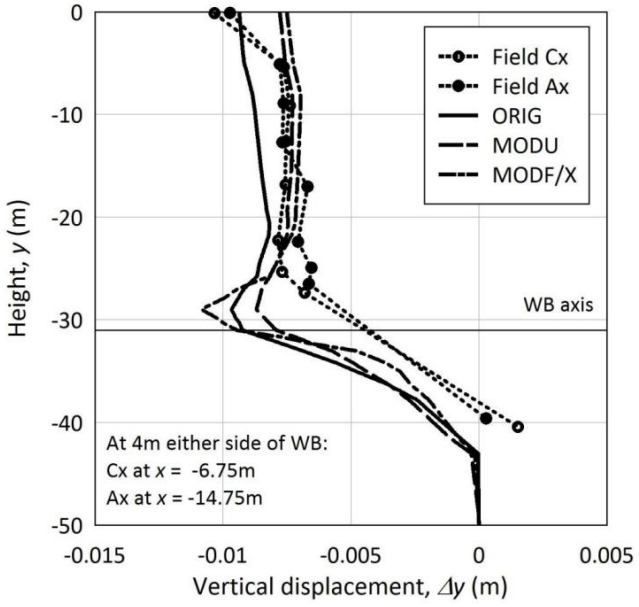

(b) Vertical displacement profiles adjacent to westbound tunnel

Figure 7.22: Displacement plots for stage CslWB

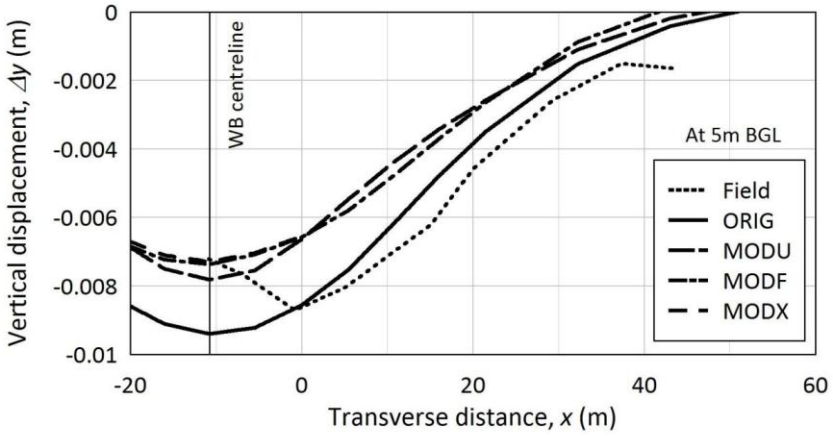

(c) Transverse settlement troughs at 5m depth

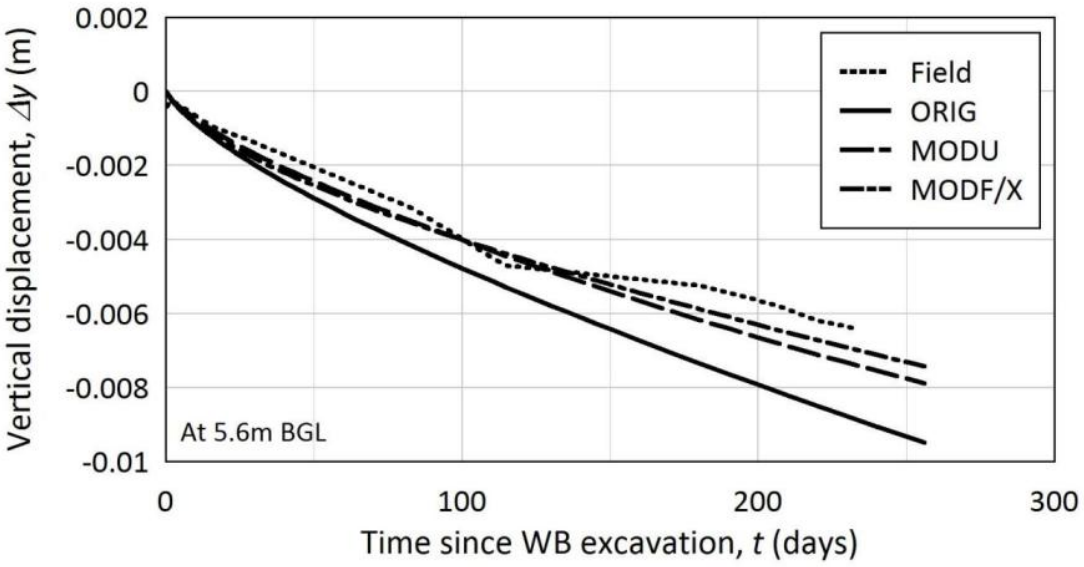

(d) Development of settlement above westbound tunnel centreline at 5.6m depth

Figure 7.22: *cont...* Displacement plots for stage CslWB

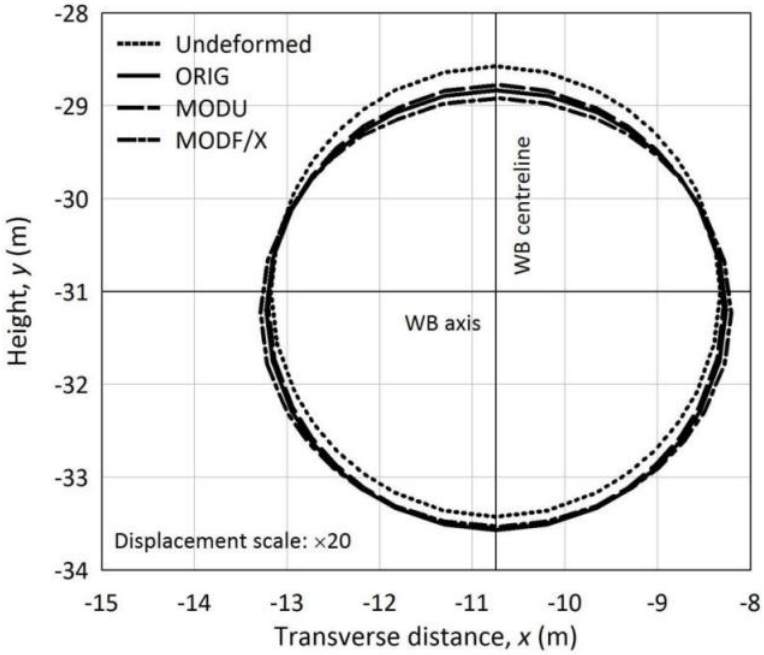

(e) Tunnel displacements for westbound tunnel

Figure 7.22: *cont...* Displacement plots for stage CslWB

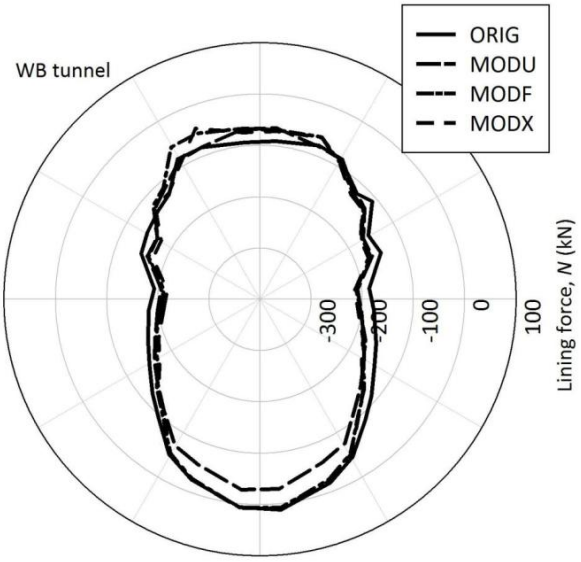

(a) Forces around westbound tunnel lining

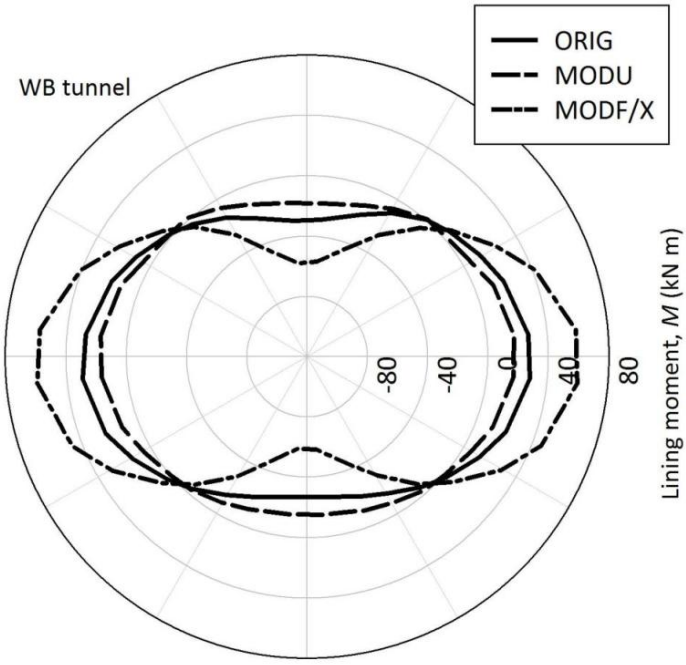

(b) Moments around westbound tunnel lining

Figure 7.23: Distributions around lining of load contributed by stage CslWB

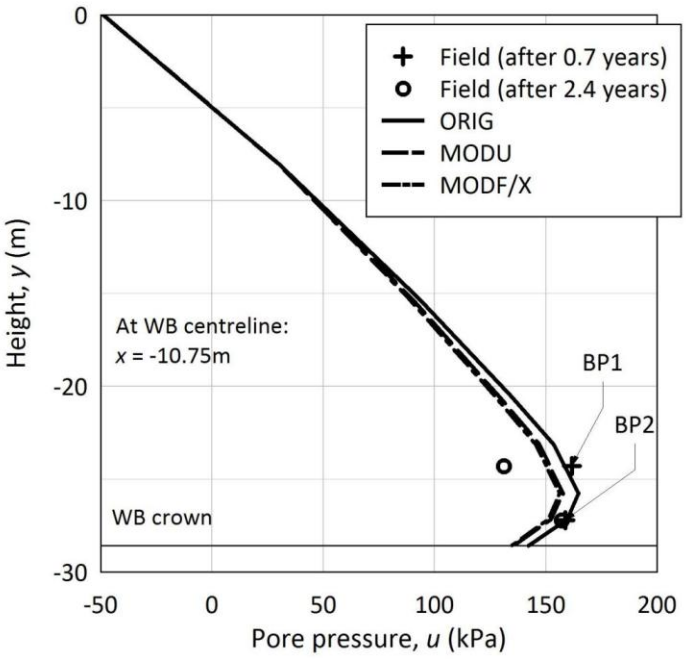

(a) Pore pressure profiles along westbound tunnel centreline

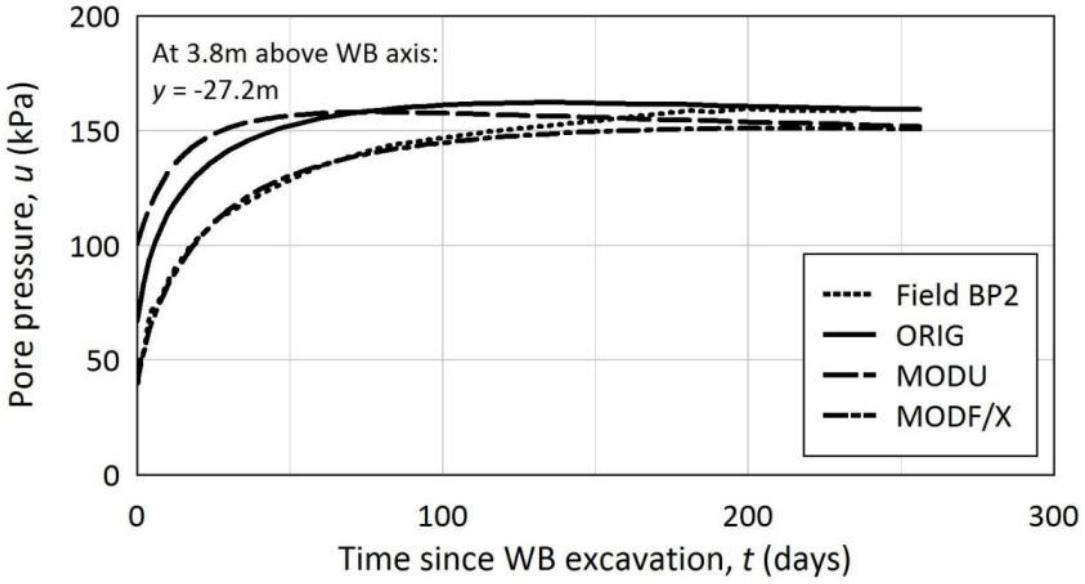

(b) Evolution of pore pressure above westbound tunnel crown

Figure 7.24: Pore pressure plots for stage CslWB

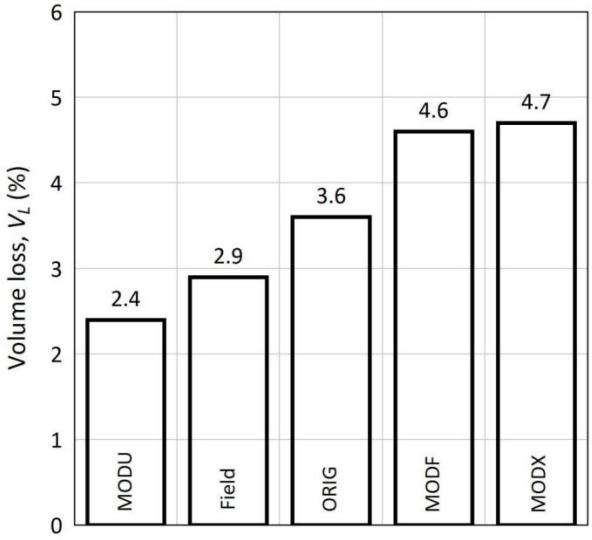

Figure 7.25: Volume losses for eastbound tunnel during stage ExcEB

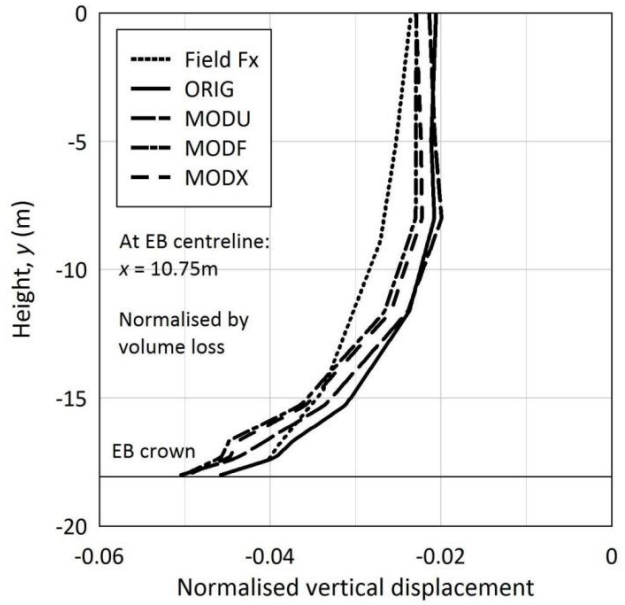

(a) Vertical displacement profiles above eastbound tunnel

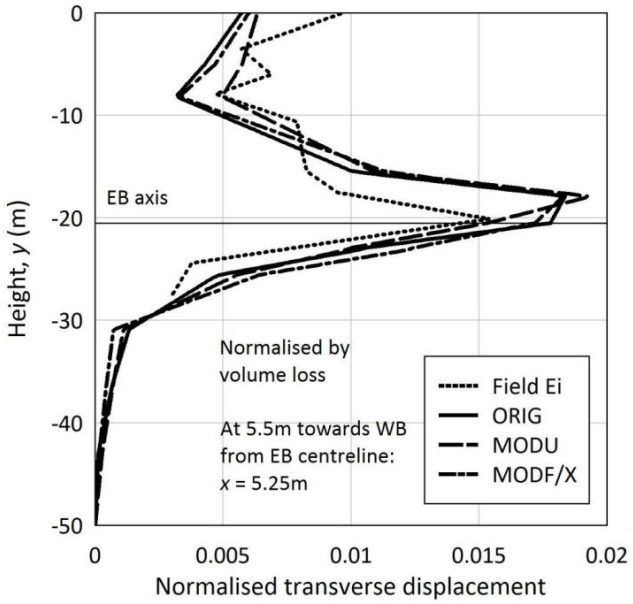

(b) Horizontal displacement profiles on near side of eastbound tunnel

Figure 7.26: Plots of displacement normalised by volume loss for stage ExcEB

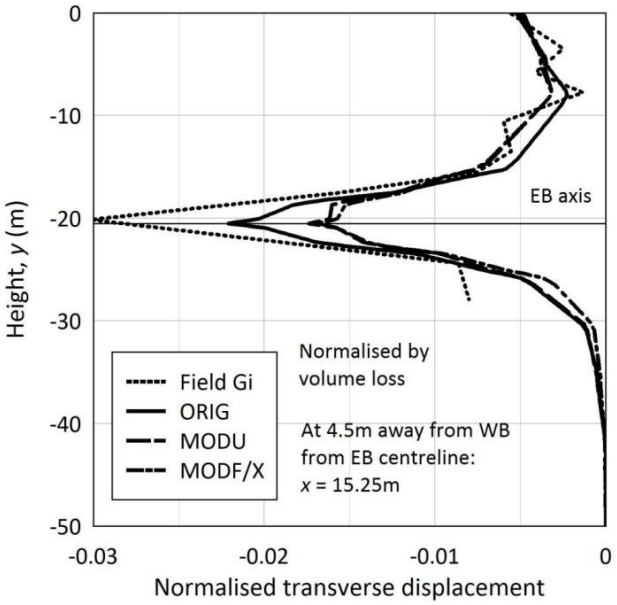

(c) Horizontal displacement profiles on remote side of east-bound tunnel

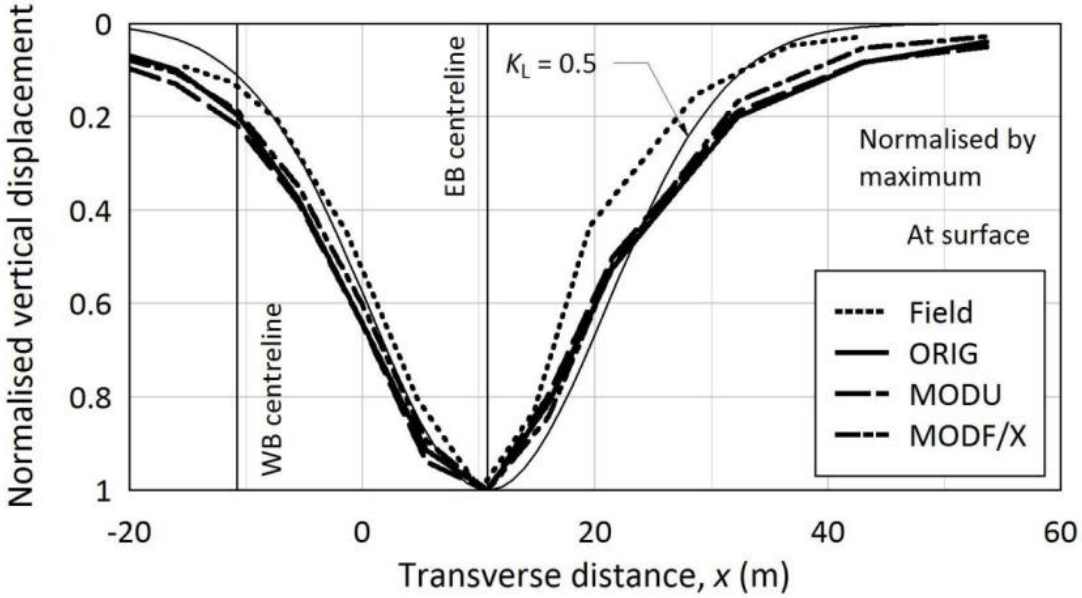

(d) Transverse surface settlement troughs

Figure 7.26: *cont...* Plots of displacement normalised by volume loss for stage ExcEB

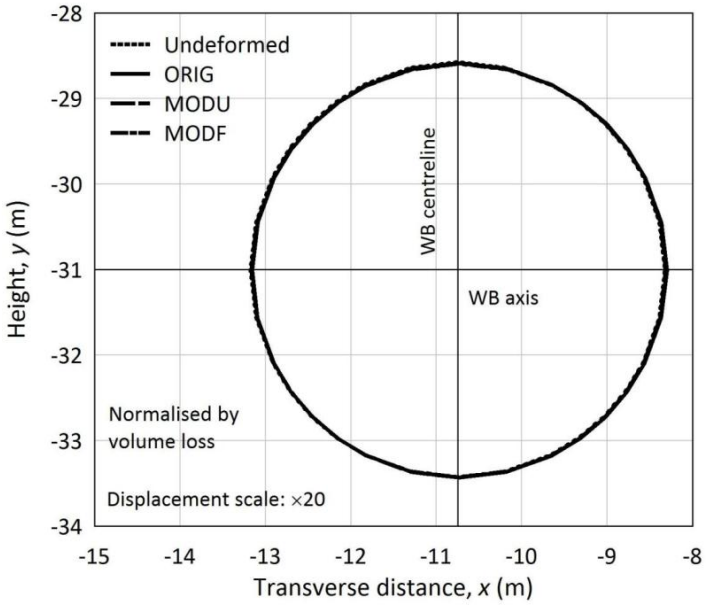

(e) Tunnel displacements for westbound tunnel

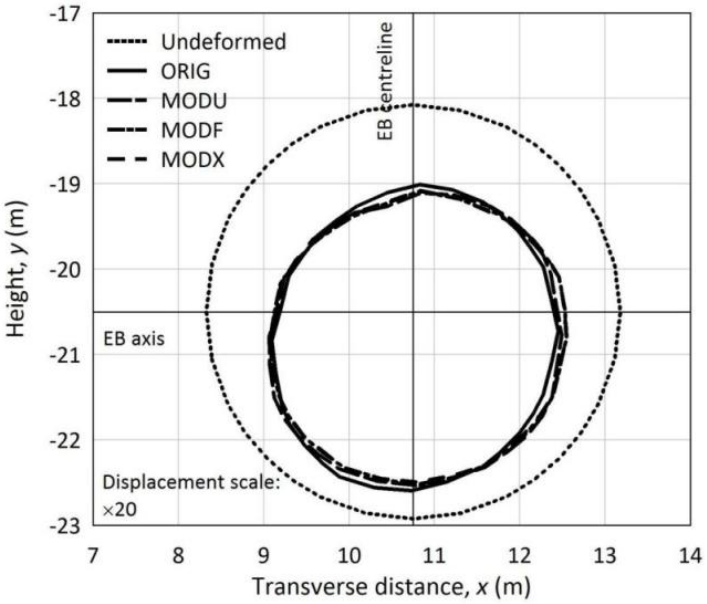

(f) Tunnel displacements for eastbound tunnel

Figure 7.26: *cont...* Plots of displacement normalised by volume loss for stage ExcEB

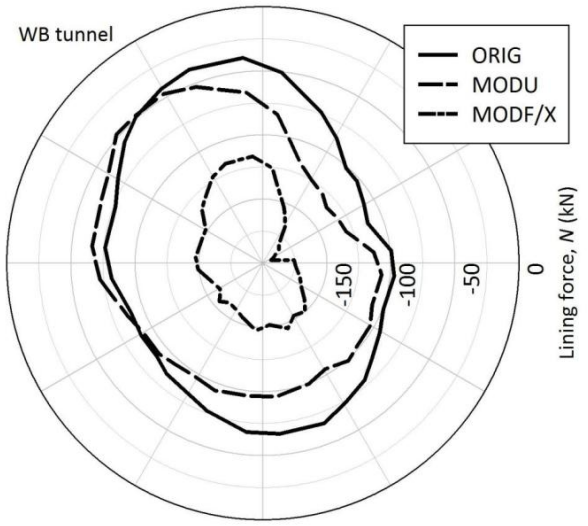

(a) Forces around westbound tunnel lining

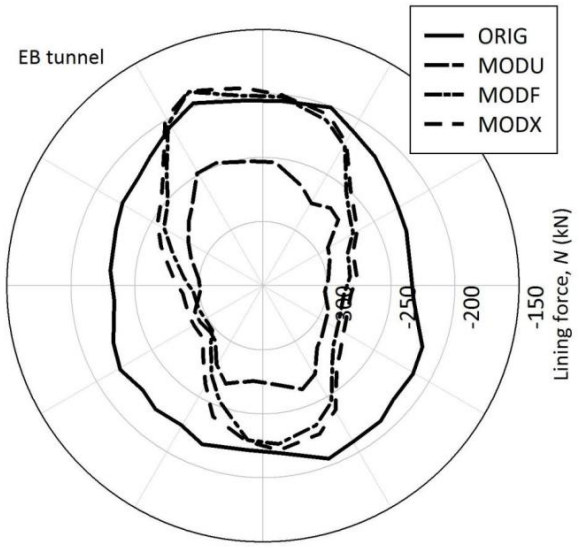

(b) Forces around eastbound tunnel lining

Figure 7.27: Distributions around lining of load contributed by stage ExcEB

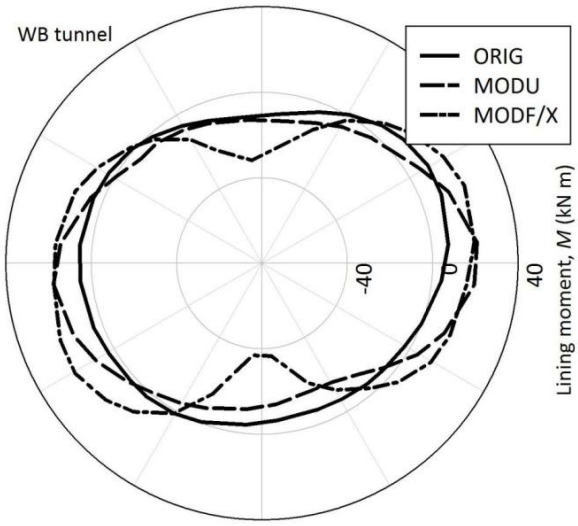

(c) Moments around westbound tunnel lining

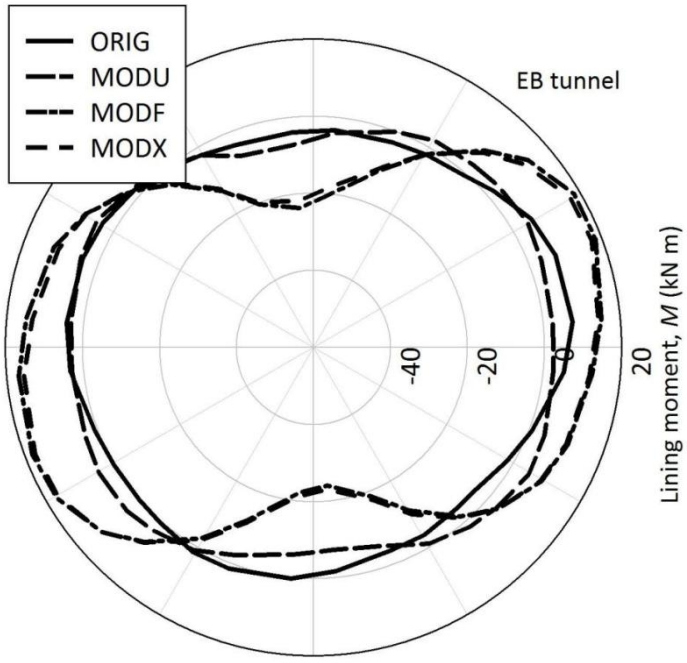

(d) Moments around eastbound tunnel lining

Figure 7.27: *cont...* Distributions around lining of load contributed by stage ExcEB

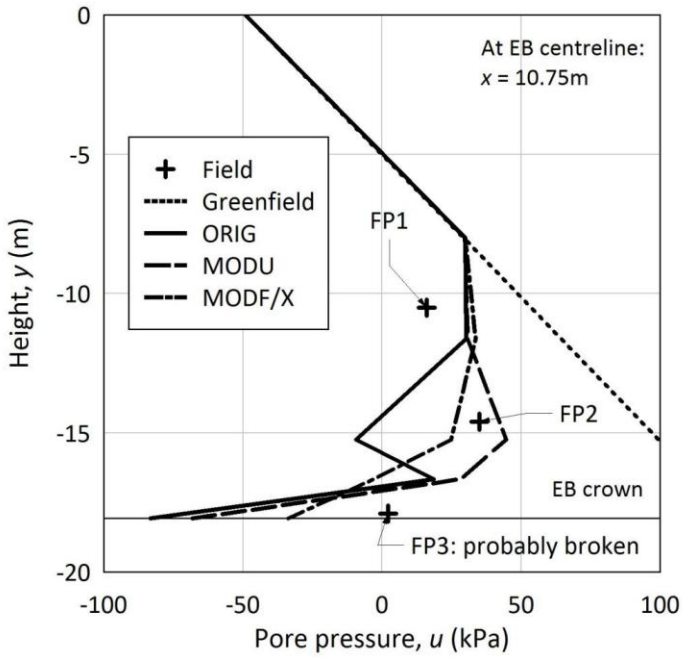

Figure 7.28: Pore pressure profiles along eastbound tunnel centreline for stage ExcEB

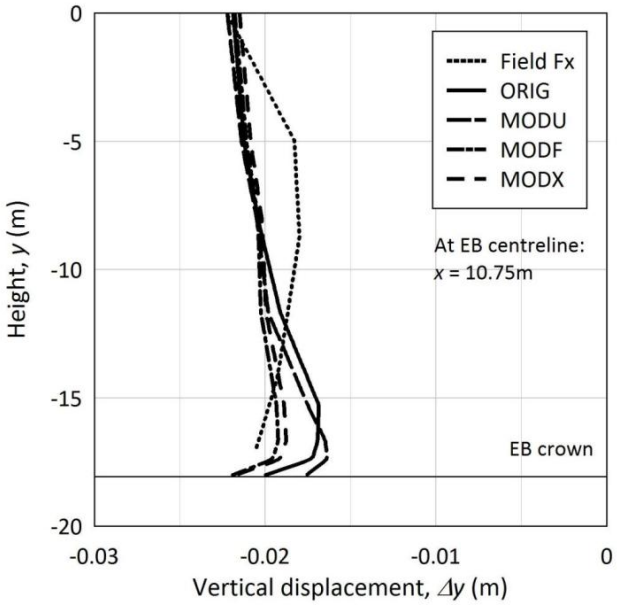

(a) Vertical displacement profiles above eastbound tunnel

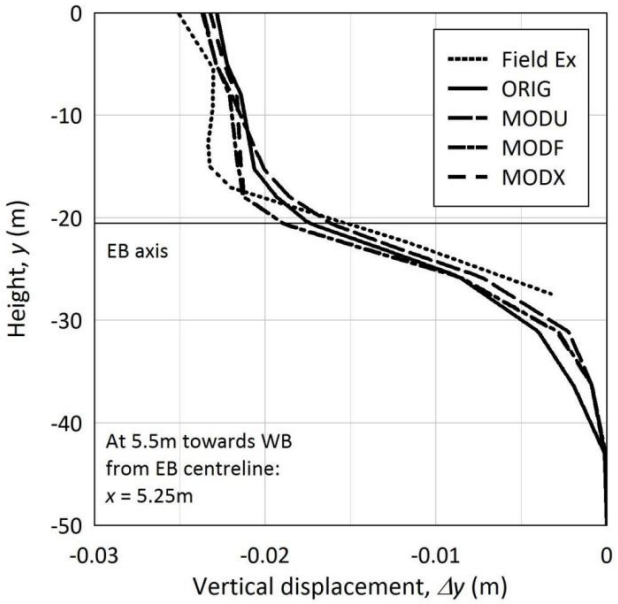

(b) Vertical displacement profiles on near side of eastbound tunnel

Figure 7.29: Displacement plots for stage CsLEB

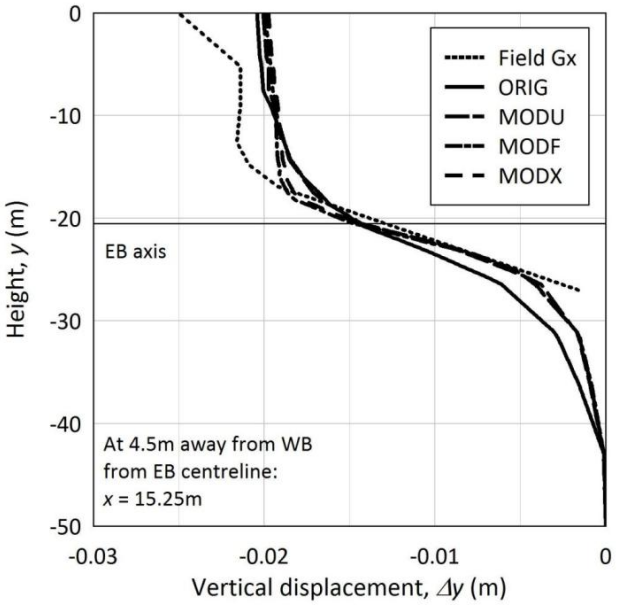

(c) Vertical displacement profiles on remote side of eastbound tunnel

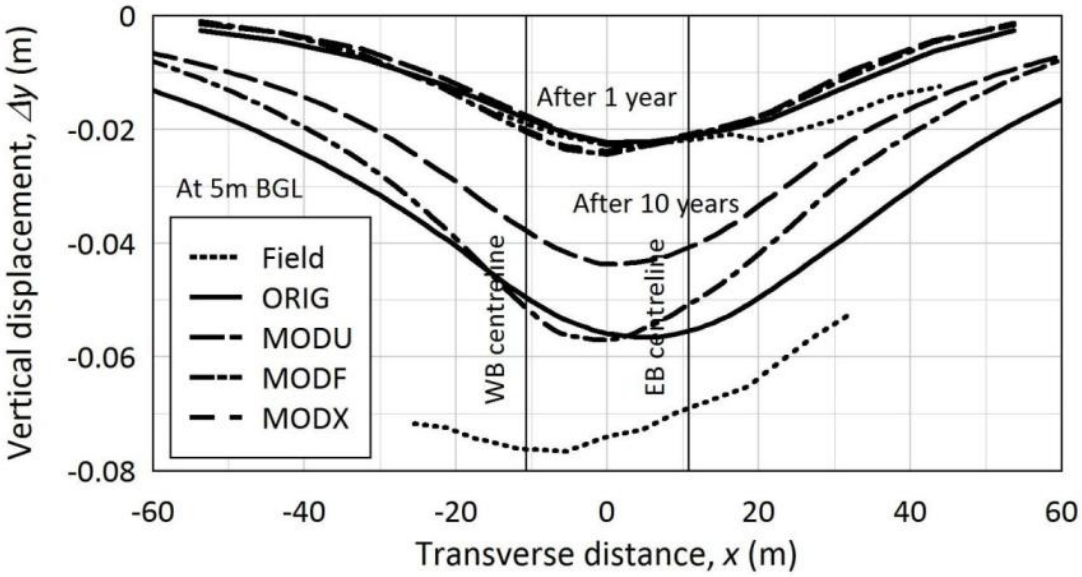

(d) Transverse settlement troughs at 5m depth

Figure 7.29: *cont...* Displacement plots for stage CslEB

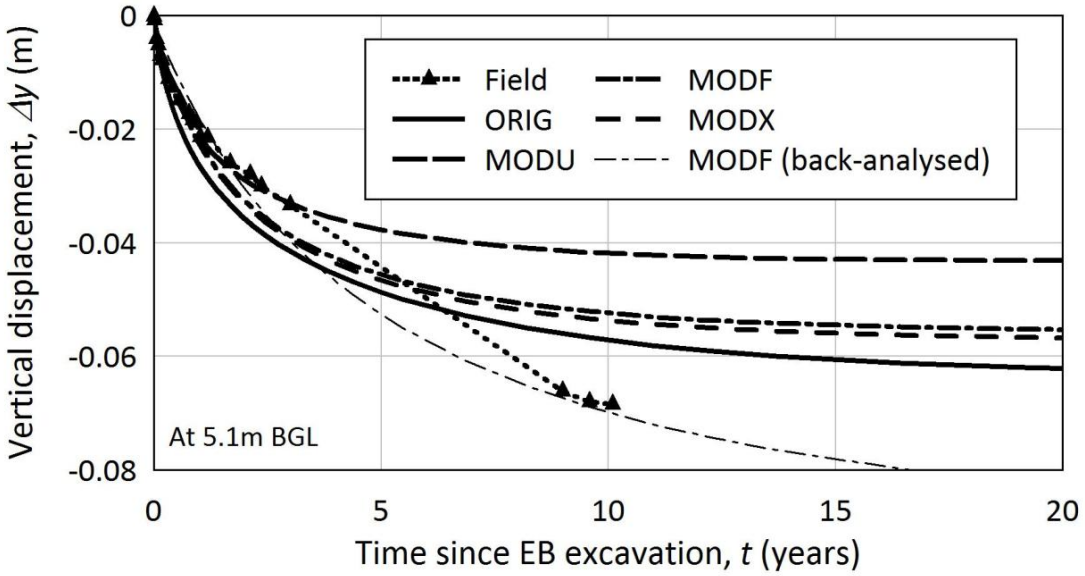

(e) Development of settlement above eastbound tunnel at 5.1m depth

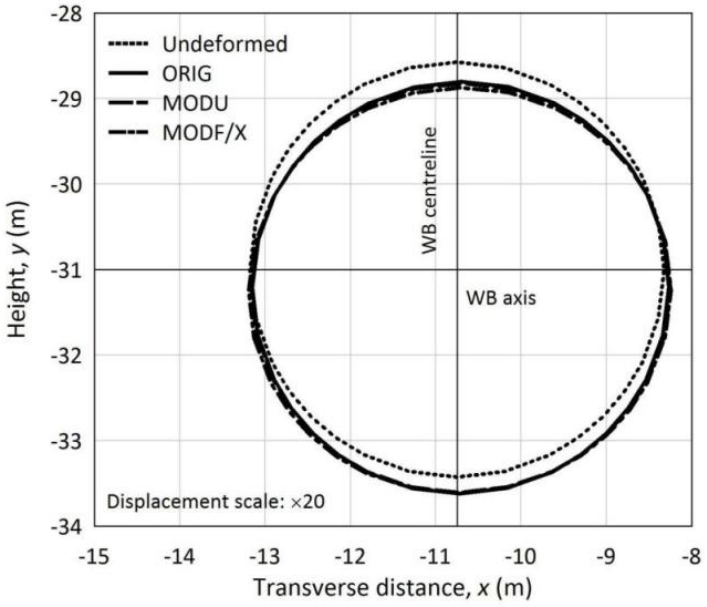

(f) Tunnel displacements for westbound tunnel

Figure 7.29: *cont...* Displacement plots for stage CslEB

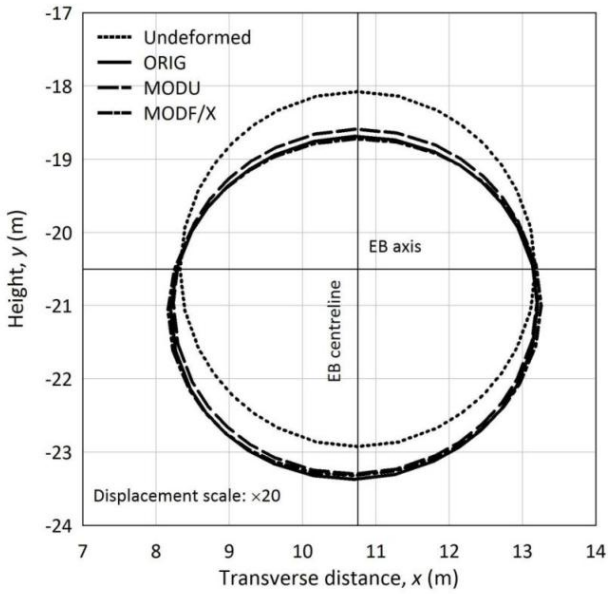

(g) Tunnel displacements for eastbound tunnel

Figure 7.29: *cont...* Displacement plots for stage CslEB

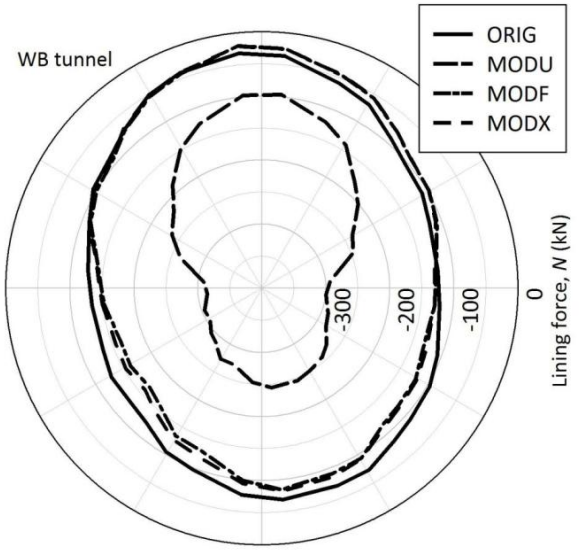

(a) Forces around westbound tunnel lining

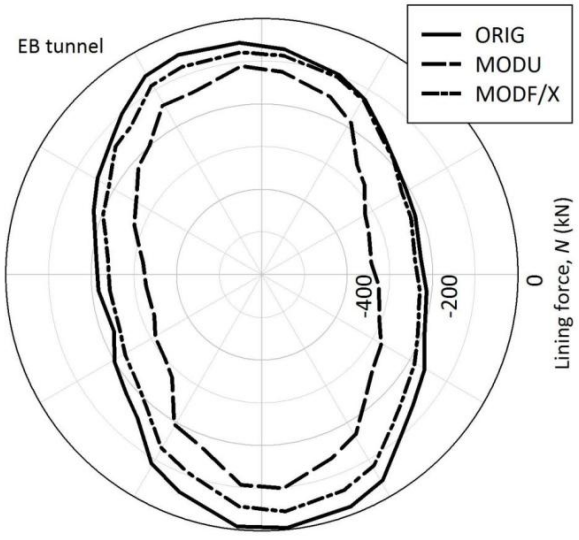

(b) Forces around eastbound tunnel lining

Figure 7.30: Distributions around lining of load contributed by stage CsLEB

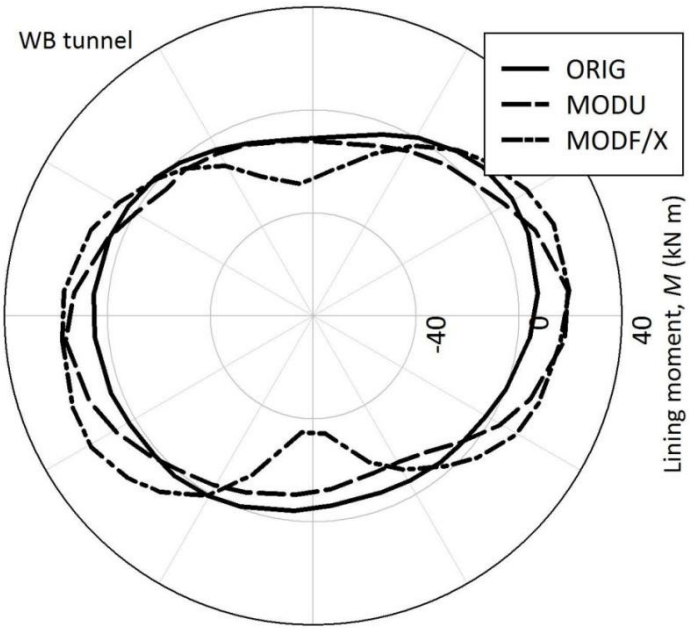

(c) Moments around westbound tunnel lining

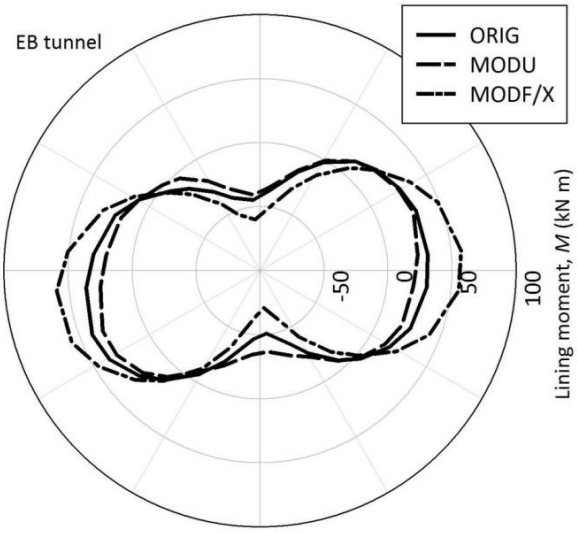

(d) Moments around eastbound tunnel lining

Figure 7.30: *cont...* Distributions around lining of load contributed by stage CslEB

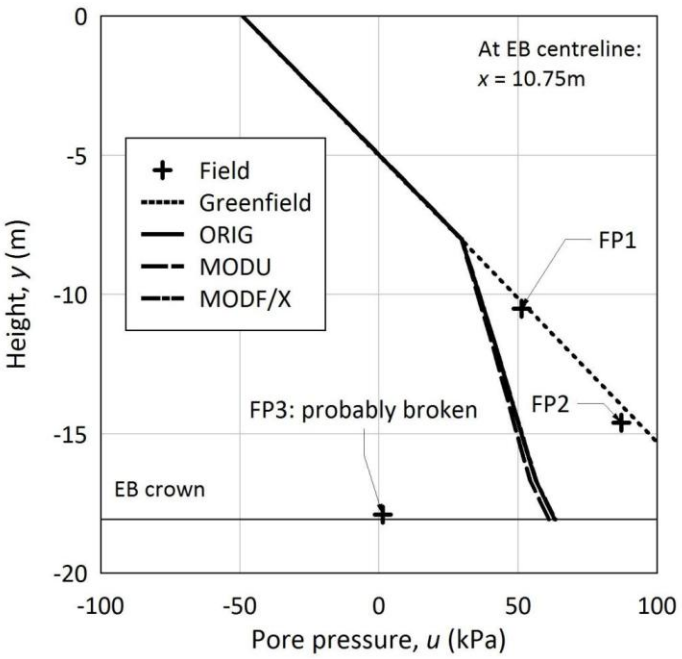

(a) Pore pressure profiles along eastbound tunnel centreline

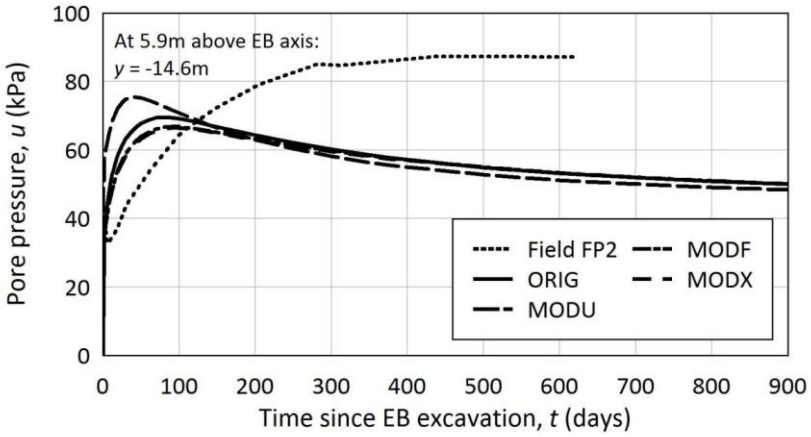

(b) Evolution of pore pressure above eastbound tunnel crown

Figure 7.31: Pore pressure plots for stage CsLEB

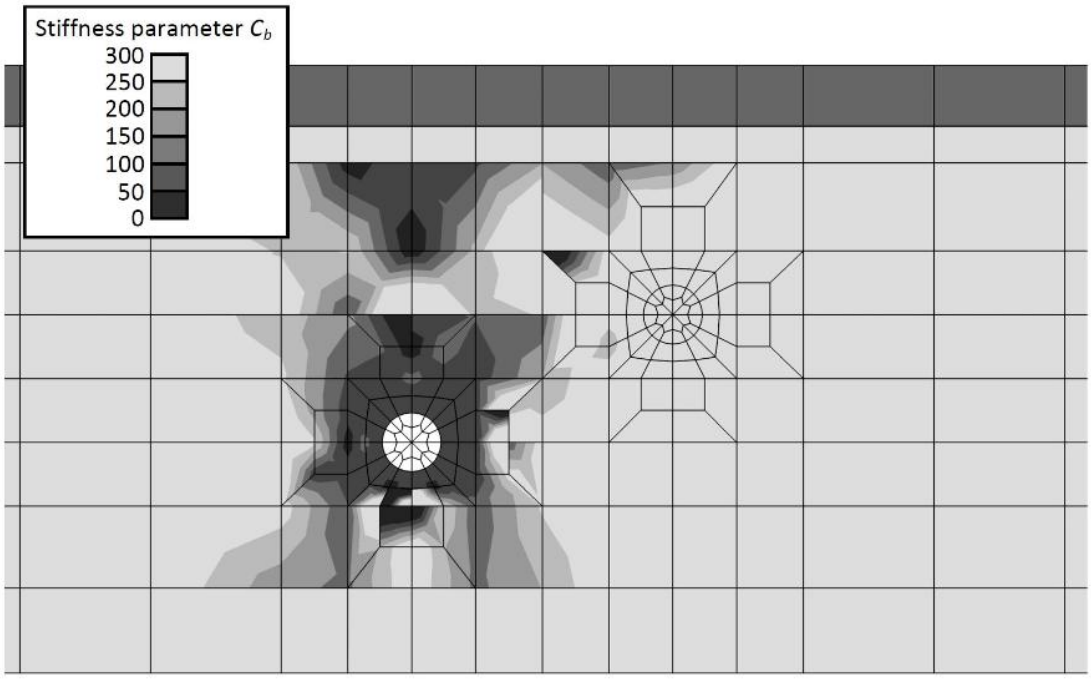

(a) For stage ExcWB

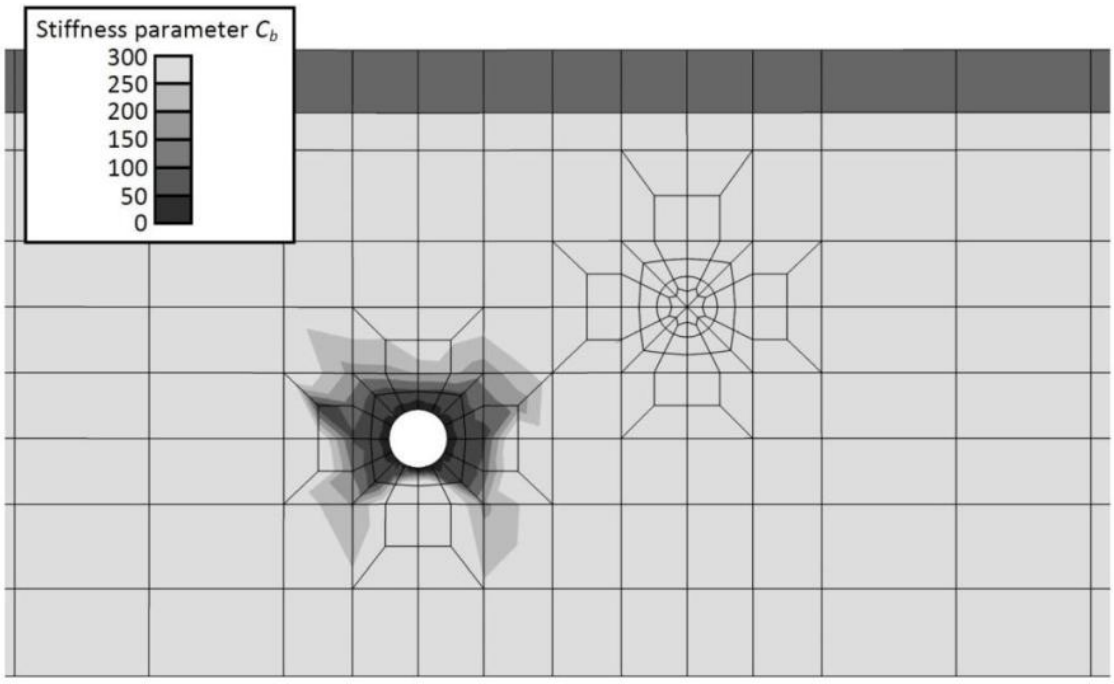

(b) For stage CslWB

Figure 7.32: Regions softened by fissures in analysis ModF

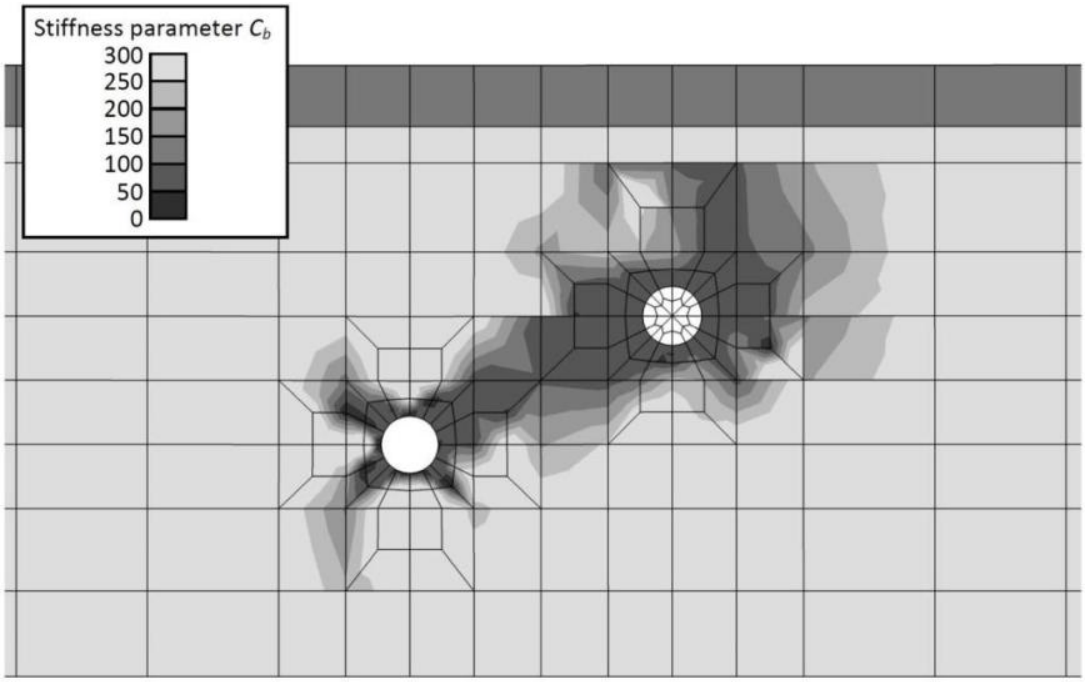

(c) For stage ExcEB

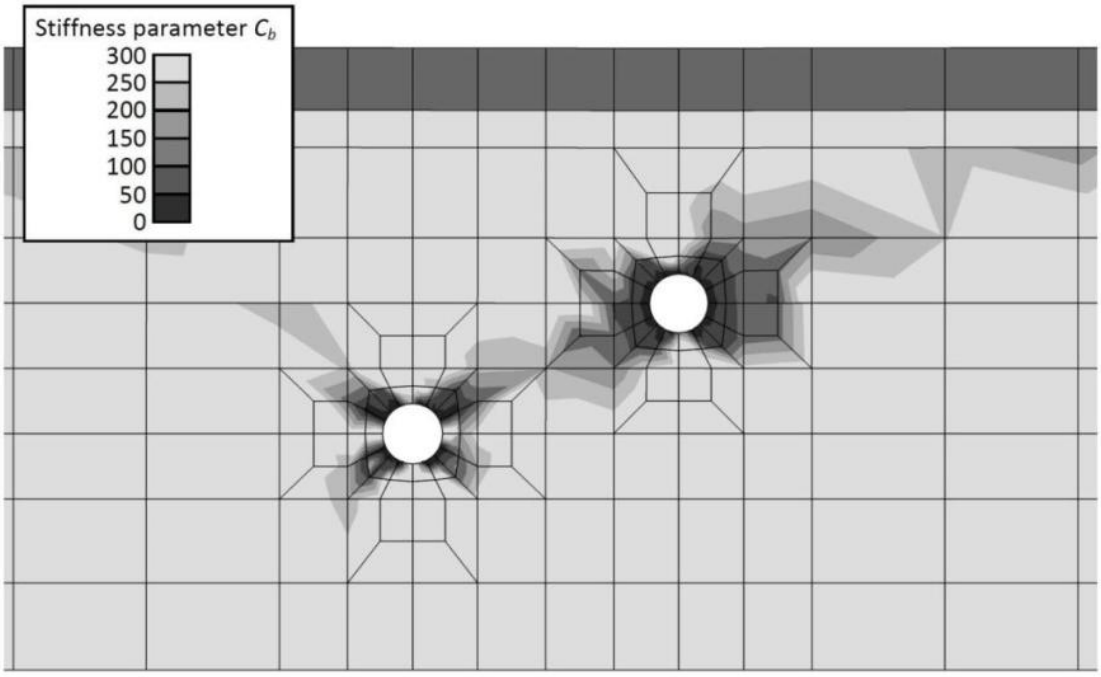

(d) For stage CslEB

Figure 7.32: *cont...* Regions softened by fissures in analysis ModF

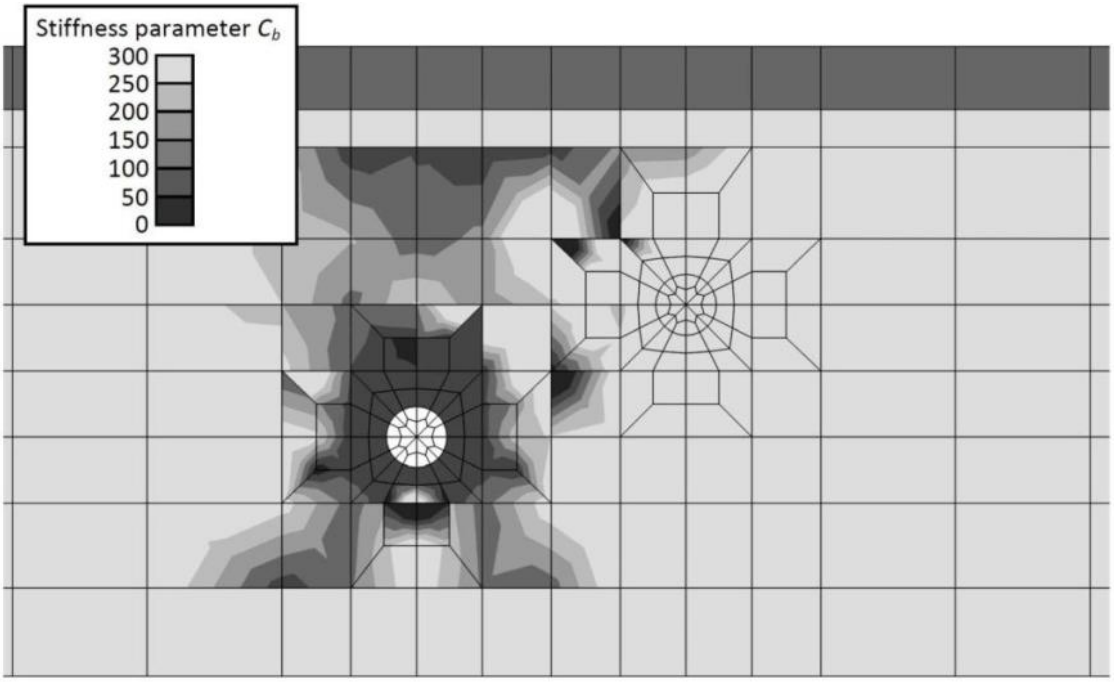

Figure 7.33: Regions softened by fissures in analysis ModX for stage ExcWB

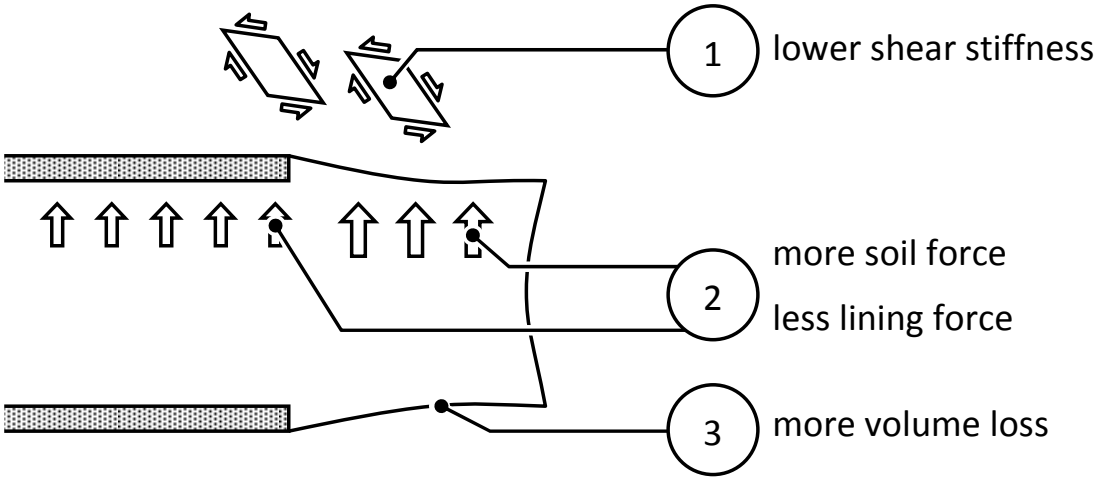

(a) For low stiffness

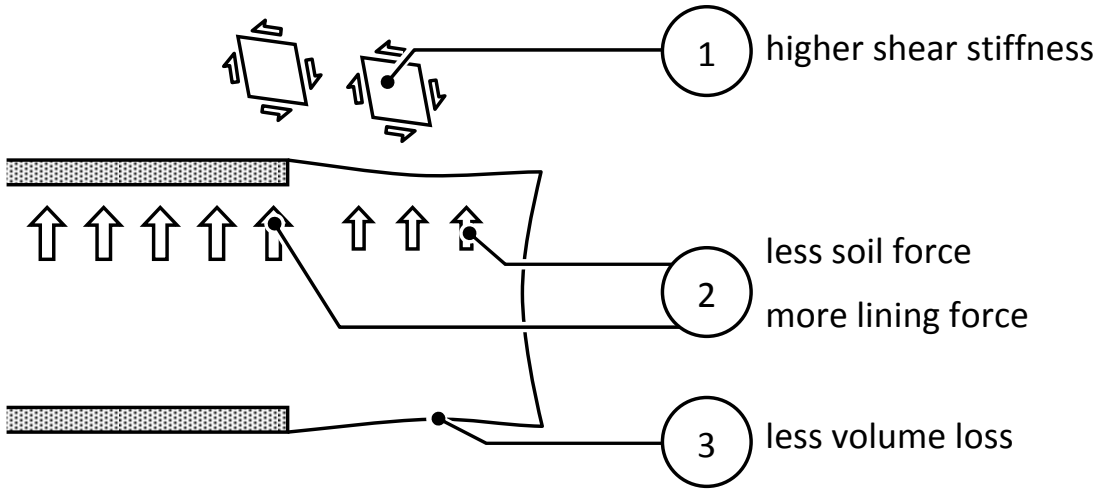

(b) For high stiffness

Figure 7.34: Influence of shear stiffness on volume loss and lining forces

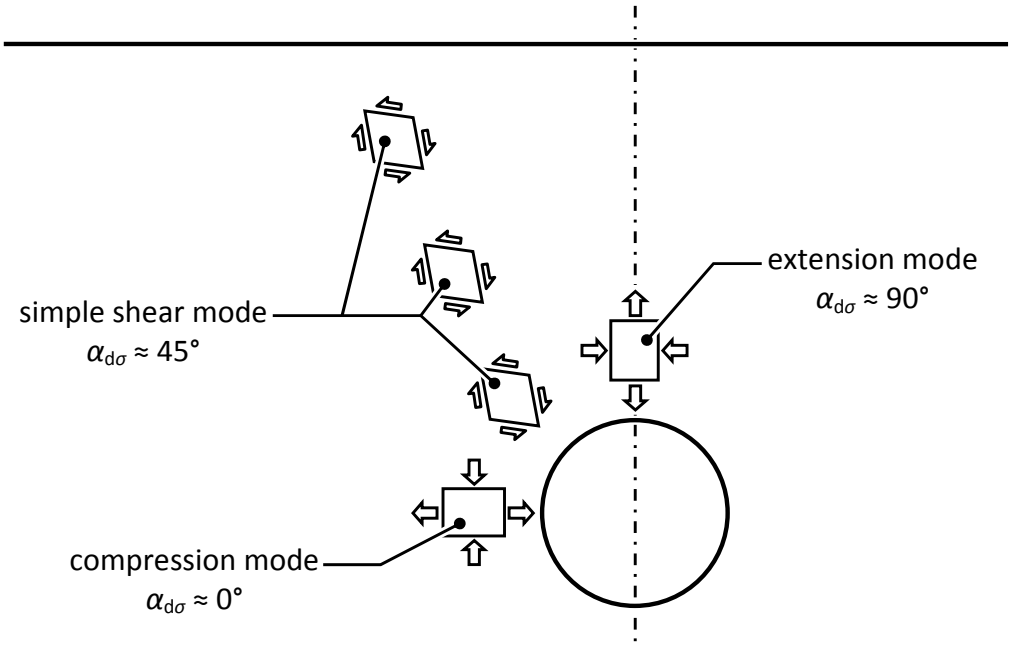

Figure 7.35: Modes of soil shearing during excavation

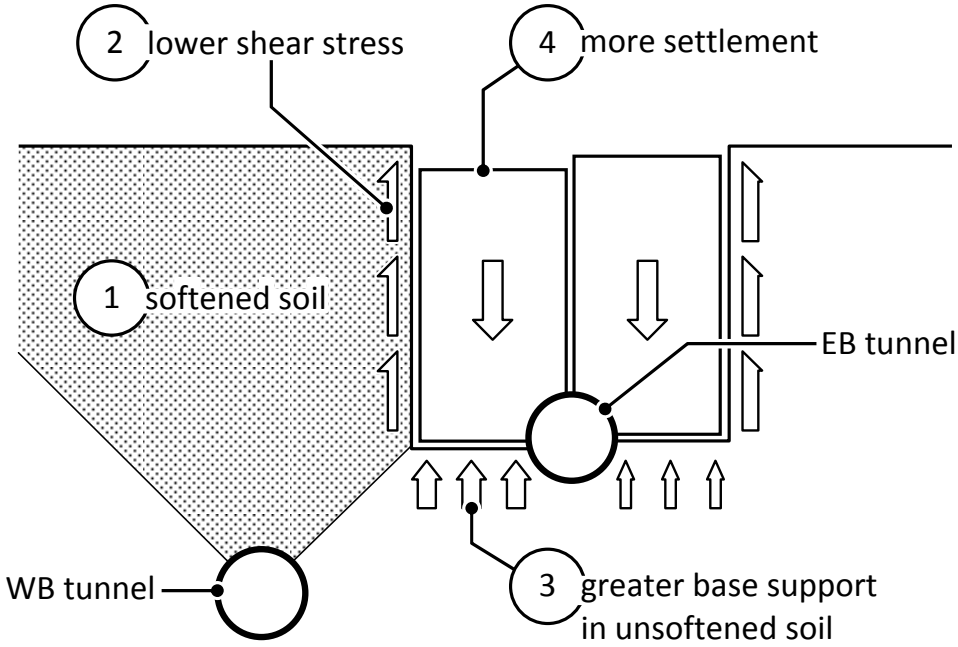

Figure 7.36: Model for asymmetrical behaviour during eastbound excavation

Chapter 8

Parametric study into single-tunnel long-term behaviour

8.1 Introduction

A parametric study was conducted to investigate factors influencing the long-term behaviour of a single tunnel. The study investigated the influence of cover-to-diameter ratio (C/D_{T}), volume loss and relative soil-lining permeability (RP).

Wongsaroj (2005) had conducted a similar study before, devising a method to predict long-term surface settlements above a single tunnel, based upon normalised charts. He also defined a relative soil-lining permeability to describe the dependence of ground movements upon permeabilities.

In this study, a new definition of relative soil-lining permeability was proposed, whilst other normalised parameters defined by Wongsaroj were also examined. The prediction method was made more comprehensive—to predict horizontal displacements as well. Simplified equations were also developed to use in place of Wongsaroj's normalised charts.

In addition, the single-tunnel analyses provided a baseline with which to identify the additional movements due to interaction in the twin-tunnel analyses, described in Chapter 9.

8.2 Method

A similar study was conducted by Wongsaroj (2005); many of the features of his analyses were adopted in these analyses because the reasoning behind them was sound and produced good results.

8.2.1 Description of meshes

Remeshing As with the St James's Park simulations, a remeshing technique was adopted to save computational time. This involved modelling excavation with a 3-D mesh to model arching at the tunnel heading, followed by modelling consolidation in a 2-D mesh; this is described in Sections 7.3.6 and 7.4.3.

Mesh geometry The single-tunnel analyses consisted of the excavation and consolidation stages for the first tunnel of the twin-tunnel analyses described in Chapter 9, so the meshes used were the same. Figure 8.1 illustrates the 3-D mesh geometries adopted for excavation; the 2-D meshes for modelling consolidation were constructed to have an identical element pattern as a transverse plane through the 3-D meshes. The mesh geometries differ in cover-to-diameter ratio (C/D_{T}) and separation-to-depth ratio (d'/z_0). Two C/D_{T} ratios were adopted: 3 and 7; and three different d'/z_0 ratios were also ran: 0.5, 2.0 and 4.5. However, for single-tunnel construction, the analyses with different d'/z_0 ratios were effectively the same, meaning that only two geometries were effectively modelled: $C/D_{\mathrm{T}} = 3$ and $C/D_{\mathrm{T}} = 7$. Time constraints limited the number of 3-D excavation analyses that could be performed, and hence the number of mesh geometries.

Quadratic element region Eight-node linear-strain soil elements were adopted, except for a region of 20-node quadratic-strain elements defined immediately around each tunnel to model variations in pore pressure and stress better. Quadratic-strain lining elements were also used. This technique was adopted in the simulations of St James's Park, described in Chapter 7. However, the region was enlarged for the parametric study—particularly above the tunnel—to ensure more realistic computation of variations close to the tunnel.

Mesh extents The width of each mesh was 600m, to locate the far-field boundaries sufficiently far away for boundary effects to be negligible; this width was verified as being suitable in Section 7.4.1. The total length of the 3-D model was $7.5z_0$, whilst the excavated length was $5.5z_0$, where z_0 is the axis depth; this was found by Wongsaroj (2005) to give a steady-state condition at the plane from which output data was extracted. This output plane was located $2.4z_0$ from the end of the model where excavation commenced, thus exceeding the minimum distance of $1.33z_0$ recommended by Wongsaroj for negligible boundary effects. To provide an idea of computational demands, the mesh with the most elements—CD7DZ45 (see Figure 8.1)—had $50,040$ elements, $88,947$ nodes and $345,096$ degrees of freedom. An excavation analysis typically required over one month to complete when using eight 2.66GHz parallel processors with 8GB of RAM. Processing of the input file required over 20GB of RAM, whilst mesh discretization typically took over 24 hours.

Excavation procedure Excavation proceeded by removing one element length of soil elements in one step, followed in the next step by activating a ring of lining elements in the same position. This was repeated to excavate the required length. The procedure is similar to that adopted in Figure 7.7, except with an unsupported length of one element (1.6m) instead of three elements long. The speed of excavation simulated the rate of advance at St James's Park, progressing at 1.6m per hour.

8.2.2 Selection of mesh parameters

Selection of C/D_T The C/D_T ratios of 3 and 7 were chosen to cover a wide range of tunnel geometries in London, as concluded by Wongsaroj (2005) after collating data on different tunnels in London. The two different C/D_T ratios were achieved by varying tunnel diameter, whilst adopting the same axis depth of 23m—Wongsaroj found this to be an average depth for tunnels in London Clay.

Selection of P/D_T The element length in the direction of excavation was chosen so that the volume loss obtained during excavation of the first tunnel was the

same for each C/D_T ratio. This was done to eliminate volume loss as an independent variable. Element length influences volume loss because it controls P/D_T, where P is the unsupported length; however, the relationship depends upon C/D_T. Suitable values of P/D_T were therefore selected by noting volume losses obtained by Wongsaroj for different C/D_T ratios. To reproduce a volume loss of approximately 2%, $P/D_T = 0.25$ and 0.5 for $C/D_T = 3$ and 7 respectively. This yielded $P \approx 1.6$m for both analyses, which was then adopted as the element length. A volume loss of 2% was estimated as being an approximate upper bound to open-face excavations in London Clay. In the end, volume losses of 2.26% and 2.34% were obtained for $C/D_T = 3$ and 7 respectively; giving an average of 2.3%.

Selection of lining thickness In addition to P/D_T ratio, lining thickness also depended upon C/D_T ratio. This was to maintain the same bending stiffness ratio, as defined by Duddeck & Erdman (1982). The procedure to select the lining thicknesses built upon that by Wongsaroj (2005) by using lining construction data from the London underground tunnels, as described in Appendix D. This led to lining thicknesses of 0.20m and 0.093m being selected for $C/D_T = 3$ and 7 respectively, to represent the bending stiffnesses of London underground linings with an equivalent uniform homogeneous concrete lining. The lining constitutive model for concrete was the same as that used in the St James's Park analyses: isotropic linear elastic stiffness with $E = 28$GPa and $\nu = 0.15$, and a concrete density of 2400kg m^{-3}.

8.2.3 Soil modelling

Profile and permeabilities The soil profile adopted is summarised below, along with permeabilities:

Soil stratum	Depth BGL (m)	k_v (m s^{-1})	k_h/k_v
Made Ground	0–5	10^{-7}	1
Terrace Gravel	5–8	5×10^{-4}	1
London Clay	8–50	2×10^{-11}	2

This profile was essentially the same as that used by Wongsaroj (2005) in his parametric study, putting the model depth at 50m. Being similar to that at St

James's Park, this soil profile was taken to be representative of a typical site in London. In the field, the permeability of London Clay would vary from site to site; evaluating the effect of such variation is beyond the scope of this study, so a homogeneous permeability was adopted for simplicity. Variations in the actual permeability of London Clay can be accommodated in the prediction method by adjusting RP. A permeability anisotropy ratio of 2 is often assumed for London Clay (Hight & Jardine, 1993; Wongsaroj, 2005), so this value was adopted as being representative of London Clay. The water table was modelled at 5m depth. The base of the model was defined as impermeable, giving a hydrostatic greenfield pore pressure profile.

Soil model The soil model described in Chapter 6—adapted from that developed by Wongsaroj (2005)—was used. Soil parameters applied to each stratum are summarised in Table 7.1. Soil model MODF was adopted for London Clay, since in Chapter 7, this model was deemed most realistic.

8.2.4 Consolidation analyses

Zero volume loss Consolidation analyses with zero volume loss during excavation were also executed, in addition to those with volume loss. This was achieved by commencing the consolidation analysis from a greenfield condition, with the tunnel wished-in-place. The zero volume loss analyses enabled the influence of volume loss to be observed.

Relative soil-lining permeabilities For the consolidation period, the lining was assigned a seepage coefficient K_{T}, as defined in Equation 7.2, allowing a range of relative soil-lining permeabilities (RP) to be explored. Twelve RP values were modelled by applying twelve values of K_{T}: 10^{-18}, 10^{-16}, 10^{-15}, 10^{-14}, 10^{-13}, 5×10^{-13}, 10^{-12}, 5×10^{-12}, 10^{-11}, 5×10^{-11}, 10^{-11}, 10^{-9} and 10^{-8}kN^{-1} m^3 s^{-1}; this covered the full range of RP, from fully impermeable to fully permeable. Such a large number of K_{T} values helped to more precisely define relationships depending upon RP. Although effectively only two excavation analyses were conducted

($C/D_{\mathrm{T}} = 3$ and 7), simulating the twelve values of K_{T} and modelling zero volume loss led to a total of 48 different consolidation analyses being conducted.

Execution The consolidation period was proceeded for 500, 000 days—equivalent to 1370 years—long enough to reach a steady-state condition.

8.3 New non-dimensional displacement

8.3.1 Previous definition

In his parametric study, Wongsaroj (2005) defined a non-dimensional measure for the maximum consolidation settlement of a transverse trough. This measure, NS_{cmax}, expressed settlement as a fraction of a theorised upper bound:

$$NS_{\mathrm{cmax}} = \frac{E'_{\mathrm{d}}}{C_{\mathrm{clay}} L_{\mathrm{c}} \gamma_{\mathrm{w}}} S_{\mathrm{cmax}} \tag{8.1}$$

where:

C_{clay}	is the clay cover
E'_{d}	is the equivalent drained 1-D elastic modulus
γ_{w}	is the bulk unit weight of water
L_{c}	is the tunnel axis depth below the water table
S_{cmax}	is the maximum consolidation settlement

8.3.2 Previous derivation

Pore pressure change Wongsaroj noted that consolidation settlements were driven by pore pressure changes. The maximum possible pore pressure change during consolidation would occur at axis depth. This would be roughly equal to $L_{\mathrm{c}}\gamma_{\mathrm{w}}$ with a permeable lining and with no negative excess pore pressure generated during excavation.

Consolidating layer Wongsaroj assumed that all consolidation occurred above the tunnel crown, in a layer of thickness C_{clay}. He defined the equivalent stiffness E'_{d} as the drained secant stiffness for 1-D consolidation of London Clay at 0.15% strain. This was to be taken at a depth of $\frac{1}{2}C_{\text{clay}}$ above the tunnel crown to be representative of the consolidating clay layer. A strain of 0.15% was chosen because this was the average vertical strain in the layer observed at the steady-state condition in simulations with a fully permeable lining and a volume loss of 1.5–2.0%.

8.3.3 New definition

Proposed formulation For this parametric study, a new non-dimensional parameter was proposed:

$$NS_{\text{cmax}} = \frac{E'_{\text{d}}}{5D_{\text{T}}L_{\text{c}}\gamma_{\text{w}}}S_{\text{cmax}} \tag{8.2}$$

where D_{T} is the tunnel diameter. This differs from Wongsaroj's formulation in two ways:

1. Firstly, the consolidating layer is taken to lie between $\pm 2.5D_{\text{T}}$ from axis depth. This is shown in Figure 8.2 for $C/D_{\text{T}} = 3$ and 7, with a fully permeable lining; here, 70–90% of consolidation occurs within this region. Previous studies also confirm this observation, as presented in Section 2.2.2. The thickness of the consolidating layer is therefore taken as $5D_{\text{T}}$ instead of C_{clay}.

2. Secondly, the definition of equivalent stiffness E'_{d} differs. Since the consolidating layer is centred about axis depth, E'_{d} is taken at axis depth instead of at $\frac{1}{2}C_{\text{clay}}$ above the tunnel crown. E'_{d} is taken at 0.08% strain, being the average vertical strain across this layer derived from settlements shown in Figure 8.2.

Horizontal displacement Horizontal displacement was non-dimensionalised in the same way, such that:

$$NH_{\text{cmax}} = \frac{E'_{\text{d}}}{5D_{\text{T}}L_{\text{c}}\gamma_{\text{w}}}H_{\text{cmax}} \tag{8.3}$$

where H_{cmax} is the maximum horizontal displacement, and NH_{cmax} its non-dimensional counterpart.

8.3.4 Deriving equivalent stiffness

In laboratory The equivalent stiffness should ideally be found from a consolidated drained (CD) triaxial compression test with zero radial strain (Wongsaroj, 2005); however, these are difficult to perform routinely. Wongsaroj therefore suggested two other methods for finding E'_{d}:

1. From a conventional CD compression test; he found little difference between E'_{d} for this test and if zero radial strain was imposed.

2. From a consolidated undrained (CU) compression test, using the equation:

$$E'_{\mathrm{d}} = \frac{2}{3}(1+\nu_{vh})E_{\mathrm{u\,sec}} \tag{8.4}$$

   where $E_{\mathrm{u\,sec}}$ is the undrained secant stiffness at the required strain, with $\nu_{vh} = 0.07$.

For parametric study For this parametric study, E'_{d} was found by simulating an oedometer test with $K_0 = 1.2$ initially. The test was executed on soil in the in-situ condition at the axis depth of 23m, giving $E'_{\mathrm{d}} = 86.8$MPa at 0.08% strain. It should be noted however that in the laboratory, an oedometer test is unsuitable for deriving E'_{d} because K_0 is likely to change during set-up.

8.4 New relative soil-lining permeability

8.4.1 Previous definition

Wongsaroj (2005) proposed a measure of relative soil-lining permeability (RP), which governs many aspects of consolidation behaviour. To derive an expression for RP, Wongsaroj assumed one-dimensional flow of water downward into the lining from the ground surface, as illustrated in Figure 8.3. The figure also shows

hydraulic head at key locations, relative to the intrados of the lining crown as a datum.

His model considered a water table located above the clay in a layer which was much more permeable. Applying Darcy's law, he equated flow through the soil to flow through the lining:

$$k_{\mathrm{S}} \frac{L_{\mathrm{c}}\gamma_{\mathrm{w}} - u_{\mathrm{T}}}{C_{\mathrm{clay}}\gamma_{\mathrm{w}}} = k_{\mathrm{T}} \frac{u_{\mathrm{T}} - 0}{\gamma_{\mathrm{w}} t_{\mathrm{T}}} \tag{8.5}$$

He then defined RP in the following way:

$$\frac{u_{\mathrm{T}}}{L_{\mathrm{c}}\gamma_{\mathrm{w}}} = \frac{1}{1 + RP} \tag{8.6}$$

with:

$$RP = \frac{C_{\mathrm{clay}} k_{\mathrm{T}}}{k_{\mathrm{S}} t_{\mathrm{T}}} = \frac{C_{\mathrm{clay}}\gamma_{\mathrm{w}} K_{\mathrm{T}}}{k_{\mathrm{S}}} \tag{8.7}$$

where:

C_{clay}	is the clay cover
γ_{w}	is the bulk unit weight of water
k_{T}	is the lining permeability
k_{S}	is the equivalent soil permeability: $\sqrt{k_{\mathrm{h}} k_{\mathrm{v}}}$
K_{T}	is the lining seepage coefficient: $\dfrac{k_{\mathrm{T}}}{\gamma_{\mathrm{w}} t_{\mathrm{T}}}$
L_{c}	is the tunnel axis depth below the water table
t_{T}	is the lining thickness
u_{T}	is the pore pressure at the lining extrados

8.4.2 New definition

Radial flow In practice, flow into the tunnel is not one-dimensional. Figure 8.3 gives an example of actual flow in the field; a better idealisation of this might be radial flow into the tunnel, which the figure also illustrates—this is the basis of the new definition of RP. For simplicity, the effects of permeability anisotropy are ignored, and the radial flow is assumed to be uniform around the tunnel.

Derivation The new expression for RP is derived by equating the volumetric flow rate through the soil per unit tunnel length (q_S) with that through the lining (q_T). To derive q_S, we consider an annular element at radius r from the tunnel, with thickness dr. The flow velocity $v(r)$ through this element is given by Darcy's law:

$$v(r) = \frac{q_S}{2\pi r} = k_S \frac{d\bar{h}}{dr} \tag{8.8}$$

where $d\bar{h}$ is the head difference across the element. This equation can be integrated to give q_S; the boundary conditions can be derived from Figure 8.3. At the lining extrados, $\bar{h} = u_T$ at $r = \frac{1}{2}D_T$. To apply the far-field boundary condition, a radius of drawdown is assumed at $r = C_{clay} + \frac{1}{2}D_T$; thus here, $\bar{h} \approx L_c$. The final expression for q_S is then:

$$q_S = \frac{2\pi k_S \left(L_c \gamma_w - u_T\right)}{\gamma_w \ln\left(\frac{2C_{clay}}{D_T} + 1\right)} \tag{8.9}$$

Lining flow per unit length q_T is also found from Darcy's law:

$$q_T = \pi D_T k_T \frac{u_T - 0}{\gamma_w t_T} \tag{8.10}$$

The two flows can be equated ($q_S = q_T$) and rearranged in the form of Equation 8.6 to find RP, as given below:

$$RP = \frac{D_T K_T \gamma_w}{2k_S} \ln\left(\frac{2C_{clay}}{D_T} + 1\right) \tag{8.11}$$

S-shaped curve Wongsaroj (2005) noted a distinctive S-shaped curve when plotting dimensionless settlement (DS) against $\log RP$, where DS is given by:

$$DS = \frac{NS_{cmax(ss)} - NS_{cmax(ssi)}}{NS_{cmax(ssp)} - NS_{cmax(ssi)}} \tag{8.12}$$

$NS_{cmax(ss)}$ is the non-dimensional steady-state settlement, $NS_{cmax(ssi)}$ is $NS_{cmax(ss)}$ for an impermeable lining, whilst $NS_{cmax(ssp)}$ is the same for a permeable lining. DS thus defines the settlement relative to the extremes of permeability behaviour.

Figure 8.4 plots the S-shaped curve for data obtained from this parametric study; compared on the figure are the old and new definitions of RP. Data points adopting the new definition fall within a tighter band; the figure shows an equation closely fitting the data.

Variation with time Chapters 4 and 5 discovered that both soil and lining permeability can change by over two orders of magnitude during the course of time, potentially changing the flow regime from fully impermeable to fully permeable, and causing RP to vary with time. It might therefore be conservative to assume a fully permeable lining when predicting displacements, since this yields the most severe movements.

8.5 New prediction method

8.5.1 Previous method

As a result of his parametric study, Wongsaroj (2005) devised a prediction method referencing normalised charts. He produced four charts, charts A–D, which are presented in Figure 8.5.

Description Chart B plots the familiar S-shaped relationship enabling DS to be found from RP, where RP is given by Equation 8.7. Chart A predicts values of $NS_{\text{cmax(ssi)}}$ and $NS_{\text{cmax(ssp)}}$. With DS derived from chart B, Equation 8.12 can then be used to obtain $NS_{\text{cmax(ss)}}$. This non-dimensional settlement is converted to actual settlement through Equation 8.1. Since this settlement is given at the steady-state condition, chart C is used to find the settlement incurred within the consolidation time of interest. In this chart, relative settlement RS_{cmax} is given by:

$$RS_{\text{cmax}} = \begin{cases} -\dfrac{S_{\text{cmax}}}{S_{\text{cmax(ss)}}} & \text{for} \quad S_{\text{cmax(ss)}} < 0 \\ \dfrac{S_{\text{cmax}}}{S_{\text{cmax(ss)}}} & \text{for} \quad S_{\text{cmax(ss)}} > 0 \end{cases} \tag{8.13}$$

whilst the dimensionless time factor T_{v} is given by:

$$T_{\text{v}} = \frac{E'_{\text{d}} k_{\text{S}} t}{{C_{\text{clay}}}^2 \gamma_{\text{w}}} \tag{8.14}$$

Chart C therefore yields S_{cmax}, the maximum settlement in the transverse trough.

Chart D then enables the trough shape to be evaluated. To describe trough shape, Wongsaroj adopts the modified Gaussian curve suggested by Vorster *et al.*

(2005):

$$S_{\mathrm{c}} = \frac{b_{\mathrm{mg}}}{(b_{\mathrm{mg}} - 1) + \exp\left[\mu \left(\dfrac{x}{K_{\mathrm{L}} z_0}\right)^2\right]} \cdot S_{\mathrm{cmax}} \tag{8.15}$$

where:

$$b_{\mathrm{mg}} = e^{\mu} \frac{2\mu - 1}{2\mu + 1} + 1 \tag{8.16}$$

Chart D provides values of K_{L} and μ in two ways:

1. **Partial numerical approach** Here, K_{L} and μ are provided for the incremental settlements caused by consolidation alone. The trough can then be added to the short-term trough to give net settlements.

2. **Total numerical approach** Here, K_{L} and μ are provided for net settlements accumulated during both excavation and consolidation.

Wongsaroj's method therefore provides prediction of the transverse settlement trough at any time during consolidation, depending upon C/D_{T} ratio, volume loss, $k_{\mathrm{h}}/k_{\mathrm{v}}$, RP and T_{v}.

8.5.2 New method: introduction

Contribution The new prediction method proposed by this parametric study sought to improve Wongsaroj's prediction method in two ways:

1. By providing a set of equations for prediction in place of normalised charts, to facilitate calculation.

2. By predicting horizontal as well as vertical displacements. Horizontal displacements, in particular, strains, are crucial to building damage (Mair & Taylor, 1997), yet a method to predict long-term horizontal displacements has not been investigated to-date.

The method also predicts horizontal strains, because it was found that horizontal strains derived from the horizontal displacement predictions might be underestimated. However, only predictions of peak strains—rather than the distribution

shape—were provided. Two peaks were predicted: $\varepsilon^{\mathrm{c}}_{\mathrm{cmax(ss)}}$ for steady-state centreline strain, and $\varepsilon^{\mathrm{f}}_{\mathrm{cmax(ss)}}$ for steady-state far-field strain, because peak horizontal strain at the centreline is opposite in sign to that in the far-field; observations show that peak strain in the far-field occurs at $1.6z_0$ from the centreline.

Description The new prediction method is presented in Figure 8.6, in seven stages:

1. Dimensionless settlement DS is first found from RP; this can be calculated from knowledge of soil and lining permeabilities, and tunnel geometry. DS determines where the displacement behaviour lies between the two extremes—fully impermeable and fully permeable linings.

2. Non-dimensional steady-state displacements are then found for the two extremes. Strains at the two extremes can also be found; the strains found are actual strains, since strains are already non-dimensional.

3. DS is used in conjunction with the values at the two extremes of permeability behaviour to find the behaviour for the particular permeability conditions in the field.

4. Non-dimensional displacements are then converted to actual field displacements: the maximum values at steady-state. Being non-dimensional by nature, strains need not be converted.

5. The steady-state movements evaluated thus far must be scaled to derive movement at the consolidation time of interest. To do this, relative displacement RS_{cmax} is found. This is defined differently to that by Wongsaroj (2005) in Equation 8.13; here:

$$RS_{\mathrm{cmax}} = \frac{S_{\mathrm{cmax}}}{S_{\mathrm{cmax(ss)}}} \tag{8.17}$$

   To evaluate RS_{cmax}, the dimensionless time factor must be calculated, along with the two parameters A_{RS} and B_{RS}.

6. RS_{cmax} then scales the steady-state maximum displacement or strain to find the value at the consolidation time of interest.

7. The maximum displacement is used to define the transverse distribution, along with shape parameters, which must also be derived. Some of these parameters have physical significance: the inflexion points of the settlement trough are $K_{\mathrm{L}} z_0$ from the centreline, whilst the peak horizontal displacements are located at a distance a_{hd} from the centreline. A distribution is not evaluated for horizontal strains.

8.5.3 New method: derivation

Relating *RP* and *DS*

The new definition for RP was adopted in the prediction method, given in Equation 8.11. The relationship between DS and RP was found by plotting data from all analyses and finding a best fit; this is illustrated in Figure 8.4. This relationship is significantly simpler than the cumulative distribution function fitted by Wongsaroj (2005) in Figure 8.5b.

Displacements at permeability extremes

The new non-dimensionalisation of settlement—given in Equation 8.2—was adopted, and applied to horizontal displacement as well (Equation 8.3).

Figure 8.7 shows the plots used to derive relationships for behaviour at the two extremes of relative soil-lining permeability. This was done for non-dimensional steady-state settlement ($NS_{\mathrm{cmax(ss)}}$) and horizontal displacement ($NH_{\mathrm{cmax(ss)}}$), and for the steady-state horizontal strains at the centreline ($\varepsilon^{\mathrm{c}}_{\mathrm{cmax(ss)}}$) and the maximum in the far-field ($\varepsilon^{\mathrm{f}}_{\mathrm{cmax(ss)}}$).

Permeable: C/D_{T} dependence For a fully permeable lining, the non-dimensional displacement or strain varies with C/D_{T}, but is relatively insensitive to volume loss; this is because movements due to tunnel drainage dominate over those due to excess pore pressure dissipation. A deeper drain—at a greater C/D_{T} ratio—would broaden the region of drawdown, resulting in greater consolidation movements. A linear relationship was assumed with C/D_{T}, based upon results from Wongsaroj (2005), who simulated an intermediate C/D_{T} ratio of 5.

Impermeable: volume loss dependence In contrast to the fully permeable lining, behaviour for a fully impermeable one is dependent upon volume loss, but varies comparatively little with C/D_{T}. For such a lining, dissipation of excess pore pressure determines consolidation movements, which in turn depends upon the volume loss incurred during excavation. Dissipation is localised to a region around the tunnel, so there is less influence from the tunnel geometry, i.e. C/D_{T}.

As expected, an impermeable lining without any short-term volume loss experiences no consolidation movement at all. There is neither drainage into the tunnel nor any excess pore pressures.

Time dependence

Dimensionless time factor Wongsaroj (2005) defined a dimensionless time factor (T_{v}), given in Equation 3.17. However, the factor is clearly not applicable to both permeable and impermeable linings. The equation assumes a drainage distance C_{clay}; however, drainage conditions for permeable and impermeable linings are different, so a single drainage distance cannot represent both. This is exemplified when RS_{cmax} is plotted against T_{v}—as shown in Figure 8.8 for selected simulation results— showing that drainage is slower for an impermeable lining. Finding a suitable drainage distance was complicated, so instead, attempts were made to fit simulation results plotted with Wongsaroj's existing definition of T_{v}.

Parabolic isochrones One estimation to fit results used parabolic isochrone theory, modelling the soil as a straight column with drainage boundaries at top and bottom. Parabolic excess pore pressure isochrones were assumed. The resulting solution comprised two stages:

$$RS_{\mathrm{cmax}} = \begin{cases} \sqrt{\dfrac{4T_{\mathrm{v}}}{3}} & \text{for} \quad T_{\mathrm{v}} < \frac{1}{12} \\ 1 - \frac{2}{3}\exp\left(\frac{1}{4} - 3T_{\mathrm{v}}\right) & \text{for} \quad T_{\mathrm{v}} > \frac{1}{12} \end{cases} \tag{8.18}$$

Figure 8.8 shows that parabolic isochrone theory overestimated the rate of settlement, in particular, during the first stage, when $T_{\mathrm{v}} < \frac{1}{12}$.

Analytical solution An analytical solution for time-dependent tunnel drainage has also been developed by Li & Flores-Berrones (2002). This is also shown in the figure; despite the good fit, the analytical solution cannot be expressed explicitly, so a new expression was sought.

New approximation Noting that the second stage of Equation 8.18 fitted the later times well, a new best-fit curve was developed from this. The equation needed modification to apply for $T_\mathrm{v} < \frac{1}{12}$, resulting in the following expression:

$$RS_\mathrm{cmax} = 1 - \frac{2}{3}\exp\left[\ln\left(\frac{3}{2}\right) - 3A_\mathrm{RS}{T_\mathrm{v}}^{B_\mathrm{RS}}\right] \tag{8.19}$$

where A_RS and B_RS are parameters depending upon C/D_T and RP.

When surface settlement occurred ($S_\mathrm{cmax} < 0$)—when the lining was permeable—adopting $A_\mathrm{RS} = 0.5$ and $B_\mathrm{RS} = 0.8$ produced a good overlap with the simulation result; this is shown in Figure 8.8. With surface heave ($S_\mathrm{cmax} > 0$)—when the lining was impermeable—the value of A_RS depended upon the C/D_T ratio. A linear relationship was assumed, such that $A_\mathrm{RS} = 0.055\dfrac{C}{D_\mathrm{T}} + 0.12$. With $B_\mathrm{RS} = 1$, a good fit was obtained. This is also illustrated in the figure, where $A_\mathrm{RS} = 0.28$ for $C/D_\mathrm{T} = 3$.

Partially permeable linings, such as with $RP = 0.17$ in the figure, gave settlements intermediate between these two extremes. However, ground movements at these RP values were relatively small (e.g. for $RP = 0.17$, maximum displacement is $\approx 5\%$ of that for permeable lining), so no attempt was made to incorporate the RP-dependence at intermediate RP values.

Figure 8.8 concurs with field observations of S-shaped curves, presented in Section 2.2.3.

Settlement distribution

Modified Gaussian trough A modified Gaussian curve, as proposed by Vorster *et al.* (2005), was assumed for the settlement trough shape; the formulation is given in Equation 8.15. This curve was chosen because the extra parameter μ enabled it to fit the wider consolidation trough better than the unmodified curve. However, the approximation deviated from the simulated troughs in two main ways:

1. **Far-field heave** All troughs with non-zero short-term volume loss exhibited heave in the far-field due to dissipation of negative excess pore pressures. Figure 8.9 presents selected settlement troughs with associated prediction curves, and this heave is evident in Figures 8.9b and d. However, the heave was acceptably small (almost 2%) relative to the maximum displacements that could occur.

2. **Multi-modal trough** Troughs with intermediate RP and non-zero short-term volume loss exhibited a multi-modal trough shape (having more than one stationary point), as exemplified in Figures 8.9b and d when $RP = 0.17$ and 0.12 respectively. However, the relatively small displacements at intermediate RP made any lack of fit in trough shape prediction acceptable.

Overall therefore, the approximation of a modified Gaussian curve was considered acceptable.

Relationships for K_L and μ Relationships to determine the curve parameters K_L and μ were found by analysing modified Gaussian curves, optimised to match each simulation. In deriving these relationships, the approximations above were duly considered.

Figure 8.11a shows optimised K_L values. The relationship $K_L = 0.8 - 6V_L$ was found to fit data suitably, and is shown on the figure. The simulations deviate from this fit in two key areas:

1. At intermediate RP, the multi-modal troughs from simulations with volume loss gave poor fits.

2. At low RP for simulations without volume loss, wider troughs were obtained.

However, displacements from these particular simulations were small, as seen in Figure 8.9, and so the simple relationship was considered an acceptable approximation.

Figure 8.11b shows optimised μ values. A two-part relationship was applied to this data:

$$\mu = \begin{cases} -0.004 & \text{for} \quad RP < 0.1 \\ 0.1 & \text{for} \quad RP \geq 0.1 \end{cases} \tag{8.20}$$

Similar deviations were noted as encountered when fitting K_{L}, but were considered acceptable since displacements for the deviating simulations were small.

Horizontal displacement distribution

A two-parameter curve was found to approximate well to the horizontal displacement distributions:

$$H_{\mathrm{c}} = \frac{3{a_{\mathrm{hd}}}^2 H_{\mathrm{cmax}} x}{|x|^3 + 2{a_{\mathrm{hd}}}^3} \tag{8.21}$$

where a_{hd} is the offset from the centreline of the maximum displacement H_{cmax}. Fits to the simulation results are shown in Figure 8.10, but show deviations in two main areas:

1. Displacement was well-predicted inside $2z_0$ from the centreline, but beyond this, inward horizontal displacement was overestimated. However, the displacements here were small relative to the maximum horizontal displacement possible; the maximum overestimation was 1.2mm: a tenth of the maximum horizontal displacement of 12mm (Figure 8.10b).

2. As with vertical settlements, more complex distributions of horizontal displacement were witnessed at intermediate RP, after there had been short-term volume loss; this is noticeable in Figures 8.10b and d.

A corollary of the first deviation above is that far-field horizontal tensile strains might be underestimated; an additional method to predict peak horizontal strains was therefore devised. However, this method is unlikely to be used in engineering practice; horizontal strains in a building would be averaged over its span (Mair *et al.*, 1996). Horizontal displacements—and hence strains—are adequately predicted within $2z_0$ from the centreline.

The offset of maximum displacement a_{hd} varies according to:

$$a_{\mathrm{hd}} = \begin{cases} 0.7z_0 & \text{for} \quad RP < 0.1 \\ z_0 & \text{for} \quad RP \geq 0.1 \end{cases} \tag{8.22}$$

This was found to fit the distributions consistently.

8.6 Validation of prediction method

8.6.1 Case histories

Wongsaroj (2005) demonstrated his prediction method by applying it to two case histories: (i) St James's Park, and (ii) the Heathrow Express trial tunnels. This section presents the application of the new prediction method to the same two case histories. Only settlement data is available for the consolidation periods, so horizontal displacements could not be validated.

St James's Park The twin-tunnel excavation at St James's Park is described in Chapter 7; more details are reported by Nyren (1998). Only calculation for the first (westbound) tunnel was attempted, since the new method does not account for interaction effects. Settlements were therefore calculated just before the second tunnel was constructed: after 256 days. The calculation was also calculated at a depth of 5m, so not to be influenced by seasonal fluctuations in the water table.

Heathrow Express Bowers *et al.* (1996) report on movements above the Heathrow Express trial tunnels. Constructed using the NATM, they comprise of three sections: Types I, II and III—each corresponding to a different sequence of drift excavation. Settlements are calculated at the time of the last recorded movements: about 1220 days after excavation. Unlike at St James's Park, the movements at Heathrow were less influenced by seasonal changes, so surface settlements could be fairly compared.

8.6.2 Input parameters

Figure 8.12 illustrates tunnel geometries for each case history. Input parameters are also shown; many of these were taken from Nyren (1998) and Bowers *et al.* (1996). Other parameters required estimation; many of the assumptions behind their selection were the same as those Wongsaroj used. These assumptions are summarised below:

St James's Park

- Equivalent stiffness E'_{d} was evaluated as detailed in Section 8.3.4. The oedometer test used to derive it adopted soil model MODF, with the same parameters as adopted in this parametric study; this model replicated ground behaviour well in the St James's Park validation analyses of Chapter 7.

- Two values of soil permeability were trialled. The first value of $k_{\mathrm{h}} = 2 \times 10^{-10}$m s^{-1} was estimated by Wongsaroj as representative for the site, from data reported by Burland & Hancock (1977) and Standing & Burland (2005). The second value of $k_{\mathrm{h}} = 5 \times 10^{-10}$m s^{-1} was back-analysed to fit the rate of settlement. $k_{\mathrm{h}}/k_{\mathrm{v}}$ was assumed as 2.

- Wongsaroj trialled three values of lining permeability k_{T}: 10^{-12}, 10^{-11} and 10^{-10}m s^{-1}. As the most permeable, $k_{\mathrm{T}} = 10^{-10}$m s^{-1} fitted the field data closest. This value was therefore adopted here.

Heathrow Express

- The water table was assumed to lie at 1m depth, based upon pore pressure measurements reported by New & Bowers (1994).

- The top of the London Clay was assumed to lie at 3m depth, also based upon New & Bowers (1994).

- Equivalent stiffness E'_{d} was evaluated from Equation 8.4, using values of $E_{\mathrm{u\,sec}}$ from undrained triaxial tests at Heathrow Terminal 5 (Hight *et al.*, 2003). $E_{\mathrm{u\,sec}} = 176$MPa was considered representative at 0.04% strain, giving $E'_{\mathrm{d}} = 126$MPa, assuming that $\nu_{vh} = 0.07$.

- $k_{\mathrm{h}} = 10^{-9}$m s^{-1} used here was considered by Wongsaroj as representative for the site, after observing horizontal permeabilities measured by Hight *et al.* (2003). Again, $k_{\mathrm{h}}/k_{\mathrm{v}} = 2$ was assumed.

- Three values for lining permeability were trialled. The first two values of 10^{-11} and 5×10^{-10}m s^{-1} were estimated by Wongsaroj as bounds on the

permeability of the shotcrete lining. The last value of 2.2×10^{-11}m s^{-1} was back-analysed to fit the maximum steady-state settlement.

- The lining thickness of 0.25m was quoted by Wongsaroj.
- Volume losses for trial tunnel Types I, II and III were 1.15, 1.05 and 1.26% respectively. Since they varied within a small range, a representative average was adopted.

8.6.3 Results

Figure 8.13 compares calculated consolidation settlements with those in the field for the two case histories, presenting the development of centreline settlement with time, and settlement troughs.

Figure 8.13a shows that adopting $k_{\mathrm{h}} = 2 \times 10^{-10}$m s^{-1} in calculations for St James's Park gave settlements developing at around half the rate as in the field. Adopting the back-analysed value of $k_{\mathrm{h}} = 5 \times 10^{-10}$m s^{-1} matched the rate in the field; this value is still acceptable as a representative soil permeability at the site. The trough in the field in Figure 8.13b is offset from the centreline; this can be attributed to a transverse variation in soil properties, highlighting the sensitivity of ground movements to spatial variation in the field. Despite this, the prediction method still reproduced a realistic trough shape.

At Heathrow, Figure 8.13c illustrates that applying the two bounds of lining permeability estimated by Wongsaroj ($k_{\mathrm{T}} = 10^{-11}$ and 5×10^{-10}m s^{-1}) gave settlements that developed three times too slowly and three times too quickly respectively. The back-analysed value of $k_{\mathrm{T}} = 2.2 \times 10^{-11}$m s^{-1} improved the fit. This value is near the bottom of the range of permeabilities back-analysed by Celestino *et al.* (2001), who obtained values between 6×10^{-11} and 10^{-8}m s^{-1} for shotcrete linings. Figure 8.13d shows that the transverse settlement distribution is well-approximated.

This illustrates the difficulty in predicting the rate of settlement: varying both lining and soil permeabilities within reasonable bounds drastically changes predictions; the same conclusion was also reached by Wongsaroj (2005) and Mair

(2008). The prediction method might therefore be limited by knowledge of in-situ permeability.

8.7 Effects on surface structures

8.7.1 Net displacements

So far, incremental displacements generated solely during the consolidation period have been presented. However, net displacements—accumulated over both excavation and consolidation—are more appropriate to examine effects on surface structures.

The net displacements and strains from analyses with non-zero volume loss are considered in Figure 8.14, highlighting the effect of consolidation on the net surface movement for each C/D_{T} ratio. Maximum values for the distributions of displacements, slope and horizontal strains are shown, together with measures of their width: trough width parameter K, and the offsets of maximum values from the tunnel centreline. Each ordinate axis is scaled so that the value after excavation lies on a line common to all plots; in this way, the effect of consolidation compared to the existing excavation movements can be easily visualised. Steady-state values for both permeable and impermeable linings are contrasted on the plots.

The figure shows that the influence of the consolidation period is strongly dependent upon permeability. For an impermeable lining, displacements and strains would reduce slightly; for instance, settlements are reduced to almost half for $C/D_{\mathrm{T}} = 7$, from 1.54 to 0.87cm. For a permeable lining however, maximum values could double or even triple, in the case of horizontal compressive strain for $C/D_{\mathrm{T}} = 7$, which increases from 0.038 to 0.114%.

8.7.2 Relation to building damage

The large increase in the maximum slope and strains suggests that building damage could become more severe during consolidation. However, it has often been noted that consolidation movements are less damaging than excavation movements because horizontal strains and settlement slopes do not increase appreciably (Mair &

Taylor, 1997). Although further building damage during the consolidation period has been reported (Harris, 2002), it is rarely observed.

The two observations of large movements and lack of building damage can be reconciled by the following possible explanations:

Widening of distributions The trough width parameter and offsets of maximum values in Figure 8.14 suggest that displacement and strain distributions widen slightly, if at all. Curvature at the ground surface might therefore not increase. This would make the deflection ratio (Mair *et al.*, 1996) less severe, so ameliorating building damage.

Lining permeability Figure 8.14 suggests that a partially permeable tunnel would induce only very small horizontal movements. However, this does not offer a complete explanation: the figure suggests that vertical movements would also be correspondingly reduced; in the field, they are still significant.

Time dependence Creep, stress relaxation or ageing might reduce the severity of ground movements; this amelioration would not occur for short-term movements.

Continuity of foundations Buildings founded upon individual footings would suffer from surface differential movements much more than those built upon continuous foundations. The predominance of continuous foundations might explain the lack of building damage.

Attribution of building damage Further building damage might have occurred so long after tunnel construction that the presence of the tunnel might be forgotten as a cause.

There is a need for further investigation to find the most likely explanation.

8.8 Summary

This chapter presented the outcomes of a parametric study into the long-term behaviour of a single tunnel, investigating the influence of C/D_{T} ratio, volume loss and relative soil-lining permeability (RP).

A prediction method was developed, which improved upon the one proposed by Wongsaroj (2005). The new method provides both vertical and horizontal surface displacement distributions by application of simple equations. Peak horizontal strains are also predicted.

In developing the prediction method, a new formulation of RP was proposed—based upon a more realistic flow regime—leading to an improved fit to simulation results. Displacement was also non-dimensionalised in a new way, in accordance with the observed distribution of sub-surface consolidation movements.

The prediction method was validated against two case histories, which demonstrated the capability of the method to yield good predictions. However, the method is limited by the determination of soil and lining permeabilities in the field. Chapters 4 and 5 also discovered that both soil and lining permeabilities can change with time; a conservative approach might therefore be to assume a fully permeable lining.

Net displacements from the simulations revealed appreciable increases in surface movement during consolidation, apparently contradicting the lack of additional building damage in the field observed during this period; this is a cause for future investigation.

Figure 8.1: Mesh geometries adopted in parametric studies

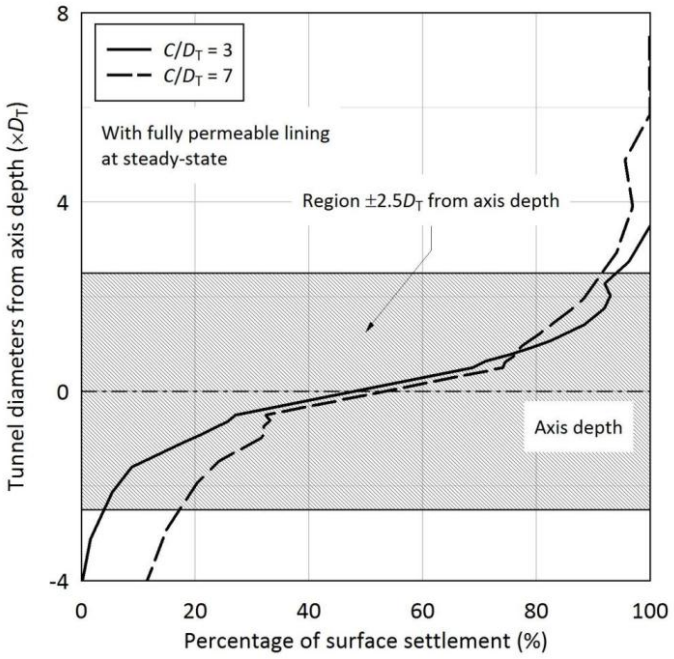

Figure 8.2: Identification of consolidating zone

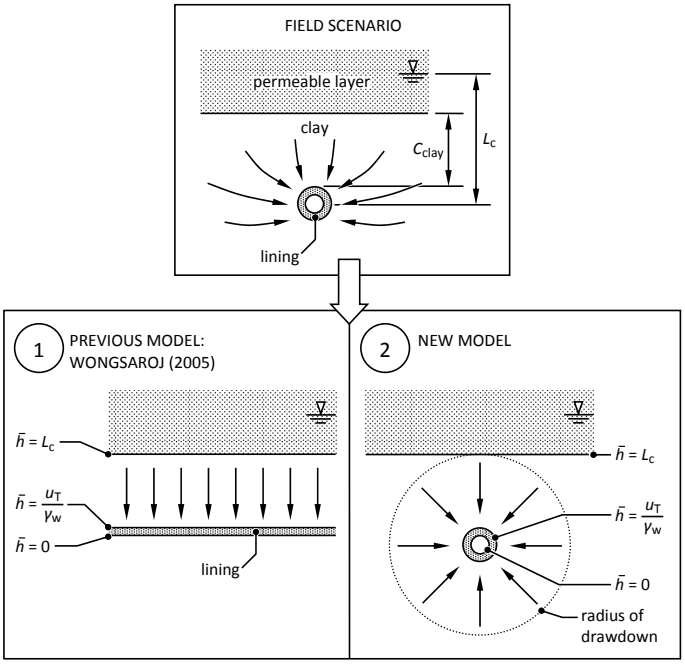

Figure 8.3: Mathematical models for deriving relative soil-lining permeability

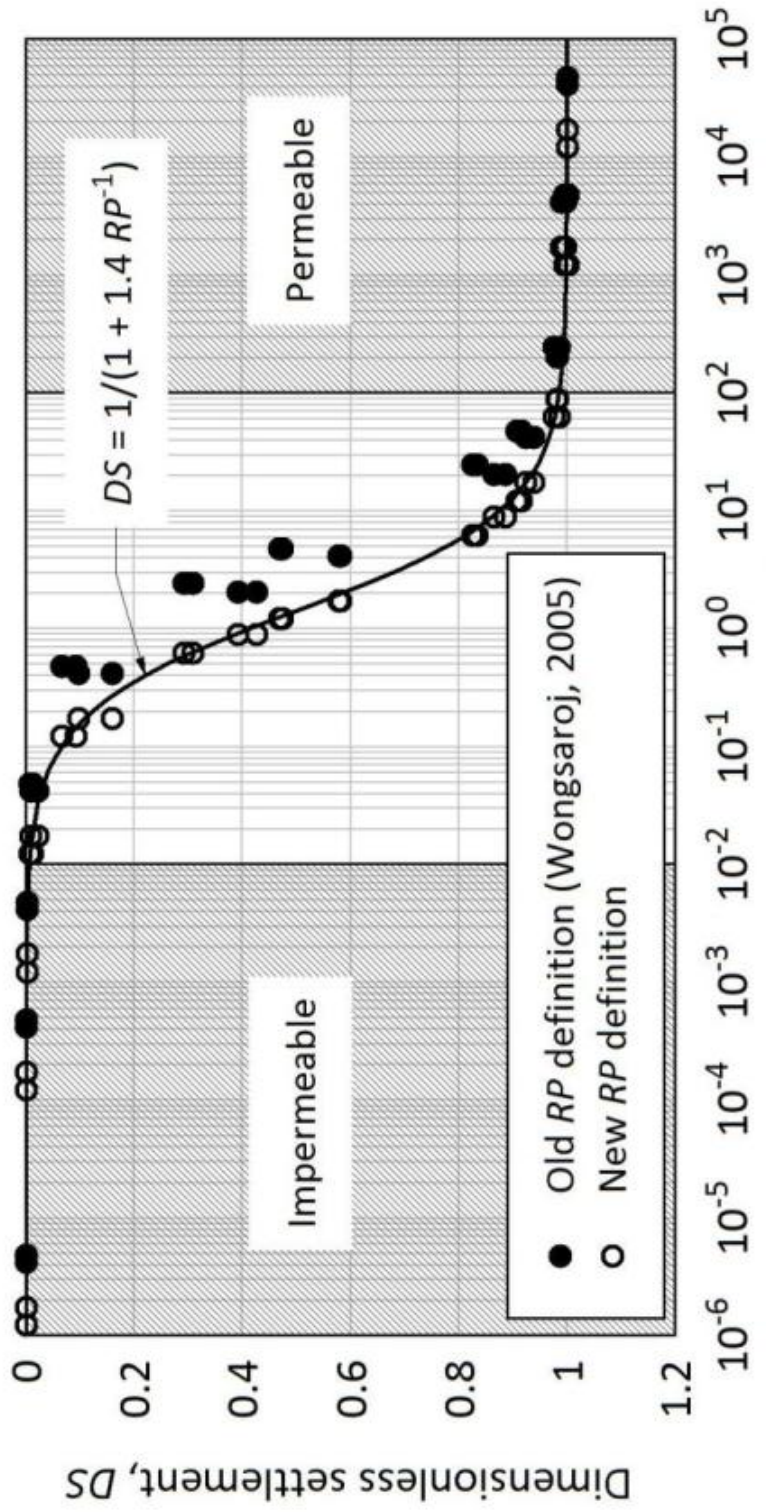

Figure 8.4: Dimensionless settlements with new and old RP definitions

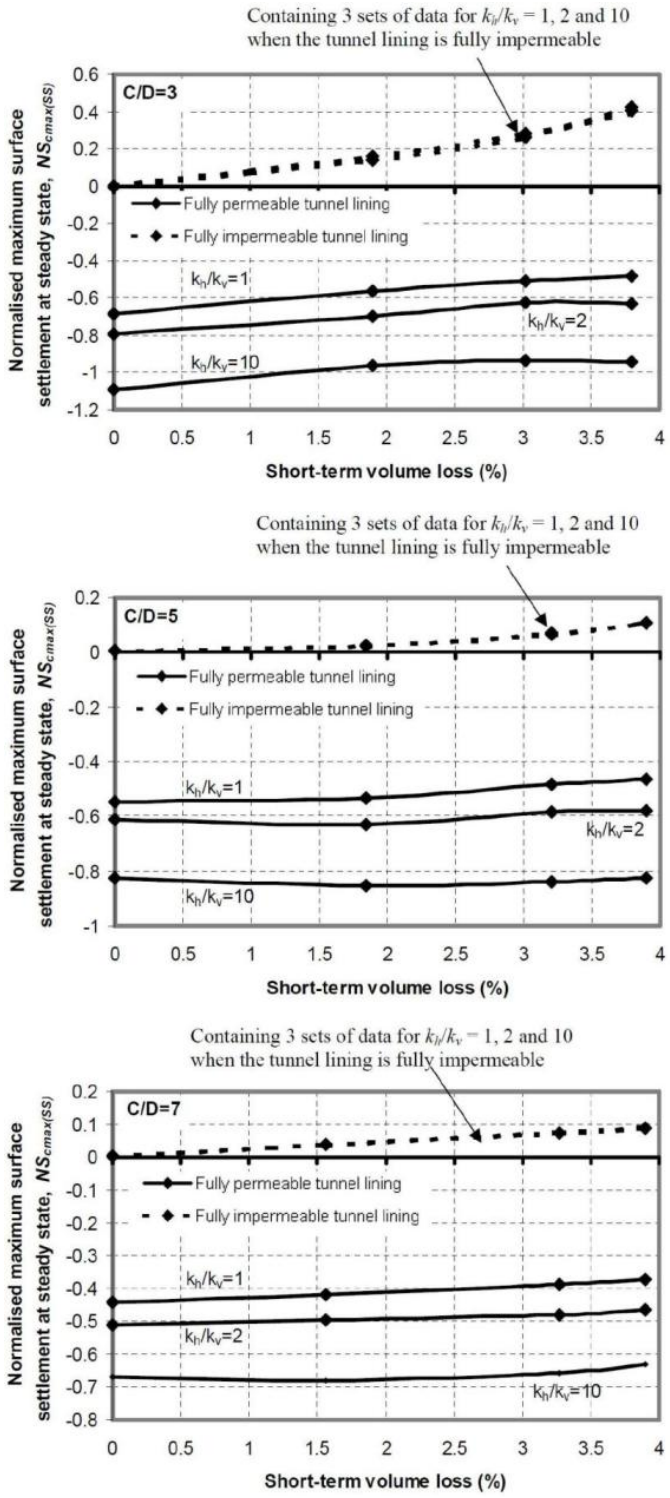

(a) Chart A: Estimating normalised steady-state maximum surface settlement at permeability extremes

Figure 8.5: Normalised prediction charts devised by Wongsaroj (2005)

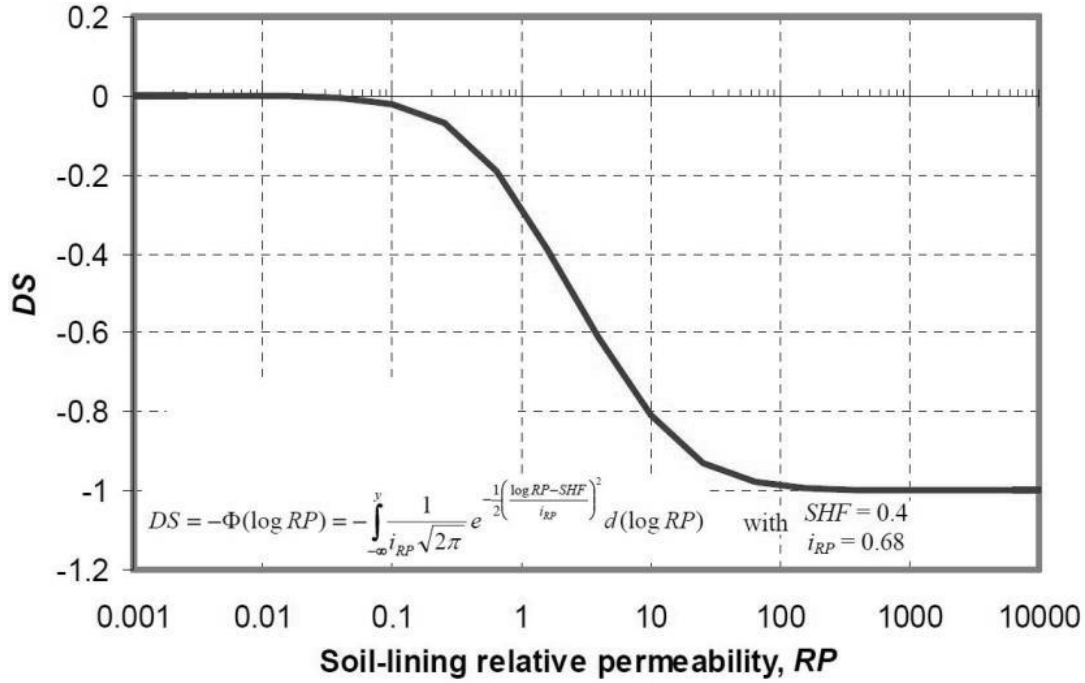

(b) Chart B: Estimating influence of permeability on settlement

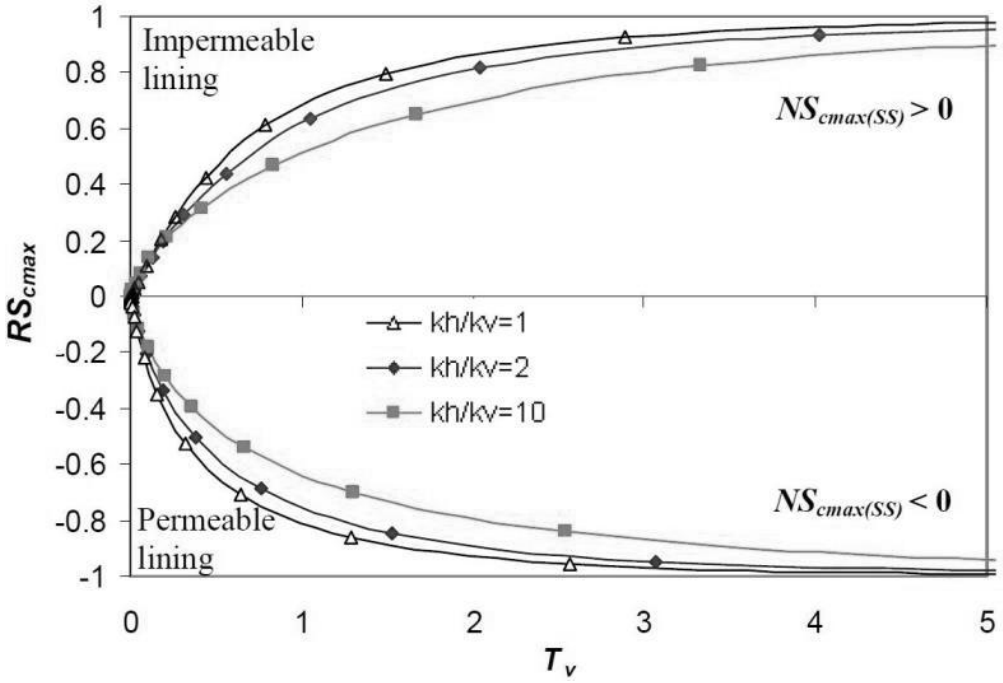

(c) Chart C: Estimating development of settlement with time

Figure 8.5: *cont...* Normalised prediction charts devised by Wongsaroj (2005)

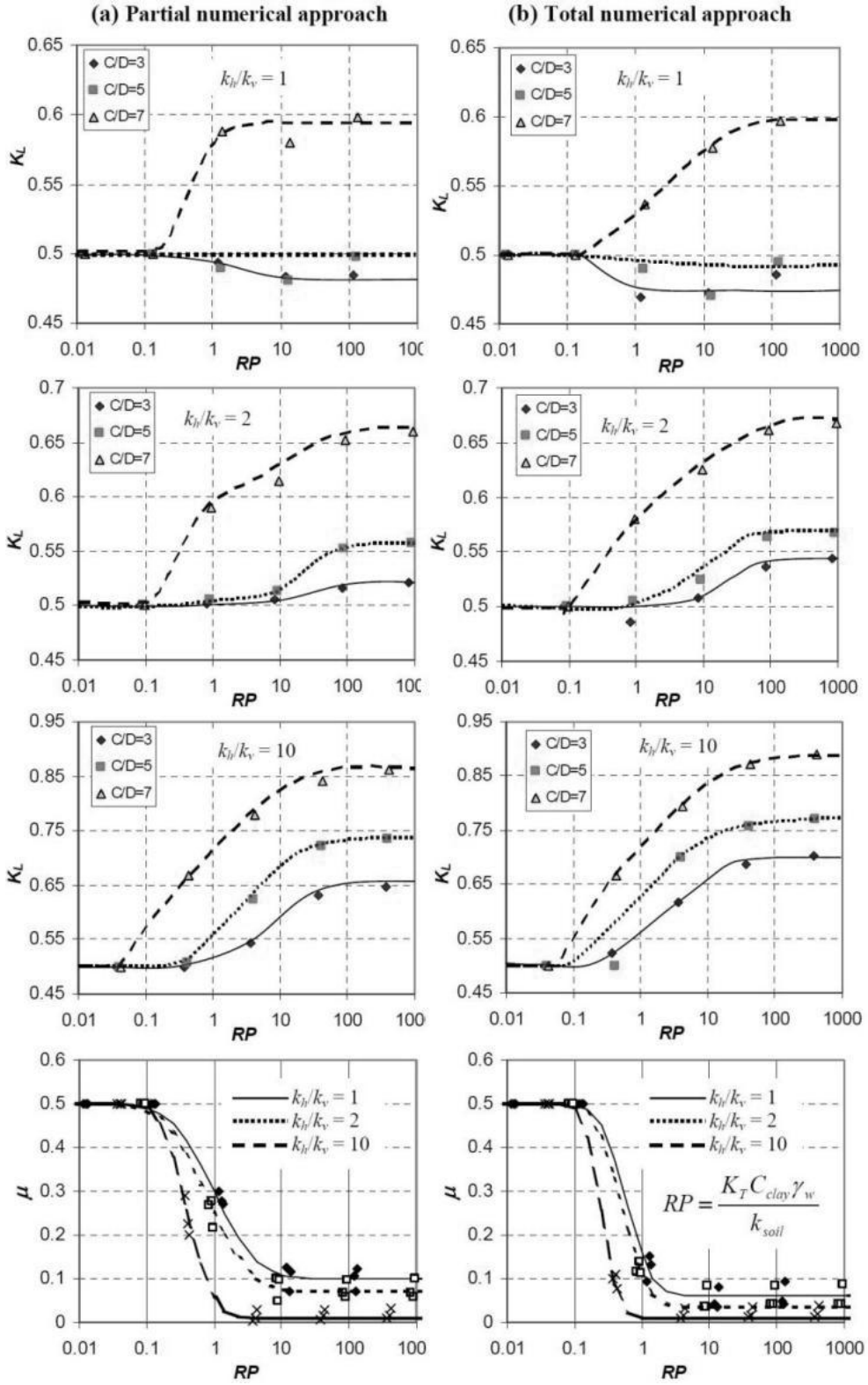

(d) Estimating trough width parameters

Figure 8.5: *cont...* Normalised prediction charts devised by Wongsaroj (2005)

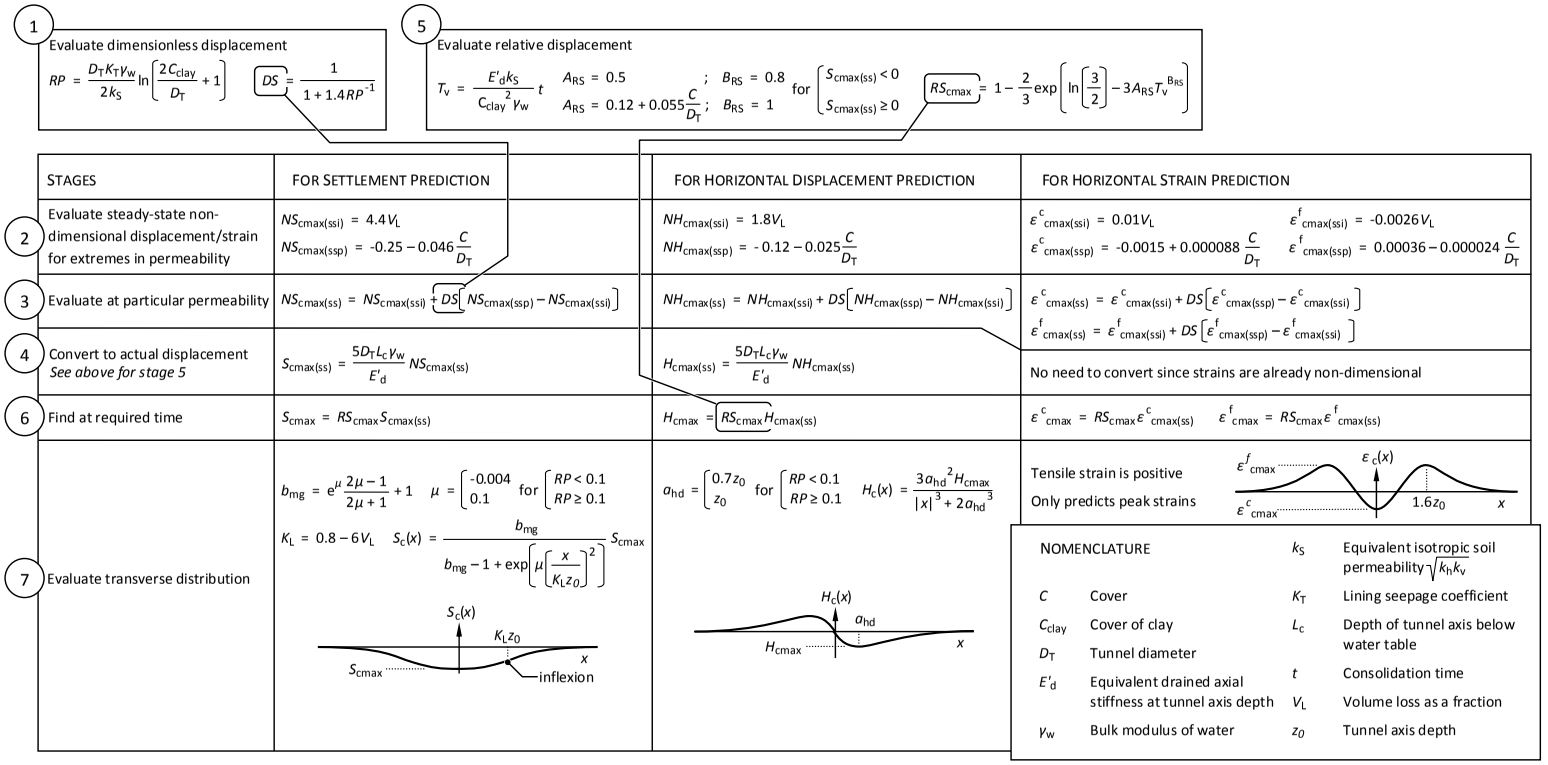

Figure 8.6: Summary of proposed prediction method

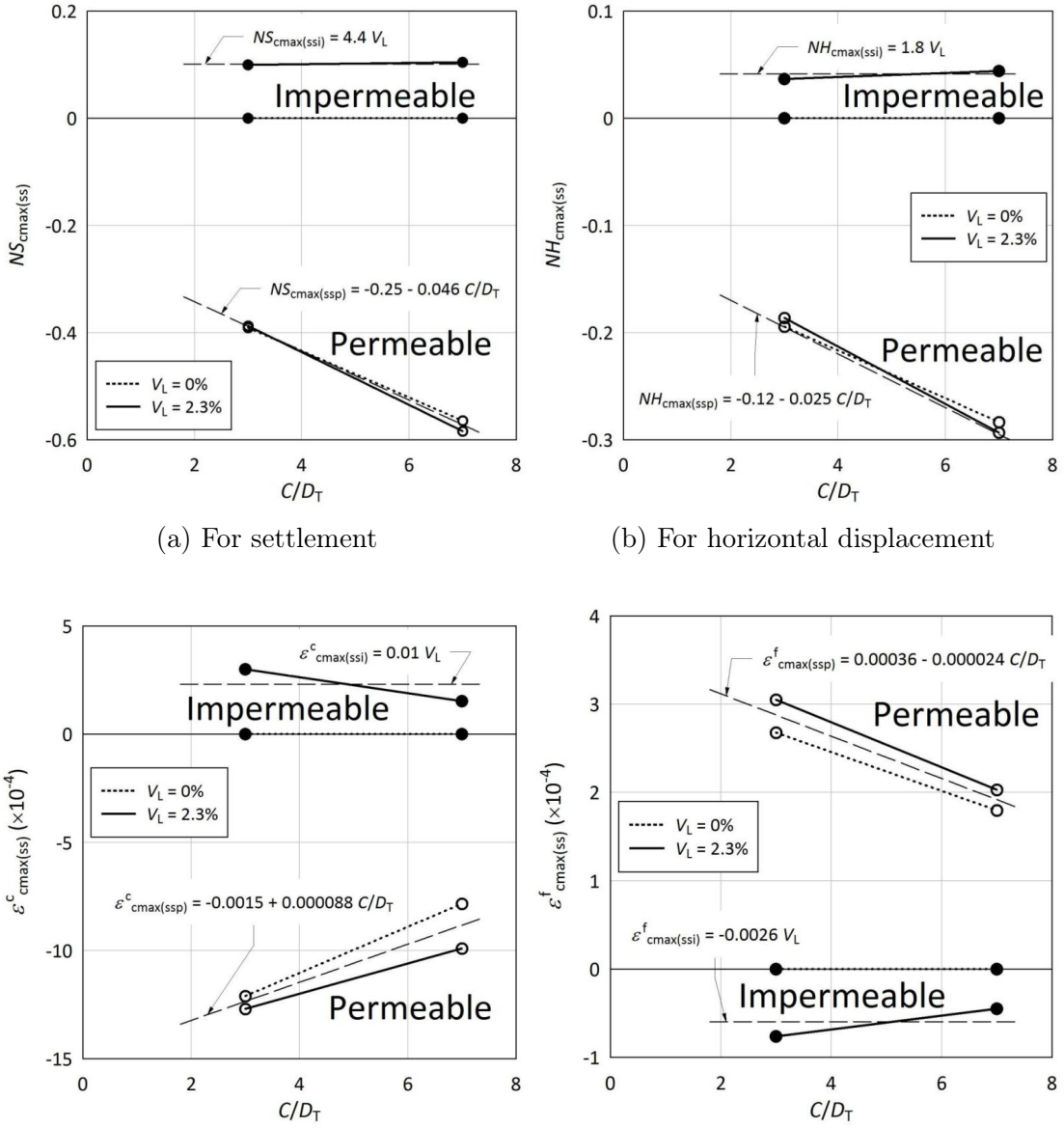

(a) For settlement

(b) For horizontal displacement

(c) For centreline horizontal strain

(d) For far-field horizontal strain

Figure 8.7: Variation of normalised steady-state maximum surface movements with C/D_T ratio

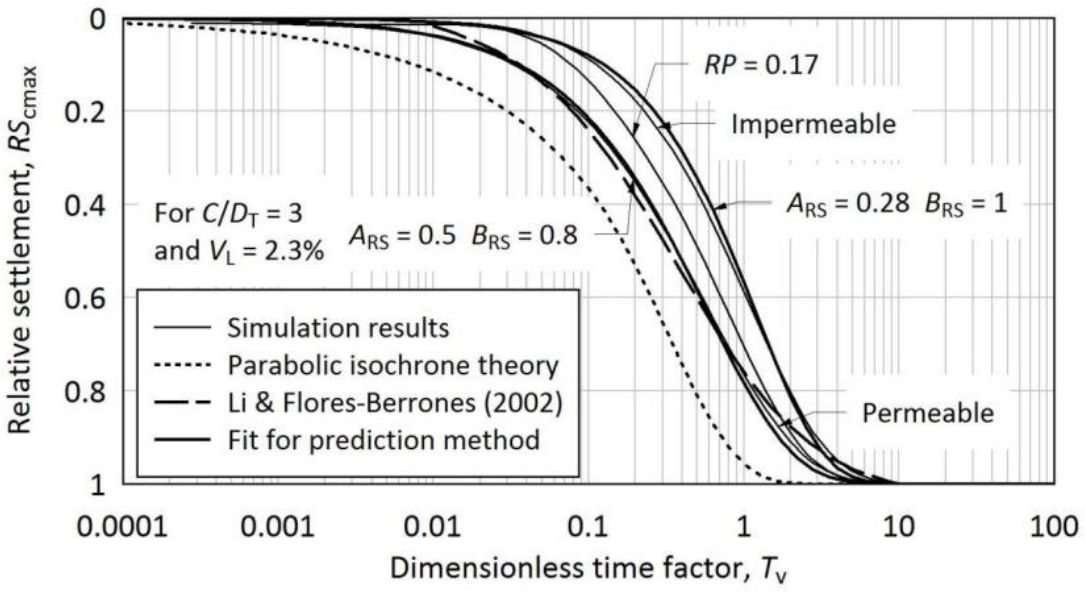

Figure 8.8: Variation of settlement with time

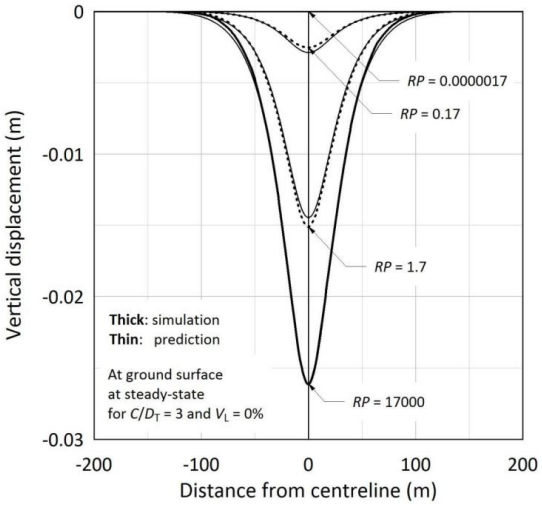

(a) For $C/D_{\mathrm{T}} = 3$ and zero volume loss

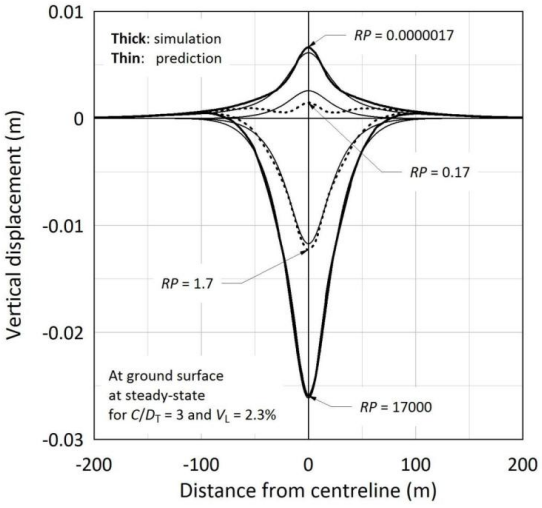

(b) For $C/D_{\mathrm{T}} = 3$ and non-zero volume loss

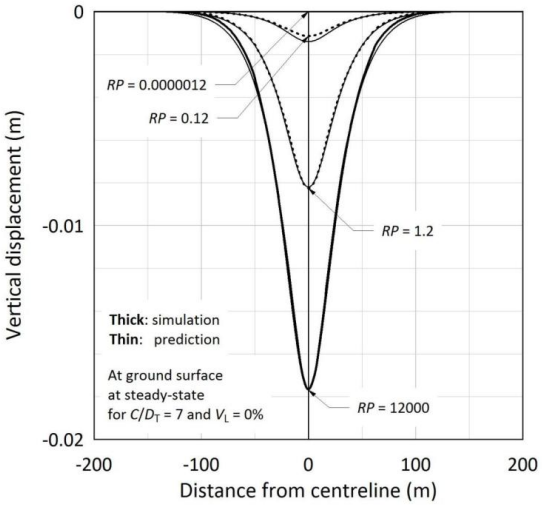

(c) For $C/D_{\mathrm{T}} = 7$ and zero volume loss

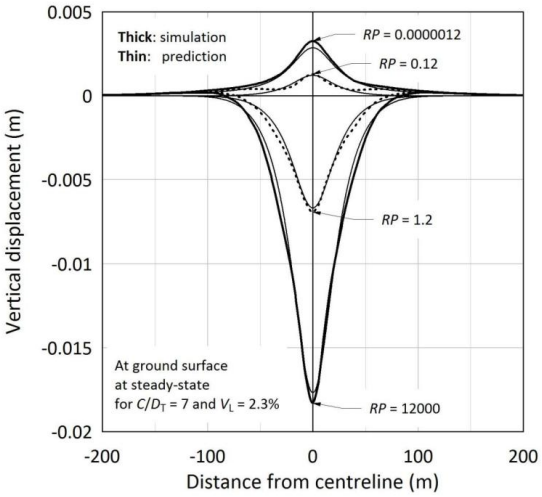

(d) For $C/D_{\mathrm{T}} = 7$ and non-zero volume loss

Figure 8.9: Predicted and simulated surface settlement troughs

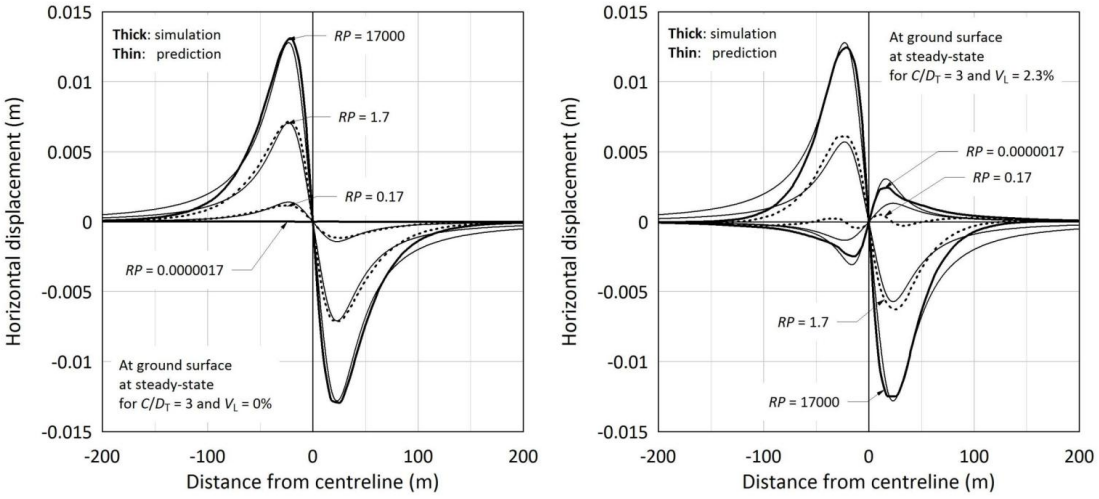

(a) For $C/D_{\mathrm{T}} = 3$ and zero volume loss (b) For $C/D_{\mathrm{T}} = 3$ and non-zero volume loss

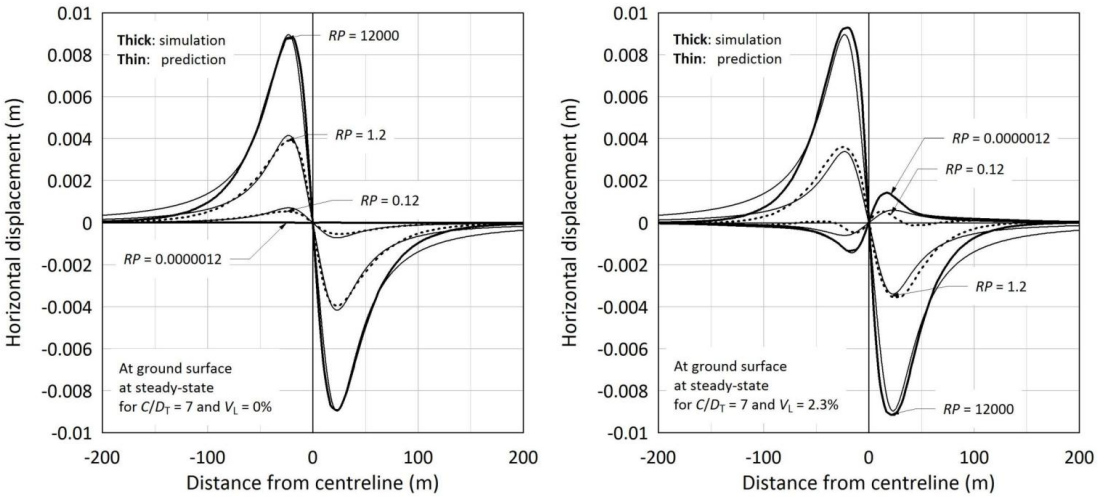

(c) For $C/D_{\mathrm{T}} = 7$ and zero volume loss (d) For $C/D_{\mathrm{T}} = 7$ and non-zero volume loss

Figure 8.10: Predicted and simulated surface horizontal displacement distributions

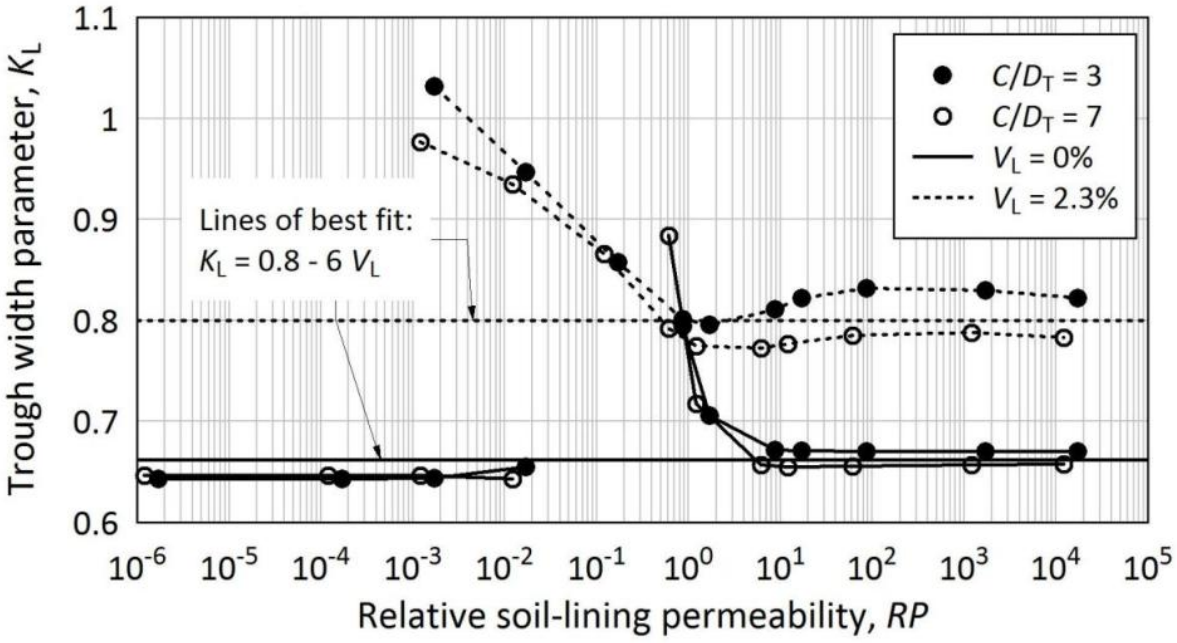

(a) For K_L

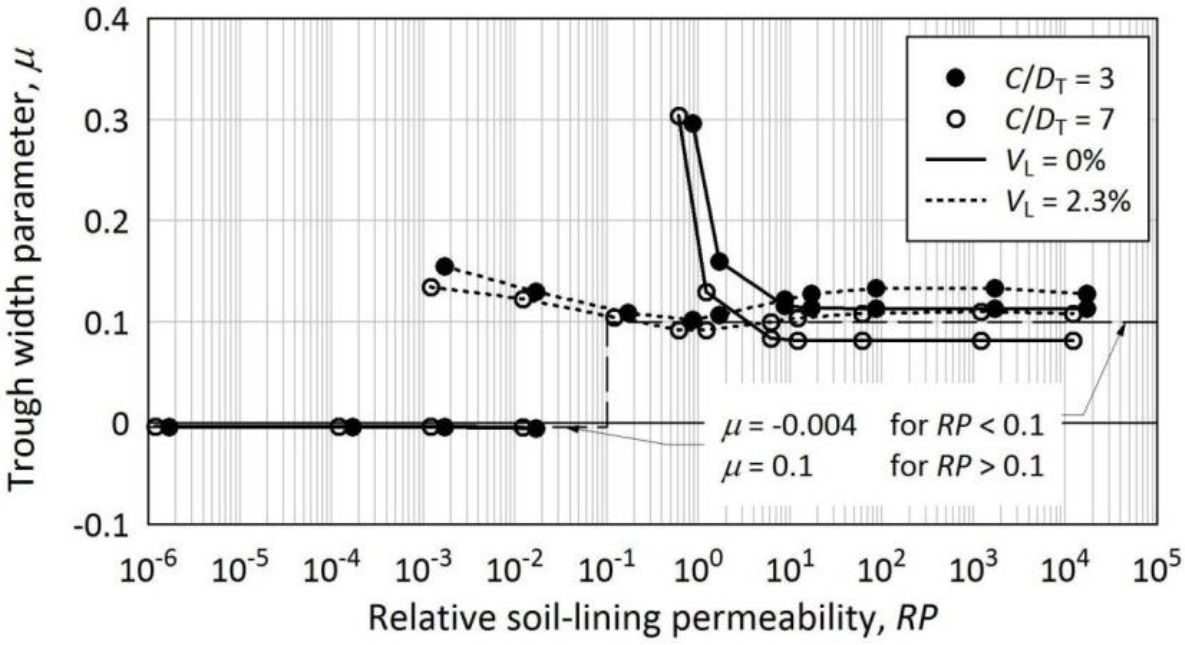

(b) For μ

Figure 8.11: Variation of trough width parameters with RP

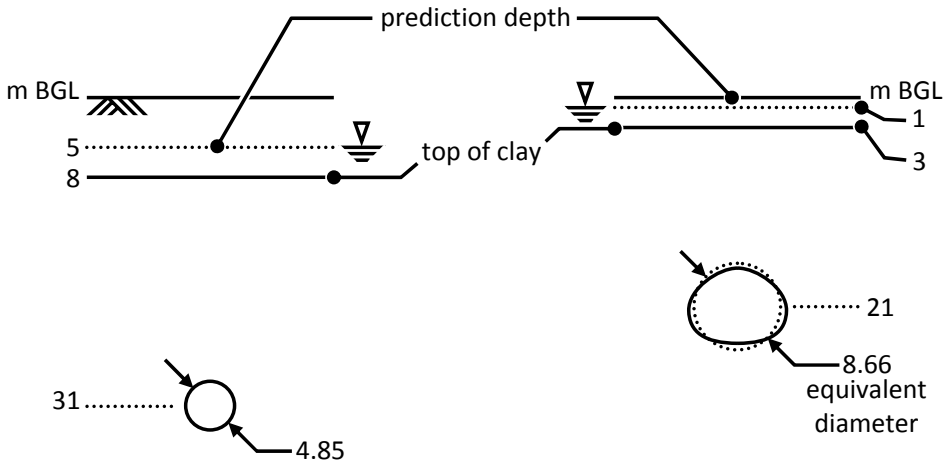

ST JAMES'S PARK

HEATHROW EXPRESS TRIAL TUNNELS

INPUT PARAMETER			ST JAMES'S PARK	HEATHROW EXPRESS
Clay cover	C_{clay}	(m)	20.6	13.7
Cover-to-diameter ratio	C/D_T		4.87	1.93
Equivalent stiffness	E'_d	(MPa)	104.7	53.9
Horizontal soil permeability	k_h	($m s^{-1}$)	2×10^{-10} 5×10^{-10}	10^{-9}
Permeability anisotropy ratio	k_h/k_v		2	2
Lining permeability	k_T	($m s^{-1}$)	10^{-10}	10^{-11} 5×10^{-10} 2.2×10^{-11}
Axis depth below water table	L_c	(m)	23.6	20
Consolidation time	t	(days)	256	1220
Lining thickness	t_T	(m)	0.2	0.25
Volume loss	V_L	(%)	3.3	1.15
Axis depth	z_0	(m)	31	21

Figure 8.12: Geometries and input parameters for case history validation

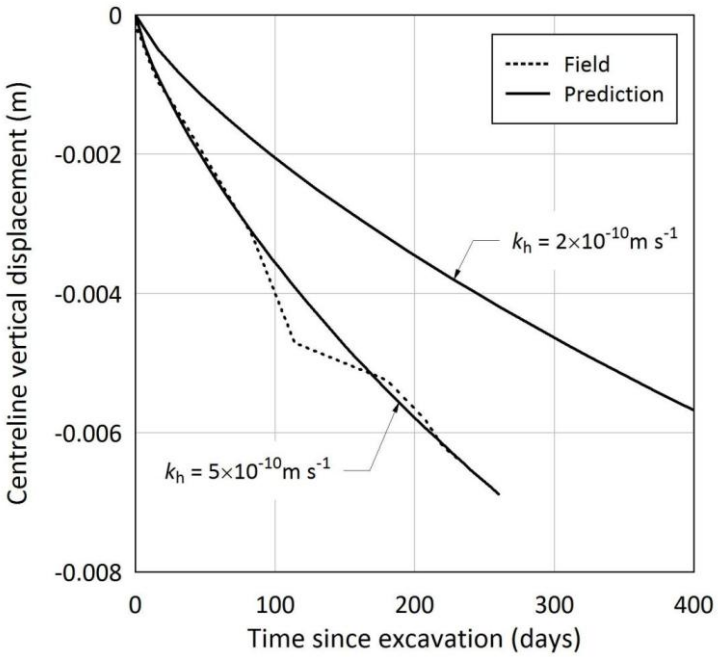

(a) St James's Park: development of settlement with time

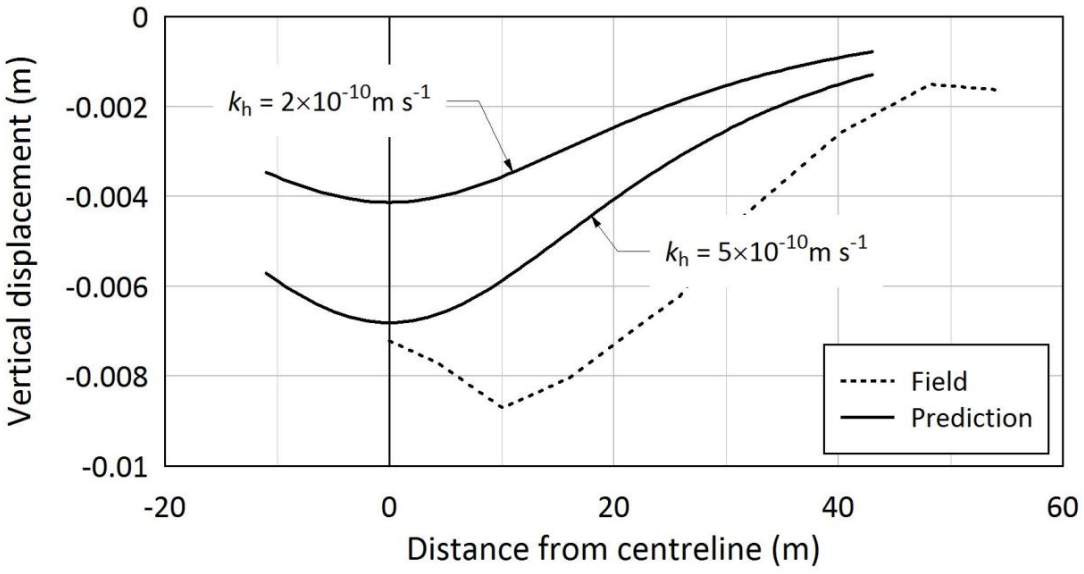

(b) St James's Park: settlement trough

Figure 8.13: Predicted and actual settlements for case history validation

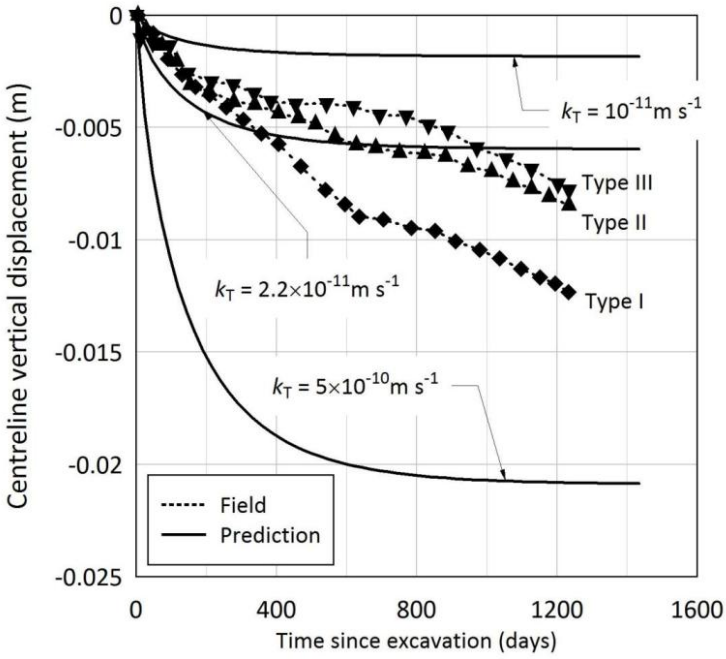

(c) Heathrow Express trial tunnels: development of settlement with time

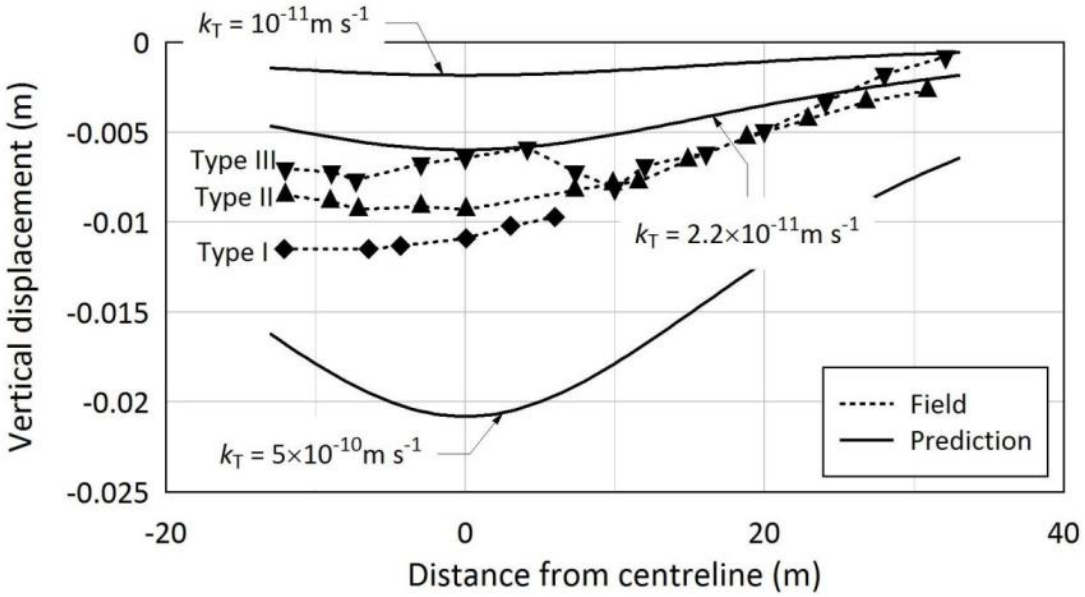

(d) Heathrow Express trial tunnels: settlement trough

Figure 8.13: *cont...* Predicted and actual settlements for case history validation

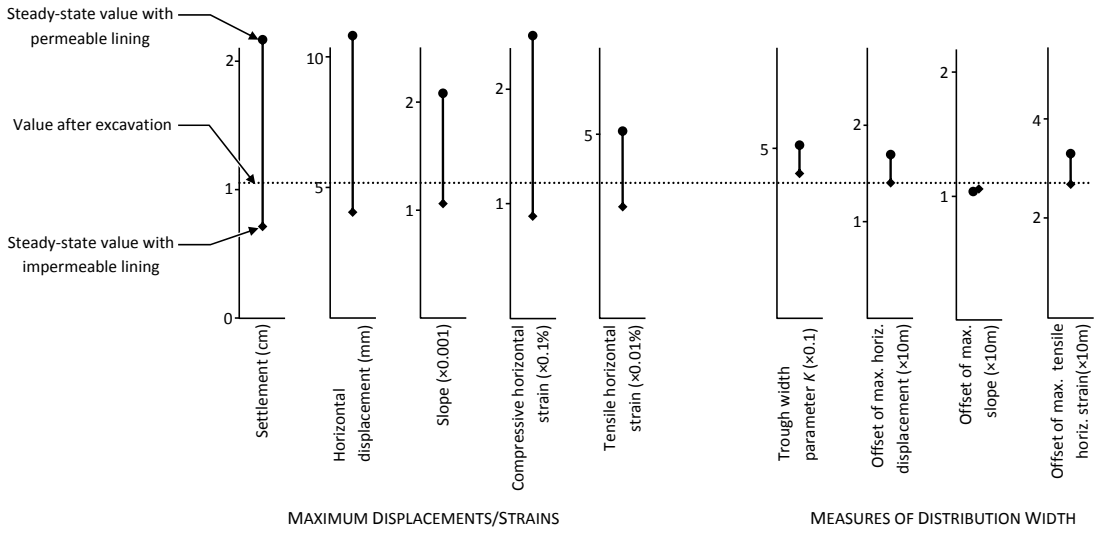

(a) At $C/D_{\mathrm{T}} = 3$

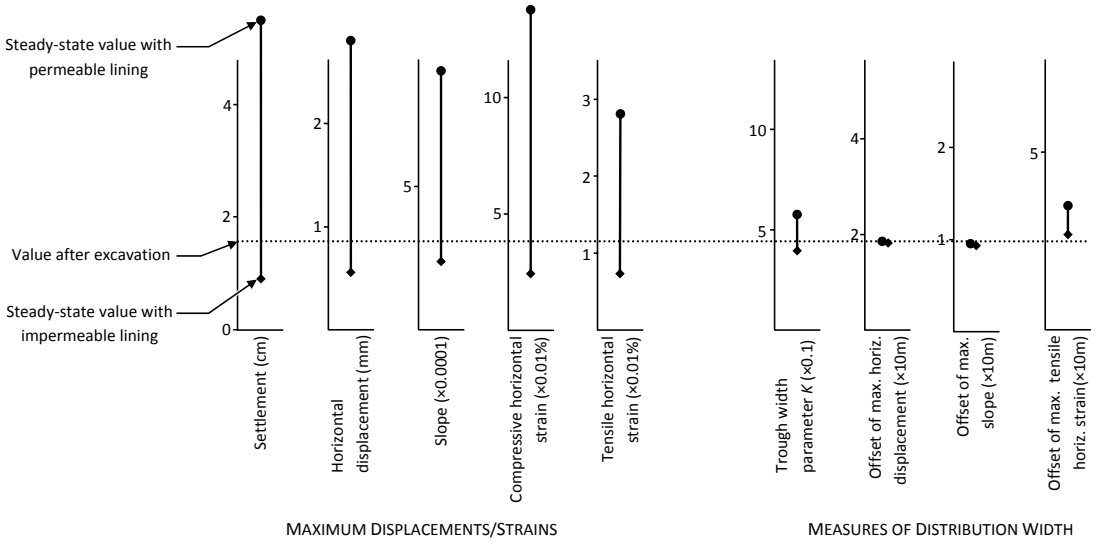

(b) At $C/D_{\mathrm{T}} = 7$

Figure 8.14: Net displacements and strains before and after consolidation

Chapter 9

Parametric study into twin-tunnel long-term behaviour

9.1 Introduction

To date, there has been no dedicated study into the interaction of closely-spaced tunnels during consolidation, despite the fact that tunnels are commonly constructed in pairs. This chapter therefore presents a parametric study into the long-term behaviour of twin side-by-side tunnels, investigating the influence of cover-to-diameter ratio (C/D_{T}), separation-to-depth ratio (d'/z_0), volume loss and relative soil-lining permeability (RP).

The study highlighted complex competing trends between interaction and pillar width, identifying key mechanisms and suggesting what long-term interaction behaviour to expect for different tunnelling conditions in the field. The influence of interaction on net surface movements was also observed to be significant.

9.2 Method

The single-tunnel parametric study was described in Chapter 8; many of its features are also shared with the twin-tunnel study, and are presented in more detail in Section 8.2. Key differences are outlined below.

9.2.1 Rest period

A remeshing technique was adopted for the twin-tunnel analyses, enabling a 3-D mesh to be used for excavation modelling, and a 2-D mesh for consolidation modelling; remeshing is detailed in Sections 7.3.6 and 7.4.3. Four analysis stages were conducted: (i) excavation of the first tunnel, (ii) an intermediate consolidation period (rest period), (iii) excavation of the second tunnel, and (iv) a final consolidation period progressing until steady-state—lasting 500,000 days (1370 years).

For the rest period between excavations, the time period to apply needed to be normalised so that different analyses could be compared fairly. However, a suitable normalised period was difficult to find because the degree of consolidation occurring within the period depended upon many factors, including geometry, permeabilities and soil stiffness.

A convenient solution was to eliminate the rest period altogether, so that the second tunnel was excavated immediately after the first. The effect of omitting the rest period is investigated in Appendix F. Here, a twin-tunnel analysis adopting a 60-day rest period is compared to one without; sixty days was considered a typical rest period in the field. Omitting the rest period had little influence on displacements, particularly at the ground surface, validating its use in analyses to ensure fair comparison.

Despite omitting the rest period, a remapping was still performed between excavating the first and second tunnels to ensure a plane-strain condition before commencing the second excavation. Output variables were therefore extracted from the output plane after the first excavation, and applied along the entire length of the mesh before excavating the second tunnel.

9.2.2 Mesh details

Six mesh geometries were trialled. The 3-D meshes adopted for excavation are illustrated in Figure 8.1; the corresponding 2-D meshes for consolidation had the same geometry as a transverse section. The meshes trialled two C/D_{T} ratios: 3 and 7; and three separation-to-depth (d'/z_0) ratios: 0.5, 2.0 and 4.5.

All other mesh details are as presented in Section 8.2—including element type, mesh boundaries, choice of C/D_{T} ratios, excavation procedure, P/D_{T} ratio (unsupported excavation length normalised by diameter), soil profile, lining thicknesses and boundary conditions. Constitutive models and soil permeabilities were also identical.

The d'/z_0 ratios were chosen to model the full range of interaction behaviour: full, intermediate and negligible interaction. To select appropriate ratios, preliminary seepage analyses were conducted to investigate the interaction in consolidation behaviour at different separations; these analyses are detailed in Appendix E.

For the analyses with volume loss, the same P/D_{T} ratio was adopted for both first and second excavations. As expected, volume loss experienced during the second excavation increased as tunnel spacing reduced: volume losses for $C/D_{\mathrm{T}} = 3$ were 2.51%, 2.25% and 2.28% respectively for $d'/z_0 = 0.5$, 2.0 and 4.5, whilst corresponding values for $C/D_{\mathrm{T}} = 7$ were 2.67%, 2.48% and 2.47%. Analyses with zero volume loss were also conducted to investigate the effect of volume loss.

9.2.3 Relative soil-lining permeabilities

Five values of relative soil-lining permeability were trialled for the twin-tunnel analyses, corresponding to lining seepage coefficients (K_{T}) of 10^{-18}, 10^{-14}, 10^{-13}, 10^{-12} and $10^{-8}\mathrm{kN}^{-1}\ \mathrm{m}^3\ \mathrm{s}^{-1}$; this spanned behaviour from fully permeable to fully impermeable. For simplicity however, only analyses with fully permeable and fully impermeable linings were used to identify trends.

Twelve values were trialled in the single-tunnel analyses to provide sufficient data for deriving the prediction equations; five values were sufficient for the twin-tunnel analyses to identify trends in interaction behaviour, since predictive equations were not being sought. Interaction behaviour was too complex to derive predictive equations with just three separation-to-depth ratios; computational resources limited the number of excavation analyses that could be performed with different mesh geometries.

In total, 60 2-D twin-tunnel consolidation analyses were performed, along with 12 3-D excavation analyses (six geometries, each with two tunnels to excavate).

9.2.4 Definition of interaction settlement

Definition To compare interaction behaviour during twin-tunnel consolidation, a steady-state interaction settlement S_c^{int} was defined:

$$S_c^{int}(x) = S_c^{twin}(x) - \left(S_c^{sgl01}(x) + S_c^{sgl02}(x)\right) \tag{9.1}$$

where:

$S_c^{twin}(x)$	is the steady-state settlement at x after excavation of both tunnels
$S_c^{sgl01}(x)$	is that after excavation of the first tunnel alone
$S_c^{sgl02}(x)$	is that after excavation of the second tunnel alone

S_c^{int} therefore represents the additional settlement incurred during twin-tunnel consolidation compared with the superposition of settlements from the two tunnels consolidating individually.

Non-dimensionalisation The interaction settlement at the mid-line between the two tunnels, S_{cmid}^{int}, is non-dimensionalised by the method described in Section 8.3.3. Thus:

$$NS_{cmid}^{int} = \frac{E'_d}{5D_T L_c \gamma_w} S_{cmid}^{int} \tag{9.2}$$

Different C/D_T ratios were simulated by modelling the same axis depth, but varying the tunnel diameter. Dividing by diameter in Equation 9.2 effectively makes the diameters the same; however, their axis depths then differ by the diameter ratio. After non-dimensionalisation therefore, the tunnel with $C/D_T = 7$ has the same diameter as when $C/D_T = 3$, but is effectively 2.14 times deeper.

9.2.5 Objective of study

Figures 9.1a and b present steady-state interaction settlement troughs for analyses with and without volume loss respectively; results are shown for a fully-permeable lining. Trends are highlighted more clearly in Figure 9.2a, where mid-line interaction settlement is plotted against separation-to-depth ratio (d'/z_0). The figure demonstrates that interaction does not monotonically decrease with separation, as it does during excavation; the relationship is more complex. With only three

d'/z_0 ratios, there were insufficient data points to describe this mathematically, and computational limitations prevented trialling more d'/z_0 ratios. No attempt was made therefore to derive predictive equations; only qualitative identification of interaction mechanisms is presented.

9.3 Proposed interaction mechanisms

9.3.1 Mechanisms A, B and C

Three possible interaction mechanisms are first proposed, based upon the results. These are summarised in Figure 9.3:

Mechanism A: strain field interaction Combination of strains from each tunnel individually causes strains in a twin-tunnel analysis to be larger than those in a single-tunnel analysis, particularly in the region between the tunnels. Since stiffness behaviour is non-linear, the larger strains will cause the soil to soften more; this encourages further straining of the soil. This not only occurs during consolidation; interaction during excavation induces additional softening before consolidation even begins. As a result, any swelling or consolidation is augmented, leading to additional heave or settlement respectively at the surface.

Mechanism B: flow supply restriction For a fully-permeable lining, inflow is governed by the ability of the surrounding soil to supply flow. If two tunnels are closely-spaced, the soil in between must supply both of them, rather than just one. The supply is therefore restricted by the finite permeability of the soil. The reduced drainage leads to less consolidation taking place, and consequently, reduced surface settlement.

Mechanism C: lateral soil compression A fully-permeable lining squats during consolidation, applying horizontal compression to the soil on either side. If two linings are closely-spaced, the soil column in between is compressed on both sides, forcing the column to extend vertically; this reduces the surface settlement.

9.3.2 Mechanisms Ai, Aii and Aiii

For Mechanism A, softening due to different causes have different extents of influence. For instance, softening caused by interaction during excavation induce strains only over a localised region around the tunnel. In contrast, the consolidation strain field induced by drainage into a permeable lining spreads over a much larger region. These different extents of influence cause interaction to vary differently with tunnel separation. To distinguish between these different behaviours, Mechanism A was decomposed into three mechanisms:

Ai: new drainage boundary Interaction of strain fields caused solely by consolidation from introducing a new drainage boundary when the lining is permeable, without volume loss. The interaction can only cause additional consolidation.

Aii: excavation interaction when permeable Softening generated by interaction during excavation augments the interaction consolidation strain of Mechanism Ai.

Aiii: excavation interaction when impermeable Swelling occurs with an impermeable lining; in a manner analogous to Mechanism Aii, interaction during excavation causes further swelling.

9.4 Simulation results & discussion

9.4.1 Use of simulation types

Investigation of mechanism characteristics is facilitated by noting three different types of simulation, which isolate the effect of different mechanisms:

Type 1: permeable with volume loss Mechanisms Ai, Aii, B and C are active when the lining is fully permeable and volume loss is modelled; troughs of interaction settlement are plotted in Figure 9.1a for this type.

Type 2: permeable without volume loss If the lining is fully permeable, but the volume loss is zero, then only Mechanisms Ai, B and C are active; Figure 9.1b presents interaction settlements for this type.

Type 3: impermeable with volume loss If the lining is fully impermeable, but the volume loss is non-zero, then only Mechanism Aiii is active; Mechanism C should not be active in this type because impermeable linings heave instead of squatting. Figure 9.1c presents corresponding interaction settlements.

This section analyses characteristics of each mechanism based upon results from each simulation type. The key findings are summarised in Figure 9.3.

9.4.2 Mechanism Ai

For Type 2, the dependence of interaction settlement on tunnel separation is presented in Figure 9.2a in the plots without volume loss. Only three mechanisms could possibly be active for Type 2: Ai, B and C. Out of these mechanisms, only Mechanism Ai can induce additional consolidation, whilst Mechanisms B and C are only active at very close spacings, and induce additional swelling. From these facts, a curve representing the contribution from Mechanism Ai can be estimated, as shown in the figure.

The Type 2 plot in the figure also shows that, except at very close spacing—when Mechanisms B and C are active—the different C/D_{T} ratios roughly agree; this implies that interaction depends only upon d'/z_0 ratio. This should be expected, since Mechanism Ai dominates at larger separations: the strain field caused by drainage into a tunnel is larger when the tunnel is deeper, explaining the dependence on d'/z_0.

The trend for Mechanism Ai superposed on the data in Figure 9.2a reflects a peak in interaction at intermediate d'/z_0. The reason behind this is revealed when observing vertical interaction strains.

Figure 9.4 illustrates profiles of vertical interaction strain at the mid-line between the tunnels, when the linings are fully permeable; interaction strain is defined analogously to interaction settlement in Equation 9.1.

Figure 9.4a shows the strain profile for Type 2. Interaction consolidation strains from Mechanism Ai are evident when $d'/z_0 = 2.0$, reaching a maximum of around 0.03% around the tunnel. When $d'/z_0 = 0.5$, these consolidation strains superpose with the swelling strains of Mechanisms B and C. The strains from Mechanism

Ai affect a region $\pm\frac{1}{4}W$ from axis level ($W \approx 40$m for $d'/z_0 = 2.0$); as tunnel separation increases, the region expands—however, the magnitude of interaction strain diminishes at the same time. The net result is that surface interaction settlement attains a peak at an intermediate d'/z_0 ratio; here the peak is at $d'/z_0 = 2.0$.

9.4.3 Mechanism Aii

Behaviour for Mechanism Aii can be deduced from Figure 9.2b, which plots the difference in interaction settlement between Types 1 and 2. If the interaction mechanisms can be assumed to act independently, then this difference can be attributed to Mechanism Aii; this being the only mechanism active in Type 1 that is not active in Type 2.

Plotting d'/D_{T} on the x-axis—rather than d'/z_0—reveals a curve which approximately fits the data, as indicated in Figure 9.2b; this suggests that interaction for Mechanism Aii is dependent upon d'/D_{T}. The reason for this is intuitive: Mechanism Aii is associated with softening around a tunnel during excavation, the extent of which is proportional to its diameter; a larger-diameter tunnel would therefore interact more.

An exception to the fitted curve in Figure 9.2b is for the closest spacing, when $C/D_{\mathrm{T}} = 3$; here, interaction settlements are less than half those that the curve predicts. This is where the assumption of independence might become invalid, since Mechanisms B and C are active at low values of W/D_{T} and d'/D_{T}; these mechanisms might then be affected by Mechanism Aii.

Figure 9.4b shows the vertical strain profile for Type 1. Compared with Type 2, Mechanism Aii is additionally active for Type 1. The figure shows that the size of the region affected by interaction from Mechanisms Ai and Aii combined is related to tunnel diameter; the region is smaller for $C/D_{\mathrm{T}} = 7$ (≈ 8m in height) because this was modelled with a smaller-diameter tunnel than when $C/D_{\mathrm{T}} = 3$ (with a region ≈ 17m in height). The region extends over a thickness approximately $\pm 1.3D$ from axis depth. This relationship is expected because the region softened during excavation is approximately proportional to diameter, and Mechanism Aii is associated with this.

9.4.4 Mechanism Aiii

Observing Figure 9.1, interaction settlements for Type 3 are an order of magnitude less than those for Types 1 and 2, implying that interaction from Mechanism Aiii is negligible. This is because swelling strains when the lining is impermeable are significantly weaker in magnitude than consolidation strains with a fully-permeable lining; superposition therefore does not lead to appreciable interaction.

9.4.5 Mechanism B & C

The effects of Mechanisms B and C are similar and difficult to distinguish, so both mechanisms are therefore discussed together to begin with.

For Type 2 in Figure 9.2a, Mechanisms B and C superpose the contribution from Mechanism Ai at very close spacing ($d'/z_0 = 0.5$), to produce the observed interaction heave (positive displacement). Here, $C/D_\mathrm{T} = 3$ encounters about one-and-a-half times the interaction since Mechanisms B and C become more influential as W/D_T reduces—and W/D_T is less for $C/D_\mathrm{T} = 3$ than for $C/D_\mathrm{T} = 7$ at the same value of d'/z_0.

Figure 9.4a shows the vertical strain profile for Type 2. Interaction swelling strains occur only when $d'/z_0 = 0.5$, since Mechanisms B and C are active at very close spacings. This swelling region spans a thickness $\pm W$ from axis level, where W is the pillar width ($W \approx 4$m for $C/D_\mathrm{T} = 3$ and $W \approx 9$m for $C/D_\mathrm{T} = 7$).

Figure 9.4b shows the vertical strain profile for Type 1. As in Figure 9.4a, Figure 9.4b shows interaction swelling strains from Mechanisms B and C superposing those from Mechanism A, for $C/D_\mathrm{T} = 3$ and $d'/z_0 = 0.5$. These swelling strains practically cancel the consolidation strains at axis level.

Flow restriction for Mechanism B One method to find the influence of Mechanism B alone is to observe the inflow into the tunnels. Figure 9.5 plots the distribution of flow velocity around the left of a pair of fully-permeable tunnels at different tunnel spacings, when the volume loss is zero. Flow velocity is normalised by the velocity resulting from radial isotropic flow into a single fully-permeable tunnel, with a drainage distance in the clay of C_clay. The same assumption was adopted

to derive relative soil-lining permeability (RP) in Section 8.4.2. The normalised flow velocity NV is therefore given by:

$$NV = \frac{D_{\mathrm{T}} \ln\left(\dfrac{2C_{\mathrm{clay}}}{D_{\mathrm{T}}} + 1\right)}{2k_{\mathrm{S}}L_c} \cdot v \tag{9.3}$$

where:

C_{clay}	is the clay cover
D_{T}	is the tunnel diameter
k_{S}	is the equivalent soil permeability: $\sqrt{k_{\mathrm{h}}k_{\mathrm{v}}}$
L_c	is the tunnel axis depth below the water table
v	is the flow velocity

The figure shows a severe reduction in flow on the side closest the neighbouring tunnel only for analyses with the closest spacing: for $d'/z_0 = 0.5$; this suggests that Mechanism B is only active at very close spacings.

There is greater interaction when $C/D_{\mathrm{T}} = 3$ compared with when $C/D_{\mathrm{T}} = 7$ ($NV = 0.1$ compared with 0.4). This suggests that Mechanism B is related to pillar width normalised by tunnel diameter, W/D_{T}; when $C/D_{\mathrm{T}} = 3$, W/D_{T} is smaller than when $C/D_{\mathrm{T}} = 7$. This relationship is intuitive because increasing W/D_{T} increases the conductivity of the soil between the tunnels.

Mechanism C is also likely to have a significant influence only upon tunnels with very close spacing, because the horizontal strain causing the interaction was observed to decay rapidly with distance from the tunnel.

9.4.6 Implications for twin-tunnel design

In Section 9.4.1, three different types of simulation were analysed to identify characteristics for each interaction mechanism. The different types were distinguished by relative soil-lining permeability and volume loss; each could therefore represent different tunnelling conditions in the field.

In practice, if the waterproofing of the lining can be considered reasonably effective, then a permeable soil-lining system might comprise a clayey soil, whereas an impermeable system might comprise a sandy soil. For volume loss, a significant

volume loss might represent open-face tunnelling, whilst a near-zero volume loss might represent closed-face tunnelling.

Only particular mechanisms are active for each simulation type, so that certain interaction behaviour (as presented in Figure 9.3) can be expected according to the tunnelling condition; this behaviour is presented below. A fourth type is added so that all tunnelling conditions are covered.

Type 1. Open-face excavation in clayey soil Greatest interaction settlement occurs at intermediate d'/z_0 (≈ 2) due to Mechanism Ai, and at close spacings ($d'/D_\mathrm{T} < 10$) due to Mechanism Aii. This corresponds to large-diameter closely-spaced tunnels excavated at relatively shallow depths; this maximises the influences of both Mechanisms Ai and Aii. Station tunnels—which are likely to possess this geometry—are therefore highly susceptible to interaction settlement after construction.

Interaction heave occurs at very close spacings ($W/D_\mathrm{T} < 4$) due to Mechanisms B and C. In this case, the overall interaction settlement would be reduced.

Type 2. Closed-face excavation in clayey soil Greatest settlement due to interaction occurs at intermediate d'/z_0 (≈ 2) due to Mechanism Ai, corresponding to moderately-spaced tunnels at relatively shallow depths; this might occur when running tunnels diverge and rise to shallower depths to meet with station tunnels.

At very close spacings, ($W/D_\mathrm{T} < 4$) interaction heave occurs due to Mechanisms B and C. Again, in this case, settlement would be counteracted by interaction heave.

Type 3. Open-face excavation in sandy soil Negligible interaction would occur, since only Mechanism Aiii is active.

Type 4. Closed-face excavation in sandy soil No consolidation occurs at all.

Reviewing this interaction behaviour, some more general observations can be stated:

- Interaction settlement—rather than heave—will almost always occur; interaction heave would only occur at relatively close spacings ($W/D_{\mathrm{T}} < 4$). Since settlement usually continues after construction, interaction would nearly always increase its severity.

- In sandy soils, interaction during consolidation would always be negligible, regardless of the tunnelling method.

- If tunnel separation and depth varies along the length of twin tunnels, longitudinal differential settlement is likely to occur, since long-term interaction effects would also vary along the length.

It should be noted that the dependence of interaction upon tunnel geometry quoted here is specific to soil with $k_{\mathrm{h}}/k_{\mathrm{v}} = 2$. The dependence will vary for other permeability anisotropies.

9.5 Importance of interaction

The complexity of twin-tunnel interaction during consolidation prompts the question of whether or not it can be ignored in numerical analyses; this is addressed by Figure 9.6.

The figure compares peak net (accumulated) surface movements for when interaction is and is not considered; when it is not considered, the consolidation movement is the superposition of the movements from two single-tunnel analyses. Maximum values of displacements, slope and strains are plotted. The values before and after consolidation are compared for the two extremes of lining permeability: fully permeable and fully impermeable. The ordinate axes are adjusted so that the value before consolidation on each plot lies along a common line, for more immediate comparison of the effect of consolidation between plots. Only the tunnel geometries exhibiting most interaction are shown, as indicated in Figure 9.2a, for each C/D_{T} ratio.

The figure shows that the relationship between vertical and horizontal movements due to interaction might be complex; interaction might increase vertical movements, whilst horizontal movements might decrease (e.g. by up to 40% with

an impermeable lining). Interaction can have a large influence, causing horizontal movement to increase two-fold, as when $C/D_T = 7$ with a permeable lining; vertical movement can increase by 20%. Interaction can also ameliorate horizontal strains (e.g. decreasing them by up to 50% when $C/D_T = 3$). Interaction has most influence upon permeable linings: when $C/D_T = 7$ for instance, interaction causes maximum horizontal displacement to increase by almost 170% for a permeable lining, but for an impermeable lining, it decreases only by 60%.

Even at moderate separations (in this case, $d'/z_0 = 2.0$), consolidation interaction cannot be ignored; horizontal movements can double, whilst vertical movements could increase significantly as well.

9.6 Summary

A parametric study to investigate the long-term behaviour of twin side-by-side tunnels was performed, investigating the effect of cover-to-diameter ratio (C/D_T), separation-to-depth ratio (d'/z_0), volume loss and relative soil-lining permeability (RP). The study identified three key interaction mechanisms during consolidation; the influence of each depended upon the twin-tunnel geometry and lining permeability.

This led to the proposition of what long-term interaction behaviour to expect for particular tunnelling conditions. Interaction nearly always augments surface settlements, and can also cause longitudinal differential settlements where twin-tunnel geometry varies along a line. Station tunnels, and the adjoining portions of running tunnels, were found to be most susceptible to interaction effects. At very close tunnel spacings, interaction would be reduced, whilst interaction could be considered negligible in sandy soils.

The effect of interaction on net surface movements was also observed. Interaction has different effects on vertical and horizontal interaction movements; horizontal movements can double, whilst vertical movements can also increase significantly. This suggests that twin-tunnel interaction during consolidation should be accounted for in long-term predictions.

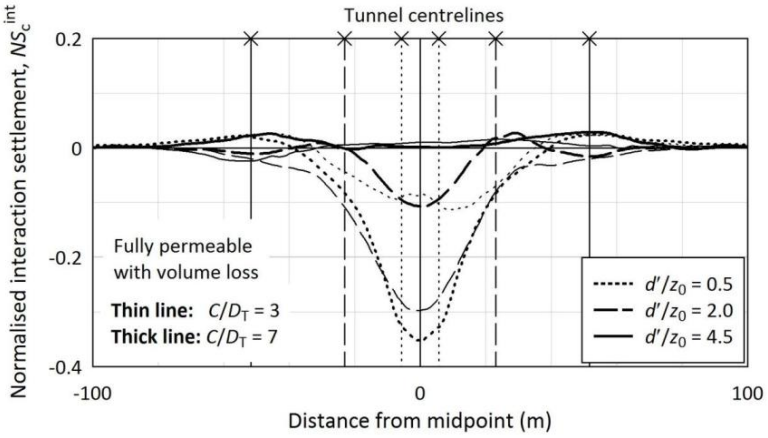

(a) For permeable lining with volume loss

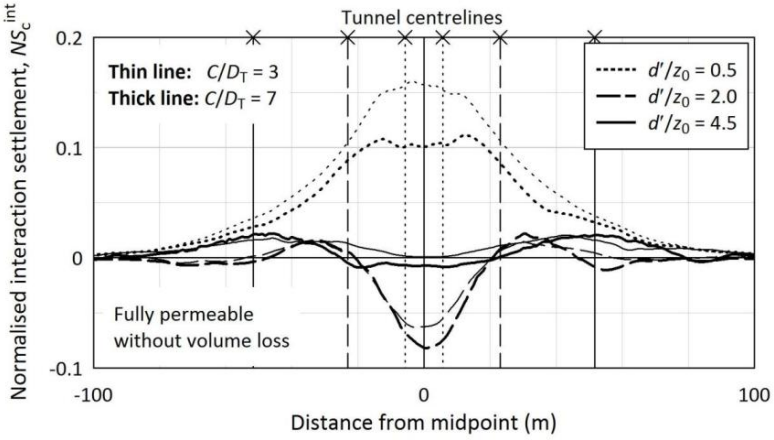

(b) For permeable lining without volume loss

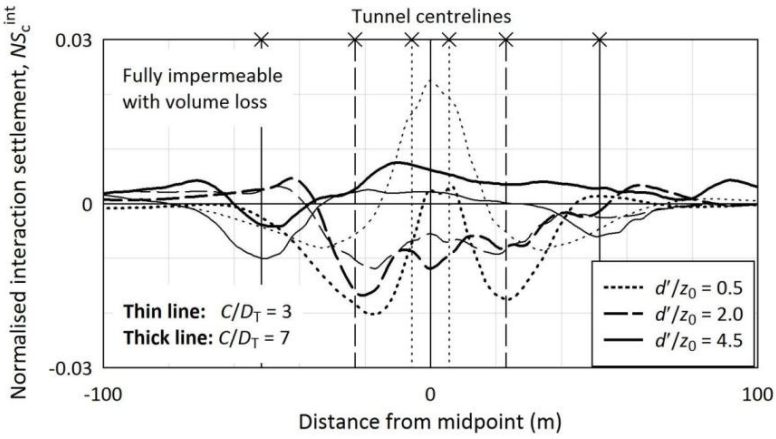

(c) For impermeable lining with volume loss

Figure 9.1: Normalised interaction surface settlement troughs

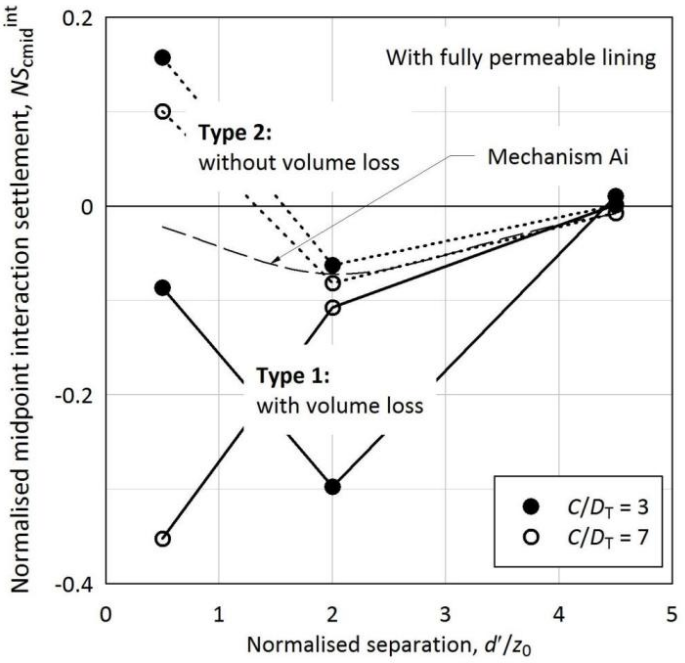

(a) For analyses with and without volume loss

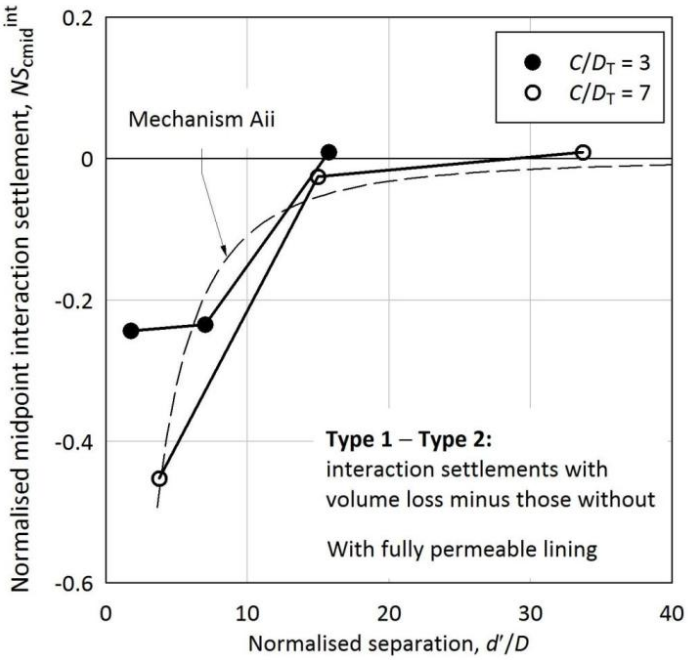

(b) For difference between analyses with and without volume loss

Figure 9.2: Variation of maximum normalised interaction surface settlement with tunnel separation

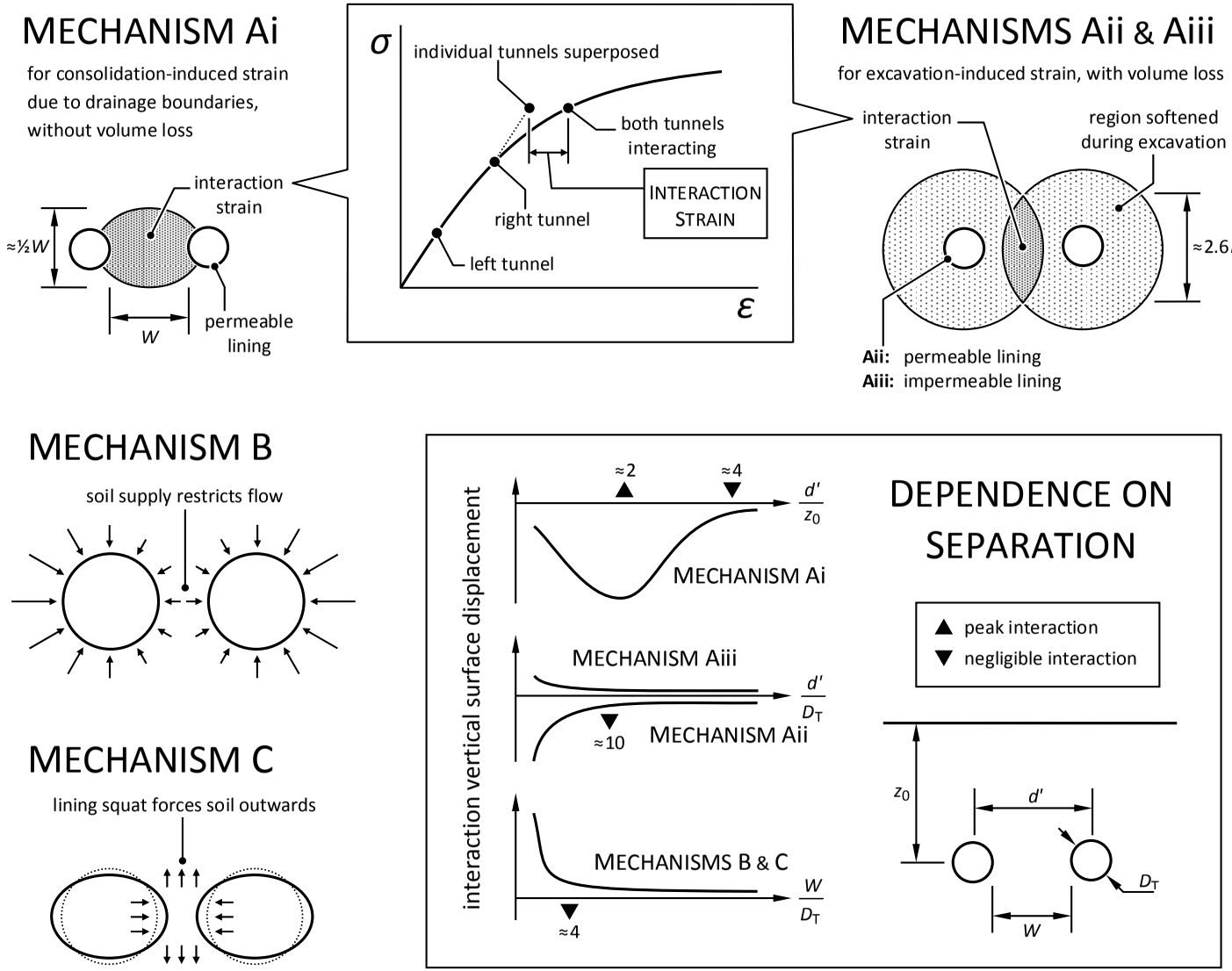

Figure 9.3: Proposed interaction mechanisms

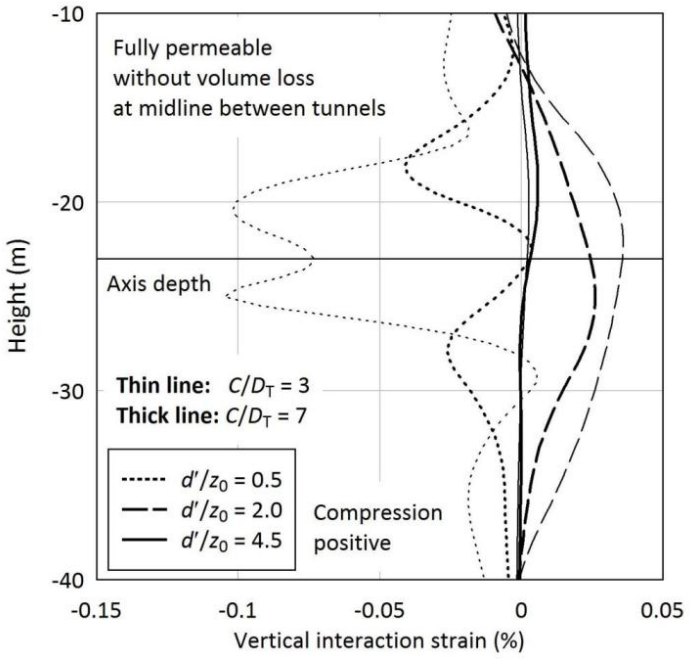

(a) Without volume loss

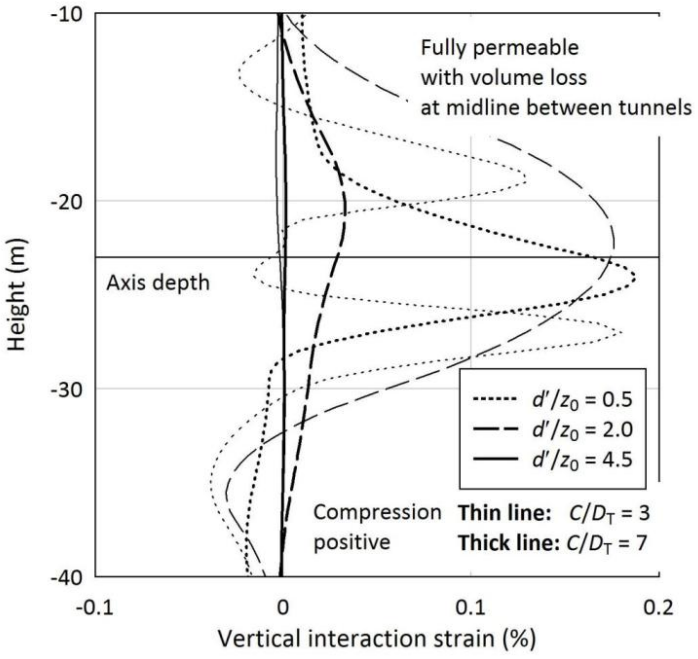

(b) With volume loss

Figure 9.4: Vertical interaction strain profiles for permeable tunnels

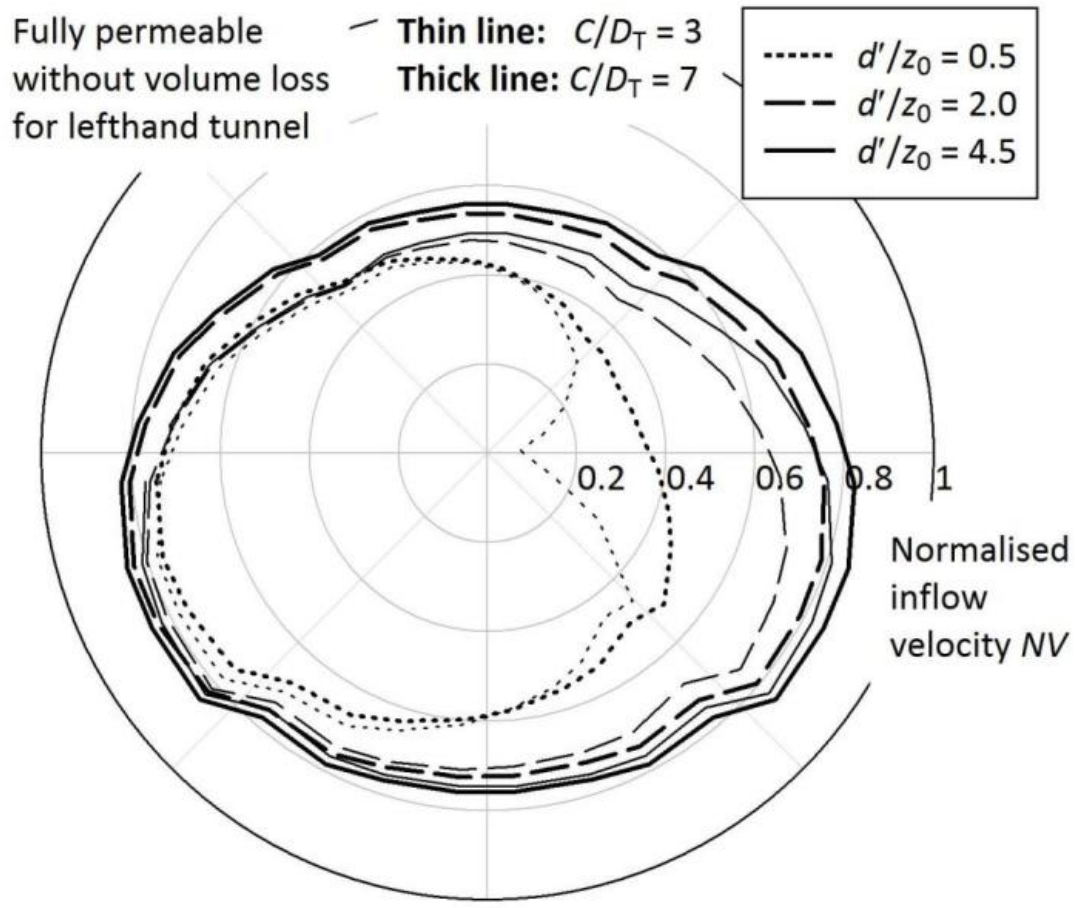

Figure 9.5: Inflow distribution around linings of closely-spaced permeable tunnels

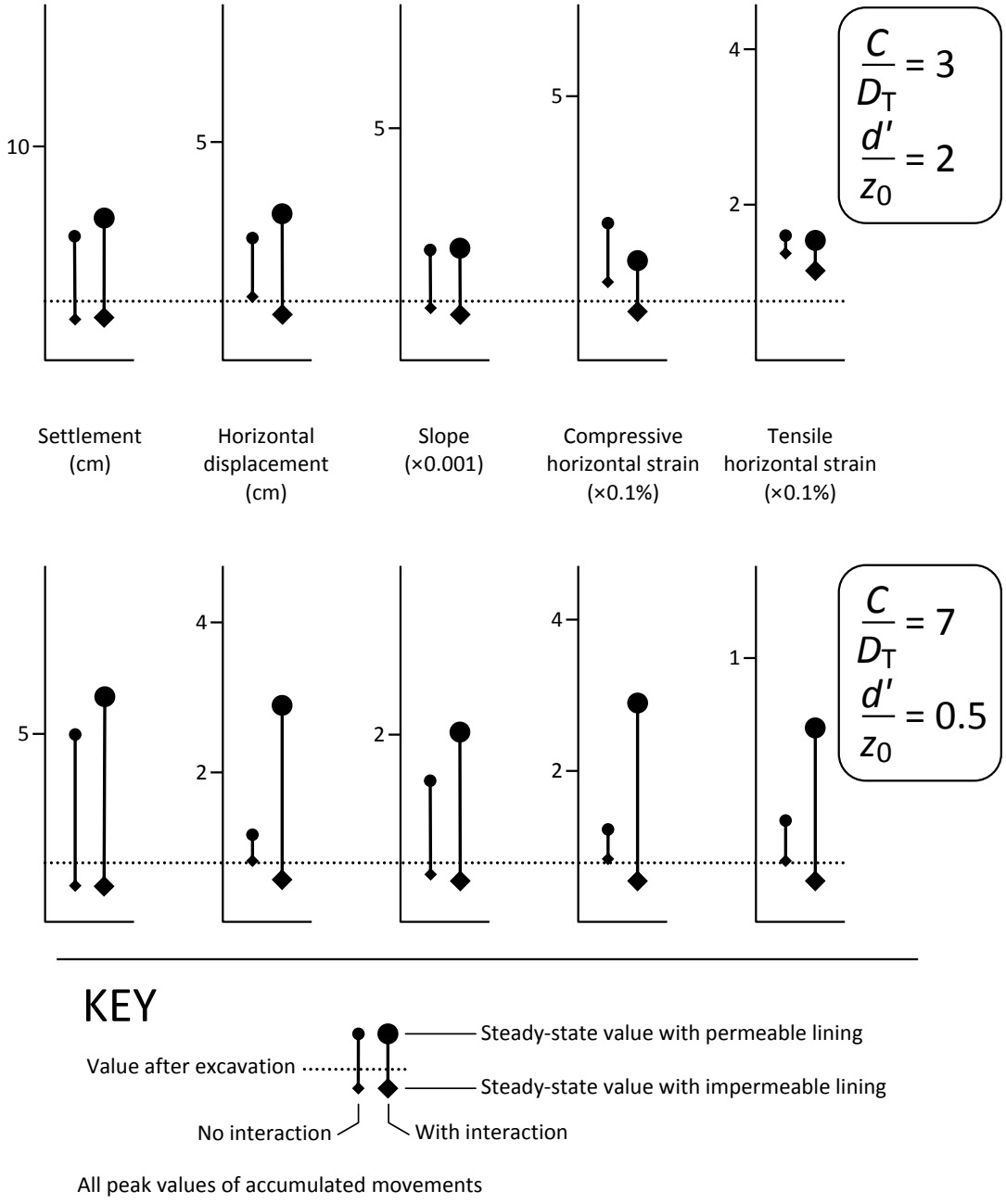

Figure 9.6: Effect of interaction on net surface movements

Chapter 10

Conclusions

10.1 Introduction

Significant long-term movements have been reported around tunnels. Previously, only the long-term behaviour of single tunnels has been investigated (Wongsaroj, 2005). However, many tunnels are constructed in pairs, and little is known about their long-term interaction. To investigate this, a numerical parametric study was conducted into the long-term behaviour of twin side-by-side tunnels. A further study also developed the existing work by Wongsaroj into single-tunnel behaviour. To validate the parametric studies, simulations were performed beforehand to replicate laboratory tests and a twin-tunnel excavation at St James's Park.

Permeability was also investigated because different soil and lining permeabilities can lead to extremes of long-term behaviour, and knowledge of permeabilities limits the accuracy of long-term predictions. The permeability of fissured London Clay and grout from London underground tunnels was therefore investigated in laboratory tests. The experimental results were obtained after the parametric studies were commenced, and so could not be incorporated in the numerical modelling.

10.2 Contributions

10.2.1 Long-term interaction mechanisms

Long-term interaction of tunnels has not previously been studied. The twin-tunnel parametric study identified the key interaction mechanisms summarised below and in Figure 9.3, along with the influence of tunnel geometry:

Mechanism A Due to interaction, larger strains are encountered during twin-tunnel than for single-tunnel construction, causing further soil softening due to lower stiffness at higher strains. This type of interaction can be divided into three sub-mechanisms:

- **Ai** Due to consolidation strains from tunnel drainage, without volume loss, leading to additional consolidation. This is dependent upon separation-to-depth ratio (d'/z_0), with peak interaction attained at an intermediate d'/z_0 ratio.
- **Aii** Due to softening during excavation with a permeable lining, leading to additional consolidation. This increases as separation-to-diameter ratio (d'/D_{T}) reduces.
- **Aiii** Due to softening during excavation with an impermeable lining. This would lead to additional swelling, but in reality this swelling is negligible.

Mechanism B With relatively closely spaced tunnels, the soil between them must supply both, which restricts tunnel inflow. This only occurs with permeable linings, and reduces consolidation. This interaction rises sharply as the normalised pillar width—W/D_{T}—becomes very small.

Mechanism C With relatively closely spaced tunnels, the soil column in between is squeezed vertically outwards by the linings squatting on either side; this reduces consolidation. Lining squat only occurs with permeable linings, and the dependence of this interaction on separation is similar to Mechanism B.

10.2.2 Expectations for long-term interaction behaviour

The following long-term interaction behaviour can be expected under the following tunnelling conditions:

- Under most tunnelling conditions, interaction will induce further surface settlement.
- With open-faced excavation in clayey soil, twin station tunnels represent the twin-tunnel geometry most susceptible to long-term interaction.
- With closed-faced excavation in clayey soil, the portions of twin running tunnel adjoining station tunnels are most susceptible to interaction.
- As tunnels become very closely spaced, settlements caused by interaction reduce.
- Longitudinal variation in twin-tunnel geometry is likely to cause longitudinal differential settlement.
- In sandy soils, long-term interaction can be considered negligible.

10.2.3 Movements causing long-term building damage

Further building damage after excavation is rarely observed and has been attributed to a less severe development in differential settlements and horizontal strains during consolidation (Mair & Taylor, 1997).

However, the parametric studies revealed appreciable increases in net surface movement during consolidation, as shown in Figure 8.14. This is most severe with a permeable lining, where horizontal strains can triple. Added to this, twin-tunnel interaction has a complex effect (Figure 9.6), potentially doubling horizontal movements, whilst also increasing vertical movements significantly.

The apparent contradiction between lack of building damage and large observed movements calls for further investigation.

10.2.4 New relative soil-lining permeability

Wongsaroj (2005) defined a relative soil-lining permeability index as a determinant for long-term behaviour between the two extremes of permeable and impermeable behaviour (Figure 8.4).

A new index was proposed by assuming a more realistic tunnel flow regime, which correlated significantly better with simulated long-term behaviour.

10.2.5 Improved single-tunnel long-term prediction

Wongsaroj (2005) produced normalised charts to predict only long-term surface settlements for a single tunnel. However, horizontal displacements are a key determinant for building damage (Mair & Taylor, 1997).

A more comprehensive prediction method was proposed in Figure 8.6, providing both vertical and horizontal surface displacements, as well as peak horizontal strains. The predictions fitted simulation results well, and successful validation with two case histories demonstrated its applicability. Simple equations instead of charts were used to ease computation.

The method also adopted an intuitive measure for non-dimensional displacement based upon observations of sub-surface consolidation.

The possibility—highlighted in Chapters 4 and 5—for both soil and lining permeabilities to evolve with time suggested that assuming a fully permeable lining would yield conservative predictions.

10.2.6 Improved soil model with fissure softening

Replicating the narrow transverse settlement trough obtained from tunnel excavation in clays has long since presented a challenge for numerical modellers (e.g. Lee & Rowe, 1989). The soil model formulated by Wongsaroj (2005) was modified, leading to narrower troughs in tunnel simulations in Chapter 7 and improved replication of laboratory stress paths in Chapter 6.

Three modifications were trialled. The first modification improved drained behaviour by adjusting model parameters and yield surface rotation. Building upon this modification, the other two modifications replicated fissure plane softening. Initiated according to a frictional criterion, softening occurred isotropically in the

first instance, and solely along the fissure plane in the second. The latter gave poor results, but the former led to significantly improved fits in laboratory test and tunnel simulations, suggesting that fissure softening might be more complex than simple shear plane softening.

The improved fit of the isotropically-softening fissure model was due to the modelling of fissure plane orientations as sub-vertical and sub-horizontal. This softened behaviour in the simple shear mode—where the major principal stress direction for a stress increment is $\alpha_{\mathrm{d}\sigma} \simeq 45°$—and effectively reduced the shear modulus G_{vh}.

This modification demonstrated that a realistic method can replicate the narrow settlement trough in the field better.

10.2.7 Grout deterioration process

Grout is usually assumed to be an impermeable barrier. However, characterisation of the permeability properties of London underground tunnel grout has revealed that deterioration increases the permeability with time in Chapter 5.

Exposure to groundwater causes carbonation and sulphate attack, and subsequent leaching of degradation products could render the grout fully permeable relative to the surrounding clay. The grout would then act as a flow path instead of a barrier.

This has implications on the numerical modelling of lining permeability, and highlights a need to mitigate grout degradation.

10.2.8 Permeability–stress fissure model

The influence of stress on permeability has previously not been investigated for fissured clays. To address this, a model describing this influence was proposed in Figure 4.13, based upon the permeability tests on fissured London Clay under cyclic confining stresses.

In-situ fissure permeability is relatively low due to interlocking fissure surfaces. After extraction however, stress relief allows surface misalignment, causing a high permeability. After this, fissure permeability reduces irrecoverably as the maximum effective stress experienced since misalignment increases; this is due to the

crushing and fracture of asperities separating the fissure surfaces. In contrast, the soil matrix permeability recovers almost elastically upon stress reversal.

A mathematical model to describe this behaviour was proposed in Figure 4.16, with the potential to account for fissure permeability changes during numerical simulations of excavation.

Fissure permeability was also found to eclipse the permeability anisotropy of the soil matrix. Numerical modelling of anisotropic permeability should therefore account for this if fissures open during a simulation.

10.3 Recommendations

10.3.1 Accounting for twin-tunnel interaction

The large and complex influence of interaction during consolidation implies that it should be accounted for in numerical analyses. Modellers should be aware that interaction during the long-term is more widespread than during excavation. In Chapter 3, it was suggested that during excavation, interaction would become negligible if $d'/z_0 > 2$. During consolidation however, twin tunnels interact over a much wider separation—perhaps up to $d'/z_0 = 4$ for $k_\mathrm{h}/k_\mathrm{v} = 2$, as in this thesis, and could interact over wider separations for greater permeability anisotropies. Long-term interaction effects would be particularly severe for station tunnels and the adjoining portions of running tunnel.

10.3.2 Omission of rest period

Excavation of two tunnels is usually separated by a rest period. In long-term twin-tunnel parametric studies, normalising this rest period to enable fair comparison between analyses is difficult because the amount of consolidation during this time depends upon many factors.

It was shown that omitting the rest period altogether provided a convenient and valid solution, which can be adopted in future time-dependent twin-tunnel parametric studies which model London Clay.

10.3.3 Numerical modelling of grout deterioration

Deterioration could cause grout permeability to change from impermeable to permeable with time. The consequent change in flow regime drastically alters the long-term behaviour, so accounting for grout permeability reduction with time would improve the realism of long-term numerical simulations.

Sufficient knowledge of grout deterioration rate would enable a time-dependent lining permeability to be assigned. Otherwise, an impermeable lining could be assumed to obtain maximum lining loads, whilst adopting a permeable lining would give maximum settlements.

10.3.4 Mitigation of grout deterioration

The increase in grout permeability is caused by its deterioration. The severity of this could be reduced by the following methods:

1. **Insertion of geomembrane** A geomembrane between the grout and soil would protect the grout from acidic groundwater. The geomembrane could be applied before lining installation, but would need protection during lining erection, and adequately watertight joints between adjacent membranes. The geomembrane itself would also help make the lining impermeable.

2. **Reduction of porosity** Reducing the grout porosity would decrease the penetration depth of groundwater into the grout, retarding its degradation. A higher water-cement ratio could achieve this, although reduced workability might require addition of plasticizers. Cement-replacement materials could instead be used, for instance, super-pulverized blast furnace slag provides carbonation resistance (Zhang *et al.*, 2004); the more compact structure of hydration products imparts lower porosity.

3. **Reduction of portlandite** The proportion of portlandite in the cement could be reduced by addition of pozzolans. During hydration, pozzolans combine with aqueous portlandite to form calcium silicates and aluminates with cementitious properties (Lea, 1970). As a key reactant for carbonation and sulphur attack, reducing the amount of portlandite would lessen the consequences of such attacks.

4. **Reduction of tricalcium aluminate content** Reducing the content of tricalcium aluminate in Portland cement imparts sulphate resistance (Domone & Jefferis, 1994), since it reacts easily with sulphates.

If successful, these methods would slow the increase in grout permeability with time, and reduce the rate of consolidation movement.

10.3.5 Acquisition of in-situ data

The acquisition of comprehensive permeability and stiffness data during the ground investigation would improve the accuracy of long-term predictions. The accuracy of the long-term single-tunnel predictions in replicating case history data was limited by the determination of soil and lining permeabilities and soil stiffness in the field. The St James's Park validation analyses also highlighted this sensitivity; Wongsaroj (2005) and Mair (2008) made similar observations.

10.4 Future work

10.4.1 Interaction charts for interaction mechanisms

Mechanisms of consolidation interaction depend essentially upon three geometric quantities: d'/z_0, d'/D_{T} and W/D_{T}. This suggests that interaction charts could be constructed as the first step towards predicting consolidation interaction settlement for twin-tunnels.

10.4.2 Horizontal displacement interaction

Interaction effects can double net horizontal surface movements, which theoretically cause building damage. Investigation into the long-term interaction of horizontal movements would help establish the effects of twin-tunnel consolidation on surface structures.

10.4.3 Relating surface movement to building damage

Numerical simulations indicate that movements develop significantly during consolidation, particularly differential settlement and horizontal strain, yet further

building damage is not observed. Further investigation into this apparent contradiction might highlight as yet unforeseen aspects of long-term changes.

10.4.4 Permeable strata

It is common to find permeable strata around tunnels, and this would have a strong influence on long-term behaviour (Harris, 2002; Wongsaroj, 2005). Studying the influence of permeable strata on long-term movements—particularly for twin tunnels—would provide insights applicable to many tunnelling sites.

10.4.5 Improved simple-shear softening

Figure 6.30 presents the observations of Nishimura *et al.* (2007) that London Clay specimens undergoing torsional modes ($\alpha_{d\sigma} \simeq 45°$) fail at lower stresses than those in direct shearing ($\alpha_{d\sigma} \simeq 0°$ and $\alpha_{d\sigma} \simeq 90°$); this anisotropy is also reflected in the stiffnesses. The isotropically-softening fissure model was able to model the softer behaviour in tests with $\alpha_{d\sigma} = 45°$ by softening on sub-horizontal and sub-vertical planes. This fissure model could be made more realistic by softening only the shear stiffness components, whilst maintaining the bulk stiffness.

Another way to improve anisotropic behaviour without modelling fissures is to apply the tangential stress rate, as implemented by Hashiguchi & Tsutsumi (2001). Conventionally, plastic strains evolve only according to the component of stress increment normal to the yield surface; however, Hashiguchi & Tsutsumi introduce a further dependence upon the tangential component, with the effect of reducing strength for stress paths with $\alpha_{d\sigma} \simeq 45°$. Additionally, their model promises to model the post-peak behaviour following shear band formation (Hashiguchi & Tsutsumi, 2003).

However, the implementation is limited to isotropic elasticity; this simplifies the mathematical formulation by maintaining independence between the hardening effects due to normal and tangential components. Generalisation for anisotropic elasticity would allow application to London Clay. Its successful implementation should improve the modelling of narrow settlement troughs in all clays, even without fissures.

10.4.6 Fissure permeability–stress investigation

The variation of fissure permeability with stress is complex, and further laboratory investigation would give deeper insights:

- Trialling different stress paths—such as simple shearing or K_0-consolidation—would relate permeability to shearing conditions.
- If single perfectly-planar fissures could be artificially created, more controlled investigation would be possible. Shear and normal stresses could be applied directly across the fissure, enabling fissure stiffness and strength also to be investigated.

Future permeability experiments should also use threaded instead of push-in fittings to reduce leakage.

The permeability model for fissured soil developed here remains to be validated in a numerical simulation. This might lead to more realistic permeability modelling.

Appendix A

Implementation of Wongsaroj's soil model

This appendix presents details concerning how the London Clay soil model—formulated by Wongsaroj (2005)—is implemented. The sections below are presented in approximately the same order as executed in the constitutive model code.

A.1 Material constants

The material constants defined for the model are:

M	gradient of critical state line in q–p' space
C_b	controls initial gradient of isotropic swelling line at load reversal
ω_s	controls non-linearity of swelling line
D, r	control non-linearity during isotropic loading and unloading
ρ_c	gradient of normal consolidation line in $\log e$–$\log p'$ space
ν_hh, ν_hv, ν_vh	drained Poisson's ratios
$G_\mathrm{hh}/G_\mathrm{vh}$	ratio of shear moduli
u_1, m	control plastic strain within the normal yield surface
β_{11}, β_{22}, β_{33}, β_{12}, β_{13}, β_{23}	components of yield surface rotation tensor

A.2 Stress path reversal parameters

Volumetric and deviatoric strains accumulated since the last stress reversal are updated at each step:

$$^{\Delta 1}\varepsilon_\mathrm{v} = \varepsilon_\mathrm{v} - \varepsilon_{\mathrm{v\,rev}} \tag{A.1a}$$

$$^{\Delta 1}\varepsilon_{\mathrm{s\,ij}} = \varepsilon_{\mathrm{s\,ij}} - \varepsilon_{\mathrm{s\,rev\,ij}} \tag{A.1b}$$

where:

ε_v	is the current volumetric strain
$\boldsymbol{\varepsilon}_\mathrm{s}$	is the current deviatoric strain tensor
$\varepsilon_{\mathrm{v\,rev}}$	is the volumetric strain at the last strain reversal
$\boldsymbol{\varepsilon}_{\mathrm{s\,rev}}$	is the deviatoric strain tensor at the last strain reversal

The current strains are updated during the step by calculating the volumetric and deviatoric strain rates:

$$\dot{\varepsilon}_\mathrm{v} = \dot{\varepsilon}_{\mathrm{ii}} \tag{A.2a}$$

$$\dot{\varepsilon}_{\mathrm{s\,ij}} = \dot{\varepsilon}_{\mathrm{ij}} - \frac{1}{3}\dot{\varepsilon}_\mathrm{v}\delta_{\mathrm{ij}} \tag{A.2b}$$

A stress reversal is defined by a scalar strain amplitude product χ (Pestana, 1994), where:

$$\chi\dot{\chi} = \begin{cases} ^{\Delta 1}\varepsilon_\mathrm{v}\dot{\varepsilon}_\mathrm{v} & \text{for} \quad \dot{\varepsilon}_\mathrm{v} \neq 0 \\ ^{\Delta 1}\varepsilon_{\mathrm{s\,ij}}\dot{\varepsilon}_{\mathrm{s\,ij}} & \text{for} \quad \dot{\varepsilon}_\mathrm{v} = 0 \end{cases} \tag{A.3}$$

The strains at the last stress reversal are then updated:

$$\varepsilon_{\mathrm{v\,rev}} = \begin{cases} \varepsilon_{\mathrm{v\,rev}} & \text{for} \quad \chi\dot{\chi} > 0 \quad \text{(loading)} \\ \varepsilon_{\mathrm{v}} & \text{for} \quad \chi\dot{\chi} \leq 0 \quad \text{(unloading)} \end{cases} \tag{A.4a}$$

$$\boldsymbol{\varepsilon}_{\mathrm{s\,rev}} = \begin{cases} \boldsymbol{\varepsilon}_{\mathrm{s\,rev}} & \text{for} \quad \chi\dot{\chi} > 0 \quad \text{(loading)} \\ \boldsymbol{\varepsilon}_{\mathrm{s}} & \text{for} \quad \chi\dot{\chi} \leq 0 \quad \text{(unloading)} \end{cases} \tag{A.4b}$$

The mean effective stress at the last stress reversal—p'_{rev}—is also updated in a similar way.

Dimensionless distances in stress space since the last stress reversal are defined along the hydrostatic axis and in the deviatoric plane, according to the formulation by Pestana (1994):

$$\xi = \begin{cases} \dfrac{p'}{p'_{\mathrm{rev}}} & \text{for} \quad p' < p'_{\mathrm{rev}} \\ \dfrac{p'_{\mathrm{rev}}}{p'} & \text{for} \quad p' \geq p'_{\mathrm{rev}} \end{cases} \tag{A.5a}$$

$$\xi_{\mathrm{s}} = \left[\left(\eta_{\mathrm{ij}} - \eta_{\mathrm{ij\,rev}} \right) \left(\eta_{\mathrm{ij}} - \eta_{\mathrm{ij\,rev}} \right) \right]^{\frac{1}{2}} \tag{A.5b}$$

where $\eta_{\mathrm{ij}} = s_{\mathrm{ij}}/p'$ represents the stress ratio in three-dimensional stress space, and $\eta_{\mathrm{ij\,rev}}$ is its value at the last stress reversal; deviatoric stress is given by $s_{\mathrm{ij}} = \sigma_{\mathrm{ij}} - p'\delta_{\mathrm{ij}}$.

A.3 Elastic stiffness matrix

The gradient of the swelling line in $\log e$–$\log p'$ space defined by Pestana (1994) was adopted, and is given by:

$$\rho_{\mathrm{r}} = \frac{1 + \omega_{\mathrm{s}}\xi_{\mathrm{s}}}{C_{\mathrm{b}}} \left(\frac{p'}{p_{\mathrm{a}}} \right)^{\frac{1}{2}} + D\left(1 - \xi^{r}\right) \tag{A.6}$$

where p_{a} is the atmospheric pressure. The bulk modulus is then given by:

$$K = \left(\frac{1+e}{e} \right) \frac{p'}{\rho_{\mathrm{r}}} \tag{A.7}$$

and the Young's moduli by:

$$E_{\mathrm{v}} = K\left(1 - 4\nu_{\mathrm{vh}} + \frac{2\nu_{\mathrm{vh}}}{\nu_{\mathrm{hv}}} - \frac{2\nu_{\mathrm{hh}}\nu_{\mathrm{vh}}}{\nu_{\mathrm{hv}}}\right) \tag{A.8a}$$

$$E_{\mathrm{h}} = E_{\mathrm{v}}\frac{\nu_{\mathrm{hv}}}{\nu_{\mathrm{vh}}} \tag{A.8b}$$

One shear modulus is given by:

$$G_{\mathrm{hh}} = \frac{E_{\mathrm{h}}}{2\left(1 + \nu_{\mathrm{hh}}\right)} \tag{A.9}$$

The other shear modulus, G_{vh}, is derived by using the material constant $G_{\mathrm{hh}}/G_{\mathrm{vh}}$. The terms in the 6×6 elastic stiffness matrix $\mathbf{D}^{\mathrm{e}}$ are then defined according to:

$$\begin{bmatrix} \dot{\sigma}_{11} \\ \dot{\sigma}_{22} \\ \dot{\sigma}_{33} \\ \dot{\sigma}_{12} \\ \dot{\sigma}_{13} \\ \dot{\sigma}_{23} \end{bmatrix} = \mathbf{D}^{\mathrm{e}} \begin{bmatrix} \dot{\varepsilon}_{11} \\ \dot{\varepsilon}_{22} \\ \dot{\varepsilon}_{33} \\ \dot{\varepsilon}_{12} \\ \dot{\varepsilon}_{13} \\ \dot{\varepsilon}_{23} \end{bmatrix} \tag{A.10}$$

The matrix is cross-anisotropic, with the 2-direction vertical; thus:

$$\mathbf{D}^{\mathrm{e}} = \frac{1}{\det \mathbf{C}^{\mathrm{e}}} \begin{bmatrix} \mathbf{F} & \mathbf{0} \\ \mathbf{0} & \mathbf{G} \end{bmatrix} \tag{A.11}$$

where:

$$\mathbf{F} = \begin{bmatrix} \frac{1}{E_{\mathrm{v}}}\left(\frac{1}{E_{\mathrm{h}}} - \frac{{\nu_{\mathrm{vh}}}^2}{E_{\mathrm{v}}}\right) & \frac{\nu_{\mathrm{vh}}}{E_{\mathrm{v}}E_{\mathrm{h}}}\left(1 + \nu_{\mathrm{hh}}\right) & \frac{1}{E_{\mathrm{v}}}\left(\frac{{\nu_{\mathrm{vh}}}^2}{E_{\mathrm{v}}} + \frac{\nu_{\mathrm{hh}}}{E_{\mathrm{h}}}\right) \\ \frac{\nu_{\mathrm{vh}}}{E_{\mathrm{v}}E_{\mathrm{h}}}\left(1 + \nu_{\mathrm{hh}}\right) & \frac{1}{{E_{\mathrm{h}}}^2}\left(1 - {\nu_{\mathrm{hh}}}^2\right) & \frac{\nu_{\mathrm{vh}}}{E_{\mathrm{v}}E_{\mathrm{h}}}\left(1 + \nu_{\mathrm{hh}}\right) \\ \frac{1}{E_{\mathrm{v}}}\left(\frac{{\nu_{\mathrm{vh}}}^2}{E_{\mathrm{v}}} + \frac{\nu_{\mathrm{hh}}}{E_{\mathrm{h}}}\right) & \frac{\nu_{\mathrm{vh}}}{E_{\mathrm{v}}E_{\mathrm{h}}}\left(1 + \nu_{\mathrm{hh}}\right) & \frac{1}{E_{\mathrm{v}}}\left(\frac{1}{E_{\mathrm{h}}} - \frac{{\nu_{\mathrm{vh}}}^2}{E_{\mathrm{v}}}\right) \end{bmatrix} \tag{A.12a}$$

$$\mathbf{G} = \begin{bmatrix} G_{\mathrm{vh}} & 0 & 0 \\ 0 & G_{\mathrm{hh}} & 0 \\ 0 & 0 & G_{\mathrm{vh}} \end{bmatrix} \tag{A.12b}$$

and $\mathbf{0}$ is a 3×3 null matrix. The determinant of the compliance matrix $\mathbf{C}^{\mathrm{e}}$ is given by:

$$\det \mathbf{C}^{\mathrm{e}} = \frac{1 + \nu_{\mathrm{hh}}}{E_{\mathrm{v}}E_{\mathrm{h}}}\left[\frac{1 - \nu_{\mathrm{hh}}}{E_{\mathrm{h}}} - \frac{2{\nu_{\mathrm{vh}}}^2}{E_{\mathrm{v}}}\right] \tag{A.13}$$

A.4 Stress invariants

Various stress invariants are defined. For the first stress invariant:

$$I' = \sigma_{\mathrm{ii}} \tag{A.14}$$

For the second stress invariant:

$$J = \frac{1}{\sqrt{6}}\sqrt{(\sigma_{11}-\sigma_{22})^2 + (\sigma_{22}-\sigma_{33})^2 + (\sigma_{33}-\sigma_{11})^2 + {\sigma_{12}}^2 + {\sigma_{13}}^2 + {\sigma_{23}}^2} \tag{A.15}$$

Deviatoric stresses are also stated relative to the rotated yield surface axis:

$$\bar{s}_{\mathrm{ij}} = s_{\mathrm{ij}} - p'\beta_{\mathrm{ij}} \tag{A.16}$$

Another stress invariant is therefore defined:

$$\bar{J}_2 = \frac{1}{2}\bar{s}_{\mathrm{ij}}\bar{s}_{\mathrm{ij}} \tag{A.17}$$

A further stress invariant describing the rotation of the yield surface is defined by:

$$J_\beta = \frac{1}{2}\beta_{\mathrm{ij}}\beta_{\mathrm{ij}} \tag{A.18}$$

The third stress invariant is given by the Lode's angle:

$$\theta = -\frac{1}{3}\arcsin\left[\frac{3\sqrt{3}}{2}\frac{\det \mathbf{s}}{J^3}\right] \tag{A.19}$$

where the determinant of the deviatoric stress matrix is given by:

$$\det \mathbf{s} = s_{11}s_{22}s_{33} - s_{11}{s_{23}}^2 - s_{22}{s_{13}}^2 - s_{33}{s_{12}}^2 + 2s_{12}s_{13}s_{23} \tag{A.20}$$

A.5 Failure criterion

The failure criterion proposed by Matsuoka & Nakai (1974) is adopted. The stress ratio at failure, M_θ must be found from:

$$M_\theta = \sqrt{3J_{2\eta}^f} \tag{A.21}$$

where $J_{2\eta}^{f}$ is the solution of the following equation:

$$(C_{\text{MN}} - 3)J_{2\eta}^{f} + \frac{2}{\sqrt{27}}C_{\text{MN}} \sin 3\theta (J_{2\eta}^{f})^{\frac{3}{2}} - (C_{\text{MN}} - 9) = 0 \tag{A.22}$$

where:

$$C_{\text{MN}} = \frac{9 - 3{M_{\text{J}}}^{2}}{\frac{2\sqrt{3}}{9}{M_{\text{J}}}^{3} - {M_{\text{J}}}^{2} + 1} \tag{A.23}$$

and M_{J} is the gradient of the critical state line in J–p' space, given by:

$$M_{\text{J}} = \frac{M}{\sqrt{3}} \tag{A.24}$$

A.6 Subloading surface definition

The normal yield surface proposed by Wheeler (1997) was adopted. In three-dimensional stress space, the sub-loading surface—defined by Hashiguchi & Chen (1998)—is described by:

$$f = 27\bar{J}_2 - \left({M_\theta}^2 - 3J_\beta\right)\left(RI_0' - I'\right)I' \tag{A.25}$$

where I_0' is I' at the intersection of the yield surface with the hydrostatic axis, and R is the ratio of the size of the sub-loading surface relative to the normal yield surface. The variable I_0' is updated at each step, so that R can be evaluated by rearranging Equation A.25 equated to zero:

$$R = \frac{27\bar{J}_2}{1 + \left({M_\theta}^2 - 3J_\beta\right){I_0'}^2} \cdot \frac{I_0'}{I'} \tag{A.26}$$

A.7 Yield surface gradient

The gradient of the yield surface must be evaluated using the chain rule:

$$\frac{\partial f}{\partial \sigma_{\text{ij}}} = \frac{\partial f}{\partial \bar{J}_2} \cdot \frac{\partial \bar{J}_2}{\partial \sigma_{\text{ij}}} + \frac{\partial f}{\partial I'} \cdot \frac{\partial I'}{\partial \sigma_{\text{ij}}} + \frac{\partial f}{\partial M_\theta} \cdot \frac{\partial M}{\partial \theta} \cdot \frac{\partial \theta}{\partial \sigma_{\text{ij}}} \tag{A.27}$$

Each of the terms is evaluated as follows:

$$\frac{\partial f}{\partial \bar{J}_2} = 27 \tag{A.28a}$$

$$\frac{\partial \bar{J}_2}{\partial \sigma_{\mathrm{ij}}} = \bar{s}_{\mathrm{ij}} \tag{A.28b}$$

$$\frac{\partial f}{\partial I'} = \left({M_\theta}^2 - 3J_\beta\right)\left(2I' - RI'_0\right) \tag{A.28c}$$

$$\frac{\partial I'}{\partial \sigma_{\mathrm{ij}}} = \delta_{\mathrm{ij}} \tag{A.28d}$$

$$\frac{\partial f}{\partial M_\theta} = -2(RI'_0 - I')M_\theta I' \tag{A.28e}$$

$$\frac{\partial M_\theta}{\partial \theta} = \frac{-{M_\theta}^2 \cos 3\theta}{3\left(C_{\mathbb{MN}} - 3 + \frac{1}{3}C_{\mathbb{MN}} M_\theta \sin 3\theta\right)} \tag{A.28f}$$

$$\frac{\partial \theta}{\partial \sigma_{\mathrm{ij}}} = \frac{\sqrt{3}}{2J^3 \cos 3\theta}\left(\frac{3\det \mathbf{s}}{J} \cdot \frac{\partial J}{\partial \sigma_{\mathrm{ij}}} - \frac{\partial \det \mathbf{s}}{\partial \sigma_{\mathrm{ij}}}\right) \tag{A.28g}$$

where:

$$\frac{\partial J}{\partial \sigma_{\mathrm{ij}}} = \frac{s_{\mathrm{ij}}}{2J}(2 - \delta_{\mathrm{ij}}) \tag{A.29}$$

And to obtain $\partial \det \mathbf{s}/\partial s_{\mathrm{ij}}$:

$$\frac{\partial \det \mathbf{s}}{\partial s_{11}} = \frac{1}{3}\left(-s_{11}s_{22} - s_{11}s_{33} + 2s_{22}s_{33} - 2{s_{23}}^2 + {s_{13}}^2 + {s_{12}}^2\right) \tag{A.30a}$$

$$\frac{\partial \det \mathbf{s}}{\partial s_{22}} = \frac{1}{3}\left(-s_{11}s_{22} + 2s_{11}s_{33} - s_{22}s_{33} + {s_{23}}^2 - 2{s_{13}}^2 + {s_{12}}^2\right) \tag{A.30b}$$

$$\frac{\partial \det \mathbf{s}}{\partial s_{33}} = \frac{1}{3}\left(2s_{11}s_{22} - s_{11}s_{33} - s_{22}s_{33} + {s_{23}}^2 + {s_{13}}^2 - 2{s_{12}}^2\right) \tag{A.30c}$$

$$\frac{\partial \det \mathbf{s}}{\partial s_{12}} = \frac{\partial \det \mathbf{s}}{\partial s_{21}} = 2(s_{23}s_{13} - s_{33}s_{12}) \tag{A.30d}$$

$$\frac{\partial \det \mathbf{s}}{\partial s_{13}} = \frac{\partial \det \mathbf{s}}{\partial s_{31}} = 2(s_{12}s_{23} - s_{22}s_{13}) \tag{A.30e}$$

$$\frac{\partial \det \mathbf{s}}{\partial s_{23}} = \frac{\partial \det \mathbf{s}}{\partial s_{32}} = 2(s_{12}s_{13} - s_{11}s_{23}) \tag{A.30f}$$

A.8 Plastic multiplier

The plastic multiplier is given by:

$$\lambda = \frac{1}{\Gamma}\left(\frac{\partial f}{\partial \boldsymbol{\sigma}}\right)^T \mathbf{D}^{\mathrm{e}}\dot{\boldsymbol{\varepsilon}} \tag{A.31}$$

where:

$$\Gamma = \left(\frac{\partial f}{\partial \boldsymbol{\sigma}}\right)^T \mathbf{D}^{\mathrm{e}}\left(\frac{\partial f}{\partial \boldsymbol{\sigma}}\right) - \frac{\partial f}{\partial R}U\left\|\frac{\partial f}{\partial \boldsymbol{\sigma}}\right\|_F - \frac{\partial f}{\partial I_0'}H \operatorname{tr}\left(\frac{\partial f}{\partial \boldsymbol{\sigma}}\right) \tag{A.32}$$

To evaluate Γ, H and U are given by:

$$U = u_1\left(\frac{1}{R^m} - 1\right) \tag{A.33a}$$

$$H = \frac{1+e}{e(\rho_{\mathrm{c}} - \rho_{\mathrm{r}})}I_0' \tag{A.33b}$$

The partial derivatives $\partial f/\partial R$ and $\partial f/\partial I_0'$ are given by:

$$\frac{\partial f}{\partial R} = -\left(M_\theta{}^2 - 3J_\beta\right) I_0' I' \tag{A.34a}$$

$$\frac{\partial f}{\partial I_0'} = -\left(M_\theta{}^2 - 3J_\beta\right) R I' \tag{A.34b}$$

The Frobenius norm of the yield surface gradient is given by:

$$\left\|\frac{\partial f}{\boldsymbol{\sigma}_{\mathrm{ij}}}\right\|_F = \sqrt{\sum_{i=1}^{3}\sum_{j=1}^{3}\left|\frac{\partial f}{\partial \sigma_{\mathrm{ij}}}\right|^2} \tag{A.35}$$

A.9 Stress rate and yield surface size

Stress rate is updated according to the plastic multiplier, determining whether behaviour is elastic or elastoplastic:

$$\dot{\sigma} = \begin{cases} \mathbf{D}^{\mathrm{e}}\ \dot{\boldsymbol{\varepsilon}} & \text{for} \quad \lambda < 0 \\ \mathbf{D}^{\mathrm{ep}}\dot{\boldsymbol{\varepsilon}} & \text{for} \quad \lambda \geq 0 \end{cases} \tag{A.36}$$

where:

$$\mathbf{D}^{\mathrm{ep}} = \mathbf{D}^{\mathrm{e}} - \frac{1}{\Gamma}\left(\mathbf{D}^{\mathrm{e}}\frac{\partial f}{\partial \boldsymbol{\sigma}}\right)^T\left(\mathbf{D}^{\mathrm{e}}\frac{\partial f}{\partial \boldsymbol{\sigma}}\right) \tag{A.37}$$

The rate of growth of the normal yield surface is given by:

$$\dot{I}_0' = H\dot{\varepsilon}_{\mathrm{v}}^{\mathrm{p}} \tag{A.38}$$

where the plastic volumetric strain rate is given by:

$$\dot{\varepsilon}_{\mathrm{v}}^{\mathrm{p}} = \lambda \frac{\partial f}{\partial \boldsymbol{\sigma}} \tag{A.39}$$

Appendix B

Implementation of fissure models

B.1 Introduction

This appendix describes the implementation of modifications to account for fissure softening in soil models ModF and ModG, introduced in Chapter 6.

Material constants

The material constants to define fissure softening are:

α_{range}	Maximum inclination of fissure plane to either vertical or horizontal directions
ϕ'_{soft}	Fissure friction angle at onset of softening
ϕ'_{range}	Range of fissure friction angle over which stiffness reduction factor ramps to minimum value
$f_{\text{fiss min}}$	Measure of minimum fissure stiffness

Shorthand notation

Many of the calculation stages below are performed twice: once for the sub-horizontal fissure range, and once for the sub-vertical range. For these stages, the notation x is introduced as shorthand for either h or v to represent the sub-horizontal and sub-vertical ranges respectively.

Ranges of fissure inclination

First, the ranges of fissure inclination are established in the first quadrant:

$$\begin{aligned} \alpha_{\mathrm{h}} &= \alpha_{\mathrm{range}} && \text{for sub-horizontal range} \\ \alpha_{\mathrm{v}} &= \frac{\pi}{2} - \alpha_{\mathrm{range}} && \text{for sub-vertical range} \end{aligned} \tag{B.1}$$

where angles are measured with respect to the horizontal plane. The ranges α_{h} and α_{v} are subsequently referred to by the shorthand notation α_{x}.

B.2 Implementation in 2-D

Softening status record

Throughout the calculation stages, two variables are updated for each fissure inclination range to record the status of fissure softening. These are:

$\alpha_{\mathrm{px\,max}}$	the inclination of the softening plane
$\phi'_{\mathrm{px\,max}}$	the friction angle mobilised on it

These are both initialised as zero, indicating a default status of no softening.

Maximum friction angle test

A simple test is first performed to save further computation if softening is not occurring: if the maximum mobilised friction angle on any plane is less than ϕ'_{soft}, then no further computation is necessary. By considering Mohr's circle, the maximum mobilised friction angle is given by:

$$\phi'_{\mathrm{mob}} = \arcsin\left[\frac{\sqrt{{\sigma_{\mathrm{d}}}^2 + \tau^2}}{\sigma_{\mathrm{m}}}\right] \tag{B.2}$$

where:

$$\sigma_{\mathrm{d}} = \frac{1}{2}(\sigma_{11} - \sigma_{22}) \tag{B.3a}$$

$$\sigma_{\mathrm{m}} = \frac{1}{2}(\sigma_{11} + \sigma_{22}) \tag{B.3b}$$

$$\tau = \sigma_{12} \tag{B.3c}$$

Maximum friction plane test

If $\phi'_{\text{mob}} > \phi'_{\text{soft}}$, then softening will occur if the plane of maximum mobilised friction angle lies within the fissure inclination ranges. Maximum friction angle is mobilised on two planes, at the inclinations:

$$\alpha_{\text{p 1}} = \frac{1}{2}\left[\frac{\pi}{2} - \arctan\left(\frac{\tau}{\sigma_{\text{d}}}\right) + \phi'_{\text{mob}}\right] \tag{B.4a}$$

$$\alpha_{\text{p 2}} = \frac{1}{2}\left[-\frac{\pi}{2} - \arctan\left(\frac{\tau}{\sigma_{\text{d}}}\right) + \phi'_{\text{mob}}\right] \tag{B.4b}$$

If either $\alpha_{\text{p 1}}$ or $\alpha_{\text{p 2}}$ fall within the ranges specified in Equation B.1, then these planes are designated softening planes. If this is true for a range x, then $\phi'_{\text{px max}}$ is set to ϕ'_{mob}, and $\alpha_{\text{px max}}$ is set to either $\alpha_{\text{p 1}}$ or $\alpha_{\text{p 2}}$ accordingly.

Bounds of ranges test

If the plane of maximum friction angle lies outside both fissure inclination ranges, then further searching is necessary to establish whether a softening plane exists. In this case, the planes mobilising the greatest friction angle within each fissure inclination range must be found. In 2-D, these planes will lie at the bounds of the ranges.

For a range x, the friction angles mobilised on these planes are given by:

$$\phi'_{\text{bnd x1}} = \left|\arctan\left(\frac{\sigma_{\text{d}}\sin 2\alpha_{\text{x}} + \tau\cos 2\alpha_{\text{x}}}{\sigma_{\text{m}} + \sigma_{\text{d}}\cos 2\alpha_{\text{x}} - \tau\sin 2\alpha_{\text{x}}}\right)\right| \tag{B.5}$$

$$\phi'_{\text{bnd x2}} = \left|\arctan\left(\frac{-\sigma_{\text{d}}\sin 2\alpha_{\text{x}} + \tau\cos 2\alpha_{\text{x}}}{\sigma_{\text{m}} + \sigma_{\text{d}}\cos 2\alpha_{\text{x}} + \tau\sin 2\alpha_{\text{x}}}\right)\right| \tag{B.6}$$

where α_{x} indicates the inclination at the bound of the range. If either $\phi'_{\text{bnd x1}}$ or $\phi'_{\text{bnd x2}}$ exceeds ϕ'_{soft} for any range x, then $\phi'_{\text{px max}}$ is set to $\phi'_{\text{bnd x1}}$ or $\phi'_{\text{bnd x2}}$ respectively, and $\alpha_{\text{px max}}$ is set to α_{x} or $-\alpha_{\text{x}}$ accordingly.

Element size

Before the stiffness reduction factor can be derived, element size is first taken into account in deriving the minimum stiffness reduction factor, as given by:

$$\zeta_{\mathrm{p\ min}} = \frac{1}{1 + \dfrac{f_{\mathrm{fiss\ min}}}{C_{\mathrm{el}}}} \tag{B.7}$$

where C_{el} is a characteristic element length provided by the numerical solver.

Reduction for isotropic softening

The reduction factor for a range x is given by the following ramped step function:

$$\zeta_{\mathrm{px}} = \begin{cases} \zeta_{\mathrm{p\ min}} & \text{for} \quad \phi'_{\mathrm{px\ max}} < \phi'_{\mathrm{soft}} \\ 1 - \left(\dfrac{\phi'_{\mathrm{px\ max}} - \phi'_{\mathrm{soft}}}{\phi'_{\mathrm{range}}} \right) (1 - \zeta_{\mathrm{p\ min}}) & \text{for} \quad \phi'_{\mathrm{soft}} \leq \phi'_{\mathrm{px\ max}} < \phi'_{\mathrm{soft}} + \phi'_{\mathrm{range}} \\ 1 & \text{for} \quad \phi'_{\mathrm{soft}} + \phi'_{\mathrm{range}} < \phi'_{\mathrm{px\ max}} \end{cases} \tag{B.8}$$

For isotropic softening, the stiffness parameter C_{b} is then reduced by the minimum of the reduction factors ζ_{px} for each range:

$$C_{\mathrm{b}} = \min |\zeta_{\mathrm{ph}}, \zeta_{\mathrm{pv}}| \cdot C_{\mathrm{b\ max}} \tag{B.9}$$

Reduction for directional softening

Directional softening—along the softening plane alone—is never implemented for 2-D numerical modelling in this thesis.

B.3 Implementation in 3-D

Softening status record

The softening status is recorded in a similar way to the 2-D implementation. Since the plane is inclined in three dimensions, the three vector components of the plane

normal—instead of a single angle—require recording; the recorded variables are thus:

$\hat{\mathbf{n}}_{\alpha\mathrm{x}}$	the unit vector normal to the softening plane
$\phi'_{\mathrm{px\,max}}$	the friction angle mobilised on it

Maximum friction angle test

As with the implementation in 2-D, the maximum friction angle is first tested. This is found from the principal stresses—σ_1, σ_2 and σ_3, in order of magnitude—which are provided by the numerical solver:

$$\phi'_{\mathrm{mob}} = \arcsin\left(\frac{\sigma_1 - \sigma_3}{\sigma_1 + \sigma_3}\right) \tag{B.10}$$

No further calculation is required if $\phi'_{\mathrm{mob}} < \phi'_{\mathrm{soft}}$.

Maximum friction plane test

If $\phi'_{\mathrm{mob}} > \phi'_{\mathrm{soft}}$, then it must be established whether any of the two planes of maximum friction angle lie within any of the fissure inclination ranges. If so, this plane is a softening plane.

The bounds of the ranges are first defined with direction cosines. These are compared with the normal vectors to the two planes of maximum friction angle, to find whether the plane lies within a range of fissure inclination.

Direction cosines for ranges The bounds of each range describe conic loci, in three dimensions. For each range, the direction cosine of the surface normal to the cone with respect to the vertical direction is given by:

$$v_{\mathrm{x}} = \cos\alpha_{\mathrm{x}} \tag{B.11}$$

Plane normals Next, the unit normal vectors to the two planes of maximum friction angle must be found. These can be stated with respect to the principal axis coordinate system (σ_1, σ_2, σ_3) as follows:

$$\hat{\mathbf{n}}_{\mathrm{p1}} = \begin{bmatrix} -\sin\alpha_{\mathrm{p}\,1} \\ 0 \\ \cos\alpha_{\mathrm{p}\,1} \end{bmatrix} \tag{B.12a}$$

$$\hat{\mathbf{n}}_{\mathrm{p2}} = \begin{bmatrix} -\sin\alpha_{\mathrm{p}\,2} \\ 0 \\ \cos\alpha_{\mathrm{p}\,2} \end{bmatrix} \tag{B.12b}$$

where:

$$\alpha_{\mathrm{p}\,1} = \frac{1}{4}(\pi + 2\phi'_{\mathrm{mob}}) \tag{B.13a}$$

$$\alpha_{\mathrm{p}\,2} = -\frac{1}{4}(\pi + 2\phi'_{\mathrm{mob}}) \tag{B.13b}$$

These unit normal vectors are then transformed to the material axes, giving:

$$\hat{n}_{\mathrm{m1}\,i} = \mathrm{T}_{\mathrm{pm\,ji}}\hat{n}_{\mathrm{p1}\,j} \tag{B.14a}$$

$$\hat{n}_{\mathrm{m2}\,i} = \mathrm{T}_{\mathrm{pm\,ji}}\hat{n}_{\mathrm{p2}\,j} \tag{B.14b}$$

where $\mathbf{T}_{\mathrm{pm}}$ is a transformation matrix, $\mathrm{T}_{\mathrm{pm\,ij}}$ being the direction cosine of the axis of i-th principal stress with respect to the axis of the j-th material direction.

Comparison Material direction 2 is vertical, and so the second component of $\hat{\mathbf{n}}_{\mathrm{m1}}$ and $\hat{\mathbf{n}}_{\mathrm{m2}}$ is compared with v_{x} for each range x to see whether the plane of maximum friction angle lies within the range. If $\hat{\mathbf{n}}_{\mathrm{m1}\,2}$ or $\hat{\mathbf{n}}_{\mathrm{m2}\,2} > v_{\mathrm{x}}$ then $\hat{\mathbf{n}}_{\alpha\mathrm{x}}$ is set to $\hat{\mathbf{n}}_{\mathrm{m1}}$ or $\hat{\mathbf{n}}_{\mathrm{m2}}$ respectively in Equations B.14a and B.14b, and $\phi'_{\mathrm{px\,max}}$ is set to ϕ'_{mob} in Equation B.10.

Bounds of range test

If the planes of maximum friction angle lie outside the fissure inclination ranges, then the existence of other softening planes within the ranges must be checked. It is assumed that in this case, the plane with the greatest friction angle will lie on

the bounds of each range. This assumption is accurate for implementation in 2-D, whilst in 3-D, it is an acceptable approximation.

To find softening planes on the bounds of the ranges, the plane with the greatest friction angle on the bounds is first found using a numerical method.

The friction angle mobilised on a plane n is found from the principal stresses (Chen & Saleeb, 1994):

$$\phi'_{\mathrm{p\,n}} = \arctan \sqrt{\frac{{\sigma_1}^2 {\hat{n}_{\mathrm{p1}}}^2 + {\sigma_2}^2 {\hat{n}_{\mathrm{p2}}}^2 + {\sigma_3}^2 {\hat{n}_{\mathrm{p3}}}^2}{\left({\sigma_1} {\hat{n}_{\mathrm{p1}}}^2 + {\sigma_2} {\hat{n}_{\mathrm{p2}}}^2 + {\sigma_3} {\hat{n}_{\mathrm{p3}}}^2\right)^2} - 1} \tag{B.15}$$

where $\hat{\mathbf{n}}_{\mathrm{p}} = [\hat{n}_{\mathrm{p1}}\ \hat{n}_{\mathrm{p2}}\ \hat{n}_{\mathrm{p3}}]^{\mathrm{T}}$ is the unit normal vector of the plane with respect to the principal axes. This is derived from the unit normal vector stated with respect to the material axes, $\hat{\mathbf{n}}_{\mathrm{m}}$, through the reverse transformation of Equations B.14a and B.14b:

$$\hat{n}_{\mathrm{p\,i}} = \mathrm{T}_{\mathrm{pm\,ij}}\, \hat{n}_{\mathrm{m\,j}} \tag{B.16}$$

where $\hat{\mathbf{n}}_{\mathrm{m}}$ is given by:

$$\hat{\mathbf{n}}_{\mathrm{m}} = \begin{bmatrix} \sqrt{1 - {v_{\mathrm{x}}}^2} \cos\theta_{\mathrm{n}} \\ v_{\mathrm{x}} \\ \sqrt{1 - {v_{\mathrm{x}}}^2} \sin\theta_{\mathrm{n}} \end{bmatrix} \tag{B.17}$$

The angle θ_{n} is the angle of $\hat{\mathbf{n}}_{\mathrm{m}}$ projected on the horizontal (1–3) plane, and rotates the plane of interest about the vertical axis (2–direction).

The search method evaluates the friction angle on 43 different planes rotated about the vertical axis, evenly distributed within the range $0 \leq \theta < 2\pi$. Out of the friction angles of these planes, the maximum is found, along with one value from each of the planes either side of it. These three friction angles allow a quadratic curve to be fitted, improving the estimate of the maximum.

This quadratic approximation gives θ at the maximum as:

$$\theta_{\max} = \frac{-\det \begin{bmatrix} {\theta_1}^2 & \phi'_{\mathrm{p\,1}} & 1 \\ {\theta_2}^2 & \phi'_{\mathrm{p\,2}} & 1 \\ {\theta_3}^2 & \phi'_{\mathrm{p\,3}} & 1 \end{bmatrix}}{2 \det \begin{bmatrix} \phi'_{\mathrm{p\,1}} & \theta_1 & 1 \\ \phi'_{\mathrm{p\,2}} & \theta_2 & 1 \\ \phi'_{\mathrm{p\,3}} & \theta_3 & 1 \end{bmatrix}} \tag{B.18}$$

where $(\theta_1, \phi'_{\mathrm{p}\,1})$, $(\theta_2, \phi'_{\mathrm{p}\,2})$ and $(\theta_3, \phi'_{\mathrm{p}\,3})$ are the three points for fitting the quadratic curve. A better estimate of maximum friction angle and the plane along which it is mobilised is then obtained by substituting $\theta_{\mathrm{n}} = \theta_{\max}$ into Equation B.17, and using Equations B.15 and B.16. This yields new values of $\hat{\mathbf{n}}_{\mathrm{m}}$ and ϕ'_{p}. If ϕ'_{p} exceeds ϕ'_{soft} for a fissure inclination range x, then these values are used to define $\hat{\mathbf{n}}_{\alpha\mathrm{x}}$ and $\phi'_{\mathrm{px\,max}}$.

Element size

Element size is accounted for in the same way as for the 2-D implementation: by applying Equation B.7.

Reduction for isotropic softening

The stiffness parameter C_{b} is reduced by applying Equations B.8 and B.9; in the same way as for the 2-D implementation.

Reduction for directional softening

For directional softening along the fissure plane, individual terms in the elastic stiffness matrix are adjusted. The terms are adjusted twice: once for each fissure inclination range.

The matrix is originally expressed with respect to the material axes. It is first transformed to axes aligned with the softening fissure plane so that the shear component along the plane can easily be identified and reduced by the corresponding stiffness reduction factor ζ_{px}. The adjusted matrix is then transformed back to the original material axes.

1. Transformation to plane axes The stiffness matrix is first transformed from material axes to fissure plane axes using the transformation tensor $\mathbf{T}_{\mathrm{mf}}$ as follows:

$$\mathrm{D}^{\mathrm{e}}_{\mathrm{f}\,ij} = \mathrm{T}_{\mathrm{mf}\,ik}\mathrm{T}_{\mathrm{mf}\,jl}\mathrm{D}^{\mathrm{e}}{}_{\mathrm{m}\,kl} \tag{B.19}$$

The tensor $\mathbf{T}_{\mathrm{mf}}$ is given by:

$$\mathbf{T}_{\mathrm{mf}} = \begin{bmatrix} \mathbf{T}_{\mathrm{mf}}^{11} & \mathbf{T}_{\mathrm{mf}}^{12} \\ \mathbf{T}_{\mathrm{mf}}^{21} & \mathbf{T}_{\mathrm{mf}}^{22} \end{bmatrix} \tag{B.20}$$

where:

$$\mathbf{T}_{\mathrm{mf}}^{11} = \begin{bmatrix} \mathrm{A}_{11}{}^2 & \mathrm{A}_{12}{}^2 & \mathrm{A}_{13}{}^2 \\ \mathrm{A}_{21}{}^2 & \mathrm{A}_{22}{}^2 & \mathrm{A}_{23}{}^2 \\ \mathrm{A}_{31}{}^2 & \mathrm{A}_{32}{}^2 & \mathrm{A}_{33}{}^2 \end{bmatrix} \tag{B.21}$$

$$\mathbf{T}_{\mathrm{mf}}^{12} = 2 \begin{bmatrix} \mathrm{A}_{11}\mathrm{A}_{12} & \mathrm{A}_{13}\mathrm{A}_{11} & \mathrm{A}_{12}\mathrm{A}_{13} \\ \mathrm{A}_{21}\mathrm{A}_{22} & \mathrm{A}_{23}\mathrm{A}_{21} & \mathrm{A}_{22}\mathrm{A}_{23} \\ \mathrm{A}_{31}\mathrm{A}_{32} & \mathrm{A}_{33}\mathrm{A}_{31} & \mathrm{A}_{32}\mathrm{A}_{33} \end{bmatrix} \tag{B.22}$$

$$\mathbf{T}_{\mathrm{mf}}^{21} = \begin{bmatrix} \mathrm{A}_{11}\mathrm{A}_{21} & \mathrm{A}_{31}\mathrm{A}_{11} & \mathrm{A}_{21}\mathrm{A}_{31} \\ \mathrm{A}_{12}\mathrm{A}_{22} & \mathrm{A}_{32}\mathrm{A}_{12} & \mathrm{A}_{22}\mathrm{A}_{32} \\ \mathrm{A}_{13}\mathrm{A}_{23} & \mathrm{A}_{33}\mathrm{A}_{13} & \mathrm{A}_{23}\mathrm{A}_{33} \end{bmatrix} \tag{B.23}$$

$$\mathbf{T}_{\mathrm{mf}}^{22} = \begin{bmatrix} \mathrm{A}_{11}\mathrm{A}_{22} + \mathrm{A}_{12}\mathrm{A}_{21} & \mathrm{A}_{11}\mathrm{A}_{23} + \mathrm{A}_{13}\mathrm{A}_{21} & \mathrm{A}_{12}\mathrm{A}_{23} + \mathrm{A}_{13}\mathrm{A}_{22} \\ \mathrm{A}_{11}\mathrm{A}_{32} + \mathrm{A}_{12}\mathrm{A}_{31} & \mathrm{A}_{11}\mathrm{A}_{33} + \mathrm{A}_{13}\mathrm{A}_{31} & \mathrm{A}_{12}\mathrm{A}_{33} + \mathrm{A}_{13}\mathrm{A}_{32} \\ \mathrm{A}_{21}\mathrm{A}_{32} + \mathrm{A}_{22}\mathrm{A}_{31} & \mathrm{A}_{21}\mathrm{A}_{33} + \mathrm{A}_{23}\mathrm{A}_{31} & \mathrm{A}_{22}\mathrm{A}_{33} + \mathrm{A}_{23}\mathrm{A}_{32} \end{bmatrix} \tag{B.24}$$

The matrix $\mathbf{A}$ is a 3×3 matrix whose rows comprise the unit vectors of the fissure plane axes. The unit vector described by the last row represents the plane normal. The other rows are defined to complete the orthonormal set. $\mathbf{A}$ is therefore given by:

$$\mathbf{A} = \begin{bmatrix} -p & \dfrac{\hat{n}_{\alpha\mathrm{x}\,1}\hat{n}_{\alpha\mathrm{x}\,2}}{p} & \dfrac{\hat{n}_{\alpha\mathrm{x}\,1}\hat{n}_{\alpha\mathrm{x}\,3}}{p} \\ 0 & -\dfrac{\hat{n}_{\alpha\mathrm{x}\,3}}{p} & \dfrac{\hat{n}_{\alpha\mathrm{x}\,2}}{p} \\ \hat{n}_{\alpha\mathrm{x}\,1} & \hat{n}_{\alpha\mathrm{x}\,2} & \hat{n}_{\alpha\mathrm{x}\,3} \end{bmatrix} \tag{B.25}$$

where:

$$p = \sqrt{\hat{n}_{\alpha\mathrm{x}\,2}{}^2 + \hat{n}_{\alpha\mathrm{x}\,3}{}^2} \tag{B.26}$$

and $\hat{\mathbf{n}}_{\alpha\mathrm{x}}$ is the unit normal vector of the softening fissure plane.

2. Stiffness reduction The reduced stiffness matrix with respect to fissure plane axes, $\mathbf{D}_{\mathrm{f}}^{\mathrm{e\,red}}$, is generated by factoring the shear stiffnesses in the plane of the fissure:

$$\mathrm{D}_{\mathrm{f}\,ij}^{\mathrm{e\,red}} = \begin{cases} \zeta_{\mathrm{px}}\mathrm{D}_{\mathrm{f}\,ij}^{\mathrm{e}} & \text{if} \quad i = 4 \quad \text{and} \quad j = 4 \\ \zeta_{\mathrm{px}}\mathrm{D}_{\mathrm{f}\,ij}^{\mathrm{e}} & \text{if} \quad i = 6 \quad \text{and} \quad j = 6 \\ \mathrm{D}_{\mathrm{f}\,ij}^{\mathrm{e}} & \text{otherwise} \end{cases} \tag{B.27}$$

3. Transformation to material axes The matrix is finally transformed back to material axes through the inverse transformation of Equation B.19:

$$\mathrm{D}^{\mathrm{e\,red}}_{\mathrm{m}\,ij} = \mathrm{T}_{\mathrm{fm}\,ik}\mathrm{T}_{\mathrm{fm}\,jl}\mathrm{D}^{\mathrm{e\,red}}_{\mathrm{f}\,kl} \tag{B.28}$$

where the transformation tensor $\mathbf{T}_{\mathrm{fm}}$ is the inverse of $\mathbf{T}_{\mathrm{mf}}$, as follows:

$$\mathbf{T}_{\mathrm{fm}} = \begin{bmatrix} \mathbf{T}^{11\,\mathrm{T}}_{\mathrm{mf}} & 2\mathbf{T}^{21\,\mathrm{T}}_{\mathrm{mf}} \\ \frac{1}{2}\mathbf{T}^{12\,\mathrm{T}}_{\mathrm{mf}} & \mathbf{T}^{22\,\mathrm{T}}_{\mathrm{mf}} \end{bmatrix} \tag{B.29}$$

Appendix C

Derivation of soil parameters by Wongsaroj

This appendix presents the determination of material properties by Wongsaroj (2005) for Made Ground, Terrace Gravel and the Lambeth Group. These properties are presented in Table 7.1.

C.1 Derivation method

Most properties were either taken from previous research, or were assumed by Wongsaroj. The derivation of other properties was more involved:

M Derived from the critical state angle of shearing resistance (ϕ'_{crit}). For the Lambeth Group, only ϕ'_{peak} was available, so $\phi'_{\text{crit}} = \phi'_{\text{peak}}$ was assumed.

$\mathbf{C_b}$ and $\boldsymbol{\omega_s}$ Determined by fitting a stiffness degradation curve to match curves given in literature.

$\boldsymbol{\rho_c}$ Derived from estimates of λ and e_0 using the equation proposed by Pestana (1994):

$$C_c = 2.303\rho_c e_0 \left[1 - \left(\frac{0.4}{e_0}\right)^2\right] \tag{C.1}$$

The compression index C_c was evaluated from λ using the equation: $C_c = \lambda \log_{10} e$.

C.2 Literature sources

The tables below summarise the literature that Wongsaroj used to derive properties for each stratum:

Property		Value	Derivation
		MADE GROUND	
γ	(kN m^{-3})	20	Addenbrooke (1996)
K_0		0.6	Potts & Zdravkovic (2001)
k	(m s^{-1})	10^{-7}	Bolton *et al.* (1998)
p'_0	(kPa)	1000	Bolton *et al.* (1998)
M		0.984	$\phi'_{crit} = 25°$ from Potts & Zdravkovic (2001)
e_0		0.65	assumed by Wongsaroj (2005)
ν		0.2	assumed by Wongsaroj (2005)
u_1		100	assumed by Wongsaroj (2005)
m		0.1	assumed by Wongsaroj (2005)
D		0	assumed by Wongsaroj (2005)
r		0	assumed by Wongsaroj (2005)
C_b		100	assumed by Wongsaroj (2005)
ω_s		15	assumed by Wongsaroj (2005)
ρ_c		0.2476	$\lambda = 0.1$ from Bolton *et al.* (1998)

Terrace Gravel			
Property		Value	Derivation
γ	(kN m^{-3})	20	Hight *et al.* (1993)
K_0		0.5	Hight *et al.* (1993)
k	(m s^{-1})	5×10^{-4}	Nyren (1998)
p'_0	(kPa)	1000	Bolton *et al.* (1998)
M		1.418	$\phi'_{\text{crit}} = 35°$ from Hight *et al.* (1993)
e_0		0.5	assumed by Wongsaroj (2005)
ν		0.2	assumed by Wongsaroj (2005)
u_1		100	assumed by Wongsaroj (2005)
m		0.1	assumed by Wongsaroj (2005)
D		0	assumed by Wongsaroj (2005)
r		0	assumed by Wongsaroj (2005)
C_{b}		400	stiffness degradation curves from Addenbrooke *et al.* (1997) and Hight *et al.* (1993)
ω_{s}		15	stiffness degradation curves from Addenbrooke *et al.* (1997) and Hight *et al.* (1993)
ρ_{c}		0.556	$\lambda = 0.1$ from Bolton *et al.* (1998)

Lambeth Group			
Property		Value	Derivation
γ	(kN m^{-3})	20	Addenbrooke (1996)
K_0		1.5	Addenbrooke (1996)
k	(m s^{-1})	5×10^{-12}	Addenbrooke (1996)
p'_0	(kPa)	3000	assumed by Wongsaroj (2005)
M		1.07	$\phi'_{\text{peak}} = 27°$ from Addenbrooke (1996)
e_0		0.65	assumed by Wongsaroj (2005)
ν		0.2	assumed by Wongsaroj (2005)
u_1		100	assumed by Wongsaroj (2005)
m		0.1	assumed by Wongsaroj (2005)
D		0.05	assumed by Wongsaroj (2005)
r		2	assumed by Wongsaroj (2005)
C_{b}		900	stiffness degradation curves from Addenbrooke *et al.* (1997) and Hight & Jardine (1993)
ω_{s}		50	stiffness degradation curves from Addenbrooke *et al.* (1997) and Hight & Jardine (1993)
ρ_{c}		0.37	$\lambda = 0.15$ from Bolton *et al.* (1998)

Appendix D

Determination of lining thicknesses for parametric study

D.1 Methodology by Wongsaroj (2005)

In conducting his parametric study, Wongsaroj (2005) recognised the need to vary the lining thickness modelled for tunnels of different diameter; this was to maintain the same bending stiffness ratio so that analyses adopting different tunnel diameters could be fairly compared. The bending stiffness ratio α_{bs} was defined by Duddeck & Erdman (1982):

$$\alpha_{\mathrm{bs}} = \frac{E_{\mathrm{S}} {R_{\mathrm{T}}}^3}{E_{\mathrm{T}} I} \tag{D.1}$$

where:

R_{T}	is the tunnel radius
E_{T}	is the lining stiffness
E_{S}	is the stiffness of the surrounding soil
I	is the second moment of area of the lining

Wongsaroj determined a suitable value of α_{bs} by averaging the bending stiffness ratio from a variety of tunnels in London Clay. To derive these however,

he needed to assume a linear variation of soil stiffness with depth, as suggested by Addenbrooke (1996). He also neglected the stiffening effect of reinforcement in concrete segments, and the softening effect of lining joints.

For this thesis, construction data for a number of London underground tunnels was available, enabling Wongsaroj's determination of lining thickness to be verified using a different method.

D.2 New methodology

The new method aims to find an effective thickness t_{eff} for a homogeneous unjointed concrete lining which represents the typical bending stiffness of London underground tunnel linings. This consists of the following stages:

1. Collating lining details from a number of London underground tunnels
2. For each lining, deriving t_{eff} and finding the radius to the neutral axis R_{eff} defined as:
$$R_{\text{eff}} = R_{\text{T}} - x_{\text{N}} \tag{D.2}$$
where R_{T} is the external tunnel radius. This accounts for different neutral axis depths x_{N}.
3. Plotting t_{eff} against R_{eff} for the linings, and fitting a proportional relationship—as predicted from Equation D.1 by Duddeck & Erdman (1982) for a homogeneous lining of uniform thickness.
4. From the proportional relationship, deriving values of t_{eff} for the tunnel radii adopted in the parametric study.

Details from 61 linings of the London underground were available, consisting of 56 bolted cast iron linings, 3 bolted spheroidal graphite iron (SGI) linings and 2 expanded concrete linings.

To derive the effective thickness t_{eff}, the effective second moment of area per unit length of tunnel I_{eff} was required. The sections below describe how this was derived for the iron and concrete linings.

D.3 Effective thickness for bolted iron sections

The cast iron and SGI segments had a U-section, with the SGI sections also possessing additional internal webs. Both types of section could be represented by a simplified section with equal bending stiffness, presented in Figure D.1a. The corresponding dimensions for each iron lining are listed in Tables D.1a and b; since the cast iron segments had no internal webs, d_2 and t_{w2} were taken as zero.

For each segment, the second moment of area was calculated, assuming linear elasticity and section thicknesses being much thinner than section depths. This was transformed to that for an equivalent concrete section using the Young's moduli for concrete and iron. For concrete, $E = 28$GPa was assumed, whilst for iron, E was taken from Craig & Muir Wood (1978): for Grade 12 cast iron, $E = 112$GPa, whilst for British Grade 700/2 SGI, $E = 176$GPa.

All of the iron linings had bolted joints; assuming these to have a high stiffness, no correction for joint flexibility was necessary. Finally, the effective thickness t_{eff} was derived, assuming a rectangular section.

D.4 Effective thickness for expanded concrete sections

The expanded concrete sections had double reinforcement, and were symmetrical about the neutral axis. The section can be represented as in Figure D.1b, and the second moment of area was calculated using linear elastic theory. E was assumed as 28GPa and 210GPa for concrete and steel respectively.

Since the expanded lining had flexible joints, the joint stiffness was assumed to be zero. The correction suggested by Muir Wood (1975) was therefore applied to account for joint flexibility:

$$I_{\text{eff}} = \left(\frac{4}{n_{\text{j}}}\right)^2 I_{\text{seg}} \tag{D.3}$$

where I_{eff} is the effective second moment of area accounting for joints, I_{seg} is that of an individual segment, and n_j is the number of joints around a ring. Since key

segments were much narrower than ordinary segments, the two joints on either side of them were therefore treated as one.

Table D.1c presents details of the two concrete linings considered.

D.5 Selection for parametric study

Figure D.2 plots effective thickness t_{eff} against effective radius R_{eff} for each lining.

A strong linear trend is evident in the bolted cast iron linings. A weaker linear trend is also indicated by the bolted SGI and expanded concrete linings, but with the effective lining thickness almost two times thinner than the bolted cast iron linings. The cast iron linings were constructed earlier when design methods were more conservative; an over-engineered design might therefore explain their greater bending stiffness.

Figure D.2 also superposes a linear fit, from which values were obtained for the parametric study. A single linear fit cannot match all types of lining on the plot; this fit therefore reflects the relative occurrence of each lining type amongst the deep-tube tunnels in London. Around 70% of these tunnels have cast iron linings, whilst practically all the rest have concrete linings (Wright, 2004). SGI linings have only been applied in the Brixton extension of the Victoria line and in the more recent Jubilee line extension. The fit is therefore skewed more towards the data from the cast iron linings.

Selected effective thicknesses for the different cover-to-diameter (C/D_{T}) ratios are summarised below:

C/D_{T}	R_{eff} (m)	t_{eff} (m)
3	3.29	0.20
7	1.53	0.093

Lining number†	External tunnel radius	External web		Internal web		Flange		Neutral axis depth	Second moment of area per unit length		Effective thickness of homogeneous concrete	Effective tunnel radius	Line
		Depth	Thickness	Depth	Thickness	Width	Thickness		For iron	Transformed to concrete‡			
	R_T	d_1	t_{w1}	d_2	t_{w2}	b	t_f	x_N	I_i	I_{cc}	t_{eff}	R_{eff}	
	m	m	m	m	m	m	m	m	$m^4 m^{-1}$	$m^4 m^{-1}$	m	m	
CI01	1.23	0.100	0.0250	0	0	0.600	0.0220	0.0217	1.96E-05	7.82E-05	0.098	1.20	JL
CI02	1.61	0.105	0.0290	0	0	0.600	0.0220	0.0241	2.60E-05	1.04E-04	0.108	1.58	JL
CI03	1.96	0.102	0.0350	0	0	0.508	0.0220	0.0266	3.21E-05	1.29E-04	0.116	1.93	JL
CI04	2.04	0.110	0.0300	0	0	0.600	0.0250	0.0255	3.04E-05	1.22E-04	0.113	2.01	JL
CI05	2.40	0.150	0.0350	0	0	0.600	0.0250	0.0382	9.09E-05	3.64E-04	0.163	2.36	JL
CI06	2.67	0.165	0.0350	0	0	0.600	0.0250	0.0430	1.21E-04	4.86E-04	0.180	2.62	JL
CI07	3.06	0.180	0.0380	0	0	0.600	0.0250	0.0495	1.69E-04	6.75E-04	0.201	3.01	JL
CI08	3.43	0.197	0.0380	0	0	0.457	0.0250	0.0613	2.72E-04	1.09E-03	0.235	3.37	JL
CI09	3.45	0.200	0.0400	0	0	0.600	0.0300	0.0550	2.41E-04	9.65E-04	0.226	3.40	JL
CI10	3.99	0.240	0.0430	0	0	0.600	0.0330	0.0693	4.41E-04	1.76E-03	0.277	3.92	JL
CI11	4.40	0.270	0.0500	0	0	0.600	0.0350	0.0836	7.02E-04	2.81E-03	0.323	4.31	JL
CI12	4.80	0.300	0.0540	0	0	0.600	0.0400	0.0947	1.02E-03	4.09E-03	0.366	4.71	JL
CI13	5.33	0.330	0.0560	0	0	0.600	0.0430	0.1060	1.39E-03	5.58E-03	0.406	5.22	JL
CI14	5.98	0.349	0.0570	0	0	0.458	0.0440	0.1232	2.02E-03	8.08E-03	0.459	5.86	JL
CI15	1.34	0.121	0.0286	0	0	0.508	0.0195	0.0305	4.60E-05	1.84E-04	0.130	1.31	U
CI16	1.69	0.165	0.0349	0	0	0.508	0.0254	0.0457	1.39E-04	5.56E-04	0.188	1.64	U
CI17	2.27	0.140	0.0349	0	0	0.483	0.0254	0.0380	8.73E-05	3.49E-04	0.161	2.23	NL
CI18	1.78	0.114	0.0318	0	0	0.495	0.0222	0.0293	4.27E-05	1.71E-04	0.127	1.75	NL
CI19	2.10	0.194	0.0318	0	0	0.508	0.0222	0.0558	2.06E-04	8.25E-04	0.215	2.04	NL
CI20	1.91	0.124	0.0318	0	0	0.508	0.0222	0.0320	5.39E-05	2.16E-04	0.137	1.87	NL
CI21	1.91	0.124	0.0318	0	0	0.508	0.0222	0.0320	5.39E-05	2.16E-04	0.137	1.87	NL
CI22	1.95	0.124	0.0318	0	0	0.508	0.0222	0.0320	5.39E-05	2.16E-04	0.137	1.92	BL
CI23	1.95	0.124	0.0318	0	0	0.559	0.0222	0.0308	4.97E-05	1.99E-04	0.134	1.92	BL
CI24	2.03	0.114	0.0445	0	0	0.356	0.0286	0.0357	7.24E-05	2.90E-04	0.151	1.99	BL
CI25	1.96	0.102	0.0349	0	0	0.406	0.0222	0.0286	3.81E-05	1.52E-04	0.122	1.93	VL
CI26	1.99	0.124	0.0318	0	0	0.508	0.0222	0.0320	5.39E-05	2.16E-04	0.137	1.96	U
CI27	2.03	0.124	0.0318	0	0	0.508	0.0222	0.0320	5.39E-05	2.16E-04	0.137	2.00	U
CI28	2.02	0.102	0.0318	0	0	0.508	0.0254	0.0254	2.87E-05	1.15E-04	0.111	1.99	VL
CI29	1.95	0.124	0.0349	0	0	0.508	0.0254	0.0324	5.77E-05	2.31E-04	0.140	1.92	U
CI30	1.95	0.124	0.0318	0	0	0.559	0.0222	0.0308	4.97E-05	1.99E-04	0.134	1.92	U
CI31	2.13	0.130	0.0318	0	0	0.508	0.0222	0.0339	6.28E-05	2.51E-04	0.144	2.10	U
CI32	2.13	0.130	0.0318	0	0	0.508	0.0222	0.0339	6.28E-05	2.51E-04	0.144	2.10	NL
CI33	2.29	0.152	0.0318	0	0	0.508	0.0254	0.0399	1.01E-04	4.04E-04	0.169	2.25	U
CI34	2.59	0.152	0.0318	0	0	0.508	0.0254	0.0399	1.01E-04	4.04E-04	0.169	2.55	U
CI35	2.29	0.152	0.0349	0	0	0.508	0.0254	0.0414	1.09E-04	4.37E-04	0.174	2.24	NL
CI36	2.44	0.152	0.0349	0	0	0.508	0.0254	0.0414	1.09E-04	4.37E-04	0.174	2.40	U

† CI denotes cast iron
‡ Assuming for concrete E = 28 GPa and for cast iron E = 112 GPa

BL Bakerloo Line
JL Jubilee Line
NL Northern Line
U Unknown
VL Victoria Line

(a) For first 36 bolted cast iron linings

Table D.1: Details of equivalent segment cross-sections from London underground linings

Lining number†	External tunnel radius	External web		Internal web		Flange		Neutral axis depth	Second moment of area per unit length		Effective thickness of homogeneous concrete	Effective tunnel radius	Line
		Depth	Thickness	Depth	Thickness	Width	Thickness		For iron	Transformed to concrete‡			
	R_T	d_1	t_{w1}	d_2	t_{w2}	b	t_f	x_N	I_i	I_{cc}	t_{eff}	R_{eff}	
	m	m	m	m	m	m	m	m	$m^4\,m^{-1}$	$m^4\,m^{-1}$	m	m	
CI37	2.59	0.152	0.0318	0	0	0.508	0.0254	0.0399	1.01E-04	4.04E-04	0.169	2.55	VL
CI38	2.67	0.152	0.0349	0	0	0.508	0.0254	0.0414	1.09E-04	4.37E-04	0.174	2.63	U
CI39	2.92	0.175	0.0349	0	0	0.508	0.0254	0.0490	1.64E-04	6.58E-04	0.199	2.87	BL
CI40	3.12	0.171	0.0349	0	0	0.457	0.0254	0.0498	1.69E-04	6.77E-04	0.201	3.07	U
CI41	3.12	0.171	0.0349	0	0	0.457	0.0254	0.0498	1.69E-04	6.77E-04	0.201	3.07	NL
CI42	3.14	0.171	0.0381	0	0	0.457	0.0254	0.0514	1.81E-04	7.24E-04	0.206	3.09	U
CI43	3.43	0.197	0.0381	0	0	0.457	0.0286	0.0593	2.74E-04	1.10E-03	0.236	3.37	U
CI44	3.43	0.197	0.0381	0	0	0.457	0.0286	0.0593	2.74E-04	1.10E-03	0.236	3.37	PL
CI45	3.66	0.197	0.0381	0	0	0.381	0.0286	0.0630	3.14E-04	1.26E-03	0.247	3.60	U
CI46	3.73	0.197	0.0381	0	0	0.457	0.0286	0.0593	2.74E-04	1.10E-03	0.236	3.67	VL
CI47	4.04	0.229	0.0381	0	0	0.457	0.0286	0.0714	4.25E-04	1.70E-03	0.273	3.97	U
CI48	4.88	0.305	0.0508	0	0	0.305	0.0381	0.1160	1.64E-03	6.57E-03	0.429	4.76	U
CI49	4.42	0.305	0.0508	0	0	0.457	0.0381	0.1044	1.24E-03	4.96E-03	0.390	4.32	NL
CI50	4.46	0.267	0.0445	0	0	0.457	0.0349	0.0867	7.59E-04	3.03E-03	0.331	4.37	U
CI51	4.42	0.305	0.0476	0	0	0.457	0.0381	0.1024	1.18E-03	4.74E-03	0.385	4.32	PL
CI52	4.57	0.305	0.0508	0	0	0.457	0.0413	0.1025	1.25E-03	5.01E-03	0.392	4.47	U
CI53	4.72	0.305	0.0540	0	0	0.457	0.0413	0.1044	1.31E-03	5.23E-03	0.397	4.62	PO
CI54	4.80	0.305	0.0508	0	0	0.457	0.0413	0.1025	1.25E-03	5.01E-03	0.392	4.70	VL
CI55	4.80	0.305	0.0508	0	0	0.457	0.0381	0.1044	1.24E-03	4.96E-03	0.390	4.70	PO
CI56	4.80	0.305	0.0508	0	0	0.457	0.0381	0.1044	1.24E-03	4.96E-03	0.390	4.70	U
SGI01	1.61	0.110	0.0180	0.080	0.0130	0.600	0.0140	0.0237	1.86E-05	1.17E-04	0.112	1.59	JLE
SGI02	2.04	0.110	0.0180	0.070	0.0130	0.600	0.0140	0.0232	1.81E-05	1.14E-04	0.111	2.01	JLE
SGI03	2.45	0.140	0.0120	0.115	0.0200	0.600	0.0150	0.0297	3.31E-05	2.08E-04	0.136	2.42	JLE
SGI04	2.98	0.105	0.0290	0.070	0.0400	1.000	0.0250	0.0215	1.64E-05	1.03E-04	0.107	2.96	JLE
SGI05	3.03	0.150	0.0130	0.110	0.0130	0.600	0.0150	0.0306	3.71E-05	2.33E-04	0.141	2.99	JLE
SGI06	2.98	0.105	0.0130	0.080	0.0200	0.600	0.0130	0.0213	1.40E-05	8.80E-05	0.102	2.96	JLE
SGI07	3.37	0.115	0.0260	0.090	0.0320	1.000	0.0130	0.0255	2.06E-05	1.30E-04	0.116	3.34	JLE
SGI08	3.40	0.150	0.0130	0.110	0.0130	0.600	0.0150	0.0306	3.71E-05	2.33E-04	0.141	3.37	JLE
SGI09	3.65	0.150	0.0280	0.125	0.0380	1.000	0.0150	0.0369	5.05E-05	3.17E-04	0.156	3.61	JLE
SGI10	3.80	0.160	0.0230	0.145	0.0130	0.600	0.0150	0.0435	7.04E-05	4.42E-04	0.174	3.76	JLE
SGI11	4.15	0.150	0.0380	0.125	0.0400	1.000	0.0130	0.0426	5.90E-05	3.71E-04	0.164	4.11	JLE
SGI12	4.28	0.150	0.0150	0.110	0.0150	0.600	0.0170	0.0315	4.19E-05	2.64E-04	0.147	4.24	JLE
SGI13	4.64	0.140	0.0310	0.115	0.0380	1.000	0.0130	0.0362	4.25E-05	2.67E-04	0.147	4.60	JLE
SGI14	4.89	0.140	0.0330	0.115	0.0380	1.000	0.0140	0.0361	4.46E-05	2.80E-04	0.150	4.85	JLE
SGI15	5.15	0.150	0.0370	0.125	0.0520	1.000	0.0150	0.0414	6.22E-05	3.91E-04	0.167	5.11	JLE
SGI16	5.15	0.150	0.0170	0.110	0.0170	0.600	0.0180	0.0328	4.64E-05	2.92E-04	0.152	5.12	JLE

† CI denotes cast iron whilst SGI denotes spheroidal graphite iron
‡ Assuming for concrete E = 28GPa, for cast iron E = 112GPa and for spheroidal graphite iron E = 176GPa

BL Bakerloo Line **PL** Piccadilly Line **U** Unknown
JLE Jubilee Line Extension **PO** Post Office Railway **VL** Victoria Line

(b) For remaining bolted cast iron linings and bolted SGI linings

Table D.1: *cont...* Details of equivalent segment cross-sections from London underground linings

Lining number†	Number of segments (excluding keys)	External tunnel radius	Segment dimensions		Reinforcement details‡		Depth of neutral axis	Second moment of area per unit length		Effective thickness of homogeneous concrete	Effective tunnel radius	Line
			Depth	Width	Depth	Area of layer		For segment*	For homogeneous ring**			
	n_j	R_T	h	b	d	A_{sr}	x_N	I_{seg}	I_{eff}	t_{eff}	R_{eff}	
		m	m	m	m	m^2	m	$m^4\,m^{-1}$	$m^4\,m^{-1}$	m	m	
CC01	12	2.06	0.153	0.610	0.102	9.90E-05	0.0763	2.97E-04	3.30E-05	0.0734	1.98	VL
CC02	12	2.43	0.200	1.000	0.160	1.51E-04	0.1000	6.75E-04	7.50E-05	0.0965	2.33	JLE

† CC denotes expanded concrete lining
‡ All segments with double reinforcement, same top and bottom
* Assuming for concrete E = 28GPa and for reinforcement E = 210GPa
** Reduction according to Muir Wood (1975)

JLE Jubilee Line Extension
VL Victoria Line

(c) For expanded concrete linings

Table D.1: *cont. . .* Details of equivalent segment cross-sections from London underground linings

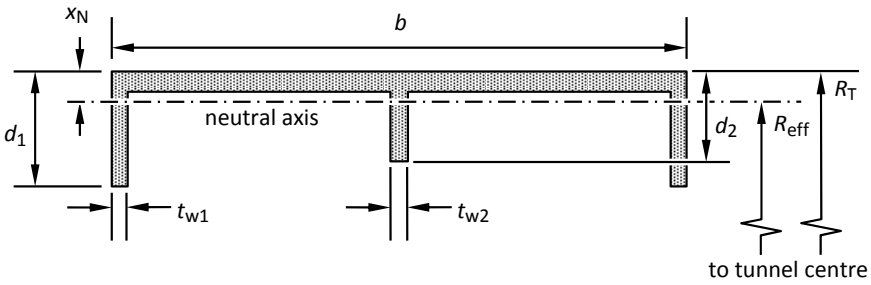

(a) For iron segments

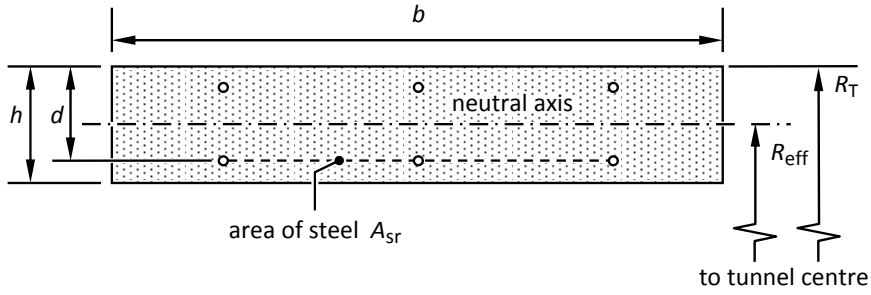

(b) For concrete segments

Figure D.1: Simplified segment cross-sections

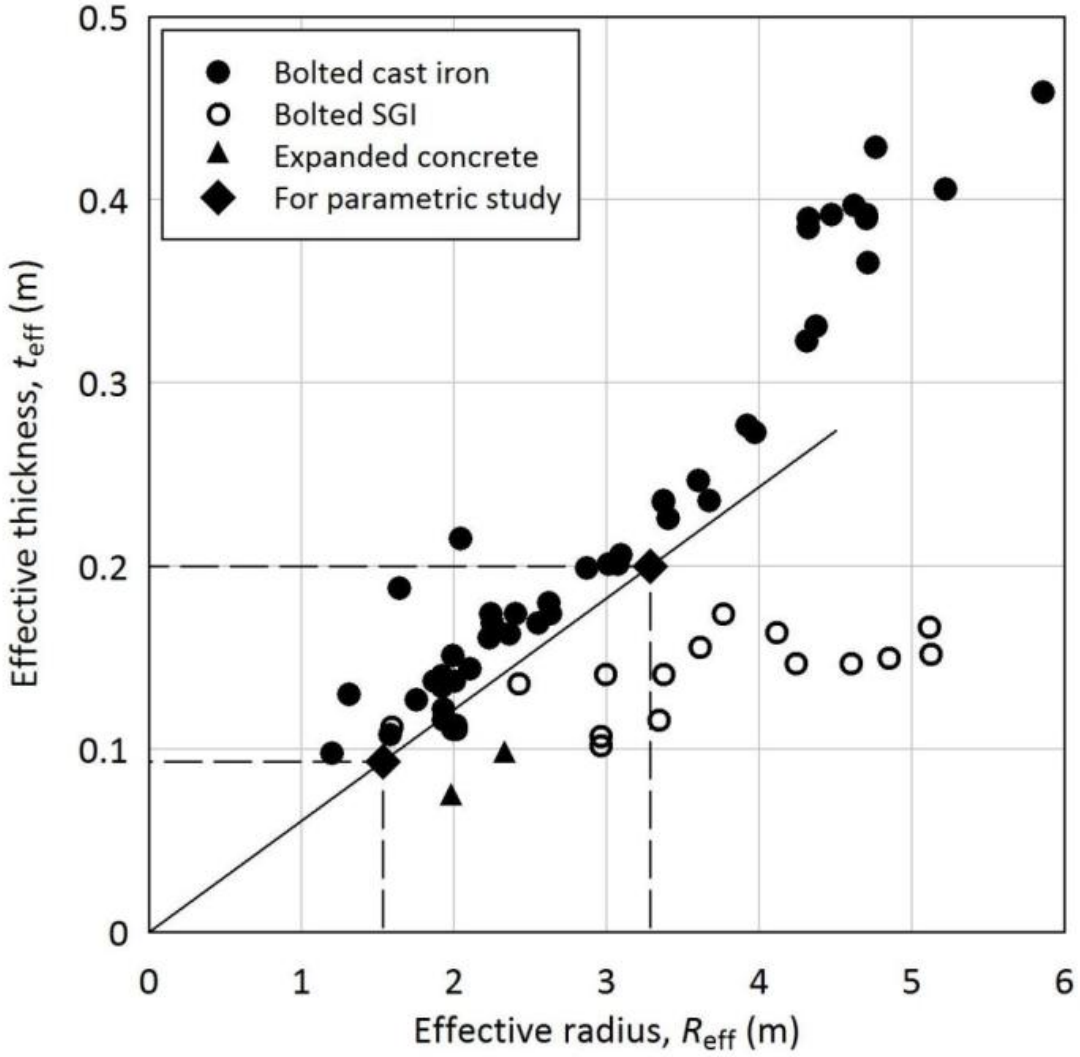

Figure D.2: Effective thicknesses and radii for London underground linings

Appendix E

Determination of tunnel separations for parametric study

E.1 Desired interaction behaviour

The twin-tunnel parametric study of Chapter 9 sought to trial as many different tunnel separations as possible. However, the large computational cost of running the excavation stages on different tunnel geometries restricted the number of tunnel separations that could be trialled to three. It was therefore desired these three tunnel separations would model full interaction, negligible interaction, and intermediate interaction behaviour.

Section 3.3.3 suggested that during excavation, interaction between two side-by-side tunnels would be negligible beyond a separation-to-depth ratio d'/z_0 of 2. However, it is well recognised that consolidation effects spread over a much wider distance than movements during excavation. This is because soil consolidates in a band extending horizontally either side of the tunnel, with the zone widening with increasing permeability anisotropy (Wongsaroj, 2005). This appendix therefore describes a study to identify suitable tunnel separations for the parametric study.

E.2 Normalising separation

Consolidation movements arise from two sources: the dissipation of excess pore pressures generated during excavation, and drainage into the tunnel lining. For a permeable lining, movements due to the latter are likely to be significantly greater than those of the former. The extent of these movements depends upon the extent of pore pressure drawdown around the tunnel; this in turn depends upon the tunnel depth, since a deeper tunnel will reduce pore pressures over a wider zone. A suitable parameter to normalise tunnel centreline separation d' is therefore the tunnel depth z_0. In this case, permeable tunnels with the same value of d'/z_0 should interact to approximately the same extent.

E.3 Seepage analysis details

Suitable values of d'/z_0 to adopt in the parametric study were determined by assessing the pore pressure drawdown between pairs of side-by-side tunnels; this was achieved by conducting 2-D seepage analyses on twin tunnels.

Various tunnel separations were trialled for the two cover-to-diameter (C/D_{T}) ratios of 3 and 7 modelled in the parametric study. To cover an adequate range of d'/z_0, five separations were trialled for $C/D_{\mathrm{T}} = 3$ and six for $C/D_{\mathrm{T}} = 7$.

Mesh dimensions were similar to those adopted in the parametric studies: the tunnels were located at 23m depth, with diameter varied to model the different C/D_{T} ratios. Each mesh was 200m wide, which was sufficient for the far-field pore pressure gradients to be sufficiently low. The height of the meshes was 50m.

An identical soil profile as that used in the parametric studies was adopted—with identical permeabilities—as listed below:

Soil stratum	Depth BGL (m)	k_v (m s^{-1})	k_h/k_v
Made Ground	0–5	10^{-7}	1
Terrace Gravel	5–8	5×10^{-4}	1
London Clay	8–50	2×10^{-11}	2

The linings were assigned a seepage coefficient K_T of $10^{-8}\text{kN}^{-1}\text{m}^3\text{s}^{-1}$: large enough to render it fully permeable relative to the soil. The initial pore pressure distribution was assumed to be hydrostatic, with the water table located at 5m depth. To simulate drainage into the tunnels, atmospheric pressure was applied at both tunnel boundaries, whilst the far-field boundaries were maintained with hydrostatic pore pressure. Pore pressures at the ground surface and at the model base were also maintained at the original values to model recharge boundaries. The analyses were run until the steady-state condition was reached.

E.4 Selection for parametric study

The steady-state pore pressure u_{ss} at axis depth, at a point midway between the two tunnels, was taken to indicate the degree of consolidation interaction. A normalised pore pressure drop was defined with respect to the far-field pore pressure u_{ff} as follows:

$$u_{norm} = 1 - \frac{u_{ss}}{u_{ff}} \tag{E.1}$$

This is plotted against the separation-to-depth ratio d'/z_0 in Figure E.1. Even though the larger-diameter tunnels exhibit slightly more interaction than those with a smaller diameter, the data fall within a narrow band.

To obtain the full range of interaction behaviour, separation-to-depth ratios for the parametric study were desired for $u_{norm} = 0.05$, 0.50 and 0.95. The selected d'/z_0 values are highlighted in Figure E.1, and summarised below:

Interaction behaviour	u_{norm}	d'/z_0
Full	0.95	0.5
Intermediate	0.50	2.0
Negligible	0.05	4.5

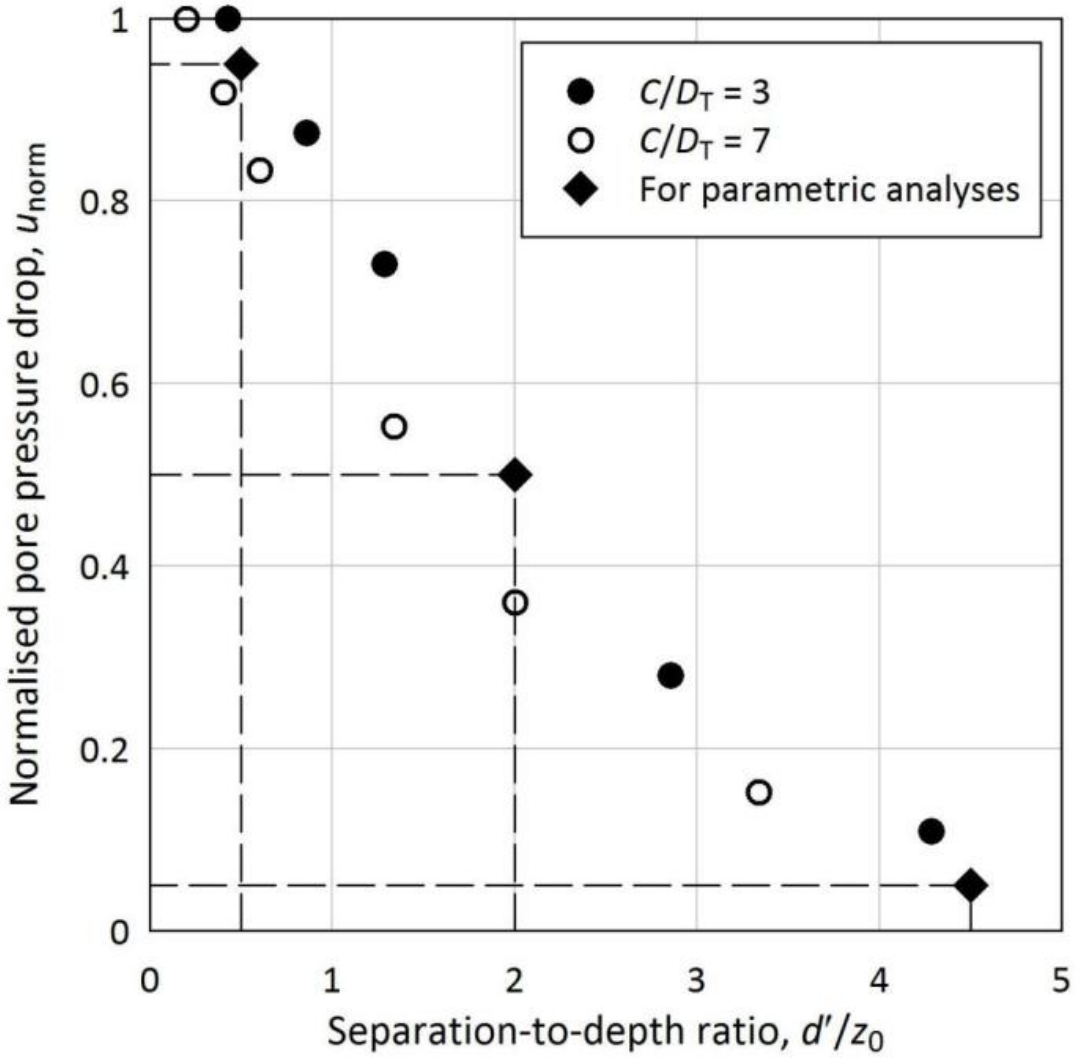

Figure E.1: Mid-point pore pressure drop for different tunnel separations

Appendix F

Influence of omitting rest period

F.1 Omission of rest period

Twin-tunnel construction in the field usually involves a rest period between excavation of each tunnel; however, normalising the rest period to compare different analyses of a parametric study is difficult, since many factors influence the degree of consolidation occurring during the period. These include tunnel geometry, soil and lining permeabilities, and soil stiffness around the tunnel. A convenient solution to this is to omit the rest period altogether, so that the second tunnel is excavated immediately after completion of the first. This enables fair comparison between analyses in the parametric study of Chapter 9.

F.2 Analyses comparing rest period

Since in reality, a finite rest period exists between tunnel excavations, it is helpful to know what difference is made by omitting the rest period. For this purpose, two analyses were compared:

1. One without a rest period between excavations
2. One including a rest period of 60 days

Sixty days was deemed a typical rest period for construction in the field.

The analyses were conducted in the same way as those in the parametric study—described in Chapter 8—except for the inclusion of a rest period. The lining permeability and tunnel configuration were selected to give the maximum consolidation changes during the rest period. This consisted of adopting the most permeable lining ($K_{\mathrm{T}} = 10^{-8}\mathrm{kN}^{-1}\mathrm{m}^3\mathrm{s}^{-1}$), the closest tunnel separation ($d'/z_0 = 0.5$) and the largest-diameter tunnels ($C/D_{\mathrm{T}} = 3$).

F.3 Influence of omitting rest period

Displacement outputs over two periods were compared:

During excavation The first period compared covered just the excavation of the second tunnel. By considering incremental displacements during this period, the impact upon excavation movements was highlighted.

At steady-state The second period extended from the greenfield condition until attainment of steady-state, after the second excavation. Displacements for this period were therefore accumulated over both excavations, the intermediate rest period (if any) and the final consolidation stage. This period therefore highlighted the net effect of rest period on the steady-state condition.

Figure F.1a shows deformed lining shapes, applying different displacement scale factors to different plots to best highlight the influence of rest period. Figure F.1b displays surface displacements. For the second excavation period, these were taken at 8m depth to exclude consolidation movements in the more permeable layers above.

F.3.1 Influence during excavation

The effect of omitting rest period upon the second excavation was to reduce the maximum surface displacement by around 8%. Volume loss into the first tunnel during the excavation increased by 5.2%, whilst volume loss into the second

decreased by 3.7%. Omitting rest period therefore notably affected excavation movements, but the effect was relatively small, and would not be expected to alter patterns of interaction behaviour appreciably.

F.3.2 Influence at steady-state

Steady-state accumulated displacements for the different rest periods demonstrated even smaller differences; maximum surface settlement decreased by less than 1% as a result of omitting rest period. The maximum convergence in diameter for the first tunnel increased by 1.5%, and for the second tunnel, it decreased by 3.5%. Overall, the influence on steady-state displacements was small. This is particularly significant for the parametric study, where consolidation surface displacements are compared. It demonstrates that results from the parametric study would also apply to construction with rest periods below 60 days, and perhaps even longer.

F.3.3 Comparison with literature

In Section 3.3.2, four zones were identified to characterise the influence of rest period upon interaction. The 60-day rest period trialled here—with $T_v \approx 0.003$—falls within the second zone, where rest period has little influence, so confirming observations.

The results verify that omission of rest period provides a valid method of resolving the difficulty of normalising rest period.

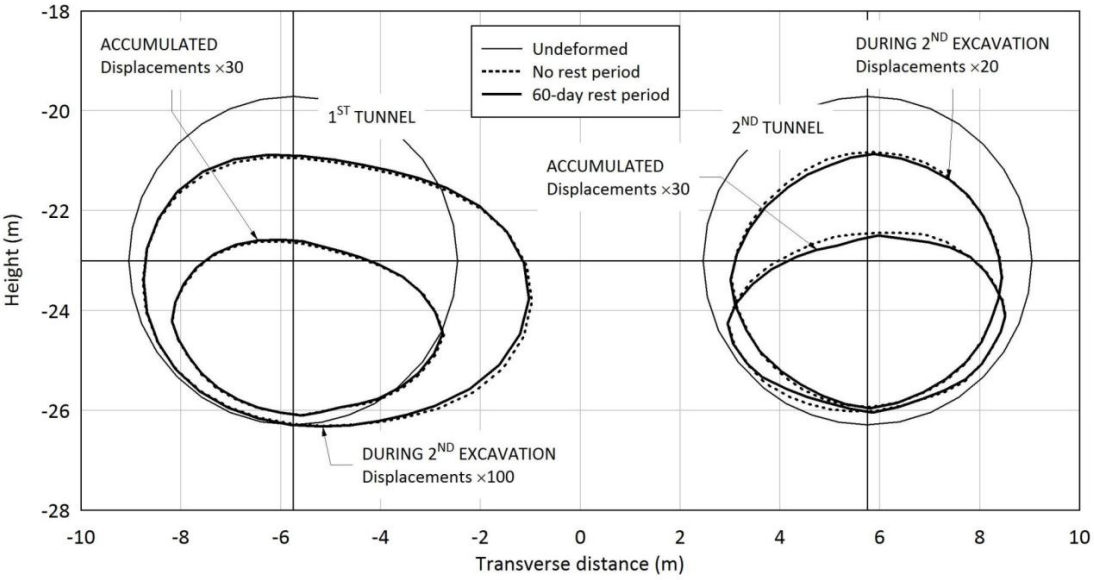

(a) At the lining

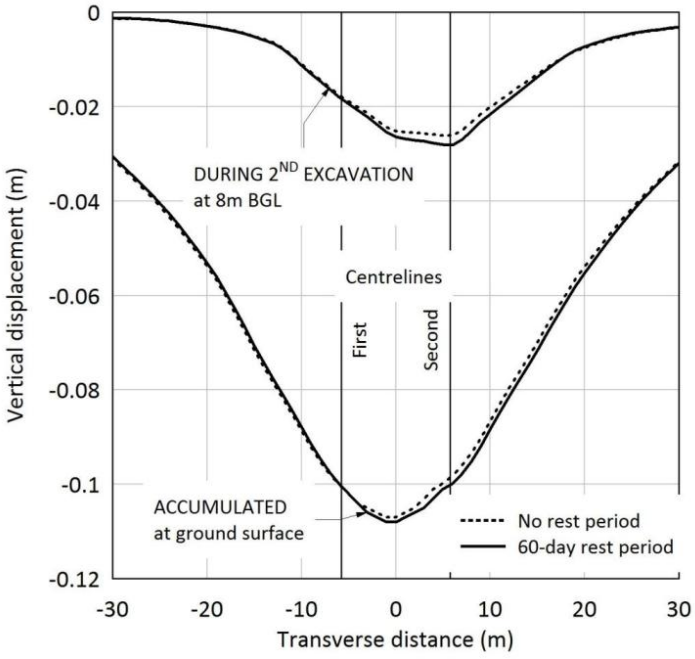

(b) At the ground surface

Figure F.1: Influence of omitting rest period on displacements

References

Addenbrooke, T.I. (1996). *Numerical analysis of tunnelling in stiff clay*. Ph.D. thesis, Imperial Col. Sci. Tech. Med., London.

Addenbrooke, T.I., Potts, D.M. & Puzrin, A.M. (1997). The influence of pre-failure soil stiffness on numerical analysis of tunnel construction. *Géotechnique*, **47**, 693–712.

Akins, K.P. & Abramson, L.W. (1983). Tunnelling in residual soil and rock. In *Proc. Rapid Exc. Tun. Conf.*, 3–24, Chicago.

American Society for Testing and Materials (1997). Standard test method for measurement of hydraulic conductivity of saturated porous materials using a flexible wall permeameter. ASTM Standard D5084-90.

Arandigoyen, M., Bicer-Simsir, B., Alvarez, J.I. & Lange, D.A. (2006). Variation of microstructure with carbonation in lime and blended pastes. *Appl. Surf. Sci.*, **252**, 7562–7571.

Barratt, D.A., O'Reilly, M.P. & Temporal, J. (1994). Long-term measurement of loads on tunnel linings in overconsolidated clay. In *Tunnelling '94*, 469–481, London.

Bennett, P.J., Kobayashi, Y., Soga, K. & Wright, P. (2010a). Wireless sensor network for monitoring transport tunnels. In *Proc. Instn. Civ. Engrs.: Geotech. Engng.*, vol. 163, 147–156.

Bennett, P.J., Soga, K., Wassell, I.J., Fidler, P.R.A., Abe, K., Kobayashi, Y. & Vanicek, M. (2010b). Wireless sensor networks for underground railway applications: case studies in Prague and London. *Smart Struct. & Sys.*, **6**, 619–639.

Bishop, A.W., Webb, D.L. & Lewin, P.I. (1965). Undisturbed sample of London Clay from Ashford Common shaft: strength and effective stress relationships. *Géotechnique*, **15**, 1–31.

Bolton, M.D., Soga, K., Mair, R.J. & Dasari, G.R. (1998). Effect of compensation grouting on tunnel lining. Report to Nishimatsu Constr. Co., Cambridge Univ.

Bowers, K.H. & Redgers, J.D. (1996). Discussion: Observations of lining load in a London clay tunnel. In *Proc. Int. Symp. Geotech. Asp. Undergnd. Constr. Soft Gnd.*, 335, London.

Bowers, K.H., Hiller, D.M. & New, B.M. (1996). Ground movement over three years at the Heathrow Express Trial Tunnel. In *Proc. Int. Symp. Geotech. Asp. Undergnd. Constr. Soft Gnd.*, 557–562, London.

British Standards Institution (1990a). Methods of test for soils for civil engineering purposes—Part 6: Classification tests. British Standard BS 1377-2:1990.

British Standards Institution (1990b). Methods of test for soils for civil engineering purposes—Part 6: Consolidation and permeability tests in hydraulic cells and with pore pressure measurement. British Standard BS 1377-6:1990.

Burland, J.B. & Hancock, R.J. (1977). Underground car park at the House of Commons, London: Geotech. aspects. *Struct. Engr.*, **55**, 87–100.

Celestino, T.B., Gomes, R.A.M. & Bortolucci, A.A. (2000). Errors in ground distortions due to settlement trough adjustment. *Tun. Undergnd. Space Tech.*, **15**, 97–100.

Celestino, T.B., Giambastiani, M. & Bortolucci, A.A. (2001). Water inflows in tunnels: back-analysis and role of different lining system. In *Proc. 2001 World Tun. Congr. VII*, 547–554, Milano.

Chan, H.T. & Kenney, T.C. (1973). Laboratory investigations of permeability ratio of New Liskeard varved soil. *Can. Geotech. J.*, **10**, 453–472.

Chapman, D.N., Ahn, S.K. & Hunt, D.V. (2007). Investigating ground movements caused by the construction of multiple tunnels in soft ground using laboratory model tests. *Can. Geotech. J.*, **44**, 631–643.

Chen, W.F. & Saleeb, A.F. (1994). *Constitutive equations for engineering materials: elasticity and modeling*, vol. 1. Elsevier, 2nd edn.

Clough, G.W. & Schmidt, B. (1981). *Soft clay engineering*, chap. Design and performance of excavations and tunnels in soft clay, 569–634. Elsevier.

Collepardi, M. (2003). A state-of-the-art review on delayed ettringite attack on concrete. *Cem. & Conc. Comp.*, **25**, 401–407.

Cooper, M.L. & Chapman, D.D. (2000). Settlement, rotation and distortion of Piccadilly Line tunnels at Heathrow. In F. Kusakabe & Miyazaki, eds., *Proc. Int. Symp. Geotech. Asp. Undergnd. Constr. Soft Gnd.*, 213–218, Balkema, Rotterdam.

Cooper, M.L. & Chapman, D.N. (1998). Movement of the Piccadilly Line Tunnels caused by the new Heathrow Express Tunnels. In *Proc. World Tun. Congr. '98 on Tunnels & Metropolises*, 249–254, Balkema, Sao Paulo.

Cooper, M.L., Chapman, D.N. & Rogers, C.D.F. (2002). Prediction of settlement in an existing tunnel caused by the second of twin tunnels. *Transp. Res. Rec.*, 103–112.

Cording, E.J. & Hansmire, W.H. (1975). Displacement around soft ground tunnels. In *Proc.* 5$^{\text{th}}$ *Pan-Amer. Conf. Soil Mech. Found. Engng.*, vol. 4, 571–633, Buenos Aires.

Craig, R.N. & Muir Wood, A.M. (1978). A review of tunnel lining practice in the United Kingdom. Supplementary Report 335, Transp. Road Res. Lab.

De Lory, F.A., Crawford, A.M. & Gibson, M.E.M. (1979). Measurement on a tunnel lining in very dense till. *Can. Geotech. J.*, **16**, 190–199.

Dewhurst, D.N., Aplin, A.C., Sarda, J.P. & Yang, Y. (1998). Compaction-driven evolution of porosity and permeability in natural mudstones: an experimental study. *J. Geophys. Res.*, **103**, 651–661.

Dimmock, P.S. (2003). *Tunnelling induced ground and building movement on the Jubilee Line Extension*. Ph.D. thesis, Cambridge Univ.

Domone, P.L.J. & Jefferis, S.A. (1994). *Structural grouts*. Blackie Academic & Professional.

Duddeck, H. & Erdman, J. (1982). Structural design models for tunnels. In *Tunnelling '82*, 83–91, London.

Eden, W.J. & Bozozuk, M. (1969). Earth pressures on Ottawa outfall sewer tunnel. *Can. Geotech. J.*, **6**, 17–32.

Franzius, J.N. (2003). *Behaviour of buildings due to tunnel induced subsidence*. Ph.D. thesis, Imperial Col. Sci. Tech. Med., London.

Fujita, K. (1981). On the surface settlements caused by various methods of shield tunnelling. In *Proc.* 11$^{\text{th}}$ *Int. Conf. Soil Mech. Found. Engng.*, vol. 4, 609–610.

Gasparre, A. (2005). *Advanced laboratory characterization of London Clay*. Ph.D. thesis, Imperial Col. Sci. Tech. Med., London.

Gasparre, A., Nishimura, S., Coop, M.R. & Jardine, R.J. (2007a). The influence of structure on the behaviour of London Clay. *Géotechnique*, **57**, 19–31.

Gasparre, A., Nishimura, S., Minh, N.A., Coop, M.R. & Jardine, R.J. (2007b). The stiffness of natural London Clay. *Géotechnique*, **57**, 33–47.

Geotechnical Consulting Group (1993). Finite element parametric study on long-term settlement caused by tunnelling. Report to Crossrail.

Ghaboussi, J. & Ranken, R.E. (1977). Interaction between two parallel tunnels. *Int. J. Numer. Anal. Meth. Geomech.*, **1**, 75–103.

Glossop, N.H. & O'Reilly, M.P. (1982). Settlement caused by tunnelling through soft marine silty clay. *Tunnels & Tunnelling*, **14**, 13–16.

Gourvenec, S.M., Mair, R.J., Bolton, M.D. & Soga, K. (2005). Ground conditions around an old tunnel in london clay. *Proc. Instn. Civ. Engrs.: Geotech. Engng.*, **158**, 25–33.

Grant, R.J. & Taylor, R.N. (2000). Tunnelling-induced ground movements in clay. In *Proc. Instn. Civ. Engrs.*, vol. 143, 43–55.

Groves, B.L. (1943). Tunnel lining with special reference to a new form of reinforced concrete. *J. Instn. Civ. Engrs.*, **20**, 29–64.

Hanya, T. (1977). Ground movements due to construction of shield-driven tunnel. In *Proc.* 9th *Int. Conf. Soil Mech. Found. Engng.*, 759–790, Tokyo.

Harris, D.I. (2002). Long term settlement following tunnelling in overconsolidated London Clay. In *Proc.* 3rd *Int. Symp. Geotech. Asp. Undergrnd. Constr. Soft Grnd.*, 393–398, Toulouse.

Hashiguchi, K. & Chen, Z. (1998). Elastoplastic constitutive equation of soils with the subloading surface and the rotational hardening. *Int. J. Numer. Anal. Meth. Geomech.*, **22**, 197–227.

Hashiguchi, K. & Tsutsumi, S. (2001). Elastoplastic constitutive equation with tangential stress rate effect. *Int. J. Plast.*, **17**, 117–145.

Hashiguchi, K. & Tsutsumi, S. (2003). Shear band formation analysis in soils by the subloading surface model with tangential stress rate effect. *Int. J. Plast.*, **19**, 1651–1677.

Hight, D.W. & Jardine, R.J. (1993). Small strain stiffness and strength characteristic of hard London Tertiary clays. In *Proc. Int. Symp. Geotech. Engng. Hard Soils—Soft Rock*, 533–551, Athens.

Hight, D.W., Pickles, A.R., De Moor, E.K., Higgins, K.G., Jardine, R.J., Potts, D.M. & Nyirenda, Z.M. (1993). Prediction and measured tunnel distortions associated with construction of Waterloo International Terminal. In *Proc. Wroth Mem. Symp.: Pred. Soil Mech.*, 317–338, Oxford.

Hight, D.W., Mcmillan, F., Powell, J.J.M., Jardine, R.J. & Allenou, C.P. (2003). Some characteristics of London Clay. In T.S. Tan, K.K. Phoon, D.W. Hight & S. Lerouil, eds., *Proc. Conf. Char. Engng. Prop. Nat. Soils*, vol. 2, 851–907, Balkema, Rotterdam, National University of Singapore.

Hight, D.W., Gasparre, A., Nishimura, S., Minh, N.A., Jardine, R.J. & Coop, M.R. (2007). Characteristics of the London Clay from the Terminal 5 site at Heathrow Airport. *Géotechnique*, **57**, 3–18.

Howland, A.F. (1980). The prediction of the settlement above soft ground tunnels by considering the groundwater response with the aid of flow net constructions. In J.D. Geddes *et al.*, eds., *Proc.* 2nd *Int. Conf.: Grnd. Mvmts. Struct.*, 345–358, Pentech Press, Cardiff.

Hulme, T.W., Shirlaw, J.N. & Hwang, R.N. (1990). Settlements during the underground construction of the Singapore MRT. In *Proc.* 10th *S. E. Asian Geotech. Conf.*, vol. 1, 521–526, Taipei.

Hunt, D.V.L. (2005). *Predicting the ground movements above twin tunnels constructed in London Clay*. Ph.D. thesis, Birmingham Univ.

King, C. (1981). The stratigraphy of the London Basin and associated deposits. Tertiary Research Special Paper 6, Backhuys.

Lea, F.M. (1970). *The chemistry of cement and concrete*. Edward Arnold, 3rd edn.

Lee, K.M. & Rowe, R.K. (1989). Deformations caused by surface loading and tunnelling: the role of elastic anisotropy. *Géotechnique*, **39**, 125–140.

Li, X. & Flores-Berrones, R. (2002). Time-dependent behavior of partially sealed circular tunnels. *Comp. & Geotech.*, **29**, 433–449.

MAIR, R.J. (1994). Discussion on paper 'Long-term movements of loads on tunnel linings in overconsolidated clay' by Barratt et al. In *Tunnelling '94*, Chapman and Hall, London.

MAIR, R.J. (1996). Settlement effects of bored tunnels. In *Proc. Int. Symp. Geotech. Asp. Undergrnd. Constr. Soft Grnd.: Session Report*, 43–53, Balkema, London.

MAIR, R.J. (2008). Tunnelling and geotechnics: new horizons. *Géotechnique*, **58**, 695–736.

MAIR, R.J. & TAYLOR, R.N. (1997). Bored tunnelling in the urban environment. In *Proc.* 14th *Int. Conf. Soil Mech. Found. Engng.*, 2353–2385, Hamburg.

MAIR, R.J., TAYLOR, R.N. & BRACEGIRDLE, A. (1993). Subsurface settlement profiles above tunnels in clays. *Géotechnique*, **43**, 315–320.

MAIR, R.J., TAYLOR, R.N. & BURLAND, J.B. (1996). Prediction of ground movements and assessment of risk of building damage due to bored tunnelling. In *Proc. Int. Symp. Geotech. Asp. Undergrnd. Constr. Soft Grnd.*, 713–718, Balkema.

MARTOS, F. (1958). Concerning an approximate equation of the subsidence trough and its time factors. In *Proc. Int. Strata Control Congr.*, 191–205, Leipzig.

MATSUOKA, H. & NAKAI, T. (1974). Stress deformation and strength characteristics of soil under three different principal stresses. In *Proc. Jap. Soc. Civ. Engrs.*, vol. 232, 59–70.

MATSUOKA, H. & NAKAI, T. (1985). Relationship among Tresca, Mises, Mohr-Coulomb and Matsuoka-Nakai failure criteria. *Soils & Found.*, **25**, 123–128.

MUIR WOOD, A.M. (1975). The circular tunnel in elastic ground. *Géotechnique*, **25**, 115–127.

NEGRO, A., SOZIO, L.E. & FERREIRA, A.A. (1996). Tunnelling in Sao Paulo, Brazil. In R.J. Mair & R.N. Taylor, eds., *Proc. Int. Symp. Geotech. Asp. Undergrnd. Constr. Soft Grnd.*, 295–300, Balkema, London.

New, B.M. & Bowers, K.H. (1994). Ground movement model validation at the Heathrow Express trial tunnel. In *Tunnelling '94*, 310–329, London.

New, B.M. & O'Reilly, M.P. (1991). Tunnelling induced ground movements; predicting their magnitude and effects (invited review paper). In *Proc.* 4th *Int. Conf. Grnd. Mvmts. Struct.*, 671–697, Pentech Press, Cardiff.

Ng, C.W.W., Zhou, X.W. & Chung, J.K.H. (2003). Centrifuge modelling of multiple tunnel interaction in shallow ground. In *Proc. 13th Eur. Conf. Soil Mech. Geotech. Engng.*, vol. 2, 759–762, Prague.

Ng, C.W.W., Lee, K.M. & Tang, D.K.W. (2004). Three-dimensional numerical investigations of new Austrian tunnelling method (NATM) twin tunnel interactions. *Can. Geotech. J.*, **41**, 523–539.

Nishimura, S. (2006). *Laboratory study on anisotropy of natural London Clay*. Ph.D. thesis, Imperial Col. Sci. Tech. Med., London.

Nishimura, S., Minh, N. & Jardine, R. (2007). Shear strength anisotropy of natural London Clay. *Géotechnique*, **57**, 49–62.

Nyren, R.J. (1998). *Field measurements above twin tunnels in clay*. Ph.D. thesis, Imperial Col. Sci. Tech. Med., London.

O'Reilly, M.P. & New, B.M. (1982). Settlements above tunnels in the United Kingdom—their magnitude and prediction. In *Tunnelling '82*, 173–181, London.

O'Reilly, M.P., Mair, R.J. & Alderman, G.H. (1991). Long-term settlements over tunnels: an eleven-year study at Grimsby. In *Tunnelling '91*, 55–64, London.

Palmer, J.H.L. & Belshaw, D.J. (1980). Deformations and pore pressure in the vicinity of a precast segmented, concrete-lined tunnel in clay. *Can. Geotech. J.*, **17**, 174–184.

Peck, R.B. (1969). Deep excavations and tunnelling in soft ground. In *Proc.* 7th *Int. Conf. Soil Mech. Found. Engng.*, 345–352, Stockholm.

Perez Saiz, A., Garami, A., Arcones, A. & Soriano, A. (1981). Experience gained through tunnel instrumentation. In *Proc. 10th Int. Conf. Soil Mech. Found. Engng.*, 345–352, Stockholm.

Pestana, J.M. (1994). *A unified constitutive model for clays and sands*. Ph.D. thesis, Massachusetts Inst. Tech., Boston.

Potts, D.M. & Zdravkovic, L. (2001). *Finite element analysis in geotechnical engineering: application*. Thomas Telford.

Rankin, W.J. (1988). Ground movements resulting from urban tunnelling; prediction and effects. In *Conf. Engng. Geol. Undergrnd. Mvmts.*, 79–92, Nottingham.

Ratnam, S. (2002). *Development of a novel self-boring permeability measurement technique*. Ph.D. thesis, Cambridge Univ.

Shin, J.H., Addenbrooke, T.I. & Potts, D.M. (2002). A numerical study of the effect of ground water movement on long-term tunnel behaviour. *Géotechnique*, **52**, 391–403.

Shirlaw, J.N. (1995). Observed and calculated pore pressures and deformation induced by earth pressure balance shield. *Can. Geotech. J.*, **32**, 181–189.

Shirlaw, J.N., Doran, S. & Benjamin, B. (1988). *Engng. Geology of Underground Movements*, chap. A case study of two tunnels driven in the Singapore "Boulder Bed" and in grouted coral sands, 93–103. Geol. Soc. Engng.: Geol. Special Pub.

Simpson, B., Lance, G.A. & Wilkinson, W.B. (1987). Engineering implications of rising groundwater levels beneath London. In *Proc.* 9th *Eur. Conf. Soil Mech. Found. Engng.*, vol. 1, 331–336, Dublin.

Simpson, B., Atkinson, A.J. & Jovičić, V. (1996). The influence of anisotropy on calculations of ground settlements above tunnels. In Mair & Taylor, eds., *Proc. Int. Symp. Geotech. Asp. Undergnd. Constr. Soft Gnd.*, 591–594, Balkema, Rotterdam.

Skempton, A.W. (1961). Horizontal stresses in an overconsolidated Eocene clay. In *Proc.* 5th *Int. Conf. Soil Mech. Found. Engng.*, 351–357, Paris.

Skempton, A.W. & Henkel, D.J. (1957). Tests on London Clay from deep borings at Paddington, Victoria and the South Bank. In *Proc.* 4th *Int. Conf. Soil Mech. Found. Engng.*, vol. 1, 100–106.

Skempton, A.W., Schuster, R.L. & Petley, D.J. (1969). Joints and fissures in London Clay at Wraysbury and Edgware. *Géotechnique*, **19**, 205–217.

Soliman, E., Duddeck, H. & Ahrens, H. (1993). Two- and three-dimensional analysis of closely spaced double-tube tunnels. *Tun. Undergnd. Space Tech.*, **8**, 13–18.

Stajano, F., Hoult, N., Wassell, I., Bennett, P., Middleton, C. & Soga, K. (2010). Smart bridges, smart tunnels: Transforming wireless sensor networks from research prototypes into robust engineering infrastructure. *Ad Hoc Networks*, **8**, 872–888.

Standing, J.R. & Burland, J.B. (1999). Report on ground characterisation to explain tunnelling volume losses in the Westminster area. Internal report, Imperial Col. Sci. Tech. Med., London.

Standing, J.R. & Burland, J.B. (2005). Unexpected tunnelling volume losses in the Westminster area, London. *Géotechnique*, **56**, 11–26.

Tavenas, F., Jean, P., Leblond, P. & Leroueil, S. (1983). The permeability of natural soft clays. Part II: Permeability characteristics. *Can. Geotech. J.*, **20**, 645–660.

Taylor, R.N. (1995). Tunnelling in soft ground in the UK. In K. Fujita & O. Kusakabe, eds., *Proc. Int. Symp. Undergrnd. Constr. Soft Grnd.*, 123–126, Balkema, Rotterdam.

Terzaghi, K. (1942). Shield tunnels of the Chicago Subway. In *J. Boston Soc. Civ. Engrs.*, vol. 3, 163–210.

Terzaghi, K. & Peck, R.P. (1967). *Soil mechanics in engineering practice*. John Wiley & Sons, 2nd edn.

Vaughan, P.R. (1994). Assumption, prediction and reality in geotechnical engineering. *Géotechnique*, **44**, 573–603.

Vorster, T.E.B., Klar, A., Soga, K. & Mair, R.J. (2005). Estimating the effect of tunnelling on existing pipelines. *ASCE J. Geotech. Geoenviron. Engng.*, **131**, 1399–1410.

Ward, W.H. & Pender, M.J. (1981). Tunnelling in soft ground—general report. In *Proc.* 10th *Int. Conf. Soil Mech. Found. Engng.*, vol. 4, 261–275, Stockholm.

Ward, W.H. & Thomas, H.S.H. (1965). The development of earth loading and deformation in tunnel linings in London Clay. In *Proc.* 6th *Int. Conf. Soil Mech. Found. Engng.*, vol. 2, 432–436, Toronto.

Webb, P.A. & Orr, C. (1977). *Analytical methods in fine particle technology*. Micromeritics Instrument Corporation.

Wheeler, S.J. (1997). A rotational hardening elasto-plastic model for clays. In *Proc.* 14th *Int. Conf. Soil Mech. Found. Engng.*, vol. 1, 431–434, Hamburg.

Wongsaroj, J. (2005). *Three-dimensional finite element analysis of short and long-term ground response to open-face tunnelling in stiff clay*. Ph.D. thesis, Cambridge Univ.

Wright, P. (2004). The tunnels team and tunnel assessments. Tube Lines Presentation.

Yimsiri, S. (2001). *Pre-failure deformation characteristics of soils: anisotropy and soil fabric*. Ph.D. thesis, Cambridge Univ.

Zhang, X., Wu, K. & Yan, A. (2004). Carbonation property of hardened binder pastes containing super-pulverized blast-furnace slag. *Cem. & Conc. Comp.*, **26**, 371–374.